Lecture Notes in Civil Engineering

Baojiang Sun · Jinsheng Sun ·
Zhiyuan Wang · Litao Chen ·
Meiping Chen *Editors*

Proceedings of The Fourth International Technical Symposium on Deepwater Oil and Gas Engineering

Springer

Lecture Notes in Civil Engineering

Volume 246

Lecture Notes in Civil Engineering (LNCE) publishes the latest developments in Civil Engineering - quickly, informally and in top quality. Though original research reported in proceedings and post-proceedings represents the core of LNCE, edited volumes of exceptionally high quality and interest may also be considered for publication. Volumes published in LNCE embrace all aspects and subfields of, as well as new challenges in, Civil Engineering. Topics in the series include:

- Construction and Structural Mechanics
- Building Materials
- Concrete, Steel and Timber Structures
- Geotechnical Engineering
- Earthquake Engineering
- Coastal Engineering
- Ocean and Offshore Engineering; Ships and Floating Structures
- Hydraulics, Hydrology and Water Resources Engineering
- Environmental Engineering and Sustainability
- Structural Health and Monitoring
- Surveying and Geographical Information Systems
- Indoor Environments
- Transportation and Traffic
- Risk Analysis
- Safety and Security

To submit a proposal or request further information, please contact the appropriate Springer Editor:

- Pierpaolo Riva at pierpaolo.riva@springer.com (Europe and Americas);
- Swati Meherishi at swati.meherishi@springer.com (Asia - except China, and Australia, New Zealand);
- Wayne Hu at wayne.hu@springer.com (China).

All books in the series now indexed by Scopus and EI Compendex database!

More information about this series at https://link.springer.com/bookseries/15087

Baojiang Sun · Jinsheng Sun ·
Zhiyuan Wang · Litao Chen ·
Meiping Chen
Editors

Proceedings of The Fourth International Technical Symposium on Deepwater Oil and Gas Engineering

Springer

Editors
Baojiang Sun
School of Petroleum Engineering
China University of Petroleum
Qingdao, Shandong, China

Jinsheng Sun
School of Petroleum Engineering
China University of Petroleum
Qingdao, Shandong, China

Zhiyuan Wang
School of Petroleum Engineering
China University of Petroleum
Qingdao, Shandong, China

Litao Chen
School of Petroleum Engineering
China University of Petroleum
Qingdao, Shandong, China

Meiping Chen
Editorial Office of Journal
of Hydrodynamics
Shanghai, China

ISSN 2366-2557 ISSN 2366-2565 (electronic)
Lecture Notes in Civil Engineering
ISBN 978-981-19-0959-7 ISBN 978-981-19-0960-3 (eBook)
https://doi.org/10.1007/978-981-19-0960-3

Preface

Deepwater is rich in oil, gas and hydrate resources, where the exploitation is known as highly difficult with high risk, high investment and high return. As the exploration and development of deepwater oil, gas and hydrate resources grow, many special technical problems are encountered, and extensive attention from industry and academic is attracted.

In order to promote the exchange and cooperation between global scholars and promote the technological progress of deepwater oil, gas and hydrate development, the *International Technical Symposium on Deepwater Oil and Gas Engineering & the International Youth Forum on Gas Hydrate* (DWOG-Hyd) series conference was founded in 2017. The first three conferences were held in Haikou and Qingdao in China from 2017 to 2019, and more than seven hundred people participated. The participants were mainly technical experts and scholars from industries and universities in China, the USA, the UK, Russia, Norway, Singapore, Canada and other countries. The DWOG-Hyd conference has formed important international influence in the field of deepwater oil, gas and hydrate exploitation research.

The fourth DWOG-Hyd conference was held on December 20 to 21, 2021, onsite in Qingdao and online, hosted by China University of Petroleum (East China), CNPC Engineering Technology R&D Company Ltd, Journal of Hydrodynamics and other institutes. The DWOG-Hyd 2021 focused on cutting-edge areas such as natural gas hydrate drilling and production, carbon dioxide storage, deepwater drilling and completion, oil and gas flow assurance and emerging hydrate-based technologies. A total of more than two thousand person-times participated both onsite and online. Participants are from ten countries including China, the USA, the UK, Canada, Brazil, Norway and Singapore, etc. Seventeen plenary speeches and seventy-seven session speeches were presented. One hundred and twenty-seven abstracts/papers were received, and forty papers were selected to publish in the proceedings.

In this book, there are nine papers for deepwater drilling and completion, thirteen papers for natural gas hydrate production, nine papers for deepwater oil and gas flow assurance and nine papers for fundamentals and emerging technologies of clathrate hydrate. A large number of new findings and novel ideas were reported.

We wish the DWOG-Hyd conference and the proceedings to be helpful to accelerate the exploration and development of deepwater oil, gas and hydrate resources.

January 2022 The Editors

Organization

Conference Committee

Chairs

Jinsheng Sun	China University of Petroleum (East China), Qingdao, China
Jianliang Zhou	CNOOC, China
Baojiang Sun	China University of Petroleum (East China), Qingdao, China

Members (Alphabet Sequence)

Guangjin Chen	China University of Petroleum (Beijing), Beijing, China
Caili Dai	China University of Petroleum (East China), Qingdao, China
Jian Hou	China University of Petroleum (East China), Qingdao, China
Xutian Hou	SINOPEC RIPE, China
Fang Huang	China University of Petroleum (East China), Qingdao, China
Yan Jin	China University of Petroleum (Beijing), Beijing, China
Shuxia Li	China University of Petroleum (East China), Qingdao, China
Xiaosen Li	Guangzhou Institute of Energy Conversion, China
Zhong Li	CNOOC Research Institute Co., Ltd, China
Shujie Liu	CNOOC Hainan Branch, China
Yikun Liu	Northeast University of Petroleum, China
Baojin Ma	CNPC Offshore Engineering Company, China
Xuwen Qin	Guangzhou Marine Geology Survey, China

Yongchen Song	Dalian University of Technology, China
Hongshu Wei	CNOOC Shenzhen Branch, China
Nengyou Wu	Qingdao Institute of Marine Geology, China
Jianmin Yang	Shanghai Jiao Tong University, China
Yongfei Yang	China University of Petroleum (East China), Qingdao, China

Youth Forum on Gas Hydrate Committee

Chairs

Zhiyuan Wang	China University of Petroleum (East China), Qingdao, China
Litao Chen	China University of Petroleum (East China), Qingdao, China

Members (Alphabet Sequence)

Jianchao Cai	China University of Petroleum (Beijing), Beijing, China
Changyin Dong	China University of Petroleum (East China), Qingdao, China
Jingchun Feng	Guangdong University of Technology, China
Guangming Fu	China University of Petroleum (East China), Qingdao, China
Yonghai Gao	China University of Petroleum (East China), Qingdao, China
Wei Guo	Jilin University, China
Ke Ke	SINOPEC RIPE, China
Gang Li	Guangzhou Institute of Energy Conversion, China
Hangyu Li	China University of Petroleum (East China), Qingdao, China
Hao Li	China University of Petroleum (East China), Qingdao, China
Yanlong Li	Qingdao Institute of Marine Geology, China
Praveen Linga	National University of Singapore, Singapore
Changling Liu	Qingdao Institute of Marine Geology, China
Shuyang Liu	China University of Petroleum (East China), Qingdao, China
Cheng Lu	Guangzhou Marine Geology Survey, China
Fulong Ning	China University of Geosicence, Wuhan
Weixin Pang	CNOOC Research Institute Co., Ltd, China
Zhengfeng Shan	CNPC Offshore Engineering Company, China

Xianzhi Song	China University of Petroleum (Beijing), Beijing, China
Xiaohui Sun	China University of Petroleum (East China), Qingdao, China
Ren Wang	CNPC Engineering Technology Research Institute, China
Xuerui Wang	China University of Petroleum (East China), Qingdao, China
Na Wei	Southwest University of Petroleum, China
Hongzhi Xu	China University of Petroleum (East China), Qingdao, China
Yuqiang Xu	China University of Petroleum (East China), Qingdao, China
Bangtang Yin	China University of Petroleum (East China), Qingdao, China
Mingjun Yang	Dalian University of Technology, China
Jiafei Zhao	Dalian University of Technology, China

Scientific Committee

Chairs

Jinsheng Sun (Convener)	China University of Petroleum (East China), Qingdao, China
Shouwei Zhou	CNOOC, China
Deli Gao	China University of Petroleum (Beijing), Beijing, China
Yang Li	SINOPEC, China
Gensheng Li	China University of Petroleum (Beijing), Beijing, China
Youhong Sun	China University of Geosciences, China

Members (Alphabet Sequence)

Rashid Hasan	Texas A&M University, USA
Hon Chung Lau	Rice University, USA
Qingping Li	CNOOC Research Institute Co., Ltd, China
Tiantai Li	Xi'an Shiyou University, China
Baoping Lu	SINOPEC RIPE, China
Hailong Lu	Peking University, China
Tao Lu	COSL, China
Dongzheng Sun	CNOOC Shanghai Branch, China
Shengxiong Yang	Guangzhou Marine Geology Survey of CGS, China

Jun Yao	China University of Petroleum (East China), Qingdao, China
Jianliang Ye	Guangzhou Marine Geology Survey, China

Publication Committee

Chairs

Baojiang Sun	China University of Petroleum (East China), Qingdao, China
Jinsheng Sun	China University of Petroleum (East China), Qingdao, China
Zhiyuan Wang	China University of Petroleum (East China), Qingdao, China
Litao Chen	China University of Petroleum (East China), Qingdao, China
Meiping Chen	Editorial Office of Journal of Hydrodynamics, China

Contents

Deepwater Drilling and Completion

Prospects of Special Ocean Engineering Equipment Application in Chinese Marine NGH Trial Production

Ye Chen[1,2(✉)], Wang Yao[2,3], Yuan Yao[1], Qi Bian[1], Xu Chen[1], and Jiahui Wang[2,4]

[1] Offshore Oil Engineering Co., Ltd., Tianjin 300461, China
upcchenye@163.com
[2] Key Laboratory of Unconventional Oil and Gas Development, Ministry of Education, China University of Petroleum (East China), Qingdao 266580, China
[3] CNOOC Research Institute, Beijing 100029, China
[4] China Petroleum Materials Co. Ltd., Beijing 100029, China

Abstract. Natural gas hydrate (NGH) is a potential alternative clean energy. According to its formation conditions such as high pressure and low temperature, the geological survey results indicate that there are abundant NGH resources buried in both the sediments of the permafrost and ocean of China, leading to the great natural advantages for the mineral industrialization. Considering the determining factors such as resource distribution, trial production progress, as well as the gap between maximum daily production rate and commercial production critical value, it is believed that the deep water especially in South China Sea will be the main battlefield for the cause of Chinese NGH development in a short term, whose specific operations always depend on the ocean engineering equipment. Based on the characteristics of NGH occurrence and its phase transitions in the marine weakly cemented shallow layers, this research summarizes and analyzes the application status of special ocean engineering equipment, such as floating body and underwater devices, applied in NGH trial production projects, then points out the potential manufacturing prospects. After comparing the symbolic floating bodies, it is implied that our current independent construction technology can satisfy the requirements derived from NGH trial production water depth in South China Sea. Actually, some indicators may even exceed the critical demands. Since these symbolic floating bodies are generally high cost with expensive daily rental, the existing cases would be like using anti-aircraft guns to fight mosquitoes. Therefore, higher technology matching should be considered preferentially for cost control. The localization multi-phase separation equipment is relative laggard, while the global higher technical level is also unable to meet the demand of deep water NGH commercial production. The related technology and equipment are in urgent need of development. ROV has the basic ability of offshore NGH survey and underwater operation, but coming to the more complex tasks, it should be gradually improved for better job. The advanced deep water seabed mining vehicle can preliminarily perform well for solid fluidization, but more targeted design and special improvement should be made in combination with the NGH characteristics. Increasing marine NGH development efficiency

B. Sun et al. (Eds.): DWOG-Hyd 2021, LNCE 246, pp. 3–9, 2022.
https://doi.org/10.1007/978-981-19-0960-3_1

and maintaining safety on the basis of meeting the requirements of trial production and environmental protection are the key points to technology research and development for ocean engineering equipment in the next stage.

Keywords: Ocean engineering equipment · Chinese NGH resource · Marine trial production · Floating body · Underwater devices · Application prospects

1 Introduction

The global energy structure is shifting with the progress of technology, and the proportion of marine oil and gas in the total fossil energy consumption is increasing year by year. Besides the petroleum and shallow gas, natural gas hydrate is also one of these marine fuel resources, capturing large amounts of flammable gas in solid cages under high pressure and low temperature [1, 2].

Because of the characteristics such as huge reserve, wide distribution and high energy density, natural gas hydrate is gradually regarded as a new potential alternative energy resource with a bright future. According to the phase equilibrium conditions, it is believed that more than 30% surface of land and 70% surface of ocean can satisfy hydrate formation requirements. The existing geological survey results indicate that there are abundant NGH resources buried in both the sediments of the permafrost (like Qilian Mountain, Tibet Plateau and Great Khingan, etc.) and ocean (like South China Sea) of China, leading to the great natural advantages for the mineral industrialization. Extracting flammable gas from the hydrate reserved in the sediments is beneficial to improve the traditional energy structure and enhance the national energy strategic security.

The marine NGH trial production projects started much later but developed rapidly, especially in the recent years. On the one hand, it is said that the total amount of hydrate deposits in continental slopes under sea water is much larger than that reserved in permafrost. On the other hand, although there are only 5 marine NGH trial production cases up to now, the production efficiencies of them are generally better with higher maximum daily production rates. Therefore, the sea area will be the main battlefield for natural gas hydrate development in the future.

To extract the flammable gas out of the solid cages buried in the sedimentary layers, a series of development methods, such as depressurization, thermal stimulation, chemical inhibitor injection, solid fluidization and CO_2 replacement, are gradually proposed based on the NGH phase transition characteristics and sedimentary properties. All these methods have their own unique merits and limitations. In which, depressurization is found to be the most widely applied in the previous trial production cases due to its low cost, little demand and convenient operation, while solid fluidization is regarded as the most suitable method for the marine loose weak-cemented sedimentary layers.

The NGH commercial production threshold is still hard to reach so far depending on the current technology and development modes. High investment cost, low gas production capacity and numerous engineering accident risks are undoubtedly important reasons, and directly or indirectly determined by the ocean engineering equipment providing supports for nearly all the operations. This research summarizes and analyzes the application status of special ocean engineering equipment, such as floating body

and underwater devices, applied in NGH trial-production projects, then points out the potential development and manufacturing prospects.

2 Floating Body

2.1 Applications in Existed Marine NGH Trial Production Cases

Common floating bodies used in offshore oil and gas exploration and development include drilling vessels and platforms. Presently, Japan and China are the only two countries around the world that have carried out the few marine NGH trial production projects, in which drilling vessels named 'Chikyu', and 'HYSY708', as well as drilling platforms named 'Blue Whale I' and 'Blue Whale II' are the symbolic floating bodies picked up respectively [3–5].

'Chikyu' is the first ocean drilling vessel all over the world that uses riser for drilling, sponsored by Japanese government, owned by JAMSTEC and operated by CDEX. The vessel is 210 m long, 38 m wide and 16.2 m high with a capacity of 200 people and a full load displacement of 57500 tons. Equipped with six full rotary thrusters of 4200 kW, one bow thruster of 2550 kW, six main diesel generators of 5000 kW and two auxiliary generators of 2500 kW, the drilling vessel has a maximum range of 20000 nautical miles, a maximum speed of 12 knots, and the capable to position at 4.5 m wave height, 23 m/s wind speed and 1.5 throttle speed. In addition, with the assistance of a derrick of 70 m high and a hook load of 1250 tons, Chikyu can adopt 10000 m pipes for drilling, and its maximum working water depth is 2500 m, which can be further extended to 4000 m.

A main function of Chikyu is to sample the seabed soil. The laboratory onboard can conduct timely petrological, paleontological, geophysical and geochemical analyses of extracted core samples. The core samples can be kept at low temperature in the refrigerated store to transported back to land for further study. Considering these characteristics, Chikyu was chosen for application in the first marine NGH trial production project in 2013. The gas hydrate buried 1000 m water depth and 300 m below mudline was obtained by depressurization.

HYSY708 is the first survey vessel with a water depth of 3000 m all over the world that integrates multi functions such as drilling, offshore working and exploration, owned by CNOOC and operated by COSL. It is 105 m long, 23.4 m wide and 9.6 m high with a full load displacement of 11600 tons. As the survey vessel with the strongest comprehensive operation ability of the same type, HYSY708 can ensure safe navigation under Grade 9 sea conditions, storm and even hurricane. Under the design draft conditions, its navigational speed is up to 14.5 nautical miles, and lifting weight is up to 150 tons. Considering its maximum working water depth of 3000 m, maximum drilling depth of 600 m below mudline, maximum sampling length of 23.5 m under constant pressure and temperature, HYSY708 was chosen to extract hydrate resources in South China Sea by solid fluidization in 2017.

Blue Whale I and Blue Whale II are two similar drilling platforms of the same series, designed by CIMC RAFFLES and verified by DNV, specially constructed for marine NGH trial production projects in 2017 and 2020. Currently, they are the world's deepest semi-submersible drilling platforms, which can be used in 95% of the world's deepwater operations. They are 117 m long, 92.7 m wide, 118 m high, and weighs

42000 tons. Equipped with hydraulic twin rigs, closed loop power system and DP3 dynamic positioning system, the operation efficiency can be improved by 30%, the fuel consumption can be reduced by 10% and the offset accuracy can be controlled within 0.5 m even under the attack of hurricane and current. Their working water depth is up to 3658 m and drilling depth is up to 15250 m.

2.2 Technology and Development Directions

The exploration results show that most of hydrate resources in South China Sea are reserved in the shallow layers under deep water, such as the loose weakly-cemented sediments with a water depth of 800–1500 m and buried depth within 500 m. Compared with common near-shore exploration and development, deep water operations need to face more frequent and violent storms, waves and currents, as well as stronger impact and corrosion effects. In addition, the increase of water depth may enhance the bending moment strength, the influence of complex internal wave flow and the effect of offset oscillation on the subsea products such as subsea pipelines. Therefore, it also puts forward higher requirements for the size, weight, positioning accuracy and stability of the floating bodies.

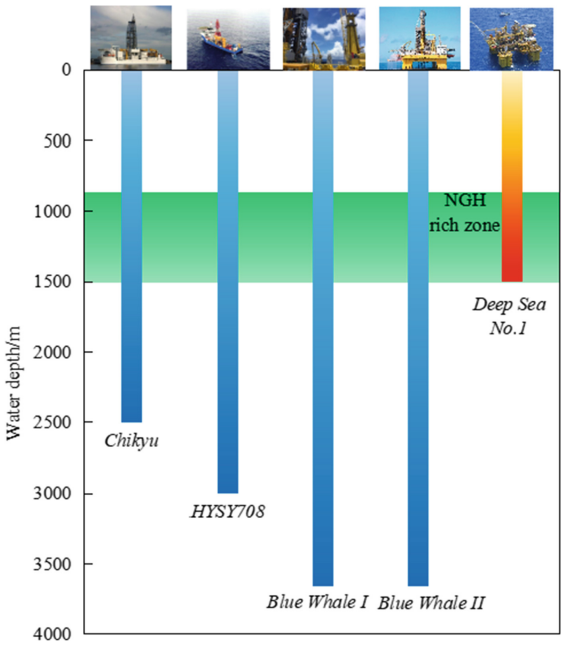

Fig. 1. Analysis of the representative floating bodies evaluated by water depth

Taking the water depth as the key reference criteria, the representative floating bodies including the ones mentioned above are evaluated through comparative analysis, as shown in Fig. 1. The results show that all of them, including Deep Sea No.1 (the world's

most advanced deep water semisubmersible production and storage platform), are competent for the demands derived from water depth of NGH drilling and production in South China Sea, indicating that the existing technology of deep water floating body technology can fully cope with the water depth challenges faced by NGH development projects in South China Sea. Some indicators may even exceed the critical demands.

The satisfaction of the technical indicator (water depth here) does not mean large-scale promotion for industrial application. More factors should be taken into consideration, for example, the total input costs. It is said that each floating body applied in marine NGH trial production cases costs hundreds of millions or even billions of dollars for construction, and the corresponding daily rental and employee fees are also expensive, resulting these cases would be like using anti-aircraft guns to fight mosquitoes. What's more, in order to alter the short-term trial production into long-term commercial production, suitable storage floating body should be selected based on these drilling floating bodies. In the follow-on process of design and construction, it is advised that higher technology matching NGH reservoir in South China Sea should be considered preferentially for cost control, and the floating body should be tailored for a better utilization.

3 Underwater Devices

Besides the large size ocean engineering equipment such as floating body, special process technology, like multi-phase separation, and certain under water devices, like remote operated vehicle and seabed mining vehicle, are also needed during marine NGH trial production. In which, the localization multi-phase separation equipment is relative laggard, while the global higher technical level is also unable to meet the demand of deep water NGH commercial production. So the related technology and equipment are in urgent need of improvement.

3.1 Remote Operated Vehicle

Remote operated vehicle (ROV) is a special underwater device used for monitoring subsea variations and executing operations. It can replace divers in hazardous, polluted and dim environments, breaking the original water depth limits and avoiding casualties. In marine NGH trial production, ROV can be applied for geology survey, core sampling and etc. [6].

'Haima' is one of the most advanced ROV which is independent-made by China. Certain key software and hardware technologies, including body structure, propeller, navigation system, heave compensator and multi-function manipulator, have been improved during the process of localization, as shown in Fig. 2. In 2014, several tests were carried out at the bottom of central basin in South China Sea, verifying that 'Haima' has the capability of underwater cable distribution, sediment sampling, subsea seismograph placement and other tasks. Since its maximum diving depth is 4502 m, much deeper than the marine gas hydrate buried positions, 'Haima' has been already used for NGH survey in South China Sea. Although the basic operations are already available, the ability of ROV to obtain more useful information and automate complex operations needs to be further enhanced with exploitation technology progress.

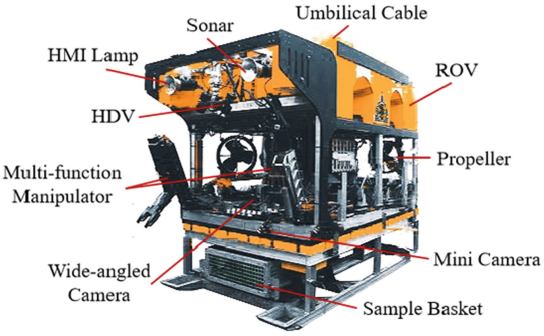

Fig. 2. Schematic diagram of core components of Chinese independent-made ROV 'Haima'

3.2 Seabed Mining Vehicle

Seabed mining vehicle is a special underwater device used for collecting subsea mineral resources in the shallow layers. Guided by ROV, it can migrate to target areas and break mineral into small blocks and pieces. As marine NGH partially distributed on the seabed surface or in the shallow layers, this underwater device can be adopted as a critical component for solid fluidization. Up to now, the domestic advanced deep water seabed mining vehicle can autonomous collect the subsea minerals with a maximum diving depth of 1305 m, while the world's advanced deep water seabed mining vehicles have more types and their diving depth is up to 1600 m or more, as shown in Fig. 3 [7].

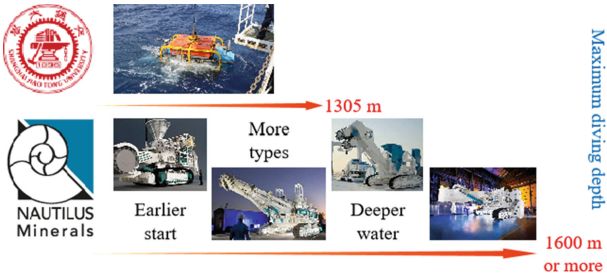

Fig. 3. Comparison of overseas and domestic advanced deep water seabed mining vehicles

After comparison, it can be seen that the existing deep-sea mining vehicles are basically capable of assisting and participating in NGH development in the South China Sea. However, targeted design and special improvement on seabed mining vehicle still need to be made in combination with the NGH characteristics, as well as the detailed process of solid fluidization.

4 Conclusions

(1) Chinese independent construction ability for floating body can satisfy the requirements of NGH trial production water depth in South China Sea now. In the follow-up works, higher technology matching should be considered preferentially for cost control.
(2) ROV and seabed mining vehicle has the primary ability of deepwater NGH survey, underwater operation and solid fluidization on seabed surface, but they should be further improved for better work.
(3) Increasing marine NGH development efficiency and ensuring safety are the key points to technology research and development for related marine devices.

Acknowledgement. The authors would like to appreciate the National Natural Science Foundation of China (No. 51876222).

References

1. Sloan, E.D., Koa, C.A.: Clathrate Hydrates of Natural Gases, 3rd edn. CRC Press, Boca Raton, FL (2007)
2. Rath, B.: Methane hydrates: an abundance of clean energy. MRS Bull. **33**(4), 323–325 (2008)
3. Kubo, Y., Mizuguchi, Y., Inagaki, F., et al.: A new hybrid pressure-coring system for the drilling vessel Chikyu. Sci. Drill. **17**, 37–43 (2014)
4. Zhou, S., Chen, W., Li, Q.P., et al.: Research on the solid fluidization well testing and production for shallow non-diagenetic NGH in deep water area. China Offshore Oil Gas **29**(4), 1–8 (2017)
5. Ye, J.L., Qin, X.W., Xie, W.W., et al.: Main progress of the 2nd gas hydrate trial production in South China Sea. Geology China **47**(3), 557–568 (2020)
6. Shen, K., Yan, Y., Yan, H.W.: Research status and development trend of deep-sea work class ROV in China. Control Inf. Technol. **3**, 1–7 (2019)
7. Fu, Q., Wang, G.R., Zhou, S.W., et al.: Development of marine NGH mining technology and equipment. Strat. Study CAE **22**(6), 32–39 (2020)

Analysis of Influence of Hydrate Decomposition on Underwater Wellhead Stability

Yang Li, Yuanfang Cheng(✉), Chuanliang Yan, Zhiyuan Wang, Yudan Peng, and Xiangfu Shan

School of Petroleum Engineering, China University of Petroleum (East China), Qingdao 266580, China
yfcheng@126.com

Abstract. During deep-water drilling, it is easy to encounter hydrate interlayers. Due to engineering disturbances, hydrates may decompose and cause the formation strength to decrease, which will cause the formation settlement and the wellhead instability. In this paper, based on the ABAQUS finite element platform, a wellhead stability calculation model for deep-water drilling encounter hydrate formations is established, and the influence of hydrate decomposition and drilling time on wellhead stability is analyzed. The research results show that the circulation of high-temperature drilling fluid in the annulus will change the formation temperature distribution. The top formation will heat slowly due to its low temperature and the cooling effect of seawater. The middle formation is greatly affected by the drilling fluid, and the lower undrilled stratum remains unchanged because it has not been disturbed by the engineering. The increase in formation temperature will cause the decomposition of hydrates, leading to a decrease in the elastic properties and strength of the near-well formation. The formation with weakened mechanical properties will produce secondary compression and consolidation, and secondary stress concentration will be formed in the hydrate saturation transition zone. This is the essential reason for the effect of hydrate decomposition on the vertical stability of the formation and wellhead. As the drilling time increases, the hydrate decomposition range increases, the bearing capacity of the formation in a larger area decreases, and the risk of underwater wellhead instability increases. However, since the hydrate decomposition area is located below the underwater wellhead at the initial moment, it will have a more serious impact on the stability of the underwater wellhead. The research in the thesis can provide a theoretical basis for the maintenance of wellhead stability in deep-water drilling.

Keywords: Deep-water drilling · Wellhead subsidence · Natural gas hydrate

1 Introduction

Natural gas hydrate is a clathrate crystal compound formed by methane molecules and water molecules under the conditions of low ambient temperature and high pore pressure. Natural gas hydrates are widely present in the shallow strata of the deep sea. During deep-water drilling, a large number of hydrate interlayers may be encountered [1]. Due

B. Sun et al. (Eds.): DWOG-Hyd 2021, LNCE 246, pp. 10–18, 2022.
https://doi.org/10.1007/978-981-19-0960-3_2

to engineering disturbances, the temperature field, pressure field and chemical field of the hydrate formation will change, leading to the decomposition of hydrate [2]. As the hydrate formation is usually shallow, the sediments are in a weakly consolidated state, and the hydrate molecules will act as a framework in the pores of the soil [3]. The decomposition of hydrate will cause the formation strength to decrease, and the soil will be compressed due to secondary compaction, which will lead to the settlement of the underwater wellhead, and even the instability of the underwater wellhead in severe cases [4].

2 Numerical Model of Effect of Hydrate Decomposition on Underwater Wellhead Stability

According to logging data from the South China Sea, natural gas hydrates are mainly found in the formation at a depth of about 200 m from the mudline, with a thickness of 25 m. Therefore, a two-dimensional axisymmetric deep-water drilling underwater wellhead stability numerical model can be established as shown in Fig. 1. The whole model can be divided into four parts, overlying strata, hydrate strata, underlying strata, and casing. The whole model can be divided into four parts, overlying strata, hydrate strata, underlying strata, and casing. The outer diameter of the strata is 200 m, of which the thickness of the overlying strata is 195 m. The thickness of the hydrate layer is 25 m, the initial saturation is 0.45, and a 2 m thick hydrate transition zone is set in the upper and lower sections of the hydrate layer. The thickness of the underlying strata is 195 m. The size of the surface conduit is $30''$, the wall thickness is $1''$, and the diameter of the wellbore in hydrate formation is $26''$. The casing only seals the overlying formation, that is, there is no seepage effect between the drilling fluid and the overlying formation, but only heat transfer. Gravity load, initial in-situ stress field, initial temperature field and initial pore pressure field varying with depth are applied to the entire model. The initial hydrate saturation field is applied to the hydrate layer. The upper boundary of the model imposes pore pressure boundary equal to the hydrostatic column pressure of seawater and temperature boundary equal to the temperature of the seabed mudline. The lower boundary of the model imposes fixed pore pressure boundary, temperature boundary and Y-direction displacement constraints. X-direction displacement constraint is imposed on the right boundary of the model; A fixed load is applied to the top of the casing, which is equal to the floating weight of the underwater wellhead, blowout preventer (BOP) and riser. The borehole section of the hydrate layer imposes drilling fluid column pressure load, pore pressure boundary and temperature boundary. The calculation of the entire model is divided into two analysis steps. Step 1 is the in-situ stress balance, and the step 2 is the analysis of the stability of the underwater wellhead during the drilling process. The selected drilling method is balance drilling with high-temperature drilling fluid. The parameters used in model calculation are shown in Table 1.

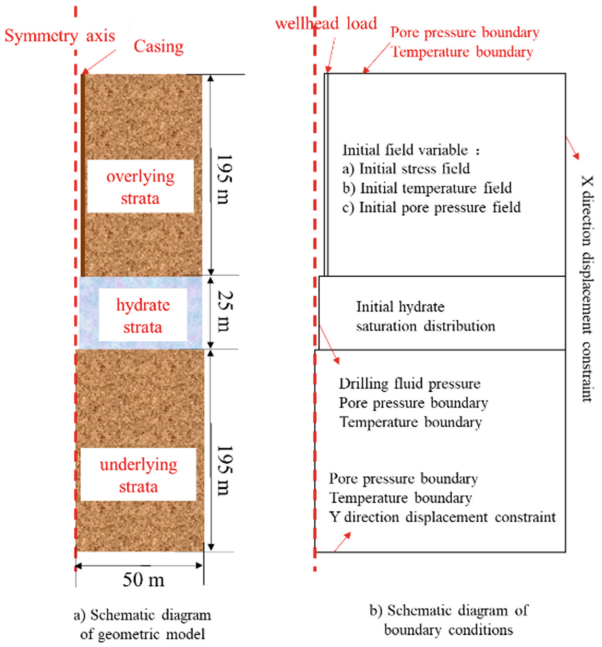

Fig. 1. Schematic diagram of the numerical model for the subsea wellhead stability in the case of penetrating hydrate-bearing sediments

3 Evolution of Underwater Wellhead Stability with Drilling Time

Figure 2 shows the formation temperature distribution of different drilling fluid soaking time. It can be seen that the circulation of high-temperature drilling fluid in the annulus will seriously change the temperature distribution of the formation, and the area near borehole will be heated due to the soaking of the drilling fluid. The top formation will heat slowly due to its low temperature and the cooling effect of seawater. The middle formation is greatly affected by the drilling fluid, and the lower undrilled stratum remains unchanged because it has not been disturbed by the engineering. For example, after the borehole is drilled for 6 h, the borehole temperature at 0.65 m formation depth is 24.8 °C, the hydrate layer borehole temperature is 30 °C, and the bottom formation remains the same as the initial temperature of 24.6 °C. At the same time, it can be seen that as the drilling time increases, the formation heated by the drilling fluid gradually increases. For example, after 6 h of drilling, the range of 220 m depth affected by drilling fluid temperature is 0.52 m, and after 24 h, this range reaches 1.04764 m. Due to the heating effect of the drilling fluid, the hydrate in the pores gradually decomposes. With the increase of the influence range of the drilling fluid temperature, the hydrate decomposition range gradually increases, as shown in Fig. 3. After 6 h of drilling, the decomposition front in the middle of the hydrate layer was 0.2264 m, or 0.68 times the radius of the borehole; after 12 h of drilling, the hydrate decomposition front advanced to 0.3067 m, which was 0.93 times the radius of the borehole.

The decomposition of hydrate will cause the formation elastic properties and strength to decrease, and the formation will be consolidated by secondary compression. Figure 4 shows the vertical deformation distribution of the hydrate layer at different drilling times. It can be seen that in hydrate decomposition area, the upper strata is deformed downwards, and the lower strata are deformed upwards. The deformation of the upper strata is higher than that of the lower strata, such as after drilling for 12 h, the deformation of the upper strata is 0.03816 m, and the compression of the lower strata is 0.01798 m. The former is 2.12 times that of the latter. This is because the upper strata not only bears the in-situ stress, but also bears the load caused by the settlement of the casing and the underwater wellhead.

Figure 5 and Fig. 6 show the mises stress distribution on the top and bottom layers of the hydrate. The formation around the borehole wall has a decrease in stress due to weakening of elastic parameters and plastic deformation. It can be seen that the upper stratum has a larger stress drop area than the lower stratum, and the maximum mises stress value of the stratum at the same time is higher, such as after 12 h of drilling, the maximum Mises stress in the upper strata is 9.67 MPa, and the lower strata is 7.13 MPa. As the drilling time increases, the location of the maximum Mise stress gradually develops toward the far well. The softening and compression of the hydrate formation caused by the decomposition of hydrate will aggravate the settlement of the underwater wellhead. Figure 7 shows the distribution cloud diagram of underwater wellhead settlement under different drilling time. It can be seen that the initial stage of hydrate decomposition has a greater impact on the underwater wellhead settlement. Such as at initial 6 h, the underwater wellhead has a settlement of 0.1365 m, while the subsea wellhead subsidence increased by 0.028 m from 6 h to 12 h, and the subsidence only increased by 0.0149 m from 12 h to 24 h. This is because, on the one hand, with the increase of drilling time, the development of the influence range of drilling fluid temperature and the range of hydrate decomposition gradually decreases. On the other hand, the initial decomposed hydrate formation is located under the casing, it has a more direct impact on the settlement of the underwater wellhead.

Therefore, when deep-water drilling encounters a hydrate layer, the decomposition of the hydrate will cause the softening of the hydrate layer and aggravate the settlement of the underwater wellhead. In the early stage of drilling fluid immersion, the hydrate decomposition front advances faster, which has a greater impact on the settlement of the underwater wellhead. As the immersion time increases, the advancing speed of the hydrate decomposition front decreases, and the subsidence speed of the underwater wellhead gradually decreases.

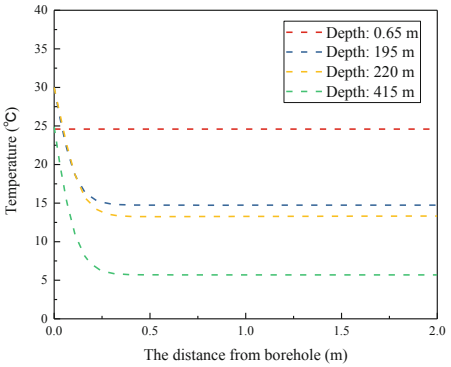

a) drilling time: 6 h

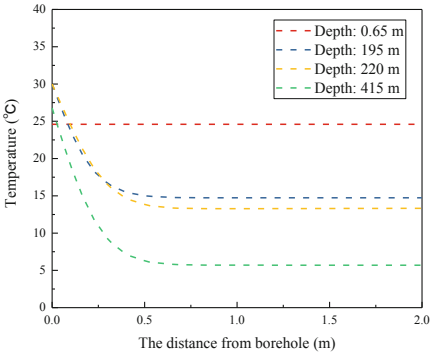

b) drilling time: 24 h

Fig. 2. Formation temperature vs. distance to the borehole wall, in cases of varied soaking time in drilling fluids

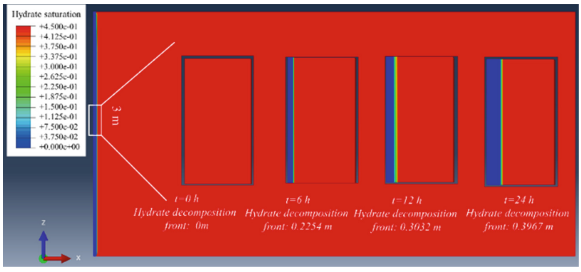

Fig. 3. Hydrate saturation vs. soaking time in drilling fluids

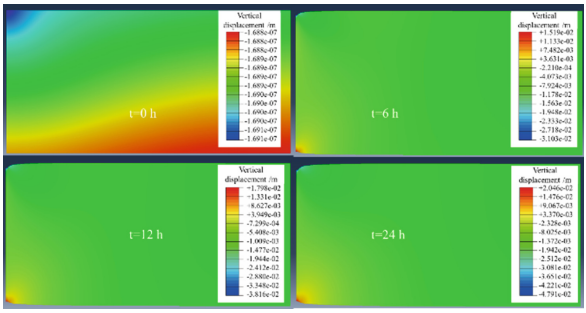

Fig. 4. Lateral deformation of the hydrate-bearing sediment vs. soaking time in drilling fluids (magnified by 30 times)

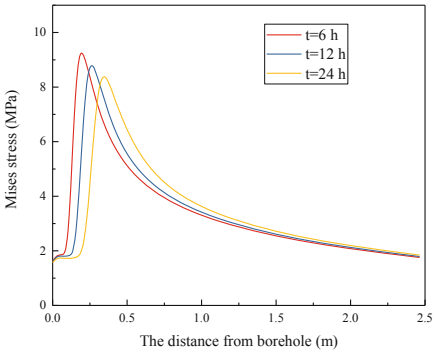

Fig. 5. Mises stress distribution of the upper formation

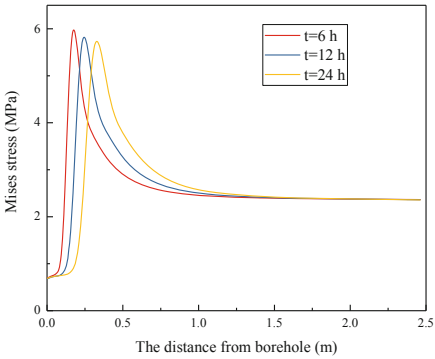

Fig. 6. Mises stress distribution of the lower formation

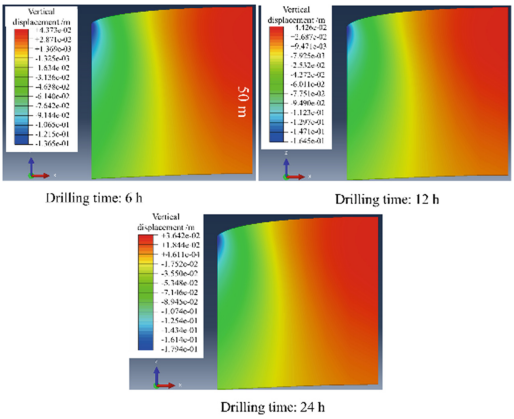

Fig. 7. Subsea wellhead subsidence vs. soaking time in drilling fluids

Table 1. Materials used in the experiments

Parameter	Value
Water depth	1300 m
Water density	1000 kg/m^3
Mudline temperature	5.67 °C
Geothermal gradient	0.0456 °C/m
Stratum density	2200 kg/m^3
Hydrate density	910 kg/m^3
Initial porosity	42.46%
Water thermal conductivity	0.6 W/m/°C
Water specific heat	4.2 kJ/kg/°C
CH_4 thermal conductivity	0.00335 W/m/°C
CH_4 specific heat	2.093 kJ/kg/°C
Hydrate thermal conductivity	0.4 W/m/°C
Hydrate specific heat	2.1 kJ/kg/°C
Formation thermal conductivity	1.5 W/m/°C
Formation specific heat	1.5 W/m/°C
Initial permeability	1 mD
Initial sediment elastic modulus	35.414 MPa
Sediment elastic modulus (S_h:0.45)	267.32 MPa
Initial sediment cohesion	0.1 MPa

(*continued*)

Table 1. (*continued*)

Parameter	Value
Sediment cohesion (S_h:0.45)	0.674 MPa
Sediment internal friction angle	30°
Sediment Poisson's ratio	0.4
Drilling fluid density	1000 kg/m^3
Drilling fluid temperature	21.25 °C
Casing elastic modulus	206.8 GPa
Casing Poisson's ratio	0.25

4 Conclusion

1. The circulation of high-temperature drilling fluid in the annulus will change the formation temperature distribution. The top formation will heat slowly due to its low temperature and the cooling effect of seawater. The middle formation is greatly affected by the drilling fluid, and the lower undrilled stratum remains unchanged because it has not been disturbed by the engineering.
2. The increase in formation temperature will cause the decomposition of hydrates, leading to a decrease in the elastic properties and strength of the near-well formation. The formation with weakened mechanical properties will produce secondary compression and consolidation, and secondary stress concentration will be formed in the hydrate saturation transition zone. This is the essential reason for the effect of hydrate decomposition on the vertical stability of the formation and wellhead.
3. As the drilling time increases, the hydrate decomposition range increases, the bearing capacity of the formation in a larger area decreases, and the risk of underwater wellhead instability increases. However, since the hydrate decomposition area is located below the underwater wellhead at the initial moment, it will have a more serious impact on the stability of the underwater wellhead.

Acknowledgement. This work is supported by the Shandong Provincial Natural Science Foundation of China (No. ZR2019ZD14), the National Natural Science Foundation of China (No. 51974353, No. 51991362), the CNPC Major Science and Technology Project (No. ZD2019-184-003).

References

1. Moridis, G.J.: Numerical studies of gas production from methane hydrates. SPE J. **8**(04), 359–370 (2003)
2. Nazridoust, K., Ahmadi, G.: Computational modeling of methane hydrate dissociation in a sandstone core. Chem. Eng. Sci. **62**(22), 6155–6177 (2007)

3. Katagiri, J., Konno, Y., Yoneda, J., et al.: Pore-scale modeling of flow in particle packs containing grain-coating and pore-filling hydrates: verification of a Kozeny-Carman-based permeability reduction model. J. Nat. Gas Sci. Eng. **45**, 537–551 (2017)
4. Liu, Y., Gamwo, I.K.: Comparison between equilibrium and kinetic models for methane hydrate dissociation. Chem. Eng. Sci. **69**(1), 193–200 (2012)
5. Li, Y., Cheng, Y., Yan, C., et al.: Mechanical study on the wellbore stability of horizontal wells in natural gas hydrate reservoirs. J. Nat. Gas Sci. Eng. **79**, 103359 (2020)

Study on Collapse Strength of Sand Control Screen Pipe with Corrosion Defect Under External Pressure

Yudan Peng[1], Baojiang Sun[1](✉), Guangming Fu[1], Xiaoyu Chen[1], Jingbo Wang[2], Mingliang Li[1], and Yuhang Tuo[1]

[1] School of Petroleum Engineering, China University of Petroleum (East China), Qingdao, Shandong, China
sunbj1128@vip.126.com

[2] Dongying Ruifeng Petroleum Technology Development Co. Ltd., Dongying, China

Abstract. At present, there are few reports on the collapse strength of screen pipe with corrosion defects under external pressure. In this paper, based on ABAQUS finite element software, a parallel screen pipe finite element model with corrosion defect under external pressure is established, and the influence of corrosion defect parameters and perforation parameters on the collapse strength of the screen pipe with corrosion defect is analyzed. The analysis results show that with the corrosion defect close to the middle of the screen pipe, the smaller the collapse strength of corrosive screen tube is; With the increase of corrosion depth and length, the collapse strength of screen pipe with corrosion defects gradually decreases, and the corrosion depth has the greatest influence on the collapse strength of screen pipe. With the change of corrosion parameters, such as corrosion length, corrosion width and corrosion depth, the deformation form of corrosion screen pipe will change. With the increase of hole size, number of circumferential holes and number of axial holes, the collapse strength of corrosive screen pipe decreases gradually. Among them, the hole size and the number of axial holes have great influence on the collapse strength of corroded screen pipe. The results of this study can provide reference for strength evaluation and life prediction of corroded screen pipes.

Keywords: Corrosion defect · Screen pipe · Hole arrangement parameter · Collapse strength · Finite element method

1 Introduction

In the development of unconsolidated sand reservoirs, the reservoir is characterised by loose cementation and low compaction, which lead to sand production from the reservoir. Reservoir sand production lead to equipment erosion, tubing sand burial and casing deformation and well wall collapsing, which can seriously affect the normal production of oil and gas wells, and it is one of the major constraints on the development of reservoirs [1, 2].

Sand control Screen pipe is an important equipment to prevent sand from entering the wellbore in large quantities. However, screen pipe in the formation is subjected to

B. Sun et al. (Eds.): DWOG-Hyd 2021, LNCE 246, pp. 19–31, 2022.
https://doi.org/10.1007/978-981-19-0960-3_3

long-term corrosion by acidic fluids such as CO_2 and H_2S in oil and gas, causing local or overall corrosion defects of screen pipe, which significantly reduce the collapsing strength of the screen pipe and increasing the risk of collapsing deformation of the screen pipe, seriously threatening the safety of sand control in oil and gas wells. At present, a great deal of research has been carried out by scholars on the collapsing strength of screen pipes without corrosion defects and on the collapsing strength of intact pipes with corrosion defects. Sun Baojiang et al. [3] established a finite element model of the screen pipe using the finite element method, analyzed the change law of the screen pipe collapsing strength under external pressure with the different hole parameter, and proposed a simplified formula for calculating the collapsing strength of the screen pipe. Peng Yudan et al. [4] established finite element models of screen pipe with different hole arrangement under external pressure with ABAQUS software and analyzed the effects of different hole arrangement on the collapsing strength of the screen tubes. Guangming Fu et al. [5] established the finite element model of the screen pipe under external pressure and bending with the FEM, analyzed influence law of bending load on the collapsing strength of the screen pipe, and proposed the formula for calculating the collapsing strength of the screen pipe under bending and external pressure load. Beltran K et al. [6] analysed the variation of the collapsing strength of parallel perforated screen tubes with different perforation parameters by experimental and finite element methods. Guo et al. [7] analysed the effect law of secondary perforation parameters on the collapsing strength of the perforating casing with the FEM. Zhu Xiaohua et al. [8] established a finite element model of casing with corrosion defects based on ANSYS analysis software and analyzed the effects of the depth of ellipsoidal defects, the length of the short axis of the ellipse and the width of penetrating defects on the strength resistance of the casing. Zhang Zhi et al. [9] established a finite element model for casing strength under different corrosion shapes and analyzed the effects of temperature and internal pressure as well as corrosion defect parameters on the equivalent stress and residual strength of corroded casing. Yang Hui and Cao Xuewen [11, 12] established finite element models for pipelines with single and double corrosion defects using the finite element method, respectively, and analyzed the influence of corrosion defect parameters on the residual strength of the pipeline.

However, little research has been reported on the collapsing strength of screen pipe with corrosion defects under external pressure, which causes problems in the evaluation of the strength of screen pipe with corrosion defects. This paper establish a finite element model of a screen tube with corrosion defects under external pressure with ABAQUS, to analyse the influence of corrosion defect parameters and hole arrangement parameters on the strength of screen tubes under external pressure, and to provide reference for the strength evaluation and life prediction of screen pipe with corrosion defects.

2 Finite Element Model Established

2.1 Assumptions

It is assumed that the corrosion defect in the screen pipe is a single volumetric defect,the screen pipe without elliptical and eccentric defects and the screen pipe with parallel hole arrangement. 1/2 FEM for the corrosion screen pipe is adopted to simplify calculations

as the corrosion screen pipe is a symmetric model. And the established corrosion screen pipe model and corrosion defect parameters are shown in Fig. 1. C3D20R element is adopted in meshing process, which can still obtain accuracy of stress and displacement with the large deformation of the mesh [13]; The mesh sensitivity analysis shows that the collapsing strength of corrosive screen can be accurately predicted when the mesh size of the model is about 20 000. The length of screen pipe is adopted more than 8 times the screen pipe diameter to reduce the influence of end effect on the accuracy of solving the collapsing strength of screen pipe.

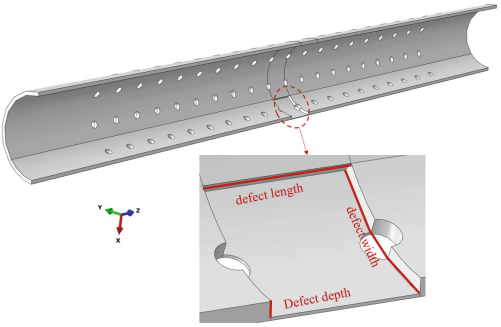

Fig. 1. Finite element model of screen pipe with corrosion defects.

2.2 Loads and Boundary Conditions

Uniform external pressure is applied to the outer surface of the screen pipe. The boundary conditions of the FEM of the screen pipe with corrosion defects are shown in Fig. 2, where the displacements in the x, y and z directions are constrained at the two end faces of the screen pipe; Applying a symmetry constraint on the symmetry plane about the Y direction – YSYMM. Risk method is adopted for solving the collapsing strength of corrosion screen pipe.

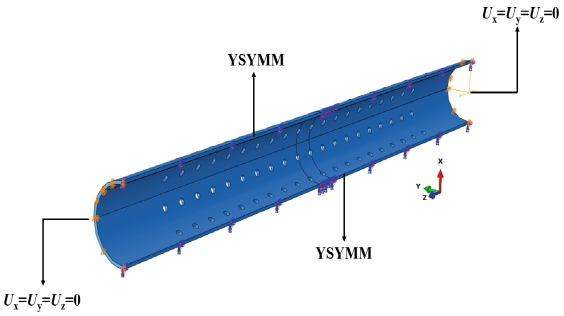

Fig. 2. Boundary conditions of finite element and corrosion defect parameters model of screen pipe

2.3 Material Parameters of Screen Pipe

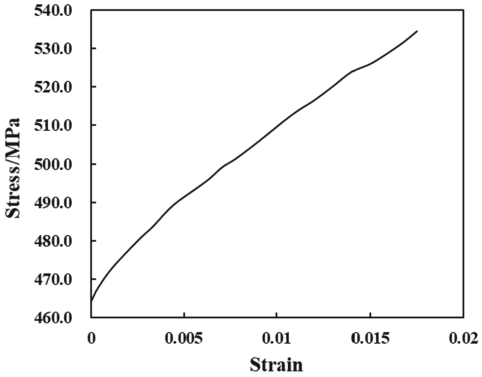

Fig. 3. Stress-strain curve of material in plastic stage

The steel grade of corrosion screen pipe is N80, the elastic modulus is 203384 MPa, the plastic strength is 464.36 MPa, and the Poisson's ratio is 0.3. The stress-strain curve of screen pipe material in plastic stage is shown in Fig. 3; It is assumed that the screen pipe material parameter property is isotropic.

3 FEM Results

The LPF curve of screen pipe with corrosion defects under external pressure is shown in Fig. 4. The stress on the screen pipe increases with increasing arc length (load) as shown in Fig. 4, and stress concentrations occur near corrosion defects and hole of the screen pipe. When the external pressure load increases to the ultimate load-bearing capacity of the screen pipe, the deformation form and stress distribution of the screen pipe are shown in Fig. 4. As the load continues to increase, the screen pipe becomes extruded from the middle and gradually expands toward pipe ends.

4 Parametric Analysis

Based on the established finite element model of screen pipe with corrosion defects, the influence of corrosion defect parameters and hole arrangement parameters on the collapsing strength of corrosion screen pipe was analyzed. The parameters of the screen pipe with corrosion analyzed in this paper are shown in Table 1.

4.1 The Influence of Corrosion Defects Location on Collapsing Strength of Screen Pipe

The selected screen pipe corrosion defect parameters are as follows: the depth of corrosion defect is 2.15 mm; The length of defect is 52.60 mm; The circumferential length

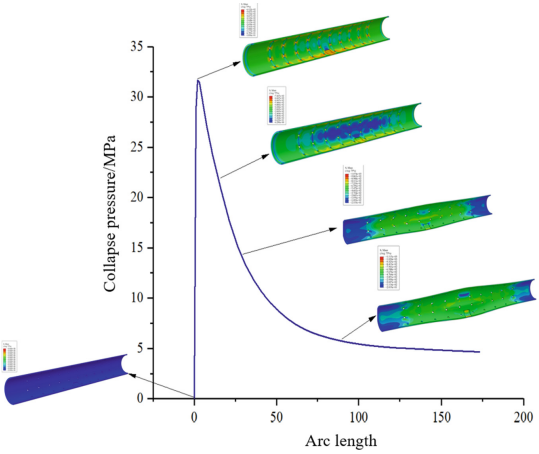

Fig. 4. LPF Curve of Screen pipe with Corrosion under external pressure

Table 1. Parameters of the screen pipe with corrosion defect

Length /mm	*D* /mm	*t* /mm	Defect location /mm	Defect Length /mm	defect width /°	defect depth /mm	d /mm	Number of axial holes	Number of circumferential holes
1400	152.60	6.46	0 73.7 147.4 173.7 200.0 673.7	0 52.6 125 250 375 500 625 750	0 30 60 90 120 150 180	0 t/6 2t/6 3t/6 4t/6 5t/6	6.35 9.5 12.7 14 16	10 14 18 20 22 26	6 8 10 12 14 16

of corrosion defect is 90.0°; The diameter of sieve hole is 12.70 mm; The number of axial holes is 20 and the number of circumferential holes is 8. The schematic diagram of corrosion defect location is shown in Fig. 5. Calculate the collapsing strength of corrosion screen pipe when the corrosion defect locations are 0 mm, 73.7 mm, 147.4 mm, 173.7 mm, 200.0 mm and 673.7 mm respectively, and the results are shown in Fig. 6. It can be seen from Fig. 6 that the location of corrosion defects has an impact on the collapsing strength of the corrosion screen pipe, and the closer the location of corrosion defects is to the middle of the screen pipe, the lower the collapsing strength of the screen pipe. When the corrosion defect is located in the middle of the screen tube (the defect location is 673.70 mm), the collapsing strength of the screen pipe is reduced by or 7.99% (2.54MPa) compared to the end of the screen pipe where the corrosion defect is located.

4.2 The Influence of Corrosion Defect Depth on the Collapsing Strength of Screen Pipe

It can be seen from the above research that when the corrosion defect is located in the middle of the screen pipe, the collapsing strength of the corrosion screen pipe is the smallest. Therefore, the corrosion defect was chosen to be located in the middle of the screen pipe to analyse the effect of the corrosion defect parameters on the collapsing strength of the screen pipe. The selected screen pipe corrosion defect parameters are as follows: The length of defect is 52.60 mm; The circumferential length of corrosion defect is 90.0°; The diameter of sieve hole is 12.70 mm; The number of axial holes is 20 and the number of circumferential holes is 8. Calculate the collapsing strength of corrosion screen pipe when the depth of corrosion defect are 0, 1.08 mm(1/6t), 2.15 mm(2/6t), 3.23 mm(3/6t), 4.31 mm(4/6t), 5.38 mm(5/6t) respectively, and the results are shown in Fig. 7. As can be seen from Fig. 7, the depth of corrosion defects has a large influence on the collapsing strength of the screen pipe, and the deeper the depth of corrosion defects, the lower the collapsing strength of screen pipe. When the corrosion defect depth is less than 1/2t, the screen pipe collapsing strength reduction degree is small; when the corrosion defect depth is more than 1/2t, the screen pipe collapsing strength reduction is significant. When the corrosion defect depth was increased from 0.00 mm to 5.38 mm (5/6 t), the collapsing strength of the screen pipe decreased by 19.80 MPa, which was 62.10% reduction in collapsing strength compared to a screen pipe with a corrosion depth of 0 mm. In addition, the corrosion defect depth affect the screen tube collapsing form. When the corrosion defect depth is less than 1/2t, collapsing deformation occurs from the middle of the screen pipe and gradually expand to the two ends as shown in Fig. 8(a). When the corrosion defect depth is more 1/2t, local extrusion deformation occurs first from the corrosion defect location, and then expand to both ends, as shown in Fig. 8(b).

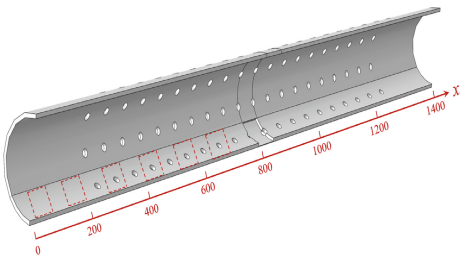

Fig. 5. Defect location of screen pipe

4.3 The Influence of Corrosion Defect Width on the Collapsing Strength of Screen Pipe

Assuming that the corrosion defect is in the middle of the screen pipe; The selected screen pipe corrosion defect parameters are as follows: The length of defect is 52.60 mm; The depth of corrosion defect is 2.15 mm(1/3t); The diameter of sieve hole is 12.70 mm; The

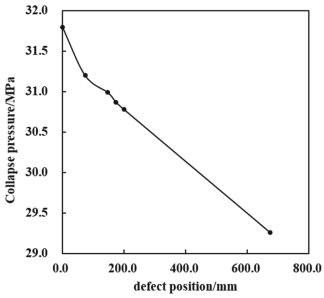

Fig. 6. The influence of corrosion defects location on collapsing strength of screen pipe

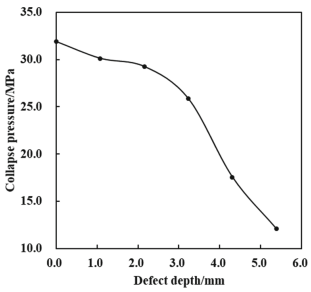

Fig.7. The influence of corrosion defect depth on the collapsing strength of screen pipe

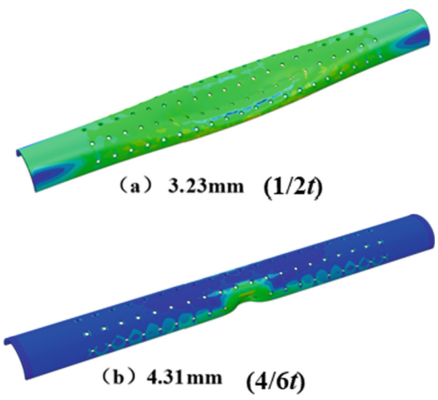

Fig. 8. Deformation patterns of screen pipe with different corrosion depths

number of axial holes is 20 and the number of circumferential holes is 8. Calculating the collapsing strength of corrosion screen pipe when the corrosion defect width are 0.0°, 30.0°, 60.0°, 90.0°, 120.0°, 150.0°, 180.0° respectively, and the results are shown in Fig. 9. As can be seen from Fig. 9, the corrosion defect width has little effect on the collapsing strength of the screen pipe, and when the defect width of the corrosion defect increases from 30.0° to 180.0°, the difference in collapsing strength of the screen pipe is only 0.65 MPa. In addition, the corrosion defect width affect the screen pipe collapsing form. When the corrosion defect width is less than 120°, collapsing deformation occurs from the middle of the screen pipe and gradually expand to the two ends as shown in Fig. 10(a). When the corrosion defect depth is more 120°, local extrusion deformation occurs first from the corrosion defect location, and then expand to both ends, as shown in Fig. 10(b).

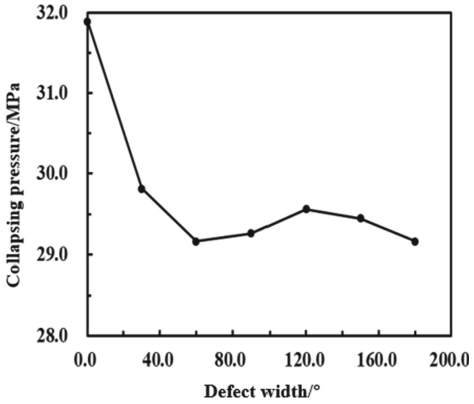

Fig. 9. The influence of corrosion defect width on the collapsing strength of screen pipe

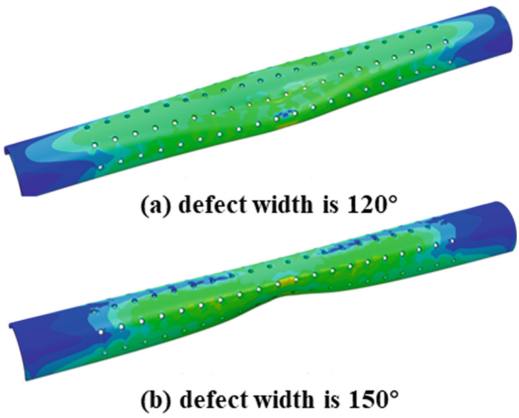

Fig. 10. Deformation patterns of screen pipe with different corrosion width

4.4 The Influence of Corrosion Defect Length on the Collapsing Strength of Screen Pipe

Assuming that the corrosion defect is in the middle of the screen pipe; The selected screen pipe corrosion defect parameters are as follows: The depth of corrosion defect is 2.15 mm(1/3*t*); The diameter of hole is 12.70 mm; The number of axial holes is 20 and the number of circumferential holes is 8. Calculating the collapsing strength of corrosion screen pipe when the corrosion defect length are 0.0 mm, 52.60 mm, 125.00 mm, 250.00 mm, 375.00 mm, 500.00 mm, 625.00 mm, 750.00 mm respectively, and the results are shown in Fig. 11.As can be seen from Fig. 11, the corrosion length has a greater effect on the collapsing strength of the screen pipe. With the increase in the length of corrosion defects, the lower the collapsing strength of the screen pipe. When the length of the corrosion defect increases from 0 to 750.00 mm, the collapsing strength of the screen pipe decreases by 12.82 MPa, which is 40.21% lower than the collapsing strength of the screen pipe without corrosion defects. When the corrosion defect length is less than 52.6 mm, collapsing deformation occurs from the middle of the screen pipe and gradually expand to the two ends as shown in Fig. 12(a). When the corrosion defect length is less than 125 mm, local extrusion deformation occurs first from the corrosion defect location, and then expand to both ends, as shown in Fig. 12(b); When the corrosion defect length is more than 125 mm, depression deformation of screen pipe from corrosion defect position as shown in Fig. 12(c).

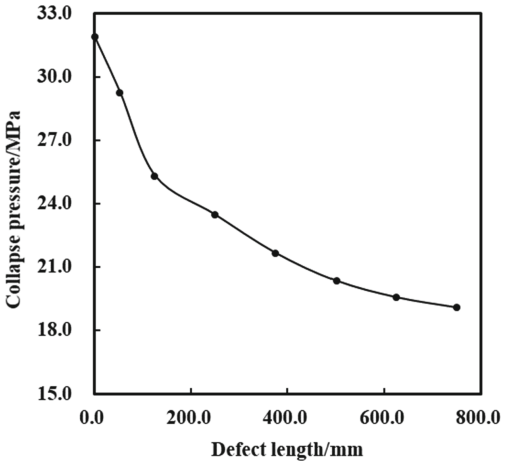

Fig.11. The influence of corrosion defect length on the collapsing strength of screen pipe

4.5 Effect of Hole Arrangement Parameters on Collapsing Strength of Screen Pipe

The above research is to study the influence of corrosion defect parameters on the collapsing strength of screen pipe while keeping the parameters of screen pipe hole distribution

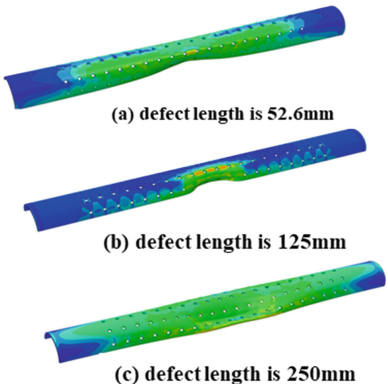

Fig. 12. Deformation patterns of screen pipe with different corrosion length

unchanged. The parameters of hole arrangement also affect the collapsing strength of the screen with corrosion defects. Therefore, the influence of hole arrangement parameters on the collapsing strength of the screen pipe with corrosion defects is analyzed in this section.

4.5.1 Effect of Different Hole Diameters on Collapsing Strength of Screen Pipe with Corrosion Defects

Assuming that the corrosion defect is in the middle of the screen pipe; The selected screen pipe corrosion defect parameters are as follows: The depth of corrosion defect is 2.15 mm(1/3t); The number of axial holes is 20 and the number of circumferential holes is 8; The corrosion defect width are 90°; The length of defect is 52.60 mm. Calculating the collapsing strength of corrosion screen pipe when the hole diameter are 6.35 mm, 9.50 mm, 12.70 mm, 14.00 mm, 16.00 mm respectively, and the results are shown in Fig. 13(a). As can be seen from Fig. 13(a), the collapsing strength of the screen pipe decreases approximately linearly with the hole diameter of the screen pipe increases. When the hole diameter was increased from 6.35 mm to 16.00 mm, the collapsing strength of the screen pipe with corrosion defects decreased by 5.91 MPa.

4.5.2 Influence of Different Circumferential Hole Numbers on the Collapsing Strength of Screen Pipe with Corrosion Defects

Assuming that the corrosion defect is in the middle of the screen pipe; The selected screen pipe corrosion defect parameters are as follows: The depth of corrosion defect is 2.15 mm(1/3t); The number of axial holes is 20; The corrosion defect width are 90°; The length of defect is 52.60 mm; The hole diameter is 12.70 mm. Calculating the collapsing strength of corrosion screen pipe when the number of circumferential holes 6, 8, 10, 12, 14 and 16 respectively, and the results are shown in Fig. 13(b). As can be seen from Fig. 13(b), the collapsing strength of the screen pipe decreases with the circumferential hole number increasing, and the effect of the number of circumferential holes on the collapsing strength of the screen pipe is not significant. When circumferential hole

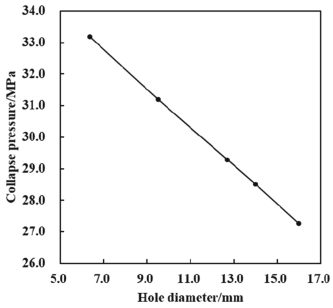

(a) hole diameter

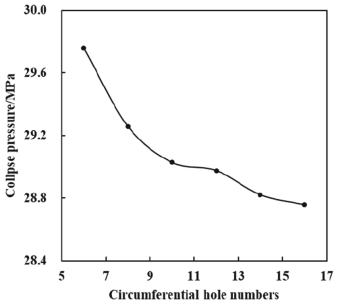

(b) the number of circumferential holes

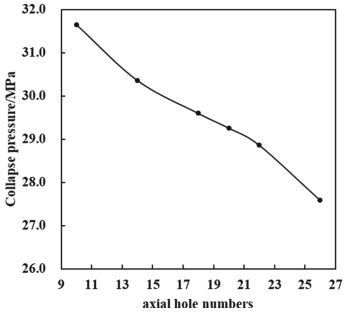

(c) the number of axial holes

Fig. 13. The influence of hole arrangement parameter on the collapsing strength of screen pipe

numbers was increased from 6 to 16, the collapsing strength of the screen pipe with corrosion defects decreased by 1 MPa.

4.5.3 Influence of Different Hole Arrangement Parameter on the Collapsing Strength of Screen Pipe with Corrosion Defects

Assuming that the corrosion defect is in the middle of the screen pipe; The selected screen pipe corrosion defect parameters are as follows: The depth of corrosion defect is 2.15 mm(1/3t); The number of circumferential holes is 8; The corrosion defect width are 90°; The length of defect is 52.60 mm; The hole diameter is 12.70 mm. Calculating the collapsing strength of corrosion screen pipe when the number of axial holes 10, 14, 18, 20, 22 and 26 respectively, and the results are shown in Fig. 13(c). As can be seen from Fig. 13(c), the collapsing strength of the screen pipe decreases with the axial hole number increasing. When axial hole numbers was increased from10 to 26, the collapsing strength of the screen pipe with corrosion defects decreased by 4.06 MPa.

5 Conclusion

A finite element model of screen pipe with corrosion defects is developed based on ABAQUS software and the influence of corrosion defect parameters and hole arrangement parameters on the collapsing strength of corrosion screen pipe was analyzed. The main conclusions of the article are summarised as follows:

When the corrosion defect is located in the middle of the screen pipe, the corrosion defect screen pipe collapsing strength is the smallest, and as the corrosion defect to the middle of the screen tube closer, the collapsing strength of screen pipe is smaller.

Collapsing strength of the screen pipe gradually decreases with the increase of corrosion defect depth and corrosion length, and defect depth has the greatest effect on the collapsing strength of the screen pipe. In addition, variations in defect depth, corrosion length and corrosion width can affect the deformation pattern of the screen pipe.

With the increase of the hole diameter, the number of circumferential holes, the number of axial holes, the collapsing strength of the screen pipe with corrosion defect gradually reduced. And the hole diameter and the number of axial holes have a significant influence on collapsing strength of screen pipe.

Acknowledgments. This work was supported by the National Natural Science Foundation of China [51890914, 51709269], the Fundamental Research Funds for the Central Universities [20CX02410A].

References

1. Wang, L., Deng, J., Zhou, J.: A physical simulation experiment on sanding in weakly consolidated sandstone gasreservoirs. Acta Petrolei Sinica **32**(6), 1007–1011 (2011)
2. Wu, G., Liu, G., Cao, Y.: Ground real-time monitoring on sand production of heavy oil reservoir. Oil Drill. Product. Technol. **38**(4), 519–525 (2016)

3. Sun, B., Peng, Y., Zhang, W.: Calculation formula of collapsing strength of screen casing and analysis of its applicability. Acta Petrolei Sinica **41**(3), 363–371 (2020)
4. Peng, Y., Sun, B., Wang, J.: Finite element analysis on anti-collapsing strength of screen pipes with different hole arrangements. China Petrol. Mach. **48**(2), 9–14 (2020)
5. Fu, G., Peng, Y., Sun, B.: Collapse pressure calculation of sand control screen tube under combined external pressure and bending. J. China Univ. Petrol. **45**(2), 78–86 (2021)
6. Beltran, K., Netto, T.: Collapse analysis of perforated pipes under external pressure. SPE, pp. 0617-0077 (2017)
7. Guo, Y.G., Blanford, M., Candella, J.D.: Evaluating the risk of casing failure due to high-density perforation: a 3D FEM case study from a deep water reservoir. SPE (2014)
8. Zhu, X., Luo, S.: The regularization of Casing corrosion defects and collapse strength analysis. Sci. Technol. Eng. **17**(9), 194-198 (2017)
9. Zhangi, Z., Kong, W., Liu, Z.: Study on residual strength of corrosion defect casing. China Sci. Paper **11**(21), 2467–2472 (2016)
10. Bangchuan, B., Changyin, D., Liang, H.: Experimental evaluation of dynamic mechanical sand screen corrosion for the high temperature pressure gas reservoir in South China Sea. Spec. Oil Gas Reserv. **27**(3), 148–156 (2020)
11. Cao, X., Zhao, L., Cui, M.: Residual strength of pipeline with double corrosion defects interaction. Oil Gas Storage Trans. **34**(4), 354–361 (2015)
12. Yang, H., Tang, Y., Chan, J.: Finite element analysis of volumetric corrosion defects of oil/gas pipeline. Oil Gas Storage Trans **34**(1), 37–41 (2015)
13. Gong, S., Hu, Q.: Buckling and collapse analyses of composite structures for deep water sandwich pipe sunder external pressure. J. Zhejiang Univ. **48**(9), 1624–1631 (2014)

Prospects of Horizontal Well Drilling in Marine Gas Hydrate Reservoir

Baojiang Sun[1(✉)], Xuefeng Li[1], Baojin Ma[2], Fei Peng[2], Zhiyuan Wang[1], and Haikang He[1]

[1] School of Petroleum Engineering, China University of Petroleum (East China), Qingdao, Shandong, China
sunbj@upc.edu.cn

[2] CNPC Offshore Engineering Company Limited, Beijing, China

Abstract. Natural gas hydrate is a new energy source that is expected to replace fossil fuels. With the further research of marine hydrates production test, natural gas hydrates have shown great application prospects. The horizontal well mining hydrates has become the key to improve the gas production, but currently there is no mature experience in the horizontal well operation of the seabed hydrate layer. In this paper, we review the drilling tools used in conventional horizontal well and the cases of seabed shallow horizontal well, as well as related techniques for inhibiting hydrates decomposition or further generation during drilling. Possible limitation in each guiding tool for horizontal well in hydrate layers are discussed. Then based on the existing research, the development direction of horizontal well operation in marine hydrate layer is prospected. Whilst there are few cases on drilling horizontal well in marine gas hydrates, the breakthroughs will depend on the research of new drilling steering tool and drilling program, as well as further study on the mechanical properties of reservoirs.

Keywords: Gas hydrate · Horizontal well · Shallow layer · Hydrate production · Steering tool

1 Introduction

Natural gas hydrates are widely distributed in the continental permafrost zone, island slopes, active and passive continental uplifts, polar continental shelves, and deep-water environments of the ocean and some inland lakes [1]. It is estimated that the organic carbon content of global hydrate is twice the total content of other fossil energy sources. More than 98% of the natural gas hydrate resources in the world are distributed on the continental shelf offshore [2].

There are mainly several ways to extract natural gas hydrates: depressurization [3–5], thermal stimulation [6–8], CO_2-CH_4 replacement [9], chemical inhibitor injection [10, 11] and solid fluidization extraction method [12, 13]. At present, the more effective method for natural gas hydrates in the shallow seabed is the depressurization method.

B. Sun et al. (Eds.): DWOG-Hyd 2021, LNCE 246, pp. 32–46, 2022.
https://doi.org/10.1007/978-981-19-0960-3_4

Japan [14] and China [15] have also adopted the depressurization method to conduct large-scale offshore methane gas hydrate developing tests in recent years. Due to the characteristics of shallow sediments, weakly cemented, unstable, and non-caprocks in the marine gas hydrate reservoirs, the "vertical well" pattern has been adopted in the production test of gas hydrates in the sea area. But the results showed that the gas production rate was lower than the acceptable standard of commercial gas production.

In the traditional oil and gas production process, horizontal wells and multi-branch wells have effectively expanded the contact range between the wellbore and the reservoir [16]. At the same time, compared with vertical wells, horizontal wells only need a smaller production pressure and are less likely to cause sand production. In addition, drilling horizontal wells with long horizontal sections can optimize well pattern to reduce the impact of foundation settlement on the wellhead due to hydrate development. Scholars have performed lots of numerical simulations and laboratory tests on natural gas hydrate production from horizontal wells [17–19], shown that horizontal wells perform better in terms of gas production and ultimate recovery. Therefore, horizontal well operation is an important method to improve the economic efficiency of marine gas hydrate production.

However, due to the special geological characteristics of the submarine shallow gas hydrate reservoir, traditional horizontal well drilling methods have been greatly restricted. In this paper, the related research progress and technical difficulties of horizontal well drilling will be reviewed, in view of the special marine geological environment of shallow seabed gas hydrates. Then the related countermeasures be improved for tackling key problem, to providing reference for horizontal well mining research of shallow hydrate in the seabed.

2 Horizontal Well Drilling Technology

2.1 Conventional Horizontal Well Drilling Technology

With the continuous improved requirements of cost reduction and efficiency in drilling development, traditional screw motors have the disadvantages of slow mechanical drilling speed, large friction torque, weak horizontal well extension ability, and difficult to control the well trajectory. The use of rotary steering technology (RST) in directional well drilling become more popular [20]. As a widely-applied technique, RST has shown its superiority in drilling rate improvement, reservoir discovery and formation protection. Rotary steering drilling technology was originally used for long-distance horizontal well drilling of shale gas, due to its outstanding economic benefits [21]. Now, RST is gradually used to tap the potential of old oil fields. The RST can expose more reservoirs, increase productivity and deal with complex formations. It is mainly used for precision drilling of horizontal wells, extended reach wells, multi-branch wells, highly deviated wells, and three-dimensional multi-target wells.

Drilling direction is mostly influenced by the direction of a drill bit and the side force applied on this drill bit. The RST guiding devices used in conventional oil and gas production can be divided into two types: push-the-bit and point-the-bit [22]. Push-the-bit rotary steering system (RSS) mainly generate pushing force on the well wall by three hydraulic sliders, and changes the drilling direction by the combined force of the reaction force of the well wall. Point-the-bit RSS uses an internal eccentric ring group to

drive the drill bit to generate eccentric force. Push-the-bit RSS have a relatively weaker tilt angle in the Schlumberger rotary guidance products. But due to its early market entry and good overall application, it is still in large-scale use. Point-the-bit RSS could avoid the interaction between the tool and the wellbore, weaken the dependency of the well wall. The quality of the well wall is better, and the risk of potential jamming is further reduced.

The second horizontal well technology is sidetrack drilling. Sidetrack drilling technology can drill up to 50–100 m of production flow path from the wellbore to the reservoir. Coiled tubing ultra-short radius radial drilling came about in the 20th century [23]. Compared to the traditional sidetrack drilling (the projectile perforation), coil tubing radial drilling can reduce operation cost and increase the drainage area of reservoir and then improve the individual well productivity greatly. It can be used in both old wells and new wells, and is especially suitable for the productivity improvement of old oilfields and development of offshore marginal field and small fields.

The process of drilling a radial horizontal well involves two steps: the first step is making a window on the casing with a specific tool, and the second step is to use a self-propelled jet bit to pull a high-pressure hose through the window of the casing to enter a horizontal well with a smaller diameter in the formation. The downhole tools involved in this drilling technology mainly include self-propelled jet drill bits, high-pressure hoses, reducing joints, coiled tubing, diverters, anchors, etc. Fix the anchor and the diverter at the "window" position of the vertical well, lower the jet bit connected to the coiled tubing to the anchor position, and use the diverter to guide the jet bit into the formation. By the reaction force of the nozzle and the thrust of the coiled tubing, the jet bit is advanced in the horizontal direction. It is a new drilling technology and has already been applied successfully and shown a huge potential.

2.2 Shallow Horizontal Well Drilling

At present, there are few reports on the drilling of horizontal wells in shallow seabed, and all these methods are in the experimental stage. In 2004, Japan organized the world's first natural gas hydrate horizontal well in the Nankai-Trough [24]. The horizontal well was kicked off at 20 m below the mudline and successfully landed horizontally when drilling to 472 m, the horizontal section was 100 m long. It took a total of 8.5 days. During the drilling process, the angle was kept building up using BHI's mud motor with a bent housing adjusted at 1.5 to 1.8°, the well hit into hydrate zone at 225 m, and continue drilling 317 m in the hydrate reservoir. It is reported that the horizontal well did not experience high friction and high torque during drilling. For various reasons, in the completed horizontal well, only a very short casing pipe (175.39 m) was set, and the completion process was not continued.

It is worth noting that a BHI's mud motor was used in the horizontal well drilling process of the seabed hydrate layer. Due to low compaction of the formation, the slope of the RSS in seabed formations is unstable. The mud motor drilling tool has a higher slope-defining ability in shallow formations than the RSS drilling tool. But with the improvement of drilling technology in recent years, the slope of the RSS is gradually

guaranteed by turning into closed circuit or transforming drilling fluid in advance, adopting lower displacement and higher weight-on-bit, and adding flexible short joints to the drilling tool combination, etc.

In 2011, Norwegian scholars proposed a new suction anchor type well foundation concept that presses the wellhead into the formation through the pressure difference between the inside and outside of the cavity [25, 26]. Compared with the conventional wellhead, the new wellhead avoids direct contact between cement and the formation, reduces cement leakage, and the casing can be pre-tilted to a certain angle inside the wellhead. Using this suction anchor well foundation, in 2016, a horizontal well was successfully drilled in shallow formations with a water depth of 400 m and a depth of 250 m below the mudline in the Barents Sea of Norway. However, this field is a reservoir of gas. The mechanical properties of the reservoir are quite different from those of the marine gas hydrate. This method of drilling shallow horizontal wells has certain reference value for drilling horizontal wells in hydrate reservoirs.

2.3 Methane Hydrate Drilling Technology

The hydrates in seabed are extremely sensitive to temperature and pressure. When the temperature of the local layer increases and the pressure decreases, the hydrates in the formation will decompose. When drilling of gas hydrate formations, the damage caused by the drilling tools to the formations resulted in the release of stresses in the well wall and near the bottom of the reservoir [27–29]. Under the temperature difference and pressure difference, drilling fluid inevitably invades the formation for heat and mass transfer, resulting in hydrate decomposition in the reservoir, which may cause serious well control problems.

In recent years, with the development of drilling equipment, a gas-liquid separation device is often used to separate the gas and liquid phases in the drilling pipeline to prevent the formation of natural gas hydrates, when designing deep-water drilling schemes in the ocean [30]. In 2013, the world's first marine hydrate trial production in the Nankai Trough, a gas separator and an electronic submersible pump were installed in the drilling pipeline to separate the gas and liquid phases in the pipeline to prevent the formation of hydrate.

3 Drilling-Related Challenge

3.1 The Ability to Control Dogleg Severity

In the marine environment, the special temperature and pressure characteristics determine the possible zone for marine hydrates. As shown in Fig. 1, below the depth where the green curve and red curve intersect, CH4 hydrate is stable and if gas exists below this depth, such as free gas in pores. It can be known that the gas hydrate stable zone is mainly located in the shallow seafloor. Therefore, it is inferred that the exploitation of horizontal wells in marine hydrates requires the completion of horizontal well operations in the shallow seafloor.

Due to the shallowness of the natural gas hydrate reservoir in the seabed, the building depth of the wellbore is insufficient. For horizontal wells designed in shallow areas, for

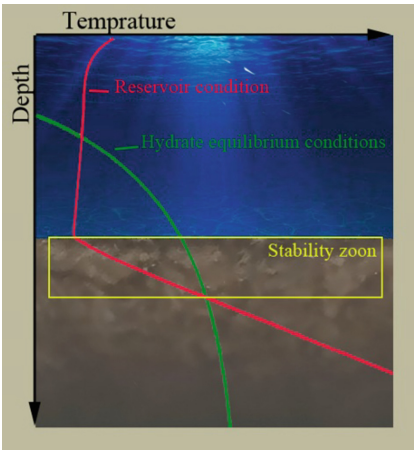

Fig. 1. Stability conditions of gas hydrate

example, building angle from 0 to 90° inclination over a vertical of 250 m, required an average of dogleg severity (DLS) of 9/30 m. To keep the DLS requirement low, it was envisaged to start building as early as possible, which incentivized the engineering team to investigate options for shortening the conductor. That is, the vertical depth from the kick point to the horizontal landing point is insufficient. Due to the limitation of vertical depth, this puts forward higher requirements for the high-angle build ability of the guide tool. The existing steering tools are usually applied to deep oil and gas reservoirs, and are not special steering tools designed for shallow horizontal drilling. Therefore, the applicability of guide tool in shallow drilling is limited, which is quite different from the drilling tool of traditional horizontal wells in oil reservoirs.

For the problem of the high DLS of shallow horizontal wells, the restriction of the horizontal well rotary steering drilling can be solved by increasing the steering tool's build rate or optimizing the kick point. Although the drilling method of the coiled tubing radius radial horizontal well is not restricted by the DLS rate, it has high requirements on the quality of the wellbore, and it needs to operate under the condition of casing, which still has great construction difficulties.

3.2 Reservoir Mechanical Properties are Unstable

During the exploration of gas hydrate reservoirs, marine gas hydrates are mainly found in the Cenozoic strata in the shallow surface of the ocean floor, which relied on appropriate pressure and geothermal gradients. The overburden layer of hydrates zone is mainly composed of thin silts interbedded with fine clay, and the mechanical strength of the formation is unstable [31]. The presence of the hydrate will significantly increase the mechanical strength of the sedimentary layer, because the hydrate in formation play the part of cement in the sandstone. If the large amount of hydrate were decomposed, the stability of the surrounding rock of the well will decrease, resulting in the wellbore collapse. When the reservoir is opened, the wellbore is easily to shrinks and collapses, increasing the friction when entering the conductor. At the same time, due to the existence

of a long seawater section, it is difficult to control the downhole mechanics during casing inserted, which may cause the casing slip into wrong place, fail to complete the well normally, further to limit the adaptability of sidetrack drilling horizontal well.

In deep water, due to poor cementation of the upper overburden layer, the shallow fracture pressure is small, the drilling mud density window between the fracture pressure and the formation pressure is narrow, and the bearing capacity is low. Compared with conventional oil and gas reservoirs, natural gas hydrate formations are softer, drilling fluid density windows are narrower, and lost circulation are more likely to occur.

The shallow weak cementation mechanical properties also increase the difficulty of horizontal well drilling. Because the sedimentary layer is relatively soft and lacks stable support [32], the push-type rotary guidance system cannot be used at this level. Although the directional rotary steering system avoids the dependence on the borehole wall and reduces the interaction between the tool and the wellbore, it is still difficult for the drill bit to obtain a stable support force during directional drilling, and cannot fully meet the requirements of trajectory control. In addition, the high rigidity of the traditional drilling, and the vibration during drilling is obvious, which further weakens the bearing capacity of the formation and results in an increase in the offset of the wellbore.

3.3 Wellhead Stability

The surface conductor, marine riser and under water wellhead are initial channels of deep-water drilling. Their stabilities are related to the whole progress of offshore drilling. Main factor weaken stability of wellhead are focused on the vibration of riser in water, lateral ocean current load, jetting depth of surface conductor [33]. The subsea wellhead is in a complicated stress state, and the risk of wellhead instability is existing. Meanwhile, the subsea silt-clay shallow foundation has low bearing capacity and high compressibility [34].

Decomposition of hydrate would further weaken the stability of wellhead. In the drilling process, interactions between hot fluid in drilling annulus space and hydrates can destabilize hydrates near the wellbore. But the decomposition rate is relatively low [27]. The reason is that the pressure in the hydrate layer is higher and the temperature increasing is limited by the relatively low thermal conductivity of the hydrate layer. But, in the development process, continuous hydrate dissociation can weaken the strength of hydrate formation, which may damage to equipment on seabed [35].

In submarine gas hydrate sediments, the pore spaces are partially occupied by the solid phase of gas hydrates. The gas hydrates in the pore can act as a cementation (bonding) agent between soil particles. The reduction in hydrostatic pressure of the hydrate reservoir, or increases in the temperature of the reservoir leads to the dissociation of the gas hydrates. The solid phase of the gas hydrates is lost and the hydrates change into the fluid phase, i.e., water and gas. When this released fluid pressure is trapped inside an area of low permeability, the effective stress, which is one of the factors of describing strength of the sediments, should be reduced and slope failure can be triggered, resulting in submarine landslides. The submarine landslides may lead to even worse situation, for example, cutting submarine cables, wellhead rollover and well-site subsidence. However, we do not have enough knowledge about the behaviors of sediments caused by dissociation of hydrates in the ground [36].

3.4 Wellbore Instability

Hydrate dissociation in the formation can lead to problems with wellbore stability, and impact adversely on the efficiency and eventually, safety of drilling operation. In the drilling with a riser, gas from the hydrates enters the returns annulus, and cannot be isolated from the rig floor. Under these conditions, the drilling fluid can become highly gasified (referred to as gas-cut mud) which lowers the mud density [37]. Further dissociation of the hydrates is promoted by this decrease of the drilling fluid pressure and a viscous cycle is established. When gas hydrates dissociate, the mechanical and physical properties of the sediments adjacent to the wellbore will change. The change in material properties associated with the dissociation includes in permeability, reduction in modulus and loss of the cementation provided by the gas hydrates.

However, the temperature of annulus mud has a more hazard in hydrate decomposition. At present, the safety and stability of the borehole wall during the drilling process has been studied by many researchers [37–41]. Most of the researchers only focused on numerical simulation, in which have shown that the temperature of drilling fluid is the main factor of hydrate decomposition. In addition, the gasification leads to lowering of the mud density, reduction of the drilling fluid pressure which may cause wellbore instability.

A further side-effect of the drilling fluid pressure reduction is reduction of its mechanical support to the wellbore that could lead to hole enlargement and possible wellbore collapse. Meanwhile, changes in mud rheological properties will impact hole cleaning capacity and combined with changes in the formation strength and pore pressure within the formation may lead to hole enlargement and wellbore collapse.

3.5 High Probability of Geological Hazards

When drilling in marine gas hydrate reservoir, the formation temperature and pressure changed by the drilling process will lead to hydrate decomposition [28]. The gas produced by the decomposition cannot be dissipated in the pores in time, lead to excessive pore pressure surrounding the well. The effective bearing capacity reducing in the sedimentary layer could easily cause natural disasters such as seabed landslides and subsidence.

In addition to the effects of hydrate decomposition, shallow seabed strata also have a series of risk problems such as unstable seabed, low bearing capacity, free gas, over pressure water, and potential seafloor instability [42]. Although the methods for identification and mitigation of these hazards are available, they are not yet mature.

4 Prospects for Horizontal Drilling Technology in Submarine Hydrate Layer

Based on the drilling challenge in hydrate layer, there are some main factors to solve challenges. 1) build horizontal well in shallow layer; 2) hold the borehole pressure; 3) optimize the drilling fluid. In the building horizontal well in shallow layer, hydro jet radial drilling and wellhead steering technology provide practicable method for finishing shallow horizontal well. Borehole pressure is the main factor to maintain the safety in drilling.

Holding the borehole pressure have significant effect on preventing the decomposition of hydrates, maintaining the wellbore stability, mitigating the geological hazards. The last factor is optimizing the drilling fluid. In this part, related technology will be reviewed.

4.1 Hydro Jet Radial Drilling

Most marine gas hydrate are wrapped in weakly cemented sand. For horizontal wells which do not require high extension distances, coiled tubing rotary jet drilling is also a feasible method. After the completion of the vertical well, the "window opening" tool was run for "window opening" and radical drilling. Horizontal drilling was performed by coiled tubing radial horizontal drilling technology, as shown in Fig. 2.

Aiming at the difficult of casing completion, some scholars have proposed casing drilling method and drill pipe drilling method. Casing drilling method refers to the simultaneous drilling and casing operation, which can reduce the effect of pumping pressure on the well wall, to maintain the stability of surrounding gas hydrate. When drilling with casing drilling method, the cuttings will be ground into fine particles. Under the effect of liquid column pressure, the particles will be squeezed into the borehole wall and the borehole surface will be covered with a certain thickness of mud cake. This phenomenon is called smear effect. This can effectively improve the leakage of drilling fluid and strengthen the stability of the wellbore. Drill pipe drilling method refers to use of large diameter drill pipes for drilling. When drilling to a predetermined depth, the drill pipe, drilling tools and drill bits in the well cannot be raised, and the drill pipe remains in the well as a casing.

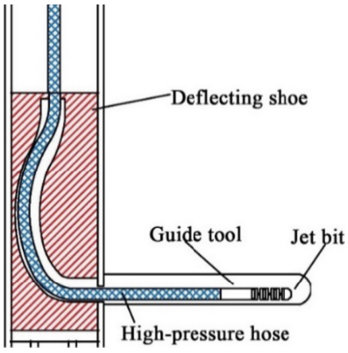

Fig. 2. Coiled tubing radial horizontal drilling technology

The jet fluid is required to have a dual function as a power medium for horizontal drilling and as a support for the fracturing fluid. That is, while the jet is using for drilling, the jet liquid is pressed into the hydrate reservoir and can form a support in the reservoir to provide a channel for natural gas to migrate to the well.

The disadvantage of sidetrack radial drilling method is the insufficient extension ability of the horizontal section. The extension ability from the wellbore to the reservoir is currently only 50–100 m. For long-distance horizontal well operations, mechanical drill bits are still required to cooperate with rotary steering drilling technology.

4.2 Wellhead Steering Technology

Conventional submarine conductor uses jet downpipe technology, and the length of the conductor is generally 60–80 m. The length of the conductor greatly shortens the vertical depth from the kick point to the horizontal landing point, which makes it difficult to drill horizontal wells in the submarine gas hydrate layer and limits the usage of rotary steering tools in shallow hydrate formations.

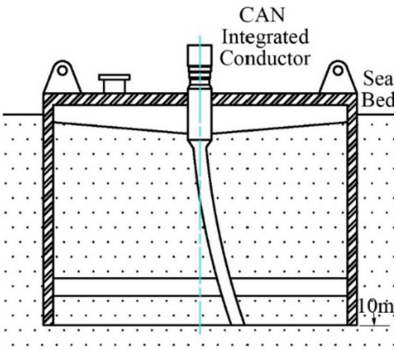

Fig. 3. CAN with integrated slender conductor

To shorten the conductor, a conductor anchor node (CAN) was designed [26]. The appearance of CAN provides a feasible idea for solving the problem of insufficient vertical depth. The CAN is like an inverted bucket. During installation, the CAN will penetrate seabed by suction pressure. Due to the large wellhead size of CAN, the wellhead stability is much higher than that of normal conductor. Compared with conventional wellheads, CAN wellheads have a shallower installation depth (10–11 m), shorter installation time (<20 h), higher stability (longitudinal bearing capacity of more than 400t), and can be reused.

Large-scale wellhead piles are more stable than traditional conductor cementing, which greatly reduces wellhead instability caused by lateral forces, and provides more stable support for the drilling of horizontal wells in the shallow layer. As shown in Fig. 3, the conductor can be pre-tilted at a certain angle inside the pile body, instead of bearing the load, which could rise the kick point. Compared with the conventional wellhead conductor structure, using CAN integrated conductor is more suitable for horizontal well drilling of subsea gas hydrate.

Based on strengthening wellhead stability and rising the kick point, the rotary steering technology currently used for drilling horizontal shale wells can be applied to horizontal well drilling in shallow seabed. However, there are still problems such as difficulty in controlling the inclined well section, unstable inclination, and insufficient extension ability. Based on the existing technology, it is necessary to realize the diversification of rotary steering technology, and optimize the combination o of drilling tool according to the characteristics of natural gas hydrate reservoirs, further increase the slope rate during actual drilling, and reduce drilling risks.

4.3 Surface Conductor Jet Drilling Technology

Surface conductor jetting drilling is a deep-water drilling technique developed to cope with loose deep-water seabed soil and prevent shallow geological disaster [43, 44]. Surface conductor is tripped in place by jetting mode, utilizing water-jet and the gravity of conductor string. When drilling to the preplanned depth, make the conductor string static, utilize the adhesion friction force of the seabed surface soil to make the conductor firm. The model of jet drilling is shown in Fig. 4. During the jetting process, the diameter of the jetted cavity should be controlled to be smaller than the conductor OD (outer diameter) to ensure the casing can penetrate into the clay by the BHA (bottom hole assembly) and its self-weight which can provide enough bearing capacity [45].

Jet pipe drilling technology is a crucial technology in deep-water drilling, it has advantages as follow: Being free of cementing, saving time, boosting drilling speed, simplifying drilling procedure and reducing cost [46].

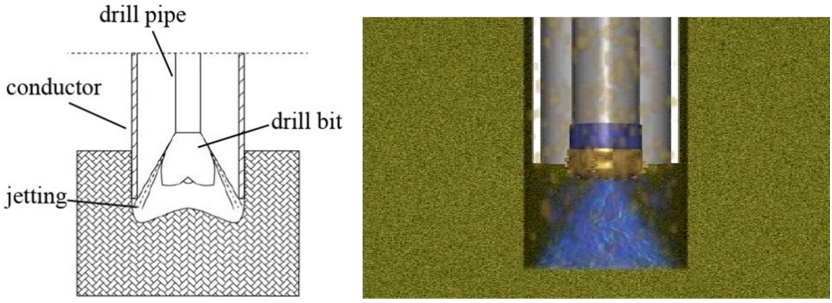

Fig. 4. The model of jet drilling

4.4 Dynamic Kill Drilling Technology

Dissociation of methane gas from its frozen lattice-like structure within the near-wellbore and until the mud and cuttings have been returned to the rig's surface separation equipment must be avoided for well control reasons [47]. Such as: 1) Blowout because of sudden gas hydrate dissociation, 2) Slope failure risk due to sudden gas hydrate dissociation, 3) Wellbore stability problems and wellbore collapse risks due to the loose sediments after gas hydrate dissociation. During the drilling process, the temperature of reservoir will rise with the fluid circulation, even though the temperature of drilling mud should be limited in the well head. If dissociation of free gas from frozen methane hydrate crystalline structures is to be avoided, the drilling process must incorporate a means of preventing near wellbore and annulus pressure drops.

On the other hand, during the deep-water drilling, there are few risers or intermediate casings for the interval of shallow formation [48]. Therefore, since the column pressure of building fluid cannot balance the formation pressure, once encountering the shallow gas or flow, the fluid with high pressure will expend to the low-pressure area in a high speed, and then form into the shallow kick, resulting a series of problems.

Hence the well control is very critical before running the intermediate casing and installing the blowout preventer. Nevertheless, wellhead blowout preventers (BOPs) have note been installed in surface drilling process, so the conventional methods cannot be used to circulate out the kick. The dynamic kill drilling (DKD) is a new method to realize effective well control [49]. The DKD is to mix the seawater into the weighted drilling fluid to form a series of drilling fluid with different density based on a certain percentage, and then to pump the weighted drilling fluid into the wellbore with high speed [50, 51], shown as in Fig. 5.

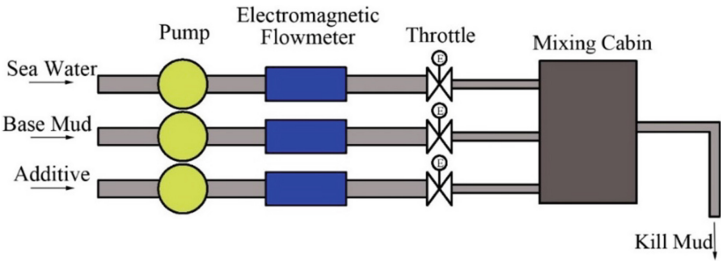

Fig. 5. DKD main devices

Dynamic kill drilling is a key technology that has the potential to solve the problem in deep-water surface drilling [52]. In this method, the mixing proportion is determined by the annular behavior through the annular pressure measurement while drilling (APWD) system, ensuring the mixture density can be maintained in the "narrow drilling window" between formation's pore pressure and fracture pressure [53].

4.5 Optimize the Drilling Fluid

It has been concluded that by cooling drilling fluid and decrease the circulation rate, the influence of drilling through gas-hydrate-bearing sediments on petroleum operations can be minimized [54]. High mud weight to increase the hydrostatic pressure may also be used to stabilize gas hydrates but caution must be exercised in its implementation as excessively high mud weight can fracture the formation and lead to lost circulation, particularly in unconsolidated marine sediments. Therefore, reducing the temperature of drilling fluid and making the pressure slightly higher than the fracture pressure of the formation are beneficial to maintaining the stability of the hydrate. Surface mud coolers may be required to chill the drilling fluid, this to avoid dissociation from an increase in temperature within the methane hydrate reservoir.

In addition, some special inhibitors or oil-based drilling fluids can also stabilize natural gas hydrates. This matter depends on the rational drilling fluids system. The drilling fluid should be able to effectively inhibit gas-hydrate aggregations in the drilling pipe and blowout preventer. In addition, for drilling in gas hydrate bearing sediments, the use of inhibitor for hydrate decomposition should be considered carefully because they prevent hydrate dissociation in the formation, but can also cause the aggregation in the borehole, if their concentration is too high.

5 Concluding Remarks

Marine gas hydrates are usually stored in shallow argillaceous siltstones in the form of cementation or pore filling, and their mechanical properties change due to their decomposition during mining. With the progress of mining, the mechanical properties of the hydrate reservoir gradually deteriorate, and the supporting force for the upper overburden gradually decreases, causing the formation to settle. Improper control will cause collapse and even geological disasters. Although the mining scheme of horizontal wells for the exploitation of marine natural gas hydrates will slow down the risks of formation subsidence and well collapse, further research is needed to ensure the reliability of horizontal wells and the safety of production. Study the effects of hydrate decomposition on foundation settlement under different reservoir conditions, and reduce the risk of wellbore stability and wellbore integrity during the entire life cycle.

Wellbore pressure is related to the stability of natural gas hydrates in the wellbore. Pressure controlled drilling technology can be used to solve the complex conditions that occur during the drilling process. When drilling in a submarine gas hydrate formation, a well drilling plan is designed to control the temperature and pressure during the drilling process. According to the actual formation characteristics, the temperature and pressure during the drilling process are jointly controlled to ensure the hydrate in the formation. It will not be decomposed in a large amount and hydrates will not be formed in the drilling pipeline, ensuring the safety of drilling in the gas hydrate layer.

Deep water hydrate reservoirs have low overburden pressure and high degree of under compaction. Compared with traditional oil and gas reservoirs, the requirements for the strength of drilling tools are greatly reduced. This means that the combination of drill bit and rotary steering tool is not necessary for the horizontal well operation of subsea hydrate reservoirs, and the jet pressure requirements for hydraulic drilling are also greatly reduced. With the gradual expansion of hydrate mining, it is necessary to design some new lightweight drilling tools to adapt to the efficient development and utilization of natural gas hydrate resources.

Funding. National Natural Science Foundation of China (No. 51890914).

References

1. Kvenvolden, K.A.: A review of the geochemistry of methane in natural gas hydrate. Organ. Geochem. **23**(11–12), 997–1008 (1995). https://doi.org/10.1016/0146-6380(96)00002-2
2. Ruppel, C.: Permafrost-associated gas hydrate: is it really approximately 1% of the global system? J. Chem. Eng. Data. **60**(2), 429–436 (2014). https://doi.org/10.1021/je500770m
3. Li, B., Li, X.-S., Li, G., Feng, J.-C., Wang, Y.: Depressurization induced gas production from hydrate deposits with low gas saturation in a pilot-scale hydrate simulator. Appl. Energy **129**, 274–286 (2014). https://doi.org/10.1016/j.apenergy.2014.05.018
4. Konno, Y., et al.: Key factors for depressurization-induced gas production from oceanic methane hydrates. Energy. Fuels. **24**(3), 1736–1744 (2010). https://doi.org/10.1021/ef901115h
5. Zhao, J., et al.: Analyzing the process of gas production for natural gas hydrate using depressurization. Appl. Energy. **142**, 125–134 (2015). https://doi.org/10.1016/j.apenergy.2014.12.071

6. Li, X.-S., et al.: Experimental investigation into methane hydrate production during three-dimensional thermal huff and puff. Appl. Energy **94**, 48–57 (2012). https://doi.org/10.1016/j.apenergy.2012.01.024
7. Yang, X., et al.: Experimental study on gas production from methane hydrate-bearing sand by hot-water cyclic injection. Energy Fuels **24**(11), 5912–5920 (2010). https://doi.org/10.1021/ef100367a
8. Linga, P., et al.: recovery of methane from hydrate formed in a variable volume bed of silica sand particles. Energy Fuels. **23**(11), 5508–5516 (2009). https://doi.org/10.1021/ef900543v
9. Jung, J.W., CarlosSanamarina, J.: CH4-CO2 replacement in hydrate-bearing sediments: a pore-scale study: research letter. Geochem. Geophys. Geosyst. **11**(12), 1–8 (2010). https://doi.org/10.1029/2010GC003339
10. Kvamme, B., Kuznetsova, T.: Hydrate dissociation in chemical potential gradients: theory and simulations. Fluid Phase Equil. **217**(2), 217–226 (2004). https://doi.org/10.1016/j.fluid.2003.02.002
11. Li, S., Zhang, L., Jiang, X., Li, X.: Hot-brine injection for the dissociation of natural gas hydrates. Petrol. Sci. Technol. **31**(13), 1320–1326 (2013). https://doi.org/10.1080/10916466.2012.716887
12. Qiu, S., Wang, G., Wang, L., Fang, X.: A downhole hydrocyclone for the recovery of natural gas hydrates and desanding: the CFD simulation of the flow field and separation performance. Energies **12**(17), 3257 (2019). https://doi.org/10.3390/en12173257
13. Zhou, S., et al.: Optimal design of the engineering parameters for the first global trial production of marine natural gas hydrates through solid fluidization. Nat. Gas Indus. B **5**(2), 118–131 (2018). https://doi.org/10.1016/j.ngib.2018.01.004
14. Oyama, A., Masutani, S.: A review of the methane hydrate program in Japan. Energies **10**(10), 1447 (2017). https://doi.org/10.3390/en10101447
15. Li, Jin-fa, et al.: The first offshore natural gas hydrate production test in South China Sea. China Geol. **1**(1), 5–16 (2018). https://doi.org/10.31035/cg2018003
16. Ehlig-Economides, C.A., Economides, M.J.: Single well reservoir management - the ultimate multibranch well challenge. In: SPE Asia Pacific Conference on Integrated Modelling for Asset Management, p. 4. Society of Petroleum Engineers, Yokohama, Japan (2000)
17. Chong, Z.R., Zhao, J., Chan, J.H.R., Yin, Z., Linga, P.: Effect of horizontal wellbore on the production behavior from marine hydrate bearing sediment. Appl. Energy **214**, 117–130 (2018). https://doi.org/10.1016/j.apenergy.2018.01.072
18. Feng, J.-C., Wang, Y., Li, X.-S., Gang Li, Y., Zhang, Z.-Y.C.: Effect of horizontal and vertical well patterns on methane hydrate dissociation behaviors in pilot-scale hydrate simulator. Appl. Energy **145**, 69–79 (2015). https://doi.org/10.1016/j.apenergy.2015.01.137
19. Tao, Y., Guan, G., Abudula, A., Yoshida, A., Wang, D., Song, Y.: Application of horizontal wells to the oceanic methane hydrate production in the Nankai Trough, Japan. J. Nat. Gas Sci. Eng. **62**, 113–131 (2019). https://doi.org/10.1016/j.jngse.2018.11.027
20. Grini, M., Rice, B., Stromberg, S.: Field development utilizing rotary steering technology. In: SPE Annual Technical Conference and Exhibition, p. 8. Society of Petroleum Engineers, New Orleans, Louisiana (2001)
21. Herrington, D., Mercer, S.: Fully mechanical 3D rotary steering technology provides economical alternative to conventional rotary steerable tools. In: SPE Annual Technical Conference and Exhibition, p. 7. Society of Petroleum Engineers, New Orleans, Louisiana, USA (2013)
22. Zhang, Y., Samuel, R.: Analytical model to estimate the directional tendency of point and push-the-Bit BHAs. In: SPE Annual Technical Conference and Exhibition, p. 12. Society of Petroleum Engineers: Houston, Texas, USA (2015)
23. Dongjun, M.A., et al.: A model of calculating the circulating pressure loss in coiled tubing ultra-short radius radial drilling. Petrol. Explor. Dev. **39**(4), 528–533 (2012). https://doi.org/10.1016/S1876-3804(12)60072-X

24. H. Takahashi, Y.T., Multi-Well Exploration Program in 2004 for Natural Hydrate in the Nankai-Trough Offshore Japan (2005)
25. Hollinger, G., Trauner, S., Dupuis, S., Breivik, D.H., Myrvoll, OH.: Transformation of mindset - cost-effective collaborative well engineering & operation delivers record horizontal appraisal well in the Barents (2017)
26. Mathis, W., Strand, H., Hollinger, G.: Case history: how to enable the horizontal development of shallow reservoirs. In: SPE/IADC Drilling Conference and Exhibition. Society of Petroleum Engineers (2017)
27. Liao, Y., Sun, X., Sun, B., Gao, Y., Wang, Z.: Transient gas–liquid–solid flow model with heat and mass transfer for hydrate reservoir drilling. Int. J. Heat Mass Transf. **141**, 476–486 (2019). https://doi.org/10.1016/j.ijheatmasstransfer.2019.06.097
28. Khabibullin, T., Falcone, G., Teodoriu, C.: Drilling through gas-hydrate sediments: managing wellbore-stability risks. SPE Drill. Compl. **26**(02), 287–294 (2011). https://doi.org/10.2118/131332-PA
29. Cheng, W., Ning, F., Sun, J., Liu, Z., Jiang, G., Li, X.: A porothermoelastic wellbore stability model for riserless drilling through gas hydrate-bearing sediments in the Shenhu area of the South China Sea. J. Nat. Gas Sci. Eng. **72**, 103036 (2019). https://doi.org/10.1016/j.jngse.2019.103036
30. Sakurai, S., Nakatsuka, T., Edwards, J., Hoskin, B.J., Manning, D.K.: An experimental study for flow assurance of the methane hydrate production test system. In: Offshore Technology Conference (2014)
31. Li, Y., et al.: Gravel sizing method for sand control packing in hydrate production test wells. Petrol. Explor. Dev. **44**(6), 1016–1021 (2017). https://doi.org/10.1016/S1876-3804(17)30114-3
32. Moridis, G.J., Reagan, M.T., Queiruga, A.F., Boswell, R.: Evaluation of the performance of the oceanic hydrate accumulation at site NGHP-02-09 in the Krishna-Godavari Basin during a production test and during single and multi-well production scenarios. Marine Petrol. Geol. **108**, 660–696 (2019). https://doi.org/10.1016/j.marpetgeo.2018.12.001
33. Yan, W., et al.: Numerical method for subsea wellhead stability analysis in deepwater drilling. Ocean. Eng. **98**, 50–56 (2015). https://doi.org/10.1016/j.oceaneng.2015.02.007
34. Xu, Y., et al.: Risk assessment method of subsea wellhead instability in consideration of uncertain factors in deepwater drilling. Arab. J. Sci. Eng. **43**(5), 2659–2672 (2017). https://doi.org/10.1007/s13369-017-3004-2
35. Li, Q., Cheng, Y., Zhang, H., Yan, C., Liu, Y.: Simulating the effect of hydrate dissociation on wellhead stability during oil and gas development in deepwater. J. Ocean Univ. China **17**(1), 35–45 (2018). https://doi.org/10.1007/s11802-018-3544-4
36. Iwai, H., Kimoto, S., Akaki, T., Oka, F.: Stability analysis of methane hydrate-bearing soils considering dissociation. Energies **8**(6), 5381–5412 (2015). https://doi.org/10.3390/en8065381
37. Freij-Ayoub, R., Tan, C., Clennell, B., Tohidi, B., Yang, J.: A wellbore stability model for hydrate bearing sediments. J. Petrol. Sci. Eng. **57**(1–2), 209–220 (2007). https://doi.org/10.1016/j.petrol.2005.10.011
38. Lin, J.-S., et al.: Assessing the geomechanical stability of interbedded hydrate-bearing sediments under gas production by depressurization at NGHP-02 Site 16 (2018)
39. Jonny Rutqvist, G.J.M.: Numerical Studies on the Geomechanical Stability of Hydrate-Bearing Sediments (2007)
40. Sun, J., et al.: Production potential and stability of hydrate-bearing sediments at the site GMGS3-W19 in the South China Sea: a preliminary feasibility study. Marine Petrol. Geol. **86**, 447–473 (2017). https://doi.org/10.1016/j.marpetgeo.2017.05.037

41. Tayber, Z., et al.: Methane hydrate stability and potential reserves in the Levant Basin southeastern Mediterranean Sea. Geoscience **9**, 306 (2019). https://doi.org/10.20944/preprints201904.0249v1
42. McConnell, D.R., Zhang, Z., Boswell, R.: Review of progress in evaluating gas hydrate drilling hazards. Marine Petrol. Geol. **34**(1), 209–223 (2012). https://doi.org/10.1016/j.marpetgeo.2012.02.010
43. Yang, J., et al.: Research of conductor setting depth using jetting in the surface of deepwater. In: International Oil and Gas Conference and Exhibition in China, p. 6. Society of Petroleum Engineers, Beijing, China (2010)
44. Yang, J., et al.: Bit stick-out calculation for the Deepwater conductor jetting technique. Petrol. Explor. Dev. **40**(3), 394–397 (2013). https://doi.org/10.1016/S1876-3804(13)60049-X
45. Wang, T., Song, B.: Study on Deepwater conductor jet excavation mechanism in cohesive soil. Appl. Ocean. Res. **82**, 225–235 (2019). https://doi.org/10.1016/j.apor.2018.09.007
46. Zhang, H., et al.: Experimental study on the down-speed of conductor pipe influenced by jetting displacement in Deepwater drilling. Adv. Petrol. Explor. Dev. **10**(2), 88–92 (2016)
47. Hannegan, D.M.: Methane hydrate drilling technology (2005)
48. Geng, J., Zhou, C., Zhao, Q.: Technology of dynamic kill drilling for drilling in the superficial layer of Deepwater. In: 2011 International Petroleum Technology Conference, Bangkok, Thailand, p. 6 (2011)
49. Xu, P., et al.: Dynamic well kill method for shallow gas pockets in deep water. Petrol. Drill. Techn. **1**, 3 (2010)
50. Gao, Y., et al.: Study on dynamic kill drilling technology in deepwater drilling. Oil Drill. Prod. Technol. **32**(5), 8–12 (2010)
51. Feng, J., et al.: Predicting pressure behavior during dynamic kill drilling with a two-phase flow. J. Nat. Gas Sci. Eng. **22**, 591–597 (2015). https://doi.org/10.1016/j.jngse.2015.01.006
52. Vieira, F., et al.: First dynamic kill drilling application for Angola's Deepwater. In: SPE Deepwater Drilling and Completions Conference, p. 9. Society of Petroleum Engineers, Galveston, Texas, USA (2014)
53. Garcia, E.M., Akers, T.J., Holster, J.L.: Shallow hazards planning in Nigeria Deepwater-Erha-7 well. In: IADC/SPE Drilling Conference, p. 15. Society of Petroleum Engineers, Orlando, Florida, USA (2008)
54. Jiang, G., et al.: Polyethylene glycol drilling fluid for drilling in marine gas hydrates-bearing sediments: an experimental study. Energies **4**(1), 140–150 (2011). https://doi.org/10.3390/en4010140

Research on Numerical Simulation of Wellbore Stability of Natural Gas Hydrate Reservoir Considering Dynamic Drilling Process

Boyu Zhou[1(✉)], Yihui Guo[2], Youqiang Liao[3], Zhiwei Hao[1], Tianju Wang[1], Wenna Zhao[1], and Junyu Deng[1]

[1] CPOE Research Institute of Engineering Technology, Tianjin, China
zhouboyu@cnpc.com.cn
[2] CNPC Tianjin Boxing Engineering Science & Technology Co., Ltd., Tianjin, China
[3] China University of Petroleum (East China), Qingdao, China

Abstract. Natural gas hydrate (NGH) is one of the potential green alternative energy sources, and its exploration and development has become one of the key directions of energy development in China. In order to solve the problem of wellbore instability in the drilling process of NGH reservoir, a wellbore stability evaluation model considering the coupling heat and mass transfer process between wellbore and reservoir during horizontal well drilling and the Thermal-Hydrosolid-Coupling (THC) mechanism in NGH reservoir is proposed, which is based on the geological conditions of NGH reservoir in Shenhu area of the South China Sea, through an example, the heat and mass transfer law between wellbore and reservoir, NGH decomposition dynamics and formation yield failure evolution law during horizontal section drilling are analyzed. The simulation results show that in the process of drilling from the heel (0 m) to the toe (400 m) in the horizontal section, the annulus temperature in the same well depth decreases continuously, the annulus temperature at the heel decreases from 15.973 °C to 15.794 °C. The NGH decomposition range starts from the heel and continues to expand to the toe, and the NGH saturation at the heel decreases from 0.4 to 0.169 (about 57.75%), where the NGH decomposition is the most. With the decomposition of NGH, the formation around the wellbore begins to yield and destroy, and the yield range continues to increase and gradually expands from the heel to the toe like the NGH saturation. When drilling to 1 h, the formation on the upper and lower sides of the wellbore at the heel first appears plastic yield. After 20 min, the formation on the left and right sides of the wellbore appears plastic yield. When drilling to 10 h, the plastic strain of the heel formation reaches 0.0586 and the maximum yield radius reaches 0.1157 m. The above work can provide theoretical reference for the variation law of formation physical parameters and wellbore stability analysis in the process of NGH reservoir drilling.

Keywords: Natural gas hydrate · Drilling · Wellbore-formation coupling · Thermal hydrosolid coupling · Wellbore stability · Numerical simulation

B. Sun et al. (Eds.): DWOG-Hyd 2021, LNCE 246, pp. 47–59, 2022.
https://doi.org/10.1007/978-981-19-0960-3_5

1 Introduction

NGH is one of the potential green alternative energy sources. Relevant studies show that the global NGH reserves are about 3000–20000 trillion cubic meters, and its total carbon content is about twice that of traditional fossil energy [1]. At present, the main methods for exploiting NGH in sea areas include depressurization, thermal stimulation, replacement, chemical injection and the combination of the above methods [2], Regardless of what type of exploitation method is adopted, the NGH reservoir needs to be opened by drilling.

However, the offshore NGH formation has the characteristics of large water depth, shallow seabed burial and under compaction. Therefore, the problem of wellbore stability is extremely prominent in the drilling process of offshore NGH reservoir [3].

Firstly, NGH formation is generally semi-consolidated and unconsolidated sandstone or argillaceous sandstone formation with weak deformation resistance [4]. Secondly, the circulation and invasion of drilling fluid will interfere with the temperature and pressure distribution of the formation during drilling, resulting in NGH decomposition, redistribution of formation stress and change of mechanical properties of the formation [5], which is very easy to cause the risk of wellbore instability.

In terms of numerical simulation of mechanical properties of NGH bearing sediments, only a few THC model have been proposed in the world, mainly including TOUGH + HYDRATE + FLAC, COHMA and MHGS. Soga et al. [6] proposed a multi field coupling model for NGH formation, which can simulate the changes of mechanical properties of NGH formation during NGH development. Zhao et al. [7] proposed the change law of mechanical strength of NGH bearing formation during the production process by simulating the three field coupling problem of seepage, heat transfer and deformation in the production process of NGH. Sun [8] simulated and analyzed the influence of NGH drilling and production process on formation physical parameters by embedding the critical state constitutive model into the multi field coupling numerical model. Taking Shenhu NGH reservoir in the South China Sea as an example, Sun [9] and others studied the wellbore stability under the condition of drilling fluid invasion through the coupling of TOUGH + FLAC3D.

By investigating the domestic and foreign literature, it is found that the current model does not specifically consider the dynamic drilling process of horizontal wells and the dynamic heat and mass transfer process between wellbore and formation. Therefore, this work establishes a wellbore-reservoir coupling wellbore stability evaluation model considering the coupling mass transfer and heat transfer law between wellbore and reservoir during horizontal well dynamic drilling and the THC mechanism of NGH reservoir. Based on the geological conditions of NGH reservoir in Shenhu area of South China Sea, the heat and mass transfer law between wellbore and reservoir, NGH decomposition dynamics and evolution law of wellbore yield failure during horizontal section drilling are analyzed through an example. This study is expected to provide a theoretical reference for the safe and efficient well construction of NGH reservoirs in the South China Sea.

2 Wellbore-Reservoir Coupling Heat and Mass Transfer Model

Micro overbalance drilling is usually used to prevent excessive reservoir pollution during NGH reservoir drilling [10]. Therefore, the high-temperature drilling fluid will invade NGH formation along wellbore due to differential pressure, resulting in NGH decomposition and the deterioration of formation mechanical properties, which significantly increases the risk of wellbore instability. In order to properly establish the mathematical model, we make the following assumptions:

(1) The fluid flow in the wellbore is one-dimensional;
(2) The influence of filter cake on drilling fluid invasion is not considered;
(3) NGH reservoir is homogeneous, with uniform porosity, permeability and saturation;
(4) The specific heat and thermal conductivity of drilling fluid, NGH, rock matrix and pipe string are constant;
(5) The density of NGH remains unchanged, NGH is incompressible and does not flow with gas and liquid.

2.1 Heat and Mass Transfer Model of the Fluid Flow in the Wellbore

Riserless drilling technology is often used in the drilling of NGH reservoir. The calculation method of annulus pressure is as follows [5]:

$$\frac{dp}{dz} + f\frac{\rho_m v_a^2}{2d_c} - \rho_m g\sin\theta = 0 \tag{1}$$

Where, p is the annulus pressure, MPa; z is the distance from mudline, m; f is the friction coefficient, dimensionless; ρ_m is the drilling fluid density, kg·m^3; v_a is the velocity of drilling fluid in annulus, m/s; d_c is the equivalent diameter of annulus, m; g is the gravitational acceleration, m/s^2; θ is deviation angle, °.

Low viscosity drilling fluid is often used in NGH reservoir drilling, and the calculation method of friction coefficient f is as follows [11]:

$$\begin{cases} f = 64/Re(\mathrm{Re} \le 2300) \\ f = 0.1927/\mathrm{Re}^{0.25}(\mathrm{Re} > 2300) \end{cases} \tag{2}$$

Where, Re is the Reynolds number.

In the process of drilling fluid circulation, there is a dynamic heat exchange process among drill string, annulus and NGH formation. According to the law of energy conservation, the heat transfer equation in the well is as follows [12]:

$$\frac{\partial T_p}{\partial t} + v_p\frac{\partial T_p}{\partial z} = \frac{2\pi r_{pi}U_p}{C_m\rho_m A_p}(T_a - T_p) \tag{3}$$

$$\frac{\partial T_a}{\partial t} = v_a\frac{\partial T_a}{\partial z} - A\left(T_a - T_p\right) + B(T_{e,0} - T_a) \tag{4}$$

$$\begin{cases} A = 2\pi r_{pi}U_p/(C_m\rho_m A_a) \\ B = 2\pi r_{ci}U_a/(C_m\rho_m A_a) \end{cases} \tag{5}$$

Where, T_a and T_p is the annulus and drill pipe temperature, respectively, °C; t is the time, s; v_p is the velocity of drilling fluid in drill pipe, m/s; r_{pi} is inner diameter of drill pipe, m; C_m is the specific heat of drilling fluid, J/(kg·°C); A_p is the area of drill pipe, m^2; T_e is the formation temperature, °C.

Comprehensive heat transfer coefficients U_a and U_p refer to the total thermal resistance of drill string to annulus and annulus to NGH formation respectively. The calculation method is as follows [13]:

$$U_p^{-1} = \frac{1}{h_{pi}} + \frac{r_{pi}\ln\left(r_{po}/r_{pi}\right)}{k_p} + \frac{r_{pi}}{r_{po}h_{po}} \tag{6}$$

$$\begin{cases} U_a^{-1} = \frac{1}{h_{ci}} + \frac{r_{ci}\ln\left(\frac{r_{co}}{r_{ci}}\right)}{k_c} + \frac{r_{co}\ln\left(\frac{r_w}{r_{co}}\right)}{k_{cem}} \\ (H_s < h \le H_c) \\ U_a^{-1} = \frac{1}{h_{hole}} (H_c < h \le H_w) \end{cases} \tag{7}$$

Where, r_{ci} is the inner diameters of casing, m; r_{po}, r_{co} and r_w are the outer diameters of drill pipe, casing and wellhole, respectively, m; k_p, k_c and k_{cem} are heat conductivities of drill pipe, casing and cement sheath, respectively, w/(m·°C); h_{pi}, h_{po}, h_{ci} and h_{hole} are convection heat transfer coefficients of inner wall of drill pipe, outer wall of drill pipe, inner wall of casing and inner wall of wellhole, respectively, w/(m·°C); H_c, H_s and H_w are depth of casing, sea and well, respectively, m.

2.2 Heat and Mass Transfer Model of the Fluid Flow in the NGH Formation

Based on the continuity equation and generalized Darcy's law, the fluid solid coupling seepage equation of NGH reservoir is obtained [14]:

$$\frac{\partial\left(\varphi\rho_g S_g\right)}{\partial t} - \nabla\cdot\left(\frac{K_{rg}\rho_g}{\mu_g}[K]\left(\nabla P_g + \rho_g g\right)\right) + \left(\varphi\rho_g S_g\right)\nabla\cdot v_s = m_g + q_g \tag{8}$$

$$\frac{\partial(\varphi\rho_w S_w)}{\partial t} - \nabla\cdot\left(\frac{K_{rw}\rho_w}{\mu_w}[K](\nabla P_w + \rho_w g)\right) + (\varphi\rho_w S_w)\nabla\cdot v_s = m_w + q_w \tag{9}$$

$$\frac{\partial(\varphi\rho_h S_h)}{\partial t} + \nabla(\varphi\rho_h S_h v_s) = -m_h \tag{10}$$

Where, φ is the porosity, dimensionless; ρ_g, ρ_w and ρ_h are the density of gas, water and NGH, respectively, kg/m^3; S_g, S_w and S_h are the saturation of gas, water and NGH, respectively, dimensionless; K_{rg} and K_{rw} are the relative permeability of gas phase and water phase, respectively, dimensionless; μ_g and μ_w are the viscosity of gas and water, respectively, mPa·s; [K] is the permeability matrix, m^2; P_g and P_w are the pressure of gas phase and water phase, respectively, MPa; v_s is the rock matrix migration velocity, m/s; m_g and m_w are the gas and water production rate of NGH decomposition in unit volume formation, respectively, $kg/(m^3\cdot s)$; m_h is the NGH decomposition rate in unit volume formation, $kg/(m^3\cdot s)$; q_g and q_w are the sources of gas and water, respectively, $kg/(m^3\cdot s)$.

The relative permeability model adopts the formula proposed by Leverett [15]:

$$K_{rg} = (1 - se)^2\left(1 - se^2\right) \tag{11}$$

$$K_{rw} = \sqrt{se}\left(1 - \left(1 - se^{1/w}\right)^w\right) \tag{12}$$

$$se = \frac{S_w - S_{wr}}{1 - S_{wr} - S_{gr}} \tag{13}$$

Where, S_{wr} and S_{gr} are the residual water saturation and residual gas saturation, respectively, dimensionless; w is the relative permeability coefficient, dimensionless, value 0.6.

Based on Kim Bishnoi [16] NGH decomposition kinetic model, the gas production rate of NGH decomposition per unit volume of formation is:

$$m_h = -M_h k_d \exp\left(\frac{\Delta E}{RT}\right) A_h\left(p_{eq} - p_e\right) \tag{14}$$

$$A_h = 0.879\frac{1 - \varphi}{r_p} S_h^{2/3} \tag{15}$$

Where, M_h is the molar mass of NGH, kg/mol; k_d is the intrinsic reaction constant of the NGH, whose value is 2.6 × 105 mol/(Pa·s·m^2); ΔE is the hydration activation energy with a value of 104,000 J/mol; R is gas constant, J/(mol·K); T is the temperature, K; p_{eq} is the NGH equilibrium pressure, MPa; p_e is the pore pressure of NGH formation, MPa; r_p is the average grain size of reservoir matrix, m.

The heat transfer model of NGH reservoir is as follows [17]:

$$\rho C\frac{\partial T}{\partial t} = \nabla \cdot (\lambda \nabla T) - \nabla \cdot [(\varphi S_g C_g \rho_g v_g + \varphi S_w C_w \rho_w v_w)T] - m_h \Delta H_D + Q_{in} \tag{16}$$

$$\rho C = (1 - \varphi)\rho_s C_s + \varphi S_h \rho_h C_h + \varphi S_g \rho_w C_w + \varphi S_g \rho_g C_g \tag{17}$$

$$\lambda = (1 - \varphi)\lambda_s + \varphi S_h \lambda_h + \varphi S_w \lambda_w + \varphi S_g \lambda_g \tag{18}$$

$$\Delta H_D = 446.12 \times 10^3 - 132.638T \tag{19}$$

Where, C_g, C_w, C_s, C_h are the specific heat of gas, water, rock matrix and NGH, respectively, J/(kg·K); ρ_s is the density of rock matrix, kg·m^3; v_g and v_w are the seepage velocity of water and gas, respectively, m/s; ΔH_D is the enthalpy change of NGH decomposition, J/mol; Q_{in} is the external heat supply, W/(m·K); λ_s, λ_h, λ_w and λ_g are the thermal conductivity of rock matrix, NGH, water and gas, respectively, W/(m·K).

2.3 Wellbore Stability Model of NGH Reservoir

In order to reflect the influence of NGH decomposition process on formation physical parameters, it is also necessary to establish the relationship equation of mechanical parameters such as elastic modulus, cohesion and permeability with formation effective stress and NGH saturation [18].

1) Dynamic model of elastic modulus
Liao [1] obtained the relationship between elastic modulus and saturation of NGH formation by regression fitting NGH pilot production field and experimental data as follows:

$$\log E_{S_{h0}} = \log E_{S_{h0}} + 1.1983 S_h \tag{20}$$

Where, E is the elastic modulus of NGH formation, MPa; Sh_0 is the initial NGH saturation, dimensionless.
2) Dynamic model of cohesion
Miyazaki et al. [19] established an empirical model between cohesion and NGH saturation as follows:

$$C_{S_h} = C_{S_{h0}} + \frac{1 - \sin\phi}{2\cos\phi} \alpha S_h^{\beta} \tag{21}$$

Where, C is the cohesion of NGH formation, MPa; α and β are the empirical coefficients, dimensionless.
3) Dynamic model of permeability
The permeability of NGH formation is jointly affected by NGH saturation and formation effective stress. This work adopts the following negative exponential equation [20]:

$$K = K_0 \exp[-(dS_h + e\sigma)] \tag{22}$$

Where, K_0 is the permeability at NGH saturation of 0, m^2; d and e are the empirical coefficients, dimensionless; σ is the effective stress, MPa.
4) Dynamic model of effective porosity
Shen [21] considered the influence of NGH decomposition and the change of formation effective stress on porosity, and obtained the calculation equation of NGH formation effective porosity:

$$\varphi = \varphi_0 (1 - S_h) \times m \bullet \exp(n \bullet \sigma) \tag{23}$$

Where, φ_0 is the porosity at NGH saturation of 0, dimensionless; m and n are the empirical coefficients, dimensionless.
5) Wellbore yield failure criterion
The formation yield failure of NGH reservoir is mainly caused by shear failure near wellbore. In this work, Mohr-Coulomb model is adopted, and the expression is as follows [22]:

$$\sigma_1 = \frac{1 + \sin\phi}{1 - \sin\phi} \sigma_3 + \frac{2C\cos\phi}{1 - \sin\phi} \tag{24}$$

Where, σ_1 and σ_3 are the maximum and minimum principal stress, respectively, MPa.

3 Simulation Results and Discussion

3.1 Basic Parameters

The NGH production test in the South China Sea shows that the buried depth of NGH layer is about 1225 m, the thickness ranges from a few meters to hundreds of meters, and the NGH saturation can be as high as 70% [10]. Table 1 gives the basic parameters of NGH reservoir [1, 23].

Table 1. Basic parameters

Parameter	Value
Depth of seawater (m)	1225.23
Depth of NGH layer (m)	1433.03–1478.63
Porosity	0.45
NGH saturation	0.4
Average permeability (mD)	10
Temperature of mudline (°C)	4
Casing inner diameter (mm)	339.7
Wellbore diameter (mm)	311.15
Drilling fluid density (kg/m^3)	1190
Rate of penetration (m/h)	40
Injection rate (L/s)	50
Injection temperature (°C)	25
Pressure of NGH formation (MPa)	14.725
Temperature of NGH formation (°C)	15
Geothermal gradient (°C/m)	0.0469
Young's modulus (MPa)	32($S_h = 0$); 96($S_h = 0.4$)
Cohesion (MPa)	0.1($S_h = 0$); 0.7($S_h = 0.4$)
Poisson's ratio	0.35
Dilation angle (deg)	10

3.2 Simulation Results

Figure 1 illustrates the temperature profile of the horizontal wellbore during drilling. As shown in the figure, as the wellbore continues to extend, the annulus temperature decreases. The annulus temperature at the heel of the horizontal well (0 m) drops from 15.973 °C to 15.794 °C. This is because the contact range between drilling fluid and

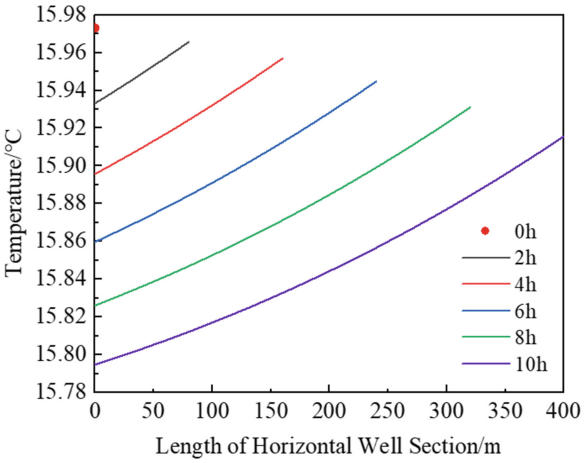

Fig. 1. Annulus temperature at different drilling times

the formation increases as well depth increases, resulting in more heat transfer from the drilling fluid to the formation.

The wellbore pressure profile when the horizontal section is drilled to 400 m is shown in Fig. 2. For the wellbore pressure, because the influence of temperature and pressure changes on the density and rheology of drilling fluid is negligible, the flow of drilling fluid in the wellbore is stable. Affected by the flow friction of drilling fluid, the annulus pressure increases with the increase of well depth. Besides, the mudline pressure is usually basically constant when drilling in NGH formation. Therefore, the pressure in the same well depth is basically unchanged during the forward extension of the wellbore.

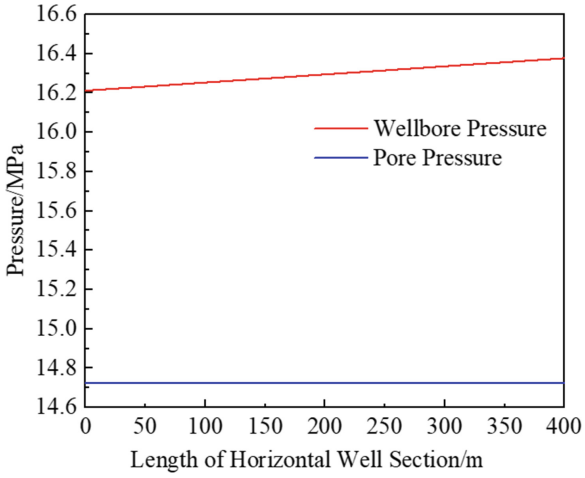

Fig. 2. Annular pressure in horizontal section

The decomposition of NGH in formation is the fundamental reason for the deterioration of formation mechanical properties, which is affected by formation temperature and pressure. Figure 3 shows the variation of near-wellbore NGH saturation over time during drilling. It can be seen that the NGH in the formation continues to decompose with the continuous extension of the wellbore, but the NGH decomposition is uneven because of the difference of pressure and temperature. The NGH decomposition range starts from the heel and continues to expand to the toe. The formation at the heel has the most NGH decomposition and the NGH saturation at the heel decreases from 0.4 to 0.169 (about 57.75%) when drilling to 400 m. This is because the formation at the heel has the longest contact time with drilling fluid, the most drilling fluid intrudes into the formation and the NGH is most significantly affected by temperature. Although the increase of pressure inhibits the NGH decomposition to a certain extent, the increase of pressure also promotes the drilling fluid to invade the NGH formation, further aggravating the NGH decomposition.

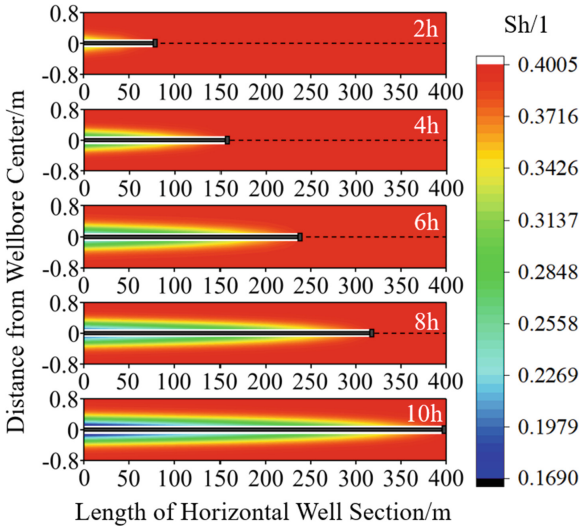

Fig. 3. Distribution of NGH saturation around the wellbore at different drilling times

The decomposition of NGH will significantly reduce the formation elastic modulus and cohesion which further weakens the mechanical strength of the formation, which is the root cause of wellbore instability. As shown in Fig. 4, with the extension of the wellbore, NGH is constantly decomposed, especially at the heel, which leads to the failure of the formation around the well, and the yield range gradually extends from the heel to the toe like the NGH saturation.

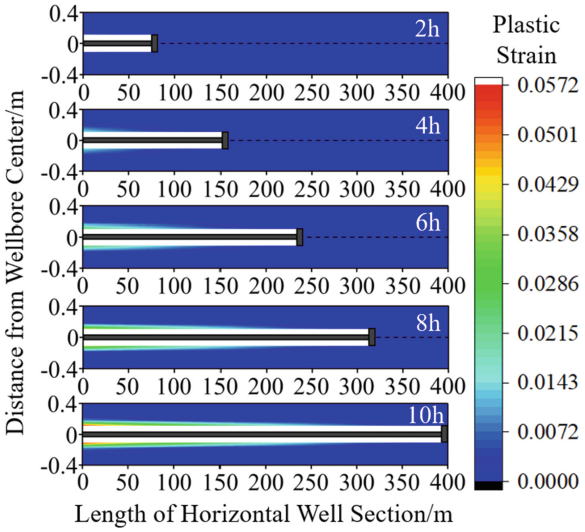

Fig. 4. Plastic strain of formation around well with different drilling time

As shown in Fig. 5, plastic strain began to occur in the formation near the heel of the well one hour after drilling. However, due to the difference between horizontal and vertical ground stress, plastic strain occurred in the formation at the upper part of the wellbore first than in the formation at the left and right sides, with a greater degree and a faster growth rate. Due to the influence of gravity, there are also differences in the force and plastic strain on the upper and lower sides of the well. The plastic strain on the immediate side of the well is slightly higher than that on the immediate side of the well. However, it is found through simulation that due to the small size of the well, the difference only accounts for 0.3% of the plastic strain on the immediate side of the well, which can be ignored.

Figure 6 describes the plastic strain of horizontal well heel formation at different drilling times. It can be seen that with the increase of drilling time, the plastic strain area of the formation around the well becomes larger. The maximum yield radius is 0.0219 m at 2 h, 0.0657 m at 6 h, 0.1157 m at 10 h, and the plastic strain reaches 0.0586. Therefore, in order to ensure the wellbore stability of NGH formation, the drilling time should be shortened.

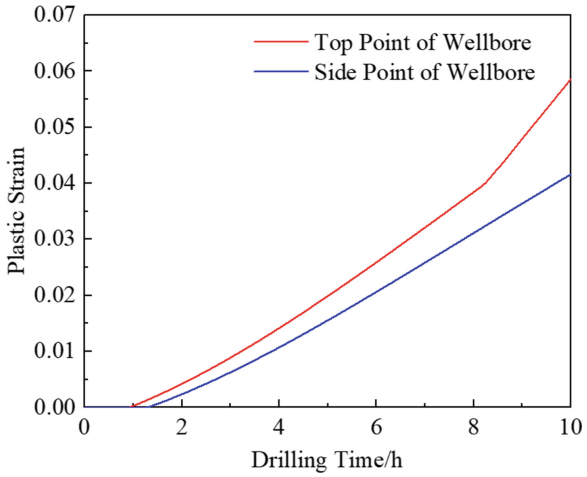

Fig. 5. Plastic strain of formation on the top and side point of wellbore

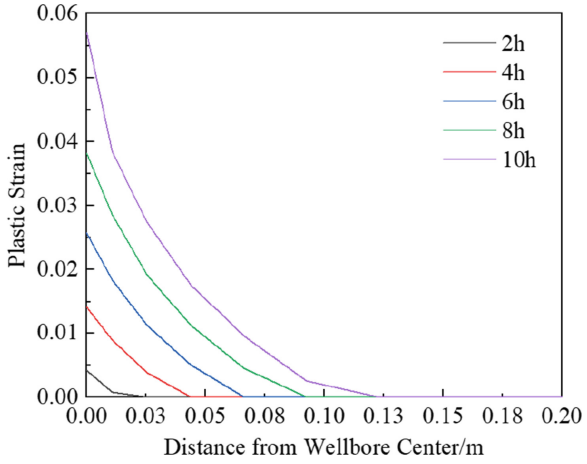

Fig. 6. Plastic strain of formation at heel at different drilling times

4 Conclusion

In this work, a wellbore stability evaluation model considering the coupling mass and heat transfer process between wellbore and reservoir during horizontal well dynamic drilling and the THC mechanism in NGH reservoir is proposed. Based on the geological conditions of NGH reservoir in Shenhu area of the South China Sea, the heat and mass transfer law between wellbore and reservoir, dynamic law of NGH decomposition and the evolution law of formation yield failure are analyzed through an example. The main conclusions are as follows:

(1) As the well extends, the annulus temperature in the same depth decreases. The annulus temperature at the heel decreased from 15.973 °C to 15.794 °C during drilling from the heel (0 m) to the toe (400 m) in the horizontal section. This is because the increase of well depth leads to the larger contact range between drilling fluid and formation and the increase of heat exchange.
(2) Due to the difference of pressure and temperature, the decomposition range of NGH increases from the heel and extends to the toe. The NGH decomposition is the most at the heel. When drilling to 400 m, the NGH saturation decreases to 0.169, about 57.75% of the decomposition. This is because the formation at the heel has the longest contact time with the drilling fluid, the most drilling fluid intrudes into the formation and the NGH is most significantly affected by temperature.
(3) With the decomposition of NGH, the formation around the well begins to yield, and the yield range keeps increasing and gradually extends from the heel to the toe like the NGH saturation. Due to the difference between horizontal in-situ stress and vertical in-situ stress, plastic yield first appeared on the upper and lower sides of the well at the heel for 1 hour, and then on the left and right sides of the well for 20 minutes. The plastic strain of formation at the heel reached 0.0586 and the maximum yield radius reached 0.1157 m after 10 hours of drilling. In order to ensure the wellbore stability of NGH formation, the drilling time should be shortened.

Acknowledgement. The authors would like to appreciate the financial support from major scientific and technological project of CNPC "Research on Basic and Key Technologies of Offshore Gas Hydrate Pilot Production Engineering" (No.: zd2019-184-004), the national key R&D plan "Dynamic Response Behavior and Control of Per Wellbore Reservoir During Natural Gas Hydrate Production" (No.: 2018yfe0126400), "Prevention and Control Process and Technical System for Safe Reservoir Exploitation Based on Productivity Optimization" (No.: 2021dq0502) supporting the national science and technology project of CNPC.

References

1. Liao, Y.Q., Wang, Z.Y., Chao, M.Z., et al.: Coupled wellbore–reservoir heat and mass transfer model for horizontal drilling through hydrate reservoir and application in wellbore stability analysis. J. Nat. Gas Sci. Eng. **95**, 104216 (2021)
2. Collett, T.S., Johnson, A.H., Knapp, C.C., et al.: Natural gas hydrates-a review. Browse Collect. **89**, 146–219 (2009)
3. Zhou, B.Y.: Study on drilling hydraulic parameter design and wellbore stability in deep water gas hydrate formation. Dissertation, China University of Petroleum (East China), Qingdao (2021)
4. Ning, F.L.: Research on wellbore stability in gas hydrate formation. Dissertation, Geological Engineering, Wuhan (2005)
5. Liao, Y.Q., Sun, X.H., Sun, B.J., et al.: Transient gas-liquid-solid flow model with heat and mass transfer for hydrate reservoir drilling. Heat Mass Tran **141**, 476–486 (2019)
6. Klar, A., Uchida, S., Soga, K.: Explicitly coupled thermal flow mechanical formulation for gas-hydrate sediments. SPE J. **18**(2), 196–206 (2013)
7. Zhao, Z.W., Bi, X.S., Fu, C.J.: Three field coupling analysis of formation stability caused by hydrate mining. J. Liaoning Univ. Eng. Technol. Nat. Sci. Ed. **33**(4), 470–475 (2014)

8. Sun, X.: Numerical simulation of sediment mechanical behavior considering the influence of hydrate decomposition. Dissertation, Dalian University of Technology (2017)
9. Sun, X., Wang, L., Luo, H., et al.: Numerical modeling for the mechanical behavior of marine gas hydrate-bearing sediments during hydrate production by depressurization. Petrol. Sci. Eng. **177**, 971–982 (2019)
10. Ye, J., Qin, X., Xie, W., et al.: Main progress of the second gas hydrate trial production in the South China Sea. Chin. Geol. **47**(3), 557–568 (2020)
11. Wang, Z., Sun, B., Wang, J., et al.: Experimental study on the friction coefficient of supercritical carbon dioxide in pipes. Int. J. Greenhouse Gas Control **25**, 151–161 (2014)
12. Liao, Y.Q., Sun, X.H., Sun, B.J., et al.: Geothermal exploitation and electricity generation from multibranch U-shaped well-enhanced geothermal system. Renew Energy **163**, 2178–2189 (2021)
13. Hasan, A.R., Kabir, C.S.: Wellbore heat-transfer modeling and applications. Petrol. Sci. Eng. **86**, 127–136 (2012)
14. Sun, X., Nanchary, N., Mohanty, K.K.: 1-D modeling of hydrate depressurization in porous media. Transp. Porous Media **58**(3), 315–338 (2005)
15. Leverett, M.C.: Capillary behavior in porous solids. Trans. AIME **142**(01), 152–169 (1941)
16. Kim, H.C., Bishnoi, P.R., Heidemann, R.A., et al.: Kinetics of methane hydrate decomposition. Chem. Eng. Sci. **42**(7), 1645–1653 (1987)
17. Zhang, H., Cheng, Y.F., Li, Q.C., et al.: Numerical analysis of wellbore instability in gas hydrate formation during deep-water drilling. J. Ocean Univ. China **17**(01), 8–16 (2018). https://doi.org/10.1007/s11802-018-3447-4
18. Zhou, B.Y., Guo, Y.H., Liao, Y.Q., et al.: Study on coupling simulation of multiple physical fields in drilling gas hydrate formation. In: Proceedings of the 31st National Symposium on Hydrodynamics, Beijing, pp. 1228–1238. Ocean Press (2020)
19. Miyazaki, K., Yamaguchi, T., Sakamoto, Y., et al.: Effect of confining pressure on mechanical properties of sediment containing synthetic methane hydrate. MMIJ **126**(7), 408–417 (2010)
20. Zhai, C., Sun, K.M., Xin, L.W., et al.: Experimental study on permeability of hydrate sediments with different saturation during effective stress rise and fall. Exp. Mech. **31**(03), 399–408 (2016)
21. Shen, H.C.: Study on fluid solid coupling numerical simulation of depressurization production in natural gas hydrate reservoir. Dissertation, China University of petroleum, Beijing (2009)
22. Sun, J., Ning, F., Lei, H., et al.: Wellbore stability analysis during drilling through marine gas hydrate-bearing sediments in Shenhu area: a case study. Petrol. Sci. Eng. **170**, 345–367 (2018)
23. Rutqvist, J., Moridis, G.J., Grover, T., et al.: Coupled multiphase fluid flow and wellbore stability analysis associated with gas production from oceanic hydrate bearing sediments. Petrol. Sci. Eng. **92–93**(4), 65–81 (2012)

Experimental Study on Strength Characteristics of Hydrate Argillaceous Siltstone Under Immersion of Drilling Fluid

Yubin Wang[1], Baojiang Sun[2(✉)], Hongzhi Xu[1], Zhenggang Gong[2], and Zhiyuan Wang[2]

[1] CNPC Engineering Technology Research Co., Ltd., Tianjin 300450, China
[2] Key Laboratory of Unconventional Oil and Gas Development, Ministry of Education, China University of Petroleum (East China), Qingdao 266580, China
sunbj1128@vip.126.com

Abstract. In order to reveal the influence of drilling fluid immersion on rock strength during open circuit drilling of hydrate argillaceous siltstone reservoir in Shenhu sea area of the South China Sea, the mechanical experiment of drilling fluid immersion in rock was carried out by using GCTS RTR-2000 rock triaxial comprehensive test system, and the influence law and internal mechanism of drilling fluid immersion on argillaceous siltstone were analyzed. The results show that the peak strength, elastic modulus, cohesion and other mechanical parameters of argillaceous siltstone decrease in varying degrees after immersion in drilling fluid. Rock softening, hydraulic splitting effect and chemical damage caused by the contact between drilling fluid components and rock are the main reasons for the weakening of rock strength. Therefore, in the drilling process of deep-water hydrate argillaceous siltstone reservoir, on the one hand, the hydrate decomposition effect caused by the drilling fluid invading the formation weakens the formation mechanical strength; On the other hand, the immersion of drilling fluid further destroys the mechanical strength of rock. Under the combined action of the two, the risk of wellbore instability during drilling is great. The research results have certain guiding significance for the field.

Keywords: Argillaceous siltstone · Peak strength · Modulus of elasticity · Wellbore instability · Drilling fluid

1 Introduction

Under the wave of energy substitution, hydrate, as a new clean energy, has become the focus of energy development all over the world in recent years. The United States, Canada and Japan have successively carried out the trial production of hydrate. China has carried out two rounds of trial production of hydrate in 2017 and 2020, both of which have been successfully carried out and made a series of major breakthroughs. The South China Sea is rich in hydrate resources, and the exploitation of hydrate is of great strategic significance to China's energy security. At present, the exploitation

B. Sun et al. (Eds.): DWOG-Hyd 2021, LNCE 246, pp. 60–71, 2022.
https://doi.org/10.1007/978-981-19-0960-3_6

of hydrate still faces a series of problems. The hydrate reservoir in the South China Sea is mostly argillaceous siltstone, which has the characteristics of weak cementation, poor diagenesis and weak formation mechanical properties [1–6]. In the process of open circuit drilling of deep-water hydrate, the reservoir rock with poor mechanical properties will be further damaged after soaking in drilling fluid, resulting in wellbore instability. The wellbore instability will lead to a series of drilling problems [7], such as logging difficulties, poor cementing quality, downhole tool lowering difficulties, etc.

The damage of drilling fluid immersion to rock can usually be characterized by the changes of parameters related to rock mechanical strength. In this regard, scholars at home and abroad have carried out a lot of basic research. Ge et al. [8–10] applied CT scanning to study the micro deformation characteristics and crack evolution law of brittle rock under external load, and pointed out that the hydration expansion and chemical alkali solution dissolution caused by drilling fluid invasion are the main causes of rock instability. Huang et al. [11] quantitatively analyzed the stress distribution around the wellbore, hydration stress and wellbore collapse cycle from the perspective of mechanics and chemical coupling of mud shale. In the aspect of mudstone hydration research, M.E. [12] conducted an indoor test, expressed the expansion pressure by using the water activity of shale, studied the flow and distribution of water in shale through thermal diffusion theory, put forward the concept of hydration stress, established relevant models, and opened up a precedent in the quantitative study of mudstone mechanical-chemical coupling. However, there are relatively few studies on the strength characteristics of argillaceous siltstone under the immersion of drilling fluid. Therefore, it is necessary to carry out some basic research on the damage effect of drilling fluid on argillaceous siltstone during deep-water drilling. Taking the argillaceous siltstone in Shenhu sea area as the research object, a series of experiments on the effect of drilling fluid immersion on rock mechanical strength are carried out, which has certain guiding significance for the exploration of wellbore stability in the process of deep-water hydrate mining.

2 Rock Sample Preparation and Experimental Methods

2.1 Sample Preparation

It is very difficult to carry out experiments in the field when studying the mechanical properties of hydrate argillaceous siltstone. Therefore, indoor preparation of soil samples for experimental research is the most commonly used means. In this paper, the test samples are obtained by crushing after mixing quartz sand and clay minerals (montmorillonite and illite), which are similar to the particle size composition of natural gas hydrate reservoir in Shenhu sea area of the South China Sea, so as to ensure the similarity of particle size composition of soil layer. The clays used in the experiment are dried and crushed. The core sample preparation equipment is used to prepare the soil sample into ϕ25 mm × 50 mm standard sample according to Test method for engineering rock mass GB/T50266-999, as shown in Fig. 1. The particle size composition of soil sample in the experiment is shown in Table 1.

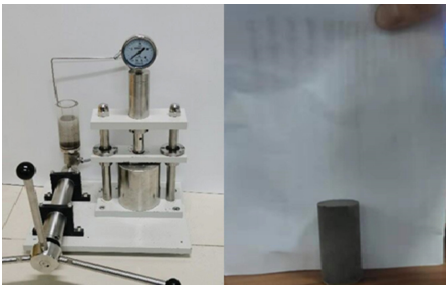

Fig. 1. Core preparation device and sample

Table 1. Grain size composition of hydrate bearing sediments in Shenhu sea area of the South China Sea [13]

Particle size	SH-7B
<4 μm	0.4
4–63 μm	23.5
63–250 μm	32.2
250–500 μm	29.1
500–2000 μm	14.8
>2 mm	0

2.2 Experimental Method

The experimental equipment in this paper is GCTS RTR-2000 high temperature and high pressure rock triaxial comprehensive test system, as shown in Fig. 2. The system is a set of closed-loop digital servo control device, which is used for simple and fast triaxial test of rock samples. It can simulate the test of uniaxial or triaxial compression, creep, relaxation, compressive strength, tensile strength, shear strength, elastic modulus, bulk modulus, shear modulus, permeability, Biot constant and other parameters of the formation rock. The design indexes of high temperature and high pressure triaxial chamber are: axial load: 1000–4600 kN, frame stiffness: 10.5 MN/mm, dynamic frequency: 0–10 Hz, confining pressure: 210 Mpa, pore pressure: 210 Mpa, core size: 25-100 mm, temperature: 150 °C, 200 °C. The whole device can realize automatic data collection, and the collected data can also automatically generate original data report, analysis report and curve chart, which has a strong intelligent function.

In order to accurately obtain the influence law of drilling fluid immersion on rock mechanical parameters, three groups of rock triaxial test experiments were carried out with effective confining pressures of 3 Mpa, 5 MPa and 7 MPa under the same immersion time. The soaking time of rock samples is 0, 1, 3 and 5 h respectively. Mechanical experiments are carried out after soaking. The rock size is ϕ25 mm × 50 mm. The specific experimental design is shown in Table 2.

Table 2. Experimental design of rock immersion with drilling fluid.

Soaking time	Effective confining pressure
0 h	3, 5, 7 MPa
1 h	3, 5, 7 MPa
3 h	3, 5, 7 MPa
5 h	3, 5, 7 MPa

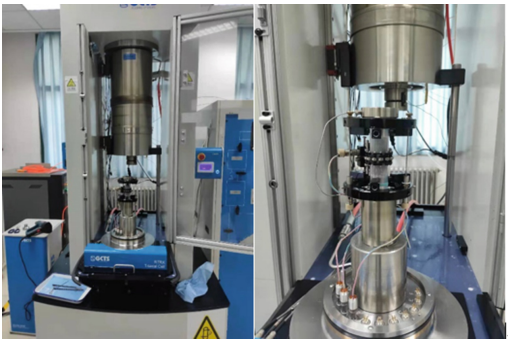

Fig. 2. GCTS RTR-2000 high temperature and high pressure triaxial tester

3 Experimental Results and Discussion

3.1 Calculation Method of Rock Mechanical Parameters

According to the experimental data obtained from rock triaxial test, the stress-strain curve of rock sample immersed in drilling fluid for different times can be drawn, as shown in Fig. 3, and then the relevant mechanical parameters of rock sample can be obtained.

The calculation formula of elastic modulus is [14]:

$$\mathrm{E} = \Delta\sigma / \Delta\varepsilon_1 \tag{1}$$

Where E is young's modulus of elasticity, MPa; $\Delta\sigma$ is the axial stress increment, MPa; $\Delta\varepsilon_1$ is the axial strain increment, mm/mm.

The natural shear strength (cohesion) C and internal friction angle φ of rock can be obtained through more than two sets of triaxial stress test data under different effective confining pressures. According the Mohr Coulomb strength criterion, the shear stress on the shear plane must overcome the inherent shear strength of the rock and the friction acting on the shear plane. The mathematical expression of M-C criterion is as follows:

$$|\tau| = C + f\sigma_n \tag{2}$$

Where τ is the shear strength of rock, MPa; σ_n is the normal stress on the shear plane, MPa; C is the cohesion of rock, MPa; f is the internal friction coefficient of rock, $f = \tan\varphi$, dimensionless; φ is the internal friction angle of rock, °.

According to the triaxial stress test data under three groups of different effective confining pressures, three stress Mohr circles can be obtained in the rectangular coordinate system. The envelope tangent to the stress Mohr circle is the M-C criterion curve, as shown in Fig. 4.

Using maximum principal stress σ_1 and minimum principal stress σ_3 to transform the Mohr-Coulomb criterion, the following results can be obtained:

$$\sigma_1 = \sigma_3 cot\left(45° - \frac{\varphi}{2}\right)^2 + 2Ccot\left(45° - \frac{\varphi}{2}\right) \tag{3}$$

The internal friction angle and cohesion of rock can be obtained by regression of multiple groups of experimental data through the above formula.

3.2 Variation of Mechanical Parameters of Argillaceous Siltstone Immersed in Drilling Fluid

It can be seen from the experimental curve in Fig. 3 that the stress-strain curve of argillaceous siltstone has no obvious compaction stage, the elastic stage is short, and the yield stage is relatively long, with obvious strain hardening characteristics; With the increase of effective confining pressure, the properties of rock tend to plastic development [15].

Figure 5 shows the variation of peak strength of argillaceous siltstone with different soaking time of drilling fluid under effective confining pressure of 3 Mpa. Figures 6, 7 and 8 show the variation laws of internal friction angle, cohesion and elastic modulus of argillaceous siltstone under different soaking time of drilling fluid. The changes of peak strength, internal friction angle, cohesion and elastic modulus of argillaceous siltstone under the immersion of drilling fluid reflect the strength characteristics of rock. It can be seen from the figure that with the increase of drilling fluid immersion time, the peak strength, cohesion and elastic modulus of rock decrease in varying degrees, and the internal friction angle has little change on the whole. Therefore, in the drilling process of deep-water hydrate argillaceous siltstone reservoir, on the one hand, a large number of hydrates in the reservoir are decomposed and the mechanical strength of the formation is weakened due to the heat exchange between the drilling fluid and the formation; On the other hand, the immersion of drilling fluid further destroys the mechanical strength of rock. Under the combined action of the two, the risk of wellbore instability during drilling is great.

There are many factors that weaken the mechanical strength of rock due to drilling fluid immersion. Firstly, due to the softness of rock, the strength of rock will be reduced after water immersion [9]. The softness of rock depends on the mineral composition and porosity. For argillaceous siltstone, the rock contains more hydrophilic and soluble minerals, and more open voids, so the rock has strong softening. Secondly, after the drilling fluid contacts with the rock, the fluid intrudes into the rock gap under the action of capillary force, permeability and hydrogen bond, resulting in stress concentration at the crack tip and "hydraulic splitting effect", resulting in the expansion of rock gap and the decrease of strength [16]. In addition, the relevant components of drilling fluid may have chemical reaction with minerals in the rock [10], so as to change the internal structure of the rock and further reduce the strength of the rock.

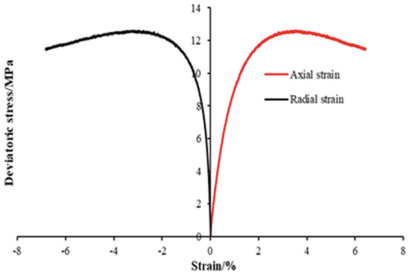

(a)Not soaked-effective confining pressure 3Mpa

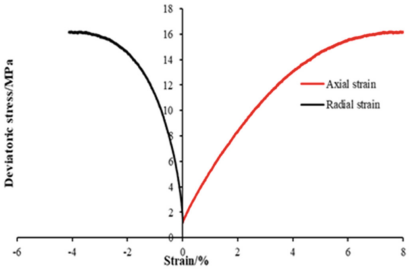

(b) Not soaked-effective confining pressure 5Mpa

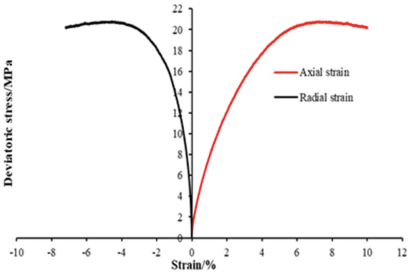

(c) Not soaked-effective confining pressure 7Mpa

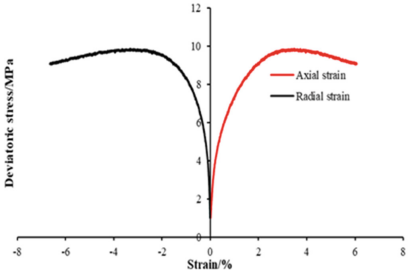

(d) Soaking for 1h-effective confining pressure 3Mpa

Fig. 3. Stress-strain curve of argillaceous siltstone

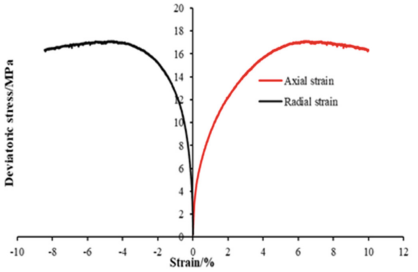

(e) Soaking for 1h-effective confining pressure 5Mpa

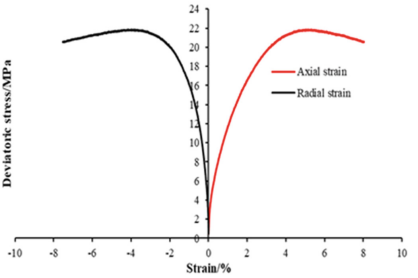

(f) Soaking for 1h-effective confining pressure 7Mpa

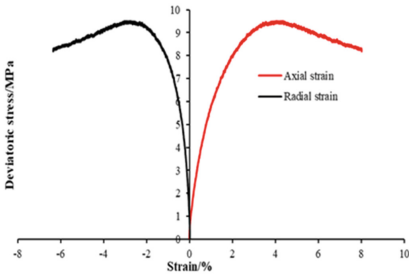

(g) Soaking for 3h-effective confining pressure 3Mpa

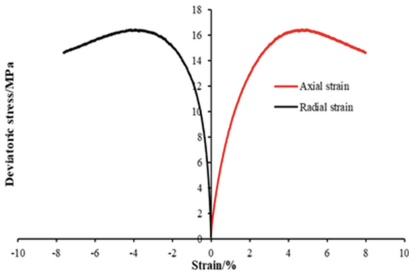

(h) Soaking for 3h-effective confining pressure 5Mpa

Fig. 3. continued

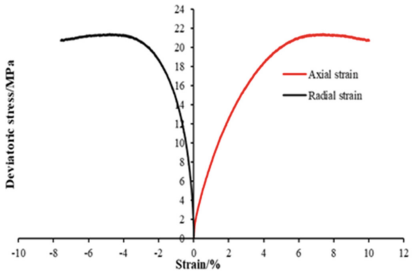

(i) Soaking for 3h-effective confining pressure 7Mpa

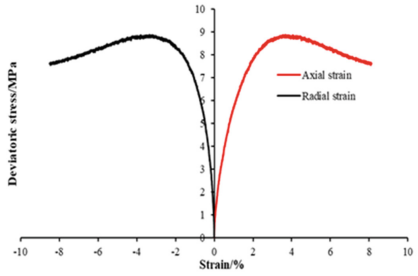

(j) Soaking for 5h-effective confining pressure 3Mpa

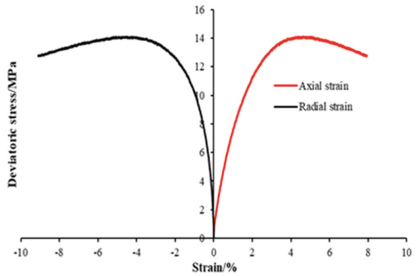

(k) Soaking for 5h-effective confining pressure 5Mpa

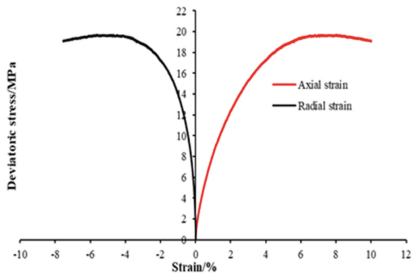

(l) Soaking for 5h-effective confining pressure 7Mpa

Fig. 3. continued

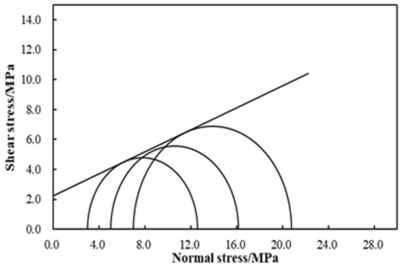

(a) Not soaked

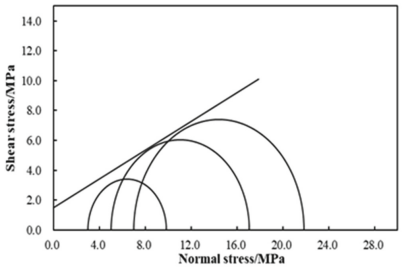

(b) Soaking for 1h

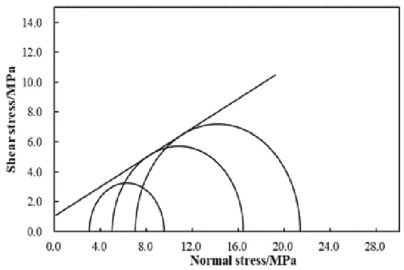

(c) Soaking for 3h

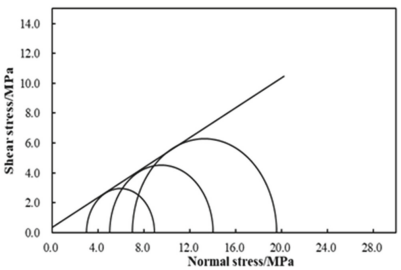

(d) Soaking for 5h

Fig. 4. Stress Mohr circle of argillaceous siltstone sample

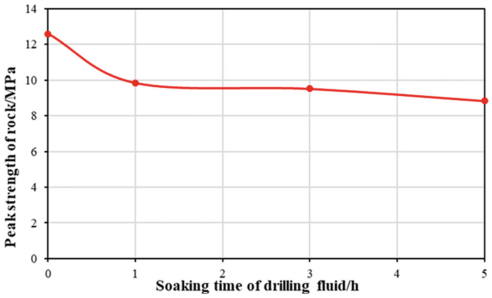

Fig. 5. Effect of drilling fluid immersion on rock peak strength

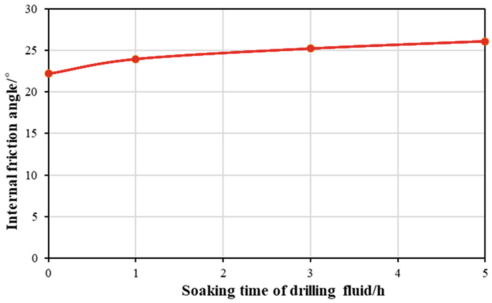

Fig. 6. Effect of drilling fluid immersion on internal friction angle of rock

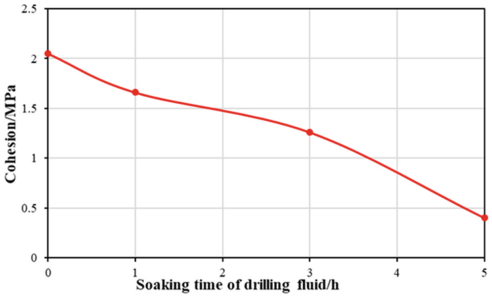

Fig. 7. Effect of drilling fluid immersion on rock cohesion

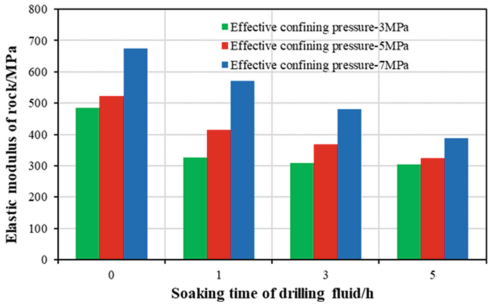

Fig. 8. Effect of drilling fluid immersion on rock elastic modulus

4 Conclusion

In this paper, according to the characteristics of hydrate argillaceous siltstone reservoir in Shenhu sea area of the South China Sea, the experimental study on the strength characteristics of reservoir rock by drilling fluid immersion is carried out. The main conclusions are as follows:

1) The peak strength, elastic modulus, cohesion and other mechanical parameters of argillaceous siltstone decreased in varying degrees after immersion in drilling fluid, and the decreasing range increased with the increase of immersion time, and the change of internal friction angle of rock was relatively stable.
2) There are many factors that weaken the mechanical strength of rock due to drilling fluid immersion. The main reasons are rock softening, hydraulic splitting effect and chemical damage caused by the contact between drilling fluid components and rock.
3) In the drilling process of deep-water hydrate argillaceous siltstone reservoir, on the one hand, due to the heat exchange between the drilling fluid and the formation, a large number of hydrates in the reservoir decompose and weaken the mechanical strength of the formation; On the other hand, the immersion of drilling fluid further destroys the mechanical strength of rock. Under the combined action of the two, the risk of wellbore instability during drilling is great.

References

1. Sloan, Jr., E.D.: Clathrate Hydrates of Natural Gases. Second Edn., Revised and Expanded. CRC Press, Boca Raton (1998)
2. Kim, H.C., Bishnoi, P.R., Heidemann, R.A., et al.: Kinetics of methane hydrate decomposition. Chem. Eng. Sci. **42**(7), 1645–1653 (1985)
3. Komatsu, Y., Suzuki, K., Fujii, T.: Sedimentary facies and paleoenvironments of a gas-hydrate-bearing sediment core in the eastern Nankai Trough. Japan. Marine. Petrol. Geol. **66**, 358–367 (2015)
4. Sun, J., et al.: Wellbore stability analysis during drilling through marine gas hydrate-bearing sediments in Shenhu area: a case study. J. Petrol. Sci. Eng. **170**, 345–367 (2018). (S0920410518305205)
5. Gao, Y., et al.: A wellbore–formation-coupled heat-transfer model in deepwater drilling and its application in the prediction of hydrate-reservoir dissociation. SPE. J. **22**, 756–766 (2017)
6. Lei, L., Santamarina, J.C.: Laboratory strategies for hydrate formation in fine-grained sediments. J. Geophys. Res. Solid Earth **123**(4), 2583–2596 (2018)
7. Zhang, R.: Study on Risk of Deepwater Gas Hydrate Formation Instability and Well Integrity during Drilling and Production. China University of Petroleum (East China) (2017)
8. Ge, X.: Deformation control law of rock fatigue failure, real-time X-ray CT scan of geotechnical testing, and new method of stability analysis of slopes and dam foundations. Chin. J. Geotechn. Eng. **30**(1), 20 (2008)
9. Kang, Y., et al.: Laboratory studies of shale fracturing behaviors with rock-drilling fluid interactions. J. China. Univ. Petrol. Edn. Nat. Sci. **40**(4), 9 (2016)
10. Yunhu, L.U., et al.: Experimental study of strength properties of deep mudstone under drilling fluid soaking. Chin. J. Rock Mech. Eng. **31**(007), 1399–1405 (2012)

11. Rongzun, H., et al.: Study on shale stability of wellbore by mechanics coupling with chemistry method. Drilling Fluid Compl. Fluid **12**(3), 8 (1995)
12. Chenevert, M.: Adsorptive pore pressures of argillaceous rocks. U.s.symposium on Rock Mechanics
13. Fang, C.H.E.N., et al.: Gas hydrate saturation and its relation with grain size of the hydrate-bearing sediments in the Shenhu area of northern south China sea. Mar. Geol. Q. Geol. **31**(5), 6 (2011)
14. Baoping, L., et al.: Advances in calculation methods for rock mechanics parameters. Petrol. Dril. Techn. **33**(5), 4 (2005)
15. Zhang, H.: Risk Assessment of Sand Production for Natural Gas Hydrate Exploitation in the Northern South China Sea. China University of Petroleum (East China) (2018)
16. Yuan, J., et al.: Wellbore stability of horizontal wells in shale gas reservoirs. Nat. Gas Indust. **32**(9), 5 (2012)

Integrity Evaluation Method of Completion Screen in Deepwater Gas Reservoirs with High Temperature and High Pressure

Bo Zhou[1], Changyin Dong[1(✉)], Chenfeng Liu[1], Liang Huang[2], Dake Fang[2], and Junyu Deng[3]

[1] Key Laboratory of Unconventional Oil and Gas Development, Ministry of Education, China University of Petroleum (East China), Qingdao 266580, China
dongcy@upc.edu.cn
[2] CNOOC (China) Zhanjiang Branch, Zhanjiang 524057, Guangdong, China
[3] Research Ltd. of Engineering Technology, CNPC, Tianjin 345000, China

Abstract. In deepwater, high-temperature and high-pressure gas reservoirs, the failure modes of screens are affected by a variety of bottom-hole environments, including water production, CO_2 gas, sand production, high temperature, high production and high speed and other conditions. Among them, under the conditions of water production and CO_2 gas, the corrosion damage of the metal screen is the main failure mode; under the condition of sand production, the screen medium is more likely to cause clogging and failure resulting in reduced production; high temperature conditions are the main factors affecting the accuracy of the screen; Under the production conditions of high output and high flow rate screens are more prone to erosion damage caused by gas carrying sand. By analyzing the failure modes of screens in high-temperature and high-pressure gas reservoirs under different bottom hole environments, the comprehensive conditions of the screens are simulated to evaluate the comprehensive performance of the screens. Based on the experimental simulation results, and mainly considering the dynamic changes of corrosion, erosion, clogging, sand retaining, accuracy change, etc., a comprehensive simulation method for screens in high-temperature and high-pressure gas reservoirs is established. In this paper, taking a gas field in South China Sea as an example, according to each individual simulation method and index system, the integrity of sand control screens are evaluated, and sand control methods and parameters are finally selected based on the evaluation results. This method can predict the high temperature accuracy change of the screen medium and the sand retaining effect, the blockage of the screen medium and the reduction of production, the dynamic condition of the screen corrosion and the damage condition of the screen erosion. Integrity evaluation is of great significance for improving the sand control effect and production efficiency of deepwater gas reservoirs with high-temperature and high-pressure.

Keywords: Integrity evaluation · Screen · Deepwater · Completion · Sand control

B. Sun et al. (Eds.): DWOG-Hyd 2021, LNCE 246, pp. 72–83, 2022.
https://doi.org/10.1007/978-981-19-0960-3_7

1 Introduction

Sand control in deepwater, high-temperature and high-pressure gas reservoirs is mainly based on independent screens. However, the effective period of sand control by independent screens has become a key issue restricting the development of high-temperature and high-pressure gas reservoirs in deepwater. According to statistics, the failure rate of open-hole screen wells after commissioning is as high as 45.6% [1].

In recent years, domestic and foreign scholars have conducted a series of researches on the strength of screen and proposed many calculation methods. Research [2, 3] respectively proposed the analysis and calculation methods of the tensile, compressive and squeezing strength of the screen/casing. There is less related study to the screen accuracy change in high temperature and high pressure. For screen clogging and sand retaining, some studies [4–6] carried out experimental research on the clogging mechanism and law, analyzed the qualitative law of the impact of particle size, flow rate and other production conditions on the clogging permeability. At present, the indoor experimental evaluation for sand retaining ability of screen is relatively mature [7–14]. For screen erosion and corrosion, few of the current researches are applied to screens. The numerical calculation model of the solid particles erosion impacting on the material surface is established to describe the erosion behavior in elbows based on the finite element (FEM) method, many CFD tools, such as ANSYS Fluent, which employed several analytical, empirical and semi-empirical models have been utilized to investigate sand erosion [15–17]. In addition, the corrosion damage evaluation experiment of downhole tubing string is usually based on specific oil and gas reservoir conditions to analyze the corrosion mechanism and prevention of tubing, casing and transportation pipelines.

For the conditions of high temperature and high pressure gas reservoirs in deep sea, there is a lack of systematic and targeted research and technical systems, and the problems of screen damage and sand production are prominent. Therefore, the integrity evaluation of screens in deepwater, high temperature and high pressure gas reservoirs needs to be developed urgently.

2 Framework

Completion screen integrity evaluation is a comprehensive evaluation of the durability of the screen under actual conditions. The screen integrity is mainly affected by the geological and production conditions of high-temperature and high-pressure gas reservoirs, as well as sand control screen itself, product structure and material parameters. According to factors such as reservoir conditions, well structure, sand control methods, and development conditions of high temperature and high pressure gas reservoirs, the possible failure modes of sand control screens and engineering risks are considered to determine the evaluation criteria which includes screen corrosion damage evaluation and screen erosion damage evaluation, accuracy evaluation, sand retaining evaluation, screen clogging and capacity evaluation.

Combining aforementioned five types of evaluation, the comprehensive effect and completeness evaluation of sand control methods will be obtained to support the optimization of high-efficiency and long-term sand control schemes for high-temperature and high-pressure gas reservoirs (Fig. 1).

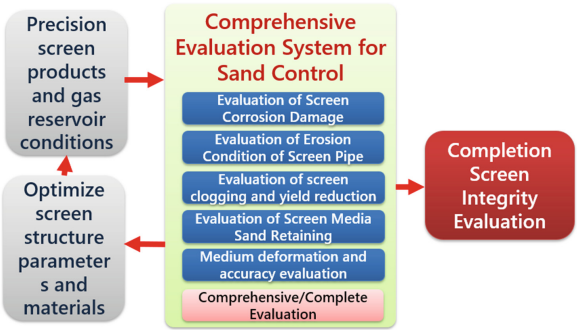

Fig. 1. Diagram of research ideas

The specific evaluation idea is to select the screen products to be evaluated, according to the evaluation method system obtained by the simulation method of the actual working conditions of the screens. The evaluation further obtains the comprehensive integrity and performance of the screen for deepwater gas reservoir conditions with high-temperature and high-pressure. The evaluation system can be used to optimize screen products, and it can also guide the optimization of screen product structural parameters and material materials based on the screen evaluation results.

3 Simulation Method

Under given production conditions (temperature, pressure, output, fluid composition and physical properties, sand production situation, etc.) and completion conditions (completion method, screen structure and material), the comprehensive simulation content of bottom hole conditions mainly includes screens accuracy change, clogging, sand retaining, corrosion and erosion. We have constructed simulation models of each process through experimental simulation methods.

3.1 Accuracy Change of Screen

The simulation of screen medium accuracy change at high temperature mainly aims to screen sand retaining. We simulated the sand-retaining result (sand passing rate) of the screen under high temperature conditions (Fig. 2).

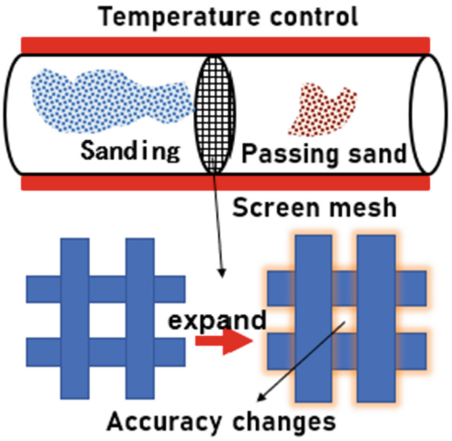

Fig. 2. Schematic diagram of accuracy change simulation method

The diameter of the mesh wire is expanded and changed under high temperature conditions, causing the mesh area to decrease. Through simulation, it is found that the accuracy of the sand retaining medium increases with the increase of the temperature expansion coefficient. With the increase of temperature, the change of sand retaining accuracy depends on the relative size of the wire diameter and pore size. If the wire diameter is greater than the sand retaining accuracy, the sand retaining accuracy will increase as the temperature increases; conversely, the sand retaining accuracy will decrease with the increase in temperature, with a small change range of 0–0.6%.

Further, we carried out experimental simulations of sand retaining effect laws at different temperatures. Under the 4 types of formation sand median size (0.21, 0.18,0.14,0.12 mm) and 4 types of sand retaining accuracy (70mesh, 80mesh, 100mesh, 120mesh), sand passing rate do not change significantly. A part experimental results are shown in Fig. 3.

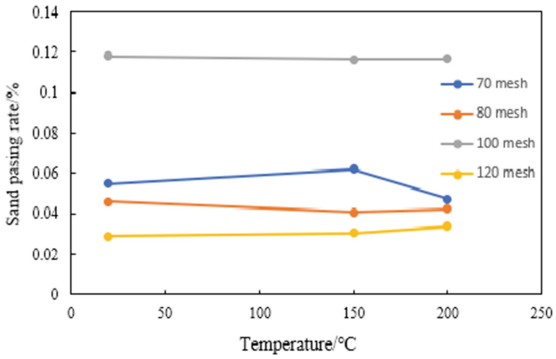

Fig. 3. Experimental results of different precision filter screens with a median particle size of 0.21 mm

The final experimental results show that under the condition of formation temperature 150–200 °C, temperature changes will not have a significant impact on the accuracy of the screen.

3.2 Screen Clogging and Sand Retaining

The clogging of the screen medium is inseparable from the sand retaining ability of the screen itself. This is a balance between the screen to keep sand retaining and maintain the capacity (Fig. 4).

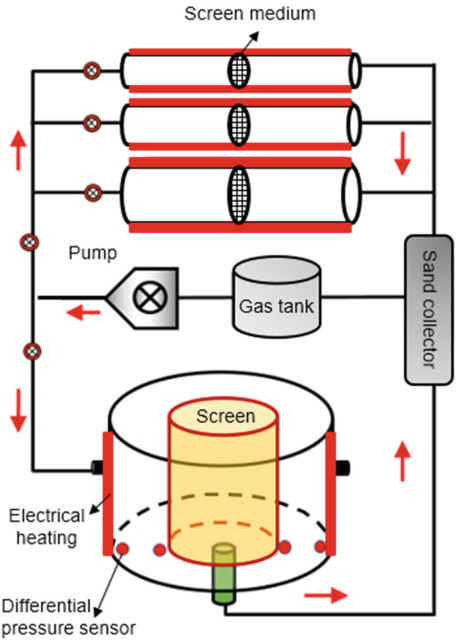

Fig. 4. Schematic diagram of screen clogging and sand retaining simulation method

The simulation of screen medium clogging conditions is aimed at screen sand retaining medium. Under different experimental (production) conditions, the permeability ratio of gravel layer clogging is basically similar over time. At the beginning of clogging, the permeability drops faster, and then gradually slows down and stabilizes [17].

Based on the experimental results of sand retaining and clogging rules, the empirical prediction model is shown in Eqs. (1) and (2). The clogging coefficient Xs is used in the model to characterize the influence of various production conditions on the specific change law of clogging permeability.

$$k_r = 1 - A_r \cdot X_S \cdot \ln(t) + B_r \tag{1}$$

$$X_s = \left(W_{Rf} X_{Rf} + W_{Rc} X_{Rc} + W_{qs} X_{qs} + W_{WSR} X_{WSR} + W_{qg} X_{qg}\right) \tag{2}$$

The clogging of the sand-retaining medium leads to changes in permeability and changes in skin coefficient and productivity. According to Dong's study [18], the relationship between production capacity ratio (PR) and basic geology, production parameters, and production time can be established to realize dynamic production capacity prediction and analysis and evaluation of clogging conditions in Eq. (3).

$$PR = \frac{q_{sc(1)}}{q_{sc(0)}} = \frac{f(x) + D(x) \cdot q_{sc(1)} + S_1}{f(x) + D(x) \cdot q_{sc(1)} + S_0} \tag{3}$$

3.3 Screen Corrosion

In the corrosion simulation of the screen, we study the difference in corrosion rate and corrosion resistance of different screen components such as the outer protective cover, base pipe, and sand retaining medium under high temperature and high pressure gas reservoir conditions (Fig. 5), as well as temperature, CO_2 partial pressure and other conditions.

The corrosion patterns of different parts of the screen are shown in Fig. 5(b) and 5(c). Due to different materials, the corrosion rate of each part is significantly different. A prediction model based on the N80 material is established, and correction coefficients is determined for other materials. The corrosion failure of the screen is characterized by the damage of the metal mesh (sand retaining medium).

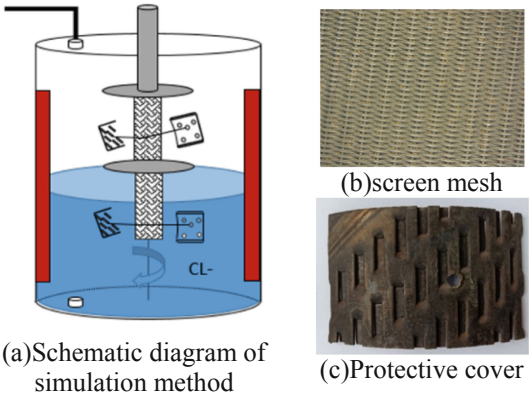

Fig. 5. Screen corrosion simulation method and part corrosion appearance

The law of influence on the corrosion rate of the screen, fitting correction to obtain an accurate prediction model (Eq. 4–5) modified based on the corrosion experiment results. Table 1 is the correction coefficient proposed by the comprehensive experimental results.

$$v_{corr} = K_t \times f_{CO_2}^{0.062} \times \left(\frac{S}{19}\right)^{0.146+0.0324\log f_{CO_2}} \times f_{(PH)} \cdot \beta_1 \cdot \beta_2 \tag{4}$$

$$RC = \frac{v_{corr} \cdot t}{HC} \tag{5}$$

Table 1. Corrosion experiment prediction model correction coefficient table

No.	Material	Correction factor
1	N80	1.0
2	304	0.3–0.4
3	316L	0.1–0.2
4	13Cr	0.45–0.6
5	P110	0.8–0.85

3.4 Screen Erosion

The screen erosion damage condition simulation is based on the erosion experiment results for the outer protective cover, sand retaining medium, and base pipe (Fig. 6).

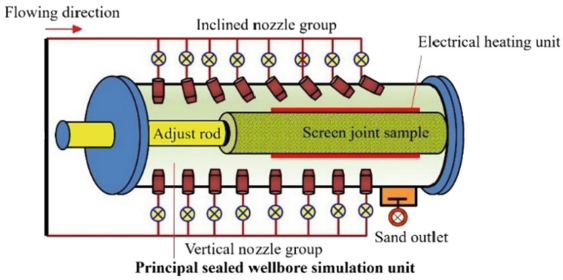

Fig. 6. Schematic diagram of screen erosion simulation method

The experimental simulation has obtained the relationship between the flow velocity, erosion angle, erosion distance and the median value particle size of formation sand and erosion rate, as shown in Fig. 7.

According to the simulation results, the erosion rate model was established, as shown in Eqs. (6), where Kc is the damage risk coefficient of the screen, which represents the comprehensive erosion resistance of the screen, and is only related to the screen material and structural parameters, and has nothing to do with the external environmental conditions.

$$V_c = K_c \cdot (1 + \frac{\alpha_{max} - \alpha}{\alpha_{max} - \alpha_{min}}) \cdot \frac{V_g^2 \cdot C_s \cdot \rho_s \cdot d_s}{L_c} \tag{6}$$

For an actual well, the erosion time Ta can be predicted based on the screen actually used, and the sand burial time Tb can be predicted based on the annulus volume and the actual sand content. If Tb > Ta, the screen is protected by sand before erosion damage. On the contrary, the above formula and Ta can be used to simulate and predict the erosion rate and erosion failure time of the screen.

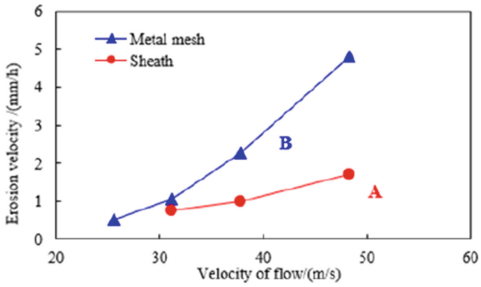

(a) Results under different flow velocity conditions

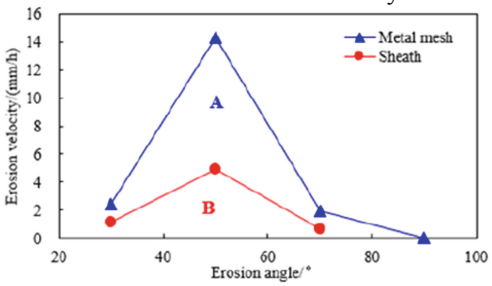

(b) Results under different flow rate conditions

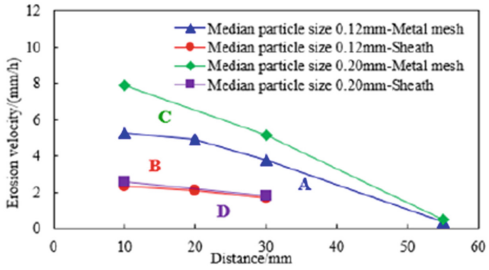

(c) Results under different distance conditions

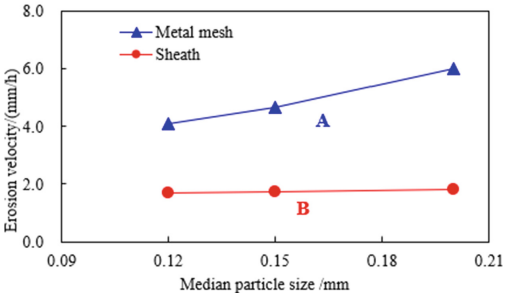

(d) Results under different median particle size conditions

Fig. 7. Simulation results under different factors

4 Evaluation System

4.1 Comprehensive Simulation for Screen at Well Bottom

After the gas well is put into production, the formation sand will gradually be produced, part of the formation sand will pass through the screen, and the other part will be blocked and deposited in the annulus between the screen and the well wall. As the production progresses, processes such as the clogging of the screen medium, the accumulation of sand in the annulus, the corrosion and erosion of the screen, and the high temperature deformation of the medium will occur at the same time.

As the production time continues, the formation sand inside the sand retaining medium will increase, and the formation sand blocked by the screen and deposited in the annulus between the screen and the well wall will also increase. With the accumulation of stratum sand, the comprehensive working conditions of the bottom of the well will undergo the following changes:

(1) The degree of clogging at screen sand retaining medium will increase, and the production capacity will decrease.
(2) At the same time, the sand retaining capacity of the screen has increased, and the sand passing speed has decreased.
(3) With the continuation of production, the corrosion and erosion of the screen will continue, and the erosion will vary with the degree of sand burial. When the formation sand fills the annulus, if erosion damage has not occurred, there is no possibility of erosion damage to the screen.
(4) The screen accuracy and material strength of the screen will change under high temperature conditions.

4.2 Evaluation Index and Grade Division

In the evaluation criteria, we prefer the evaluation index to characterize the integrity of the screen. The accuracy change is characterized by the accuracy change rate, the screen retention and sand clogging are characterized by sand passing rate and production capacity ratio, the erosion is characterized by comprehensive damage risk coefficient, and the corrosion is characterized by corrosion damage rate. The performance of each individual effect is normalized to a dimensionless evaluation index between 0–1, and the comprehensive adaptability evaluation index is calculated by the weighted average method, and the evaluation chart of the comprehensive index is formed as shown in Fig. 8.

The comprehensive evaluation index K is calculated by weighting 5 individual indexes, and the specific weight coefficient is based on the actual well performance.

According to the statistical law of various indicators of actual wells, we have preliminarily divided the evaluation grade (excellent, good, moderate, poor) of each individual evaluation indicator. The value of the comprehensive evaluation index Rs of sand retaining performance is greater than 0.85 as excellent, between 0.75–0.85 as good, and between 0.65–0.75 as medium or worse.

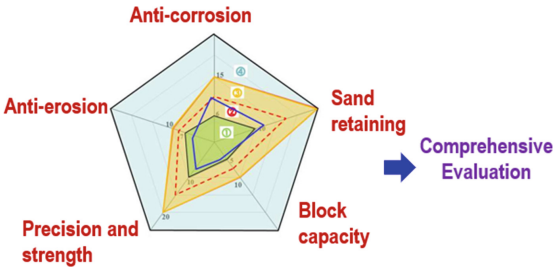

Fig. 8. Evaluation chart of the comprehensive index

5 Application

In this paper, a typical well in a gas reservoir in South China Sea is used for comprehensive analysis and integrity evaluation application.

The production section of the well in the gas reservoir is 535 m in length, with a production rate of 410,000 m^3/day and a pressure of 13.94 MPa. The CO_2 content in natural gas is 10.25%. The well uses Excelflo composite screen and Excluder screen. The screen material is 13Cr80, 316L stainless steel, and the screen accuracy is 0.115 mm uniform sintered mesh. Using the above data, also including formation sand screening data, formation water data, etc., the calculation and evaluation of typical well cases are carried out. The results are shown in the Table 2.

After comprehensive evaluation of the well screen, the following results are obtained. Since the formation sand d50 is selected according to the average value of 0.081 mm, which matches the accuracy of 0.115 mm, the sand retaining performance is slightly lower. Due to the high CO_2 content (10.25%), the risk of screen corrosion is relatively high. At the same time, the capacity ratio is within a reasonable range. In general, the overall adaptability of the well screen for sand control is good.

Table 2. Evaluation results of each index in the application

Evaluation items	Calculation parameters		Dimensionless index	Evaluation results
	Type	Value		
Sand retaining	Sand passing rate	74.204%	0.129	Worse
Clogging and productivity	Final capacity ratio	0.6554	0.873	Excellent
Anti-corrosion	Corrosion damage rate	12.77%	0.662	Medium
Anti-erosion	Erosion damage risk coefficient	0.3636	0.794	Good
Accuracy change	Accuracy change rate	-0.048%	0.995	Excellent

6 Conclusion

This paper studies and establishes the comprehensive performance and integrity evaluation method and index system of the screen, and clarifies the comprehensive performance evaluation process of the screen, which can be used for the comprehensive integrity evaluation of the high-temperature and high-pressure gas reservoir screen. Using the constructed completion screen integrity evaluation method, comprehensive evaluation analysis and comparison of screens were carried out for a well in the Gas Field in South China Sea. The results show that the well in the Gas Field has a low risk of erosion damage, moderate sand retaining and clogging indicators, and good overall adaptability of the screen for sand control.

Symbol Description

t— the experiment time
kr—the clogging permeability ratio
Ar, Br— fitting coefficients
Xs— comprehensive plugging coefficient
WSR—Accuracy ratio between formation sand and screen
Rf—fine sand content
RC—clay content
qs—sand content
qg—gas production strength
W_{Rf}, W_{Rc}, W_{qs}, W_{WSR}, W_{qg}—weight coefficient
$q_{SC(0)}$—gas production before sand control (standard condition)
$q_{SC(1)}$—gas production after sand control (standard condition)
S_0—skin coefficient before sand control
S_1—skin coefficient after sand control
f(x), D(x)—calculation items, which depend on different gas well productivity models
v_c—erosion velocity
Kc—fitting coefficient
Cs—volumetric content of sand in the gas
qs—sand content
ρs—sand particle density
ds—sand particle size
Lc—erosion distance
α—erosion angle
αmax—maximum erosion angle
αmin—minimum erosion angle
v_{corr}—corrosion rate
β_1 and β_2—Correction coefficient
Hc—Total thickness of medium
Rc—Corrosion damage rate

Acknowledgement. This work was financially supported by the National Natural Science Foundation of China (Grant No. 51774307, 52074331) and funded by the China National Petroleum Corporation Science and Technology Major Special Project (ZD2019-184).

References

1. Chen, Y.: The optimization and application of sand control method in an oil field of Bohai bay. Petrochem. Indus. Technol. **23**(6), 113–114 (2016)
2. Mathisen, A.M., Aastveit, G.L., Alteraas, E.: Successful installation of stand alone sand screen in more than 200 wells- the importance of screen selection process and fluid qualification. Soc. Petrol. Eng. (2007)
3. Tallin, A., Han, Y., Wong, G.: Analysis of sand screen integrity in depleting sandstone reservoir. Soc. Petrol. Eng. (2016)
4. Hu, C.Z., et al.: Laboratory research on plugging mechanism in gravel packed well. J. China. Univ. Petrol. (Edn. Nat. Sci.) **28**(3), 40–42 (2004)
5. Wu, Y.X., et al.: Research of influence of high temperature on mechanical screen strength. Oil Field Equip. **46**(5), 43262 (2017)
6. Procyk, A., et al.: Sand control screen erosion: prediction and avoidance. In: SPE Technical Conference and Exhibition (2015)
7. Pinkert, S., Grozic, J.L.H.: Failure mechanisms in cemented hydrate-bearing sands. J. Chem. Eng. Data **60**(2), 376–382 (2015)
8. Dong, C.Y., et al.: Experimental study on selection of mechanical screens and sand retention precision design for horizontal wells in a gas field. J. China Univ. Petrol. (Edn. Nat. Sci.) **39**(6), 104–109 (2015)
9. Dong, S.X., et al.: Test and analysis of sand-control screen corrosion in thermal production wells using multiple thermal fluids. Chem. Eng. Oil Gas. **42**(03), 287-289+293 (2013)
10. Li, Y., et al.: A new strength criterion and constitutive model of gas hydrate-bearing sediments under high confining pressures. J. Petrol. Sci. Eng. **109**(5), 45–50 (2013)
11. Chanpura, R.A., Hodge, R.M., Andrews, J.S., Toffanin, E.P., Moen, T., Parlar, M.: A Review of Screen selection for Standalone Applications and a New Methodology. SPE 127931 (2013)
12. Ma, S., Xiong, Y., Yu, D., Liu, L., Jun, X., Du, J.: Research on precision design of sand control on high yield offshore gas field. Oil Drill. Prod. Technol. **06**, 48–51 (2013)
13. Butler, R.M., Stephens, D.J.: The gravity drainage of steam-heated heavy oil to parallel horizontal wells. J. Can. Pet. Technol. **20**(02), 90–96 (1981)
14. Alghurabi, A., et al.: CFD numerical simulation of standalone sand screen erosion due to gas-sand flow. J. Nat. Gas Sci. Eng. **85**, 103706 (2021)
15. Fucheng, D., Jingen, D., Lianbo, H., Baohua, Y., Qiang, T., Yi, X.: Simulation research on the erosion of slotted screen for the unconsolidated sand formation. Arab. J. Sci. Eng. **39**(6), 5237–5243 (2014). https://doi.org/10.1007/s13369-014-1205-5
16. Zhang, R., et al.: Analysis and simulation of erosion of sand control screens in deep water gas well and its practical application. J Petrol. Sci. Eng. **189**, 106997 (2020)
17. Dong, C.Y., et al.: Experimental study of sand retaining media plugging pattern in sand control well and quantitative prediction model for plugging degree. Exp. Mech. **32**(03), 351–360 (2017)
18. Dong, C.Y., et al.: Sand control productivity prediction and evaluation model for horizontal gas wells. Petrol. Drill. Technol. **37**(05), 20–25 (2009)

Study on Throttling Characteristics of Hydraulic Cylinder Throttle Valve and Control Strategies for MPD

Hao Shen[1], Hao Li[1], Baojiang Sun[1(✉)], Xuerui Wang[1], Chengzhen Shi[1], Meipeng Ren[2], and Zhiming Yin[2]

[1] Key Laboratory of Unconventional Oil and Gas Development, Ministry of Education, China University of Petroleum (East China), Qingdao 266580, China
sunbj1128@vip.126.com

[2] CNOOC Research Institute Company Limited, Beijing 100028, China

Abstract. The surface choke manifold is the core part of the Managed Pressure Drilling system, on which the adjustment of the throttle valve components is very important for exquisite control of the pressure in the wellbore. Whereas there are still few field experiments of hydraulic throttle valve under gas-liquid two-phase flow, of which lack significance for field guidance, so it is necessary to conduct further study in this area. By building a field full-scale experimental platform, taking drilling fluid as the experimental object, and using a new cylindrical throttle valve, the pure liquid phase and gas-liquid two-phase flows experiments were carried out respectively. Taking into account the pressure bearing capacity of the experimental system, the throttle valve's opening adjustment ranged from 19%-100% in the experiment. The experimental results showed that the new cylinder throttle valve had a good linearity when the opening was lower than 40%, and its invalid opening interval was 80–100%. During the pure liquid phase flow experiment, when the drilling fluid displacement was changed from 15L/s to 20L/s, the choke pressure varied from 0.5MPa to 7.3 MPa. When the opening was less than 40%, the choke pressure changed rapidly, the smallest opening unit was recommended while operating and when the opening was between 40% and 80%, the choke pressure did not change significantly, the opening unit could be changed based on actual needs while operating and the choke pressure was basically unchanged when the opening was between 80% and 100%, in which it was suggested that the operation of the valve be avoided. Under the gas-liquid two-phase flow experiment, the initial void fraction was changed from 0.3321 to 0.4484, the drilling fluid displacement was changed from 15L/s to 20L/s, the choke pressure ranged from 1.09–9.7MPa, and when the initial void fraction reached at the maximum of 0.4484, under the same opening and liquid phase displacement, the choke pressure was the largest, and the other laws showed were basically the same as those under the experiment of pure liquid phase flow. By comparing the curves of choke pressure with opening in pure liquid phase and gas-liquid two-phase, it was found that the choke pressure in gas-liquid two-phase was larger under the same liquid displacement and the same opening, which conformed to the law. In addition, considering the gas disturbance, it was suggested to slow down the operation of the valve in gas-liquid

B. Sun et al. (Eds.): DWOG-Hyd 2021, LNCE 246, pp. 84–94, 2022.
https://doi.org/10.1007/978-981-19-0960-3_8

two-phase flow. The throttling characteristic experiments of pure liquid and gas-liquid two-phase flows of the hydraulic cylinder throttle valve are good references for the Managed Pressure Drilling in field, and meaningful for guidance.

Keywords: Cylinder throttle valve · Throttling characteristics · Field experiment · Managed pressure drilling · Gas-liquid two-phase flow

1 Introduction

Managed Pressure Drilling (MPD) is an important technology developed in recent years which can effectively control downhole pressure to solve complex drilling problems. When operating in complex areas, MPD can greatly improve the drilling speed, thus shortening the drilling time and making drilling operations safer [1]. Throttle valve is a choke element with variable resistance in the pipeline system [2], which can control the fluid flow by changing the choke's cross section or the choke length, and then control the differential pressure at both ends and it is widely used in petroleum industry [3, 4]. In MPD system, the back pressure at the wellhead is controlled by adjusting the throttle valve's opening on the choke manifold, so as to maintain the balance of wellhead pressure during the whole drilling process [5]. Therefore, it is of great significance to study the throttle valve's throttling characteristics through experiment for the field operation of MPD.

Scholars at home and abroad have made some achievements in the choke's pressure-drop theory and the numerical simulation of the flow field inside the throttle valve, but the field experimental studies on the relationship between the opening and pressure drop in the two-phase flow inside the throttle valve is relatively few, and the guidance for the field operation still needs improvement. In 1986, R. Sachdeva et al. [6] studied the boundary conditions of critical flow and subcritical flow in the two-phase flow inside the wellhead throttle valve and the transformation between them, and proposed a new mathematical model that could predict the flow rate and critical conditions between the critical flow and subcritical flow through experiments. In 2007, B. Guo et al. [7], based on Sachdeva's [6] choke model, added a flow coefficient through throttling to the equation to improve its calculating errors. In 2013, Yu Min et al. [8] established the theoretical equation for the calculation of choke pressure drop and verified the calculating method through field experiments. In 2015, Guorong et al. [9] tested a new type of throttle valve for MPD, and found that its linear pressure control was good by combining the theoretical derivation with numerical simulation analysis. In 2018, Qu Junbo et al. [10] obtained the analytical formula of spool stroke and pressure drop at both ends of the wedge-shaped throttle valve in MPD through the theoretical analysis, and gained the effective range of adjustment of the wedge-shaped throttle valve by combining with the drilling field data. In 2020, Yang Yousheng et al. [11] experimentally studied the throttling characteristics of the valve port of the moving seat throttle valve, and found that the pressure at the valve port of the moving seat throttle valve decreased rapidly, and the smaller the opening, the greater the pressure drop.

In this paper, a full-size field experimental platform was set up, and experiments of throttling characteristics of the hydraulic cylinder throttle valve under single-phase and

gas-liquid two-phase flows were conducted successively. The change of choke pressure with opening under different drilling fluid's displacement in single phase flow and the choke pressure varied with the opening under the same drilling fluid displacement but with different initial void fraction in gas-liquid two-phase flow were studied respectively. The experiments are significant and practically meaningful for the operation of throttle valve in the process of MPD in field.

2 Experimental Section

2.1 Equipment and Materials

Hydraulic cylinder throttle valve has a relatively simple structure and is easy to manufacture. By adjusting the throttle valve spool to raise the height of throttling, so as to achieve the control of pressure. The hydraulic cylinder throttle valve used in this experiment was designed and manufactured according to API Spec 16C standard. It has good throttling performance, corrosion resistance, long service life, and safe and reliable operation.

The throttle valve's throttling characteristics experimental system (pure liquid phase and gas-liquid two-phase) contained a cementing pump, a pressure sensor, a gas flowmeter, standard seven-meter lines, a choke manifold system, and two gas compressor vehicles. The cementing pump truck was connected to one side of the choke manifold system with a seven-meter standard pipeline. In the two-phase flow experiment, the gas compressor vehicles were needed, which were also connected to the choke manifold system on the same side with the above standard pipeline to transport gas and provide gas source pressure. On the other side of the choke system, to recover or recycle the liquid used in the experiment by connecting it to a liquid storage tank.

From the Fig. 1 below, the throttle valve used in the experiments has a nominal diameter of 103 mm, choke diameter of 50 mm and stroke of 50.8 mm. The valve is driven by hydraulic pressure.

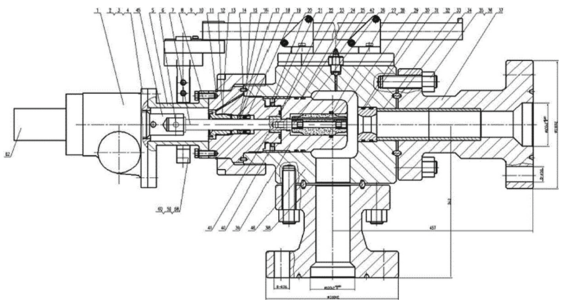

Fig. 1. Diagram of the structural parameters of hydraulic cylinder throttle valve

The liquid used was water-based drilling fluid transported from the field, and the gas pumped in the two-phase flow experiment was air. During the experiment, the temperature ranged from 20 °C to 40 °C, the pressure was below 15MPa, and the liquid's displacement changed to 15L/s and 20L/s respectively. The drilling fluid's density was

1.55 g/cm^3, and the viscosity was 23 mPa·s. The drilling fluid's surface tension was 73.97 dyn/cm. The above fluid's parameters were set at room temperature and pressure and parameters under other temperature and pressure needed to be converted according to relevant formulas.

2.2 Experimental Scheme and Process

In the pure-liquid phase flow experiment, the displacement in the experimental pipeline was adjusted to 15 L/s and 20 L/s by cementing pump truck, and the throttle valve's experiment was carried out with field drilling fluid. Specifically by adjusting the throttle valve's opening from 19% to 100%, and the opening was increased by 10% each time. The pressure data corresponding to different opening degrees were collected and recorded through the pressure sensor inside the pipe. Several groups were carried out at each group of displacement and opening, and a total of 32 groups were completed. Collecting data for at least one minute each time after the pressure gauge's value became stable. When it came to the gas-liquid two-phase flow experiment, the influence of different displacements were studied: The drilling fluid's displacement in the experimental pipeline was adjusted to 15 L/s and 20 L/s respectively by cementing pump truck, and a fixed amount of air was input into the choke system by gas compressor vehicles to make the void fraction fixed before throttling. The other operations were the same as the last experiment, and a number of groups were carried out at each group of displacement and opening, and it was 55 groups in total. The influence of different void fraction was studied in the gas-liquid two-phase flow experiment: Under certain drilling fluid's displacement, making the void fraction vary four times before throttling by pumping a fixed amount of gas to the choke system. The rest of the operations were the same as the former two experiments, several groups were completed, and it was 53 groups in total. Figure 1 is the flow chart of these experiments.

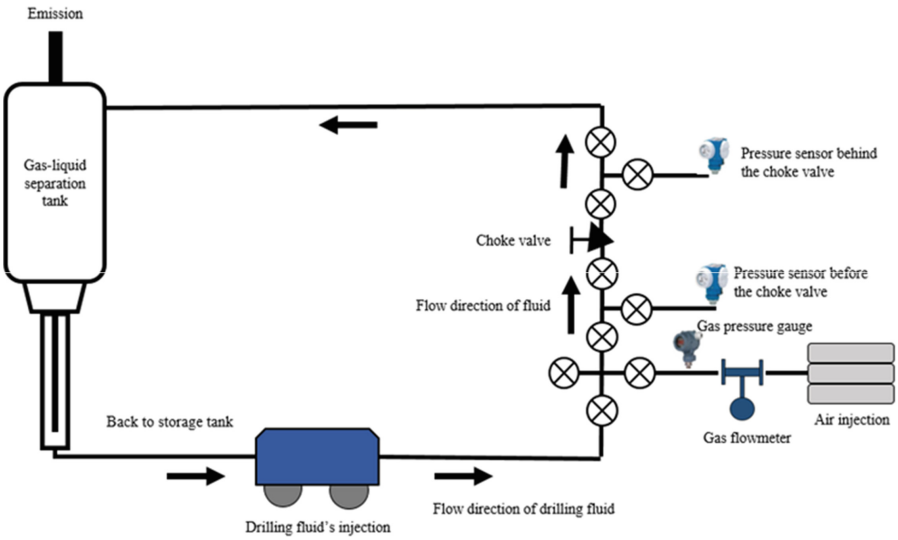

Fig. 2. Flow chart of the experiment of throttling characteristics of hydraulic cylinder throttle valve

3 Experimental Results and Discussion

Based on the experimental scheme, according to the change of experimental conditions, the experimental results are divided into three parts to analyze the throttling characteristics of the throttle valve under three different experimental conditions (Fig. 2).

3.1 Analysis on the Experiment of Throttling Characteristics with Drilling fluid's Different Displacements in Pure Liquid Flow

From Fig. 3 below, it could be seen that when the opening was lower than 40%, the choke pressure changed significantly with opening. When the opening was greater than 40%, the choke pressure did not change significantly with the opening's variation. Under the same opening, the greater the drilling fluid displacement, the greater the choke pressure.

In addition, there was a certain linear relationship between the choke pressure and the opening within the range of 25–40%.

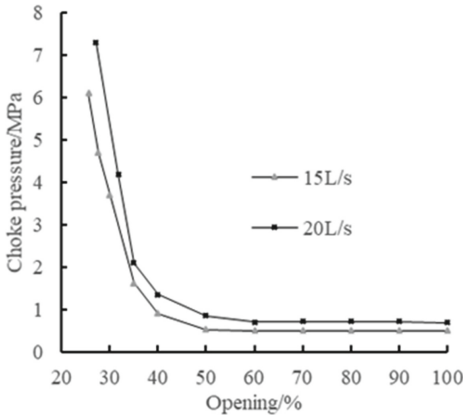

Fig. 3. Curves of choke pressure varying with opening at different displacement of drilling fluid

3.2 Analysis on the Experiment of Throttling Characteristics with Drilling fluid's Different Displacements in Gas-Liquid Two-Phase Flow

The initial void fraction described in Figs. 4, 5, 6 is the sectional void fraction at standard atmospheric pressure when the throttle valve is fully open in gas-liquid two-phase flow.

Based on Fig. 4, the initial void fraction was 0.4. When the opening was less than 40%, the control of opening to choke pressure was significant, and its strength weakened with the increase of the opening. When the opening was more than 40%, the control of opening to choke pressure was very weak. And when the opening was more than 80%, choke pressure was no longer affected by opening. Additionally, when the opening was 20–40%, the cylinder throttle valve had a good linearity, and it was suggested to take this as the actual operating range in field.

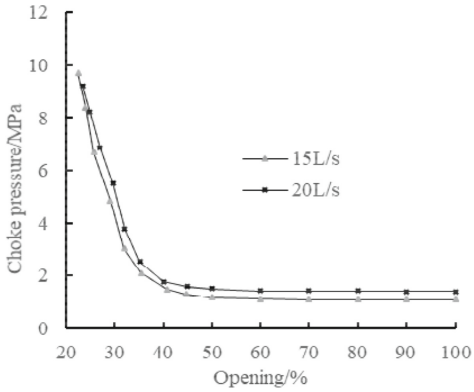

Fig. 4. Curves of choke pressure changing with opening at different displacement of drilling fluid when void fraction is 0.4

3.3 Analysis on the Experiment of Throttling Characteristics with Different Initial Void Fractions in Gas-Liquid Two-Phase Flow

Figure 5 shows the three-dimensional bar chart of void fraction and choke pressure changing with the opening.

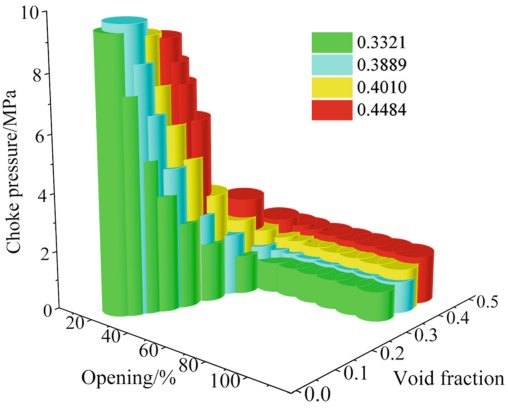

Fig. 5. Bar chart of choke pressure changing with opening and void fraction at different initial void fractions for drilling fluid displacement of 15 L/s

As can be seen from Fig. 5, with the decrease of the opening, the void fraction in the two phases at each initial void fraction decreased, and the corresponding choke pressure increased. The choke pressure and void fraction formed a spiral upward curve when the opening decreased.

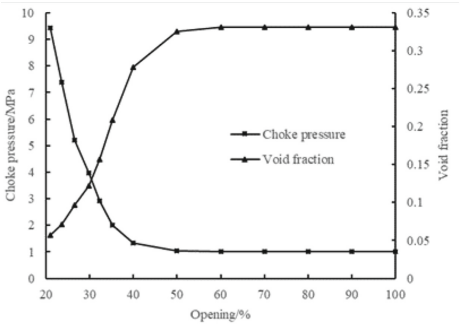

(a) The initial void fraction is 0.3321

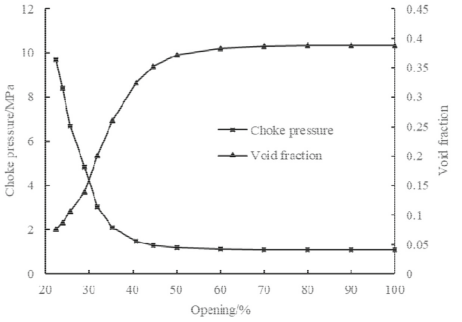

(b) The initial void fraction is 0.3889

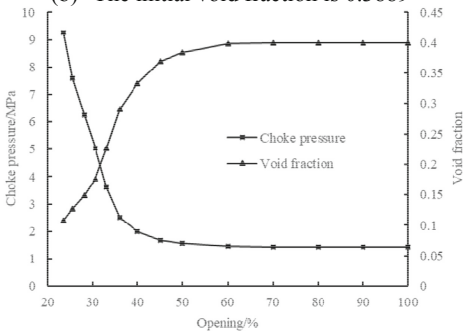

(c) The initial void fraction is 0.4010

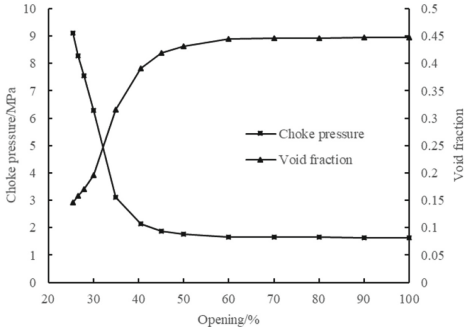

(d) The initial void fraction is 0.4484

Fig. 6. Curves of choke pressure and void fraction changing with opening at different initial void fractions when the drilling fluid displacement is 15 L/s

In Fig. 6, from graph (a) to (d), it could be easily seen that the choke pressure and void fraction showed an adverse tendency with the increase of the opening, which was that the choke pressure did increase when the opening increased while the void fraction decreased at different initial void fraction.

4 Pressure Control Strategies of Hydraulic Cylinder Throttle Valve

In the following analysis, based on the experimental data of the experiments, the two adjacent opening points in the experiment were regarded as a half-open and half-closed interval in the same experiment, and the one with the smaller opening was included in the interval, while the one with the larger opening belonged to the next interval. Absolute amplitude of choke pressure change represented the value of choke pressure change caused by 1% opening change in a certain opening range, which was abbreviated to AACPC.

As can be seen from Fig. 7, when the opening was less than 30%, the choke pressure controlled by 1% of the opening had exceeded 0.5 MPa, and the adjusted opening within this range could not meet the requirements for exquisite control of pressure, range of which also called the overshoot opening range.

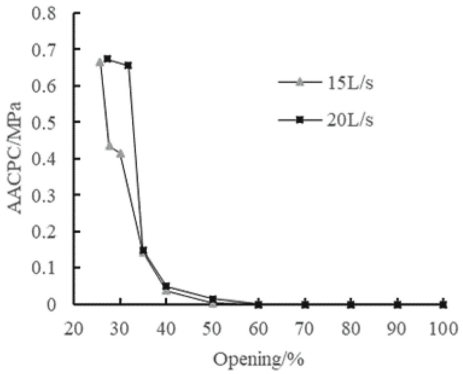

Fig. 7. Curves of absolute amplitude of choke pressure change (AACPC) with opening under the drilling fluid single-phase flow

When the opening was between 35–80%, the choke pressure controlled by 1% opening was less than 0.1MPa, range of which called the effective pressure control opening range. When the opening was greater than 80%, no matter how the opening was changed, the choke pressure would not change, range of which called the invalid opening range.

As can be seen from Fig. 8, under gas-liquid two-phase flow, when the initial void fraction was 0.4, the overshoot opening range expanded. When the opening is about 32%, the choke pressure controlled by 1% was greater than 0.5 MPa, and the effective pressure control opening range shrank roughly to 37–80%, while the invalid opening range remained unchanged.

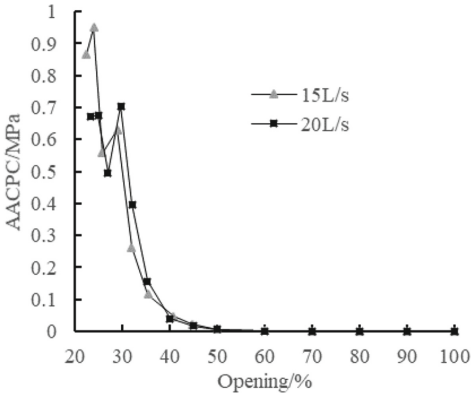

Fig. 8. Curves of AACPC with opening under gas-liquid two-phase flow when the initial void fraction is 0.4

It can be seen from Fig. 9 that the AACPC increased with the increase of initial void fraction.

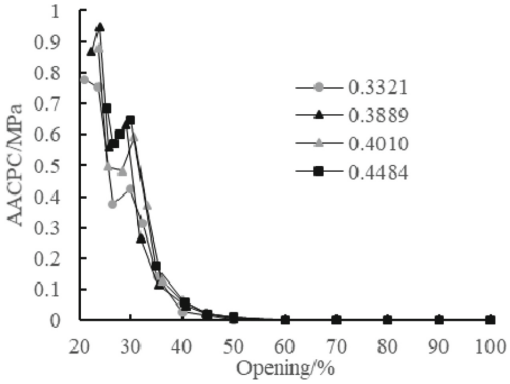

Fig. 9. Curves of AACPC with opening at different initial void fractions under gas-liquid two-phase flow when the displacement of drilling fluid is 15 L/s

And the AACPC decreased with the increase of opening at different initial void fractions, and the decreasing amplitude kept going down.

By comparing Fig. 3 and Fig. 4, it was found that under the same liquid phase displacement and opening, the choke pressure at the initial void fraction of 0.4 was higher than that under the single-phase flow of drilling fluid. The comparison in Fig. 7, Fig. 8 and Fig. 9 also confirmed this feature for the reason that under the same liquid displacement, the addition of gas would increase the overall composition, and then increase the pressure.

In the pure liquid phase flow, the choke pressure and the opening were in a non-linear relationship from the whole view, but the linear relationship between two was good within a certain opening range. In order to reduce the effect of fluid flow and it was

recommended to keep the value of pressure sensor get stable more quickly, the throttle valve was supposed to be operated moderately and slowly. It was suggested that when the throttle valve was operated in the overshoot opening range, it was good to use the smallest opening unit to adjust; when the throttle valve was at the effective pressure control opening range, it was favorable to change the opening operation unit in real time based on actual needs; It was suggested to avoid the invalid opening range to save the operation time and cost. In the gas-liquid two-phase flow, because of the increased gas disturbance in the flow, the fluid pressure was unstable. When operated, the operation could refer to that of sing-liquid phase flow's, and after each operation, it was advised to wait for the value of the pressure sensor to stabilize for a period of time before reading. If the stable value met the requirements, continue to the next step.

5 Conclusion

By setting up the throttling characteristics experimental platform of the valve under pure-liquid phase and gas-liquid two-phase flows, using the drilling fluid as a flowing medium, setting different fluid displacements in single phase flow, different drilling fluid's displacements and initial void fractions in gas-liquid two phase flow, then adjusting the opening of the throttle valve, next collecting the choke pressure data corresponding to different opening of the throttle valve in the throttling process, and finally obtained the curves containing the choke opening and the choke pressure, the following conclusions could be drawn:

(1) For this hydraulic cylinder throttle valve, when the opening was less than 40%, the choke pressure changed significantly with the opening; when the opening was greater than 40%, the choke pressure did not change significantly with the opening; when the opening was in the range of 25% to 40%, there was a certain linear relationship between choke pressure and opening.

(2) When the initial void fraction was 0.4, under the same opening, the larger the displacement of drilling fluid, the higher the choke pressure. As the opening decreased, the choke pressure kept increasing; when the opening was less than 40%, the opening was more significant for the control of choke pressure, and this controlling intensity weakened as the opening degree increased. When the opening was greater than 40%, the opening controlled the choke pressure very weakly, and when the opening was greater than 80%, the opening had almost no effect on the choke pressure.

(3) As the opening decreased, the choke pressure and the void fraction under different initial void fractions in gas-liquid two-phase flow had an opposite relationship with the opening. When the opening was lower, the void fraction of the gas was constantly decreasing but the corresponding choke pressure was constantly increasing; the choke pressure and the void fraction formed a spirally rising curve in the process of reducing the opening, which conformed to the law. And when the opening was less than 40%, the cylinder throttle valve had better linearity.

(4) All throttle valve's operations should be moderately slow to prevent the effect of fluid flow. For the hydraulic cylinder throttle valve used in these experiments, when the opening in the experiment of pure liquid phase flow was less than 40%, it was suggested to use the smallest opening unit for operation. When the opening was between 40–80%,

it could be operated more flexibly according to the actual conditions, and it was advised to avoid the operation in the invalid opening range which stood for the opening of 80–100% of the hydraulic cylinder throttle valve; for the experiment of gas-liquid two-phase flow, after each operation, it was recommended to ensure the values of pressure sensors before and after the valve were stable and fulfilled requirements.

Symbol Description

MPD—Managed Pressure Drilling.
AATPC—Absolute amplitude of choke pressure change, MPa.

Acknowledgement. The authors acknowledge the support from the General Foundation of National Natural Science Foundation (52074325), National Natural Science Foundation (52004315), Natural Science Foundation of Shandong Province (ZR2020QE113).

References

1. Zhu, H.: Numerical Simulation and Experimental Research on Working Mechanism of Throttle valve in Managed Pressure Drilling. Southwest Petroleum University (2014)
2. Zhou, J., et al.: Failure analysis and structure optimization of throttle valve core. China Petrol. Mach. **47**(12), 131–138 (2019)
3. Liu, M.: Function analysis of choke and kill manifold and its application in drilling ship. China New Technol. Prod. **01**, 50–51 (2019)
4. Wang, H., et al.: Analysis of invalidation characteristics and causes of throttle valves in gas wells. Chem. Eng. Equip. **08**, 85–86 (2020)
5. Wang, G., et al.: Linear throttle valve and its control technology for managed pressure drilling. Acta Petrol. Sin. **38**(08), 955–962 (2017)
6. Sachdeva, R., et al.: Two-Phase Flow Through Chokes. SPE-15657-MS (1986)
7. Guo, B., Al-Bemani, A.S., Ghalambor, A.: Improvement in Sachdeva's multiphase choke flow model using field data. J. Can. Pet. Technol. **46**(05), 22–26 (2007)
8. Yu, M., et al.: The calculation method and test research of choke pressure drop in killing well. Neijiang Technol. **34**(05), 61+46 (2013)
9. Wang, G., et al.: Numerical simulation and experimental study of working mechanisms of a throttle valve used in MPD. Mech. Sci. Technol. Aerosp. Eng. **34**(08), 1254–1258 (2015)
10. Qu, J., et al.: Study on choke pressure drop law of wedge throttle valve in managed pressure drilling. Chem. Mach. **45**(03), 328–332 (2018)
11. Yang, Y., Zhang, Q., Li, H.: Simulation and experimental study on orifice characteristics of moving seat throttle valve. Hydromech. Eng. **48**(10), 137–142 (2020)

Estimation of Formation Parameters Based on Void Fraction Measurement Outside Riser in Deepwater Drilling

Jing Zhao, Bangtang Yin(✉), and Wei Zhang

School of Petroleum Engineering, China University of Petroleum (East China), Qingdao 266580, China
yinbangtang@163.com

Abstract. A gas kick often occurs when the formation exceeds the mud hydrostatic pressure in the borehole, causing severe drilling accidents and low penetration in deepwater drilling operations. Thus, early kick detection and efficient kick control have become increasingly important for safe and rapid drilling. However, the prediction and access of formation parameters under overflow effect and complex downhole drilling conditions have not been treated in detail. Therefore, we propose a novel method based on the combination of void content monitoring and gas-liquid two phase flow model to predict the formation parameters after gas kick. The results indicate that the Doppler ultrasonic wave signal can reflect the variation of gas void fraction. Besides, the gas void fraction depends on the formation parameters. This work can realize early gas kick detection and control as well as formation parameters prediction, which could be used to prevent or reduce blowout accidents.

Keywords: Gas kick · Void fraction · Formation parameters · Doppler ultrasonic wave · Gas-liquid two phase flow

1 Introduction

Exploration and development of oil and gas have moved on to regions with complex geological and morphological conditions due to conventional oil and gas already remaining in later production period [1]. When drills in the formation with abnormal high pressure, a gas kick often occurs and even causes blowout accidents, which affects the process of drilling [2]. Therefore, well control and blowout prevention has important significance for safe drilling.

Accurately acquiring formation parameters after recognizing overflow is not only the means of preventing blowout but also the base of realizing well control [3]. Thus, formation properties accessing after overflow based on gas void fraction measurement have become a key issue in deepwater drilling. Yin et al. [4] proposed a method to detect the gas kick and the results showed the correlations between the Doppler ultrasonic signals and gas void fraction as well as the effectiveness and reliability of this monitoring system. Besides, Ren et al. [5] stated that Doppler ultrasound examination is a better

B. Sun et al. (Eds.): DWOG-Hyd 2021, LNCE 246, pp. 95–102, 2022.
https://doi.org/10.1007/978-981-19-0960-3_9

method to realize the gas kick early detection. Furthermore, Geng et al. [6] demonstrated that influx gas could lead to wave attenuation in Doppler ultrasonic tests. Moreover, safety risk analyses of offshore drilling were conducted based on theoretical analysis and experiment research [7]. The gas kick early detection and influx gas evaluation have become integral parts of deepwater-well control. However, prediction and evaluation of formation parameters for estimating the gas kick characteristics and mud flow properties remain poorly understood.

In this paper, we present a method for formation parameters prediction after overflow based on the gas void fraction measurement outside riser in offshore deepwater drilling. A gas-liquid phase flow model is established to calculate the flow characteristics and obtain the gas void chart of depth and gas void fraction. Additionally, combining with gas void fraction measured through Doppler ultrasonic wave, we predict the permeability and other formation parameters according to the and propose strategies for well control.

2 Calculation of Gas-Liquid Two Phase Flow

2.1 Gas-Liquid Two Phase Flow Model

Gas flow in the borehole can be described by the two-phase flow model during the gas invasion process [8]. The continuity equation of gas and drilling mud are given as follows:

$$\frac{\partial\left(\rho_g \phi_g\right)}{\partial t} + \frac{\partial\left(\rho_g v_g \phi_g\right)}{\partial z} = 0 \tag{1}$$

$$\frac{\partial\left(\rho_f \phi_f\right)}{\partial t} + \frac{\partial\left(\rho_m v_m \phi_m\right)}{\partial z} = 0 \tag{2}$$

The momentum equation is expressed as:

$$\begin{aligned} &\frac{\partial}{\partial t}\left(\rho_g u_g \phi_g + \rho_m u_m \phi_m\right) + \frac{\partial}{\partial z}\left(\rho_g u_g^2 \phi_g + \rho_m u_m^2 \phi_m\right) \\ &+g\left(\rho_g \phi_g + \rho_m \phi_m\right) + \frac{dp}{dz} + \left|\frac{dp}{dz}\right|_f = 0 \end{aligned} \tag{3}$$

The temperature field can be described through Eq. (4).

$$T = h(z) \tag{4}$$

The friction of fluid is given as follows:

$$\left|\frac{dp}{dz}\right|_f = f\left(h, \rho_g, \rho_m, u_m, l, \phi_g\right) \tag{5}$$

The density of drilling mud is assumed as a constant value, while that of gas is given as follows:

$$\rho_g = \frac{3484.4\gamma_g}{ZT} \tag{6}$$

The velocities of gas and mud in bubble flow and slug flow can be described by Eqs. (7) and (8).

$$u_g = \frac{Q_g + Q_m}{A} + 1.53\left[gl\left(\rho_m - \rho_g\right)\Big/\rho_m^2\right]^{0.25} \tag{7}$$

$$u_g = 1.2\frac{Q_g + Q_m}{A} + 0.35\left[gl\left(\rho_m - \rho_g\right)/\rho_m\right]^{0.5} \tag{8}$$

The gas void fraction and mud fraction in the borehole are given as follows:

$$\phi_g = u_{sg}/u_g \tag{9}$$

$$\phi_m = 1 - \phi_g \tag{10}$$

This model can be used to describe the gas invasion process in deepwater drilling. In this paper, we propose a method to predict the formation parameters after overflow, as shown in Fig. 1.

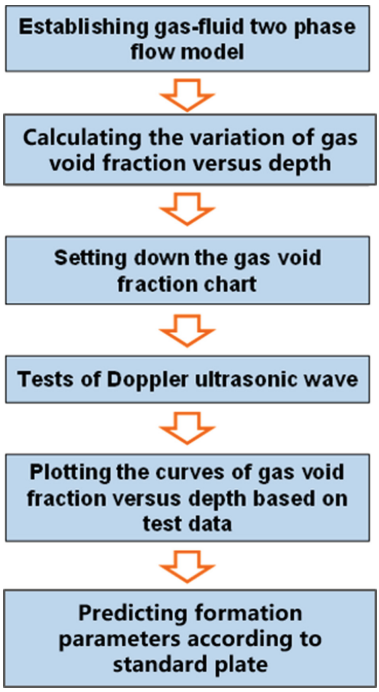

Fig. 1. Flow chart of this model

2.2 Calculation of Gas Void Fraction

The correlation between gas void fraction and depth is obtained through using this model mentioned above. The parameters are determined according to the previous studies and geological data in the South China Sea, as shown in Table 1.

Table 1. Materials used in the experiments

Parameter	Value
Depth of water	1500 m
Total depth	3500 m
Sea surface temperature	10.5 °C
Flow rate	30 L/s
Mud density	1.2 g/cm^3
Initial formation pressure	33 MPa
Permeability	10 md, 50 md, 100 md, 150 md, 200 md

Figure 2 depicts the variation of gas void fraction versus depth under different permeability. The results indicate that the gas void fraction differs versus depth and changes abruptly at the depth of 1500 m. This is mainly caused by the changes of pipe diameter. Besides, the increase of permeability brings in gas void fraction rising.

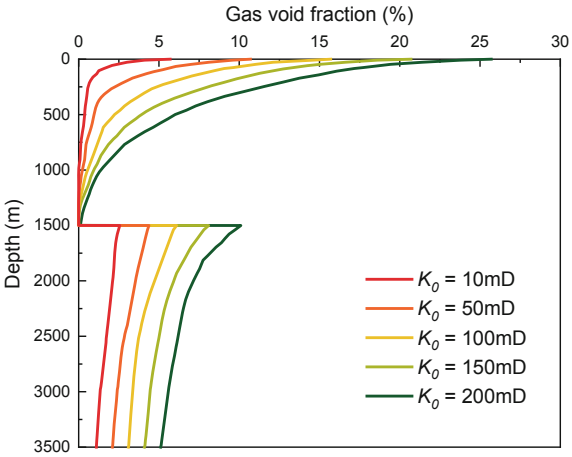

Fig. 2. Variation of gas void fraction versus depth under different permeability

According to the calculation results, the differences between the gas void fraction at different depths are obvious. The gas void fraction is less than 5% with permeability of 10 md, while that reaches 27.6% with the permeability of 200 md under the gas invasion process.

Additionally, the variation of formation parameters alter the gas void fraction under the conditions of the deepwater drillling. Once gas invasion occurs, the flow changes, which will cause overflow and even blowout under high permeability. Thus, the prediction of formation parameters has pivotal meaning in gas invasion prevention and risk control.

3 Gas Void Fraction Measurement

Figure 3 illustrates the Sketch of gas void fraction measurement with Doppler ultrasonic wave. The attenuation of Doppler ultrasonic wave can reflect the variation of gas void fraction in the borehole. The transmitting and receiving sensors are installed per 100 m, which can monitor the gas void fraction. According to the data from Doppler ultrasonic wave, the gas void fraction versus depth is obtained during the deepwater drilling process.

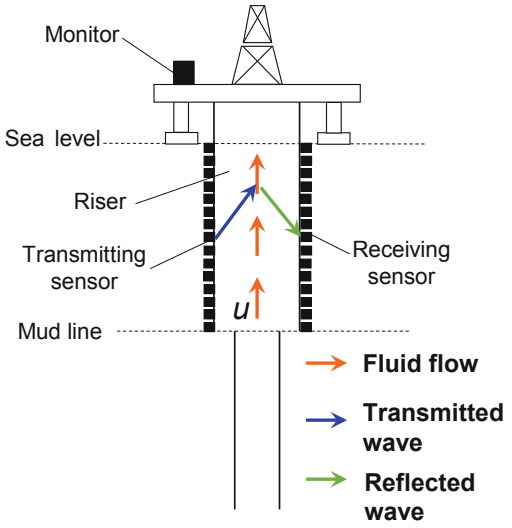

Fig. 3. Sketch of gas void fraction measurement [4]

Figure 4 shows the relationship between the gas void fraction and depth during the experiments. The results indicate that the gas void fraction increases gradually with the increasing depth. The gas void fraction exceeds 15% at the wellhead.

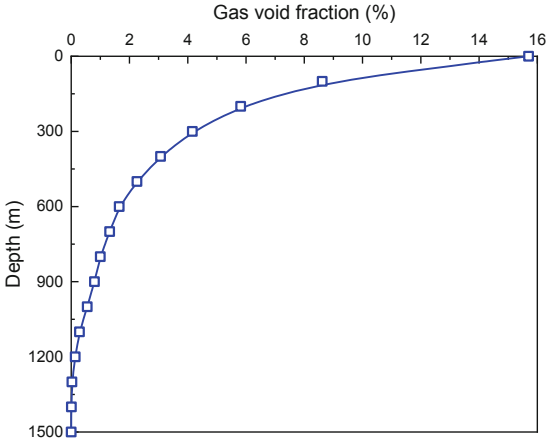

Fig. 4. Correlation between the gas void fraction and depth in tests

4 Formation Parameter Prediction

4.1 Prediction Method

Combining the calculation model mentioned above and the gas void fraction tests, we proposed a method to predict the formation parameter after gas invasion during deep-water drilling. Firstly, the gas void fraction calculation charts can be obtained based on the model with considering different formation parameters. In addition, the formation parameters (i.e. permeability) can be determined through comparing the test curves and the calculation charts for gas void fraction. Thus, we can get a best approximation from the gas void fraction calculation charts, which could be used as the actual value of the identified formation parameter (i.e. permeability).

4.2 Identifying the Formation Parameters

Specifically, the formation parameters (i.e. permeability) can be identified by combining the test data and chart obtained through the model. Based on the calculation results of gas void fraction obtained from this proposed model, we can plot the gas void fraction charts with different permeability(i.e.10 md, 50 md, 100 md, 150 md, 200 md). Compared with the gas void fraction with different permeability, we could find a similar curve in the charts according to the test curve in Fig. 4. The permeability of identified curve in Fig. 2 represents the actual permeability in the tests. Thus, the formation parameters can be obtained through the gas void fraction charts calculated by the proposed model in this paper.

4.3 Case Study

As stated above, the correlation between gas void fraction and depth is determined, as shown in Fig. 4. This test result shows the relationship between the gas void fraction and depth with certain permeability and porosity. Furthermore, the results can be used to predict the formation parameter (i.e. permeability). Using the curve from the test, we can compare and match the real curve with a correlation chart to further acquire the permeability of the formation, such as Fig. 5. The curve obtained from tests is similar to the curve in the correlation chart under permeability of Line 3, indicating that the reference value of the permeability under the test condition is in the range of 100–110 md. Thus, we can obtain a good approximation.

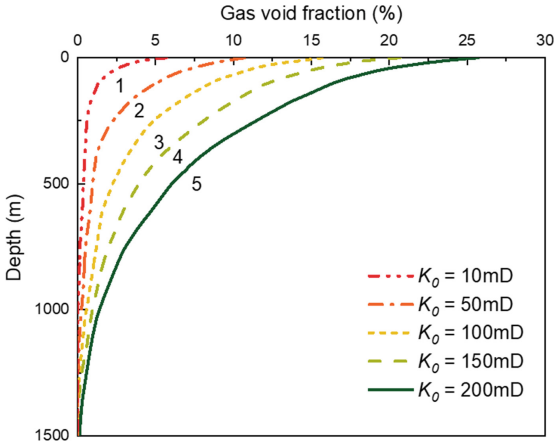

Fig. 5. Calculation chart

5 Conclusion

This paper presents a novel method by combining gas void content monitoring and a gas-liquid two phase flow model to predict the formation parameters after overflow. The gas void fraction measurement and application in deepwater drilling are shown in detail. Besides, the formation permeability is determined based on the curve obtained from the test and the correlation chart. The main conclusions are summarized as follows:

The gas void fraction depends on the total well depth as well as formation parameters. The high permeability brings in an obvious increase in gas void fraction, which can increase the risk of blowout incidents.

Combining the test data and correlation chart, the formation parameters can be identified effectually before the blowout. This method can be used to prevent blowout and realize well control in deepwater drilling.

Symbol Description

Φ_g, Φ_m—Gas and drilling mud faction in borehole
u_g, u_m—Gas and drilling mud velocity of flow
ρ_g, ρ_m—Gas and drilling mud density in borehole
z—Total well depth
t—Gas invasion time
p—Pressure
h—Friction along the borehole
T—Temperature
Z—Z-factor
γ_g—Relative density of natural gas
Q_g—Volume of invasion gas
Q_m—Volume of drilling mud in circulation
u_{sg}—Gas superficial velocity

Acknowledgments. This paper was sponsored by Natural Science Foundation of Shandong (NO. ZR2020ME095, ZR2021ME001); National Natural Science Foundation of China (Nos. 51991363, Nos. 52074325). These financial supports are gratefully acknowledged. We recognize the support of China University of Petroleum (East China) for the permission to publish this paper.

References

1. Sun, Z.Y., Zhou, J.L., Gan, L.F.: Safety assessment in oil drilling work system based on empirical study and analytic network process. Saf. Sci. **105**, 86–97 (2018)
2. Abimbola, M., Khan, F., Khakzad, N.: Dynamic safety risk analysis of offshore drilling. J. Loss Prev. Process Ind. **30**, 74–85 (2014)
3. Yin, B., Li, B., Liu, G., Wang, Z., Sun, B.: Quantitative risk analysis of offshore well blowout using bayesian network. Saf. Sci. **135**, 105080 (2021)
4. Yin, B., et al.: A gas kick early detection method outside riser based on doppler ultrasonic wave during deepwater drilling. Pet. Explor. Dev. **47**(4), 846–854 (2020)
5. Ren, M.P., et al.: The Characteristics and identification method of gas-liquid two flow overflow in deepwater drilling. J. Eng. Thermophys. **28**(1), 86–92 (2016)
6. Geng, Y., et al.: Study on real-time ultra sonic kick detection technique along riser during deep water drilling operations. China Offshore Oil Gas **28**(1), 86–92 (2016)
7. Abimbola, M., Khan, F., Khakzad, N.: Dynamic safety risk analysis of offshore drilling. J. Loss Prev. Process Ind. **30**, 74–85 (2014)
8. Li, X.F., et al.: Study on two-phase gas-liquid flow during gas kick. J. Eng. Thermophys. **25**(1), 73–76 (2004)

Natural Gas Hydrate Production

Visual Experimental Study on Hydrate Dissociation in Porous Media

Ningtao Zhang, Shuxia Li(✉), Litao Chen, and Jianbo Zhang

Key Laboratory of Unconventional Oil and Gas Development, Ministry of Education, China University of Petroleum (East China), Qingdao 266580, China
lishuxia@upc.edu.cn

Abstract. As a new type of unconventional energy, the research of natural gas hydrate is of great importance. The dissociation of hydrate in porous media has a significant influence on the hydrate development process; however, studies of the instantaneous dissociation characteristics of hydrate are still lacking. In this paper, the instantaneous hydrate dissociation induced by depressurization was investigated using a microfluidics device. The direct proof of the induced local re-formation of the hydrate by the gas-liquid flow was given during the dissociation process. And the gas-liquid-solid phase saturation played a significant role in hydrate dissociation. High hydrate saturation (Sh: 78.1%) affected pore connectivity, causing hydrate to dissociate with pressure spread, generating a distinct hydrate dissociation front. However, under the conditions of high water saturation (Sw: 96.2%, Sh: 3.3%) or high gas saturation (Sg: 60.6%, Sh: 16.0%), the pore connectivity was better, the pressure spread rapidly, and the hydrate dissociated simultaneity in the pores. Therefore, hydrate saturation was the key to inhibiting the rate of hydrate dissociation and affected the mass transfer. At the same time, there were phenomena such as expansion, growth, coalescence, and retention of bubbles during dissociation. Compared with high gas saturation, a large number of microbubbles were generated during the dissociation process under high water saturation and high hydrate saturation, which might have an impact on the future gas production efficiency. These findings are beneficial for understanding the microscale mechanisms of the hydrate dissociation efficiency, which may provide a theoretical foundation for future natural gas hydrate development.

Keywords: Hydrate · Depressurization · Hydrate reformation · Methane microbubbles · Microfluidics

1 Introduction

The share of natural gas in the world's primary energy consumption is increasing year by year as the world's energy structure transforms to low carbon [1]. As an ice-like substance formed when natural gas and water are combined at high pressure and low temperature, natural gas hydrate has the advantages of wide distribution, large reserves, and low pollution [2]. Therefore, natural gas hydrate has great development potential.

B. Sun et al. (Eds.): DWOG-Hyd 2021, LNCE 246, pp. 105–114, 2022.
https://doi.org/10.1007/978-981-19-0960-3_10

The hydrate dissociation has a significant impact on the exploration and development of natural gas hydrate. Although more studies and summaries on the dissociation of hydrate in porous media have been published in recent years, several key questions need to be addressed before exploitation. The first question concerns the ease with the direct observation of the instantaneous hydrate dissociation process. X-ray computed tomography (CT), magnetic resonance imaging (MRI) have been extensively applied. CT technology can monitor the internal spatial structure of sediment accurately, but the long scanning time and intermittent observation method of CT technology make it difficult to record the instantaneous process of hydrate nucleation and growth in pores [3]. Although MRI technology can represent the material composition distribution in pores, its spatial resolution is poor, making it difficult to meticulously depict local pore structure and gas-liquid-solid distribution [4, 5]. Thus, the research of the instantaneous dissociation characteristics of hydrate with the use of CT and MRI technology is still limited. The stop-and-go depressurization method has a significant difference from the direct depressurization. A better observation method is vital if we are to gain an understanding of the dynamic evolution of pore structures with instantaneous hydrate dissociation induced by depressurization.

A second question concerns the influence of gas-liquid-solid phase saturation on hydrate dissociation. Heat/mass transfer, phase transition, and multiple fluid seepage are involved in the hydrate dissociation process. Gas-liquid-solid phase saturation is potentially related to these factors. For example, some scholars found that gas-liquid flow during the hydrate dissociation would cause the re-formation of hydrate according to the feedback of the temperature of the measuring points [6]. At the same time, the initial distribution of hydrate can further affect gas production at the dissociation stage [7, 8]. However, a lack of observational evidence at the pore scale means that many of the assumptions currently made about how gas-liquid-solid phase saturation influences the hydrate dissociation process have not been verified. Thus, it is essential to investigate the influence of gas-liquid-solid phase saturation on hydrate dissociation with direct observation.

Microfluidics technology, in contrast to other pore-scale technologies like CT and MRI, provides a non-destructive, quick, and low-cost experimental approach [9–11]. In this paper, the dynamic evolution of pore structures with instantaneous hydrate dissociation induced by depressurization was investigated at the pore scale using a micromodel representing sediments in the laboratory. The influence of the gas-liquid-solid phase saturation on hydrate dissociation, as well as the hydrate re-formation, was studied. And the evolution characteristics of microbubbles during hydrate dissociation were discussed, including CH4 bubble expansion, growth, coalescence, and retention.

2 Experimental Section

2.1 Materials and Apparatus

The experimental system diagram is depicted in Fig. 1. The entire experimental system is divided into four sections: fluid supply, temperature control, pressure control, and data collection. The laboratory produces deionized water, and pure methane gas (99.99%) is acquired from Yantai Deyi Gas Co., Ltd. in China. The CCD (Charge-coupled Device)

camera is installed above the micromodel and illuminated by a cold light source. During the test, videos are captured. The micromodel used to form hydrate can work in a high-pressure environment (withstand 8 MPa inside). Figure 2(a) and (b) shows a picture of the overall 3D structure of the micromodel and a physical picture of the etched porous network. Parameters of the etched porous network are shown in Fig. 2(c). The phases of gas-liquid-solid in pores may be easily identified due to the difference in refractive index.

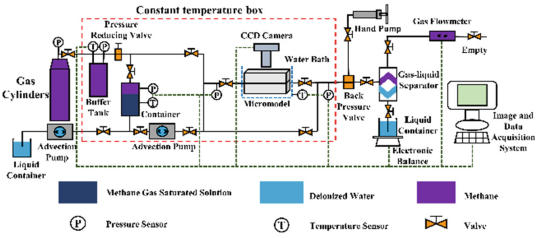

Fig. 1. System diagram of the experimental

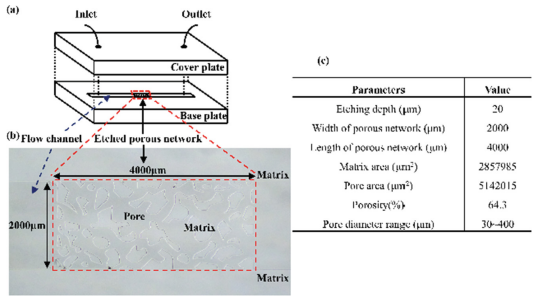

Fig. 2. The micromodel used in this study. (a) 3D etched pore structure; (b) a physical picture of the etched porous network; (c) parameters of the etched porous network

2.2 Experimental Procedures

The main experimental procedures can be summarized as five steps. (1) Loading of experimental materials and vacuum processing of the experimental system. Deionized water was injected into the container first, and then the whole system was vacuumed for 1 h. The gas buffer tank was then injected with methane gas. (2) Reducing the system temperature. The constant temperature box was adjusted to reduce the temperature of the gas in the buffer tank and the deionized water in the container to about 274.15K, while the water bath's temperature was also cooled. (3) Hydrate formation. Different distribution and morphology of hydrates in the pores were formed, while the gas-liquid-solid phase saturation and the formation pressure were controlled. (4) Depressurization for hydrate dissociation. When the formation of the hydrate was complete, the back pressure valve was adjusted to dissociate the hydrates according to the pressure drop range.

(5) Data processing. During the hydrate formation, the experimental device's temperature and pressure data were gathered and recorded, and the CCD camera continually recorded changes in the phase saturation of gas-liquid-solid. The image was processed and segmented using ImageJ software. The details of the experimental conditions are summarized in Table 1.

Table 1. Experimental conditions for hydrate dissociation.

Exp	P_f/MPa	P_{eq}/MPa	P_d/MPa	Before dissociation		
				S_g (%)	S_W (%)	S_h (%)
1	5	3	2.74	10.2	53.5	36.3
2	4.22	3	0.88	0.6	96.2	3.3
3	6	4	3.84	60.6	23.4	16.0
4	4.52	3	2.8	4.3	17.7	78.1

P_f = the formation pressure; P_{eq} = the phase equilibrium pressure; P_d = the dissociation pressure.

3 Experimental Results and Discussion

Observing hydrate phase transition and the dynamic evolution of pore structures in porous media is significant for understanding the instantaneous dissociation characteristics of hydrate. Moreover, gas-liquid-solid phase saturation can affect hydrate re-formation at the dissociation stage. Thus, it is essential to investigate the process of hydrate dissociation at different liquid-solid phase saturation.

3.1 A Certain Amount of Free Gas and Free Water in Pores Before Hydrate Dissociation

Figure 3 shows the process of hydrate dissociation when a certain amount of free gas and free water was in pores. In this experiment, hydrate dissociation mainly consists of four stages. Initially (Fig. 3b), as the pore pressure began to decrease, the original gas phase in the pores began to expand while some bubbles were generated from at the hydrate boundary. Then (Fig. 3c), the flow of gas and liquid induced local re-formation of hydrate at the inlet. Over time (Fig. 3d), hydrates dissociated with the propagation of pressure and some bubbles become more dispersed, reunite and deform. Eventually (Fig. 3b), there were more small bubbles staying in the pores. The main processes of hydrate dissociation were extremely fast, with time scales on the order of milliseconds. Because pressure propagation takes time during hydrate dissociation, the pressure at the inlet was larger than the phase equilibrium pressure within a specific length of time, and the gas-liquid flow increased the contact area of the gas-liquid and promoted hydrate re-formation.

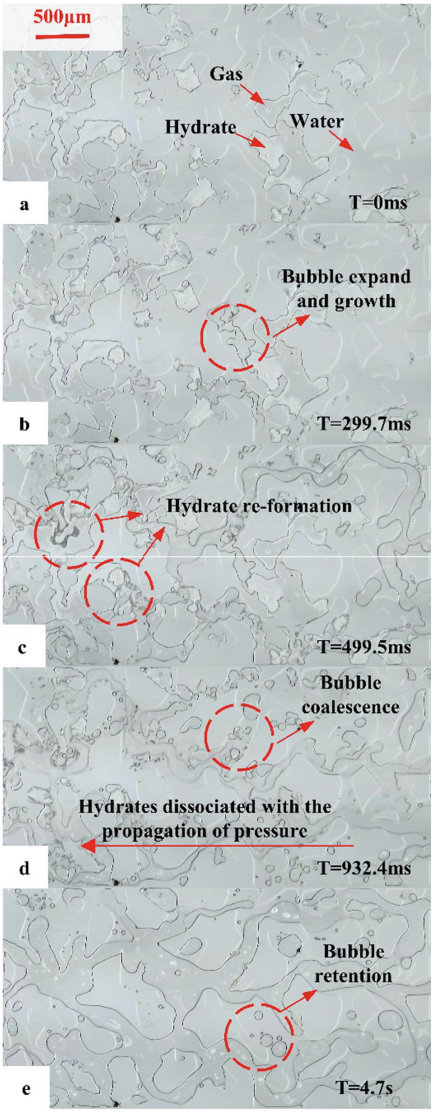

Fig. 3. The process of hydrate dissociation when a certain amount of free gas and free water was in pores (Exp.1)

3.2 Hydrate Dissociation at Different High Phase Saturation

(1) High water saturation

Figure 4 shows the process of hydrate dissociation at high water saturation. In this experiment, the process of hydrate dissociation was relatively simple. Because the hydrate saturation was low, the pore connectivity was good and the pressure spread faster. After the bubbles expanded and formed (Fig. 4b), all hydrates dissociated simultaneity (Fig. 4c). In the later stage of dissociation (Fig. 4d), the gas dissolved in the liquid was continuously resolved and randomly distributed in the pores.

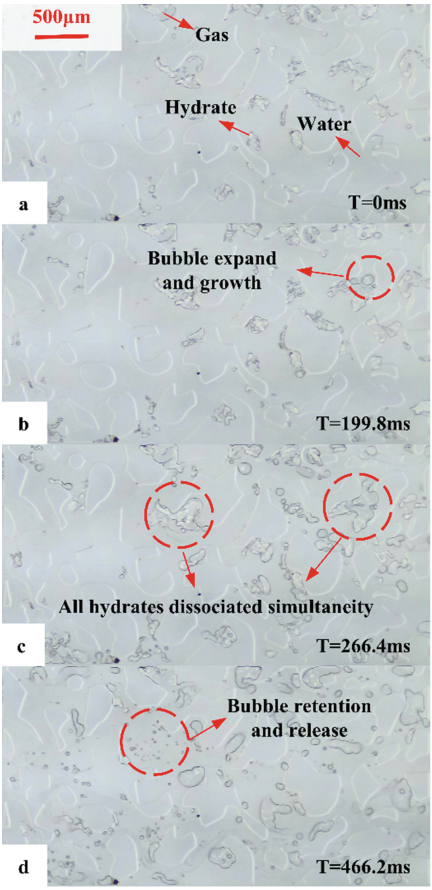

Fig. 4. The process of hydrate dissociation at high water saturation (Exp. 2)

(2) High gas saturation

Figure 5 depicts the process of hydrate dissociation at high gas saturation. Similar to the process of hydrate dissociation at high water saturation, pore connectivity was very good under low hydrate saturation, and all hydrates also dissociated simultaneity. The difference was that the gas phase in the pores was the main continuous phase, the gas

produced by dissociation and expansion immediately merged into the gas phase in the pores, so there were fewer small bubbles generated in the pores, and the pore structure changes relatively little, and the water phase attached to the grain surface as it is.

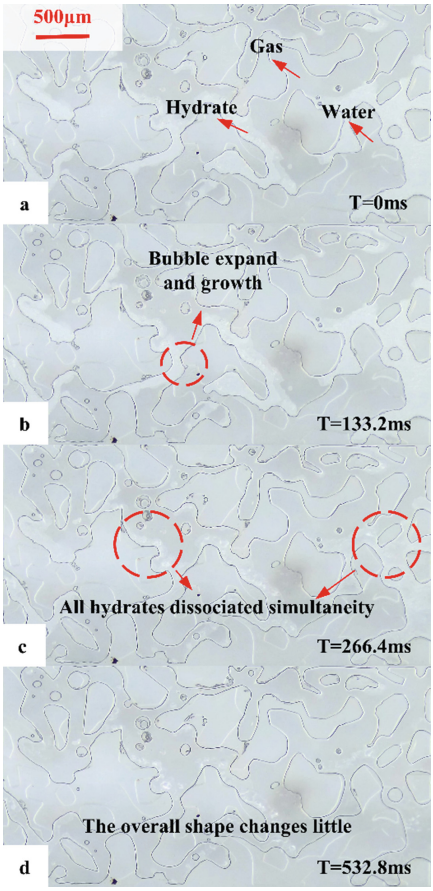

Fig. 5. The process of hydrate dissociation at high gas saturation (Exp. 3)

(3) High hydrate saturation

Figure 6 illustrates the process of hydrate dissociation at high hydrate saturation. Before hydrate dissociation (Fig. 6a), the pores were completely blocked by hydrate. Pore connectivity was very bad at high hydrate saturation. In the initial stage (Fig. 6b), as the pressure drops, some gas began to flow at the outlet. Over time, hydrates dissociated with the propagation of pressure. This also caused an interesting phenomenon. By comparing Fig. 6 c and Fig. 6d, it is found that hydrate re-formation also occurred with the propagation of pressure. At the end of dissociation (Fig. 6e), more and more bubbles were resolved from the liquid.

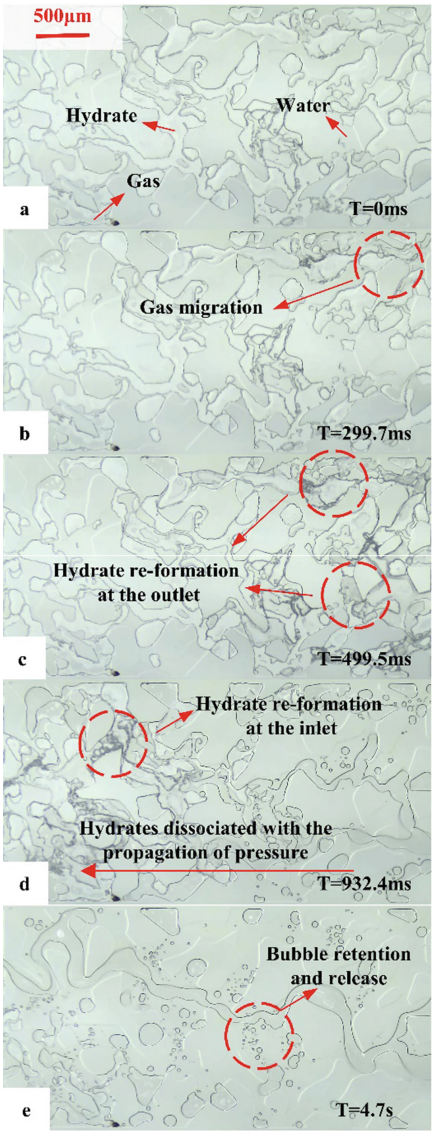

Fig. 6. The process of hydrate dissociation at high hydration saturation (Exp. 4)

4 Conclusion

The purpose of this article is to investigate the dynamic evolution of pore structures with instantaneous hydrate dissociation induced by depressurization in porous media, as well as to identify the influence of gas-liquid-solid phase saturation on hydrate dissociation. The following conclusions can be taken from the experimental results at the pore scale:

(1) Gas-liquid-solid phase saturation plays a significant role in hydrate dissociation. Gas-liquid-solid phase saturation is related to mass transfer, phase transition, and multiple fluid seepage in the hydrate dissociation process.
(2) When a certain amount of free gas and free water was in pores, the dissociation was accompanied by the re-formation of hydrates, and hydrates dissociated with the propagation of pressure.
(3) The pore connection was good during the hydrate dissociation process at high water or gas saturation. Hydrates would not form, and all hydrates would dissociate simultaneity.
(4) The pore connection was poor during the hydrate dissociation process at high hydrate saturation. Hydrate re-formation, as well as the hydrate dissociation, occurred with the propagation of pressure.
(5) The expansion, growth, coalescence, and retention of bubbles were observed during hydrate dissociation.

Acknowledgement. This work is supported by the Major Program of the National Natural Science Foundation of China (51991365), National Natural Science Foundation of China (52074334, 51974347), which are gratefully acknowledged.

References

1. Petroleum, B.: Energy Outlook 2020. BP, London (2020)
2. Sloan, E.D., Koa, C.A.: Clathrate Hydrates of Natural Gases, 3rd edn. CRC Press, Boca Raton (2007)
3. Kou, W., Li, X., Wang, Y., et al.: Pore-scale analysis of relations between seepage characteristics and gas hydrate growth habit in porous sediments. Energy **218**, 119503 (2021)
4. Kleinberg, R.L., Flaum, C., Griffin, D.D., et al.: Deep sea NMR: methane hydrate growth habit in porous media and its relationship to hydraulic permeability, deposit accumulation, and submarine slope stability. J. Geophys. Res. Solid Earth **108**(B10), 2508 (2008)
5. Zhang, L., Kuang, Y., Dai, S., et al.: Kinetic enhancement of capturing and storing greenhouse gas and volatile organic compound: micromechanism and micro-structure of hydrate growth. Chem. Eng. J. **379**, 122357 (2020)
6. Li, X., Wang, Y., Li, X., et al.: Experimental study of methane hydrate dissociation in porous media with different thermal conductivities. Int. J. Heat Mass Trans. **114**, 118528 (2019)
7. Dai, S., Santamarina, J.C., Waite, W. F., et al.: Hydrate morphology: physical properties of sands with patchy hydrate saturation. J. Geophys. Res. Solid Earth **117**(B11) (2012)
8. Ren, X., Guo, Z., Ning, F., et al. Permeability of hydrate-bearing sediments. Earth-Sci. Rev. **202**, 103100 (2012)

9. Wang, S., Cheng, Z., Liu, Q., et al. Microscopic insights into CH4 hydrate formation and dissociation in sediments using microfluidics. Chem. Eng. J. **248**(7), 117227 (2021)
10. Tohidi, B., Anderson, R., Clennell, M.B., et al.: Visual observation of gas-hydrate formation and dissociation in synthetic porous media by means of glass micromodels. Geology **29**(9), 867–870 (2001)
11. Pandey, J.S., Strand, R., Solms, N.V., et al.: Direct visualization of CH_4/CO_2 hydrate phase transitions in Sandstone Pores. Cryst. Growth Des. **21**, 2793–2806 (2021)

Numerical Simulation of Combined Depressurization Production of Natural Gas Hydrate and Shallow Gas

Fengrui Zhao[1,2] and Shuxia Li[1,2(✉)]

[1] Key Laboratory of Unconventional Oil and Gas Development, China University of Petroleum (East China), Qingdao 266580, Shan-dong, China
lishuxia@upc.edu.cn

[2] College of Petroleum Engineering, China University of Petroleum (East China), Qingdao 266580, Shan-dong, China

Abstract. Natural gas hydrate (NGH) usually coexists with the shallow gas at the bottom. The combined production of NGH and shallow gas can greatly reduce the cost of hydrate production. Therefore, it is of great significance to study the combined exploitation of NGH and shallow gas. Based on the geological data of hydrate reservoirs, this paper divides the coexistence modes of NGH and shallow gas into three types: type A (upper hydrate and underlying free gas), type B (upper hydrate, permeable interlayer and underlying free gas), type C (upper hydrate, impermeable interlayer and underlying free gas). The geological model of combined depressurization production of NGH and shallow gas is established by numerical simulation. The gas production performance of combined depressurization is calculated under different coexistence modes. The influence of parameters such as permeability, thickness and area of interlayer on gas production in type B coexistence modes are analyzed. The results show that the accumulative gas production of combined production is the highest in the type A, B and C coexistence modes. In the type B coexistence mode, when only hydrate is exploited, the lower the permeability is, the thicker the thickness is, and the larger the area is of the interlayer, the more the interlayer seepage is hindered. Therefore, the thickness, area and permeability of the interlayer have an important impact on the production performance of hydrate reservoirs. This study can provide theoretical basis for the combined production of NGH and shallow gas in the future.

Keywords: Natural gas hydrate · Shallow gas · Coexistence modes · Combined production · Depressurization

1 Introduction

As global climate change and the greenhouse effect become more serious, the world's demand for clean energy is increasing year by year. As important clean energy, the proportion of natural gas consumption is also growing rapidly in the energy structure [1]. Natural gas hydrate (combustible ice) is an ice-packed substance formed by natural gas and water under low temperature and high pressure. It has huge reserves and is mainly

B. Sun et al. (Eds.): DWOG-Hyd 2021, LNCE 246, pp. 115–123, 2022.
https://doi.org/10.1007/978-981-19-0960-3_11

distributed in sea bottom slope land and permafrost [2]. According to previous studies, a large number of hydrocarbon gases will migrate to the upper strata from the deep oil and gas reservoirs. The structures such as gas chimney, faults and connecting fractures in the strata provide an upward channel for the migrated fluid. The migrated gas and water will form a natural gas hydrate stability zone (GHSZ) under appropriate temperature, pressure and structural conditions, and accumulate shallow gas below. It can be seen that there is a spatial coexistence relationship between NGH, lower shallow gas and deep oil and gas [3, 4]. Collett et al. [5] proposed natural gas hydrate oil-gas system; Wu [6] and Sun [7] focused on the seepage geological structure on gas migration; Lei [8] put forward three basic coexistence modes between hydrate and oil and gas resources from the perspective of geological reservoir formation; Liu [9] and Xin [10] focused on the feasibility of hydrate as caprock and the gas source of the reservoir. In conclusion, the obtained geological characteristics can provide the evidence for the coexistence of hydrate and traditional oil and gas reservoirs. However, the definition of the concept of coexistence modes mostly lies in the geological accumulation theory and methods, and there is no definite conclusion in the simulation. At present, scholars at home and abroad have conducted a lot of research on the numerical simulation of natural gas hydrate exploitation by the depressurization [11–14], but the models mostly use pure hydrate, hydrate combined with free gas or free water as the research objects. Few numerical simulation studies have been conducted from the perspective of coexistence of oil and gas reservoirs. Therefore, from the perspective of reservoir formation, this paper divides the coexistence modes of NGH and shallow gas into three types: type A (upper hydrate and underlying free gas), type B (upper hydrate, permeable interlayer and underlying free gas), and type C (upper hydrate, impermeable interlayer and underlying free gas). The geological model of combined depressurization production of NGH and shallow gas is established by numerical simulation. The gas production performance of combined depressurization is calculated under different coexistence modes. The influence of parameters such as permeability, thickness and area of interlayer on gas production in type B coexistence modes are analyzed.

2 Numerical Simulation of Combined Depressurization Production of NGH and Shallow Gas

2.1 Coexistence Mode of NGH and Shallow Gas

From the perspective of development, this paper divides the coexistence modes of NGH and shallow gas into three types. Type A is composed of upper hydrate and underlying free gas, simulates the upward migration of deep gas, and forms GHSZ under appropriate temperature, pressure and structural conditions. With the continuous migration and diffusion of gas, shallow gas reservoirs are formed in the bottom of hydrate; type B is composed of upper hydrate, middle permeable interlayer and lower shallow gas. The permeable interlayer is used to simulate fluid seepage channels such as gas chimney, fault and fracture between hydrate and gas reservoir; type C is composed of upper hydrate, middle impermeable barrier and lower shallow gas layer. The impermeable interlayer is used to simulate the geological structure of seepage channel plugging caused by geological structure changes. The conceptual diagram of three types of occurrence modes is shown in the Fig. 1.

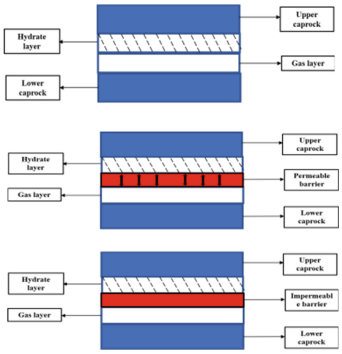

Fig. 1. Conceptual diagram of coexistence modes of A (upper), B (middle) and C (lower)

2.2 Model of Numerical Simulation

The geological model of the three types of coexistence modes is established by using numerical simulation software, taking type B as an example, as shown in Fig. 2. Numerical model of type B coexistence mode includes upper overburden, hydrate layer, middle permeable interlayer, underlying gas layer and underlying caprock. The thickness of hydrate layer is 20 m, the thickness of the underlying gas layer is 20 m, and the upper and lower caprocks are set at 30 m. The model size is 250 m * 250 m * 100 m. The I and J directions are divided into 29 grids on the model plane, and the grids near the well are encrypted. The horizontal grid distribution is 12 * 20 m, 5 * 4 m and 12 * 20 m. There are 40 grids in K direction. The longitudinal grid distribution of hydrate layer, middle permeable interlayer, underlying gas layer, upper and lower caprocks are 20 * 1 m, 1 * 5 m, 10 * 2 m and two 5 * 6 m, respectively.

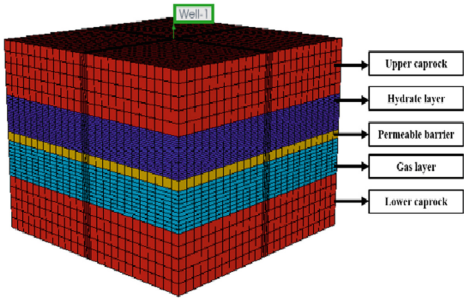

Fig. 2. Numerical model of type B coexistence mode

The water depth in the model area is 1200 m, and the depth of the hydrate layer from the seabed is 230 m. The initial pressure at the bottom interface of hydrate layer is 13.83 MPa, and its initial temperature is 14.15 °C. The ground temperature gradient is set at 5 °C/100M, and the pressure gradient is set at 100 M/MPa. The simulated production pressure is set at 4 MPa, and the simulated production time is 3 years. The detailed parameter settings are shown in Table 1.

2.3 Numerical Simulation Scheme Design

In this paper, when the numerical simulation of depressurization production is carried out for the three types of coexistence modes of A, B and C, three production modes are adopted: only producing hydrate layer, only producing gas layer and combined production of hydrate and gas layer. Then the gas production effects are compared and analyzed under different schemes.

Table 1. Basic parameters of coexistence mode

Reservoir types	Parameter	Value
Hydrate layer	Porosity φ	0.4
	Horizontal permeability $K_{i,j}$ (10^{-3} μm^2)	35
	Vertical permeability K_k (10^{-3} μm^2)	1
	Hydrate saturation Sh	0.6
	Water saturation S_w	0.4
Gas layer	Porosity φ	0.4
	Permeability K (10^{-3} μm^2)	75
	Gas saturation Sg	0.4
	Water saturation S_w	0.6
Upper and lower caprock	Porosity φ	0.15
	Permeability K (10^{-3} μm^2)	1
	Water saturation Sw	1
Permeable interlayer	Thickness H (m)	5
	Porosity φ	0.1
	Gas saturation S_g	0.05
	Water saturation S_w	0.95
	Permeability K (10^{-3} μm^2)	7.5
Impermeable interlayer	Thickness H (m)	5 m
	Porosity φ	0.1
	Water saturation S_w	1
	Permeability K (10^{-3} μm^2)	0.001
Relative permeability parameters	Irreducible water saturation S_{irw}	0.5
	Irreducible gas saturation S_{irg}	0.05
	Attenuation index of water permeability n_{w}	4
	Attenuation index of gas permeability n_{g}	5

3 Results and Discussion

3.1 Gas Production Performance of Combined Production Under Different Coexistence Modes

Figure 3, 4 and 5 show the gas production performance of different production schemes under three coexistence modes. As shown in the figure, the change trend of gas production dynamic curve is generally similar. The combined production mode has the highest cumulative gas production in each coexistence mode.

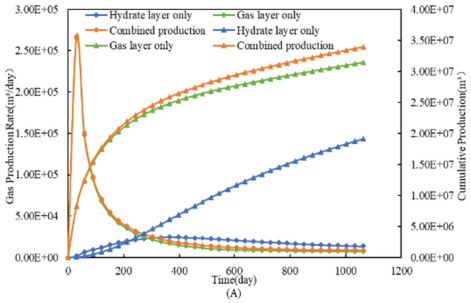

Fig. 3. Changes in gas production dynamics with time under type A coexistence mode

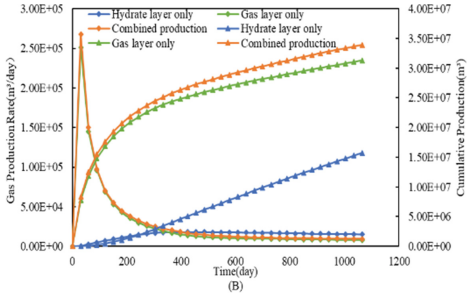

Fig. 4. Changes in gas production dynamics with time under type B coexistence mode

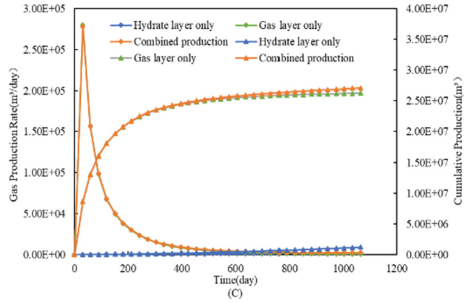

Fig. 5. Changes in gas production dynamics with time under type C coexistence mode

At the initial stage of production, the gas production rate of only gas production and combined production increases rapidly, which is much higher than that of only hydrate production. After reaching the peak value, the gas production rate decreases rapidly. The gas production rate of only hydrate production is the same as that of the first two, but the peak is obviously low, and the gas production rate in the middle and later stage exceeds that of the first two production methods. The reason of this phenomenon is that the pressure drop of hydrate is difficult to propagate and the hydrate decomposition is slow at the early stage of production. However, the gas in the gas zone is highly mobile. Under the action of high production pressure difference, the gas can be quickly produced from the bottom of the hole, leading to the gas production peak of extremely high, and the pressure drop in the gas zone can quickly spread. With the decrease of reservoir pressure and gas amount near the well, the gas production rate decreases rapidly. In the case of only hydrate production, there is a phenomenon that the gas in the gas layer escapes into the hydrate layer and produces. In the early stage of production, gas interlayer seepage is hindered by hydrate, which leads to the peak of gas production lag and decrease. The presence of impermeable interlayer blocks the interlayer seepage and makes the gas production curve show the same trend as that of only hydrate production.

3.2 Influencing Factors of Gas Production Dynamics

According to the above study, due to the strong seepage capacity of gas, the gas production rate in the early stage will increase rapidly and then decrease in the case of gas layer production and combined production, and the effect of interlayer hindering gas seepage is difficult to be reflected in the curve. Therefore, in order to clarify the influence of interlayer geological parameters on gas production more clearly, this section discusses the influence of permeability, thickness and area of interlayer on gas production in the type B coexistence mode when only hydrate is exploited.

3.2.1 Interlayer Permeability

Based on the previous model, the permeability of the interval was set as 7.5 md, 75 md and 0.75 md, respectively. Other parameters remain unchanged to study the influence of interval permeability on gas production.

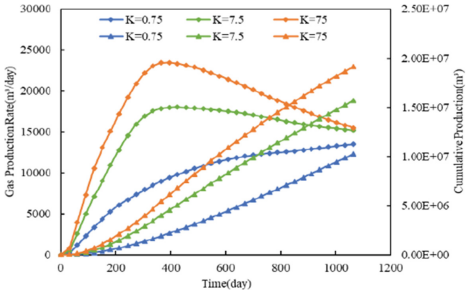

Fig. 6. Variation of gas production with time under different permeability of interlayer

It can be seen from Fig. 6 that under the same production conditions, the greater the permeability of the interlayer, the higher the gas production rate, and the higher the final cumulative gas production. The reason is that the inhibition of gas seepage in the gas layer is weakened with the increase of interlayer permeability. With gas flowing into the gas hydrate layer and producing, the pressure of gas layer decreases simultaneously, and the pressure drop propagation promotes the decomposition of gas hydrate at the bottom.

3.2.2 Interlayer Thickness

Based on the previous model, the thickness of the interval was set as 5 m, 15 m and 25 m, respectively. Other parameters remain unchanged to study the influence of interlayer thickness on gas production.

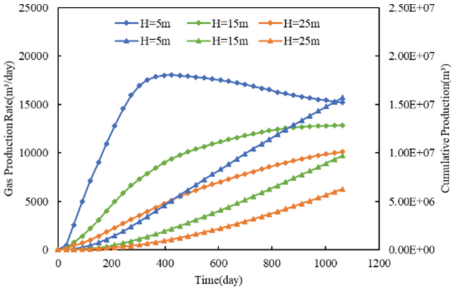

Fig. 7. Variation of gas production with time under the different thickness of the interlayer

It can be seen from Fig. 7 that with the increase of interlayer thickness, the lower the gas production rate and cumulative gas production. Due to the increase of the interlayer thickness, it is more difficult for the free gas to escape the hydrate layer. The decrease of gas production rate in the early stage leads to a slow decrease of the pressure in the gas layer, and the increase of the thickness of the interlayer hinders the propagation of pressure drop, which affects the decomposition rate of hydrate in the middle and late stage, resulting in a large gap between the gas production rate and accumulated gas production in the late stage.

3.2.3 Interlayer Area

Firstly, the area of the simulation model is normalized to 1. The blocking effect of the interlayer area on gas seepage was studied by setting different area ratios of the interlayer layer. Here the area ratios are 0.25, 0.5 and 0.75, respectively.

It can be seen from Fig. 8 that with the decrease of the interval area, the gas production rate and accumulative gas production both increase, but the increase is slowing down. The reason is that with the decrease of the area of the interlayer, the ability of interlayer to inhibit gas flow into hydrate layer is weakened. Therefore, the gas production rate is improved, the gas pressure drop accelerates, and the hydrate decomposition at the boundary of the interlayer is accelerated, leading to the increase of accumulated gas production.

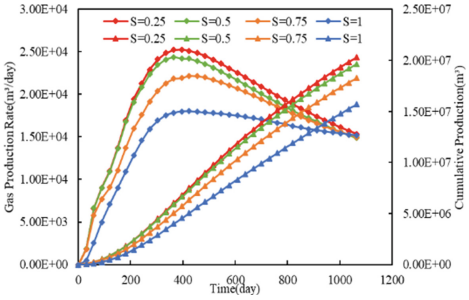

Fig. 8. Variation of gas production with time under different area of interlayer

4 Conclusion

(1) The numerical simulation results show that under the coexistence modes of type A (the upper part of gas hydrates and underlying free gas), type B (upper hydrate, interlayer permeability and the underlying free gas), and type C (upper hydrate, impermeable interlayer and underlying free gas), the cumulative gas production of combined production is the highest.

(2) When only hydrate is exploited in type B coexistence mode, the lower the permeability is, the thicker the thickness is, and the larger the area is of the interlayer, the more the interlayer seepage is hindered, the smaller the cumulative gas production is.

Acknowledgement. This work is supported by the Major Program of the National Natural Science Foundation of China (51991365), National Natural Science Foundation of China (52074334,51974347), which are gratefully acknowledged.

References

1. Petroleum, B.: Statistical Review of World Energy. BP, London (2021)
2. Makogon, Y.F., Holditch, S.A., Makogon, T.Y.: Natural gas hydrates—a potential energy source for the 21st century. J. Petrol. Sci. Eng. **56**(1–3), 14–31 (2007)
3. Sassen, R., Sweet, S.T., Milkov, A.V., et al.: Thermogenic vent gas and gas hydrate in the Gulf of Mexico slope: is gas hydrate decomposition significant. Geology **29**(2), 107–110 (2001)
4. Grauls, D.: Gas hydrates: importance and applications in petroleum exploration. Mar. Pet. Geol. **18**(4), 519–523 (2001)
5. Collett, T.S., Johnson, A.H., Knapp, C.C., et al.: Natural gas hydrates: energy resource potential and associated geologic hazards. AAPG Memoir **89**. AAPG (2010)
6. Wu, S., Gong, Y., Mi, L., et al.: Study on hydrocarbon leakage system and associated gas hydrate reservoirs in the deepwater basin of northern South China Sea. Geoscience **24**(03), 433–440 (2010)
7. Sun, Y., Wu, S., Dong, D., et al.: Gas hydrates associated with gas chimneys in fine-grained sediments of the northern South China Sea. Mar. Geol. **311**, 32–40 (2012)

8. Lei, X., Lin, G., Miao, Y., et al.: Accumulation coexistence models of natural gas hydrate and conventional hydrocarbon: an approach. Marine Origin Petro. Geol. **18**(01), 47–52 (2013)
9. Liu, J., Wang, S., Yan, W.: Research on coexistence between marine gas hydrate and deepwater oil. J. Trop. Oceanogr. **34**(02), 39–51 (2015)
10. Xin, S.: Correlation study on natural gas hydrate and hydrocarbon accumulation. Geol. Resour. **27**(02), 204–208 (2018)
11. Grover, T., Holditch, S.A., Moridis, G.: Analysis of reservoir performance of Messoyakha gas hydrate field. In: The Eighteenth International Offshore and Polar Engineering Conference, OnePetro (2008)
12. Gaddipati, M., Myshakin, E., Boswell, R., et al.: Gas production modeling from a complex 3-D description of marine hydrate deposits. In: The 7th International Conference on Gas Hydrates (2011)
13. Giraldo, C., Klump, J., Clarke, M., et al.: Sensitivity analysis of parameters governing the recovery of methane from natural gas hydrate reservoirs. Energies **7**(4), 2148–2176 (2014)
14. Li, S., Wu, D., Wang, Z., Liu, J., et al.: Numerical simulation of dissociation front of ShenHu hydrate reservoirs by depressurization. Sci. Sin. (Phys. Mech. Astron.) **49**(03), 116–126 (2019)

Numerical Simulation on Sensitivity of Related Parameters for Hydrate Dissociation by Depressurization

Wei Cui(✉), Yixian Yu, Wenbo Wang, and Jiaqi Xiao(✉)

Qilu University of Technology, Jinan 250353, China
1506304292@qq.com, jiaqixiao@qlu.edu.cn

Abstract. With the spread of the world energy crisis, natural gas hydrate, as a new clean energy resource, has attracted widespread attention. Hydrate depressurization recovery is considered to be one of the most effective methods due to its economic benefits and feasibility. However, there are still many tasks to the realization of commercial hydrate recovery.

In this study, we combined the continuity equation, the kinetic reaction equation and other auxiliary equations, and established a mathematical model in 2D cylindrical coordinate system. Then the model was discretized and solved by the finite difference method. Furthermore, Sensitivity of main control parameters to pressure distribution and gas productivity in hydrate dissociation were analyzed. The conclusions are obtained as follows: 1. In the process of hydrate decomposition, the greater the initial permeability and the initial porosity, the faster the pressure transmission, the greater the gas production rate, the greater the cumulative gas production. 2. The reservoirs with higher initial hydrate saturation have slower pressure transmission speed, lower gas production rate. 3. Comparing the influence of the initial permeability on gas production rate with that of the initial porosity, and the hydrate saturation, it can be seen that the gas production rate is more sensitive to the initial permeability.

Keywords: Natural gas hydrate · Decomposition · Control parameters · Sensitivity · Numerical simulation

1 Introduction

Although these two trial production [1, 2] in the Shenhu area of the South China Sea were very successful compared with others, there are still many tasks to the realization of commercial hydrate recovery [3, 4].

A reliable numerical simulation is crucial to study the sensitivity of the permeability, the porosity, and the hydrate saturation to the pressure distribution and the productivity for better production plan design [5–8].

B. Sun et al. (Eds.): DWOG-Hyd 2021, LNCE 246, pp. 124–131, 2022.
https://doi.org/10.1007/978-981-19-0960-3_12

2 Methodology

2.1 Mathematical Model

In this study, we combined the continuity equation, the kinetic reaction equation and other auxiliary equations, and established a mathematical model in 2D cylindrical coordinate system.

Only gas and liquid are considered in the flow, which complies with the Darcy's law.

We ignored the gravity influence, the secondary formation of the gas hydrates, and the formation compressibility.

For a reservoir with the thickness h, the borehole radius *r_w*, and the decomposition zone radius *r_e*, the daily gas production *V_g*(*m*ˆ3/d) and the cumulative gas production *Q_g* (*m*ˆ3) up to *t_*0(day) are calculated by the following formulas: Calculation of daily gas production rate V_g:

$$V_g = \int_0^h \int_{r_w}^{r_e} 2\pi r m_g d_r d_z \tag{1}$$

Calculation of cumulative gas production Q_g:

$$Q_g = \int_0^{t_0} V_g d_t \tag{2}$$

2.2 Initial Values and Boundary Conditions

In the z direction, the upper and lower formations are assumed non-permeable. The middle hydrate reservoir can be divided into many small layers; In the r direction includes the borehole and many cylindrical zones. Each layer has different initial values for the parameters including the absolute permeability, the porosity, the saturation, and the production well pressure.

2.3 Finite Difference and Discrete Solution

After the initial values and boundary conditions are given, the continuity equation is discretized by finite difference, resulting in the pressure matrix equation of the water component. Solving this equation system, we obtained the dynamic parameters of the hydrate decomposition.

$$\begin{aligned} &A(i,j)(P_w)^{n+1}_{(i-1,j)} + C(i,j)(P_w)^{n+1}_{(i,j-1)} + E(i,j)(P_w)^{n+1}_{(i,j)} + B(i,j)(P_w)^{n+1}_{(i+1,j)} \\ &+D(i,j)(P_w)^{n+1}_{(i,j+1)} = Q(i,j) \end{aligned} \tag{3}$$

Written as a matrix equation in the form (21), and then write a program to solve the problem, the process is as follows:

$$\begin{bmatrix} F_{11} & B_{11} & \cdots & D_{11} & & & & \\ A_{21} & E_{21} & B_{11} & \vdots & \ddots & & & \\ \vdots & A_{31} & E_{31} & \vdots & & \ddots & & \\ C_{12} & \cdots & \cdots & \ddots & & & & \\ & & \vdots & & \ddots & & \vdots & \\ & & & & & & D_{mn-1} & \\ & & & & & & \vdots & \\ & & & & & & B_{m-1n} & \\ & & & & C_{mn} & \cdots & A_{mn} & E_{mn} \end{bmatrix} \begin{bmatrix} P_{11} \\ P_{21} \\ \vdots \\ P_{12} \\ \vdots \\ P_{mn-1} \\ \vdots \\ P_{m-1n} \\ P_{mn} \end{bmatrix} = \begin{bmatrix} Q_{11} \\ Q_{21} \\ \vdots \\ Q_{12} \\ \vdots \\ Q_{mn-1} \\ \vdots \\ Q_{m-1n} \\ P_{mn} \end{bmatrix} \tag{4}$$

1) Input the initial parameter value; 2) Solve the matrix equation; 3) Calculate the gas pressure of each grid node, compare the gas pressure with the hydrate phase equilibrium pressure, and judge whether the hydrate is decomposed; 4) Solve the hydrate, water, gas Saturation distribution of each phase; 5) Set a reasonable time step and enter the loop solution.

3 Model Validation

Comparing the simulation results with trial production data in the Shenhu area in Fig. 1, the daily gas production changes in a similar trend, which verifies the effectiveness of the numerical simulation in this study.

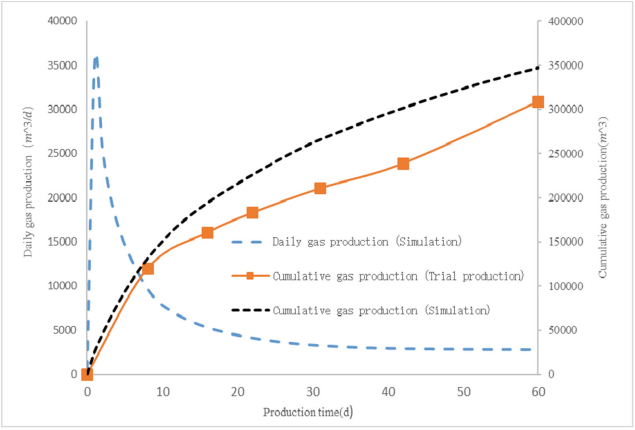

Fig. 1. Comparison of gas production calculation results and trial production data

4 Simulation Results

With the modeling of hydrate discovery by depressurization, the sensitivity of the permeability, the porosity, and the hydrate saturation to the pressure distribution and the productivity are analyzed. the results are as follows:

4.1 Intrinsic Permeability

The initial intrinsic permeability distribution in hydrate layer is shown in Fig. 2a. By initial permeability, there are eight layers from the bottom to the top: D01, D02, D03, D04, D05, D06, D07, D08. Other parameters of all formations are the same. From Fig. 2b–f, it's obvious that the larger the initial permeability, the faster the pressure transfers.

From Fig. 3 we can see, the greater the initial value of intrinsic permeability, the greater the value of gas production rate per unit thickness per unit time under the same production time. As time goes by, the gas production rate in the formation rapidly increases for the first 60 days, and then (60–1000d) gradually decreases.

In Fig. 4, as the initial permeability value increases, the gas production increases significant.

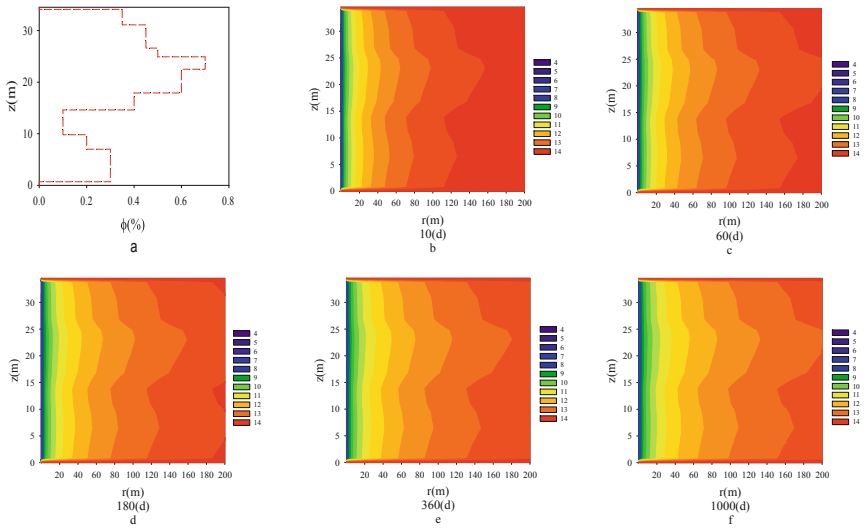

Fig. 2. The initial porosity of the reservoir and the pressure distribution map during the depressurization mining process

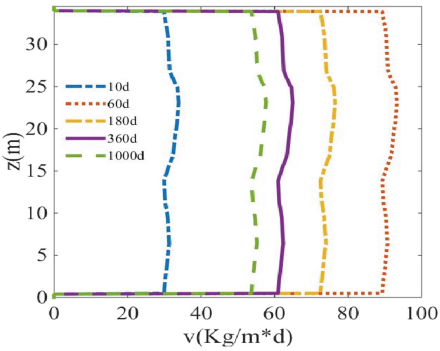

Fig. 3. Evolution of gas production rate in different initial porosity

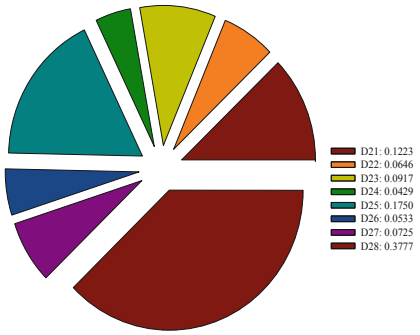

Fig. 4. Contribution rate of gas production in different porosity formations (after model improving)

4.2 Initial Porosity

By the initial porosity value, there are 8 layers from the bottom to the top: D11, D12, D13, D14, D15, D16, D17, D18 in Fig. 5.

From Fig. 5b–f, it can be seen that the larger the initial porosity, the faster the movement speed of the decomposition outer edge (the pressure is just lower than the initial value), which is similar to the initial permeability. But the initial porosity has relatively smaller effect on the pressure transmission than the initial permeability.

The larger the initial porosity value, the larger the gas production rate as we can see in Fig. 6.

From Fig. 7, Layer D12, D14, and D16 have the same thickness, while the initial porosity value increases sequentially, the cumulative gas production increases sequentially.

Layer D13 and D17 of the same thickness have a large difference in initial porosity values, but the gas production contribution rate is close.

Comparing the influence of the initial permeability on gas production rate with that of the initial porosity, it can be seen that the gas production rate is more sensitive to the initial permeability.

4.3 Initial Hydrate Saturation

By initial hydrate saturation, there are 8 layers from the bottom to the top: D21, D22, D23, D24, D25, D26, D27, D28 in Fig. 8.

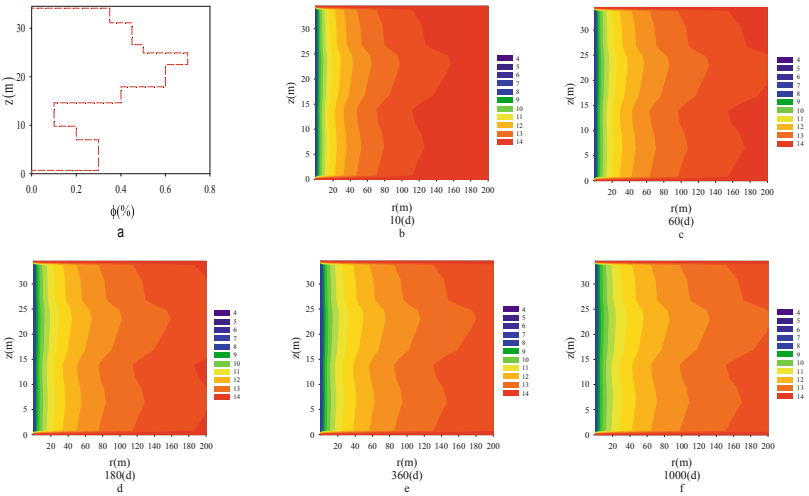

Fig. 5. The initial porosity of the reservoir and the pressure distribution map during the depressurization mining process

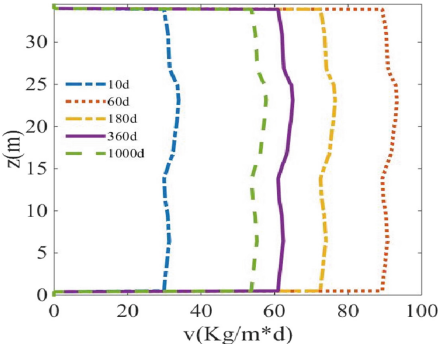

Fig. 6. Evolution of gas production rate in different initial porosity

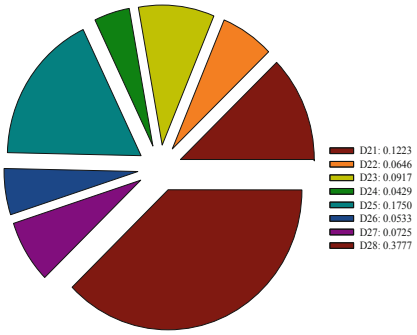

Fig. 7. Contribution rate of gas production in different porosity formations (after model improving)

From Fig. 8b–f, it can be seen that under relatively low initial permeability (5 md), reservoirs with higher initial hydrate saturation show slower movement speed of the decomposition outer edge.

We can see in Fig. 9. Reservoirs with relatively lower initial saturation have higher gas production rate, while, reservoirs with relatively higher saturation have slower gas production rate.

From Fig. 10, the gas production rate in all layers increases rapidly in the first 60 days, and then (60–540d) the gas production rate decreases with time.

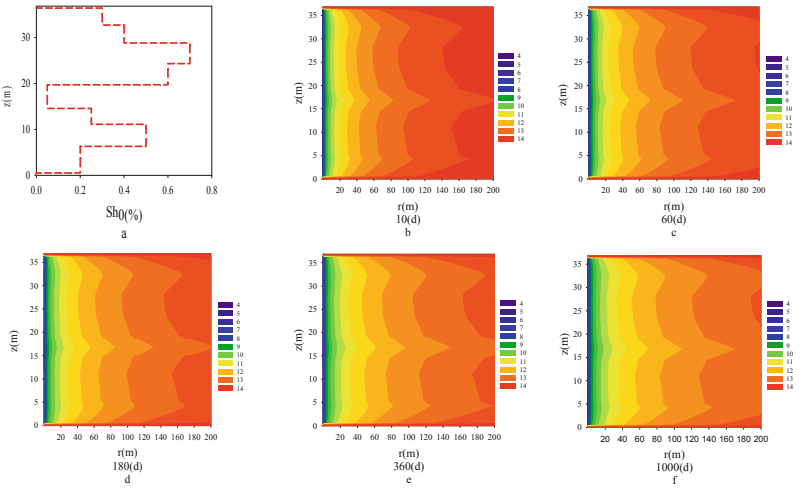

Fig. 8. The initial saturation of the reservoir and the pressure distribution map during the depressurization mining process

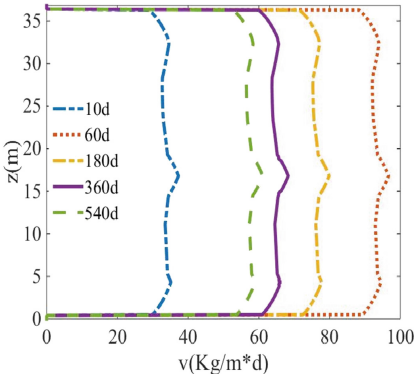

Fig. 9. Evolution of gas production rate in different initial saturation

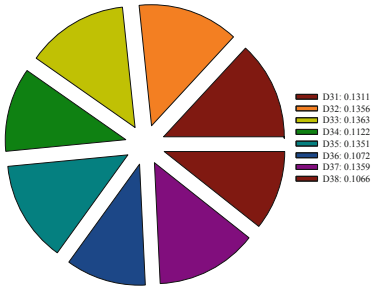

Fig. 10. Contribution rate of gas production in different saturation formations (after model improving)

5 Conclusion

In the process of hydrate decomposition, the greater the initial permeability and the initial porosity, the faster the pressure transmission, the greater the gas production rate, the greater the cumulative gas production.

The reservoirs with higher initial hydrate saturation have slower pressure transmission speed, lower gas production rate.

Comparing the influence of the initial permeability on gas production rate with that of the initial porosity, and the hydrate saturation, it can be seen that the gas production rate is more sensitive to the initial permeability.

Acknowledgement. The authors would like to appreciate professor Xiao for his careful guidance and help.

References

1. Li, J.F., Ye, J.L., Qin, X.W., et al.: The first offshore natural gas hydrate production test in South China Sea. China Geol. **1**(1), 5–16 (2018)
2. Jianliang, Y., Xuwen, Q., Wenwei, X., et al.: Main progress of the second gas hydrate trial production in the South China Sea. Geol. China **47**(03), 557–568 (2020)
3. Wan, Y., Wu, N., Hu, G., et al. Reservoir stability in the process of natural gas hydrate production by depressurization in the Shenhu area of the South China Sea. Nat. Gas Ind. **5**(6), 631–643 (2018)
4. Yu, T., Guan, G., Wang, D., et al.: Numerical investigation on the long-term gas production behavior at the 2017 Shenhu methane hydrate production site. Appl. Energy **285,** 116466 (2021)
5. Moridis, G.J., Kowalsky, M.: Depressurization-induced gas production from Class 1 and Class 2 hydrate deposits. SPE Res. Eval. Eng. **10**(05), 458–481 (2007)
6. George, J., et al.: Gas production potential of disperse low-saturation hydrate accumulations in oceanic sediments. Energy Conver. Manag. **48**(6), 1834–1849 (2007)
7. Uddin M., Wright, F., Dallimore, S., et al. Gas hydrate dissociations in Mallik hydrate bearing zones A, B, and C by depressurization: effect of salinity and hydration number in hydrate dissociation. J. Nat. Gas Sci. Eng. **21**, 40–63 (2014)
8. Yoshihiro, K., et al.: Key findings of the world's first offshore methane hydrate production test off the coast of Japan: toward future commercial production. Energy Fuels **31**(3), 2607–2616 (2017)

Numerical Investigation on Dissociation Performance of Natural Gas Hydrate in Reservoirs by Depressurization

Lin Dong(✉) and Hualin Liao

School of Petroleum Engineering, China University of Petroleum (East China), Qingdao 266580, China
donglinupc@163.com

Abstract. The velocity of dissociation front is key factor to reflect the hydrate production process. However, the characteristics of dissociation front and formation responses during hydrate production are not studied in detail. To investigate the dissociation performance of gas hydrate, we conduct a numerical model to simulate the process of gas extraction from formation by depressurization. The distribution of hydrate, water, and gas saturation varies during production process. The hydrate saturation decreases in near-well region, while the gas saturation increases. The dissociation zone expands and dissociation front moves from well to formation. This work can provide a reference for natural gas development.

Keywords: Natural gas hydrate · Dissociation performance · Front movement · Gas extraction · Physical fields

Symbol Description

P_i	Initial pore pressure
T_i	Initial temperature
S_h,S_w	Hydrate and water saturation
P_f	Well pressure
T_f	Well temperature
λ_h, λ_w, λg, λ_s	Thermal conductivity of hydrate, water, gas, and sand
C_s,C_w,C_g,C_r,C_h	Specific heat of sediments,water, gas, rock,and hydrate
ρ_r, ρ_h, ρ_d	Density of rock, hydrate, and drilling fluid
K_0	Initial permeability (hydrate-free)
ΔE_a	Activation energy
M_{H2O}, M_{CH4}, M_h	Molar mass of water, methane, and hydrate
r_w	Borehole radius
φ	Porosity
k_{d0}	Intrinsic kinetic constant
N_h	Hydration number
S_{wr},S_{gr}	Irreducible water and gas saturation
P_0	Gas entry value

B. Sun et al. (Eds.): DWOG-Hyd 2021, LNCE 246, pp. 132–141, 2022.
https://doi.org/10.1007/978-981-19-0960-3_13

1 Introduction

Natural gas hydrate (NGH) is one of the most important sources of alternative energy, which draws the attention to the whole world [1, 2]. Generally, NGH widely exists in oceanic and permafrost regions under the condition of high pressure and low temperature [3]. Driven by the energy demand and technological advancement, natural gas hydrate production is conducted worldwide to extract natural gas from the reservoirs, such as the South China Sea and the Eastern Nankai Trough [4, 6].

Changes in physical fields and dissociation front are important for analyzing production performance during gas extraction from natural gas hydrate reservoirs [6]. Zheng et al. [7] studied the controlling mechanisms of hydrate dissociation front with the lab-scale and field-scale models. The results indicate that using optimized characteristic time is a key factor in estabilishing calculation models. Afterward, A pragmatic criterion was developed to illustrates the relations among controlling mechanisms, hydrate dissociation modes, and characteristics of dissociation front [8]. Besides, the investigation on advance of dissociation front is essential for optimizating gas production and preventing the risks [9]. However, the dissociations on characteristics of dissociation front and formation responses during hydrate production are insufficient.

In this paper, we investigate the dissociation performance of gas hydrate reservoirs by depressurization method. The responses of pore pressure and temperature of formation are discussed. Besides, the distribution of hydrate, water, and gas saturation as well as dissociation front of hydrate are studied. This work can provide a reference for the practical application and numerical simulation in natural gas hydrate development.

2 Numerical Model

2.1 Governing Equations

The continuity equation of hydrate, water, and gas are given as follows:

$$\frac{\partial(\varphi\rho_h S_h)}{\partial t} = -m_h \tag{1}$$

$$\frac{\partial(\varphi\rho_w S_w)}{\partial t} - \nabla\cdot\left[\frac{K_{rw}K\rho_w}{\mu_w}(p_w + \rho_w g)\right] = m_w \tag{2}$$

$$\frac{\partial(\varphi\rho_w S_w)}{\partial t} - \nabla\cdot\left[\frac{K_{rw}K\rho_w}{\mu_w}(p_w + \rho_w g)\right] = m_w \tag{3}$$

The dissociation process of hydrate in the reservoirs can be described by the Kim-Bishoni kinetic model.

$$m_g = k_{d0}\exp\left(\frac{\Delta E_a}{RT}\right)M_{CH_4}A_{rs}(p_e - p_g) \tag{4}$$

$$A_{rs} = \varphi S_h\sqrt{\frac{\varphi(1-S_h)}{2K}} \tag{5}$$

$$K = K_0(1 - S_h)^n \tag{6}$$

Correspondingly, the generation rate of water and dissociation rate of hydrate are showed as follows:

$$m_w = m_g N_h \frac{M_{H_2O}}{M_{CH_4}} \tag{7}$$

$$m_h = -m_g \frac{M_H}{M_{CH_4}} \tag{8}$$

$$P_e = \exp\left(A_0 + A_1 T + A_2 T^2 + A_3 T^3 + A_4 T^4 + A_5 T^5\right) \tag{9}$$

$$p_w = p_g - p_c \tag{10}$$

The energy conservation is expressed as:

$$\begin{aligned} &\frac{\partial\left[\rho_w \varphi S_w C_w T + \rho_g \varphi S_g C_g T + \rho_h \varphi S_h C_h T + \rho_s (1-\varphi) C_s T\right]}{\partial t} + \\ &\nabla \cdot \left(\rho_w \varphi S_w \mathbf{v}_{w,t} C_w T + \rho_g \varphi S_g \mathbf{v}_{g,t} C_g T\right) = \nabla \cdot \lambda_{eff} \nabla T + Q_h \end{aligned} \tag{11}$$

$$Q_h = \frac{m_h}{M_h}(B_1 + B_2 T) \tag{12}$$

The heat transfer coefficient of the HBS can be determined by the sediments, hydrate, water, and gas.

$$\lambda_{eff} = (1 - \varphi)\lambda_s + \varphi\left(S_g \lambda_g + S_w \lambda_w + S_h \lambda_h\right) \tag{13}$$

Capillary pressure is given based on Van-Genuchten model.

$$p_c = p_0 \left[\left(\frac{S_w - S_{wr}}{1 - S_{wr}} \right)^{-1/\lambda} - 1 \right]^{1-\lambda} \tag{14}$$

The relative permeability of water and gas endpoints of hydrate-free sediments are calculated by the following equations.

$$K_{rw} = K_{rwo} \left(\frac{S_w - S_{wr}}{1 - S_{wr}} \right)^{n_w} \tag{15}$$

$$K_{rg} = K_{rgo} \left(\frac{S_g - S_{gr}}{1 - S_{gr}} \right)^{n_g} \tag{16}$$

2.2 Model Descriptions

Figure 1 shows the cylindrical model of natural gas hydrate reservoir. The radius is 100 m and the height is set as 20 m. A well is designed in the centre of this model which is used for producing natural gas from this reservoir.

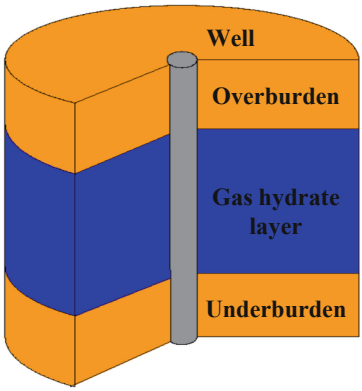

Fig.1. Model construction for the simulation.

2.3 Initial and Boundary Conditions

The initial conditions in this model are determined by referring the previous studies [10]. The initial formation temperature and pore pressure are set as 288.15K and 14MPa, respectively. Besides, the initial water and hydrate saturation are 0.5 and 0.5, respectively.

The parameters are determined according to the previous studies and geological data in the South China Sea [11, 12], as shown in Table 1.

Table 1. Parameters used in this model.

Parameter	Value
Initial pore pressure, P_i	14 MPa
Initial temperature, T_i	288.15 K
Hydrate saturation, S_h	0.5
Water saturation, S_w	0.5
Well pressure, P_f	4.0 MPa
Well temperature, T_f	278.15K
Thermal conductivity of hydrate, λ_h	2.0 $W{\cdot}m^{-1}{\cdot}K^{-1}$
Thermal conductivity of water, λ_w	0.6 $W{\cdot}m^{-1}{\cdot}K^{-1}$
Thermal conductivity of gas, λ_g	0.07 $W{\cdot}m^{-1}{\cdot}K^{-1}$
Thermal conductivity of sand, λ_s	1.0 $W{\cdot}m^{-1}{\cdot}K^{-1}$
Specific heat of sediments, C_s	1000 $J{\cdot}kg^{-1}{\cdot}K^{-1}$
Specific heat of water, C_w	4200 $J{\cdot}kg^{-1}{\cdot}K^{-1}$
Specific heat of gas, C_g	2180 $J{\cdot}kg^{-1}{\cdot}K^{-1}$

(*continued*)

Table 1. (*continued*)

Parameter	Value
Specific heat of hydrate, C_h	2220 J·kg^{-1}·K^{-1}
Density of rock, ρ_r	2600kg/m^3
Density of hydrate, ρ_h	920kg/m^3
Density of drill fluid, ρ_f	1019kg/m^3
Initial permeability (hydrate-free), K_0	10 mD
Activation energy, ΔE_a	81084.20J·mol^{-1}
Molar mass of water, M_{H2O}	18.016g·mol^{-1}
Molar mass of methane gas, M_{CH4}	16.042g·mol^{-1}
Molar mass of methane hydrate, M_h	124.138g·mol^{-1}
Borehole radius, r_w	0.15 m
Porosity, φ	0.40
Intrinsic kinetic constant, k_{d0}	3.6×10^4 mol·m^{-2}·Pa^{-1}·s^{-1}
Hydration number, N_h	6
Irreducible water saturation, S_w	0.3
Irreducible water saturation, S_{gr}	0.05
λ	0.7
Gas entry value, P_0	10^5Pa
C_f	33.72995
C_1	13521
C_2	−4.02

3 Results and Discussions

3.1 Description of Specimens

Figure 2 shows the distribution of pore pressure during gas hydrate production. The pore pressure increases from near-well region to far well formation. The depressurization and hydrate dissociation lead to the changes in the pore pressure field, which reflects the mass transfer process with the multi-phase flow.

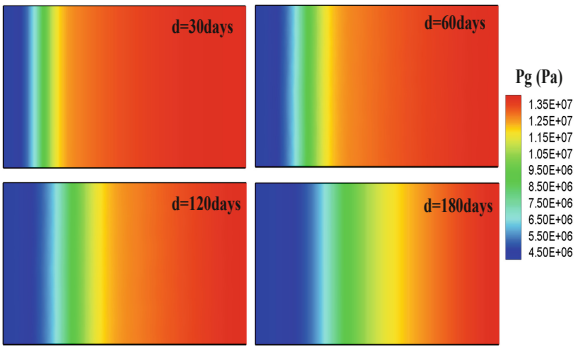

Fig. 2. Variation of pore pressure versus production time

Figure 3 illustrates the distribution of temperature in the natural gas hydrate formation. The temperature increases from well to formation, which is caused by the heat transfer and hydrate dissociation. The distribution of temperature varies during production process due to the heat and mass transfer.

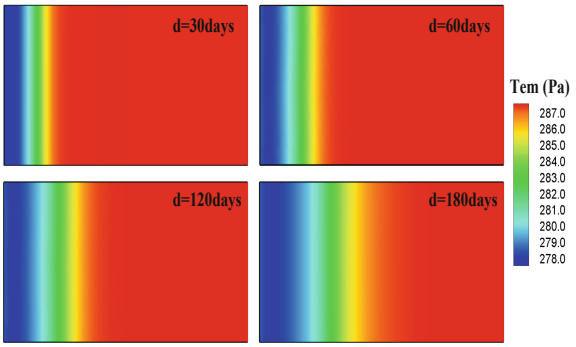

Fig. 3. Variation of the temperature of formation versus production time

3.2 Variation of Hydrate, Gas, and Water Saturation

Distribution of hydrate and water saturation during gas hydrate production are displayed in Figs. 4 and 5. The results indicate that the hydrate saturation decreases significantly with production time. Meanwhile, it is lower near well induced by the hydrate dissociation compared with that in the zone far from the well.

In addition, the water saturation increases due to the produced water from the hydrate dissociation. The water in the formation is also extracted to the ground. These factors affect the water distribution in the formation. The phase transition of hydrate occurs during production, which brings in variation of hydrate and water saturation.

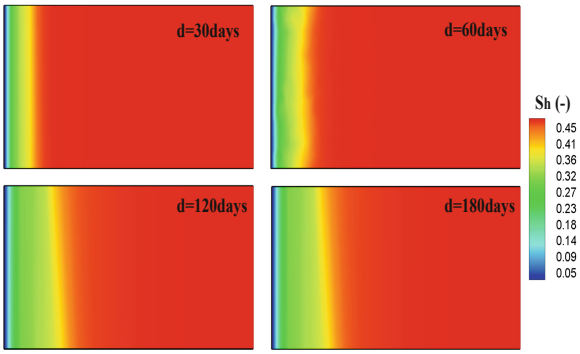

Fig. 4. Distribution of hydrate saturation during hydrate production

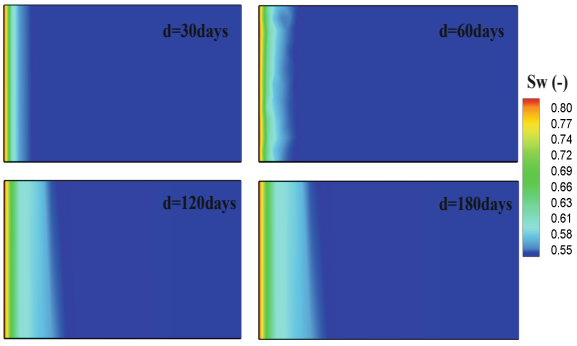

Fig. 5. Distribution of water saturation during hydrate production

Similarly, the gas saturation increases in near well region, which is caused by the hydrate dissociation and gas extraction, as shown in Fig. 6. The gas produced through hydrate dissociation is extracted from the formation, which leads to the variation of gas saturation and changes in distribution characteristics.

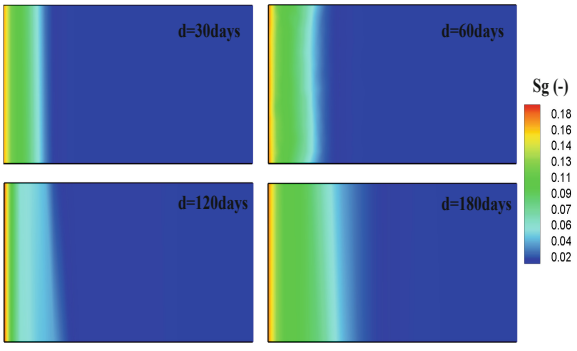

Fig. 6. Distribution of gas saturation during hydrate production

3.3 Hydrate Dissociation Front

Figure 7 demonstrates the variation of hydrate saturation during gas extraction. It can be observed that the hydrate saturation in near-well region is lower. The dissociation zone expands with production time, as shown in Fig. 7(b). The hydrate dissociation front moves toward the further bore zone due to the changes in the dissociation zone.

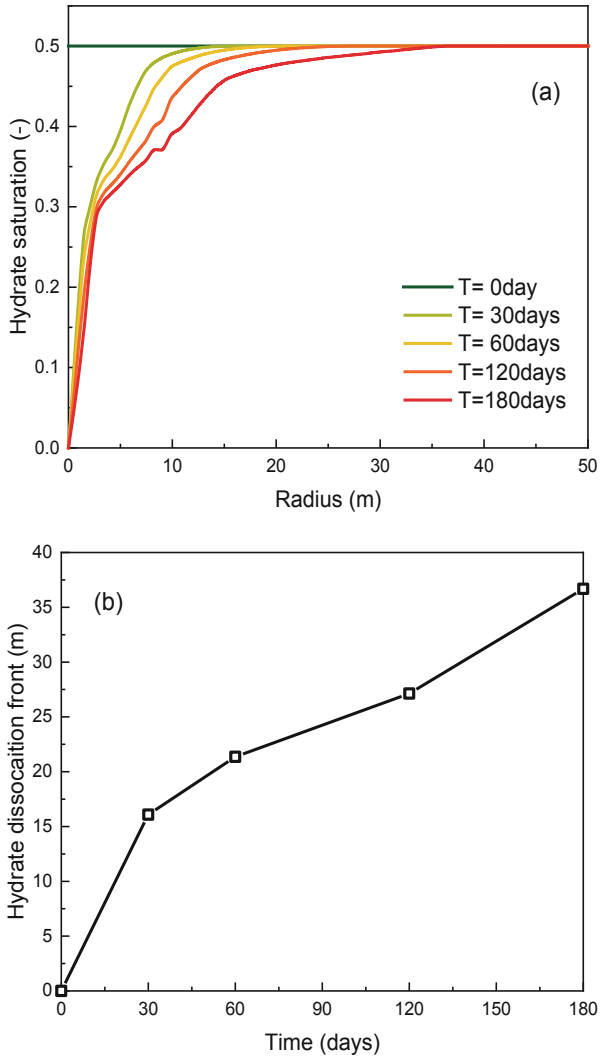

Fig. 7. Variation of hydrate saturation and dissocation front during production

As mentioned above, the controlling mechanisms of hydrate dissociation and characteristics of dissociation front depend on the pressure and temperature conditions of the

well and the properties of the formtation. The dissociation front reflects the production process of the natural gas hydrate.

4 Conclusion

Based on the results and discussions presented above, the conclusions are obtained as below:

(1) Dissociation performance of natural gas hydrate in the formation is a complex process associated with heat and mass transfer as well as phase transition. Numerical simulation on hydrate production provides the references of dissociation characteristics and changes in physical fields for analyzing natural gas hydrate production.
(2) Distribution of multi-physical fields varies during hydrate dissociation, which is determined by the gas extraction as well as the heat and mass transfer process. The hydrate saturation decreases in near-well formation, while the gas saturation increases.
(3) The dissociation zone expands, and hydrate dissociation front moves to far well formation with production time. The multi-field responses of natural gas hydrate reservoirs are related to the hydrate dissociation performance during natural gas hydrate production.

Acknowledgments. This research was supported by , Graduate School Innovation Program of China University of Petroleum (YCX2019020). These financial supports are gratefully acknowledged. We recognize the support of China University of Petroleum (East China) for the permission to publish this paper.

References

1. Boswell, R., Collett, T.S.: Current perspectives on gas hydrate resources. Energy Environ. Sci. **4**(4), 1206–1215 (2011)
2. Chong, Z.R., Yang, S.H.B., Babu, P., Linga, P., Li, X.: Review of natural gas hydrates as an energy resource: prospects and challenges. Appl. Energy **162**, 1633–1652 (2016)
3. Waite, W.F., et al.: Physical properties of hydrate-bearing sediments. Rev. Geophys. **47**(4), 1–38 (2009)
4. Malagar, B.R.C., Lijith, K.P., Singh, D.N.: Formation & dissociation of methane gas hydrates in sediments: a critical review. J. Nat. Gas Sci. Eng. **65**, 168–184 (2019)
5. Qin, X., et al.: The response of temperature and pressure of hydrate reservoirs in the first gas hydrate production test in South China Sea. Appl. Energy. **278**, 115649 (2020)
6. Yu, T., Guan, G., Abudula, A., Yoshida, A., Wang, D., Song, Y.: Gas recovery enhancement from methane hydrate reservoir in the Nankai Trough using vertical wells. Energy (Oxford) **166**, 834–844 (2019)
7. Zheng, R., Li, S., Cui, G.: Determining the controlling mechanisms of hydrate dissociation front using optimized characteristic time. Fuel. **298**, 120805 (2021)

8. Zheng, R., Li, S., Li, Q., Li, X.: Study on the relations between controlling mechanisms and dissociation front of gas hydrate reservoirs. Appl. Energy **215**, 405–415 (2018)
9. Bhade, P., Phirani, J.: Gas production from layered methane hydrate reservoirs. Energy **2**, 686–696 (2015)
10. Feng, Y., et al.: Numerical analysis of gas production from layered methane hydrate reservoirs by depressurization. Energy **166**, 1106–1119 (2019)
11. Sun, X., Luo, T., Wang, L., Wang, H., Song, Y., Li, Y.: Numerical simulation of gas recovery from a low-permeability hydrate reservoir by depressurization. Appl. Energy **250**, 7–18 (2019)
12. Wan, Y., et al.: Reservoir stability in the process of natural gas hydrate production by depressurization in the shenhu area of the south China sea. Nat. Gas Indus. B **5**(6), 631–643 (2018)

The Facilitative Behaviors of Underlying Gas Toward Hydrate-Bearing Sediment Formation and Dissociation

Guangjun Gong, Jia-nan Zheng, Guojun Zhao, Mingjun Yang(✉), and Yongchen Song

Key Laboratory of Ocean Energy Utilization and Energy Conservation of Ministry of Education, Dalian University of Technology, Dalian 116024, China
yangmj@dlut.edu.cn

Abstract. Methane hydrate with the underlying gas, a new alternative energy source in the future, has attracted great attentions all over the world. The methane hydrate-bearing sediment core samples using the marine sediments from the South China Sea were remolded. A methane reservoir employed to hold underlying gas was connected with the core holder to simulate underlying gas layers below the hydrate layers. In this study, the formation and production characteristics of the remolded cores (water saturation 65%) with the different underlying gas pressure (7.4–8.5 MPa) at the constant confining pressure (8.7 MPa) were studied. The results indicated that the underlying gas is an effective driving force for hydrate formation due to its constant supply of gas for consumption. In addition, it is the presence of underlying gas that reduces the pressure difference between the inlet and outlet of remolded samples, increasing the gas-water contact area. The higher underlying gas pressure, the more pronounced the promotion effect. The hydrate saturations of the core samples were ranged from 31.2% to 38.3%. In addition, the underlying gas could promote the dissociation of methane hydrate using the depressurization method by providing the heat for hydrate reservoirs. It was found that it reduced the damage to the core samples by effective stress and the improved the gas recovery due to the presence of the underlying gas. The results of this study are significant for guiding the spot production process of marine sediments deposits with the underlying gas.

Keywords: Methane hydrate · Underlying gas · Effective pressure · Gas production

1 Introduction

Methane hydrate, a potential energy source, is the one of the largest untapped reservoir of unknown energy on Earth for the humanity [1, 2]. Methane hydrate composed of water and methane under low temperature and high pressure conditions are known as cage hydrate. Methane hydrate is mostly white or light grey crystals, which are also known as “combustible ice” [3]. According to technical data on hydrate exploration, methane hydrate is mainly found in the marine sediments and permafrost regions such as South

B. Sun et al. (Eds.): DWOG-Hyd 2021, LNCE 246, pp. 142–152, 2022.
https://doi.org/10.1007/978-981-19-0960-3_14

China Sea, Gulf of Mexico, Indian Ocean, Alaska Arctic and Qinghai [4]. In addition, it is also noted that methane hydrate is characterized by large amount of resources, shallow burial, high energy density and cleanness [5, 6]. Because of the impermeability of methane hydrate, it is often used as the sealing layer of its underlying gas. The underlying gas layer is an important component of the hydrate reservoir. Analysis of logging, seismic, sedimentary rock and geochemical test data from 32 sites in the South China Sea, the Northeast Basin of Japan, the northern Gulf of Mexico and the Eastern Basin of India has revealed the widespread presence of the underlying gas [7, 8]. The need and urgency for the commercial exploitation of hydrate is reinforced by the presence of underlying gas. As a result, the safe and efficient extraction of gas hydrate with underlying gas will be a hot research issue in the coming decades.

The main principle of hydrate exaction is to obtain methane gas and other substances from hydrate by breaking the temperature and pressure of phase equilibrium [9]. Currently, main methods of exploitation hydrate are depressurization [10], thermal injection [11], carbon dioxide replacement [12], inhibitor injection [12], hydraulic fracturing [13] and combination of these methods. In terms of economics, environmental friendliness and simple operation, depressurization is considered to be the most economically effective method [14]. There are many researches related to methane hydrate have carried out extensive experiments using the depressurization. Similarly, some countries, Japan and China, have successfully conducted several hydrate exploitation tests using the depressurization method in the eastern Nankai Trough in 2013 and 2017, in the South China Sea in 2017 and 2020, respectively [10]. However, few experiments and tests take into account the effect of underlying gas on dissociation and gas production via depressurization in-situ conditions.

Confining pressure employed to imitated in-situ conditions is defined as the pressure exerted it from the surrounding environment [15]. It is commonly accepted that confining pressure is related to water depth, thickness and density of the overlying pressure [16]. The core holder, the most suitable experimental equipment, is capable of exerting the confining pressure. Studies have found that confining pressure controls the distribution and pore structure of hydrate, which have a significant influence on the efficiency and capacity of gas production [17]. Zhao et al. [15] investigated the effect of confining pressure to the gas behavior of methane hydrate and found that it had a strong inhibiting effect on hydrate production especially in the later stages of gas production. According to Wu et al. [18] among the proposed methods, it was confining pressure that controlled gas being from hydrate by impacting the gas permeability. In addition, Li et al. [19] also founded that the gas production decreases with increasing effective stress at a constant confining pressure. Therefore, understanding the effect of confining pressure on the gas characteristics of methane hydrate with underlying gas is of vital importance to realize the controllable exploitation of hydrate using depressurization method.

There are few laboratory-scale hydrate production experiments using the real marine sediments. In this study, the core remolded by using the marine sediments was injected with methane at different underlying pressure (7.5–8.5 MPa) to form hydrate at constant confining pressure (8.7 MPa). Firstly, the formation characteristics of hydrate-bearing sediment with different underlying gas pressure were studied in terms of hydrate saturation and pressure difference between inlet and outlet of remolded core. Then the

dissociation and gas production characteristic of remolded core were investigated using depressurization method. The average dissociation rate and gas recovery at different underlying gas pressure were compared and analyzed during the process of depressurization. The results of this work on the joint gas production of the methane hydrate and underlying gas could provide insightful guidance for commercial exploitation in the future.

2 Experimental Section

2.1 Materials

The experimental materials used in the experiments consisted mainly of methane gas, deionized water and marine sediment. The purity and supplier of experimental materials was shown in the Table 1.

Table 1. Purity and supplier of experimental materials

Substance	Mole fraction purity	Supplier
Methane gas	GC 0.99999 mol%	Dalian Special Gases Corporation, China
Deionized water	18.2 MΩ·cm	Laboratory-made
Marine sediment	–	Shenhu Sea of South China Sea, LW3-H4–1 C-06,123 m

2.2 Apparatus

The Fig. 1 illustrated an experimental apparatus used to study the phase change process and characteristics of methane hydrate with underlying gas using depressurization. The apparatus consisted mainly of core holder, methane reservoir, water bath, gas collector and valves. The core holder (FCH series, Core laboratories CO., USA), a place used to put the remolded marine sediment samples, was divided into the core chamber and confining chamber by rubber. The inlet and outlet of confining pressure chamber were used as the inlet and outlet of the confining pressure fluid, respectively. The core holder was immersed in water sink and its temperature was mainly controlled indirectly by the circulating water bath. Methane reservoir was employed to pre-cool methane gas and to allow methane gas from methane cylinder (up to 20 MPa) to the inlet of the core holder so that better simulate methane hydrate reservoirs with underlying gas. There was gas collector used to collect the gas being produced form methane hydrate. The volume of methane reservoir and gas collector made of stainless steel was 1 L, 4 L respectively. The control valve (Fisher-Baumann, USA) coupled with a self-turned PID Controller (OMEGA CN2120 Ramp/Soak Controller) was used to set the ideal dissociation pressure at which hydrate would break down. The confining pressure was mainly controlled by plunge pump (250 L, Haian Petroleum Scientific Research Instrument co., ltd., China)

and maintained by injecting a certain amount of deionized water at the constant pressure or constant rate. Pressure gauges with an accuracy of 0.1 MPa were used to measure gas pressure, inlet pressure, outlet pressure, produced gas pressure and confining pressure. One T-type thermocouple (±0.1 K) was installed on the bottom of core holder to measure temperature changes during the phase transition process. At the same time, the measured experimental data was collected and stored by the data acquisition system via the A/D digital conversion module. In particular, it should be noted that the gas production pipeline used in this experiment 1/6 in pipe.

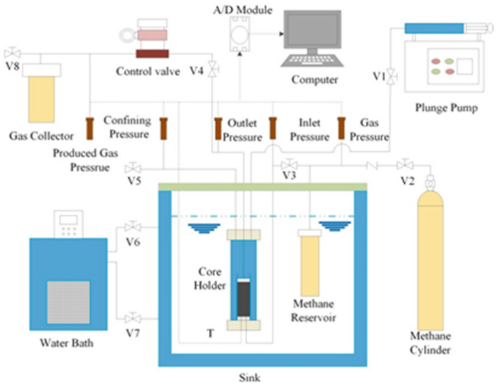

Fig. 1. Schematic diagram of the experimental apparatus

2.3 Experimental Steps

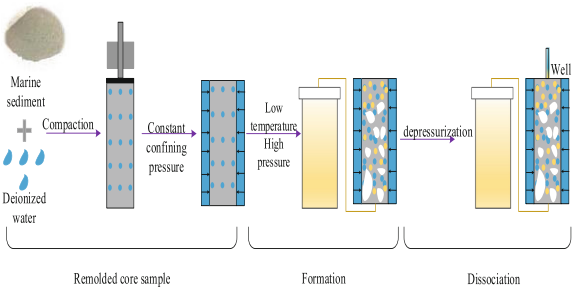

Fig. 2. Schematic diagram of the experimental procedure

As shown in the Fig. 2, the experimental procedure was divided into three main parts: consisting mainly of remolded core sample, formation and dissociation.

First and foremost, the process of remolded core was carried out in the following steps:

(1) The marine sediments were dried in a high precision dryer at a temperature of 383 K for 24 h in order to better remove the moisture.

(2) The calculated dried marine clay was broken up in a blender and evenly mixed with a certain amount of deionized water.
(3) The core was remolded using wet tamping method for compaction and stratified sample making.
(4) The core was transferred rapidly to core holder and the permeable membranes were placed at the both ends. After that, the pipes were connected and vacuumed and leak-tested lines.

Then, there was injection methane to form the methane hydrate at low temperature and high pressure. The core holder was passed into the methane gas with the pressure of 1 MPa at 3–4 times in order to eliminate the effect of air on hydrate formation. A circulating cooling water bath was turned on and set to 274 K, while deionized water was injected to confining chamber via the plunger pump to increase the confining pressure at constant rate. The valve was opened and the pre-cooled underlying gas was passed through the pipe into the core chamber. At same time, the confining pressure increased as the pore pressure inside the core increased until it reached the desired value. The confining pressure was always greater than the pore pressure, which was used to protect the core rubber from excessive deformation. As hydrate formation continued with gas consumption, it was considered to be complete when the pressure change was less than 0.001 MPa over 10 h period.

Finally, methane hydrate were dissociated using the depressurization. The back pressure valve was set 2 MPa until the pore pressure inside the core was equal to the set value and the dissociation of hydrate was completed. After that, the data acquisition system was shut down and experimental apparatus were disassembled for cleaning and repeated for the next round of experiments.

In addition, the date processing process can be found in our previous literature [20]. In brief, the hydrate saturation can be calculated from the consumption of the injected underlying gas pressure. The average dissociation rate of hydrate is the average of the rate of hydrate dissociation throughout the whole depressurization process. The gas recovery rate is the ration between the gas produced and the gas injected.

3 Experimental Results and Discussion

In this study, the methane hydrate with different underlying gas pressure in core holder was formed in the remolded core sample. Improving the pressure of the underlying gas was an effective measure to further increase the hydrate saturation. The depressurization was used to induce the gas production of the methane hydrate. In terms of the heat replenishment and the damage of effective stress, the underlying gas can not only be beneficial to the gas production by the transferring heat, but also reduce effective damage to the remolded core by constant gas replenishment. Table 2 shows the specific conditions of experiment and main experimental results.in addition, the water saturation and the confining pressure of remolded core were 65%, 8.7 MPa, respectively.

Table 2. The experimental conditions and results

Case	P_u (MPa)	S_h (%)	Av_{dis} (mol/min)	R_g (%)	ΔP (MPa)
1	7.5	31.2	0.072	64.6	0.9
2	7.8	34.3	0.078	67.8	0.62
3	8.1	35.6	0.082	71.8	0.57
4	8.3	37.5	0.084	75.1	0.51
5	8.5	38.3	0.086	78.9	0.45

3.1 The Formation of Methane Hydrate with the Underlying Gas

The underlying gas had a significant positive importance on hydrate formation. The underlying gas provided sufficient gas for hydrate formation, and reduced the pressure difference between the inlet and outlet pressure in remolded core sample. The schematic diagram about the effect of underlying gas on hydrate formation was shown in Fig. 3. On the one hand, the high-pressure underlying gas provided a huge force for hydrate formation. On the other word, the reduced pressure difference between the inlet and outlet corresponded to an increased gas-water contact area.

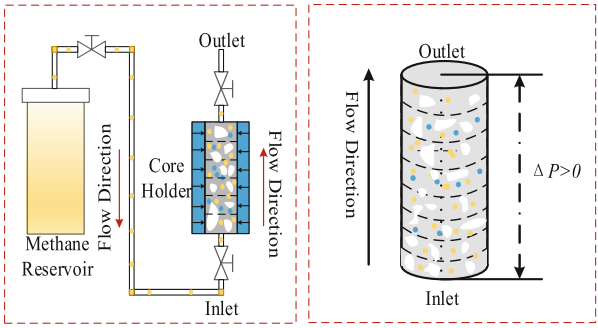

(a) Supplied gas (b) Reduced differential pressure

Fig. 3. Schematic diagram of the underlying gas on hydrate formation

3.1.1 Effect of Underlying Gas on Hydrate Formation

The underlying gas, providing the great driving force for hydrate formation, is a key factor to improve the hydrate saturation. The formation of hydrate is influenced by the driving forces, which take various forms such as pressure, temperature and fugacity differences, but mainly fugacity differences.

The expression of fugacity differences was shown in Eq. (1) [15].

$$n_h = F_A K_O A_S \exp\left(\frac{-\Delta E}{RT}\right)\left(f_{eq} - f_g\right) \tag{1}$$

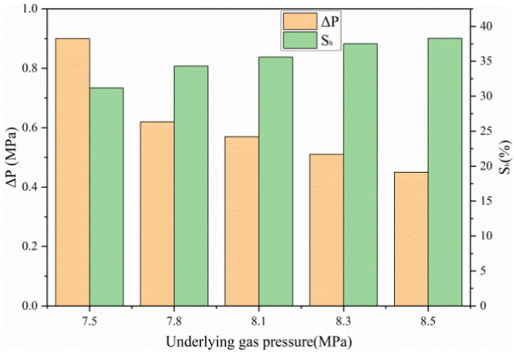

Fig. 4. The hydrate saturation and pressure difference of remolded core with different underlying gas pressure

where F_A denotes the area adjustment factor, K_O represents the hydration reaction constant, A_S denotes the surface area for the reaction, E refers to the hydration activation energy, f_g and f_{eq} are the gas phase fugacity and the equilibrium fugacity of methane gas under the temperature T, respectively. The fugacity of methane at each (P, T) can be obtained from the REFPROP Model of the National Institute of Standards and Technology [21]. The higher the underlying gas pressure, the greater the fugacity difference. As shown in Fig. 4, the facilitation phenomenon became more pronounced as the underlying gas pressure increased. The underlying gas pressure changes from 7.5 MPa to 8.5 MPa and the hydrae saturation increases from 21.1% to 38.3%, correspondingly. On average, the hydrate saturation increases by 17.2% for each 1MPa increase in underlying gas pressure.

Similarly, the higher the lower underlying gas pressure, the lower the pressure difference between the inlet and outlet of remolded core. As shown in Fig. 4, the underlying gas pressure increased of 1 MPa reduced the pressure differential by 0.45 MPa on average. The stressing effect of the constant confining pressure and the non-permeability of hydrate resulted in a certain pressure difference between the inlet and outlet of the remolded core during the process of hydrate formation [22, 23]. It was the presence of pressure difference that intended to reduce the contact area of gas-water. Conversely, the underlying gas pressure reduced the pressure difference and increased the gas-water contact area, which further facilitates the improvement of hydrate saturation.

3.2 The Dissociation of Methane Hydrate with the Underlying Gas

The underlying gas can also have a positive effect on the dissociation of methane hydrate. The schematic diagram about the effect of underlying gas on hydrate dissociation was shown in Fig. 5. The facilitative effect is manifested in two main ways: (1) provided heat for dissociation; (2) reduced effective pressure damage. On the one hand, the dissociation of hydrate is a complex process of heat absorption. In other words, the dissociation of hydrate inevitably caused temperature fluctuations and lowers the temperature of the hydrate-bearing reservoir. However, the underlying gas was the constant temperature that was equal to the temperature before hydrate dissociation. On the other word, it was

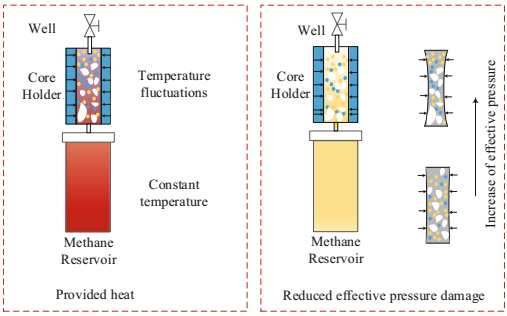

Fig. 5. Schematic diagram of the underlying gas on hydrate dissociation

the presence of hydrate slowed the reduction in core pressure. However, the confining pressure was constant. This just reduced the effective pressure damage to the remolded core. In general, the underlying gas facilitates the dissociation of hydrate and improved the gas recovery from the temperature and effective stress perspective, respectively.

3.2.1 Effect of Underlying Gas on Hydrate Dissociation

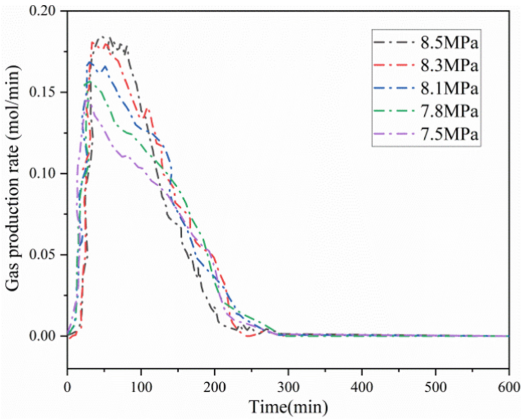

Fig. 6. The gas production rate of remolded core with different underlying gas pressure

The rate of gas production is a key factor in measuring the ability of the hydrate reservoir to produce gas. And the gas production rate of remolded core with different underlying gas pressure was shown in Fig. 6. The rate of gas production increased for approximately the first 50 min of depressurization, a phenomenon was attributed to the significant release of free gas, the continued dissociation of hydrate and the partial production of underlying gas pressure. As the depressurization reaction continues, the driving force of the fluids decreased accordingly.

It can be clearly seen that the higher the pressure of the underlying gas, the longer the gas production rate continues at high speed. After approximately 60 min, the gas

production rate began to gradually decrease. In general, the higher the underlying gas pressure, the greater the flow drive force provided and the corresponding higher the gas production rate. At the same time, the constant temperature of the underlying gas provided continuous heat for hydrate decomposition, accelerating the rate of hydrate decomposition and gas production.

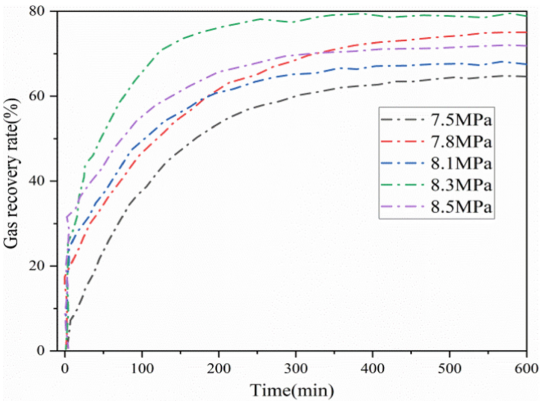

Fig. 7. The gas recovery rate of remolded core with different underlying gas pressure

The gas recovery rate is one of the most important indicators of the economics of gas production from hydrate reservoir. The gas recovery rate at different underlying gas pressure was presented in Fig. 7. It is clear to see that the higher underlying gas pressure the better the recovery of the gas.

In terms of the effective pressure, the presence of underlying gas pressure rerduced the damage to the remolded core. The effective pressure of remolded core was calculated by the Eq. (2):

$$\Delta \mathrm{P}_e = P_c - (P_i + P_0)/2 \tag{2}$$

Where $\Delta \mathrm{P}_e$ denotes the effective pressure, P_c denotes the constant confining pressure, P_i and P_0 are the inlet pressure and outlet pressure of remolded core, respectively. The underlying gas pressure was equal to the inlet pressure of remolded core because they are always connected through the pipeline during the entire process of depressurization. The underlying gas flows through the core via pipeline into the gas collector. Firstly, the underlying gas was added to the core sample and then slowed the reduction of pore pressure in the core. In addition, the effective pressure calculated by the Eq. (2) reduced when the underlying gas pressure rose. The lower the effective pressure, the less damage the pore structure and fluid channels within the sediment core, which was conducive to the gas recovery.

4 Conclusion

The effects of underlying gas on the formation and gas production behaviors of methane hydrate using the depressurization were investigated in this study. The remolded core

sample (water saturation 65%, and the constant confining pressure 8.7 MPa) within the core holder was synthesized by the marine sediment obtained from the South China Sea. And the different underlying gas pressure (7.5–8.5 MPa) was injected to form the hydrate. The corresponding conclusions were summarized as follows:

(a) The underlying gas improving the hydrate saturation of remolded core samples is a key factor by reducing the pressure difference and increasing the driving force for hydrate formation.
(b) The underlying gas likewise promotes the entire dissociation of hydrate reservoirs: increasing the gas production rate and improving the gas recovery rate. This phenomenon is attributed to the underlying gas providing the heat for dissociation and reducing the effective damage on remolded core.

Acknowledgement. The authors would like to appreciate National Natural Science Foundation of China (51822603, 51676025), the Innovation Foundation of Science and Technology of Dalian (2019J11CY012) and the Fundamental Research Funds for the Central Universities of China (DUT21ZD103).

References

1. Chong, Z.R., Pujar, G.A., Yang, M., Linga, P.: Methane hydrate formation in excess water simulating marine locations and the impact of thermal stimulation on energy recovery. Appl. Energy **177**, 409–421 (2016)
2. Yin, Z., Khurana, M., Tan, H.K., Linga, P.: A review of gas hydrate growth kinetic models. Chem. Eng. J. **342**, 9–29 (2018)
3. Yu, T., Guan, G., Abudula, A., Yoshida, A., Wang, D., Song, Y.: Application of horizontal wells to the oceanic methane hydrate production in the Nankai Trough, Japan. J. Nat. Gas Sci. Eng. **62**, 113–131 (2019)
4. Yang, M., Zheng, J.-N., Gao, Y., Ma, Z., Lv, X., Song, Y.: Dissociation characteristics of methane hydrates in South China Sea sediments by depressurization. Appl. Energy **243**, 266–273 (2019)
5. Zhao, J., Liu, D., Yang, M., Song, Y.: Analysis of heat transfer effects on gas production from methane hydrate by depressurization. Int. J. Heat Mass Transf. **77**, 529–541 (2014)
6. Yin, Z., Huang, L., Linga, P.: Effect of wellbore design on the production behaviour of methane hydrate-bearing sediments induced by depressurization. Appl. Energy **254**, 113635 (2019)
7. Zhai, C., Sun, K., Xin, L., Wang, T.: Experimental study of permeability variation of hydrate bearing sediments with different saturations during effective stress loading-unloading process. J. Exp. Mech. **31**(3), 399–408 (2016)
8. Zhai, C., Sun, K.-M., Xin, L.-W., Tian, S.: Experimental study of permeability of sand soil bearing sediments containing methane hydrates. J. Wuhan Univ. Technol. **37**(8), 78–82 (2015)
9. Xiaochun, L.I., Ying, W., Ning, W.E.I.: Research on measuring method of permeability by using storage-variable transient pulse method. Chin. J. Rock Mech. Eng. **27**(12), 2482–2487 (2008)
10. Babu, P., Kumar, R., Linga, P.: Pre-combustion capture of carbon dioxide in a fixed bed reactor using the clathrate hydrate process. Energy **50**, 364–373 (2013)

11. Song, Y., et al.: The status of natural gas hydrate research in China: a review. Renew. Sustain. Energy Rev. **31**, 778–791 (2014)
12. 樊栓狮, 汪集旸: Progress of gas hydrate studies in China. Chine. J. Process Eng. **6**(6), 997–1003 (2006)
13. Sun, Y., Li, S., Lu, C., Liu, S., Chen, W., Li, X.: The characteristics and its implications of hydraulic fracturing in hydrate-bearing clayey silt. J. Nat. Gas Sci. Eng. **95**, 104189 (2021)
14. Waite, W.F., Kneafsey, T.J., Winters, W.J., Mason, D.H.: Physical property changes in hydrate-bearing sediment due to depressurization and subsequent repressurization. J. Geophys. Res.-Solid Earth **113**(B7) (2008)
15. Zhao, J., Zheng, J.-N., Ma, S., Song, Y., Yang, M.: Formation and production characteristics of methane hydrates from marine sediments in a core holder. Appl. Energy **275**, 115393 (2020)
16. Miyazaki, K., Tenma, N., Aoki, K., Sakamoto, Y., Yamaguchi, T.: Effects or confining pressure on mechanical properties of artificial methane-hydrate-bearing sediment in triaxial compression test. Int. J. Offshore Polar Eng. **21**(2), 148–154 (2011)
17. Yang, M., Dong, S., Zhao, J., Zheng, J.-N., Liu, Z., Song, Y.: Ice behaviors and heat transfer characteristics during the isothermal production process of methane hydrate reservoirs by depressurization. Energy **232**, 121030 (2021)
18. Wu, Z., Liu, W., Zheng, J., Li, Y.: Effect of methane hydrate dissociation and reformation on the permeability of clayey sediments. Appl. Energy **261**, 114479 (2020)
19. Li, B., Li, X.-S., Li, G., Jia, J.-L., Feng, J.-C.: Measurements of water permeability in unconsolidated porous media with methane hydrate formation. Energies **6**(7), 3622–3636 (2013)
20. Zhao, J., Zheng, J.-N., Kang, T., Chen, B., Yang, M., Song, Y.: Dynamic permeability and gas production characteristics of methane hydrate-bearing marine muddy cores: experimental and modeling study. Fuel **306**, 121630 (2021)
21. Zhao, J., Zheng, J.-N., Li, F., Yang, M.: Gas permeability characteristics of marine sediments with and without methane hydrates in a core holder. J. Nat. Gas Sci. Eng. **76**, 103215 (2020)
22. Yan, K., Li, X., Chen, Z., Zhang, Y., Xu, C., Xia, Z.: Methane hydrate formation and dissociation behaviors in montmorillonite. Chin. J. Chem. Eng. **27**(5), 1212–1218 (2019)
23. Dai, S., Santamarina, J.C., Waite, W.F., Kneafsey, T.J.: Hydrate morphology: physical properties of sands with patchy hydrate saturation. J. Geophys. Res. Solid Earth **117** (2012)

The Investigation of Efficiency During the Exploitation of Gas Hydrates by Depressurization

Zhiqiang Liu, Linlin Wang(✉), and Shihui Yu

State Key Laboratory of Petroleum Resources and Prospecting, China University of Petroleum, Beijing 102249, China
linlin.wang@cup.edu.cn

Abstract. Gas hydrate, the most potential alternative energy source, is widespread on the ocean and permafrost. However, one of the critical issues for hydrate exploitation is the low efficiency of gas recovery. Understanding the governing mechanism during exploitation is crucial for enhancing recovery efficiency. In this work, the exploitation of gas hydrate from bearing sediments by depressurization is simulated. The processes of heat transfer, fluid flow, and kinetic dissociation are taken into full consideration during hydrate exploitation. Besides, the production pressure is further analyzed. It finds that the exploitation process can be divided into two processes, that are controlled by fluid flow and heat transfer, respectively. The additional energy will be supplied by heat transfer if the sensible heat is not enough for the dissociation of gas hydrate, which greatly extends the time cost. This finding may be useful for predicting the production efficiency and optimization of the gas recovery from hydrate-bearing sediments.

Keywords: Gas hydrate · Depressurization · Production efficiency · Governing mechanism

1 Introduction

Gas hydrate is an ice-like crystalline substance composed of gaseous and water substances [1]. It can form and stabilize in permafrost regions or deep ocean sediments with high pressure and low temperature [2–4]. Gas hydrate is recognized as the most potential alternative energy sources because the organic carbon in gas hydrate is nearly twice of that in the proved fossil fuels over the world [5–7]. Depressurization is regarded as the most economic method to exploit gas hydrate bearing sediments, whose principle is to lower the pressure to disrupt the stabilization of gas hydrate and promote its decomposition [8–10]. Although a lot of tests were conducted in the past three decades, there are still some issues in the production efficiency. The dissociation of gas hydrate is an endothermic process, thus, the sufficient heat supplement must be insured timely for the continuous production [11]. The hydrate exploitation mainly involves fluid flow, heat transfer, and kinetic dissociation. Specifically, they can be represented by the intrinsic permeability, thermal conductivity, and kinetic reaction rate, respectively. It has also

B. Sun et al. (Eds.): DWOG-Hyd 2021, LNCE 246, pp. 153–161, 2022.
https://doi.org/10.1007/978-981-19-0960-3_15

been reported that the main governing process of hydrate reservoirs changed with initial pressure and intrinsic permeability [12, 13]. There is still no consensus on governing mechanisms during the exploitation of gas hydrates.

In this work, numerical analysis is applied for the research on the production features of gas hydrate by depressurization. After revealed the governing mechanisms of two recovery methods, the influence of actual condition on the production efficiency is further considered. The evaluation model has been proposed to predict the production efficiency.

2 Numerical Modeling

Numerical simulations are conducted by Tough + Hydrate, which can model multiphase behavior, the non-isothermal hydration reaction, and fluid and heat flow under the typical conditions of natural gas hydrate deposits [14]. A 1D numerical model with 100m in length is established and discretized into 1000 grids to investigate the depressurization process. Following the experiences of hydrate production test, the production well is located at the left end of the model. The constant-temperature and pressure boundary conditions are assigned to the first grid and the boundaries of no mass and heat flux are settled at right end of the model.

As mentioned before, it is correlated to the intrinsic permeability, thermal conductivity, and kinetic reaction rate. Therefore, these three parameters are selected to investigate the features under exploitation simulation of gas hydrate. Parameters adopted in these cases are shown in Table 1.

Table 1. Materials used in the experiments

Name	Value
Initial hydrate saturation	0.5
Initial water saturation	0.5
Initial pressure, MPa	6
Production pressure, MPa	2.7
Initial temperature, °C	5
Thermal conductivity, W/(m·K)	3.1
Permeability, m^2	2.96×10^{-13}
Intrinsic reaction constant, $mol/(m^2 \cdot Pa \cdot s)$	36000
Porosity	0.3

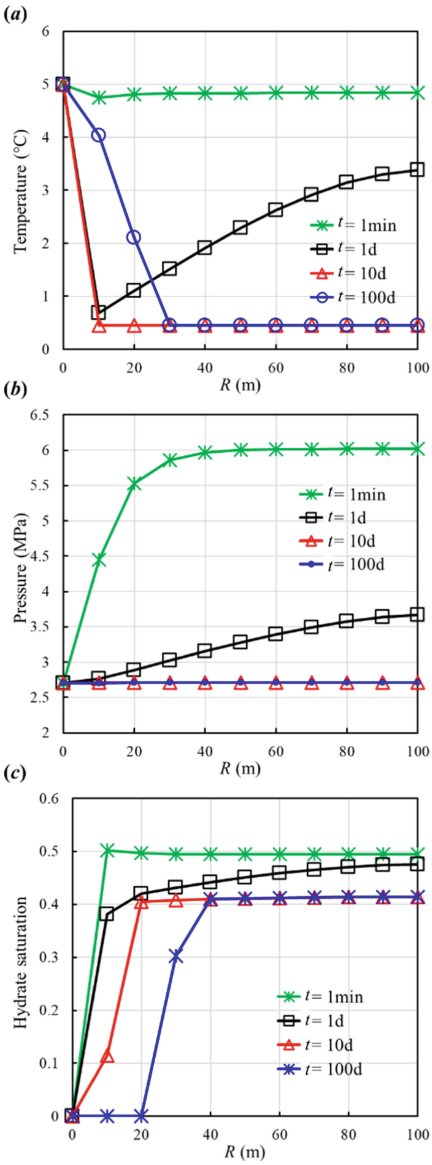

Fig. 1. Simulation results of the exploitation by thermal stimulation: (a) the evolution of temperature; (b) the evolution of pressure; (c) the evolution of hydrate saturation

3 Simulation Results and Discussion

3.1 Governing Mechanisms

Figure 1 has illustrated the evolution of temperature, pressure, and saturation. In the absence of an external heat source, the strongly endothermic reaction of hydrate dissociation is fueled by the heat provided by its own heat capacity. Consequently, temperature is expected to decline in Fig. 1(a) during the hydrate exploitation corresponding to the location of dissociation front in Fig. 1(c). However, the lack of heat supply will greatly reduce the production efficiency afterwards. It shows that the temperature and pressure both varies a lot during depressurization. Once the pressure drops to the equilibrium pressure, gas hydrates begin to dissociate, and the temperature decreases because of the endothermic effect, corresponding to the hydrate dissociation front. Accordingly, the exploitation of gas hydrate can be simply divided into depressurization and endothermic dissociation.

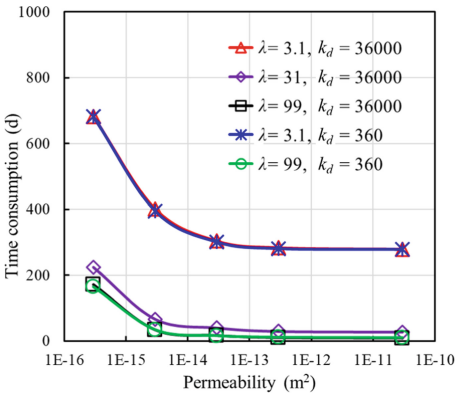

Fig. 2. The influence of different governing mechanisms.

The influence of three governing mechanisms is further considered in Fig. 2. The intrinsic reaction constant has little influence. The time consumption for the recovery decreases with the increases of permeability and thermal conductivity. But when the thermal conductivity is high and permeability is low, the variations in production time is mainly determined by permeability. Similarly, the production time with high permeability and low conductivity is controlled by the thermal conductivity. These phenomena correspond to the two distinct processes mentioned above, and it can be expressed by the combination of heat transfer (TC_H) and fluid flow (TC_T)

$$TC = TC_H + TC_T \propto f(k) + f(\lambda) \tag{1}$$

TC is the time consumption for 50% recovery of methane hydrate in the reservoir, d. It reveals that the production efficiency of gas recovery process is dependent on two distinct processes.

3.2 Two Distinct Processes

1. The Term of Fluid Flow

In the term of fluid flow, the time consumption of exploitation is dependent on TC_H, which is proportional to the reciprocal of permeability. So, this process can be characterized by a typical hydraulic diffusion process, which can be rewritten as

$$TC_H \propto \frac{\mu C_t}{k} \tag{2}$$

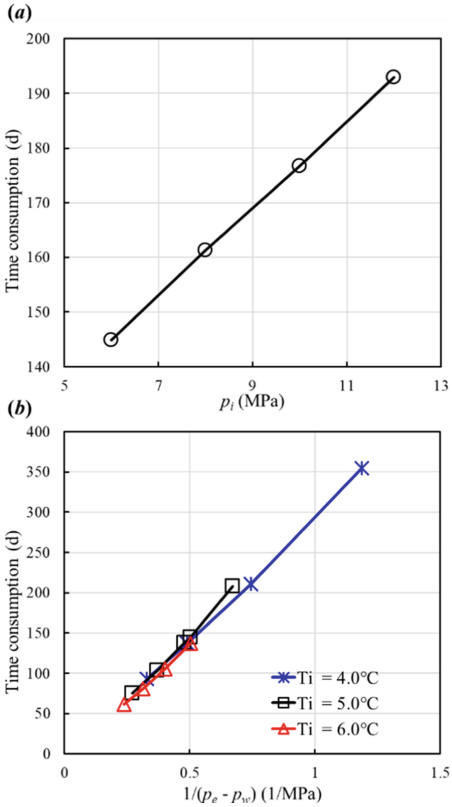

Fig. 3. The influence of (a) initial pressure and (b) initial temperature.

The influence of initial temperature T_i and pressure p_i is shown in Fig. 3. The increasing production pressure p_w will reduce the time consumption, opposing with the increasing initial pressure. In this case, the initial temperature (i.e., the equilibrium pressure p_e) has little effect on the production efficiency. It indicates that higher initial pressure cost more time to drop the pressure to the equilibrium pressure, that is, large difference between p_i and p_e corresponds to the low production efficiency. Meanwhile,

the large difference between p_w and p_e accelerate the dissociation of gas hydrate and enhance the efficiency.

2. The term of heat transfer

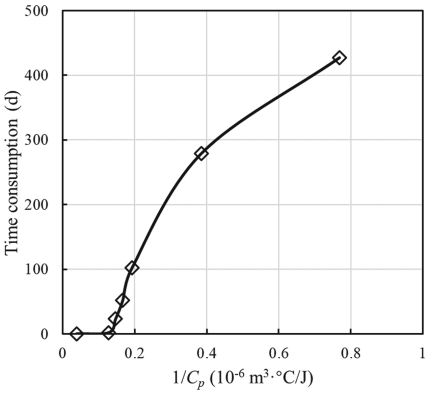

Fig. 4. The effect of heat capacity

In the term of heat transfer, the time consumption is inversely proportional to the thermal conductivity and decreases with the heat capacity (Fig. 4). Small heat capacity affect little on the production efficient because the sensible heat of the surrounding directly supplies the hydrate dissociation. Larger heat capacity provides more sensible heat. Assuming the time consumption is linear with C_p in a reasonable region, we get

$$\mathrm{TC}_T \propto \frac{1}{C_p \lambda} \tag{3}$$

Compared with the term of fluid flow, p_i has no effect on production efficiency from Fig. 6. The time consumption increases with decrease of the pressure difference, while rising of the initial temperature will reduce the production efficiency.

Specially, the time consumption is segmented when $p_w = 2.65$ MPa, which involves two processes. As presented in Fig. 6(a), the hydrate saturation drops down in a short time, and then the dissociation front moves outward from left side. However, when $p_w =$ 2.6 MPa, the hydrate has dissociated a certain degree over the layer, but the movement of dissociation front does not occur. Therefore, high permeability causes a small pressure gradient in the reservoir, and gas hydrate proceeds endothermic dissociation at the same time, leading to a uniform decrease of hydrate in Fig. 5(b). Meanwhile, when the heat is not enough to provide for the dissociation of hydrate (i.e., the difference between p_w and p_e is small), additional heat must be supplied by the boundary heat source through heat transfer to sustain the phase transition. Moreover, the time cost in Fig. 6(a) is much longer than that in Fig. 6(b), leading to the segmentation of the curve.

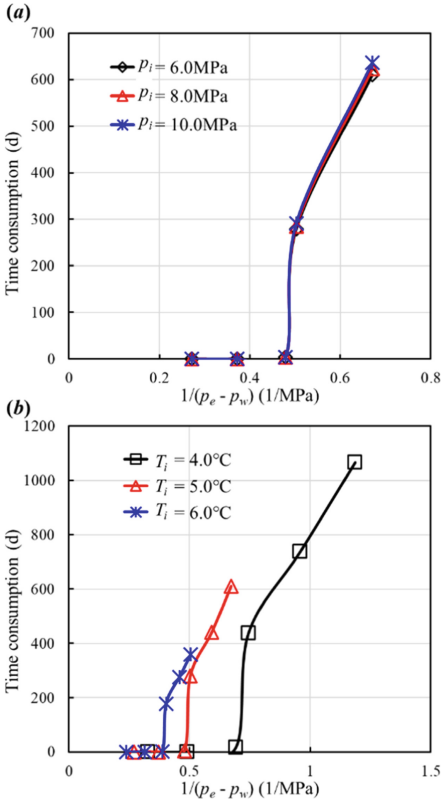

Fig. 5. The influence of (a) initial pressure and (b) initial temperature.

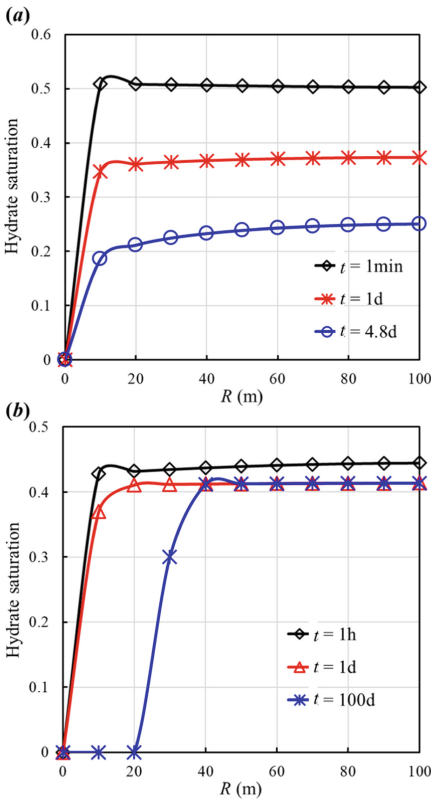

Fig. 6. The evolution of hydrate saturation under different production pressure: (a) p_W = 2.6 MPa; (b) p_W = 2.7 MPa.

4 Conclusion

The exploitation of gas hydrate by depressurization is simulated here. The governing mechanisms and the influence of actual conditions are investigated in the research. We find the kinetic dissociation has nearly no effect on the hydrate exploitation. The process can be divided into fluid flow and heat transfer. The term of fluid flow is a typical hydraulic diffusion, while the term of heat transfer involves in two types of heat supply when the in-situ formation energy is insufficient. The insufficient supply leads subsequent heat transfer from boundary, extending the production time dramatically. The impact of production efficiency by the heat transfer term is higher than that by the fluid flow term. Therefore, the term of heat transfer will be a key point to improve the efficiency of hydrate exploitation. These findings are anticipated to give us a fundamental understanding of dissociation behaviors of hydrate reservoirs and benefit making appropriate recovery plans.

Acknowledgement. The authors would like to appreciate National Natural Science Foundation of China (U20B6005) and National Natural Science Foundation of China (Grant No. 51809275).

Symbol Description

t Time
p Pressure
T Temperature
TC Time consumption
C_t Compressibility
C_p Heat capacity
μ Viscosity
k Permeability
k_d Intrinsic reaction constant
λ Thermal conductivity

References

1. Sloan, E.D., Koa, C.A.: Clathrate Hydrates of Natural Gases, 3rd edn. CRC Press, Boca Raton (2007)
2. Kvenvolden, K.A.: Gas hydrate—a major reservoir of carbon in the shallow geosphere? Chem. Geol. **71**(1–3), 41–51 (1988)
3. Max, M., Johnson, T.A.: hydrate petroleum system approach to natural gas hydrate exploration (2017)
4. Moridis, G.J., Silpngarmlert, S., Reagan, M.T., et al.: Gas production from a cold, stratigraphically-bounded gas hydrate deposit at the Mount Elbert gas hydrate stratigraphic test well, Alaska north slope: implications of uncertainties. Mar. Pet. Geol. **28**(2), 517–534 (2011)
5. Chong, Z.R., Yang, S., Babu, P., et al.: Review of natural gas hydrates as an energy resource: prospects and challenges. Appl. Energy **162**, 1633–1652 (2016)
6. Boswell, R., Collett, T.S.: Current perspectives on gas hydrate resources. Energy Environ. Sci. **4**(4), 1206–1215 (2011)
7. Klauda, J.B., Sandler, S.I.: Global distribution of gas hydrate in ocean sediment. Energy Fuels **19**(2), 459–470 (2005)
8. Zhang, K., Moridis, G.J., Wu, N., et al.: Evaluation of alternative horizontal well designs for gas production from hydrate deposits in the Shenhu area, South China sea. In: International Oil and Gas Conference and Exhibition in China. Society of Petroleum Engineers (2010)
9. Zhao, J., Liu, Y., Guo, X., et al.: Gas production behavior from hydrate-bearing fine natural sediments through optimized step-wise depressurization. Appl. Energy **260**, 114275 (2020)
10. Guo, X., Xu, L., Wang, B., et al.: Optimized gas and water production from water-saturated hydrate-bearing sediment through step-wise depressurization combined with thermal stimulation. Appl. Energy **276**, 115438 (2020)
11. Chen, Z., Feng, J., Li, X., et al.: Preparation of warm brine in situ seafloor based on the hydrate process for marine gas hydrate thermal stimulation. Ind. Eng. Chem. Res. **53**(36), 14142–14157 (2014)

12. Jamaluddin, A.K.M., Kalogerakis, N., Bishnoi, P.R.: Modelling of decomposition of a synthetic core of methane gas hydrate by coupling intrinsic kinetics with heat transfer rates. Can. J. Chem. Eng. **67**(6), 948–954 (1989)
13. Tsypkin, G.G.: Effect of liquid phase mobility on gas hydrate dissociation in reservoirs. Fluid Dyn. **26**(4), 564–572 (1991)
14. Yilong, Y., Tianfu, X., Xin, X., et al.: Multiphase flow behavior of layered gas hydrate reservoir induced by gas production. Geofluids **2017**, 1–15 (2017)

Gas Hydrate Exploitation Technology by Mixed Gas Replacement

XueWen Cao[1], HongChao Wang[1], KaiRan Yang[1], YanBo Shao[2], ZiLong Nan[2], and Jiang Bian[1(✉)]

[1] College of Pipeline and Civil Engineering, China University of Petroleum, Qingdao 266580, China
bj@s.upc.edu.cn

[2] China Petroleum Engineering and Construction Corporation North China Branch, Cangzhou 266071, China

Abstract. CO_2 replacement for natural gas hydrate extraction is considered as a new type of extraction method in which the damage to hydrate structure can be reduced and CO_2 can also be storaged, thus reducing carbon emission and mitigating the greenhouse effect. The low replacement efficiency has been one of the major reasons preventing the industrial application of CO_2 replacement method. In order to solve this problem, a mixed gas extraction technology of CO_2 with N_2 or H_2 is proposed, which can play the role of both replacement and purging, and can improve the efficiency of hydrate development while achieving CO_2 gas sequestration compared with the pure CO_2 gas replacement technology. In this paper, the mechanism and impact mechanism of different gas mixture replacement mining technologies are described in detail. In addition, based on this technology, the combined technology application of mixed gas injection mining technology with plant flue gas utilization technology, methane steam reforming technology and other industrial chain technologies is summarized. The combined mining technology has many benefits and will be the mainstream development direction for hydrate development in the future. This paper evaluates the advantages of the combined technology from the energy, economic and environmental perspectives, and analyzes the challenges encountered by the current technology and the directions to address them. Finally, some shortcomings of the existing research methods are pointed out, and future research work is envisioned.

Keywords: Displacement · Purging · Hydrate exploitation · CO_2 sequestration

1 Introduction

Natural gas hydrates are widely distributed in deep submarine gravels in terrestrial permafrost zones and continental margins. The global carbon reserves of natural gas hydrates in shallow parts of the lithosphere at depths up to 2000 m are estimated to be 2×10^{16} m^3, which is twice the total carbon content of existing fossil fuels, about 27% are distributed in frozen rocks, and 90% of the ocean contains natural gas hydrates [1].

B. Sun et al. (Eds.): DWOG-Hyd 2021, LNCE 246, pp. 162–169, 2022.
https://doi.org/10.1007/978-981-19-0960-3_16

Natural gas hydrate resembles snow or loose ice, and it is combustible when exposed to fire, usually white in color, commonly known as combustible ice [2]. In general, natural gas hydrate formation requires the following conditions: (1) the presence of liquid water or supersaturated water vapor in the gas phase; (2) low temperature and high pressure; (3) the presence of crystal nuclei or gas streams and temperature-pressure perturbations in the system. For these reasons, hydrates in the natural environment are often generated at 1200–1500 m of seafloor and 200–1000 m of permafrost zone [3]. There are three common types of gas hydrate structures, namely type I, type II and type H [4]. The density of gas hydrates is related to the occupancy of the pore, the type of hydrate and the molecular weight of the guest molecules [5], which is generally between 0.8 and 1.2 g/cm3. The thermal conductivity of gas hydrates is 0.5 W/m-K, which is only 1/5 of the thermal conductivity of ice. The thermal conductivity of hydrates increases slowly with temperature, which is the opposite of the temperature-dependent trend of ice, but the spectral, mechanical, and transfer properties of hydrates are similar to those of ice.

CO_2 replacement is a novel method for natural gas hydrate extraction, which can recover both CH_4 and CO_2, and the formation of CO_2 hydrate during the replacement process can maintain the mechanical stability of the formation, thus avoiding geological disasters such as submarine landslides and collapses. However, the low replacement efficiency is still one of the major reasons preventing the industrial application of natural gas hydrate extraction by CO_2 replacement. In addition, the injection of CO_2 mixture containing small molecules such as N_2/H_2 is an effective means to enhance the replacement efficiency, which is more economical than the injection of single CO_2. It can also be combined with industrial chain technologies for natural gas applications to produce the required gas mixture for injection, achieving the dual effect of natural gas hydrate development and utilization.

2 CO_2 and N_2/H_2 Gas Mixture Replacement Exploiting

2.1 Replacement Mechanism

Under geological temperature and pressure conditions, a gas mixture of hydrate formers CH_4, CO_2 and N_2 will form sI hydrates [6], so it can be expected that the addition of N_2 can provide additional control of hydrate equilibrium by a third component during gas exchange between CO_2 and CH_4 in natural gas hydrates. When more N_2 is added to CO_2 as a second guest, the phase equilibrium curve of the mixture approaches that of pure N_2, with more demanding phase equilibrium conditions compared to pure CO_2 [7].

Park et al. [8] initially investigated the gas exchange phenomenon occurring between binary gas mixtures of CO_2 and N_2 and sI NGH by spectroscopic methods, and they found that N_2 molecules attack the CH_4 molecules in the small cage and eventually occupy the position. the CO_2 molecules remain preferentially substituted for the CH_4 molecules in the large cage of sI. On the other hand, N_2 molecules are comparable in size to CH_4 and are expected to compete with CH_4 for occupancy of the small cage. Therefore, since the molecular exchange process takes place in the absence of hydrate decomposition, the use of CO_2-N_2 binary mixtures will significantly improve the recovery of CH_4 from NGH due to the complementary roles of CO_2 and N_2 in the exchange process. Based

on this hypothesis, they experimentally demonstrated that the use of binary CO_2-N_2 mixtures under non-water conditions increased the fraction of CH_4 recovered to 85% [9], which indicated a significant increase in CH_4 recovery compared to 64% obtained with pure CO_2 (Fig. 1). Lee et al. [10] investigated the process of flue gas replacement of natural gas hydrates and found that nitrogen molecules preferentially entered small cages of sI hydrate and replaced methane molecules, thus improving the efficiency of hydrate replacement. The results showed that there was no significant decomposition and hydrate generation during the flue gas replacement process, and only part of the cage structure was deformed or destroyed. Liu et al. [11] investigated the feasibility of the N_2/CO_2 methane replacement reaction by simulation and concluded that the gas mixture replacement process includes thermodynamically dominated CO_2 replacement and kinetically dominated N_2 replacement. The replacement of CH_4 with CO_2 in a large cage and the replacement of CH_4 with N_2 in a small cage with negative Gibbs free energy implies that both of these processes can occur. However, replacing CH_4 with CO_2 in small cages is not feasible. Meanwhile, N_2 diffuses faster than CO_2 in hydrates, which is beneficial to improve the replacement rate of the process.

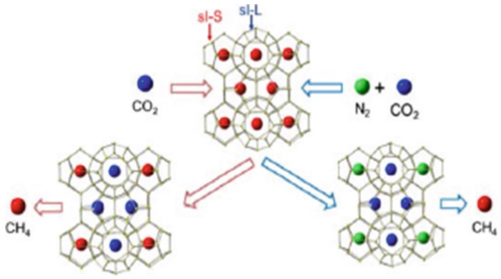

Fig. 1. Microscopic diagram of methane hydrate extraction by CO_2+N_2 gas mixture replacement

Similar to the mechanism of CO_2/N_2 injection, CO_2/H_2 injection can also enable natural gas hydrate extraction. Ding et al. [12, 13] performed a replacement reaction with 60% H_2 and CO_2. They found that the replacement efficiency of the CO_2/H_2 mixture was up to 71.12%, but the gas phase CH_4 concentration was not high, only 28%–30%. There was no water in the replaced sample. In contrast, the replacement efficiency of pure CO_2 could reach 50.22%, and the gas-phase CH_4 concentration could reach about 50%. Therefore, they concluded that H_2 was present in the replacement agent only as a replacement promoter.

Chen et al. [14–16] studied the effects of hydrogen content ratio, gas flow rate, and gas injection method on the CO_2/H_2 gas mixture on the recovery rate. Increasing the hydrogen content ratio is beneficial to improve the recovery efficiency of CH_4. Multiple rounds of gas injection can increase the rate of hydrate decomposition, but at a later stage, the concentration of CH_4 in the product gas decreases, which increases the separation cost of the later process. Different from the replacement mechanism of CO_2/N_2 mixture, CO_2/H_2 replacement has two processes: gas exchange and pressure reduction. In the depressurization process, the hydrate dissociates to produce free water. the increase of CO_2 concentration will increase the gas production of the replacement process, but at

the same time the time of gas production will also increase. When the CO_2 concentration is low, the total CH_4 recovery increases, even if the hydrate is completely decomposed. However, when the CO_2 concentration is below 18%, the recovery of CH_4 is almost from the bucketing mechanism.

2.2 Technology Development

With 78% of N_2 in air and air being abundantly available at any time and any place, the cost of feedstock can be further reduced when using air or a mixture of CO_2 and air to extract natural gas hydrates. In 2014, Hyery et al. [17] experimentally simulated the process of extracting natural gas hydrates from air as well as a mixture of CO_2 and air. In the study Hyery demonstrated the extraction of NGH with a mixture of air and CO_2/air, arguing that the process of air extraction of NGH from permeable subsea sediments is accompanied by the release of CH_4 (decomposition of NGH) and the replacement of CH_4 and air. Hyery investigated the injection of air into the hydrate layer and the mixture of air and CO_2, respectively.

Flue gas is the exhaust gas from power plants after combustion to generate electricity and is mainly composed of CO_2, N_2 and a small amount of other gases. Using flue gas replacement to extract hydrate can not only reduce the cost of CO_2 separation, but also improve the efficiency of CH_4 hydrate recovery. Chen [18] et al. proposed a hydrate chain energy system (Fig. 2) to improve the overall extraction efficiency. This is the first conceptual process proposed for the natural gas utilization chain generated by hydrate replacement. The process is a carbon cycle system based on liquefied gas/methane substitution of hydrates. Exhaust gas (mainly CO_2 and N_2) from the plant is injected into the formation to replace the extracted natural gas hydrates. The gas mixture obtained from the extraction process can be transported nearby to a nearby plant for utilization, or it can be separated by the hydrate method and yield relatively pure CH_4, which can then be transported in the form of hydrates and finally used in a gas power plant or gas-fired power plant. Based on this, a virtuous cycle of energy utilization is achieved by using hydrate based separation and transportation processes.

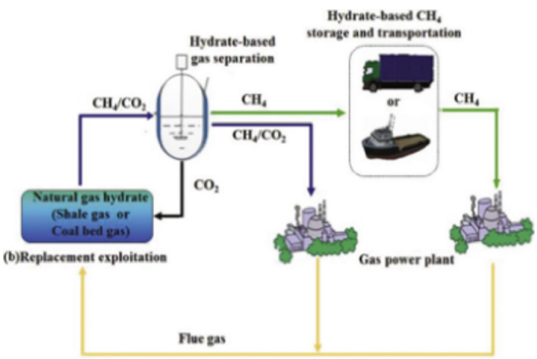

Fig. 2. Carbon cycle system based on flue gas/methane substitution for hydrates

Wang et al. [19] proposed a new production method of methane steam reforming with CO_2/H_2 injection instead of flue gas (CO_2/N_2), the principle of which is shown in Fig. 3. In this mining scheme, CH_4 obtained from natural gas hydrate-bearing sediments is reformed with steam on the platform to produce a CO_2/H_2 gas mixture. These gas mixtures are then partially separated to produce pure H_2 as a product and the carbon-rich CO_2/H_2 gas mixture is injected into the hydrate-bearing sediments for cyclic production. This method has the following advantages: first, the hydrate dissociation rate is high, and the injection of CO_2/H_2 gas mixture reduces the CH_4 partial pressure and breaks the phase equilibrium of natural gas hydrate; second, CO_2 is reinjected into the hydrate layer to replace CH_4, reducing green gas emissions and forming CO_2 hydrate to keep the formation stable. Meanwhile, considering that the generation of CO_2 hydrate reduces the CO_2 content and the decomposition of CH_4 hydrate increases the CH_4 content, the $CO_2/H_2/CH_4$ mixture is partially separated in the formation environment; thirdly, the steam reforming produces a CO_2/H_2 mixture. This method is easier to separate than the CH_4/N_2 mixture produced by the flue gas injection method; fourth, the pressure of the separated CO_2/H_2 mixture (2–7 MPa) is more suitable for high pressure injection when CH_4 steam reforming is performed on the platform. Therefore, significant savings in gas pressurization and transportation costs can be achieved compared to using flue gas.

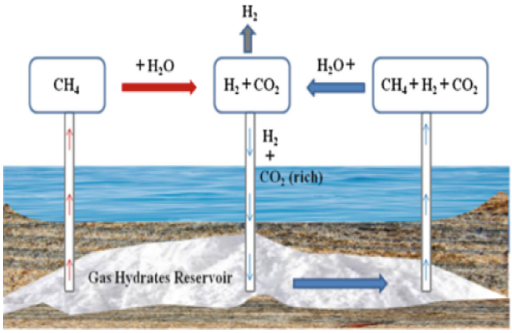

Fig. 3. Process combining methane steam reforming with CO_2/H_2 replacement

Xu et al. [20] proposed the use of integrated gasification combined cycle (IGCC) waste gas to replace mining. H_2 not only has similar effects to N_2, but also can be used as an energy gas together with CH_4 to avoid further separation. Li et al. [21] used IGCC syngas to recover CH_4 from natural gas hydrate not only to significantly improve the recovery efficiency of CH_4, but also to successfully separate CO_2 from IGCC syngas to obtain high-quality H_2 energy.

3 Sweep of N_2/H_2

CO_2 injection replacement for natural gas hydrate extraction produces a blowing effect on hydrate reservoir at the earliest, because the injection of large amount of CO_2 will significantly reduce the escape of CH_4 gas in the gas phase and thus stimulate hydrate

decomposition. However, since CO_2 is prone to hydrate formation, it plays a limited role in blowdown, but small molecule gases such as N_2/H_2 are not prone to hydrate formation, so adding N_2/H_2 and other gases can play a good role in blowdown,, and the effect is similar to that of pressure-reducing extraction. The difference is that the static pressure of the reservoir does not need to drop, which is beneficial to maintain the mechanical stability of the reservoir and is better than the simple pressure-reducing extraction method. However, it needs to increase the subsequent cost of gas separation, especially for the separation of N_2 and CH_4, and there is no more cost effective separation method [5].

Waage et al. [22] studied the diffusion of gas mixtures (CO_2-N_2/H_2) in sI hydrates using molecular simulations. They claimed that H_2 molecules diffuse faster in the sI hydrate structure, readily entering the occupied cage and facilitating the departure of CH_4 from the cage, while N_2 cannot do so [23]. It is suggested that H_2 is more favorable than N_2 for the decomposition of hydrates. Their study showed that the addition of H_2 can increase the volumetric diffusion rate of CH_4 and CO_2 in sI hydrates. The slow diffusion of injected gas in natural gas hydrates determines the importance of diffusion coefficient for hydrate extraction. Xu et al. [24] demonstrated the replacement mechanism of CO_2, N_2, and H_2 as displacing agents. The results showed that the smaller the diffusing gas molecules in the porous medium, the faster the hydrate diffusion rate, which facilitates the recovery of CH_4. The addition of H_2 or N_2 molecules in the system weakens the van der Waals forces between CH_4 molecules and hydrate cage, which leads to the deformation of hydrate cage. The result is that CH_4 molecules can be replaced by N_2 or H_2 in both large and small cages. Therefore, it has a great impact on improving the recovery efficiency of CH_4.

4 Conclusion and Outlook

1. The injection of pure CO_2 and pure N_2/H_2 gas are two extreme cases, the former is mainly replacement and the latter is mainly purging. To balance both purging and replacement, a mixture of CO_2 and N_2/H_2 gas should be injected.
2. The mechanism of small molecule gas such as N_2/H_2 to promote replacement in mixed gas replacement extraction of natural gas hydrate needs to be further studied so that the efficiency of hydrate extraction can be better improved.
3. Optimize methane recovery rate, CO_2 recovery ratio and CO_2/CH_4 replacement production of natural gas hydrate. In order to improve the production efficiency, it is necessary to improve the recovery rate, recovery injection ratio and gas production concentration; otherwise, the low injection ratio and low CH_4 concentration of produced gas will lead to the complexity and high energy consumption of the subsequent separation process.
4. The joint application of other industrial chain technologies with hydrate development also needs to be developed vigorously so as to reduce the cost of natural gas hydrate development. Waste gas heat is also a good source of heat, and future hydrate development should be a process of conversion and utilization of multiple low-grade energy sources to obtain high-quality energy.

Acknowledgements. This work was supported by the National Natural Science Foundation of China (Grant No. 52074341 and No. 51874340) and the Project of China Petroleum Engineering Construction Co., Ltd. (Grant No. CPECC2020KJ07).

References

1. Zhang, W.-L., He, Y.-M., Sun, Y.-H.: Research history and development trend of natural gas hydrate. Broken Block Oil Gas Field (02), 8–10+89 (2005)
2. Sloan, E.D.: Fundamental principles and applications of natural gas hydrates. Nature **426**(6964), 353–363 (2013)
3. Jinxing, D.A., Huang, S., et al.: Genetic types of gas hydrates in China. Pet. Explor. Dev. **44**(6), 887–898 (2017)
4. Van der Waals, J.H., Platteeuw, J.C.: Clathrate solutions. Adv. Chem Phys **2**(21), 1–55 (1959)
5. Guangjin, C., Changyu, S., Qinglan, M.: Gas Hydrate Science and Technology. Chemical Industry Press, Beijing (2008)
6. Sloan, E.D., Koh, C.A.: Clathrate Hydrates of Natural Gases, 3rd edn. CRC Press, Boca Raton (2007)
7. Kang, S.P., Lee, H., Lee, C.S., Sung, W.M.: Hydrate phase equilibria of the guest mixtures containing CO_2, N_2 and tetrahydrofuran. Fluid Phase Equil. **185**, 101–109 (2001)
8. Lee, H., Seo, Y., Seo, Y.-T., Moudrakovski, I.L., Ripmeester, J.A.: Recovering methane from solid methane hydrate with carbon dioxide. Angew Chem. Int. Ed. **42**, 5048–5051 (2003)
9. Park, Y., et al.: Sequestering carbon dioxide into complex structures of naturally occurring gas hydrates. Proc. Nat. Acad. Sci. **103**, 12690–12694 (2006)
10. Lee, Y., Kim, Y., Lee, J., Lee, H., Seo, Y.: CH_4 recovery and CO_2 sequestration using flue gas in natural gas hydrates as revealed by a micro-differential scanning calorimeter. Appl. Energy **150**, 120–127 (2015)
11. Liu, J., Yan, Y., Xu, J., Li, S., Chen, G., Zhang, J.: Replacement micro-mechanism of CH_4 hydrate by N_2/CO_2 mixture revealed by abinitio studies. Comput. Mater. Sci. **123**, 106–110 (2016)
12. Ding, Y.-L., Xu, C.G., Yu, Y.S., Li, X.-S.: Methane recovery from natural gas hydrate with simulated IGCC syngas. Energy **120**, 192–198 (2017)
13. Ding, Y., Wang, H., Xu, C., Li, X.: The effect of CO_2 partial pressure on CH_4 recovery in CH_4-CO_2 swap with simulated IGCC syngas. Energies **13**(5), 1017 (2020)
14. Wang, X.-H., et al.: Gas production from hydrates by CH_4-CO_2/H_2 replacement. Appl. Energy **188**, 305–314 (2017)
15. Sun, Y.-F., et al.: Natural gas hydrate exploitation by CO_2/H_2 continuous injection-production mode. Appl. Energy **226**, 10–21 (2018)
16. Sun, Y.-F., et al.: Gas hydrate exploitation using CO_2/H_2 mixture gas by semi-continuous injection-production mode. Appl. Energy **240**, 215–225 (2019)
17. Kang, H., Koh, D.Y., Lee, H.: Nondestructive natural gas hydrate recovery driven by air and carbon dioxide. Sci. Rep. **4**, 6616 (2014)
18. Chen, J., Wang, Y.-H., Lang, X.-M., Fan, S.-S.: Energy-efficient methods for production methane from natural gas hydrates. J. Energy Chem. **24**(5), 552–558 (2015)
19. Wang, X.H., Sun, Y.F., Wang, Y.F., et al.: Gas production from hydrates by CH_4-CO_2/H_2 replacement. Appl. Energy **188**, 305–314 (2017)
20. Sun, Y.-F., et al.: Natural gas hydrate exploitation by CO_2/H_2continuous Injection-Production mode. Appl. Energy **226**, 10–21 (2018)
21. Sun, Y.-F., et al.: Gas hydrate exploitation using CO_2/H_2 mixture gas by semi-continuous injection-production mode. Appl. Energy **240**, 215–225 (2019)

22. Xu, C.-G., Cai, J., Yu, Y.-S., Chen, Z.-Y., Li, X.-S.: Research on micro-mechanism and efficiency of CH_4 exploitation via CH_4-CO_2 replacement from natural gas hydrates. Fuel **216**, 255–265 (2018)
23. Waage, M.H., Trinh, T.T., van Erp, T.S.: Diffusion of gas mixtures in the sI hydrate structure. J. Chem. Phys. **148**, 214701 (2018)
24. Sun, Y.F., Wang, Y.F., Zhong, J.R., et al.: Gas hydrate exploitation using CO_2/H_2 mixture gas by semi-continuous injection-production mode. Appl. Energy **240**, 215–225 (2019)

Experimental Study on Methane Hydrate Formation and Dissociation in the Sediments of South China Sea

Mingjun Yang, Xinru Wang, Jie Zhao, and Jianan Zheng(✉)

Key Laboratory of Ocean Energy Utilization and Energy Conservation of Ministry of Education, Dalian University of Technology, Dalian 116024, China
zhengjn@dlut.edu.cn

Abstract. The depressurization is regarded as the most economical and feasible method for the exploitation of natural gas hydrate. In this paper, the depressure-producing process of methane hydrate generated in the sediments of the South China Sea through two modes of constant injection of deionized water pressure and injection of methane gas was studied. The results show that: When the reservoir reaches the state of gas saturation, there is a large amount of methane and water less than 20% of porosity. When the reservoir reaches the state of water saturation, there is a large amount of methane and water less than 20% of porosity. The ratio of free gas in the total gas production of the reservoir have little influence on the gas production schedule of the previous stage in the production process. In addition, in this paper, the depressurization mining process with the reactor connected with the underlying gas and the depressurization mining process without the reactor connected with the underlying gas are also studied, and found that the time required to produce of hydrate reservoir connecting underlying gas is shorter than that of hydrate reservoir no connecting underlying gas. In the process of hydrate exploitation, the underlying gas past through the reservoir, and promoted the methane hydrate decomposition.

Keywords: Hydrate · Exploitation · Underlying gas

1 Introduction

Methane hydrate is a solid crystalline compound composed of water and gas molecules. Water molecules surround guest gas molecules through hydrogen bonds to form a cage lattice, which is stabilized by van der Waals force [1]. Methane hydrate deposits are widely distributed in Marine sediments with high pressure and low temperature and permafrost regions [2], which will be an important energy source in the coming decades [3]. Methane hydrate deposition is produced by changing pressure and temperature (P-T) conditions to make methane hydrate decomposition lower than phase equilibrium conditions [4]. The dissociation process of hydrate is essentially a multi-phase and multi-component heat and mass transfer problem, which is combined with internal dynamics

B. Sun et al. (Eds.): DWOG-Hyd 2021, LNCE 246, pp. 170–178, 2022.
https://doi.org/10.1007/978-981-19-0960-3_17

and fluid flow behavior [5]. Since 2018, researchers have conducted a number of experimental studies on hydrate production processes. Song et al. [6] generated methane hydrates with different initial hydrate saturation in a pressure vessel, compared the gas production rate, gas production rate and energy efficiency of the three methods, and analyzed the driving force of hydrate dissociation at different decompression stages. Zhao et al. [7] conducted methane hydrate dissociation experiments in three porous media with production pressures of 2.2 MPa, 2.6 MPa and 3.0 MPa respectively, and divided the methane gas generation process into three main stages: free gas release, hydrate decomposition under the action of reservoir sensing heat, and hydrate decomposition under the action of environmental heat transfer. Song et al. [8] studied the influence of permeability of core-scale hydrate sediments on gas production by thermal simulation method, and found that although the optimal permeability is related to gas production rate, gas production rate is faster in relatively low permeability reservoirs and less time is needed to complete the dissociation process. Chong et al. [4] studied the gas and water production curves of methane hydrate formed in an environment of excess water simulating ocean location. Yang et al. [9] simulated two types of gas hydrate deposition under the monitoring of MAGNETIC resonance imaging (MRI): one is formed by excess gas, and the other is over depressurization formed by excess water. They found that under the condition of excess gas, a larger decompression range improved the average dissociation rate and gas production rate of MH. Chen et al. [10] analyzed the change of hydrate distribution and the influence of water migration on the dissociation of methane hydrate (MH) under different back pressures and flow rates, and found that the chemical potential difference between hydrate and water phase leads to the decomposition of MH in the flow process, and the decomposition rate of MH increases with the decrease of back pressures and the increase of flow velocity. When MH dissociation rate is low, it takes longer time for flow channel to appear, change and disappear, and a new method of flow erosion to improve gas hydrate development is proposed. Zhao et al. [11] analyzed and applied confining pressure to simulate the seabed environment by injecting methane repeatedly into cores and reshaping Marine sediments containing hydrates with different hydrate saturation. They found that the higher the core water content, the greater the hydrate saturation and the longer the hydrate separation time. Sun et al. [12] analyzed the effects of sea-gas flow rate and initial hydrate saturation on the production of methane hydrate (MH), and found that sea-gas flow could effectively promote hydrate dissociation and inhibit hydrate transformation. With the increase of sea-water flow rate and the decrease of gas flow rate, heat and mass transfer rate accelerated, and the average MH dissociation rate increased. Zheng et al. [13] reconstructed water-saturated hydrate sediments with initial conditions of 6 MPa, 3 °C and hydrate saturation of 20%, and adopted a basic decomposition method of simple depression-reduction to 2 MPa and a compensation process of injecting hot water at a certain temperature (20 °C, 30 °C and 40 °C) into the deposit. They found that reduced water saturation was conducive to gas generation. At high gas rate, the gas saturation should be controlled above 25% by water absorption. In this paper, two different pressurization modes of hydrate generation and two different depressurization modes of hydrate exploitation are used to produce methane hydrate, and their effects on the reservoir characteristics of methane hydrate generation and methane hydrate exploitation characteristics are analyzed.

2 Experimental Section

2.1 Materials and Apparatus

This experiment device is shown in Fig. 1, the experiment device simulation including and excluding underlying gas hydrate step-down recovery process, mainly by the high-pressure reaction kettle, injection pump (ISCO pump), gas storage system, constant temperature water bath, underlying tank, the back pressure valve, pressure sensor, thermocouple and data acquisition system, including gas storage system composed of gas liquid separator and propane tanks. The reactor is made of 316 stainless steel with an internal volume of 1038 ML. There is a layer of water bath outside the reactor, water bath temperature range is -10–30 °C, water bath temperature is set to 2 °C, control reactor temperature is 3–4 °C. The reaction kettle is connected with the methane cylinder through a pressure regulating valve. Injection pump is a high precision injection pump used to inject water into the kettle at a constant flow rate. A water bath is provided outside the injection pump, and the temperature of the water bath is set at 2 °C. The water temperature of the control injection pump is 3–4 °C, which is consistent with the temperature of the reaction kettle. Backpressure valves are used to maintain constant gas production pressure. The volume of the gas-liquid separator is 502 mL, and the volume of the gas storage tank is 3050 mL, respectively, to collect the produced water and methane.

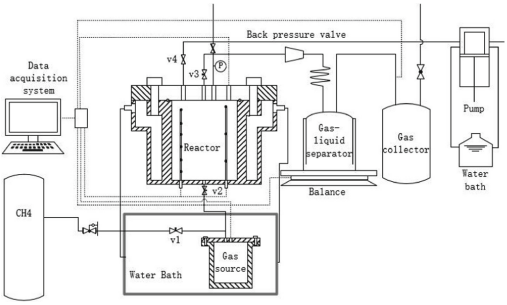

Fig. 1. Schematic of the apparatus for gas hydrate experiment

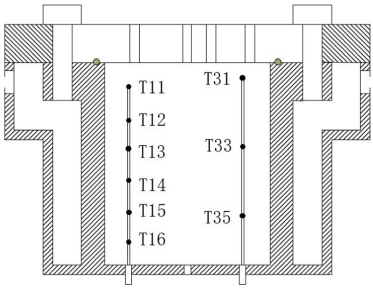

Fig. 2. Diagram of thermocouple distribution in reaction kettle

The precision of electronic scale is ±0.1 g, used for weighing the quality of water from gas-liquid separator. The thermocouple temperature test accuracy is ±0.1 K, which is mainly distributed in the high-pressure reaction kettle (as shown in Fig. 2). The pressure sensor is distributed in the reaction kettle, the underlying gas tank and the gas collecting tank, which is used to measure and record the real-time temperature and pressure. Thermocouple and pressure sensor are connected with A/D module, A/D module and balance are connected with the acquisition system, real-time data collection, and save to the computer.

2.2 Experimental Procedure

700 g of South China Sea soil dried at 110 °C for 24 h was filled into the high pressure reaction kettle; Cool the reactor to 3.5 °C; Fill the reactor with methane gas to 1 MPa, and then slowly discharge the gas, repeat three times to empty the air in the reactor; Inflate the reaction kettle to 3 MPa; ISCO pump was used to inject deionized water into the reactor at a constant flow rate of 10 mL/min, and the pressure to the reactor was 4 MPa, 4 MPa and 3.5 MPa, respectively. After 12 h stabilization, methane or deionized water is injected into the reactor and pressurized to 8 MPa, 6.6mpa and 8MPa, respectively, to make methane hydrate saturated with gas or water. Then, the back pressure valve was set to 2 MPa, 3 MPa and 3 MPa, respectively. The back pressure valve was opened to decompose methane hydrate, and the underlying gas was connected during decomposition.

3 Experimental Results and Discussion

In this paper, the experiment of hydrate formation and decomposition in sediments of south China Sea was carried out by combining two different pressurization modes of hydrate formation and two different depressurization modes of hydrate extraction, and its influence on hydrate extraction characteristics was analyzed. The two pressure relief modes are deionized water injection and methane gas injection, respectively. The two pressure relief modes are the reaction kettle connected with the underlying gas during pressure relief mining and the reaction kettle alone pressure relief mining.

3.1 Temperature and Pressure Characteristics of Reservoir Decomposition of Underlying Gas Hydrates

The temperature change trend of the nine temperature measuring points T11–T16 and T21–T23 is roughly the same. In this paper, the decomposition process is divided into two stages. The first stage is from the beginning of decomposition to the decomposition of 95% methane hydrate, and the second stage is from the decomposition of 95% methane hydrate to the complete decomposition of methane hydrate. The first stage lasts for 70min. In this stage, the pressure of the reactor drops rapidly in the first 10min and slowly after 10min, because the regulation value of the back pressure valve of the reactor exhaust port is 2 MPa. When the exhaust valve V3 (Fig. 1) is opened at the beginning of mining, The unbound methane gas (free gas for short) enters the gas storage system through the exhaust port first, the reservoir pressure decreases, and the methane hydrate begins to

decompose. At the same time, open the underlying gas production valve V2, methane gas through the reservoir into the gas storage system, so the underlying gas pressure decreases rapidly. The gas storage system pressure rises from zero. Each temperature measuring point change trend first reduce and then increases, temperature measuring point T11, T21 temperature drop range is very large, probably because the two temperature measuring point close to the vent (as shown in Figs. 1 and 2), the free gas near the first through the valve 3 and back pressure valve into the low pressure gas storage system that is Joule-Thomson effect [14]. Temperature measurement points T12 and T22 are close to the above two temperature measurement points (as shown in Figs. 1 and 2), and the temperature drops due to the influence of heat transfer, which is delayed in time, because heat transfer takes time, while other temperature measurement points are far away from each other and have little influence. Another reason for the decrease of temperature in the kettle is the heat absorption of methane hydrate decomposition in the reservoir. The temperature rise at about 60 min is due to heat transfer due to the temperature difference between the reservoir and the outside.

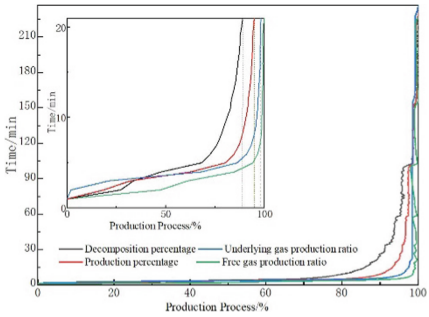

Fig. 3. Gas production schedule of depressurized exploitation of gas hydrate reservoirs containing underlying gas

The second stage lasted 158 min. In this stage, the temperature of each temperature measuring point gradually rose until it was stable, the pressure of the reaction kettle decreased by 0.06 MPa, and the pressure of the underlying gas decreased by 0.03 MPa.

In the process of depression-relief exploitation of hydrate simulated in this experiment, the methane gas entering the gas storage system includes three parts: free gas, gas produced by hydrate decomposition and gas produced by underlying gas. The mining process lasted 228 min, and the free gas was produced first in 21 min. As shown in Fig. 3, 88.89% of the hydrate in the reservoir is decomposed, 98.1% of the underlying gas is produced, and 94.7% of the total gas production is completed. Therefore, the vast majority of free and underlying gas is produced in the first 21 min of the production process, and in the following 216 min of production, the main source of production is methane gas generated from the decomposition of reservoir hydrate.

3.2 Effect of Underlying Gas on Decompression Rate of Hydrate Reservoir

In the process of mining, the hydrate reservoir connected with underlying gas takes 70 min from the beginning of mining to 95% hydrate decomposition, and the hydrate reservoir not connected with underlying gas takes 182 min from the beginning of mining to 95% hydrate decomposition, as shown in Fig. 4. It takes 155 min for methane hydrate reservoirs connected with underlying gas to be completely decomposed during depressors exploitation. At this time, 94% of hydrate reservoirs not connected with underlying gas are decomposed, as shown in Fig. 5.

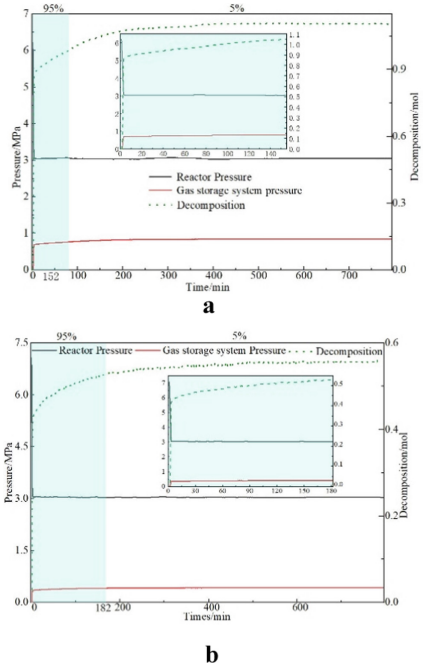

Fig. 4. a Decomposing pressure and decomposing quantity of reservoir with underlying gas hydrates b Decomposing pressure and decomposing quantity of reservoir without underlying gas hydrates

The accumulation of hydrate connected with underlying gas is faster than that of hydrate not connected with underlying gas, which may be due to the fact that during the exploitation of hydrate connected with underlying gas, the underlying gas passes through the reservoir and promotes the decomposition of methane hydrate. In addition, the back pressure of hydrate reservoir with connected underlying gas is 3 MPa, and that without connected underlying gas is 2 MPa. The slow exploitation of hydrate reservoir without connecting underlying gas may also be caused by high back pressure, relatively small reservoir pressure in the kettle and pressure difference of gas storage system.

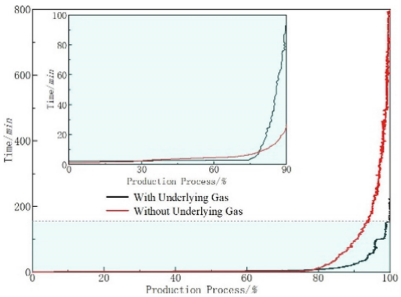

Fig. 5. Gas production schedule diagram of depressurized gas hydrate reservoirs with and without underlying gas hydrate reservoirs

3.3 Depressurization and Decomposition of Hydrate Formation Under Different Pressure Methods

In this paper, the characteristics of methane hydrate formed by methane pressurization in sediments with different porosity in the South China Sea are compared. Both Case1 and Case3 are pressurized with methane. The methane hydrate saturation generated in Case1 is 17.2%, and that generated in Case3 is 12%. The methane hydrate saturation generated by Case1 is 43% lower than that generated by Case3. This may be due to the different porosity of the reservoirs in Case1 and Case3. The porosity of the south China sea sediment in Case1 is 12.14% and that in Case3 is 8.71% (Fig. 6).

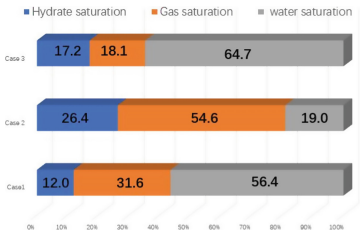

Fig. 6. Saturation of different experimental conditions

The amount of hydrate generated by methane pressurization (Case2) is about twice that generated by water pressurization (Case3). The reservoir hydrate saturation of methane pressurization (Case2) is 26%, while that of water pressurization (Case3) is 17.2%, as shown in Fig. 7. This indicates that there is excess water in the reservoir. The amount of methane hydrate generated when methane gas enters the reservoir and combines with the original water in the reservoir is more than that generated when water enters the reservoir and combines with the original water in the reservoir. In Case2 experiment, there is still a large amount of methane gas in the reservoir after stable formation. In Case3 experiment, 18.1% methane gas with stable residual saturation was generated, and it was difficult for the remaining water in the reservoir to combine with these small

amounts of methane gas to form hydrate. In Case2 experiment, 19.0% water was generated, and it was difficult for the remaining methane gas in the reservoir to combine with these small amounts of water to form hydrate.

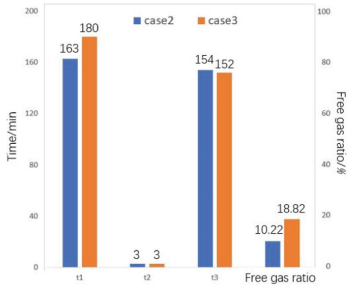

Fig. 7. Gas production time and free gas proportion under methane and water pressure

When the reservoir reaches gas saturation state, there is a lot of methane and a little water in the reservoir, and the water content is generally less than 20% of the porosity. When the reservoir reaches water saturation state, there is a lot of methane and a little water in the reservoir, and the methane content is generally less than 20% of the porosity.

In the mining process, the time taken by Case2 and CasE3 to produce gas to 95% is roughly the same, as shown in Fig. 7. As a result, the first phase of gas production in case2 and case3 was roughly the same, and the remaining 5% of methane hydrate in case3 was slowly decomposing. Hydrate reservoir generation yes hydrate reservoir generation nearly two times, the free part of the total gas accounted for more than case3 than Case2, and the experimental results show that the progress that the first of the two phase of gas is roughly same, this shows that the total output of hydrate and free gas in the gas reservoir of exploitation of the first stage of the gas progress had little effect.

4 Conclusion

In this paper, it is found that the majority of free gas and underlying gas in the hydrate reservoir connected with underlying gas are produced in the first 21 min of the exploitation process, and in the following 216 min of exploitation process, the main source of production is methane gas generated by the decomposition of reservoir hydrate. In addition, the hydrate reservoir connected with underlying gas is faster than that not connected with underlying gas, which may be due to the fact that in the exploitation process of hydrate reservoir connected with underlying gas, the underlying gas passes through the reservoir and promotes the decomposition of methane hydrate, resulting in high back pressure of exploitation, which may also lead to the slow exploitation of hydrate reservoir. When the reservoir reaches gas saturation state, there is a lot of methane and water less than 20% of porosity in the reservoir, and when the reservoir reaches water saturation state, there is a lot of methane and water less than 20% of porosity in the reservoir. The amount of hydrate in the reservoir and the proportion of free gas in the total gas production have little influence on the gas production schedule in the first stage of

exploitation. In the following study, we conducted a further study on the factors affecting the decomposition rate of methane hydrate in the reservoir.

Acknowledgement. [1] Outstanding Youth Program of National Natural Science Foundation of China (51822603): Mechanism of gas hydrate phase transition, 2019–2021, Responsible Person: Mingjun Yang.

[2] Fok Yingdong Foundation for Young Teachers, Ministry of Education (161050):Basic research on phase transformation mechanism and control of natural gas hydrate,2018–2021, Responsible Person: Mingjun Yang.

[3] Dalian Science and Technology Innovation Fund (2019J11CY012): Hydrate formation mechanism and blockage detection technology in oil and gas pipelines, 2019–2021, Responsible Person: Mingjun Yang.

References

1. Yin, Z., Khurana, M., Tan, H.K., Linga, P.: A review of gas hydrate growth kinetic models. Chem. Eng. J. **342**, 9–29 (2018)
2. Yang, M., Zheng, J.-N., Gao, Y., Ma, Z., Lv, X., Song, Y.: Dissociation characteristics of methane hydrates in South China Sea sediments by depressurization. Appl. Energy **243**, 266–273 (2019)
3. Chong, Z.R., Yang, S.H.B., Babu, P., Linga, P., Li, X.-S.: Review of natural gas hydrates as an energy resource: prospects and challenges. Appl. Energy **162**, 1633–1652 (2016)
4. Chong, Z.R., Pujar, G.A., Yang, M., Linga, P.: Methane hydrate formation in excess water simulating marine locations and the impact of thermal stimulation on energy recovery. Appl. Energy **177**, 409–421 (2016)
5. Yin, Z., Chong, Z.R., Tan, H.K., Linga, P.: Review of gas hydrate dissociation kinetic models for energy recovery. J Nat Gas Sci Eng **35**, 1362–1387 (2016)
6. Song, Y., et al.: Evaluation of gas production from methane hydrates using depressurization, thermal stimulation and combined methods. Appl. Energy **145**, 265–277 (2015)
7. Zhao, J., Zhu, Z., Song, Y., Liu, W., Zhang, Y., Wang, D.: Analyzing the process of gas production for natural gas hydrate using depressurization. Appl. Energy **142**, 125–134 (2015)
8. Song, Y., Kuang, Y., Fan, Z., Zhao, Y., Zhao, J.: Influence of core scale permeability on gas production from methane hydrate by thermal stimulation. Int. J. Heat Mass Transf. **121**, 207–214 (2018)
9. Yang, M., Fu, Z., Jiang, L., Song, Y.: Gas recovery from depressurized methane hydrate deposits with different water saturations. Appl. Energy **187**, 180–188 (2017)
10. Chen, B., Yang, M., Sun, H., Wang, P., Wang, D.: Visualization study on the promotion of natural gas hydrate production by water flow erosion. Fuel **235**, 63–71 (2019)
11. Zhao, J., Zheng, J.-N., Ma, S., Song, Y., Yang, M.: Formation and production characteristics of methane hydrates from marine sediments in a core holder. Appl. Energy **275**, 115393 (2020)
12. Sun, H., Chen, B., Yang, M.: Effect of multiphase flow on natural gas hydrate production in marine sediment. J. Nat. Gas Sci. Eng. **73**, 103066 (2020)
13. Zheng, J.N., Wang, X.R., Ma, Z.Q., Yang, M.J.: Production behaviors of water-saturated methane hydrate deposits during the depressurization with/without thermal water compensation process. Energy Fuels **35**(2), 1638–1647 (2021)
14. 高祎: 多类型甲烷水合物藏降压开采特性研究. 硕士. 大连理工大学 (2019)

Numerical Simulation of Producing Natural Gas Hydrate by Air Injection

Wu Ying[1], Jiakai Ji[1], Haotian Wang[1], Yuhang Zhang[1], Pengcheng Jing[1], Yuxiang Xia[1], and Litao Chen[1,2(✉)]

[1] School of Petroleum Engineering, China University of Petroleum (East China), Qingdao 266580, China
chenlt@upc.edu.cn

[2] Key Laboratory of Unconventional Oil and Gas Development, Ministry of Education, China University of Petroleum (East China), Qingdao 266580, China

Abstract. In this paper, a numerical simulation study is carried out for the extraction of natural gas hydrate by air injection. The air method of natural gas hydrate extraction uses the principle of chemical potential difference to inject a large amount of compressed air into the natural gas hydrate reservoir to reduce the partial pressure of CH_4 in the gas phase. Due to the chemical potential difference between the solid phase and the gas phase, CH_4 in the solid phase will escape to the gas phase until the equilibrium state. A two-dimensional gas hydrate extraction model is developed to simulate the intrinsic process of gas hydrate extraction by the air method at different saturation levels, to study the way each factor contributes to the gas production and to evaluate the production capacity. The results verify the feasibility of gas hydrate extraction by air injection, and analyze the gas and water production pattern and hydrate solid phase concentration variation of air injection extraction.

Keywords: Ocean natural gas hydrate · Air injection · Numerical simulation

1 Introduction

Natural gas hydrates are ice-like, non-chemical crystalline compounds composed of water and natural gas when mixed under high pressure and low temperature conditions [1]. Gas hydrates are mainly found in deep-sea sediments, and their organic carbon content is nearly twice that of conventional fossil energy sources, and their reserves are huge. Compared with traditional energy sources such as oil and coal, natural gas hydrates are cleaner and have better combustion performance, making them an important part of meeting the needs of human life in the future. As a potential alternative energy source with huge resource potential, natural gas hydrates have shown great interest in the world, but a sound theory and technology for commercial gas hydrate extraction has not yet been developed.

At present, the main methods of natural gas hydrate extraction include depressurization, thermal excitation, chemical inhibitor injection, replacement, etc. [2]. The pressure

B. Sun et al. (Eds.): DWOG-Hyd 2021, LNCE 246, pp. 179–187, 2022.
https://doi.org/10.1007/978-981-19-0960-3_18

reduction method is considered to be the most promising extraction method, which destroys the hydrate phase equilibrium conditions by reducing the pressure to break it down, but there are problems such as low efficiency and serious sand emission [3]. The thermal excitation method decomposes gas by heating the system temperature higher than the gas hydrate phase equilibrium temperature, but the heat loss is serious and the efficiency is not high. The chemical inhibitor injection method destroys the gas hydrate phase equilibrium conditions by inhibitor injection, but it is expensive and easy to contaminate the formation. The replacement method replaces the methane molecules in the gas hydrate by injecting carbon dioxide to produce carbon dioxide hydrate, but it is inefficient and expensive. Thus, disrupting the phase equilibrium conditions of natural gas hydrates is the most effective way to break them down, but there is still an urgent need for an efficient and economical development method to achieve commercial development of natural gas hydrates.

In this paper, we propose a novel method of gas hydrate extraction by air injection [4, 5]. As shown in Fig. 1, by injecting a large amount of air into the hydrate reservoir, the large amount of injected air will reduce the partial pressure of methane gas in the system. Because of the chemical potential difference between the gas and solid phases at this point, methane molecules within the natural gas hydrate will continue to escape into the gas phase until the chemical potentials of the two become equal at some point.

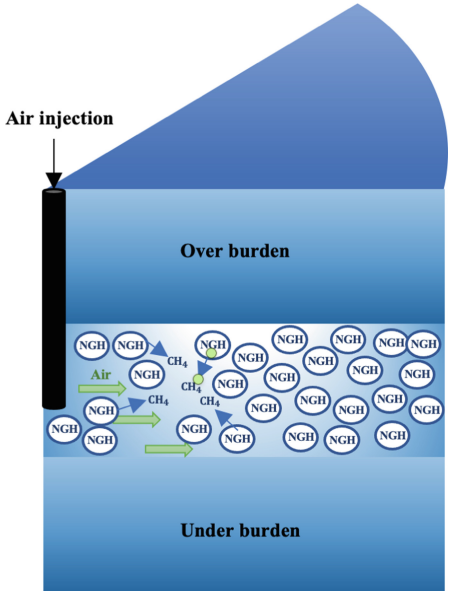

Fig. 1. Schematic diagram of gas hydrate extraction by air injection

After reaching the new thermodynamic equilibrium, the chemical sites of CH_4 in the gas and hydrate phases are equal and are expressed in Eq. (1) as:

$$\mu_{CH_4}^{G} = \mu_{CH_4}^{H} \tag{1}$$

Where, $\mu^{G}_{CH_4}$ and $\mu^{H}_{CH_4}$ denote the chemical sites of CH_4 in the gas phase and the hydrate phase, respectively [6].

In this paper, we mainly use CMG-STARS to simulate the gas hydrate extraction by air injection, in which the geological model of gas hydrate is established based on the test recovery data of gas hydrate reservoir in Shenhu Sea, South China Sea [7].

2 Numerical Simulation

2.1 Model Construction

In the model of gas hydrate extraction by air injection, five components are considered: water, $CH_4 - HYD$, CH_4, oxygen, and nitrogen. Water is the liquid phase; $CH_4 - HYD$ is the solid phase; and CH_4, oxygen and nitrogen are the gas phases. Because the composition of air is composed of oxygen (21%), nitrogen (78%) and rare gases and other substances (1%), the air injected in the simulation is replaced by oxygen and nitrogen, and the ratio of oxygen to nitrogen is 21:78. The decomposition of natural gas hydrate to produce water and CH_4 has a complex phase transition mechanism, so in order to simplify the model to explore the feasibility of the air injection method for natural gas hydrate extraction, the following assumptions are introduced in the The following assumptions are introduced in the model: 1) CH_4 and water generate SI hydrate, without considering oxygen, nitrogen and water to generate hydrate; 2) water is pure water and liquid phase all the time, without considering the influence of ice phase and salinity; 3) the percolation of water phase and liquid phase is in accordance with Darcy's law; 4) dissolution of oxygen and nitrogen in water is not considered; 5) the upper and lower cap layers are impermeable boundary layers and hydrate layers only have heat transfer, ignoring The effect of mass transfer between upper and lower cover layer and hydrate layer is ignored. Following the above assumptions, the numerical model of gas hydrate extraction by air injection is established as follows [8]:

1) Kinetic equation for the decomposition reaction of hydrate generation:

$$CH_4(g) + nH_2O(l) \leftrightarrow CH_4 \cdot nH_2O(s) \pm \text{heat} \tag{2}$$

where: n is the $CH_4 - HYD$ hydration number and takes the value of $n = 5.75$.

2) Hydrate decomposition rate equation:

$$-d_{n_H}/d_t = K_{rd}A_s(f_e - f_g) \tag{3}$$

Where:

n_H: the amount of gas in hydrate form at moment t (mol);
A_s: the total surface area of hydrate particles;
K_{rd}: rate constant of hydrate decomposition;
f_e: methane fugacity under three-phase equilibrium conditions;
f_g: methane fugacity in the gas phase;

The rate of hydrate decomposition is proportional to the surface area A_s of the decomposing particles and the driving force generated by the difference between the methane fugacity f_e and the methane fugacity f_g in the gas phase under three-phase equilibrium conditions.

And K_{rd} is the hydrate decomposition rate constant can be expressed by Eq. (4) as:

$$K_{rd} = K_d^0 Exp(-\Delta E/RT) \tag{4}$$

where K_d^0 is the intrinsic decomposition rate constant of the hydrate, independent of temperature.

3) Porosity equation:

$$\phi = \phi_0(1 - S_h) \tag{5}$$

Where:

ϕ: effective porosity;
ϕ_0: initial porosity;
S_h: hydrate saturation;

4) Permeability equation:

$$k(\phi) = k_0(\phi/\phi_0)^{\varepsilon}[(1 - \phi_0)/(1 - \phi)]^2 \tag{6}$$

Where:

ϕ: effective porosity;
ϕ_0: initial porosity;
ε: is an empirical parameter varying between 1, 3, 5 and 10;
$k(\phi)$: is the effective permeability;
k_0: is the initial permeability;

5) Equilibrium pressure equation [9]:

$$P_e = y_i P_g / X_i \tag{7}$$

Where:

P_e: equilibrium pressure;
y_i: molar fraction of CH_4 in the gas phase;
X_i: the molar fraction of CH_4 in the liquid phase;
$y_i P_g$: the partial pressure of CH_4 in the gas phase;

2.2 Model Parameters

In this paper, a geological model is established using the data published in the first test production of ShenHu in the South China Sea, which considers the reservoir containing subducted gas hydrate reservoir. This simulation area is a cylinder with a radius of 200 m and 20 m. The extraction method of one injection and one extraction is adopted, with injection wells located at the outer edge of the cylinder and extraction wells located at the center of the cylinder. The gas injection volume is 100×10^4 m^3/d and the temperature is 25 °C.

It is assumed that the depth of the subsea level is 1495 m. The upper and lower cover layers are both 20 m and impermeable boundaries, and the underlying gas formation contains only gas and water phases with saturation of 0.3 and 0.7, respectively, and the other relevant formation parameters and physical properties are shown in Table 1.

Table 1. Reservoir parameters

Parameter	Value
Deposit density ρ	2600 kg/m^3
Deposit specific heat capacity C	1000 $J \cdot kg^{-1} \cdot °C^{-1}$
Hydrate-Bearing Layer (HBL) thickness	30 m
Porosity Φ	0.35
Permeability K	2.9 mD
Initial temperature (at base of HBL) T_B	14.23 °C
Initial pressure (at base of HBL) P_B	16.27 MPa
Initial solid concentration ($CH_4 - HYD$)	2616 $gmole/m^3$

3 Results and Discussion

3.1 Gas Production and Water Production Law

Simulating the gas hydrate reservoir in the Shenhu Sea for air injection mining, the cumulative gas production results calculated from the simulation are given in Fig. 2. From Fig. 2, it can be seen that the CH_4 production enters a period of stagnation after the initial rapid rise, and continues to rise when the time reaches 2500 days, while the water production keeps rising slowly, although the rate of water production gradually slows down with increasing time. The gas and water produced in the initial stage are mainly free gas and pore water in the lower volatile gas formation [10]. A large amount of air is injected into the lower volatile gas formation and continuously drives the gas and water in the lower volatile gas formation into the wellbore, but some of the air also enters the hydrate reservoir with the lower volatile gas, which causes the hydrate reservoir pressure to rise and also generates some hydrate. The stagnation for a period of time after

all the CH_4 in the downgradient formation is displaced by air is mainly due to the large injection volume which causes the gas and water in the downgradient formation to be displaced quickly, and the injected air forms a circulation channel between the injection and production wells. Most of the injected gas flowed into the production wells from the circulation channel of the lower volcanic formation, and could not enter the reservoir completely to reduce the partial pressure of CH_4 in the hydrate reservoir, thus causing the decomposition of hydrate. However, as the air is extracted, the pore water in the hydrate reservoir is also extracted along with the air, and more air enters the natural gas hydrate reservoir after the pore space in the hydrate reservoir is vacated, and the CH_4 in the gas phase further decreases to the critical methane concentration, and then the hydrate starts to decompose in large quantities. At this time, the temperature and pressure conditions in the hydrate reservoir are still within the phase equilibrium conditions, and the hydrate is not decomposed because of the decrease of the pore water outflow pressure.

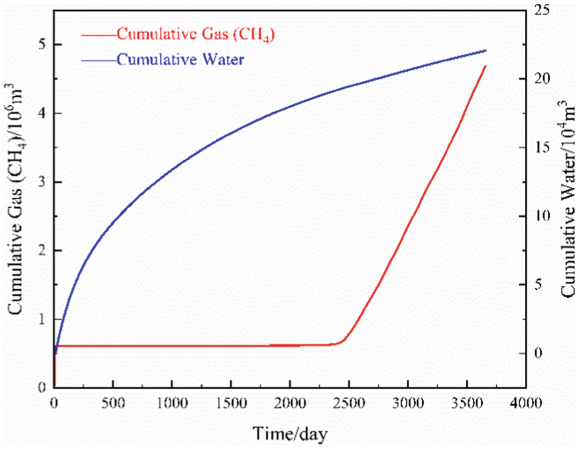

Fig. 2. Cumulative gas and water production

Figure 3 shows the variation of gas production rate of hydrate decomposition and the proportion of CH_4 to total gas production with time after 2500 days, from which it can be seen that the gas production rate gradually increases. From the simulation results, the gas produced by hydrate decomposition caused by air injection accounts for more than 85% of the total CH_4 production, and the proportion of CH_4 to total gas production is basically higher than 1‰, which verifies the feasibility of gas hydrate extraction by air injection.

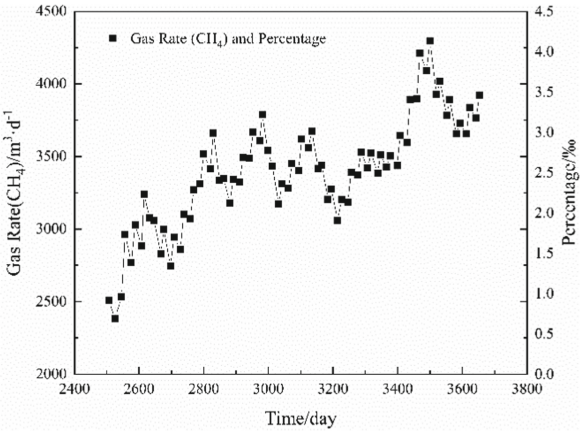

Fig. 3. Gas rate (CH_4) and percentage

3.2 Hydrate Saturation Variation Law

Figure 4 shows the variation of hydrate solid phase concentration in the reservoir with time, and the solid phase concentration is an equivalent expression of saturation, where Well-1 is a production well. It can be seen from Fig. 4 that hydrate in the reservoir did not decompose in the early stage of mining. In the middle of the hydrate reservoir near the extraction well, a part of the injected air carries free gas from the underlying gas formation into the reservoir, which raises the hydrate reservoir pressure and generates a part of hydrate at the same time. When the time reached 2190 days, a small amount of hydrate decomposed near the injection wells, and then the hydrate gradually decomposed along the radial direction from the injection wells. At 2555 days, a small amount of hydrate decomposed near the production well, and the hydrate generated in the previous period also gradually decomposed. After that, the hydrate decomposition area gradually spreads from the extraction wells and injection wells to the middle of the reservoir, and the hydrate decomposition area gradually increases, and the gas production rate also increases.

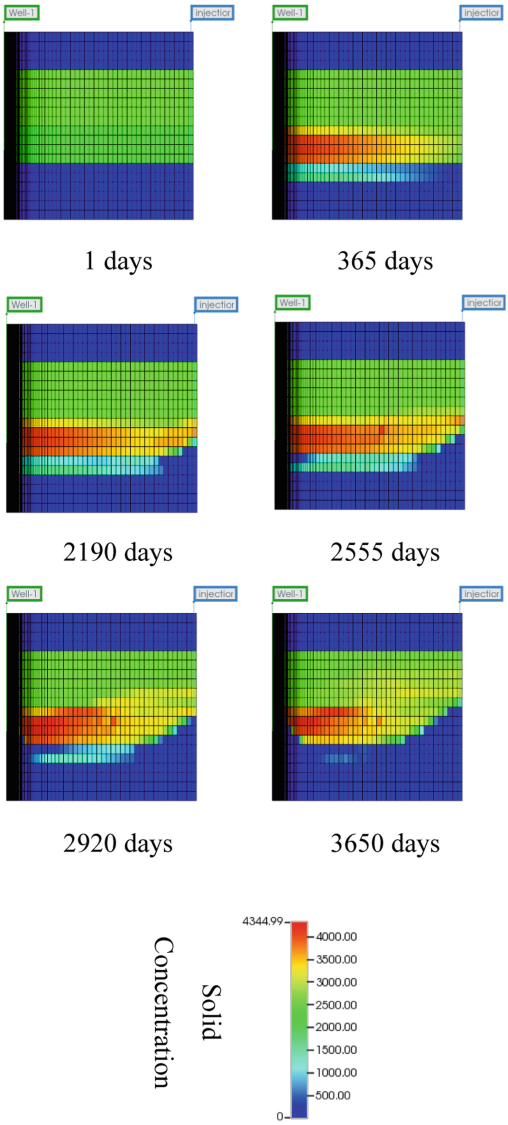

Fig. 4. Solid concentration

4 Conclusion

1) Air injection mining of natural gas hydrate reservoirs is feasible in principle and technology, and the simulation results show that the cumulative gas production over ten years of mining is 4.68×10^6 m^3, of which the CH_4 extracted by air method accounts for more than 85%, and the rest is the lower volatile gas driven by air injection.

2) There is still room for improvement in the efficiency of air-injection extraction of gas hydrate reservoirs, and the proportion of CH_4 to the total gas produced is basically higher than 1‰, which meets the minimum standard for gas separation, but the separation is more difficult.
3) The gas production in the middle stage of extraction of gas hydrate reservoir by air injection is basically zero, mainly because the formation of gas circulation channels leads to the direct output of most of the injected gas, and the extraction wells can be shut down after the replacement of the lower vapor free gas to enhance the partial pressure effect of air on CH_4.
4) The extraction method of air injection for gas hydrate reservoirs can be combined with the pressure reduction method and heat injection method to further improve the extraction efficiency. Alternatively, the CO_2 content can be increased in the injected air, and CO_2 can be used to replace part of CH_4 to achieve sequestration of CO_2 while extracting hydrate [11, 12].

References

1. Sloan, E.D., Koa, C.A.: Clathrate Hydrates of Natural Gases, 3rd edn. CRC Press, Boca Raton, FL (2007)
2. Li, L., Li, X., Wang, Y., et al.: Investigating the interaction effects between reservoir deformation and hydrate dissociation in hydrate-bearing sediment by depressurization method. Energies **14**(3), 548–564 (2021)
3. Lee, J.: Experimental study on the dissociation behavior and productivity of gas hydrate by brine injection scheme in porous rock. Energy Fuels **24**(1), 456–463 (2010)
4. Okwananke, A., Yang, J., Tohidi, B., et al.: Enhanced depressurisation for methane recovery from gas hydrate reservoirs by injection of compressed air and nitrogen. J. Chem. Thermodynamics **117**, 138–146 (2018)
5. Ahn, Y.H., Kang, H., Koh, D.Y., et al.: Production of natural gas hydrate by using air and carbon dioxide. Int. J. Chem. Mol. Eng. **9**(7), 808–812 (2015)
6. Holder, G.D., Corbin, G., Papadopoulos, K.D.: Thermodynamic and molecular properties of gas hydrates from mixtures containing methane, argon, and krypton. Ind. Eng. Chem. Fundam. **19**(3), 282–286 (1980)
7. Li, J.F., Ye, J.L., Qin, X.W., et al.: The first offshore natural gas hydrate production test in South China Sea. China Geol. **1**(1), 5–16 (2018)
8. Selim, M.S., Sloan, E.D.: Heat and mass transfer during the dissociation of hydrates in porous media. AIChE J. **35**(6), 1049–1052 (2010)
9. Mckoy, V., Sinanoğlu, O.: Theory of dissociation pressures of some gas hydrates. J. Chem. Phys. **38**(12), 2946–2956 (1963)
10. Koh, D.Y., Ahn, Y.H., Kang, H., et al.: One-dimensional productivity assessment for on-field methane hydrate production using CO_2/N_2 mixture gas. AIChE J. **61**(3), 1004–1014 (2015)
11. Hassanpouryouzband, A., Yang, J., Okwananke, A., et al.: An experimental investigation on the kinetics of integrated methane recovery and CO_2 sequestration by injection of flue gas into permafrost methane hydrate reservoirs. Sci. Rep. **9**(1), 1–9 (2019)
12. Seo, Y., Park, S., Kang, H., et al.: Isostructural and cage-specific replacement occurring in sII hydrate with external CO_2/N_2 gas and its implications for natural gas production and CO_2 storage. Appl. Energy **178**, 579–586 (2016)

Numerical Study of Reservoir Stability in Depressurized Exploitation of Natural Gas Hydrate Reservoir

Mingyu Xue, Yuanfang Cheng(✉), Zhiyuan Wang, Zhenhai Liu, Bo Sun, and Xiangfu Shan

School of Petroleum Engineering, China University of Petroleum (East China), Qingdao 266580, China
yfcheng@126.com

Abstract. Natural gas hydrate (NGH) is widely distributed in the South China Sea and has high exploitation potential. Aiming at the problems of reservoir compression and mudline settlement in the depressurized exploitation of NGH reservoirs. This paper proposed a 2D thermal-hydrologic-mechanical-chemical (THMC) coupling model by finite element simulation software. The effect of different production pressure difference on vertical displacement of reservoir top, reservoir bottom and mudline during production process was analyzed through numerical simulation. The results indicated: 1) The extraction of NGH will cause reservoir compression. In the early stage of production, both the sedimentation rate of reservoir top and uplift rate of reservoir bottom are large, and decreases gradually as production goes on; 2) With the increase of production pressure difference, the subsidence of reservoir top and uplift of reservoir bottom increase, and the difference of vertical displacement of mudline is not obvious. The simulation results show the effect of production pressure difference on the mechanical stability of NGH reservoir. In addition, the numerical simulation method of large-scale NGH reservoir is obtained, which provides a thought for large-scale numerical simulation of NGH reservoir under different exploitive modes.

Keywords: Natural gas hydrate · Reservoir settlement · Multi-field coupling · Numerical simulation

Symbol Description

h Hydrate
g Gas
w Water

1 Introduction

Natural gas hydrate (NGH), which is a kind of crystal compound formed by natural gas and water molecules under the environment of high pressure and low temperature [1–3].

B. Sun et al. (Eds.): DWOG-Hyd 2021, LNCE 246, pp. 188–195, 2022.
https://doi.org/10.1007/978-981-19-0960-3_19

NGH has more abundant reserves and higher energy efficiency than traditional fossil fuels, and has been suggested to be a potential renewable energy resource in the future [4, 5]. The principle of exploiting NGH is to destroy the phase equilibrium condition of hydrate in porous media. The decomposition of NGH will lead to reservoir depletion during the production process, and the reservoir will be deformed under the action of stress change [6–8]. The serious deformation will restrict the long-term safe and efficient exploitation of natural gas hydrate.

It is difficult to conduct experimental simulation on NGH exploitation. Numerical simulation is mostly used to solve this problem [9–11]. However, most of the current numerical simulation focuses on the prediction of production capacity and the optimization of various exploitive method and ignores the reservoir deformation. In this paper, a thermo-hydrologic-mechanical-chemical (THMC) coupling model is proposed to study the influence relationship between the change of production pressure difference and the deformation amount of NGH reservoir at the first 30 days of production.

2 Mathematical Model

2.1 Reaction Kinetics Equations of Hydrate

The kinetics of the hydrate dissociation reaction are described as follows [12]:

$$\frac{\mathrm{d}m_{\mathrm{g}}}{\mathrm{d}t} = K_{rd} M_g A_{dec} (f_e - f_g) \tag{1}$$

$$\frac{\mathrm{d}m_{\mathrm{h}}}{\mathrm{d}t} = \frac{\mathrm{d}m_g}{\mathrm{d}t} \frac{nM_w + M_g}{M_g} \tag{2}$$

$$\frac{\mathrm{d}m_{\mathrm{w}}}{\mathrm{d}t} = \frac{\mathrm{d}m_g}{\mathrm{d}t} \frac{nM_w}{M_g} \tag{3}$$

Where n is the coefficients of the decomposition reaction which based on the Kim-Bishnoi model of the hydrate kinetics; f_e is the gas fugacity in equilibrium with water and gas hydrate; f_g is the local gas fugacity.

The hydrate phase equilibrium is described by the following equation [13]:

$$P_e = \exp(e_1 + \frac{e_2}{T_e}) \tag{4}$$

The decomposition rate of the hydrate K_{rd} can be calculated by the following formula:

$$K_{rd} = K_{d0} \exp(\frac{\Delta E_d}{RT}) \tag{5}$$

The boundary area of hydrate and liquid phase is represented by A_{dec} as the following equation:

$$A_{dec} = \phi S_h A_{HS} \tag{6}$$

2.2 Energy Conservation Equations

The energy conservation equation is as follows [14–16]:

$$\begin{aligned}&\left[\begin{array}{l}(1-\varphi)\rho_r C_{pr}+\varphi S_h\rho_h C_{ph}\\ +\varphi S_g\rho_g C_{pg}+\varphi S_w\rho_w C_{pw}\end{array}\right]\frac{\mathrm{d}T}{\mathrm{d}t}\\ &+\nabla\cdot\left[\left(\rho_g\vec{u}_g C_{pg}+\rho_w\vec{u}_w C_{pw}\right)T\right]\\ &-\nabla\cdot(\lambda_c\nabla T)=-\frac{\mathrm{d}m_h}{\mathrm{d}t}\Delta H_D+Q_{in}\end{aligned}\tag{7}$$

The effective heat conduction λ_c is described based on the method of volume average:

$$\lambda_c=(1-\varphi)\lambda_r+\varphi(S_w\lambda_w+S_g\lambda_g+S_h\lambda_h)\tag{8}$$

The absorption heat of hydrate dissociation was expressed as follows [13]:

$$Q_h=\Delta H_{\mathrm{D}}\frac{\mathrm{d}m_h}{\mathrm{d}t}\tag{9}$$

$$\Delta H_{\mathrm{D}}=446.12\times10^3-132.638T\tag{10}$$

2.3 Mass Balance Equations

The mass balance equations for the gas, water, and hydrate are as follows [17]:

$$\begin{aligned}&\frac{n_{\mathrm{g}}}{B_{\mathrm{g}}}\frac{\mathrm{d}P_{\mathrm{g}}}{\mathrm{d}t}+\nabla\cdot\left[-\frac{K_{\mathrm{h}}k_{\mathrm{g}}}{\mu_{\mathrm{g}}}\left(\nabla P_{\mathrm{g}}-\rho_{\mathrm{g}}\mathbf{g}\right)\right]\\ &=\frac{1}{\rho_{\mathrm{g}}}\frac{\mathrm{d}m_{\mathrm{g}}}{\mathrm{d}t}-n\frac{\mathrm{d}S_{\mathrm{g}}}{\mathrm{d}t}-S_{\mathrm{g}}\frac{\mathrm{d}\varepsilon_{\mathrm{v}}}{\mathrm{d}t}+n_{\mathrm{g}}\beta_{\mathrm{g}}\frac{\mathrm{d}T}{\mathrm{d}t}\end{aligned}\tag{11}$$

$$\begin{aligned}&\frac{n_{\mathrm{w}}}{B_{\mathrm{w}}}\frac{\mathrm{d}P_{\mathrm{w}}}{\mathrm{d}t}+\nabla\cdot\left[-\frac{K_{\mathrm{h}}k_{\mathrm{w}}}{\mu_w}(\nabla P_{\mathrm{w}}-\rho_{\mathrm{w}}\mathbf{g})\right]\\ &=\frac{1}{\rho_{\mathrm{w}}}\frac{\mathrm{d}m_{\mathrm{w}}}{\mathrm{d}t}-n\frac{\mathrm{d}S_{\mathrm{w}}}{\mathrm{d}t}-S_{\mathrm{w}}\frac{\mathrm{d}\varepsilon_{\mathrm{v}}}{\mathrm{d}t}+n_{\mathrm{w}}\beta_{\mathrm{w}}\frac{\mathrm{d}T}{\mathrm{d}t}\end{aligned}\tag{12}$$

$$n\frac{\mathrm{d}S_{\mathrm{h}}}{\mathrm{d}t}=\frac{1}{\rho_{\mathrm{h}}}\frac{\mathrm{d}m_{\mathrm{h}}}{\mathrm{d}t}-S_{\mathrm{h}}\frac{\mathrm{d}\varepsilon_{\mathrm{v}}}{\mathrm{d}t}+n_{\mathrm{h}}\beta_{\mathrm{h}}\frac{\mathrm{d}T}{\mathrm{d}t}\tag{13}$$

The absolute permeability of porous media in the medium calculated by:

$$K_h=K_0(1-S_h)^n\tag{14}$$

Where K_0 is the original permeability of porous media without hydrate.

The relative permeability of the water and gas phase in the porous media are using the equations as follow [18]:

$$k_g=\left(\frac{\frac{S_g}{S_w+S_g}-S_{gr}}{1-S_{gr}-S_{wr}}\right)^{ng}\tag{15}$$

$$k_w=\left(\frac{\frac{S_w}{S_w+S_g}-S_{wr}}{1-S_{gr}-S_{wr}}\right)^{nw}\tag{16}$$

2.4 Solid Mechanics Equations

Based on the principle of effective stress, the static equilibrium equation of hydrate reservoir is established as follows:

$$\sigma_{ij,j} + f_i - (\alpha \delta_{ij} \overline{P})_{,j} = 0 \tag{17}$$

$$\overline{P} = P_g S_g + P_w S_w \tag{18}$$

Where, $\sigma_{ij,j}$ is total stress tensor; δ_{ij} is Kronecker function, $\delta_{ij} = 1,\ i = j$; $\delta_{ij} = 0, i \neq j$.

Geometric equation is calculated by [19]:

$$\varepsilon_{ij} = \frac{1}{2}\left(u_{i,j} + u_{j,i}\right) \tag{19}$$

The constitutive equation in the form of increment as follow:

$$d\sigma_{ij} = D_{ijkl} d\varepsilon_{kl} \tag{20}$$

3 Experimental Results and Discussion

3.1 Geometry Model Description

The model geometry in this study is depicted in Fig. 1. The axial symmetry thermal-hydrologic-mechanical-chemical (THMC) coupled model sized of 1000 × 500 m is established with product well located at the axis of symmetry besides it passes through the upper 20 m of the hydrate bearing layer. The upper boundary is the sea floor at a water depth of 1000 m. The model is divided into five layers, the fourth layer L4 representing hydrate bearing layer.

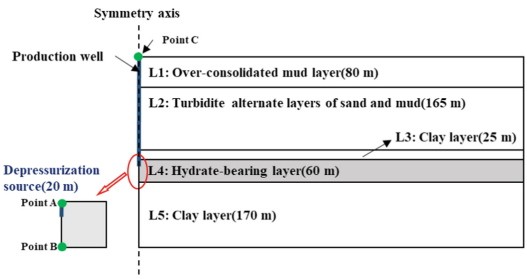

Fig. 1. Geometry of the geomechanical model

3.2 Initial Conditions

Pore pressure conditions are specified for the pressure distribution, with a pressure of 14.6 MPa at the bottom of the domain and 9.8 MPa at the top. The temperature at the top is 277 K and the geothermal gradient is 0.03 K/m. The vertical and horizontal stress gradients are computed assuming a uniform bulk density for the sediments of 1828.75 kg/m^3. The basic parameters of each layer for model are shown in Table.1, and the thermal of hydrate, methane, water and formation rock are listed in Table.2. For analysis the reservoir stability influenced by production pressure, set the production pressure to 4 MPa (Case1), 5 MPa (Case2), 6 MPa (Case3), respectively. Thus the production pressure difference at the bottom hole is 8 MPa, 7 MPa, 6 MPa.

Table 1. Basic parameters of each layer for model

Parameter	L1	L2	L3	L4	L5
Initial shear modulus(MPa)	78	197	236	250	254
Initial bulk modulus(MPa)	201.67	426.83	511.33	541.67	550.33
Poisson's ratio	0.3	0.3	0.3	0.3	0.3
Initial porosity	0.5	0.44	0.44	0.4	0.23
Intrinsic permeability(m^2)	2.4×10^{-16}	3.7×10^{-17}	2.8×10^{-17}	6.8×10^{-13}	3.2×10^{-17}

Table 2. Basic parameters of each layer for model

Parameter	Hydrate	Gas	Water	Rock
Density(kg/m^3)	920	0.85	1000	2200
Thermal conductivity(W/(m·K))	1600	4000	2093	1000
Specific heat(J/(kg·K))	0.393	0.044	0.6	1.5

4 Results and Discussion

The vertical displacement of three points were monitored during the simulation process. (Point A represents the top of the hydrate bearing layer, Point B represents the bottom of the layer, Point C is the mudline intersects the axis of symmetry, respectively. As shown in the Fig. 1.The relation curve between vertical displacement and time of above three points are shown in the Fig. 2.

It can be observed that both Point A and Point C settle downward, Point B shows uplift. This condition indicates that production of NGH via depressurization reduces

the strength of the hydrate bearing layer due to the loss of hydrate and increases in effective stress from the pore pressure. Those processes cause the compaction of the NGH reservoir. Under the combined influence of bottom uplift and top downward of reservoir, the mudline occurs a small displacement.

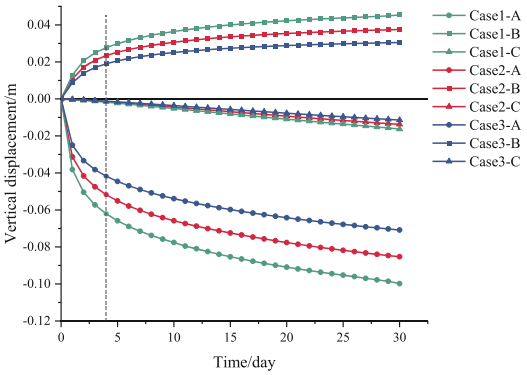

Fig. 2. Comparison of different cases of vertical displacement at Point A, Point B, Point C versus time

It can be observed that the vertical displacement of three points changed at a higher rate in the previous few days. This is mainly because the fast dissociation of hydrate at the beginning of production.

It can also be known from the figure that the vertical displacement of the three points increases with the increase of production pressure difference. This is because the increase of production pressure difference accelerates the decomposition rate of NGH, resulting in the increase of reservoir deformation.

5 Conclusions

1) NGH production will cause the top of the reservoir to sink, the bottom of the reservoir to uplift and there will be a small downward displacement on the mudline.
2) In the early stage of production, the deformation rate of the reservoir is lager, and gradually decreases as time goes on.
3) The increase of the production pressure difference will accelerate the decomposition of NGH and further lead to the increase of reservoir deformation.

Acknowledgement. This work is supported by the Shandong Provincial Natural Science Foundation of China (NO. ZR2019ZD14), the National Natural Science Foundation of China (NO. 51974353, NO. 51991362), the CNPC Major Science and Technology Project (NO. ZD2019–184-003).

References

1. Sloan, E.D., Jr., Koh, C.A.: Clathrate Hydrates of Natural Gases, 3rd edn. CRC Press, New York (2007)
2. Ruppel, C., Boswell, R., Jones, E.: Scientific results from Gulf of Mexico gas hydrates Joint Industry Project Leg 1 drilling: introduction and overview. Mar. Pet. Geol. **25**(9), 819–829 (2008)
3. Torres, M.E., Trehu, A.M., Cespedes, N., et al.: Methane hydrate formation in turbidite sediments of northern Cascadia, IODP Expedition 311. Earth Planet. Sci. Lett. **271**(1–4), 170–180 (2008)
4. Chen, L., Feng, Y., Okajima, J., et al.: Production behavior and numerical analysis for 2017 methane hydrate extraction test of Shenhu, South China Sea. J. Nat. Gas Sci. Eng. **53**, 55–66 (2018)
5. Chong, Z.R., Moh, J.W.R., Yin, Z., et al.: Effect of vertical wellbore incorporation on energy recovery from aqueous rich hydrate sediments. Appl. Energy **229**, 637–647 (2018)
6. Wan, Y., Wu, N., Hu, G., et al.: Reservoir stability in the process of natural gas hydrate production by depressurization in the Shenhu area of the South China Sea. Nat. Gas Ind. B **5**(6), 631–643 (2018)
7. Wang, Y., Feng, J.C., Li, X.S., et al.: Methane hydrate decomposition and sediment deformation in unconfined sediment with different types of concentrated hydrate accumulations by innovative experimental system. Appl. Energy **226**, 916–923 (2018)
8. Hyodo, M., Li, Y., Yoneda, J., et al.: Effects of dissociation on the shear strength and deformation behavior of methane hydrate-bearing sediments. Mar. Pet. Geol. **51**, 52–62 (2014)
9. Hou, J., Xia, Z., Li, S., et al.: Operation parameter optimization of a gas hydrate reservoir developed by cyclic hot water stimulation with a separated-zone horizontal well based on particle swarm algorithm. Energy **96**, 581–591 (2016)
10. Sakamoto, Y., Komai, T., Kawamura, T., et al.: Laboratory-scale experiment of methane hydrate dissociation by hot-water injection and numerical analysis for permeability estimation in reservoir: Part 1-Numerical study for estimation of permeability in methane hydrate reservoir. Int. J. Offshore Polar Eng., **17**(01) 2007
11. Wu, N., Li, Y., Wan, Y., et al.: Prospect of marine natural gas hydrate stimulation theory and technology system. Nat. Gas Ind. B **8**(2), 173–187 (2021)
12. Clarke, M.A., Bishnoi, P.R.: Measuring and modelling the rate of decomposition of gas hydrates formed from mixtures of methane and ethane. Chem. Eng. Sci. **56**(16), 4715–4724 (2001)
13. Selim, M.S., Sloan, E.D.: Heat and mass transfer during the dissociation of hydrates in porous media. AIChE J. **35**(6), 1049–1052 (1989)
14. Liu, L., Lu, X., Zhang, X.: Numerical analysis on evolution of natural gas hydrate decomposition region in hydrate-bearing sediment. Acta Petrolei Sinica **35**(5), 941–951 (2014)
15. Sun, X., Mohanty, K.K.: Kinetic simulation of methane hydrate formation and dissociation in porous media. Chem. Eng. Sci. **61**(11), 3476–3495 (2006)
16. Bai, Y., Li, Q., Yu, X., Feng, G.: Numerical study on dissociation of gas hydrate and its sensitivity to physical parameters. China Ocean Eng. **21**(4), 625–636 (2007)
17. Zhai, C., Sun, K., Xin, L., et al.: Numerical simulation research of deformation and fracture of the formation near the wellbore during the heat injection exploitation of natural gas hydrates. J. Geomech. **23**(6), 821–828 (2017)

18. Moridis, G J.: User's manual for the hydrate v1. 5 option of TOUGH+ v1. 5: A code for the simulation of system behavior in hydrate-bearing geologic media. Lawrence Berkeley National Lab (LBNL), Berkeley, CA (United States) (2014)
19. Freij-Ayoub, R., Tan, C., Clennell, B., et al.: A wellbore stability model for hydrate bearing sediments. J. Petrol. Sci. Eng. **57**(1–2), 209–220 (2007)

Numerical Simulation of the Mining of Heterogeneous Hydrate Reservoir Considering Formation Sand Production and Subsidence

Linchao Yang[1] and Liang Zhang[1,2(✉)]

[1] School of Petroleum Engineering, China University of Petroleum (East China), Qingdao 266580, China
zhlupc@upc.edu.cn

[2] Key Laboratory of Unconventional Oil and Gas Development, Ministry of Education, China University of Petroleum (East China), Qingdao 266580, China

Abstract. Based on the multi-field coupling mathematical model of hydrate decomposition, this paper describes the multiphase flow production law and the interphase transformation process of the heterogeneous hydrate reservoirs through numerical simulation. The simulation results show that the hydrate tends to decompose outward along with the heterogeneous high-permeability reservoirs, and it is easy to form "earthworm-like caves". Part of the silt sand will deposit around the well and block the pore throat. Under the effect of stress, the formation subsidence will compress the pores and reduce the gas production by 20.47%. At the same time, the compression and broken of the reservoir rocks also increased the sand production by 21.78%. For high-saturation reservoirs, proper reservoir modification can be considered to release early productivity. For low-saturation reservoirs, attention should be paid to the excessive sand production rate in the early stage. The lower critical velocity and larger started frequency factor can promote the migration of silt and increase sand production. A large deposition frequency factor represents a high precision of sand control. The formation around the wellbore is blocked by a large amount of silt sand, and even more than 80% of the pore space is filled, which has a serious impact on the subsequent production of hydrate reservoirs.

Keywords: NGH · Heterogeneous reservoir · Formation sand production · Formation subsidence

1 Introduction

The natural gas hydrates in the Shenhu area of the South China Sea are mainly found in unconsolidated silt sediments on the shallow seafloor. The content of fine silt and clay is as high as 70–80%, which is a typical argillaceous siltstone hydrate reservoir [1]. This type of hydrate reservoir has fine sediment particle size, high clay content, low permeability and poor cementation. Due to the above problems, the productivity cannot

B. Sun et al. (Eds.): DWOG-Hyd 2021, LNCE 246, pp. 196–209, 2022.
https://doi.org/10.1007/978-981-19-0960-3_20

be released, and the phenomenon of silt sand migration is prominent [2]. Therefore, the economic value of hydrate exploitation in the South China Sea is greatly reduced.

According to the extensive investigations, it has been found that the hydrate decomposition, fluid migration, and the crushed reservoir rocks are the main controlling factors of sand production [3, 4]. In addition, the hydrate saturation, porosity, permeability, and silt sand composition also have an important impact on sand production and formation subsidence [5]. The detachment and migration of the particles are mainly concentrated near the wellbore in the early stage, and the formation subsidence near the wellhead is the largest [6]. In the long-term mining process, the decompression rate needs to be controlled to balance the relationship between productivity, reservoir stability and sand production [7].

In summary, there is no relevant research on the mechanism and laws of formation sand production, formation subsidence and pore throat blockage caused by hydrate decomposition in heterogeneous reservoirs, and there is no clear conclusion on the relationship between formation sand production and the change of productivity. Therefore, this paper integrates the multi-field coupling mathematical model of hydrate exploitation and establishes a numerical simulation model of multiphase flow of hydrate decomposition considering the formation sand production and subsidence. And the multiphase flow mechanism and gas production laws of heterogeneous hydrate reservoirs are revealed.

2 Mathematical Model

2.1 Reaction Kinetic Model of Hydrate Formation and Decomposition

The rate of hydrate formation and decomposition is proportional to the driving force (the difference between the phase equilibrium pressure of hydrate and the pressure of gas phase). Hydrate formation and decomposition can be expressed in Eqs. (1) [8] and (2) [9].

$$n_f = k_f^0 exp\left(-\frac{E}{RT}\right)\left(\phi_f^2 A_{\mathrm{HS}} S_h S_w + \phi_f A_{\mathrm{HS}} S_w\right)\left[p_g - p_e\right] \tag{1}$$

$$n_d = k_d^0 exp\left(-\frac{E}{RT}\right)\phi_f^2 A_{\mathrm{HS}} S_h S_w\left[p_e - p_g\right] \tag{2}$$

where n_f and n_d are the hydrate formation and decomposition rates, mol/m^3; ${k_f}^0$ and ${k_d}^0$ are the reaction frequency factors of hydrate formation and decomposition, mol/(s·MPa·m^2); E is the reaction activation energy, J/mol; A_{HS} is specific surface area of hydrate particles, m^2/m^3; R is the ideal gas constant, J/(mol·K); p_e is the phase equilibrium pressure of hydrate, MPa; φ_f is the fluid porosity, fraction.

2.2 The Model of the Particle Detachment-Migration-Deposition

The critical velocity of water (V_{cfs}) is introduced for the particles. Only when the water flow velocity is larger than the critical velocity, the particles can be detached (or started) and converted from a solid phase to an aqueous phase [10].

Particle detachment: SFP (solid) → WFP (aqueous)

$$n_{fs} = n_{rfs}\exp\left(-\frac{E_{fs}}{RT}\right)\left(\frac{V_w - V_{cfs}}{V_{ref}}\right)\varphi C_{sfp} \cdot \varphi_f \rho_w S_w X_{wfp} \tag{3}$$

Particle deposition: WFP (aqueous) → SFP (solid)

$$n_{fd} = n_{rfd}\exp\left(-\frac{E_{fd}}{RT}\right)\varphi C_{sfp} \cdot \varphi_f \rho_w S_w X_{wfp} \tag{4}$$

where n_{fs} is the reaction rate of particle detachment, mol/min/cm^3; n_{fd} is the reaction rate of particle deposition, mol/min/cm^3; n_{rfs} is the reaction frequency factor of particle detachment, cm^3/min/mol; n_{rfd} is the reaction frequency factor of particle deposition, cm^3/min/mol; E_{fs} is the reaction activation energy of particle detachment, J/mol; E_{fd} is the reaction activation energy of particle deposition, J/mol; V_{cfs} is the critical water flow velocity to start particles, cm/min; V_w is the water flow velocity, cm/min; V_{ref} is the reference flow velocity, cm/min; T is the temperature, K; ρ_w is the molar density of water, mol/cm^3; S_w is the water saturation, fraction; X_{wfp} is the mole fractions of particles in aqueous phase; C_{sfp} is the mole concentrations of particles in the solid phase, mol/cm^3.

2.3 The Model of Stress Change and Formation Deformation

In the process of hydrate decomposition, formation deformation is mainly related to the conversion relationship between stress (σ), strain (ε) and displacement (u). If the change of momentum is neglected, the relationship between the above three parameters is transformed as follows [11]:

$$\Delta \cdot \sigma - \rho_r B = 0 \tag{5}$$

$$\sigma = \sigma' + \alpha p I \tag{6}$$

$$\sigma' = C : \varepsilon - \eta \Delta T I \tag{7}$$

$$\eta = \begin{cases} \frac{E\beta_r}{(1-2v)}, \text{ strain} \\ \frac{E\beta_r}{(1-v)}, \text{ stress} \end{cases} \tag{8}$$

$$\varepsilon = \frac{1}{2}[\nabla u + (\nabla u)^T] \tag{9}$$

where σ is the total stress tensor, Pa; B is the body force/unit mass of solid grain, m/s^2; σ' is the effective stress tensor, Pa; ρ_r is the solid grain density, kg/m^3; α is the Biot's number; p is the pressure, Pa; I is the identity matrix; C is the tangential stiffness tensor, Pa; ε is the volumetric strain of bulk volume; η is the thermoelastic coefficient, Pa/^{o}C; ΔT is the change in temperature, ^{o}C; E is Young's modulus, Pa; v is the Poisson's ratio; β_r is the linear thermal coefficient of bulk volume, 1/^{o}C; u is the displacement vector, m.

2.4 The Model of Formation Porosity-Permeability

The model comprehensively considers the reservoir hydrate saturation, silt sand content, formation deformation, then the change of reservoir fluid porosity and permeability during the exploitation of hydrate reservoir can be described as follows [12]:

$$\phi_f = \phi - \phi_h + \phi_{\mathrm{fs}} - \frac{\sigma}{1-\phi_d} - \phi \cdot \varepsilon_v \tag{10}$$

$$K = K_0 \left(\frac{\phi_f}{\phi_{\mathrm{f0}}}\right)^N \left(\frac{1-\phi_{f0}}{1-\phi_{\mathrm{f}}}\right)^2 \tag{11}$$

where Φ_h is the volume of hydrate per unit pore volume, m^3/m^3; Φ_{fs} is the volume of liquefied sand per unit pore volume, m^3/m^3; Φ_d is the plug porosity, the value is 0; ε_v is the volume strain; K_0 is the initial permeability of the reservoir, 10^{-3} μm^2; N is the power law coefficient, the value is 5.

3 Numerical Simulation Model

3.1 Model Parameters

The Shenhu sea area is located in the middle section of the land slope outside the Pearl River Estuary in China. The reservoir sediments are in a fluid plastic state, which is a typical argillaceous siltstone reservoir. Based on relevant geological data, the main parameters of the model are shown in Table 1.

Table 1. Main parameters of the model

Parameters	Value
Water depth, m	1200
Mudline temperature, °C	3.62
Temperature gradient, °C/100 m	4.63
Pressure gradient, MPa/100 m	11.99
Reservoir thickness, m	60
Average matrix porosity, %	30 (0.06–0.55)
Average permeability, 10^{-3} μm^2	0.5 (0.1–15.4)
Hydrate saturation, %	30
Poisson's ratio, fraction	0.3
Young modulus, kPa	$10^6 \rightarrow 10^5$

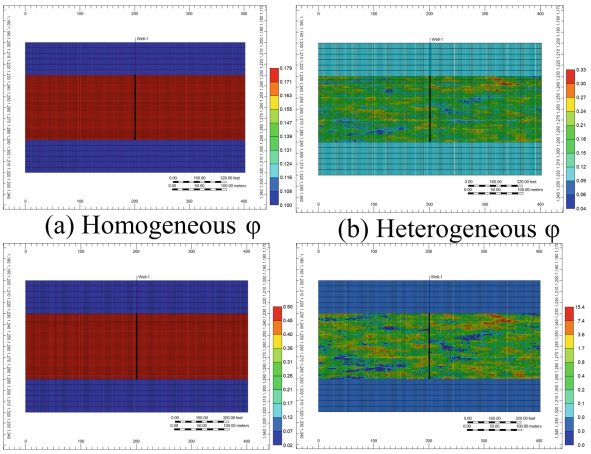

Fig. 1. Porosity and permeability distribution

3.2 Heterogeneity Setting

The vertical 2D geological model is established according to the model parameters. To make the porosity and permeability distribution of the formation conform to the sedimentary rhythm, the fine reservoir heterogeneity field is shown in Fig. 1.

3.3 Simulation Scheme

First, the fluid-solid production law of the basic model and the change of reservoir properties are simulated and analyzed. Secondly, the sensitivity schemes of the heterogeneous model are shown in Table 2.

Table 2. Simulation scheme

Sensitivity parameters	Value
σ	Consider*, no consider
S_H, %	10, 30*, 50
V_{cfs}, *m/d*	0.009*, 0.05, 0.5
n_{rfs}, $s^{-1}mol^{-1}$	0.001, 0.01, 0.1*, 1
n_{rfd}, $s^{-1}mol^{-1}$	0.0002, 0.002*, 0.01, 0.02

4 Simulation Result Analysis

4.1 Basic Law Analysis

4.1.1 Changes of Reservoir Properties

Figure 2 is the comparison of the field diagrams of the homogeneous/heterogeneous model after 5 years. It can be seen from the figure that the homogeneous hydrate is evenly decomposed outward, while the heterogeneous hydrate is preferentially decomposed along the high permeability zone. In the heterogeneous model, and the decomposition front of hydrate can reach about 130 m. The permeability of the layers with particles migration increases obviously, forming obvious "earthworm-like holes". [13].

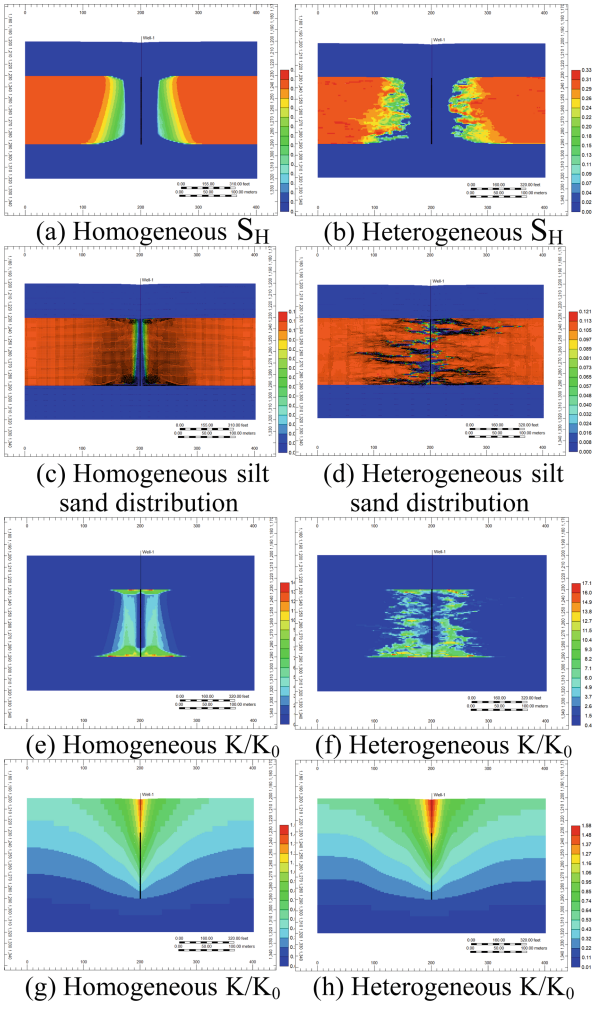

Fig. 2. Comparison of the basic field diagrams

However, some silt sand particles can deposit and block the pore throat around the wellbore, reducing the permeability. Because the near-well stress is the most concentrated, the formation subsidence around the wellhead is the most obvious, and the maximum subsidence of the heterogeneous model is 1.58 m.

4.1.2 Fluid-Solid Production Law

Figure 3 shows the fluid-solid production law of homogeneous/heterogeneous models. It can be seen from the figure that the gas, water and sand production of the heterogeneous model is higher than that of the homogeneous model. The gas production increases by 38.89%, the water production increases by 26.78%, and the sand production increases by 34.21%. For the heterogeneous reservoir, the initial water production rate reaches the maximum of 80.56 m^3/d, the sand production rate is also the maximum of 3.9 m^3/d, and the sand production is mainly concentrated in the first 60 days. Affected by sand production, the pore space is released, and the initial gas production rate can reach 1957.46 m^3/d. When the temperature of the reservoir decreases and the silt sand blocks the near-well pore throat, the production rates of gas, water and sand all drop rapidly. In the end, the cumulative sand production was 733.7 m^3, the cumulative gas production was 67.53 × 10^4 m^3, and the cumulative water production was 7194.41 m^3.

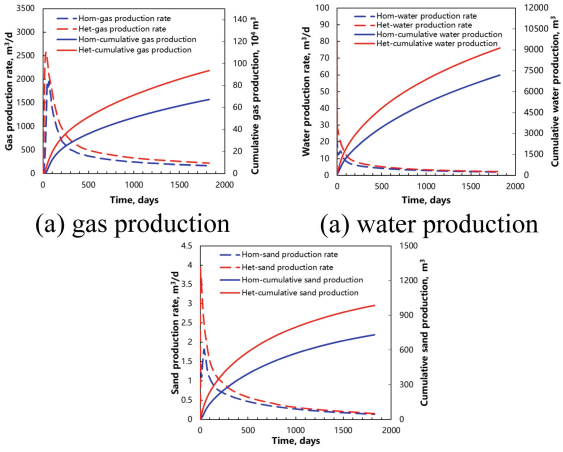

(a) gas production (a) water production

(c) sand production

Fig. 3. Fluid-solid production law

4.2 Sensitivity Factor Analysis

4.2.1 Crustal Stress

The influence of crustal stress on characteristics of fluid-solid production is shown in Fig. 4. The concentrated stress will reduce gas production from 117.93 × 10^4 m^3 to 93.79 × 10^4 m^3. According to Fig. 4(d), concentrated stress compresses formation pores,

limiting hydrate decomposition and reducing gas production. However, when the pore space of the formation is compressed, the water production increases by 12.93%, and the higher water velocity will drive more silt sand detaching. Meanwhile, the formation rock is crushed under the action of concentrated stress, and the sand production increases by 21.78%.

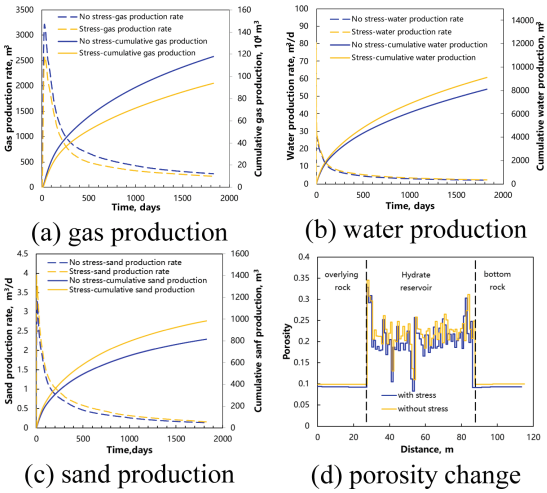

Fig. 4. Fluid-solid production law and porosity change

4.2.2 Hydrate Saturation

Hydrate saturation is set to 10%, 30% and 50%, respectively. The production characteristics of fluid-solid under different saturation are shown in Fig. 5. The reservoir with low hydrate saturation has higher initial permeability and higher water production. However, the variation of gas production is complicated. When the hydrate saturation is 50%, the porosity and permeability of the reservoir are extremely small, and the initial production release is severely limited. With the pressure slowly decreasing, the gas production rate of the reservoir with high hydrate saturation increases to the maximum. Finally, the decomposition front of hydrate with saturation of 50% is within 30m (Fig. 6(b)), and the hydrate with saturation of 10% is completely decomposed. It can be predicted that the reservoir with higher hydrate saturation will produce more gas with a longer production cycle. In terms of sand production, the sand production rate of the reservoir with low hydrate saturation is large in the early stage. In summary, the reservoir with low hydrate saturation should pay attention to the large amount of sand production in the early stage, and the reservoir with high hydrate saturation can be considered for reservoir reformation in the field, which is conducive to the rapid release of initial productivity. Figure 5(d) shows the formation subsidence with different hydrate saturation. When the hydrate saturation is high, the stress concentration effect is significant and the formation subsidence is more obvious (the maximum subsidence is 1.74 m.).

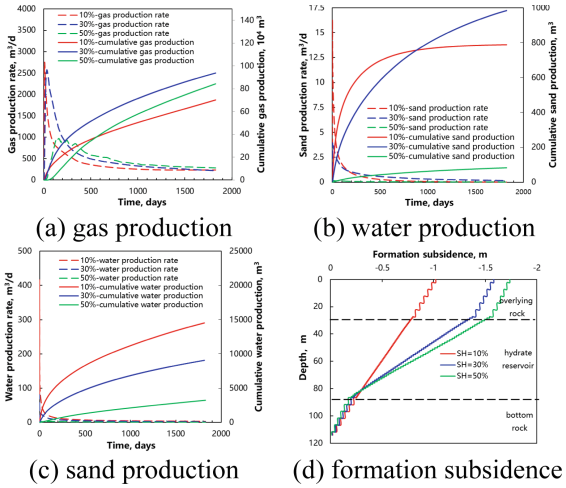

(a) gas production (b) water production

(c) sand production (d) formation subsidence

Fig. 5. Production law and formation subsidence

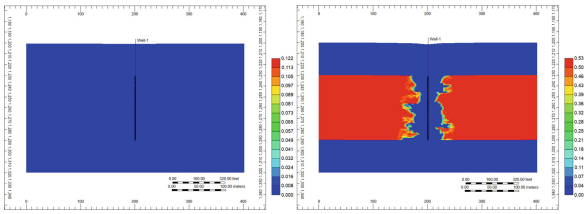

(a) S_H=10% (b) S_H=50%

Fig. 6. Distribution of hydrate saturation

4.2.3 Critical Velocity of Water

Only when the water flow velocity is larger than the critical velocity, the particles can be detached (or started) and converted from a solid phase to an aqueous phase. It can be seen from the Fig. 7 that the smaller critical velocity leads to the larger sand production. When the critical flow velocity increases to a certain value, the formation of sand disappears. The migration of sand particles also releases the pore space, and the productivity is also increased. However, the risk of sand burial caused by excessive sand production should be considered. At the same time, the low critical velocity causes a large amount of migrated sand to deposit near the wellbore, and the permeability of the reservoir decreases. This is also the reason for the low gas production rate at the later with low critical velocity. In addition, the deposited particles in the pores play the role of the rock skeleton, so the formation subsidence is also the minimum (1.58 m). Figure 8 shows the influence of the critical velocity on the movable silt sand distribution in the formation. When the critical velocity increases to 0.5 m/d, the “earthworm-like caves” have completely disappeared.

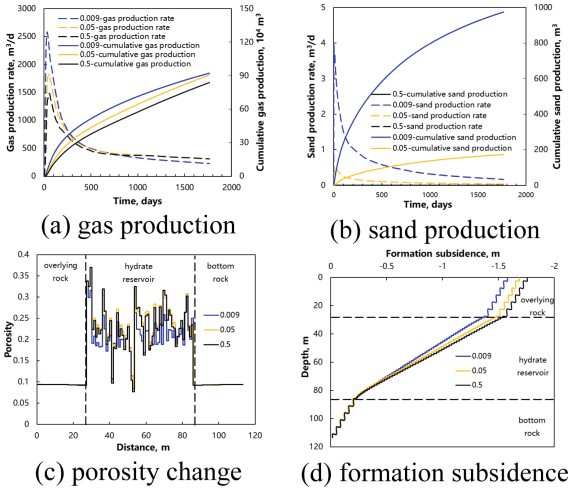

Fig. 7. Production law and formation subsidence

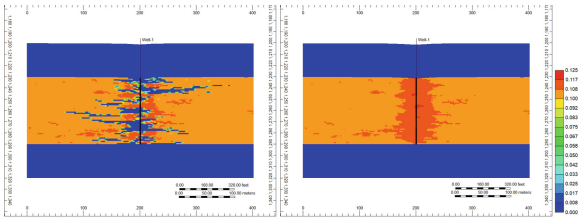

Fig. 8. Distribution of pore movable silt sand content

4.2.4 Started Frequency Factor

The started frequency factor reflects the detachment speed of silt when the water velocity reaches the critical velocity. According to the Fig. 9, the large started frequency factor leads to a large amount of silt sand production, with a range of 85.15–1101.31 m^3. In the early and middle stages, the large started frequency factor can promote the detachment and migration of silt sand, the pore space is released, and the hydrate productivity is increased. In the later stage, a large amount of silt sand is likely to cause blockage of the pores around the wellbore and reduce gas production. At the same time, a large amount of blocked silt sand plays a role as the rock skeleton, and the formation subsidence is also smaller. Figure 10 shows the influence of started frequency factor on the distribution of movable silt sand. The larger frequency factor makes the “earthworm-like cave” extend into the deep formation.

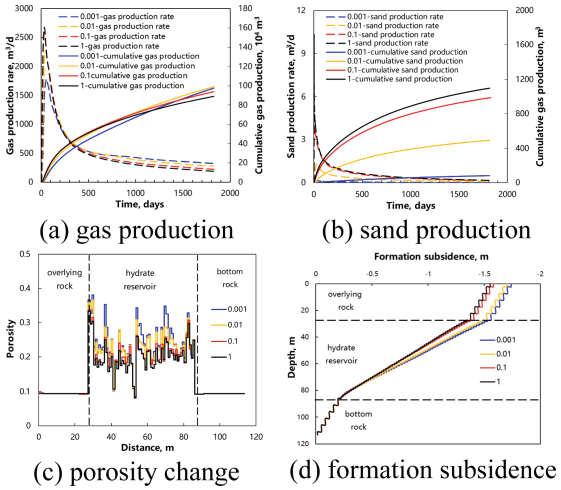

Fig. 9. Production law and formation subsidence

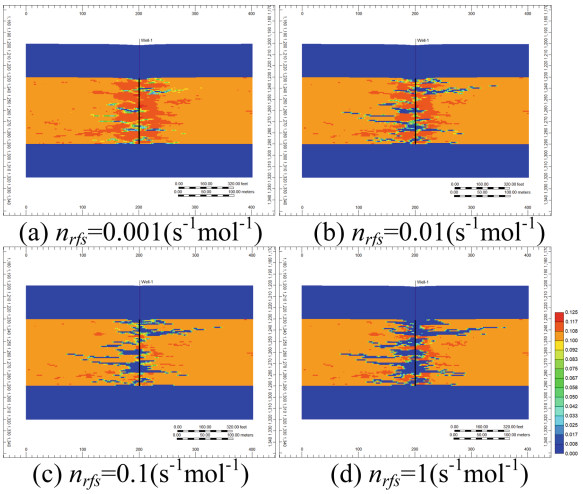

Fig. 10. Distribution of pore movable silt sand content

4.2.5 Deposition Frequency Factor

The deposition frequency factor means the deposition rate of migrating silt sand particles. Most of the silt sand will come out with water in a small deposition frequency factor, and cannot block the pore throat, so the gas and water production are higher. If the deposition factor reaches 0.01 $s^{-1}mol^{-1}$, the near-wellbore area is blocked by deposited silt sand, and 88% of the pore volume is filled in the worst case (Fig. 13). The blockage seriously limits the normal exploitation of hydrate reservoirs, and the complete decomposition area of hydrate is only concentrated within 10 m around the wellbore (Fig. 12(b)). On the other hand, the silt sand blocked in the pore plays a role of rock skeleton, and the

formation subsidence decreases and even appears uplift. In summary, the value of the deposition frequency factor corresponds to the sand control precision of the screen tube. Although the larger sand control precision can prevent the risk of sand burial effectively, it also increases the risk of pore throats blockage, and forced depressurization mining may cause geological problems (Fig. 11).

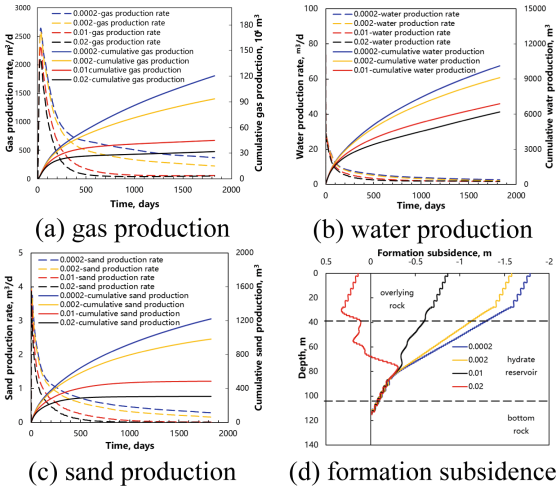

Fig. 11. Production law and formation subsidence

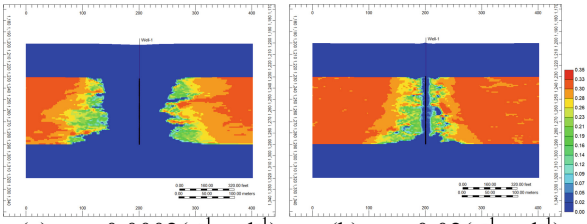

Fig. 12. Distribution of hydrate saturation

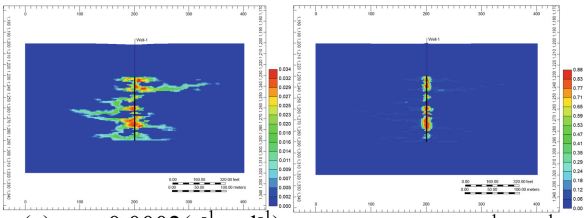

(a) n_{rfd}=0.0002($s^{-1}mol^{-1}$) (b) n_{rfd}=0.02($s^{-1}mol^{-1}$)

Fig. 13. Distribution of deposited silt sand content

5 Conclusions

In this paper, the numerical simulation is carried out to reveal the multi-phase flow mechanism and fluid-solid production law of heterogeneous hydrate reservoir, and the conclusions are as follows:

(1) The hydrate preferentially decomposes outwards along with the high permeability formation in heterogeneous reservoirs, and it is easy to form "earthworm-like holes". However, some silt sand will deposit near the well and block the pore throat, reducing the gas production rate.
(2) Considering the crustal stress, the formation subsidence near the wellbore is the largest, reaching 1.58 m. The formation subsidence also compresses the pores, damaging the permeability and reducing the gas production by 20.47%. Excessive hydrate saturation will affect the release of early productivity, and lower hydrate saturation should pay attention to the vast sand production in the early stage. Lower critical velocity and higher started frequency factor can promote the detachment and migration of sand, which is conducive to the release of hydrate productivity. However, excessive sand production also increases the risk of pore throat blockage and wellbore sand burial. A large deposition frequency factor represents a high sand control precision. Although the risk of sand burial can be effectively avoided, the productivity is also severely limited, so appropriate sand control precision should be selected in the field.

Acknowledgement. This research is supported by the National Natural Science Foundation of China (No.51974347) and the General Project of Shandong Natural Science Foundation (ZR2020ME090). We also appreciate the reviewers and editors for their constructive comments to make the paper high quality.

Symbol Description

φ Porosity.
S_H Hydrate saturation.
K Current permeability.
K_0 Initial permeability.

References

1. Dallimore, S.R., Collett, T.S.: Intrapermafrost gas hydrates from a deep core hole in the Mackenzie Delta, Northwest Territories, Canada. Geology **23**(6), 527–530 (1995)
2. Collett, T., Bahk, J.J., Baker, R., et al.: Methane hydrates in nature-current knowledge and challenges. J. Chem. Eng. Data **60**(2), 319–329 (2014)
3. Oyama, H., Nagao, J., Suzuki, K., et al.: Experimental analysis of sand production from methane hydrate-bearing sediments applying depressurization method. J. MMIJ **126**(8/9), 497–502 (2010)
4. Ghassemi, A., Pak, A.: Numerical simulation of sand production experiment using a coupled lattice Boltzmann-discrete element method. J. Petrol. Sci. Eng. **135**, 218–231 (2015)
5. Li, Z.H.: Experimental Study on Sediment Deformation during Natural Gas Hydrate Dissociation by Depressurization. Tianjin University, Tianjin (2018)
6. Rutqvist, J., Moridis, G. J.: Coupled hydrologic, thermal and geomechanical analysis of well bore stability in hydrate-bearing sediments. In: Offshore Technology Conference, Houston, Texas, USA (2008)
7. Ning, F.L., Sun, J., Liu, Z., et al.: Prediction of sand production in gas recovery from the Shenhu hydrate reservoir by depressurization. In: Proceedings of the 9th International Conference on Gas Hydrate, Denver, Colorado, USA, ICGH9 (2017)
8. Vysniauskas, A., Bishnoi, P.R.: A kinetic study of methane hydrate formation. Chem. Eng. Sci. **38**(7), 1061–1072 (1983)
9. Kim, H.C., Bishnoi, P.R., Heidemann, R.A., et al.: Kinetics of methane hydrate decomposition. Chem. Eng. Sci. **42**(7), 1645–1653 (1987)
10. STARS manual. Computer Modelling Group (2012)
11. Li, S.X., Ding, S.Y., Wu, D.D., et al.: Analysis of stratum subsidence induced by depressurization at an offshore hydrate-bearing sediment. Energy Fuels **35**(2), 1381–1388 (2021)
12. Tien, C., Payatakes, A.C.: Advances in deep bed filtration. AIChE J. **25**(5), 737–759 (1979)
13. Dong, C.Y., Yan, Q.L., Li, Y.L., et al.: Numerical simulation of sand production based on a grain scale microcosmic model for natural gas hydrate reservoir. J. China Univ. Petrol. **43**(6), 77–87 (2019)

Study on Seepage and Mass Transfer Characteristics During CO_2 Storage in Saline Aquifer

Weixin Zhang, Bohao Wu, Pengfei Lv, Shaohua Li, and Lanlan Jiang(✉)

Key Laboratory of Ocean Energy Utilization and Energy Conservation of Ministry of Education, Dalian University of Technology, Dalian 116024, China
lanlan@dlut.edu.cn

Abstract. CO_2 storage in saline aquifer is considered to be the most potential and most promising method to alleviate greenhouse effect and neutralize CO_2. Rock wettability and heterogeneity study is crucial for CO_2 storage in saline aquifer due to the complex geological structure of submarine surroundings. In this study, CO_2 dynamic displacement process and imbibition process in sand cores were captured by CT scanning technology in different conditions (40 °C, 8 Mpa and 25 °C, 0.1 Mpa). Experiment result shows that stronger wettability is conducive to the occurrence of CO_2 snap off and increases the safety of CO_2 capillary capture and storage, while imbibition of weaker wettability porous media is more stable but CO_2 is difficult to capture. Moreover, CO_2-salt water interface was divided into three categories (interface aggregation nodes, interface clusters and interface monomers) and interface evolution low was quantified by the liner relationship of relative interface area (*RIA*) and salt water saturation (*Sw*). Upward imbibition is beneficial for CO_2 storage according to the *RIA* of the upward imbibition process is about 1.3 times that of downward when salt water saturation keeps the same. Finally, the heterogeneity of the mixed sand significantly increases the contact area of the two phases than uniform sand for the same Reynolds number. The microscopic transport mechanism and morphological distribution characteristics of CO_2-salt water in the pores in this paper has some implication for practical CO_2 long-term and safe storage in saline aquifer.

Keywords: CO_2 storage · CT · Wettability · Interface between two phases

Symbol Description

Sw	salt water saturation
RIA	relative interface area
PV	pore volume
a_i	specific interface area

B. Sun et al. (Eds.): DWOG-Hyd 2021, LNCE 246, pp. 210–220, 2022.
https://doi.org/10.1007/978-981-19-0960-3_21

1 Introduction

CO_2 reduction and CO_2 neutralization have become the consensus of more and more people. CO_2 storage in saline aquifer has enormous potential to significantly slow the pace of global climate change by bury massive CO_2 in deep saline aquifers.

The storage efficiency of storage CO_2 largely depends on the properties of the target reservoir rock [1–3]. Rock wettability and heterogeneity study is crucial for CO_2 storage in saline aquifer due to the diverse composition of rock and the complex geological structure of submarine surroundings. As a non-invasive technology, X-ray CT imaging can generate three-dimensional pore-scale images with micro-level spatial resolution, which is critical for visualizing mass transfer process. Gao [4] studied the characteristics of Estaillades carbonate rock, which is different from previous sandstone studies and found that it has complex heterogeneity. Brusseau [5] studied the interface distribution in different types of porous media and found that the specific interface area and the maximum specific interface area are inversely proportional to the median particle size of the porous media.

Moreover, the CO_2-salt water interface is the main area of mass transfer between each phase during the storage process. To better understand the CO_2 dissolution process and CO_2-salt water mass transfer in the pores, it is necessary to study the evolution law of the CO_2-salt water interface. For the interface between phases in two-dimensional porous media, the interface area between phases can be directly measured by the displacement experiment in the micro-etched glass plate of the porous media [6, 7]. Jettestuen et al. simulated the process of imbibition in a three-dimensional sandstone, and observed the retraction of the interphase interface into the pores, the expansion of the wetting phase film and the snap-off effect [8]. The interface plays a vital role in the mass transfer process of each phase, but this time-varying process lacks sufficient quantitative analysis [9].

We have established a set of experimental methods based on the microfocus X-ray CT system to measure the mass transfer of CO_2 under complex conditions of multi-components. Using CT continuous scanning to obtain the microscopic pore structure of the sand-filled sample and the dynamic evolution process of the CO_2-salt-water interface. Then with the help of image processing technology, we explored the impact of the wettability and heterogeneity of different reservoir components on CO_2 storage. In addition, we studied the changes of the CO_2-brine phase interface under different salt water injection flow rates, that realizing the dynamic visualization of the CO_2-salt water interface. The microscopic transport mechanism and morphological distribution characteristics of CO2-salt water in this paper has some implication for practical CO_2 long-term and safe storage in saline aquifer [10, 11].

2 Experimental Method

2.1 Materials and Setup

Figure 1 is a diagram of the microscopic visualization test system of CO_2-salt water mass transfer characteristics. The experimental system is mainly composed of three parts: micro-focus X-ray CT visual imager (resolution is 4 μm), injection and recovery system, and temperature and pressure control system. In the reactor used in this experiment, the

part of the tube wall through which X-rays penetrate is made of polyether ether ketone (PEEK), which ensures the quality of CT imaging while minimizing the attenuation of X-rays [12]. ISCO piston pumps are used in the experiment as the gas injection, water injection and pressure control system. A circulating temperature controller is used to control the temperature of the injected fluid to simulate the environment of the porous medium of the saline aquifer reservoir. Finally, we use high-precision pressure sensors and thermocouples to monitor and automatically collect the temperature and pressure data of the system.

In the filled sandstone core, artificial glass sand with different particle sizes (produced by Japan's AS-ONE company) and natural quartz sand, dolomite and feldspar sand (purchased from Hebei sand quarry) were used. The shape of glass sand is a relatively regular sphere, while the shapes of quartz sand, dolomite and feldspar sand are irregular. The mineral composition of each sand is single, and its specific particle size distribution is shown in Table 1. During the process of filling the core, a combination of multiple filling layer by layer and several shaking by percussing is used, which can not only avoid delamination during the filling process, but also ensure that the sand core is compacted well. Then graphite electric heating tape is used to heat it up to the experimental temperature. For the experiment, the gas used is high-purity CO_2 with a purity of 99.9% and the salt water is made up of deionized water and 3% sodium chloride (Analytical Pure AR, Tianjin Komiou Chemical Reagent Co., Ltd.) to simulate the salinity of saline water in underground reservoirs. In addition, potassium iodide with a mass fraction of 6% is added as a contrast agent to enhance the contrast between gas and salt water in CT images.

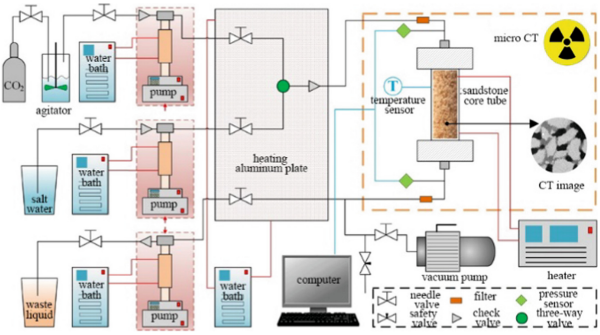

Fig. 1. Schematic diagram of experimental device

2.2 Experimental Approach

(1) Preparation of porous medium and two-phase fluid: placing the porous medium into the reactor before the experiment, and then connecting the experimental pipeline according to Fig. 1. High-pressure gas is used to clean the pipeline and leak detection to ensure that there is no liquid residue in the pipeline. Before each experiment starts, vacuuming for 20 min to remove the gas. A sodium chloride solution with a mass

Table 1. Types and detailed parameters of sand used in the experiment.

Sand type	Particle size/mm	Average particle size/mm
Glass sand BZ06	0.500–0.710	0.6
Glass sand BZ04	0.350–0.500	0.4
Glass sand BZ02	0.177–0.250	0.2
Rough quartz sand	0.355–0.425	0.4
Fine quartz sand	0.180–0.212	0.2
Rough feldspar	0.355–0.425	0.4
Fine feldspar	0.180–0.212	0.2
Rough dolomite	0.355–0.425	0.4
Fine dolomite	0.180–0.212	0.2

Table 2. CO_2 saturation of each layer after the displacement process of layered sand filling core.

Rock stratum	SCO_2 (40 °C, 8 MPa)		SCO_2(25 °C, 101 kPa)	
	0.1 mL/min	0.3 mL/min	0.6 mL/min	0.3 mL/min
BZ06	0.80	0.81	0.80	0.78
BZ02	0.18	0.10	0.06	0.07
Quartz	0.14	0.07	0.06	0.12
Dolomite	0.74	0.55	0.24	0.29

fraction of 3% is prepared, and potassium iodide with a mass fraction of 6% is added as a contrast agent.

(2) Displacement process: after vacuuming, the sand-filled core is injected with salt water through the liquid injection pump. The pressure and temperature are controlled to slowly rise to the requirements of the specific experimental conditions, and the core is left alone for 12 h to keep the core fully saturated with salt water. Then CO_2 was injected into the sand-filled core at a rate of 0.1 mL/min. The injecting is not stopped until CT image acquisition process starts, and CO_2 is continued injected after the image acquisition is completed.

(3) Imbibition process: after the displacement process, salt water saturated with CO_2 is injected into the sand-filled core at an injection rate of 0.1 mL/min, and CT images of the inhalation process are collected in the same way as the displacement process until the inhalation the process is over.

(4) Grayscale image stack acquisition: before injecting salt water, CT continuous scanning is used to obtain the image slice stack of the porous medium saturated with CO_2; then salt water is injected at a constant flow rate, and CT scanning is used to obtain salty water at different pore volume (PV) moments. Change the salt water injection rate, change the porous medium, etc., and repeat the above experiment.

(5) Perform voxel imaging, segmentation and extraction on the obtained gray-scale image stack: According to the image slice stack obtained in step 4, threshold segmentation is performed using the density difference of each phase to obtain the distribution of the phase fluid; quantify the components characterize based on the gray-scale data.

2.3 CT Image Analysis

The processing of the original image mainly includes noise reduction, segmentation and extraction of each phase, and three-dimensional visualization analysis. In order to obtain a clear internal image of the pore, this study used ImageJ and 3D visualization Avizo software to preprocess the original CT image slice stack. Use ImageJ software to crop the image first, leaving the porous medium area only, and then adjust and increase the contrast of the image. The gas phase density is small, so it appears black, and the sandstone density is the largest, and it appears bright white on the grayscale image. The salt water solution with KI added as a contrast agent is somewhere in between, showing off-white.

The experiment uses a calculation method based on CT image parameters. The porosity φ of the filled sandstone core is calculated by the formula (1), where CT_{brine}^{sat} and CT_{CO2}^{sat} are the images of the sand core saturated with salt water and the sand core saturated with CO_2 respectively.CT_{brine} and CT_{CO2} are images of the reactor kettle filled with CO_2 and salt water respectively.

$$\varphi = \frac{CT_{brine}^{sat} - CT_{CO2}^{sat}}{CT_{brine} - CT_{CO2}} \tag{1}$$

In the same way, during the experiment, CO_2 is injected into the sand-filled sand core saturated with salt water. After reaching the steady state, CT scan was performed to obtain the experimental image CT_{exp}, and then the spatial distribution of CO_2 saturation was calculated using the formula (2):

$$S_g = \frac{CT_{exp} - CT_{CO2}^{sat}}{CT_{CO2}^{sat} - CT_{brine}^{sat}} \tag{2}$$

3 Results and Discussion

3.1 The Influence of Wettability and Heterogeneity

3.1.1 The Influence of Wettability on CO_2 Displacement and Capture Characteristics

Table 2 shows the CO_2 saturation value of each sand-filled layer after the completion of the layered sand-filled core displacement [13]. It can be clearly seen that when the pore structure is similar, the wettability will have a serious impact on the flow and distribution of the CO_2 phase. In the supercritical CO_2 state, when the injection rate is low (0.1 mL/min), the CO_2 phase is stably displaced in the dolomite layer with poor

wettability, occupying most of the pore space of the dolomite layer, and obtaining high CO_2 saturation (0.74). But in the quartz sand layer with strong wettability, there is an obvious capillary fingering phenomenon. CO_2 only displaces a small part of the pores and breaks through, resulting in a lower CO_2 saturation (0.14). As the injection rate increases to 0.3 mL/min, the displacement of CO_2 in the weakly wetted dolomite layer also becomes significantly unstable. CO_2 is unevenly distributed in the pore space of the dolomite, and the saturation drops to 0.55. Further increase (0.6 mL/min), CO_2 in the dolomite layer can almost only flow along the outer pore space, forming a larger finger in the internal pores, and the saturation is further reduced to 0.24. As for the quartz layer, the increase in the injection rate also makes CO_2 trapped in the outer pore space to flow, cannot enter the inner pore space, and the CO_2 saturation is very low. Under the condition of gaseous CO_2, because the viscosity difference between CO_2 and salt water is greater, the displacement process is also more unstable, but the CO_2 saturation (0.29) of the dolomite layer with worse wettability is still greater than that of the strong wettability quartz sand layer (0.12).

Figure 2 shows the dynamic change process of the CO_2 phase in the inhalation process of mixed glass sand and quartz sand. It can be seen from the figure that as the inhalation process progresses, the CO_2 phase will continue to snap off, changing from a continuous phase to an isolated phase. For strongly wetted porous media, capillary fingering is prone to occur in the displacement process, resulting in relatively low CO_2 saturation, but for the inhalation process, strong wettability is conducive to the occurrence of snap off, increasing the safety of C capillary capture and storage. For weakly wettable porous media, the displacement process is more stable and the CO_2 saturation is higher. However, the inhalation process is mainly piston displacement, and CO_2 is difficult to capture, which is not conducive to the safety of CO_2 storage. As for the stratum structure, the structure with strong sealing of the cap layer, the address with poor wettability can be chosen for CO_2 storage, in order to achieve a larger CO_2 storage capacity [6].

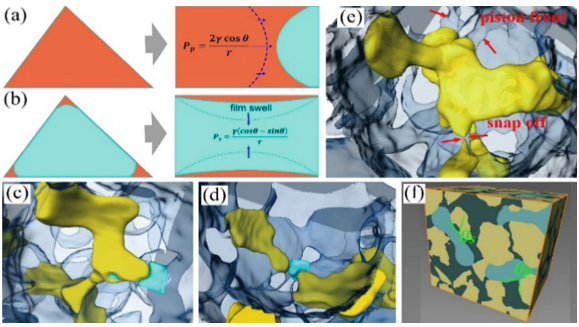

Fig. 2. The piston flooding front and snap-off effect in the pores of glass sand and quartz sand-filled sand cores: (a) The mechanism of the piston flooding front is shown (blue indicates CO_2); (b) CO_2 snap-off mechanism indicates; (c) Piston displacement front occurs (yellow indicates CO_2); (d) CO_2 snap off occurs in the throat; (e) CO_2 piston displacement front edge and snap off occur simultaneously in the throat; (f) The local contact angle when CO_2 is snap-off and the front edge of the piston displacement.

3.1.2 Influence of Heterogeneity on CO_2 Displacement and Capture Characteristics

For structurally heterogeneous cores, at the displacement stage, under supercritical CO_2 conditions, when the injection rate is low (0.1 mL/min), CO_2 first occupies most of the pore space of the BZ06 rock above the core. However, in BZ02 formation with small pores, CO_2 forms two larger branches and develops along the place containing BZ06 sand in the formation. And then it enters BZ06 formation with large pores below the core and occupies most pores, resulting in high CO_2 saturation of BZ06 formation (0.80) and low saturation of BZ02 formation (0.18). In other word, the CO_2 injection rate of the quartz + dolomite layered sand-filled core increases, the CO_2 saturation of both rock layers will decrease. For BZ06 + BZ02 layered sand filling core, with the increase of injection rate, CO_2 saturation is still displaced stably in BZ06 formation, and CO_2 saturation does not decrease (0.81 at 0.3 ml/min injection rate and 0.80 at 0.6 ml/min injection rate). For BZ02 formation, the CO_2 displacement process becomes more unstable, the CO_2 displacement changes from two larger branches to only one displacement path, and the CO_2 saturation decreases to only 0.06 at the injection rate of 0.6 ml/min. Comparing the supercritical CO_2 displacement and gaseous CO_2 displacement processes at the same rate, it is found that the displacement of CO_2 also becomes unstable in the BZ02 rock formation with smaller pores and has no obvious effect on the BZ06 formation. It shows that the changes of injection rate and fluid viscosity mainly affect the rock stratum with small pore structure, but have little effect on the rock stratum with large pores.

During the inhalation process, this experiment found that CO_2, which is the non-wetting phase, also ruptured within a single hole. Analyzing the fractured CO_2 in a single hole, there will be many fractured CO_2 phases in a single hole, and the fractured phases are close to the inner wall of the pore. The shape factor distribution of the fracture phase CO_2 and the comparison of the volume size with the pore volume are calculated. It is found that the shape factors of most isolated CO_2 phases are mainly distributed between 1 and 1.3, and their shape is similar to a sphere (the sphere shape factor is 1), and the volume of almost all fractured isolated CO_2 phases is much smaller than the pore volume. In the mixed glass sand porous medium, there is no obvious CO_2 phase fracture. The main reason for this difference is that the pore structure of the two sand-filled cores is different. Figure 2 shows the comparison of the interface characteristics between the fractured CO_2 phase and the unruptured CO_2 isolated phase. For the CO_2 phase without fracture, the size of the isolated CO_2 phase is relatively large, usually several pores, and there is a part of the contact area between the CO_2 phase and the salt water (medium silver region). When the CO_2 phase ruptures, the isolated CO_2 phase has a smaller volume, generally much smaller than a pore, and the contact area between CO_2 and salt water is also larger.

3.2 Evolution of the Interface Between Phases in the Process of Dissolution and Storage

3.2.1 Types of Phase Interface Evolution

The time-varying CO_2-salt water interface during the salt water imbibition process is shown in Fig. 3, in which only some representative experimental data are shown. *PV*

stands for pore volume (pore volume). In the three-dimensional rendering, each isolated CO_2-salt-water interface is rendered into the corresponding colour according to its size, so as to directly and effectively show the evolution of each isolated interface in the pore.

As CO_2 is gradually split and dissolved by salt water, especially in the later stage of the mass transfer process, only a small amount of CO_2 bubbles occupy the pore space. Therefore, the interface area between the phases is related to the shape of the bubble, but not the same as the surface area of the bubble. The interphase interface with irregular and slender shape can extend to multiple pores, but the monomer area is small. On the contrary, the interphase interface with regular shape and larger area can occupy 2−3 pores. Another phenomenon is that the CO_2-salt water interface is usually located in the void of the pore throat. At this time, CO_2 and salt water are attached to the surface of the porous medium. This type of two-phase bonding will pinch the CO_2-salt-water interface. In order to facilitate effective classification and observation, this chapter divides the CO_2-salt water interface area into three categories based on the data results of all experiments, according to their quantity and area characteristics: interface aggregation nodes, interface clusters and interface monomers.

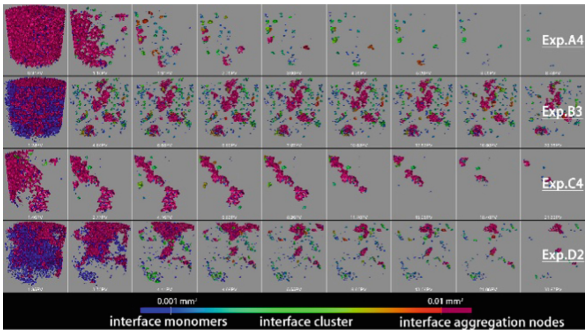

Fig. 3. The time-varying CO_2-salt water interface in the process of salt water absorption

In this study, the interphase interface with an interface area greater than 0.01 mm^2 is called the interface aggregation node, as shown in Fig. 3. The interface aggregation node is composed of interconnected interface clusters, which is significantly larger than other kinds of interphase interfaces, but the number is smaller. During the mass transfer process, the interfacial aggregation nodes further evolved when the salt water invaded, and their number and size decreased. However, more than one interface aggregation node can continue to remain connected and always exist until only a small amount of CO_2 bubbles are left. In Fig. 3, voxels with a color distribution range between red and cyan are classified as interface clusters, and the evolution of the interface is represented by the color gradient. Due to the intrusion of the wetting phase, some parts of the CO_2 phase aggregation node will return from the pore throat to the pores. At this time, the interfacial tension causes the leading part of the non-wetting phase to fragment into interface clusters. The interface between the salt water phases is defined as the interface monomer. For the CO_2 bubbles captured in a single pore, the CO_2-salt water interface is restricted to the pore throat or the corner of the pore. The evolution mode of the

interface monomer does not depend on the flow conditions, but has a certain degree of randomness.

3.2.2 Quantitative Relationship Between Phase Interface Area and Salt Water Saturation

Brusseau [14] conducted air-water displacement and imbibition experiments and found that the air-water phase interface area decreases linearly with the increase of water saturation, which conforms to the linear relationship:

$$a_i = a \times S_w + b \tag{3}$$

Where a_i is the specific interface area, S_w is the salt water saturation, and a and b are constant parameters.

The relationship between specific interface area a_i and salt water saturation S_w under different PV in some experimental groups is shown in Fig. 4, where each data point is calculated from its corresponding two-dimensional slice image, and the solid line represents the linear relationship of each experimental data set Mode. Taking into account a large number of data points (for example, there are more than 2500 points in Exp. D3) and inevitable systematic errors, this strong linear correlation strongly confirms that the specific interface area a_i will vary with the CO_2-salt water two-phase mass transfer process. As the salt water saturation S_w increases, it decreases linearly. During the mass transfer process, the data points of the specific interface area a_i gradually move along the regression line to the zero point, and the distribution range of the data points gradually shrinks.

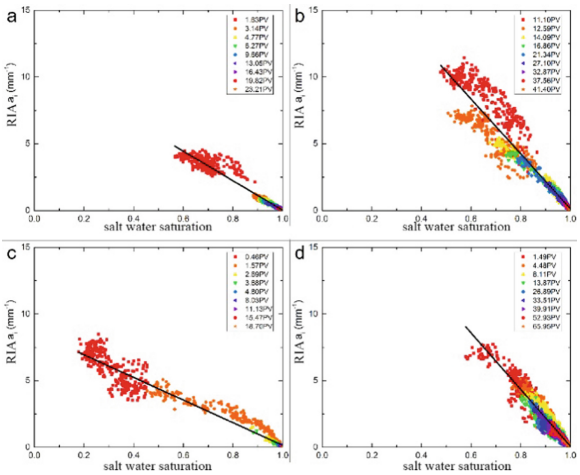

Fig. 4. The relationship between specific interface area and salt water saturation under different PV in some experimental groups.

When quantifying the relationship between the interface area of CO_2-salt water and the degree of salt water saturation, the surface area of the porous media can be

measured, in order to exclude the influence of different porous media particle sizes on the characteristics of the interface area between the phases. According to it, the interface area between CO_2 and salt water is normalized to obtain the relative interface area between CO_2 and salt water, which is recorded as *RIA* (relative interface area). Figure 4 visually shows the linear relationship between relative interface area RIA and salt water saturation. It can be found that for the same salt water saturation, *RIA* of the upward imbibition process is about 1.3 times that of the downward imbibition process. This feature corresponds to Fig. 4. The shape of the interphase interface of the Exp. A experimental group is more irregular, resulting in a larger interphase interface area. As the Reynolds number increases, the slope of the linear relationship in the uniform sand experiment has an increasing trend, while the slope of the linear relationship in the mixed sand experiment is not directly related to the Reynolds number. Under the same Reynolds number, the heterogeneity of the mixed sand significantly increases the contact area of the two phases, so the relative interface area RIA in the mixed sand experiment is larger than that in the uniform sand experiment.

4 Conclusion

This paper uses four sand-filled cores (mixed glass sand, quartz sand, BZ06 + BZ02 layered sand-filled cores and quartz + dolomite layered sand-filled cores) to visualize the CO_2 displacement process and imbibition process under different experimental conditions. In the flow experiment, the microscopic influence mechanism of wettability and heterogeneity on CO_2 displacement and capture characteristics was studied from the pore scale. It is found that during the displacement process, the wettability layered structure and pore layered structure will reduce the permeability of rocks, especially small pore rock formations and strong wettability rock formations, which reduces the storage capacity of CO_2 phase. The increase of the salt water concentration will cause the deterioration of the continuity of the water phase after the displacement process is completed. This phenomenon is more obvious in the strong wettability porous media, and the deterioration of the wettability will reduce the CO_2-salt water phase interface area. During the inhalation process, CO_2 phase rupture was observed, and CO_2 capillary capture was more likely to occur in areas where the wettability or pore structure changed.

The experiment was carried out to measure the area of the CO_2-salt-water interface in homogeneous and heterogeneous sand-filled sand cores, and the evolution of the interface between the phases in the process of dissolution and storage was comprehensively analyzed. The microscopic transport mechanism and morphological distribution characteristics of CO_2-salt water in the pores in this paper has some implication for practical CO_2 long-term and safe storage in saline aquifer.

References

1. Chadwick, R.A., Zweigel, P., Gregersen, U., Kirby, G.A., Holloway, S., Johannessen, P.N.: Geological reservoir characterization of a CO_2 storage site: the Ultra Sand, Sleipner Northern North Sea. Energy **29**(9–10), 1371–1381 (2008)

2. Metz, B., Davidson, O., De Coninck H.: IPCC special report on carbon dioxide capture and storage Working Group III of the Intergovernmental Panel on Climate Change (2005)
3. Niu, B., Al Menhali, A., Krevor, S.C.: The impact of reservoir conditions on the residual trapping of carbon dioxide in Berea sandstone. Water Resour. Res. **51**(4), 2009–2029 (2015)
4. Gao, Y., Qaseminejad Raeini, A., Blunt, M.J., Bijeljic, B.: Pore occupancy, relative permeability and flow intermittency measurements using X-ray micro-tomography in a complex carbonate. Adv. Water Resour. **129**(April), 56–59 (2019)
5. Scanziani, A., et al.: In Situ characterization of three-phase flow in mixed-wet porous media using synchrotron imaging. Water Resour. Res. **56**(9), 1–21 (2020)
6. Wu, B.: Investigation on two-phase flow and mass transfer characteristics of co_2 sequestration in saline aquifer. Dalian University of Technology (Dalian), Dalian (2020)
7. Lv, P.: Pore to core scale influence mechanism of wettability and heterogeneity on co_2 sequestration in saline aquifer. Dalian University of Technology (Dalian), Dalian (2019)
8. Andrew, M., Bijeljic, B., Blunt, M.J.: Pore-scale imaging of trapped supercritical carbon dioxide in sandstones and carbonates. Int. J. Greenh. Gas Control **22**, 1–14 (2014)
9. Chen, C.Y., Horne, R.N., Fourar, M.: Experimental study of liquid-gas flow structure effects on relative permeabilities in a fracture. Water Resour. Res. **40**(8) (2004)
10. George, F.O.: Measurement and estimation of soil water characteristic (April) (2020)
11. Jettestuen, E., Helland, J.O., Prodanovič, M.: A level set method for simulating capillary-controlled displacements at the pore scale with nonzero contact angles. Water Resour. Res. **49**(8), 4645–4661 (2013)
12. Lv, P., et al.: Pore-scale imaging and analysis of phase topologies and displacement mechanisms for co_2-brine two-phase flow in unconsolidated sand packs. Water Resour. Res. **53**(11), 9127–9144 (2019)
13. Jiang, L., Wu, B., Liu, Y., Suekane, T., Wang, D.: Dynamic evolution of the CO_2-brine interfacial area during brine imbibition in porous media. Int. J. Heat Mass Transf. **128**, 1125–1135 (2018)
14. Brusseau, M.L., Peng, S., Schnaar, G., Murao, A.: Measuring air-water interfacial areas with X-ray microtomography and interfacial partitioning tracer tests. Environ. Sci. Technol. **41**(6), 19–1961 (2007)

Study on the Movement of Hydrate Decomposition Front Under Different Control Mechanisms

Zhidong Hu and Shuxia Li(✉)

China University of Petroleum (East China), Qingdao 266580, China
lishuxia@upc.edu.cn

Abstract. The development of natural gas hydrate reservoirs is mainly affected by the three control mechanisms of decomposition, flow and heat transfer. The movement of the hydrate decomposition front is closely related to the development of hydrate reservoirs, and it has a direct impact on the hydrate reservoir's gas production, pressure, temperature, and other production dynamics. As a result, studying the movement of the decomposition front under various control mechanisms is crucially significant to the development of hydrate reservoirs. Using numerical simulation, this paper establish a one-dimensional hydrate reservoir depressurization model to investigate the decomposition front movement law under single control mechanisms (decomposition control, flow control, and heat transfer control) and coupled control mechanisms (decomposition-heat transfer control, decomposition-flow control, decomposition-heat transfer control, flow-heat transfer control). The results show that under a single control mechanism, when the decomposition control plays a leading role, the decomposition front movement rate remains stable; when heat transfer control or flow control plays a leading role, the movement rate of the decomposition front decreases significantly in the later stage; under the coupled control mechanism, the decomposition mode is stable and non-piston. When decomposition-flow control or decomposition-heat transfer control plays the leading role, the movement rate of the decomposition front remains essentially constant in the later stage, exhibiting linear characteristics; when flow-heat transfer control takes the lead, the movement rate of the decomposition front gradually decreases. Therefore, the movement of the decomposition front is very different under the action of different control mechanisms. This study can provide a reference for the actual production dynamic control of hydrate reservoirs in the future.

Keywords: Hydrate · Decomposition front · Control mechanism

1 Introduction

Natural gas hydrate is a non-polluting, clean energy source. Hydrate reservoirs are widely distributed on land and sea, abundant in resources. It is estimated that the carbon content of hydrates in nature is more than twice that of known fossil fuels worldwide, and it is an ideal potential alternative energy source in the 21st century [1–3]. Despite the abundance

B. Sun et al. (Eds.): DWOG-Hyd 2021, LNCE 246, pp. 221–228, 2022.
https://doi.org/10.1007/978-981-19-0960-3_22

of hydrate resources, our research on hydrate reservoir development is still in its early stages. China is a big energy consumer country, so it is necessary to study the technology of hydrate exploitation and development. Natural gas hydrate is different from traditional oil and gas resources. It is mostly found in the pores of the medium as solids. The cementation of the reservoir sediments gradually weakens as the hydrate decomposition front moves, resulting in a decrease in the formation's stability and strength, which may cause geological disasters [4, 5]. Different control mechanisms govern the movement of the decomposition front. The study of the movement of the hydrate decomposition front under different control mechanisms is beneficial for understanding and analyzing the production dynamics of hydrate reservoirs on the one hand; on the other hand, it is beneficial for accurate judgment and predicting formation stability. In this paper, a one-dimensional depressurization model is established by numerical simulation to investigate the movement of the decomposition front under a single control mechanism and a coupled control mechanism.

2 Control Mechanism and Criterion of Hydrate Decomposition

The production dynamics of natural gas hydrate reservoirs are mainly affected by the three control mechanisms of decomposition, flow and heat transfer. If the hydrate reservoir can provide sufficient heat for hydrate dissociation and has sufficient capacity for fluid flow, and the decomposition rate is low, then the hydrate decomposition control mechanism is decomposition control; if the hydrate reservoir can provide sufficient heat and the hydrate decomposition rate is quickly, and the flow resistance is large, the hydrate decomposition control mechanism is flow control; when the hydrate reservoir has a large decomposition rate and low flow resistance, while the heat supply is limited, the hydrate decomposition control mechanism is heat transfer control.

The criterion of judging the control mechanism is characteristic time [6]. The characteristic time of fluid flow controlling mechanism was defined as the time it took for the gas phase to flow through the whole length of hydrate reservoir; the characteristic time of hydrate dissociation controlling mechanism was defined as the time it took to dissociation the hydrate in a unit volume of hydrate reservoir; the characteristic time of heat transfer controlling mechanism was defined as the time it took for the gas phase to transfer the heat in the unit length of hydrate reservoir through the unit area by heat conduction.

The formula for the three characteristic times is as follows:

(1) Flow control:

$$\tau_1 = \frac{\varnothing \mu_g L^2}{k_0 \Delta P} \tag{1}$$

(2) Decomposition control:

$$\tau_2 = \frac{\varnothing \rho_h S_h}{k_d^0 e^{\frac{-\Delta E}{RT_i}} \sqrt{\frac{\varnothing^3}{2k_0} M_h \Delta P}} \tag{2}$$

(3) Heat transfer control:

$$\tau_3 = \frac{L^2 \rho_g C_g}{K_g} \tag{3}$$

3 Analysis of the Moving of the Decomposition Front Under Different Control Mechanisms

This paper employs CMG to simulate the production performance of hydrate reservoir via depressurization, A one-dimensional hydrate reservoir model with a length of 1 m is established, which is discretized into 50 grids with lengths of 0.02 m each. The grid's width and height are both 0.1 m. Table 1 displays the main parameters of hydrate reservoirs.

Table 1. The main parameters

Parameter	Value
Hydrate saturation	0.4
Porosity	0.3
Permeability	1.0×10^{-13} m^2
Reservoir pressure	6 MPa
Bottom hole pressure	3 MPa
Reservoir temperature	5 °C
Activation energy	8.1×10^4 J/mol
Response frequency factor	3.6×10^4 mol/m^2/pa/s
Specific heat capacity	1020 J/kg/K
Thermal conductivity	0.5 W/m/K

3.1 Decomposition Front Movement Under a Single Control Mechanism

The special parameter settings of different control mechanisms are shown in Table 2, other parameters that do not changed refer to Table 1. Taking decomposition control as an example, the characteristic time is calculated according to Eqs. (1)–(3), $\tau 1 = 1.0 \times 10^6$; $\tau 2 = 1.41 \times 10^7$; $\tau 3 = 2.04 \times 10^3$. Decomposition control has the largest eigenvalue, then decomposition control plays a leading role.

Table 2. The special parameters

Mechanism	Parameter	Value
Flow control	Bottom hole pressure	3.5 MPa
	Permeability	1.0×10^{-13} m^2
Decomposition control	Response frequency factor	3.6×10^3 $mol/m^2/pa/s$
	Porosity	0.4
Heat transfer control	Gas specific heat capacity	1500 J/kg/K
	Thermal Conductivity	0.05 W/m/K

The movement of the decomposition front under different control mechanisms is shown in Fig. 1.

When decomposition is the primary control, the front edge movement rate of the decomposition remains constant. Other factors have little effect on the decomposition front in this case, and a stable movement speed can be maintained. When flow is the primary control, the decomposition front moves at a relatively fast rate in the early stage, and the reduction in pressure in the previous stage causes the hydrate to decompose rapidly. However, due to the high resistance of gas-water flow capacity, the hydrate decomposition front's movement rate is rapidly reduced. When heat transfer is the primary control, the front movement rate of the decomposition remains relatively high. Due to the decrease in pressure during the initial stage of depressurization, the hydrate decomposes quickly, and the reservoir has a high specific heat capacity and can continue to provide heat for the hydrate's decomposition. Afterwards, as the propagation of the reservoir temperature decreased in the later stage, the movement speed of the hydrate decomposition front decreases faster.

3.2 Decomposition Front Movement Under the Coupling Control Mechanism

The special parameter settings of different control mechanisms are shown in Table 3, and the parameters that do not need to be changed refer to Table 1. Taking decomposition-flow coupling control as an example, the characteristic time is calculated according to Eqs. (1)–(3), $\tau 1 = 3.60 \times 10^6$; $\tau 2 = 3.92 \times 10^6$; $\tau 3 = 2.04 \times 10^3$. In this case, the characteristic time of decomposition control and flow control are not much different, and both of these are far greater than that of the heat transfer control, so the decomposition-flow coupling control plays the leading role.

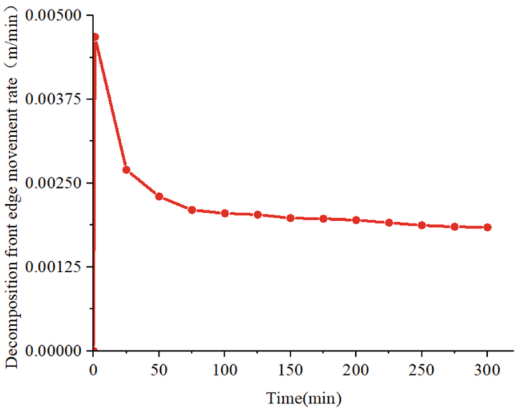

(a)

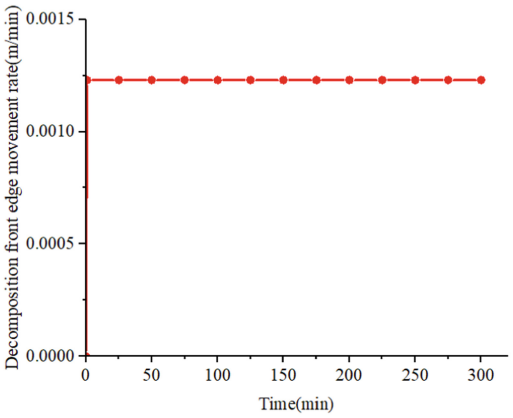

(b)

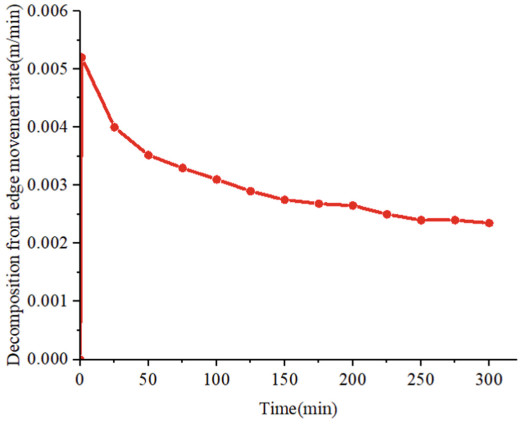

(c)

Fig. 1. The movement rate of the decomposition front (a) flow control; (b) decomposition control; (c) heat transfer control.

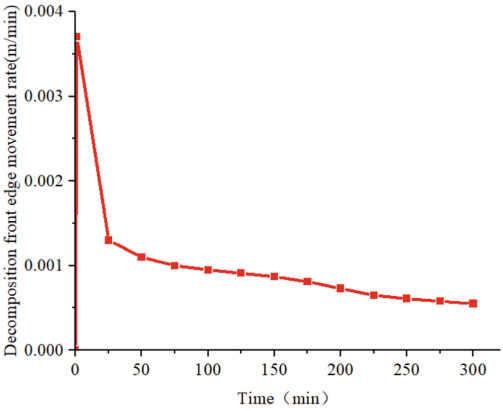

(a)

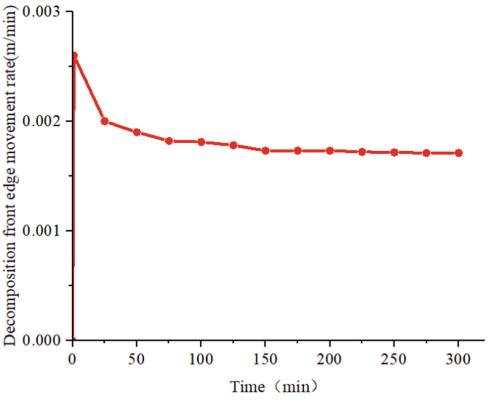

(b)

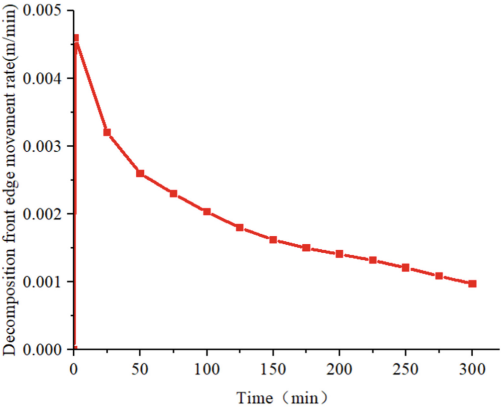

(c)

Fig. 2. The movement rate of the decomposition front under different coupling control mechanisms. (a) decomposition-flow; (b) decomposition-heat transfer; (c) flow-heat transfer

Table 3. The special parameters

Mechanism	Parameter	Value
Decomposition-Flow coupling control	Response frequency factor	1.0×10^4 mol/m^2/pa/s
	Permeability	3.6×10^{-14} m^2
Decomposition-heat transfer coupling control	Response frequency factor	1.0×10^4 mol/m^2/pa/s
	Gas specific heat capacity	1500 J/kg/K
Flow-heat transfer coupling control	Gas specific heat capacity	1500 J/kg/K
	Thermal Conductivity	0.05 W/m/K
	Permeability	2.8×10^{-14}m^2

The movement of the decomposition front under different coupling control mechanisms is shown in Fig. 2.

When the coupling control is decomposition-flow, the movement rate of the decomposition front is relatively high in the early stage. The reason is that the decomposition control plays the primarily role in this stage. After that, the flow control effect increases gradually, so the decomposition front movement rate decreases. When the coupling control is decomposition-heat transfer, the temperature decreases during the decomposition process, so the movement rate of the hydrate decomposition front decreases. When the coupling control is flow-heat transfer, the movement rate of the decomposition front always shows a gradual decrease. It is because the flow of gas and water is restricted, which hinders the further decomposition of hydrate. Furthermore, the temperature decreases rapidly in the later stage of decomposition, which makes the decomposition more slowly.

4 Conclusion

(1) In the case of a single control mechanism, when decomposition is the primary control, the decomposition front movement curve exhibits a linear characteristic, and the hydrate decomposition front movement rate remains essentially constant. When flow is the primary control function, the movement rate of the decomposition front gradually decreases as gas-water flow resistance increases in the later stages of depressurization; when heat transfer is the primary control, the temperature of the hydrate reservoir rapidly decreases, and the movement rate of the hydrate decomposition front is lower in the later stages of decomposition.

(2) In the case of coupling control mechanism, when decomposition-flow or decomposition-heat transfer is the primary control, due to the decrease of the hydrate decomposition rate constant, the movement rate of the hydrate decomposition front does not gradually decrease in the later stage as that of the flow control, and it still maintains a relatively stable movement rate. When the flow-heat transfer plays a dominant role, due to the increase of flow resistance and the decrease of temperature in the later stage of decomposition, the movement rate of the front edge of hydrate decomposition is lower.

Symbol Description

$\varnothing$—Porosity
k_0—Permeability, 10^{-13} m^2
ρ_h—Density of hydrate, kg/m^3
S_h—Hydrate saturation
C_g—Gas specific heat capacity, J/kgK
K_g—Thermal conductivity of gas, W/mK
M_h—Molar mass of hydrate, kg/mol
ΔE—Thermal conductivity of gas, J/mol
k_d^0—Reaction rate constant, mol/m^2/pa/s
L—Reservoir size, m

Acknowledgement. This work is supported by the Major Program of the National Natural Science Foundation of China (51991365), National Natural Science Foundation of China (52074334, 51974347), which are gratefully acknowledged.

References

1. Li, S., Jiang, X., Liu, C.: The simulation of gas production from hydrates by depressurization at a constant pressure. Pet. Sci. Technol. **30**(9), 855–863 (2012)
2. Lin, D., Gong, J.: Research progress of formation and flow properties of natural gas hydrate. Contemporary chemical industry. Xiandai Huagong/Modern Chem. Ind. **34**(11), 24–29 (2017)
3. Makogon, Y.F., Holditch, S.A., Makogon, T.Y.: Natural gas-hydrates — a potential energy source for the 21st century. J. Petrol. Sci. Eng. **56**(1–3), 14–31 (2007)
4. Delli, M.L., Grozic, J.: Prediction performance of permeability models in gas-hydrate-bearing sands. SPE J. **18**(02), 274–284 (2013)
5. Sakamoto, Y., Komai, T., Miyazaki, K., et al.: Laboratory-scale experiments of the methane hydrate dissociation process in a porous media and numerical study for the estimation of permeability in methane hydrate reservoir. J. Thermodyn. **2010**(1), 9879–9884 (2010)
6. Zheng, R., Li, S., Li, Q., et al.: Study on the relations between controlling mechanisms and dissociation front of gas hydrate reservoirs. Appl. Energy **215**, 405–415 (2018)

Deepwater Oil and Gas Flow Assurance

Numerical Simulation of Hydrate Particle Migration and Deposition in Horizontal Pipe Flow

Zhengfeng Shan[1], Xiansi Wang[1], Yubin Wang[2], Jihao Pei[3], and Zhiyuan Wang[3(✉)]

[1] CNPC Offshore Engineering Co., Ltd., Tianjin 300450, China
[2] CNPC Engineering Technology Research Co., Ltd., Tianjin 300450, China
[3] China University of Petroleum (East China), Qingdao 266580, China
wangzy1209@126.com

Abstract. During the development of deep-water gas wells, the low temperature and high pressure environment near the mudline is easy to form hydrate in the wellbore, resulting in severe hydrate plugging risk. In this paper, the traditional discrete phase model is optimized by establishing the hydrate particle transport model and the judgment criterion of particle deposition on the pipe wall, so as to numerically simulate the hydrate particle transport and deposition law in the pipe flow. Through the simulation, we get the velocity distribution and concentration distribution of hydrate particles in the pipe flow. It is found that the deposition rate of particles generated in the gas core can reach about 7%, which decreases with the increase of gas velocity and increases with the increase of particle size. This conclusion confirms the importance of hydrate particles deposition in the gas core to the overall hydrate deposition, which lays a foundation for the accurate calculation of hydrate deposition blockage.

Keywords: Natural gas hydrate · Particle migration · Particle deposition · Numerical simulation

1 Introduction

Deepwater oil and gas drilling and development has the characteristics of high investment, technology and high risk. The problem of hydrate flow guarantee has become one of the key problems restricting deepwater oil and gas development [1]. The deep and shallow formation has the environment of low temperature and high pressure. Once the gas and water molecules produced by the formation meet the phase equilibrium conditions for hydrate formation, hydrate will be generated in the production string, choke line and BOP, deposit and attach to the pipe wall, resulting in the reduction of the inner diameter of the pipeline, which may cause the wellbore, valves, BOP and choke line to be blocked by hydrate and serious safety accidents. Therefore, the study on the migration and deposition law of hydrate particles is of great significance to predict the location of hydrate blockage.

B. Sun et al. (Eds.): DWOG-Hyd 2021, LNCE 246, pp. 231–239, 2022.
https://doi.org/10.1007/978-981-19-0960-3_23

The main driving force of hydrate research is to solve the thorny problem of hydrate flow assurance. Once hydrate is formed, the particle aggregates formed are not deposited in-situ, but transported and deposited under the action of gas carrying. At present, the mechanism of hydrate particle migration and accumulation is not fully understood. Fidel Dufour et al. believe that the aggregation process of hydrate particles was like a chemical reaction. When hydrate particles contact with water droplets, water droplets quickly nucleate and crystallize into hydrate particles and adhere to the original hydrate particles (aggregates) [2]. Based on the population balance model, Colombel et al. put forward the theory that contact aggregation mechanism and shear limited aggregation mechanism are unified to explain hydrate aggregation [3].

Hydrate deposition refers to the process that the hydrate generated in the pipe reaches the pipe wall and adheres to the pipe wall. At present, many studies on hydrate particle deposition were based on the deposition of solid particles. In 1977, Friedlander and Johnstone proposed the free flight model [4]. After the relaxation process, the particles moved to the pipe wall in free-flight. In 1993, fan and Ahmadi proposed an empirical correction formula for particle deposition considering the effects of surface roughness and gravity [5]. In 2010, based on the previous studies, Jassim used CFD technology to simulate the experiment of single hydrate particle deposition, and proposed a theoretical model for calculating single hydrate particle deposition in gas dominated system [6]. Di Lorenzo et al. carried out an indoor experimental study on hydrate formation and transport in the annular mist flow in the pipeline for the first time, and obtained a large number of experimental data, such as hydrate formation rate, hydrate layer growth rate on the pipe wall, etc. [7]. Aman et al. studied the effects of gas phase velocity and sub-cooling on hydrate formation and deposition in pipelines with gas phase as continuous phase, and found that the droplet entrainment rate in gas phase was very important to hydrate formation and pipeline blockage [8]. Wang et al. discussed the hydrate deposition characteristics in the annular mist, and preliminarily found that hydrate particles generated by droplets in the gas core and hydrate particles generated at the liquid film on the pipe wall will deposit and adhere on the pipe wall [9].

At present, there are abundant researches on hydrate deposition blockage, but most of them are theoretical analysis and model establishment for the macro phenomenon of hydrate blockage. Few studies pay attention to the movement state of hydrate particles near the pipe wall in the gas phase, and usually ignore the influence caused by this part of particle deposition in the process of establishing hydrate blockage prediction model. In this paper, the migration and deposition characteristics of hydrate particles in gas core are simulated by the optimized DPM model, and the migration and deposition characteristics of particles are obtained, which provides a theoretical basis for the accurate prediction of hydrate deposition plugging.

2 Solving Model

2.1 Numerical Model

Because this paper mainly focuses on the migration and deposition of hydrate particles in the pipe flow, and in order to simplify the numerical simulation process, we make the following assumptions:

(1) The pipe flow is an isothermal process, while ignoring the mass transfer process between gas and liquid, that is, the formation and decomposition of hydrate are not considered.
(2) The hydrate particles in the pipe flow are spheres.
(3) The particle volume concentration is less than 10%, that is, only the interaction between particles and fluid is considered, and the interaction between particles is ignored.

The numerical models used in this paper are mainly turbulence model and discrete phase model (DPM). Among them, the turbulence model adopted the standard k-e model, and its turbulent flow energy equation and diffusion equation could be expressed by the following formula (1)–(2).

$$\frac{\partial}{\partial t}(\rho k) + \frac{\partial}{\partial x_i}(\rho k u_i) = \frac{\partial}{\partial x_j}\left[\left(u + \frac{u_t}{\sigma_k}\right)\frac{\partial k}{\partial x_j}\right] + G_k + G_b - \rho e - Y_M \tag{1}$$

$$\frac{\partial}{\partial t}(\rho e) + \frac{\partial}{\partial x_i}(\rho e u_i) = \frac{\partial}{\partial x_j}\left[\left(u + \frac{u_t}{\sigma_e}\right)\frac{\partial e}{\partial x_j}\right] + C_{1e}\frac{e}{k}(G_k + C_{3e}G_b) - C_{2e}\frac{e^2}{k} \tag{2}$$

In DPM model, the trajectory equation of particles is mainly solved according to the differential equation of particle force in Cartesian coordinate system. The form of the force balance equation of particles in Cartesian coordinate system (taking the X coordinate as an example) can be shown by formula (3), in which the first term on the right of formula (3) represents the unit mass drag force on particles, the second term is the gravity term, and the third term is other forces on particles in X direction.

$$\frac{du_p}{dt} = F_D(u - u_p) + \frac{g_x(\rho_p - \rho)}{\rho_p} + F_x \tag{3}$$

Among them, the drag force F_D can be calculated by the formula (4)–(6).

$$F_D = \frac{18\mu}{\rho_p d_p^2}\frac{C_D Re_p}{24} \tag{4}$$

$$Re_p = \frac{\rho d_p |u - u_p|}{\mu} \tag{5}$$

$$C_D = a_1 + \frac{a_2}{Re_p} + \frac{a_3}{Re_p} \tag{6}$$

When the particles move near the wall, due to the change of flow field and the interaction between wall and particles, the particles will also be affected by Saffman lift force and wall adhesion. When there is a velocity gradient in the flow field, Saffman lift force will be generated due to the velocity difference between the upper and lower sides of hydrate particles. When the fluid flows over a solid surface, in the area far away from the wall (until the fluid is very close to the wall), the fluid makes a non-rotational motion, and due to the viscosity of the fluid, the non-slip motion is made on the wall, and the transition between the two areas will produce a very large velocity gradient. Because the

fluid velocity gradient near the wall is large, the Saffman lift will have a great impact on the particle motion, which can be calculated by formula (7) [10].

$$F_L = 1.615\mu d_p^2 \left(\frac{\rho_g}{\mu}\frac{du}{dz}\bigg|_{z=d/2}\right)^{0.5} u_p \tag{7}$$

The adhesion force between hydrate particles and the wall is the sum of all molecular and atomic attraction between two objects, and its calculation method is shown in formula (8) [10].

$$F_A = \frac{A_{hm} d_p}{12h^2} \tag{8}$$

Since the particles have no high-speed rotation near the wall, they have good electrostatic elimination characteristics, and Magnus force, basset force and electrostatic force can be ignored. Therefore, the stress of hydrate particles in pipe flow can be accurately described by formula (3). The stress state of particles on the pipe wall can be seen in the Fig. 1. By integrating the time step of formula (3), the hydrate particle velocity at each position can be obtained. Through the following formula (9), the particle trajectory equation and additional equation describing particle mass/heat transfer can be obtained.

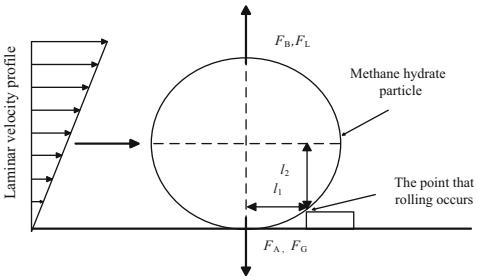

Fig. 1. Schematic diagram of stress state of hydrate particles on pipe wall

$$\frac{dx}{dt} = u_p \tag{9}$$

2.2 Judgment of Particle Deposition

When the particles move to the pipe wall, the boundary conditions of general DPM only include collision reflection, escape and wall capture. However, previous studies have found that after the hydrate particles contact the wall, only a small part of them will deposit on the wall, resulting in the growth of the hydrate layer, and most of the particles will return to the gas core under the action of gas drag. Previous studies have found that particle rotation is the key factor for hydrate particles to deposit on the wall. G.M. Burdick et al. quantitatively characterized the motion characteristics of hydrate particles

on the wall by introducing the critical particle Reynolds number [10]. If the Reynolds number is greater than the critical value, the particle will leave the wall. The established hydrate particle deposition judgment criteria is shown by formula (10):

$$Re_{\mathrm{p}} \geq \frac{-\mathrm{F_A} \cdot l_2}{(1.7009 \cdot 3\pi \cdot l_1) + \left(1.615\left(\frac{\rho_g \mathrm{d}u}{\mu\ \mathrm{d}z}\Big|_{z=\frac{d}{2}}\right)^{\frac{1}{2}} d_p \cdot l_2\right) + \left(0.943993 \cdot 2\pi d_p\right)} \frac{\rho_g}{\mu^2} \tag{10}$$

The UDF provided by Fluent can realize the user's personalized needs by writing code programs and dynamically linking to the solver. In this paper, the compiled UDF is used to judge the complex boundary conditions of discrete phase particles. Based on the stress analysis of particles on the pipe wall, through the user-defined macro Define_DPM_ BC implements the custom particle and wall removal mechanism, and embeds the source code into the shared library to link with Fluent.

3 Numerical Solution Process and Result Analysis

3.1 Simulation Method and Parameters

The simulation is transient and uses the Eulerian-Lagrangian method (Eulerian method is used to solve the N-S equation for gas and Lagrangian method is used to solve the particle trajectory equation for hydrate particles). Since the turbulent diffusion of particles has a great impact on the solution of the particle trajectory equation, the influence of particles on the continuous phase is taken into account in this simulation. Firstly, the convergent continuous phase flow field is obtained by k-epsilon model, and then the discrete phase model is created for coupling calculation.

The physical model used in the simulation is a cylindrical pipe with a length of 1.5 m and a diameter of 0.1 m. The grid is divided by O-grid method (It can be seen in Figs. 2). The simulation conditions are temperature 275 k and pressure 6 MPa. The gas component is pure methane, the liquid content is 5%, the gas velocity is 10 m/s, and the liquid velocity is 0.08 m/s. Through calculation, it can be obtained that the gas viscosity under this condition is $1.172 * 10^{-5}$ Pa·s. The gas density is 48.669 kg/m^3 and the surface tension is 0.075 N/m.

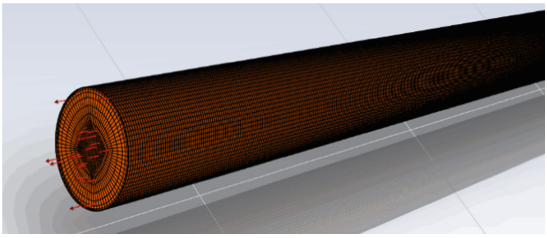

Fig. 2. Schematic diagram of meshing

3.2 Results and Analysis

We intercepted the migration velocity of hydrate particles at different sections, as shown in Figs. 3, and found that the particle movement velocity in the gas core area is high, which can reach 8 m/s, while the particle movement velocity at the pipe wall is small, which can reach 0.001 m/s. This is because in the gas core region, the particles are only dragged by the gas in the turbulent core region, so that the particles move together with the gas core. In the near wall region, a large number of particles collide and rebound with the wall or roll and slide along the wall, which loses most of the kinetic energy, reduces the velocity, and even some particles deposit due to the adhesion of the wall.

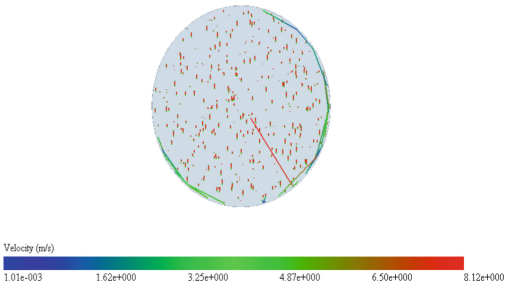

Fig. 3. Particle velocity distribution in pipe flow

We also get the concentration distribution of hydrate along the axial direction of the pipeline under different gas velocities. It can be seen from the Fig. 4 that the hydrate particle concentration is mainly concentrated in the rear section of the pipeline, and the maximum particle concentration is concentrated at the bottom of the pipeline. This is because the radial motion of particles in pipe flow is mainly affected by particle gravity. At the same time, it is found that the greater the gas velocity, the stronger the shear force exerted by the gas on the hydrate particles, so the smaller the concentration distribution of hydrate particles on the wall, and the more uniform the concentration distribution of hydrate particles.

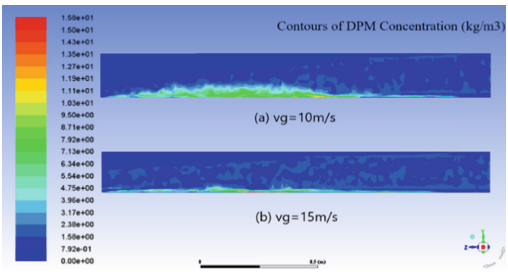

Fig. 4. Particle concentration distribution at different gas velocities

By capturing the hydrate deposition particles on the wall, we obtain the total number of particles injected and the number of particles deposited on the pipe wall, and calculate

the deposition rate of hydrate particles in the gas phase, as shown in the Fig. 5. It can be seen from the figure that the maximum particle deposition rate can reach about 7%, which shows that the role of hydrate particles generated in the gas core in the overall hydrate deposition cannot be ignored. The hydrate deposition blockage prediction model should take into account the hydrate particles deposition generated in the gas core. At the same time, it is found that the deposition rate decreases with the increase of gas velocity and increases with the increase of particle size, and the larger the particle size, the smaller the influence of gas velocity on deposition.

The influence of gas velocity on deposition rate is reflected in two aspects. First, with the increase of gas velocity, the greater the turbulent kinetic energy of the fluid, the stronger the fluid pulsation, the greater the kinetic energy obtained by the particles in the fluid due to pulsation, which makes the rebound energy of the particles greater, so the probability of deposition after collision with the wall decreases. Second, with the increase of gas velocity, the shear effect of gas is stronger, and the particles that have reached the wall are easier to return to the gas flow under the action of shear force, resulting in the reduction of wall deposition probability. The influence of particle size on particle deposition is mainly reflected in gravity. The larger the particle size is, the greater the gravity the particles are subjected to, and the easier it is to deposit at the bottom of the pipe wall.

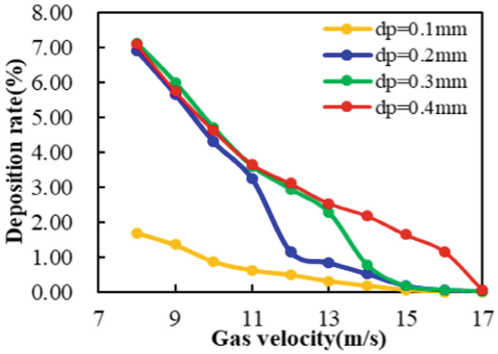

Fig. 5. Variation curve of particle deposition rate with gas velocity and particle size

4 Conclusion

Based on the stress characteristics of hydrate particles in pipe flow, this paper establishes hydrate particle migration model and deposition judgment criteria on the pipe wall, and optimizes the traditional DPM model in Fluent, in order to accurately predict the migration and deposition law of hydrate particles in pipe flow. Through numerical simulation, we get the velocity distribution and concentration distribution of hydrate particles in the pipeline. It is found that the migration velocity of hydrate particles is characterized by high velocity in the gas core and low velocity near the pipe wall, and its migration is mainly affected by gravity. At the same time, the simulation also shows that the deposition rate of hydrate particles in the gas core is up to about 7%, which

decreases with the increase of gas velocity and increases with the increase of particle size, which further explains the importance of hydrate particle deposition in the gas core to the growth of the overall hydrate layer. This result provides a theoretical basis for the accurate prediction of the growth rate of hydrate deposition layer.

Symbol Description

u, u_p—Fluid and particle velocities, m/s
G_k, G_b, Y_M—Turbulent kinetic energy generated by laminar velocity gradient, turbulent kinetic energy generated by buoyancy, fluctuation caused by transition diffusion in compressible turbulence, J
g_x—Gravitational acceleration in X direction, m/s^2
ρ_p, ρ—Particle and fluid density, kg/m^3
F_D, F_L, F_A, F_x—Drag, Saffman lift, adhesion, other forces, N
σ_e, σ_k—Prandtl number of turbulence in e equation and K equation
l_1, l_2—Particle rotation arm, m
μ—Dynamic viscosity, N·s/m^2
d_p—Particle size, mm
C_D—Drag coefficient
Re_p—Particle Reynolds number
a_1, a_2, a_3,—Empirical coefficient
k—Turbulent kinetic energy, J
e—Diffusivity
u_t—Turbulent velocity, m/s

Acknowledgement. The work was supported by the CNPC's Major Science and Technology Projects (ZD2019-184-003).

References

1. Sloan, E.D., Jr.: Fundamental principles and applications of natural gas hydrates. Nature **426**(6964), 353–363 (2003)
2. Fidel-Dufour, A., Gruy, F., Herri, J.M.: Rheology of methane hydrate slurries during their crystallization in a water in dodecane emulsion under flowing. Chem. Eng. Sci. **61**(2), 505–515 (2006)
3. Colombel, E., Gateau, P., Barre, L., et al.: Discussion of agglomeration mechanisms between hydrate particles in water in oil emulsions. Oil Gas Sci. Technol. **64**(5), 629–636 (2009)
4. Friedlander, S.K., Marlow, W.H.: Smoke, dust and haze: fundamentals of aerosol behavior. Phys. Today **30**(9), 58–59 (1977)
5. Fan, F.-G., Ahmadi, G.: A sublayer model for turbulent deposition of particles in vertical ducts with smooth and rough surfaces. J. Aerosol Sci. **24**(1), 45–64 (1993)
6. Jassim, E., Abdi, M.A., Muzychka, Y.: A new approach to investigate hydrate deposition in gas-dominated flowlines. J. Nat. Gas Sci. Eng. **2**(4), 163–177 (2010)

7. Di Lorenzo, M., Aman, Z.M., Kozielski, K., et al.: Underinhibited hydrate formation and transport investigated using a single-pass gas-dominant flowloop. Energy Fuels **28**(11), 7274–7284 (2014)
8. Aman, Z.M., Di Lorenzo, M., Kozielski, K., et al.: Hydrate formation and deposition in a gas-dominant flowloop: initial studies of the effect of velocity and subcooling. J. Nat. Gas Sci. Eng. **35**, 1490–1498 (2016)
9. Wang, Z., Zhang, J., Chen, L., et al.: Modeling of hydrate layer growth in horizontal gas-dominated pipelines with free water. J. Nat. Gas Sci. Eng. **50**, 364–373 (2018)
10. Burdick, G.M., Berman, N.S., Beaudoin, S.P.: Hydrodynamic particle removal from surfaces. Thin Solid Films **488**(1–2), 116–123 (2005)

Study on Erosion Wear Law of Pipe String with Sand and Liquid-Carrying in Gas Storage

Hemin Yang, Zhiyuan Wang(✉), Yangyang Zhang, and Xiao Liu

School of Petroleum Engineering, China University of Petroleum (East China), Qingdao 266580, China
wangzy1209@126.com

Abstract. At present, there are few reports of erosion wear law of pipe string with sand and liquid-carrying in gas storage, and the erosion law in the multiphase flow of oil and gas gathering and transmission pipeline is not fully applicable to the analysis of pipe string with sand and liquid-carrying in gas storage. Since the natural gas density under high temperature and pressure is 10–100 times higher than that under normal temperature and pressure, it is necessary to comprehensively analyze the stress state of sand particles in the pipe string under two conditions of sand-containing only in the early stage of gas production, and sand-containing and liquid- carrying in the later stage of gas production the gas storage. By considering the buoyancy, pressure gradient force, additional mass force, and Saffman lift of particles, which is used to be neglected during the erosion study in multiphase flow of oil and gas gathering and transmission line, the coupling effect of gas-solid and gas-liquid-solid during erosion is more comprehensive, and then the erosion law in the pipe string of gas storage is carried out using the CFD method and Fluent Software, which has important theoretical guidance and practical significance to ensure the safe and efficient injection and production of gas storage.

Keywords: Gas storage · Pipe string · Erosion law · Analog simulation · Sand content · Liquid-carrying

1 Introduction

At present, the location of China's natural gas fields does not match the demand. There is a large difference in natural gas demand across quarters, and the contradiction between supply and demand is prominent. According to statistics, in 2020, my country's demand for liquefied natural gas was further expanded. The net import volume of natural gas was 142.8 billion m^3, and the external dependence reached 43% [1]. Zhou [2] predicts that in the next 15 years under the background of carbon neutrality, China's natural gas market is still in a stable growth period, and the natural gas consumption will reach 650 billion m^3 in 2035. In order to realize the functions of natural gas peak shaving, supply protection and strategic reserve, gas storage has become an inevitable demand when China's natural gas develops to a certain scale. With the accelerating pace of gas storage construction in China and the increasing number of gas storage around cities, the safety of gas storage has become more and more important.

B. Sun et al. (Eds.): DWOG-Hyd 2021, LNCE 246, pp. 240–250, 2022.
https://doi.org/10.1007/978-981-19-0960-3_24

Different from the pursuit of stable production of oil and gas reservoirs, gas store mostly adopt the modes of long-term fast injection and production and strong injection and production, and the injection and production string is mostly the same string, which puts forward higher requirements for the pipe string of gas reservoirs. Moreover, under long-term alternating load, the reservoir is more prone to fatigue damage and high sand production risk, which further aggravates the pipe string erosion and makes it more difficult to manage the safe operation of the pipe string. The above shows that it is urgent and necessary to carry out the research on the erosion law of pipe string in gas storage [3, 4].

Erosion is a phenomenon that the fluid and its carrying phase (such as droplets, sand particles, etc.) impact the material surface at a certain speed and angle, resulting in material deformation and loss. Most gas storage pipe strings are plastic materials (N80, P110, S13cr, 13Cr, etc.) [5]. Scholars at home and abroad have conducted a lot of research on the erosion wear of plastic materials and achieved many results. However, these results mostly consider the simplification of particle force and are mostly applicable to the analysis of erosion wear law of gathering and transmission pipeline or under special working conditions. There are few reports on the erosion research of gas storage pipe string based on CFD method and Fluent Software. The essential reason is that the gas storage pipe string has the characteristics of deflecting, high gas production intensity, complex interaction between sand particles and droplets and liquid film, and difficult tracking of particle trajectory, which brings great challenges to the research on the degree and law of pipe string erosion [6, 7].

Therefore, based on the actual deflection mode of pipe string in a gas storage, this paper establishes the vertical section and inclined section models of the 5 m actual pipe string of the gas storage. On the basis of comprehensively considering the force on the particles in the gas production pipe string of the gas storage, combined with the CFD method and Fluent Software, the standard k ~ ε turbulence model and Mclaury erosion model [8] are selected for simulation, and the parameters are calculated and input to explore the influence law of flow velocity, particle diameter, sand content and water content the erosion of gas storage pipe string.

2 Parameters and Research Scheme of Gas Storage

The preliminary production data of a depleted gas reservoir and the design parameters of gas storage are shown in Table 1.

Using the fluent simulation software, five groups of simulation are carried out for the vertical pipe section and inclined pipe section under the actual working conditions of gas production in the gas storage. The parameter input is shown in Table 2 below.

Table 1. Parameters of a gas storage

Formation pressure	37.8 MPa
Formation temperature	177.8 °C
String density	7850 kg/m^3
Particle density	2650 kg/m^3
pipe diameter	177.8 mm
Design production	1680000 m^3/d

Table 2. Analog parameter input.

	Case1	Case2	Case3	Case4	Case5
Pipe section	Vertical pipe	Vertical pipe	Vertical pipe	Inclined pipe	Inclined pipe
Flows (m/s)	6.12–30.6	6.12	6.12	4.12	4.12
Sand content (g/s)	6.2	12.4–62	6.2	0.01–0.1	0.1
Particle diameter (um)	40	40	40–120	40	40
Water content (%)	0	0	0	0	1–10

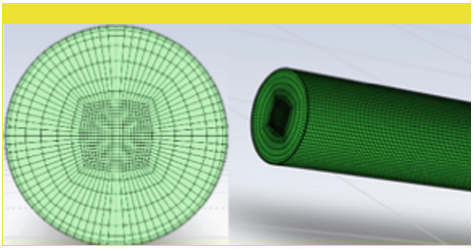

Fig. 1. Model meshing

3 Fluent Analogue Simulation

3.1 Modeling and Meshing

According to the size of the pipe string used in the production site of the gas storage, the geometric models of the vertical section and inclined section of the pipe string are established by Spaceclaim Software, the thickness of the boundary layer is set by ICEM.

Software and the structural grid is divided, as shown in Fig. 1, and the grid independence is tested. As shown in Fig. 2, the optimal number of grids is determined to be 880000.

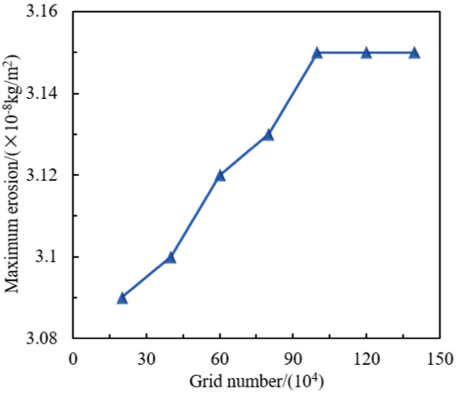

Fig. 2. Grid independence test

3.2 Particle Stress Analysis

Assuming that the shape of particles is spherical, on the basis of previous studies only considering gravity and drag force, considering that the density of natural gas under high temperature and high pressure is 10–100 times that under normal temperature and pressure [9], the buoyancy F_B (the formula (1)), additional mass force F_M(the formula (2)), pressure gradient force F_P (the formula (3)) and Saffman lift F_S (the formula (4)) of particles in the pipe string can not be ignored, Therefore, the above forces between gas-solid and gas-liquid-solid are considered in Fluent simulation calculation, so as to make the simulation closer to the actual production situation of gas storage and study the erosion wear of gas storage pipe string.

$$F_B = \rho V_P g \tag{1}$$

$$F_P = -\frac{\pi d_p^3}{6}\frac{\partial p}{\partial h} \tag{2}$$

$$F_M = 0.5\frac{\pi d_p^3}{6}\rho a_p \tag{3}$$

$$F_s = 1.61 d_p^2 (\rho\mu)^{0.5}(v - v_p)|dv/dy|^{0.5} \tag{4}$$

3.3 Analysis on Erosion Law of Pipe String

Based on the temperature and pressure field of the pipe string in a gas storage, the simulation parameters of continuous phase and discrete phase are calculated and input. Select standard k ~ ε turbulence model is used to calculate, the fluent DPM model is used to set the interaction between particles and continuous phase, and the McLaury erosion model [8] is selected as the judgment basis of pipe string erosion amount to explore the erosion law of vertical section and inclined section of pipe string.

$$ER = C * F_s * V_p^n * F(\alpha) \tag{5}$$

3.3.1 Analysis on Erosion Law of Vertical Section of Pipe String

3.3.1.1 Effect of Flow Velocity on Pipe String Erosion

Assuming that the injected particles are spherical and other influencing factors remain unchanged, change the flow velocity to study the change of the maximum erosion amount of the pipe string. In order to ensure the full development of the flow field, inject particles after the flow field converges (about 1.5 s) to obtain the overall and local enlarged nephogram of the pipe string erosion amount, as shown in Fig. 3. It can be seen from the nephogram that the erosion degree of the pipe string wall is relatively uniform. Under different flow velocity, the maximum erosion amount of the pipe string changes with time, as shown in Fig. 4. It can be seen from the figure that the maximum erosion amount of the pipe string increases with the increase of time, because when the number of particles injected is the same, the kinetic energy of the particles increases with the increase of flow velocity, and the impact force when the particles hit the wall increases, Thus, the erosion amount of the pipe string increases; With the increase of particle kinetic energy, the frequency of the same number of particles hitting the wall also increases, which will also increase the change of erosion amount. Finally, the maximum erosion amount of pipe string shows an exponential growth trend with the increase of flow velocity, as shown in Fig. 5.

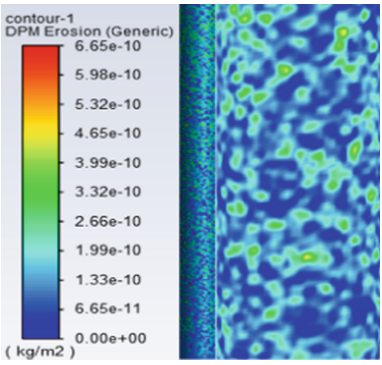

Fig. 3. Nephogram of erosion amount in vertical section of pipe string

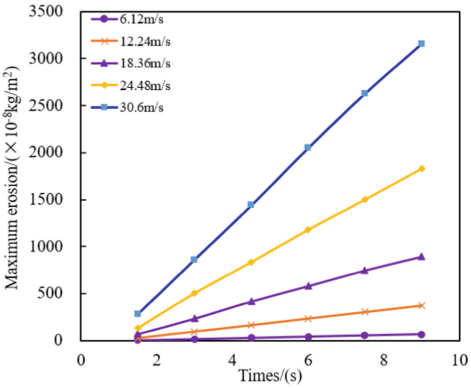

Fig. 4. Variation of maximum erosion amount of pipe string with time

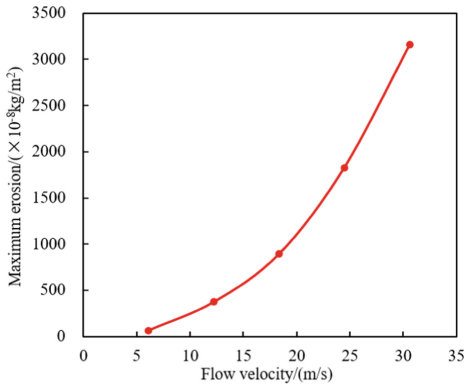

Fig. 5. The maximum erosion amount of pipe string varies with flow velocity

3.3.1.2 Effect of Particle Mass Flow on Pipe String Erosion

Assuming that the injected particles are spherical and other influencing factors remain unchanged, change the particle mass flow to study the change of the maximum erosion amount of the pipe string. The particle injection time is the same as the above setting. The maximum erosion amount of the pipe string changes at any time under different particle mass flow, as shown in Fig. 6. The maximum erosion amount of the vertical pipe section of the pipe string increases with the increase of the particle mass flow. This is because when other conditions remain unchanged, increasing the mass flow of particles will increase the number of particles injected into the pipe string per unit time, increase the probability of particles hitting the wall, make more particles hit the inner wall of the pipe string, cause erosion to the pipe string, and finally lead to a roughly linear increase in the maximum erosion of the pipe string with the increase of particle mass flow, as shown in Fig. 7.

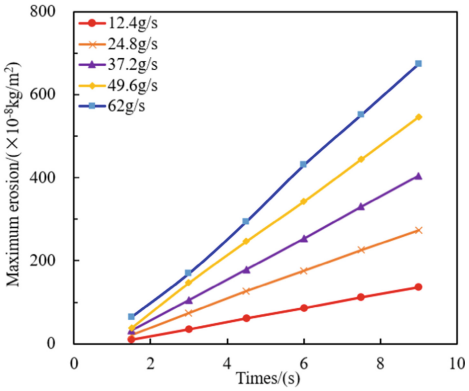

Fig. 6. Variation of maximum erosion amount of pipe string with time

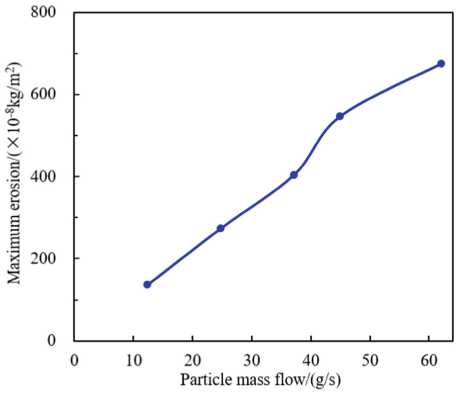

Fig. 7. The maximum erosion amount of pipe string varies with particle mass flow

3.3.1.3 Effect of Particle Diameter on Pipe String Erosion

Assuming that the injected particles are spherical and other influencing factors remain unchanged, change the particle diameter to study the change of the maximum erosion amount of the pipe string. The particle injection time is the same as the above settings. Under different particle diameter, the maximum erosion amount of the pipe string changes with time, as shown in Fig. 8. It can be seen from the figure that the maximum erosion amount of the pipe string decreases with the increase of the particle diameter, This is because when the particle mass flow remains unchanged, the increase of particle diameter means that the number of particles injected decreases, and the number of particles impacting the inner wall of the pipe string decreases, resulting in the decrease of the maximum erosion amount of the pipe string with the increase of particle diameter, as shown in Fig. 9.

Unfortunately, this conclusion is consistent with the results of some scholars, but because the particle diameter studied is relatively small, the "particle size effect" of the particles is not found, that is, the erosion amount of the pipe string decreases with the

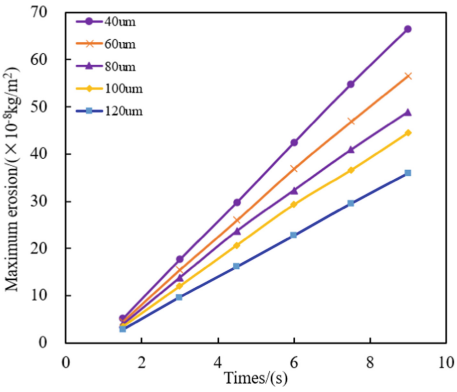

Fig. 8. Variation of maximum erosion amount of pipe string with time

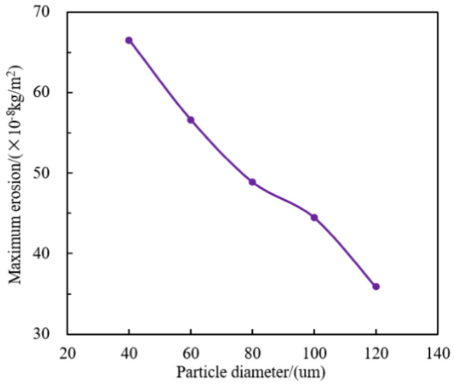

Fig. 9. The maximum erosion amount of pipe string varies with particle diameter

increase of the particle diameter, but when the particle diameter increases to a certain value, and then continues to increase the particle diameter, the erosion amount of pipe string will also increase. In the follow-up work, it is necessary to further study the influence of particle diameter on the erosion of gas storage pipe string [10–12].

3.3.2 Analysis on Erosion Law of Inclined Section of Pipe String

3.3.2.1 Effect of Particle Mass Flow on String Erosion

Assuming that the injected particles are spherical and other influencing factors remain unchanged, change the particle mass flow to study the change of the maximum erosion amount in the inclined section and the change of the maximum erosion amount of the pipe string with time, as shown in Fig. 10. The erosion law of the particle mass flow on the inclined section of the pipe string is consistent with that of the verticle section, which is not repeated.

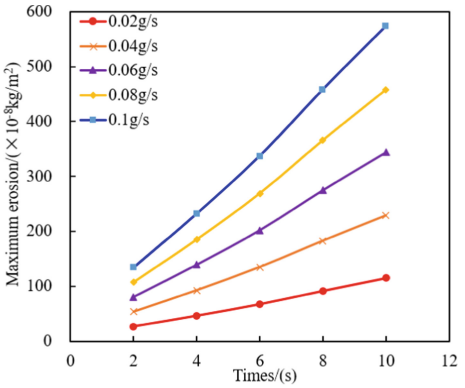

Fig. 10. Variation of maximum erosion amount of pipe string with time

3.3.2.2 Effect of Water Content on String Erosion

Assuming that the injected particles are spherical and other influencing factors remain unchanged, the Euler-DPM model in Fluent simulation software is used to set the first item of continuous phase as gas phase and the second item as liquid phase. The settings of flow velocity, particle mass flow and particle diameter are shown in case 5 in Table 2. The variation of maximum erosion amount with water content in inclined section of string is studied.The nephogram of gas-liquid volume fraction is shown in Fig. 11. It is found that due to the small volume fraction of the liquid phase, the liquid phase is dispersed by the gas phase during injection at the inlet of the pipe string, showing the state distribution of discrete droplets. With the continuous injection of the liquid phase, the droplets continue to gather along the pipe string, at the upper end of the inclined pipe string, the liquid phase is distributed as a continuous phase, and the maximum erosion amount of the pipe string changes with time, as shown in Fig. 12. It can be seen from the figure that under the production condition of low water content, The change of water content has little impact on the erosion of pipe string. Compared with the erosion amount of pipe string without water, the maximum erosion amount of pipe string is little different. Some scholars have found that the existence of liquid film will alleviate the erosion effect of pipe string, but the interaction between sand particles, liquid droplets and liquid film needs to be further discussed [13, 14].

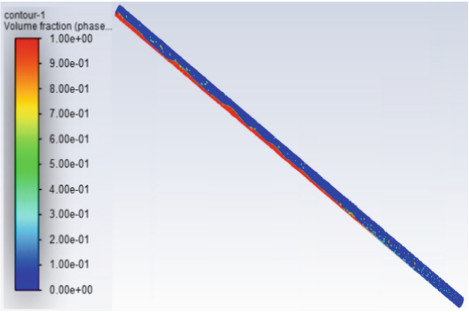

Fig. 11. Nephogram of gas-liquid volume fraction

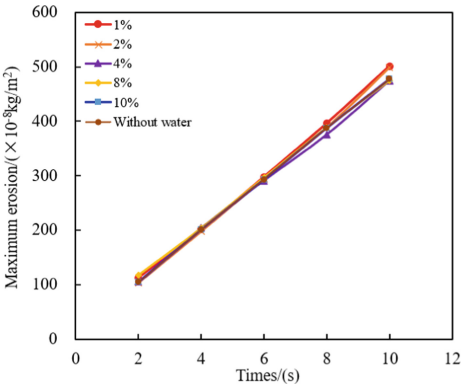

Fig. 12. Variation of maximum erosion amount of pipe string with time

4 Conclusion

The buoyancy F_B, additional mass force F_M, pressure gradient force F_P and Saffman lift F_S of particles can not be ignored. By considering the above forces of particles, the gas-solid, gas-liquid-solid coupling effect during erosion in pipe string is more comprehensive. The erosion simulation of vertical and inclined sections of pipe string with sand and liquid-carrying in gas storage is carried out. The result shows that on the premise that other conditions remain unchanged, the maximum erosion amount of pipe string increases with the increase of flow velocity, presenting an exponential trend; With the increase of particle mass flow, the maximum erosion amount of pipe string increases linearly. Due to the small particle size, the maximum erosion amount decreases with the increase of the particle diameter, but the "particle diameter effect" of the particles is not found, so further simulation is also needed. When the water content is low, the maximum erosion amount of the pipe string changes little with the water content. The interaction between sand, droplets, and liquid film needs to be further discussed. Under the accelerating trend of gas storage construction in China, the research on the erosion law of pipe string under different working conditions has important theoretical guidance and practical significance to ensure the safe and efficient injection and production of gas storage.

Symbol Description

ρ—Particle density, kg/m^3
V_p—Volume of particles, m^3
g—Normal setting 9.81, kg/m^2
d_p—Particle diameter, m
$\frac{\partial p}{\partial P}$-—Pressure gradient, pa/m
a_p—Acceleration of particles, kg/m^2
μ—Viscosity of natural gas, mPa·s

v—Continuous phase velocity, m/s
v_p—Particle velocity, m/s
dv/dy—velocity gradient, 1/s
ER—Pipe string erosion, kg/m^2
C—Empirical constant
n—Speed index
F_s—Particle shape coefficient, Spherical particle, $F_s = 1$
$F(\alpha)$—Particle impact angle function

References

1. Ding, G., Ding, Y., Li, Y., et al.: Development prospect of underground gas storage inChina under carbon neutralization strategy. Oil Gas Storage Transp. 1–11 (2021)
2. Zhou, S., Wang, J., Liang, Y.: Development of China's natural gas industry during the 14th Five-Year Plan in the background of carbon neutrality. Nat. Gas Ind. **02**(41), 171–182 (2021)
3. Sui, Y., Lin, T., Liu, X., et al.: The influence of alternating load on sand production law of injection/production wells of underground gas storages. Oil Gas Storage Transp. **38**(3), 303–307 (2019)
4. Yi, F.: Analysis on sand production law of Shuang 6 gas storage. In: 2018 National Natural GasAcademic Conference. Natural Gas Professional Committee of China Petroleum Society (2018)
5. Li, G., Liu, F., Song, G., et al.: Matching techniques of process pipe string for injection and recovery wells in Dazhangtuo underground gas storage. Nat. Gas Ind. (09), 156–158 (2004)
6. He, Z., He, T., Yi, W., et al.: Development suggestions and production technologies and development of Sinopec's gas storage of depleted gas reservoir type. Geol. Explor. **56**(03), 605–613 (2020)
7. Najafifard, F.: Predicting near wall particle behavior withapplication to erosion simulation. The University of Tulsa (2014)
8. Mclaury, B.S.: Predicting solid particle erosion resulting from turbulent fluctuations in oil field geometries. The University of Tulsa (1996)
9. Li, H.: Theoretical and experimental research on gas-sand two-phase flow in natural gas exploration. Sichuan University (2004)
10. Peng, W., Cao, X.: Analysis on erosion of pipe bends induced by liquid-solid two-phase flow. J. Chin. Soc. Corros. Prot. **35**(06), 556–562 (2015)
11. Chen, Z.: Numerical simulation on erosion and wear of fracturing manifold and analysis of the mechanical behavior. Dalian University of Technology (2021)
12. Xu, X.: Numerical simulation of solid particle erosion and wear in oil and gas pipelines. Liaoning University of Ptroleum and Chemical Technology (2020)
13. Liu, M., Liu, H., Zhang, R.: Numerical analyses of the solid particle erosion in elbows for annular flow. Ocean Eng. **105**, 186–195 (2015)
14. Peng, W.: Study on the solid particle erosion mechanism of pipe bend for multiphase flow. China University of Petroleum (East China) (2017)

Analysis of Combined Gas Lift and Electric Submersible Pump Lifting Wellbore Fluid Production in a Heavy Oil Block in South China Sea

Na Xu, Yonghai Gao(✉), Hongxing Yuan, Xinyao Su, Shaoqiang Li, and Yaqiang Qi

School of Petroleum Engineering, China University of Petroleum (East China), Qingdao 266580, China
upcgaoyh@126.com

Abstract. In recent years, as a kind of unconventional oil energy, heavy oil has large reserves and wide distribution, and the issue of marine heavy oil exploitation has gradually attracted attention. Especially, the temperature near the mud line was low, the viscosity of heavy oil increases exponentially, and it was difficult to flow. Therefore, taking appropriate lifting measures to improve wellbore flow had become the focus of current research. In this paper, multi-phase flow dynamic theory was used to model artificial lift of heavy oil well in a certain block in the South China Sea, including gas lift, gas lift-electric submersible pump (GL-PCP) combined thermal insulation pipe technology. Compared with no lifting measures, the fluidity of heavy oil vertical wellbore was explored. The simulation results showed that the liquid production of heavy oil increased obviously with the injection of natural gas. With the addition of electric submersible pump, the liquid production effect of gas lift was improved compared with that of single lift, and the pressure gradient was obviously reduced. In addition, the fluid temperature near the mud line was low, and the minimum temperature could be appropriately raised by combining the insulation pipe. It was of great significance to optimize artificial lifting method of heavy oil and ensure wellbore fluidity.

Keywords: Offshore heavy oil · Gas lift · Gas lift-electric submersible pump · Fluid producing

1 Introduction

The depletion of light crude oil reserves has led to the increasing importance of unconventional oil and gas. Heavy oil plays an important role. Developing new technologies to increase offshore heavy oil recovery by 5–10%. According to the latest oil and gas resource evaluation data, the accumulative proven oil and gas reserves in China's offshore areas are $53 * 10^8$ t and $14.37 * 10^{11}$ m^3, which were mainly distributed in Bohai Sea, Pearl River Estuary and other basins [1–3]. Heavy oil has high viscosity and is extremely sensitive to temperature. Ambient temperatures near the deep cement line were often in the single digits, and some offshore fields suffered from poor liquidity and low fluid

B. Sun et al. (Eds.): DWOG-Hyd 2021, LNCE 246, pp. 251–257, 2022.
https://doi.org/10.1007/978-981-19-0960-3_25

production even when exploration results showed good reservoir properties and shallow water. As the viscosity of heavy oil is greatly affected by temperature, heating were often used to improve wellbore fluidity in Bohai oilfield, including cable (electromagnetic) heating, rod pump heating, insulation pipe, etc. However, in some offshore oil fields, the results of field trial production could not reach the ideal state in the testing process of using progressing cavity pump heating and coiled tubing gas lift.

Due to environmental constraints, there were fewer offshore exploratory wells compared to land, and the actual situation of the oil reservoir was not well understood. When the actual reservoir performance was significantly different from the forecast, it was necessary to pull up the tubing string and redesign the equipment parameters, which made it impossible to carry out other lifting. The gas lift equipment was simple, without lifting column and wide range of displacement, which was very suitable for offshore oilfield production [4, 5]. The pump displacement of electric submersible pump could be well matched with the gas lift displacement without conflict. When the depth of oil well was increasing, the single lifting method need to continuously pressurize and increase power, resulting in the limitations of equipment working condition resistance, shortened repair free period, huge investment consumption and so on. Combined lift was generally considered on the surface to be suitable for ultra-deep wells over 4,500 m deep [6]. When oil fields were distributed offshore and deep heavy oil wells, combined lifting could also be applied, which had important reference significance for future Marine heavy oil exploitation.

2 Temperature-Pressure Model of Combined Gas Lift and Electric Submersible Pump

2.1 Model Hypothesis

In order to facilitate the establishment of the combined electric submersible pump-gas lift model, the assumptions were as follows:

(1) Formation fluids instantaneously mix with injected gas.
(2) The two-phase flow in the wellbore was one-dimensional flow along the wellbore direction.
(3) Each phase fluid was regarded as a continuous medium composed of numerous fluid particles.

2.2 Model Building

Before calculating the temperature and pressure of the well, it was necessary to understand the inflow behavior of the well. This was a prerequisite for modeling [9]:

$$Q_l = J_l\left(p_r - p_{wf}\right) \tag{1}$$

Among them, Q_l was liquid production, m^3/d; J_l was the liquid production index, $m^3/(d.MPa)$; p_r was formation pressure; p_{wf} was the bottom hole pressure, MPa.

When gas-liquid two-phase flow state appears in wellbore, the change of pressure would lead to complex change of flow pattern, presenting different morphology, and then change the pressure gradient along the wellbore. The total pressure drop was divided into four parts: gravity pressure drop, friction pressure drop, acceleration pressure drop and pump work pressure drop, considering gas lift and electric submersible pump work [7].

$$-\frac{dP}{dZ} = \rho g sin\theta + f\frac{\rho}{d}\frac{v^2}{2} + \rho v\frac{dv}{dZ} + \rho\frac{dW}{dZ} \tag{2}$$

Among them, $\frac{dP}{dZ}$ was the pressure gradient, Pa/m; ρ was the fluid density, kg/m^3; g was the acceleration of gravity, m/s^2; θ is the Angle between the pipe and the horizontal direction, °; f was the two-phase resistance coefficient, dimensionless; d was the diameter of the circular tube, m; v was the apparent flow rate of mixed phase, m/s; W was Lifting system energy, J;

Friction coefficient and liquid holdup should be determined to calculate wellbore flow pressure gradient, and in the heavy-oil combined lifting method, viscosity characteristics of heavy oil were key parameters in the calculation of liquid holdup and friction coefficient. In this study, viscosity changes after dissolved gas of heavy oil were calculated by the dissolved gas heavy oil model proposed by D.Brant Bennion [8]:

$$lg\left[lg(\mu)\right] = A_1 + A_2 \cdot T + A_3 \cdot p + A_4\frac{P}{T} + A_5\frac{T^2}{P} + A_6 \cdot API^\circ \tag{3}$$

Among them, μ was the viscosity of heavy oil after dissolved gas, mpa.s; A_1–A_6 was a constant, dimensionless; P was pressure, MPa; T was temperature, K.

In the process of modeling the temperature of the multiphase flow with the combined electric submersible pump and gas lift, it was necessary to calculate the temperature iteratively from the bottom of the tubing upwards along the wellhead. The gas lift equipment was placed at the upper part of the whole system, and the electric submersible pump was located at the lower part of the system. Thus, the temperature field calculation model was as follows [9]:

$$T_{out} = T_{in} - \left[\frac{K_L(T_S - T)}{G_f C_f} - \frac{gcos\theta}{C_f}\right]\Delta h + \Delta t \tag{4}$$

Among them, T_{out} was the fluid outflow temperature, °C; T_{in} was the inflow temperature of fluid, °C; T was the temperature between the injected gas and the gas injection point in the oil jacket annulus, °C; T_S was the temperature of injected gas at the casing annulus wellhead, °C; G_f was the mass flow rate of wellbore fluid, kg/s; C_f was the specific heat of wellbore fluid, J/(kg.°C); Δh was the interval length, m; Δt was the temperature increase of upper cable of electric submersible pump, °C.

When the annulus injected gas at different temperatures into the gas lift valve [9]:

$$G_{lt} \cdot C_{plt} + G_{gt} \cdot C_{pgt} \cdot (T_t - T) = G_{gin} \cdot C_{pgin} \cdot (T - T_{in}) \tag{5}$$

Among them, C_{plt} was the specific heat of formation produced fluid, J/(kg.°C); C_{pgt} was the specific heat of gas, J/(kg.°C); G_{lt} was the mass flow rate of produced fluid, kg/s;

G_{gt} was the mass flow rate of produced gas, kg/s; G_{gin} was the injected gas mass flow rate, kg/s; C_{pgin} was the specific heat of injected gas, J/(kg.°C); T_{in} was the temperature of formation produced fluid, °C; T was the temperature of formation fluid and gas mixture, °C; T_{in} was injection temperature degree, °C.

3 Analysis of Simulation Results

3.1 Model Validation

Taking a heavy oil block in the South China Sea as an example, the well depth was 3,500 m, the water depth was 158 m, the vertical well, the sea surface ambient temperature was 30 °C, the temperature near the bottom mud line was 5 °C, the reservoir temperature was 135 °C, and the pressure was 40 MPa. The overall well structure was shown in Fig. 1. The gas-lift valve was 2000 m away from the wellhead, the injected gas was natural gas, the gas temperature was 20 °C, the electric submersible pump was set 3300 m away from the wellhead, the viscosity of heavy oil was 181 mPa.s, the density was 0.87 g/cm^3, the content of each carbon component was shown in Table 1, and the heat conduction coefficient of tubing and casing was 48 W/(m. °C).

Table 1. Heavy oil components

Components	The mole fraction/%	Components	The mole fraction/%
C1–C10	1.3	C11–C20	34
C21–C30	56.7	C30+	8

3.2 Analysis of Liquid Production

Figure 2 showed the change curves of tubing fluid production under three different lifting conditions: no measure, gas lift, GL-ESP. The horizontal axis was the length of tubing from bottom to wellhead. Without any lifting measures, the well production was stable at 29.8 m^3/d. After the injection of natural gas, it could be seen that the liquid production at the gas injection point had a significant increase, and the liquid production could reach about 51 m^3/d. After the addition of electric submersible pump on the basis of gas lift, the fluid production was also increased to a certain extent compared with the first two types, and the final wellhead fluid production can reach about 55 m^3/d. Through the comparison of the three, it could be seen that after gas lift and electric submersible pump were added into the heavy oil wellbore, the liquid production of heavy oil was improved, and the advantage of combined lift was greater than that of single lift.

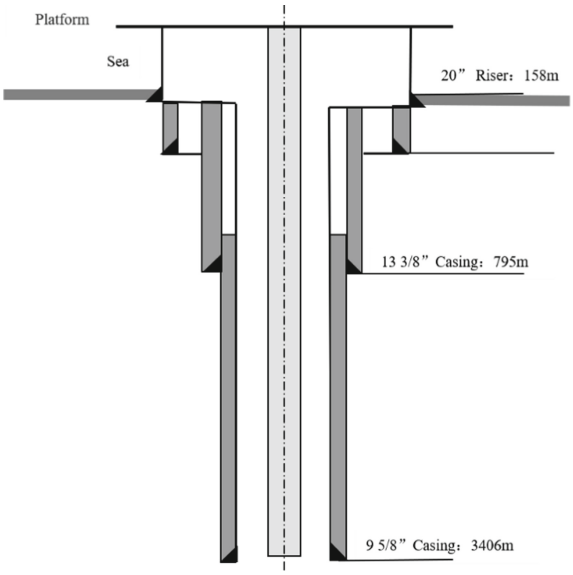

Fig. 1. Well structure of the well

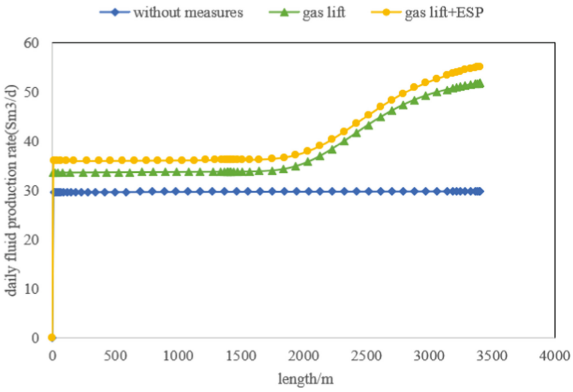

Fig. 2. Fluid production from heavy oil wellbore with different lifting measures

3.3 Temperature Analysis

As shown in Fig. 3, wellbore temperature change curves along the wellbore under three different lifting conditions of no measure, gas lift, GL-ESP were obtained respectively. It could be seen that the low ambient temperature near the mud line made the liquid production temperature appear an obvious inflection point, about 12–15 °C; After the injection of natural gas, the temperature mutation of 3–4 °C occurred at the injection point. The small change of the mutation temperature might be due to the large flow rate of wellbore liquid, low injection temperature and low flow rate, and no big fluctuation

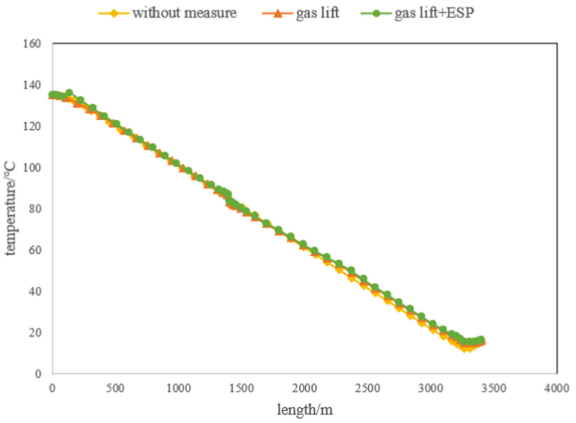

Fig. 3. Wellbore temperature curves of heavy oil with different lifting measures

occurs after the two-phase mixing. After the electric submersible pump was added, the temperature increased to a certain extent due to the pump working temperature.

3.4 Pressure Analysis

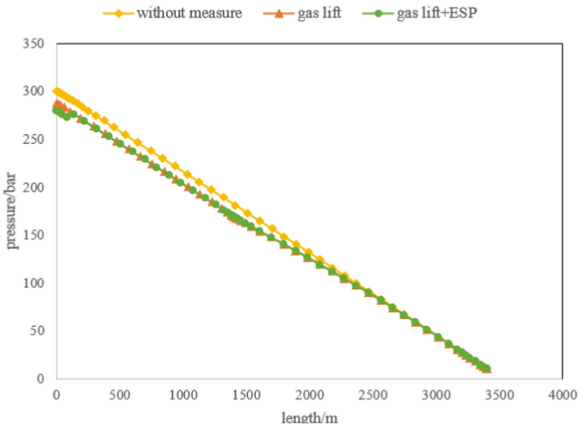

Fig. 4. Wellbore pressure variation curve of heavy oil with different lifting measures

As shown in Fig. 4, variation curves of wellbore pressure along the wellbore under three different lifting conditions of no measure, gas lift, GL-ESP were obtained respectively. It was observed that the wellbore pressure gradient decreased with gas injection compared to no lift. The change in wellbore pressure using GL-ESP is similar to that of gas lift alone.

4 Conclusion

In view of the wellbore flow problem of a heavy oil block in the South China Sea, the feasibility and application effect of GL-ESP combined lifting for improving heavy oil flow were analyzed theoretically for the first time.

Analysis of numerous measures, gas lift, GL+ESP three different lifting methods of heavy oil wellbore fluid producing, the change of temperature, pressure curve, found that compared with no lifting measures, gas lift, GL-ESP two ways could effectively increase the production, to reduce the pressure gradient, and the combination lifting effect was superior to the single gas lift; In addition, the temperature near the mud line was low, so it was suggested to cooperate with insulation pipe to reduce wellbore temperature loss and improve the fluidity of heavy oil.

References

1. Jia, C.Z.: Development challenges and future scientific and technological researches in China's petroleum industry upstream. Acta Pet. Sin. **41**(12), 1445–1464 (2020)
2. Xie, Y.H.: Progress and thinking of CNOOC oil and gas exploration under the background of low oil prices. China Offshore Oil Gas **33**(01), 1–12 (2021)
3. Aitken, K.J., Allan, D., Holmes, J.D.: Combined ESP/auto gas lift completions in high GOR/high sand wells on the Australian Northwest shelf. SPE 64466 (2000)
4. Jiang, Y.: Optimization of borehole viscosity reducing method while offshore heavy oil lifting. China University of Petroleum, Beijing (2016)
5. Yu, J.F., Lv, X.M., Liu, S.J., et al.: Adaptive analysis on offshore heavy oil lifting. Petrochem. Ind. Technol. (6), 2 (2015)
6. Mali, P., Al-Jasmi, A.: Evaluation of artificial lift modes for heavy oil reservoirs. Paper Presented at the SPE Heavy Oil Conference-Canada, Calgary, Alberta, Canada, June 2014
7. Sun, D.X., Tan, C.D., Kan, C.X., et al.: Coupling model of GL-ESP combined lift for offshore oil well. China Pet. Mach. **45**(9), 6 (2017)
8. Han, J.W.: Study of flow characteristics of heavy oil solution gas. China University of Petroleum (East China), Qingdao (2018)
9. Qiu, Z.J.: Analysis and research on combined lift design of electric submersible pump and gas lift. China University of Petroleum, Beijing (2018)

Experimental Study on Hydrate Anti-agglomerants Performance of Plant Extracts in Oil-Water System

Jiakai Ji, Pengcheng Jing, Yuxiang Xia, Haotian Wang, Xin Jiang, and Litao Chen(✉)

Key Laboratory of Unconventional Oil and Gas Development, Ministry of Education, China University of Petroleum (East China), Qingdao 266580, China
chenlt@upc.edu.cn

Abstract. Pipeline blockages and ruptures caused by natural gas hydrates are the main problems in ensuring the flow of oil and gas, especially in the deep sea and pipeline throttle parts. Anti-agglomerant is one of the effective methods to prevent the blockage of natural gas hydrate. In this work, a high-pressure hydrate rocking reactor was used to evaluate the inhibitory properties of saponins extract, soapwort extract, camellia seed extract and sapindus extract on methane hydrate polymerization. The hydrate volume fraction and the position image of the slider are used to reflect the inhibition performance of the plant extract on methane hydrate. The data shows that plant extracts can promote the formation of methane hydrate. Compared with the system without anti-agglomerant, the volume fraction of methane hydrate increased respectively by 11.28, 11.78, 12.1, 13.57% when the concentration of the extract of saponins was 0.5, 1, 1.5, and 2 wt%. And as the concentration of saponins extract increases, its effect on promoting hydrate formation is more obvious. Judging from the position image, as the concentration increases, the saponins extract and soapwort extract can delay the methane hydrate blockage time. This phenomenon is not observed in the camellia seed extract and the sapindus extract. When the concentration of soapwort extract is 1.5 wt%, it has a certain anti-agglomerant effect, and the slider is not completely blocked by the hydrate in the end, and it moves in the range of 110 mm to 128 mm. camellia seed extract and sapindus extract have no anti-agglomerant effect.

Keywords: Methane · Hydrate · Anti-agglomerant · Plant extract · Experiment

1 Introduction

Gas hydrates are non-stoichiometric clathrate crystal substances formed by water and small molecular gases such as methane (CH4), ethane (C2H6), carbon dioxide (CO2) and hydrogen sulfide (H2S), so they are also called clathrate hydrates [1, 2]. At present, there are three types of hydrate structures that have been discovered, which are customarily referred to as structure I (sI), structure II (sII) and structure H (sH) [3]. The blockage of natural gas hydrates in pipelines is a major flow safety issue in the oil and gas industry. In the development of deep-water oil and gas, the high-pressure and low-temperature

B. Sun et al. (Eds.): DWOG-Hyd 2021, LNCE 246, pp. 258–266, 2022.
https://doi.org/10.1007/978-981-19-0960-3_26

environment at the mudline on the seabed makes it easy for hydrate to form, deposit and block in the pipeline. The blockage of natural gas hydrate in the pipeline will cause safety risks to the transportation and production system, and may cause significant economic losses [4].

Inhibition of hydrate formation in the pipeline is achieved by dehydration, depressurization, heating or chemical methods. Depressurization and heating methods can easily lead to the risk of pipeline rupture. Chemical methods usually use thermodynamic inhibitors, kinetic inhibitors and anti-agglomerants to inhibit the formation and blockage of hydrates [5]. Among them, the thermodynamic inhibitor breaks the phase equilibrium conditions of the hydrate, so that the formation of the hydrate requires a higher pressure and lower temperature, thereby inhibiting the formation of the hydrate. Kinetic inhibitors can inhibit hydrate nucleation and delay the time of hydrate formation. Anti-agglomerant can be adsorbed on the surface of the hydrate particles to prevent the crystal particles from further agglomerating, so that the hydrate particles can be suspended and dispersed without clogging [6].

Methanol is often used as a thermodynamic inhibitor to prevent the formation of hydrates in oilfields, but its amount is large, the cost is high, and the pollution is serious. Kinetic inhibitors are limited by the high subcooling [7]. Sorbitol [8], rhamnolipids [9] and some plant-extracted anti-agglomerants discovered in recent years are the few environmentally friendly hydrate anti-agglomerants so far. Plant-derived anti-agglomerants have the characteristics of good water solubility, easy biodegradation, and environmental friendliness [10]. In this work, several kinds of plants were extracted, their extracts were obtained, and the performance evaluation experiments of anti-agglomerants were carried out on several plant extracts.

2 Experimental Section

2.1 Materials

The materials and reagents used in the experiment are shown in Table 1.

2.2 Apparatus

As shown in Fig. 1, the instruments used in the experiment are: constant temperature magnetic stirrer, vacuum pump, high-pressure hydrate rocking reactor. Figure 1 shows the experimental equipment in this experiment. The high-pressure stainless steel reactor with a design pressure of 30.00 MPa provides a place for the formation and decomposition of hydrates. Each kettle has a capacity of 150 ml, and there are 4 reaction cells in total. There are sliders in the cell, which can be used to determine whether the hydrate is blocked or not. A cooling water bath and a gas cylinder are used to provide the required temperature and pressure for the experimental system. The data collection terminal can display and record the experimental temperature and pressure in real time. The temperature sensor range is 223.15 K to 373.15 K, the measurement accuracy is $\pm$ 0.1 K, the pressure sensor range is 0 MPa to 40 MPa, the accuracy is $\pm$ 0.25%, and the position sensor's working temperature range is 233.15 K to 348.15 K. The gas cylinder provides the gas source, and the vacuum pump is used to extract the air in the cell.

2.3 Experimental Steps

The experiment is divided into two parts: plant extraction and evaluation of anti-agglomerant.

The first is the extraction part: the plant grinding powder is placed in an oven at 353.15 K and dried for 24 h, 5 g is weighed and placed in a flask, 100 ml of deionized water is added, fixed in a water bath, and the temperature is set to 353.15 K. Turn on the thermostatic magnetic stirrer, heat and reflux for 4 h, perform suction filtration while it is hot, and dry the obtained filtrate to obtain a solid-phase plant extract.

The experiment of anti-agglomerant evaluation:

(1) Use deionized water to repeatedly clean the cell and dry it
(2) Mix 5# white oil, deionized water and plant extracts according to a certain ratio and add them into the kettle, tighten the end cap of the reaction kettle, evacuate sequentially, and set the water bath to 289.15 K;
(3) After the temperature in the cell is stable, turn on the gas cylinder switch, and pass high-purity methane gas into the cell. When the experimental pressure is reached, turn off the switch;
(4) Turn on the rocking kettle rocking system, at this stage the methane is quickly dissolved in the white oil;
(5) The pressure in the kettle is stable at about 8MPa, the temperature of the water bath is set to 273.15 K, the temperature is reduced at a constant cooling rate, the data acquisition system is turned on, and the temperature, pressure and position data in the kettle are recorded;
(6) After the temperature and pressure are stabilized again, it indicates that the hydrate formation is complete. Turn off the water bath and data acquisition system, turn off the rocking system, exhaust the gas in the kettle, and pour out the waste liquid in the reaction kettle;
(7) Replace other plant extracts and repeat (1) to (6).

2.4 Calculation of Hydrate Volume Fraction

The amount of methane gas after dissolution equilibrium $n1$:

$$n_1 = \frac{P_1 V_1}{ZRT_1} \tag{1}$$

Among them, P_1 is the stable pressure after dissolution equilibrium, MPa; T_1 is the stable temperature after dissolution equilibrium, K; V_1 is the gas volume in the kettle, mL; Z is the compressibility factor of methane at the temperature and pressure can be obtained by the Patel-Teja equation of state, R is the ideal gas constant, taking $8.314\ \mathrm{J \cdot mol^{-1} \cdot K^{-1}}$.

The amount of methane gas after the hydrate formation pressure stabilizes n_2:

$$n_2 = \frac{P_2 V_2}{ZRT_2} \tag{2}$$

Where: P_2 is the stable pressure after hydrate formation, MPa; T_2 is the stable temperature after hydrate formation, K; V_2 is the volume of gas in the kettle, mL.

Then the amount of methane gas consumed is:

$$n_{gas} = n_1 - n_2 \tag{3}$$

The molecular formula of methane hydrate is $CH_4 \cdot 6H_2O$, that is, 1 mol hydrate is composed of 1 mol methane and 6 mol water. The mass of the hydrate formed and the water consumed can be calculated based on the amount of methane gas consumed.

Volume of hydrate formed V_{hyd}:

$$V_{hyd} = \frac{m_{hyd}}{\rho_{hyd}} \tag{4}$$

Hydrate volume fraction ϕ:

$$\phi = \frac{V_{hyd}}{V_{hyd} + V_{oil} + V_{water} - V_{water,conv}} \tag{5}$$

Where: V_{hyd} is the volume of methane hydrate, mL; V_{oil} is the volume of the oil phase, mL; V_{water} is the volume of the water phase; $V_{water,conv}$ is the volume of water converted to hydrate in the system, mL.

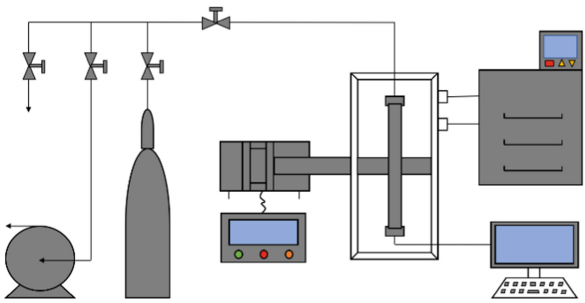

Fig. 1. Schematic diagram of high-pressure hydrate rocking device

3 Experimental Results and Discussion

A total of 4 groups of plant extract evaluation experiments were done. The water content of the experiment is 30%, the equilibrium pressure of dissolution is 8MPa, and the concentration of the plant extract is 0.5 wt%, 1 wt%, 1.5 wt% and 2 wt%, respectively.

Table 1. Materials used in the experiments

Name	Specification	Manufacturer
Deionized water	18.2 MΩ·cm	Lab homemade
CH4	99.999%	Xinkeyuan Gas Co., Ltd.
Saponins powder	100–200 mesh	Yaozhiyuan Medicinal Materials Co., Ltd.
Soapwort extract		Shaanxi Mufei Biological Technology Co., Ltd.
Camellia seed powder		Kaihua Junong Agricultural Development Co., Ltd.
Sapindus powder		Haozhou Congshen Chinese Medicine Firm
Mineral white oil	5#	Mojiezuo Petrochemical (Shanghai) Co., Ltd.

3.1 No Anti-agglomerant

Figure 2 shows the blank group, that is, the hydrate formation temperature, pressure, hydrate volume fraction and slider position curve without anti-agglomerant.

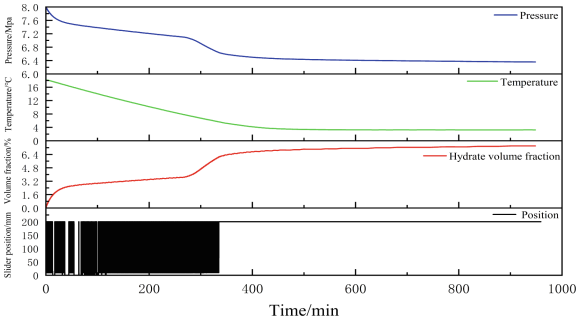

Fig. 2. Temperature, pressure, hydrate volume fraction and position curve in the cell

As the temperature drops to a certain value, the pressure drops suddenly, and hydrates are formed at this time. As the temperature continues to decrease, large amounts of hydrates are formed. When the volume fraction increases to 5.64%, the slider completely stops moving. At this time, it is only 5.3 h from the cooling point. After that, the slider has been blocked at the position of 200 mm. The final hydrate volume fraction was 7.42%, indicating that without the addition of anti-agglomerants, hydrate blockage is prone to occur in the system. Even if the amount of hydrate formation is small, there is a greater risk of hydrate blockage.

3.2 Contains Anti-agglomerant

As shown in Fig. 3, by analyzing the position images of different concentrations of the Ginsenoside extract, it can be found that the slider is not blocked immediately after the hydrate begins to form, and as the concentration of Ginsenoside extract increases, the duration of the movable range of the slider increases from 320 min. By 480 min, it shows that the saponins extract can delay the blockage time of hydrate. However, as the hydrate volume fraction increases, the sliders are eventually completely blocked.

Comparing the position images of different concentrations of soapwort extract, it is found that as the concentration increases, the duration of the movable range of the soapwort extract does not increase, but shows a trend of first decreasing and then increasing. When the concentration is 1.5 wt%, after the temperature and pressure are stabilized, the hydrate will no longer be formed, and the hydrate volume fraction will reach the maximum value. At this time, the slider is not completely blocked, and the position range is 110 mm to 128 mm. At this concentration, the polymerization will be inhibited. The effect is better than that of saponins extract. If it is compounded with other synergists, it may have a more significant inhibition effect, which can be further studied in the future.

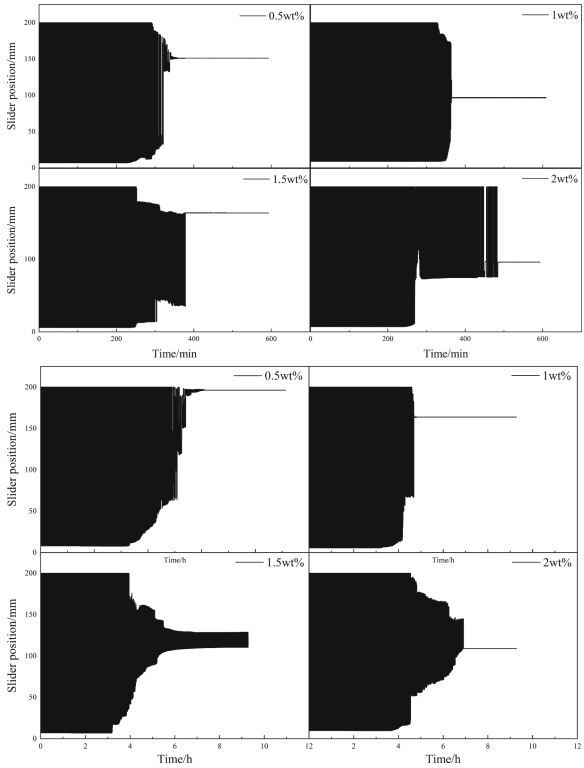

Fig. 3. Slider position image of saponins extract (up) and soapwort extract (down) at different concentrations

As can be seen from the position image in Fig. 4, no matter at low or high concentration, camellia seed powder extract and sapindus extract have no anti-polymerization effect. With the large amount of hydrate formation, the volume fraction increases, and the blocks are eventually jammed in a certain position.

Table 2 lists the hydrate volume fraction and the final hydrate volume fraction when plant-extracted anti-agglomerants are blocked at different concentrations.

It can be seen from the hydrate volume fraction in Table 2 that with the increase of the concentration of the saponins extract, the final hydrate volume fraction increases, indicating that it has a certain promoting effect on the formation of hydrates. This trend can also be observed in soapwort extract, but camellia seed extract and sapindus extract did not show a tendency to increase the final hydrate volume fraction as their concentration increased.

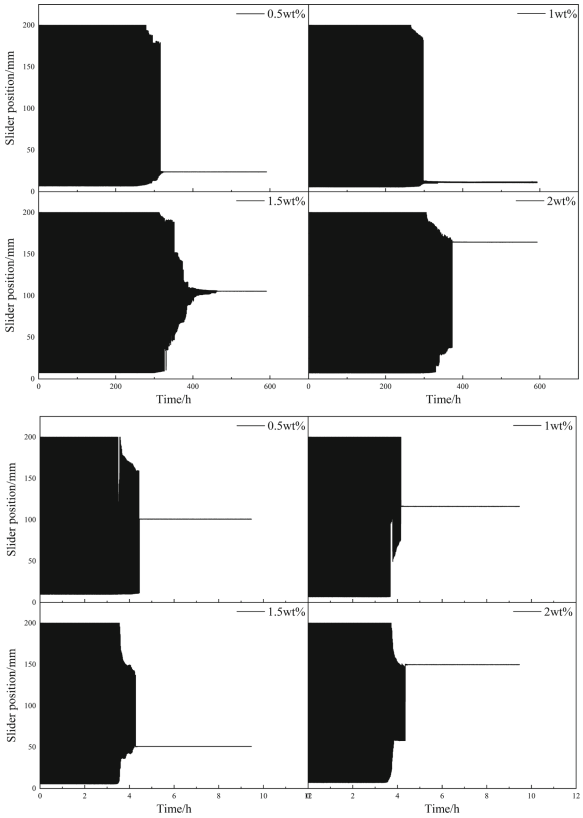

Fig. 4. Slider position images of camellia seed extract (up) and sapindus extract (down) at different concentrations

Table 2. Hydrate volume fraction

Name	Concentration/wt%	Hydrate volume fraction at blockage/%	Final hydrate volume fraction/%
No inhibitor	–	5.64	7.42
Saponins extract	0.5	6.48	18.7
	1	8.52	19.2
	1.5	10.8	19.52
	2	11.32	20.99
Soapwort extract	0.5	8.24	23.75
	1	12.76	24.39
	1.5	13.54	26.04
	2	15.47	23.87
Camellia seed extract	0.5	6.27	17.72
	1	5.76	10.94
	1.5	9.78	20.37
	2	7.43	15.96
Sapindus extract	0.5	3.16	4.03
	1	4.08	19.83
	1.5	5.12	8.14
	2	6.2	10.63

4 Conclusion

In this work, under the experimental conditions, the soapwort powder, camellia seed powder and sapindus powder were extracted and evaluated the hydrate inhibition performance of the saponins extract, soapwort extract, camellia seed extract, and sapindus extract. It was found that the saponins extract had the effect of delaying the hydrate blockage time, and as the concentration of the saponins extract increased, the effect of delaying the hydrate blockage time increased significantly, but in the end the hydrate was completely blocked. Soapwort extract also has a certain effect of promoting the formation of hydrates, and the slider is not completely blocked at a concentration of 1.5 wt%, and has a certain inhibitory effect. In the future, it will become a better anti-agglomerant through the potential of compounding. However, the camellia seed extract and the sapindus extract have no anti-aggregation effect.

Acknowledgement. The authors would like to appreciate the financial support from National Natural Science Foundation of China (grant Nos. 51991365, 51876222) and CNPC Major R&D Project (grant No. ZD2019-184-002).

References

1. Chen, G.J., Sun, C.Y., Ma, Q.L.: Gas Hydrate Science and Technology. Chemical Industry Press (2008)
2. Sloan, E.D., Koa, C.A.: Clathrate Hydrates of Natural Gases, 3rd edn. CRC Press, Boca Raton (2008)
3. Mohammadi, A.H., Richon, D.: Phase equilibria of methane hydrates in the presence of methanol and/or ethylene glycol aqueous solutions. Ind. Eng. Chem. Res. **49**(2), 925–928 (2010)
4. Chen, J., Yan, K.L., Chen, G.J., et al.: Insights into the formation mechanism of hydrate plugging in pipelines. Chem. Eng. Sci. **122**, 284–290 (2015)
5. Joshi, S.V., Grasso, G.A., Lafond, P.G., et al.: Experimental flowloop investigations of gas hydrate formation in high water cut systems. Chem. Eng. Sci. **97**(7), 198–209 (2013)
6. Xu, S., Fan, S., Fang, S., et al.: Pectin as an extraordinary natural kinetic hydrate inhibitor. Sci. Rep. **6**(1), 23220 (2016)
7. Yan, K.L., Sun, C.Y., Chen, J., et al.: Flow characteristics and rheological properties of natural gas hydrate slurry in the presence of anti-agglomerant in a flow loop apparatus. Chem. Eng. Sci. **106**, 99–108 (2014)
8. Xu, Z., Sun, Q., Gao, J., et al.: Experiment and model investigation of D-sorbitol as a thermodynamic hydrate inhibitor for methane and carbon dioxide hydrates. J. Nat. Gas Sci. Eng. **90**(1), 103927 (2021)
9. York, J.D., Firoozabadi, A.: Comparing effectiveness of rhamnolipid biosurfactant with a quaternary ammonium salt surfactant for hydrate anti-agglomeration. J. Phys. Chem. B **112**(3), 845 (2008)
10. Wang, X.Q., Qin, H.B., Ma, Q.L., et al.: Development of hydrate anti-agglomerant based on analysis of active components of plant extract. Chem. Prog. **35**(12), 7 (2016)

Discrimination Model of Critical Gas Velocity in Partial Falling Area of Kill Fluid in Deepwater Blowout

Lichen Guan[1], Zhiyuan Wang[1(✉)], Wenqiang Lou[1], Xueqi Liu[1], Dalin Sun[1], Peng Liu[1], and Wei Wang[2]

[1] School of Petroleum Engineering, China University of Petroleum (East China), Qingdao 266580, China
wangzy1209@126.com

[2] No. 5 Oil Production Plant, PetroChina Changqing Oilfield Company, Xi'an 710200, Shanxi, China

Abstract. In the unconventional well killing process of deepwater blowout, the movement state of kill fluid at the injection point is the key to the success of kill operation. In this paper, the vertical and visual killing fluid drop device designed by ourselves is used for experiment. It is found that the falling of kill fluid is not the relationship between "0" and "1", that is, when the gas velocity is lower than the critical gas velocity, the kill fluid will fall completely, otherwise the kill fluid will rise. The kill fluid injected into the wellbore is partially rising and partially falling. A discriminant model was established for the two critical gas velocities in part of the falling area. Compared with the experimental data, the fitting is good, which proves the accuracy of the model.

Keywords: Unconventional well killing · Kill fluid drop · Critical liquid carrying velocity of gas · Flow pattern conversion

1 Introduction

With the rapid development of national economy, China's demand for oil and gas is increasing. At present, China has become the second largest oil consumer in the world. Due to the relative shortage of domestic oil and gas resources, oil and gas production is difficult to support the rapid economic development, and the contradiction between supply and demand is becoming increasingly prominent [1]. The lack of oil and gas production has become the bottleneck of social development. In order to alleviate the energy problem, China actively develops deep-sea oil and gas resources. Deep water oil and gas production involves problems such as poor stability of seabed mudstone, easy formation of hydrate near mud line, limited working space, especially frequent invasion of high-pressure shallow gas, and narrow safe operation density window, which makes well control and killing operation face great challenges [2].

Well killing in petroleum exploration and development is to inject sufficient volume and appropriate performance of well killing fluid into the wellbore and re-establish

B. Sun et al. (Eds.): DWOG-Hyd 2021, LNCE 246, pp. 267–281, 2022.
https://doi.org/10.1007/978-981-19-0960-3_27

an effective hydrostatic column in the wellbore to balance the formation pressure and control the blowout accident [3]. However, the construction premise of conventional well killing method is to realize safe shut in, the drilling tools in the wellbore are at the bottom of the well, and the circulation of kill fluid can be realized [4]. In the process of well killing, it is always ensured that the bottom hole pressure is slightly greater than the formation pressure [5]. For special circumstances such as swabbing caused by tripping out without timely grouting, lack of shut in conditions at the wellhead after overflow, blowout of drilling fluid in the wellbore, no drilling tool in the well or the plugging of drilling tool is difficult to remove, and the drilling tool is not at the bottom of the well, the conventional well killing method cannot be applied, but the unconventional well killing method can only be applied [6].

In the process of unconventional well killing, the flow in the wellbore is complex and the pressure changes greatly [7]. The parameters such as liquid phase velocity, gas phase velocity and wellbore inclination will affect the flow in the wellbore and finally affect the well killing results. The motion state of kill fluid at the injection point is the key to the success of well killing [8]. The motion state of kill fluid after entering the wellbore is related to the rheological and physical parameters of fluid in the wellbore [9]. According to the previous research on the liquid carrying theory of gas wells, there is a critical liquid carrying gas velocity [10]. When the gas velocity in the wellbore is greater than the critical liquid carrying gas velocity, the kill fluid rises completely. When the gas velocity in the wellbore is less than the critical liquid carrying gas velocity, the kill fluid begins to fall. The common critical liquid carrying gas velocity models include minimum pressure gradient model, droplet model and liquid film model. According to previous studies, the reverse flow of liquid film is the reason for the fall of kill fluid [11].

In order to study the law of kill fluid drop and accurately predict the critical liquid carrying gas velocity, a vertical and visual kill fluid drop experiment is carried out. It is found that there are partial rise and partial fall of kill fluid drop. According to the two critical points of kill fluid drop, a discrimination model is established and compared with the experimental data, The results show that the model can accurately describe the critical gas velocity of kill fluid.

2 Kill Fluid Drop Test

In order to explore the law of killing fluid falling, a vertical and visual “killing fluid falling flux experimental device” is designed to carry out killing fluid falling experiments under different apparent gas velocity, apparent liquid velocity and different killing fluid viscosity.

2.1 Experimental Device

Vertical visual killing fluid drop experiment was carried out at room temperature and atmospheric pressure. The experimental device is mainly divided into three parts: gas input part, liquid input part and vertical visualization experiment part. The experimental device is shown in Fig. 1.

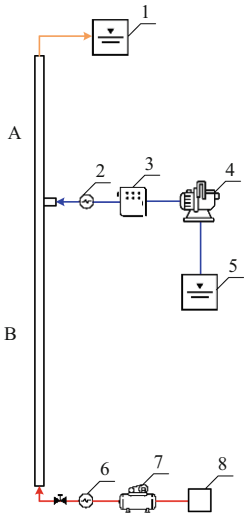

Fig. 1. Schematic diagram of visual kill fluid drop test device

In Fig. 1, 1 is a water tank for holding the liquid ejected from above the pipe; 2 is liquid float flowmeter, which is used to measure liquid flow rate; 3 is the liquid speed control box, which is used to control the speed of the gear pump; 4 is a gear pump, pumping liquid to the pipeline; 5 is a water tank containing experimental liquid; 6 is the gas float flowmeter, which is used to measure the gas flow rate; 7 is air compressor and 8 is gas-liquid separator.

The two sections of pipelines A and B constitute the vertical visualization experiment part. The length of section A is 3.28 m, the length of section B is 8.88 m, the total length of the pipeline is 12.16 m, the inner diameter is 4 cm, and the diameter of the liquid injection port is 3 cm. The material is plexiglass. In the vertical visualization experiment, the gas and liquid are mixed with each other to simulate the falling process of the kill fluid.

The red line in Fig. 1 represents the gas input part, which is composed of gas-liquid separator, high-pressure air compressor, high-pressure gas storage tank, high-pressure gas injection pipeline, high-pressure gas injection valve, etc. it is mainly used to provide experimental gas and inject the gas into the vertical visualization experiment part according to a certain flow.

The blue line in Fig. 1 represents the liquid input part, which is composed of high-pressure pipeline, liquid storage tank, gear pump, liquid velocity control box, etc. it is mainly used to provide experimental liquid and inject the liquid into the vertical visualization experiment part according to a certain flow.

2.2 Experimental Materials

In the experiment, the gas is air at room temperature, the liquid is water and sodium carboxymethyl cellulose solution with different viscosity. The model of food grade sodium carboxymethyl cellulose (CMC) is FH9 and the material is powder. It is produced

by Zhejiang Qinuo food ingredients Co., Ltd. and other parameters comply with gb1904–2005. The experimental water is laboratory tap water.

When preparing sodium carboxymethyl cellulose solution, first add 1000 L water into the plastic bucket, accurately weigh a certain amount of sodium carboxymethyl cellulose powder with an electronic balance, add a small amount of sodium carboxymethyl cellulose powder into the water several times using a dosage cup, and stir with a mixer. Stir with a mixer for several times to completely dissolve the sodium carboxymethylcellulose powder. The viscosities of each group were 18 mPa · s, 33 mPa · s, 40 mPa · s and 51 mPa · s respectively.

2.3 Experimental Process

During the experiment, the gas phase is compressed by the air compressor, buffered by the gas bottle, transported by the high-pressure pipeline, and injected into the wellbore after pressure regulation by the pressure regulating valve. The liquid phase is transported through the gear pump and into the wellbore through the infusion pipeline. At the beginning of the experiment, first open the gas channel, and then open the liquid channel after the air flow is stable to inject a fixed flow of liquid. In the experiment, the gas velocity gradually increased. After the gas was stable, the gear pump speed was adjusted, and the liquid was injected into the tube at a constant liquid velocity. The rise and fall of the liquid were observed and recorded at the liquid outlet by DV. After the liquid rises stably, cup the liquid from 1, and record the time and liquid volume. Multiple groups of experiments are carried out at the same gas velocity and liquid velocity to reduce the experimental error. After recording, stop liquid injection, greatly increase the gas velocity, blow out the residual liquid in the wellbore from the upper outlet to the liquid storage tank, and adjust the gas velocity for the next group of experiments. The drop of kill fluid under different gas velocity, liquid velocity and liquid viscosity was measured.

3 Falling Mechanism of Kill Fluid

3.1 Analysis on Falling Form of Kill Fluid

The movement state of kill fluid at the injection point is the key to the success of well killing. The motion state of kill fluid is affected by many factors, such as gas velocity, liquid velocity, liquid viscosity and so on. At present, the models used to distinguish the falling of liquid in the wellbore mainly include droplet model, liquid film model and flow pattern transformation model. In 1969, Turner [12] took the vertical well as the research object and assumed that the droplets in the wellbore were spherical. Through the stress analysis of the droplets with the largest diameter, as shown in Fig. 2, the critical gas velocity was obtained. Turner believes that when the gas velocity is greater than the critical gas velocity, the liquid will rise completely, otherwise the liquid will fall. However, most experimental results show that the drop of droplets is not the main reason for the drop of kill fluid. When the liquid film falls, the droplets still move upward. Therefore, it is considered that the theoretical basis of droplet model is insufficient. The liquid film theory attributes the falling of the liquid in the wellbore to the minimum

interfacial shear stress, and the flow pattern transformation model considers that the transformation between annular fog flow and slug flow corresponds to the falling of the liquid. Although the above three models have made great contributions to gas well effusion, they have good prediction results. However, in the well killing operation, the injection of kill fluid often has the initial speed, and the two working conditions are different. Moreover, the above three models involve the critical flow rate of gas. It is considered that when the gas velocity is greater than the critical flow rate, the liquid will rise completely, and when it is less than the critical flow rate, the liquid will fall. However, through experiments, it is found that the fall of kill fluid is not the opposite relationship between "0" and "1", and there is a situation of partial rise and partial fall of kill fluid.

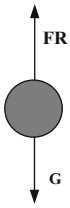

Fig. 2. Stress analysis diagram of Turner droplet

Figure 3 is the experimental image and its corresponding diagram under the condition of the same liquid velocity and different gas velocity. It can be seen that when the gas velocity is small, the kill fluid falls completely. With the increase of gas velocity, the killing fluid has the state of partial rise and partial fall. When the gas velocity is greater than the critical gas velocity, the kill fluid rises completely.

(1) As shown in Fig. 3 (a), when the gas velocity is small, the kill fluid completely falls under the action of gravity, and some droplets move upward in the center of the pipeline.
(2) As shown in Fig. 3 (b), with the gradual increase of gas velocity, the shear force between gas-liquid interface increases, the flow direction of some kill fluid changes, and the kill fluid presents two motion states: rising and falling. The gas-liquid two-phase flow pattern presents annular fog flow above the injection port, and the gas-liquid two-phase countercurrent flow occurs below the injection port. In this gas velocity range, the disturbance of the liquid film intensifies, and the liquid film disturbance leads to the increase of the fluctuation of the liquid film. According to the Kelvin Helmholtz instability, the disturbance wave breaks, the rising droplets in the wellbore increase, and the thickness of the liquid film below is the largest. When the amplitude of the wave reaches a certain degree, it forms a bridging of the liquid film, so that the gas takes the kill fluid away from the wellbore. Although some kill fluid falls, the falling amount is affected by many factors, which is difficult to ensure the success of killing in time. At the same time, it leads to the waste of kill fluid, resulting in economic losses and potential safety hazards.

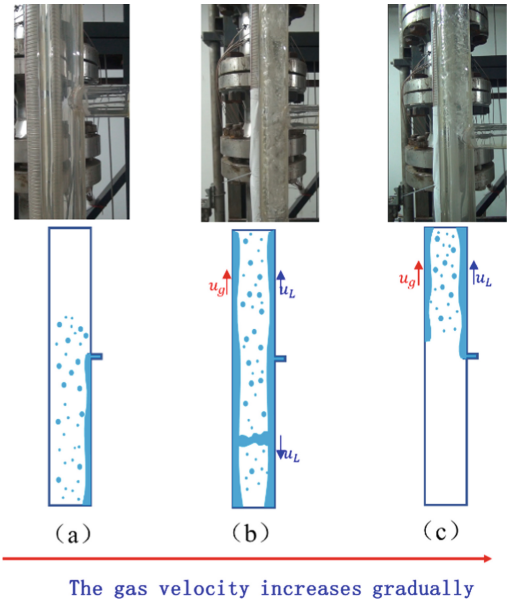

Fig. 3. Experimental image and corresponding diagram

(3) As shown in Fig. 3 (c), when the gas velocity is higher than the critical gas velocity, the kill fluid will not fall, and there is annular mist flow above the injection port. At this time, the kill fails.

3.2 Kill Fluid Drop Test Results

In the experiment, take the rising kill fluid from above the vertical visualization experimental pipeline, and record the time and flow. By comparing with the liquid flow at the liquid inlet, the falling proportion of kill fluid is obtained. Figure 4 shows the drop ratio of kill fluid under different viscosity, different liquid velocity and different gas velocity.

It can be seen from Fig. 4 that the falling proportion of kill fluid and gas velocity curve has the same trend under different conditions, and there is a partial falling of kill fluid. In this paper, the gas velocity corresponding to the complete falling of kill fluid is defined as the complete falling gas velocity of kill fluid, as shown in point m in Fig. 5, where the falling ratio of kill fluid is 1; The point where the kill fluid begins to fall is defined as the initial falling gas velocity of the kill fluid, as shown in point n in Fig. 5. With the increase of kill fluid displacement, the complete falling gas velocity of kill fluid decreases, and the initial falling gas velocity of kill fluid changes little, indicating that the increase of kill fluid displacement is conducive to the falling of kill fluid.

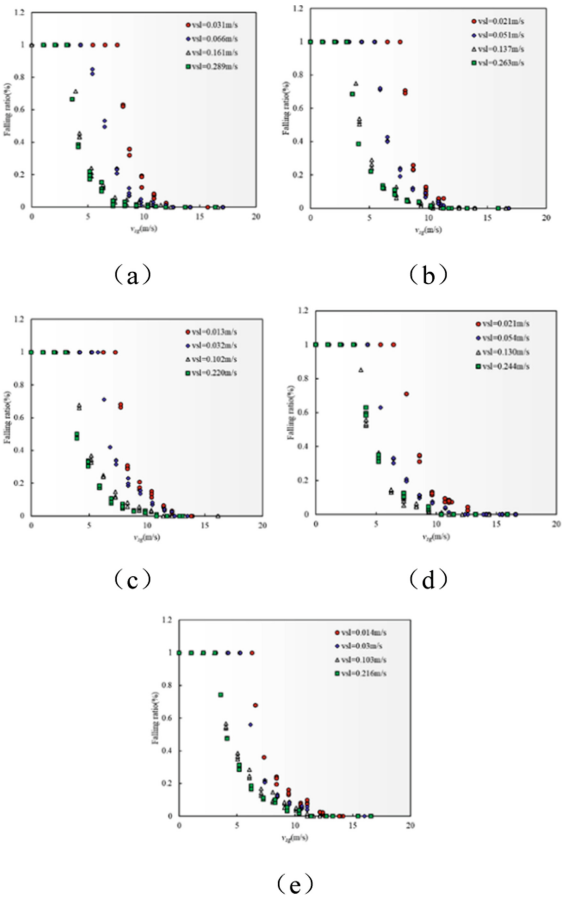

Fig. 4. Falling ratio of kill fluid under different liquid viscosities: (a) experimental liquid viscosity is 1 mPa·s; (b) experimental liquid viscosity is 18 mPa·s; (c) experimental liquid viscosity is 33 mPa·s; (d) experimental liquid viscosity is 40 mPa·s; (e) experimental liquid viscosity is 51 mPa·s.

Figure 5 is a schematic diagram of the falling proportion of kill fluid with water as the experimental liquid, in which the liquid velocity is 0.032 m/s. It can be found that it is different from the previous models. The drop of kill fluid is not a simple 0–1 relationship, that is, the gas velocity is greater than the critical liquid carrying gas velocity, and the kill fluid rises completely, otherwise all the kill fluid falls. There is an area where the killing fluid is partially falling, as shown in the area B in Fig. 5. Therefore, an independent model cannot accurately divide the area of the killing fluid. It is necessary to combine the existing models to accurately judge the falling situation of the kill fluid.

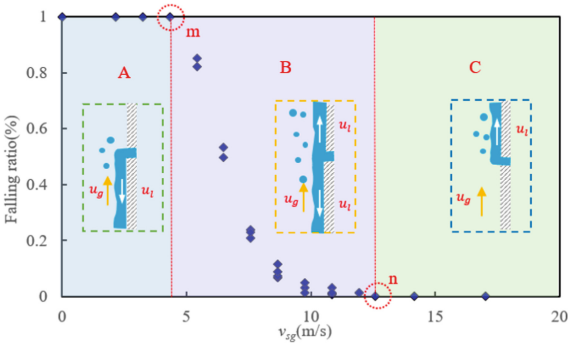

Fig. 5. Falling proportion of kill fluid (Vsl = 0.066 m/s, viscosity: 1 mPa · s)

4 Criteria for Critical Drop of Kill Fluid

4.1 Initial Drop Criterion of Kill Fluid at Low Liquid Holdup

At low liquid holdup, the liquid film model proposed by Li Jinchao and others is used in this paper [13]. The model considers that when the shear stress between the liquid film and the pipe wall is 0, the liquid in the wellbore falls, as shown in Fig. 6.

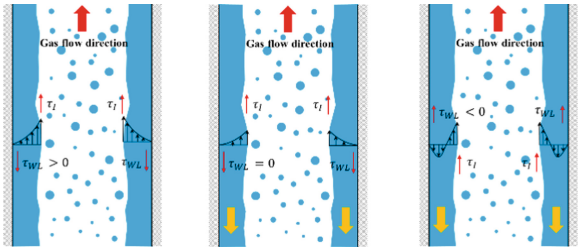

Fig. 6. Schematic diagram of liquid film velocity [13]

Therefore, it is first necessary to determine the velocity distribution of the liquid film. Assuming that the thickness of the liquid film is uniform, take micro elements in the liquid film and conduct force analysis. It can be obtained when the gas-liquid interface friction is equal to the sum of the friction between the liquid and the wall, the gravity of the liquid film and the wellbore pressure drop.

$$\left(\tau + \frac{\partial \tau}{\partial y}\mathrm{d}y\right) \cdot 2\pi[(R-y) - \mathrm{d}y]\mathrm{d}z - \tau \cdot 2\pi(R-y)\mathrm{d}z$$
$$-\rho_{\mathrm{L}} g \cdot 2\pi(R-y)\mathrm{d}y\mathrm{d}z - \frac{\mathrm{d}p}{\mathrm{d}z}\mathrm{d}z(R-y)\mathrm{d}y = 0 \tag{1}$$

$$\tau = \mu_{\mathrm{L}} \frac{\partial v}{\partial y} \tag{2}$$

The liquid film velocity is zero at the pipe wall, The shear stress at the gas-liquid interface is τ_I, The liquid film thickness is δ_F. According to the boundary conditions and simultaneous formula (1) (2), the liquid film velocity distribution can be obtained.

$$v = \frac{B}{\mu_{\mathrm{L}}}\left[-\frac{y(2R-y)}{4} - \frac{(R-\delta_{\mathrm{F}})^2}{2}\ln\frac{R-y}{R}\right] - \frac{\tau_1(R-\delta_{\mathrm{F}})}{\mu_{\mathrm{L}}}\ln\frac{R-y}{R} \tag{3}$$

By integrating formula (3), the relationship between gas-liquid interface shear stress and liquid film thickness and liquid apparent velocity can be obtained.

$$\tau_1 = \frac{(\rho_{\mathrm{L}}-\rho_{\mathrm{C}})g\cdot\overline{B} - \mu_{\mathrm{L}}v_{\mathrm{SL}}}{\left[\frac{4}{D\left(1-2\tilde{\delta}_{\mathrm{F}}\right)}\cdot\overline{B} + 4D\left(1-2\tilde{\delta}_{\mathrm{F}}\right)\cdot\overline{A}\right]} \tag{4}$$

In the above formula,

$$\tilde{\delta}_{\mathrm{F}} = \frac{\delta_{\mathrm{F}}}{D}$$

$$\overline{A} = -\frac{(1-2\delta_{\mathrm{F}})^2}{8}\ln\left(1-2\tilde{\delta}_{\mathrm{F}}\right) + \frac{\left(\delta_{\mathrm{F}}^2-\delta_{\mathrm{F}}\right)}{4}$$

$$\overline{B} = \frac{-D^2\tilde{\delta}_{\mathrm{F}}^4 - D^2\tilde{\delta}_{\mathrm{F}}^2 + 2D^2\tilde{\delta}_{\mathrm{F}}^3}{2} - D^2\left(1-2\tilde{\delta}_{\mathrm{F}}\right)^2\cdot\overline{A}$$

At the wall, the shear stress between the liquid film and the wall can be obtained by substituting y = 0 into formula (3).

$$\tau_{\mathrm{WL}} = \frac{\tau_{\mathrm{l}}}{\left(1-2\tilde{\delta}_{\mathrm{F}}\right)} - (\rho_{\mathrm{L}}-\rho_{\mathrm{C}})gD\left(\tilde{\delta}_{\mathrm{F}}-\tilde{\delta}_{\mathrm{F}}^2\right) \tag{5}$$

When the shear stress between liquid film and wall is 0, the relationship between gas-liquid interface shear stress and dimensionless liquid film thickness under critical conditions can be obtained.

$$\tau_{\mathrm{I}} = (\rho_{\mathrm{L}}-\rho_{\mathrm{C}})gD\left(\tilde{\delta}_{\mathrm{F}}-\tilde{\delta}_{\mathrm{F}}^2\right)\left(1-2\tilde{\delta}_{\mathrm{F}}\right) \tag{6}$$

The gas-liquid interface shear stress of annular fog flow can also be expressed by the following formula.

$$\tau_{\mathrm{I}} = \frac{1}{2}f_{\mathrm{I}}\rho_c\frac{v_{\mathrm{SGC}}^2}{\left(1-2\tilde{\delta}_{\mathrm{F}}\right)^4} \tag{7}$$

In formula (7), the gas-liquid interface friction resistance coefficient fI uses the modified Wallis correlation.

$$f_I = 0.005\left(1+380\tilde{\delta}_{\mathrm{F}}\right) \tag{8}$$

In formula (4), the gas-liquid interface friction resistance is a function of the dimensionless liquid film thickness and the liquid apparent velocity. In formula (6), the gas-liquid interface friction resistance is a function of the dimensionless liquid film thickness. Given the liquid apparent velocity, the corresponding gas-liquid interface friction resistance and dimensionless liquid film thickness can be obtained. Using the obtained data and formula (7), the critical gas phase apparent velocity can be obtained [13].

4.2 Initial Drop Criterion of Kill Fluid Under High Liquid Holdup

When the liquid holdup is large, the liquid film model will no longer be applicable. The falling of kill fluid in the wellbore involves flow pattern transformation [14]. The flow pattern transformation model considers that the transformation between annular fog flow and slug flow corresponds to the falling of liquid in the wellbore. Barnea model [15] is used to solve the critical gas phase apparent velocity. In 1986, Barnea [16] proposed a unified model for the transition from annular mist flow to intermittent flow. He believed that when the gas core is interrupted by liquid at any point in the pipeline, the annular mist flow transitions to slug flow, and proposed the mechanism of liquid film instability: Part of the liquid film near the pipe wall flows downwards causing the air core at the inlet to be blocked.

The instability criterion can be obtained by the instantaneous solution of the following dimensionless equation.

$$Y = \frac{1 + 75\alpha_L}{(1-\alpha_L)^{\frac{5}{2}}\alpha_L} - \frac{1}{\alpha_L^3}X^2 \tag{9}$$

$$Y \geq \frac{2 - \frac{3}{2}\alpha_L}{\alpha_L^3\left(1 - \frac{3}{2}\alpha_L\right)}X^2 \tag{10}$$

In the above formula,

$$X^2 = \frac{\left(\frac{dp}{dx}\right)_{LS}}{\left(\frac{dp}{dx}\right)_{GS}} = \frac{\frac{4}{D}f_{LS}\frac{\rho_L U_{SL}^2}{2}}{\frac{4}{D}f_{GS}\frac{\rho_G U_{SG}^2}{2}}$$

$$Y = \frac{(\rho_L - \rho_G)g\sin\beta}{\left(\frac{dp}{dx}\right)_{GS}}$$

$$f_1 = 0.046\mathrm{Re}_L^{-0.2}$$

When the following formula is met, the gas core is blocked and flow pattern conversion occurs.

$$\frac{A_L}{A \cdot R_{sm}} = \frac{\alpha_L}{R_{sm}} \geq 0.5 \tag{11}$$

Rsm is the minimum liquid holdup to form a bridged blocked gas channel, approximately equal to 0.48. The transition boundary of flow pattern is intuitively expressed by apparent gas velocity and apparent liquid velocity.

$$\left(\rho_{L.} - \rho_g\right)gD\sin\beta = 2f_{GS}\rho_G U_{SG}^2\frac{1 + 75\alpha_L}{(1-\alpha_L)^{\frac{3}{2}}\alpha_L} - \frac{2}{\alpha_L^3}f_{LS}\rho_L U_{SL}^2 \tag{12}$$

When the pipe diameter is known, the liquid holdup equation can be obtained.

$$\alpha_L = F(U_{SG}, U_{SL}, \rho_L, \rho_G) \tag{13}$$

By substituting formula (11) into formula (13) and taking Rsm = 0.48, the transition boundary between slug flow and annular fog flow can be obtained.

Comparing the experimental data with the model, as shown in Fig. 7, it can be found that the experimental data fit well with the model. Bring the basic experimental data into the model, calculate the gas velocity at the falling point of kill fluid under different conditions, and compare it with the gas velocity obtained from the experiment, as shown in Fig. 8. The error between the gas velocity at the falling point of kill fluid obtained by the model and the experimental data is less than 10%, which proves that the model can better describe the gas velocity at the falling point of kill fluid.

4.3 Criteria for Complete Drop of Kill Fluid

Select the complete falling point of kill fluid under different viscosity and liquid velocity, and draw the relationship between the liquid velocity and the complete falling gas velocity of kill fluid, as shown in Fig. 9.

It can be seen from the figure that under a certain viscosity, with the increase of liquid velocity, the gas velocity at the complete falling point of kill fluid gradually decreases. Similarly, at a certain liquid velocity, with the increase of viscosity, the gas velocity at the complete falling point of kill fluid decreases gradually. It can be seen that with the increase of liquid velocity and kill fluid viscosity, the thickness of liquid film in the wellbore increases, the cross-sectional area of gas core decreases, and the actual flow rate of gas increases, which leads to the increase of liquid film disturbance, and the disturbance wave is easier to be broken and carried out outside the well.

In order to determine the gas velocity at the complete falling point of kill fluid, the gas velocity at the complete falling point of kill fluid is fitted by Reynolds number, bond number and Froude number. Formula (14) can be obtained.

$$\mathrm{Re}_g = 8665.6\mathrm{Re}_L^{0.168} Bd^{-0.099} Fr^{-0.489} \tag{14}$$

By comparing the gas Reynolds number at the complete falling point of kill fluid obtained from the experiment with the gas Reynolds number obtained by the model, it can be found that the error is within 12%, so the model can accurately determine the gas velocity at the complete falling point of kill fluid (Fig. 10).

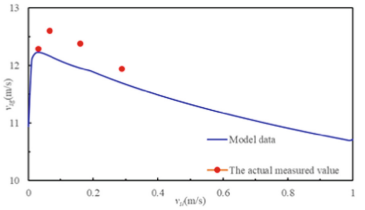

(a)

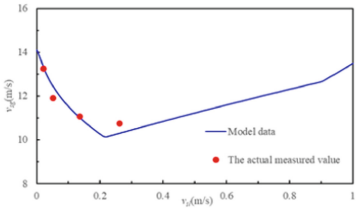

(b)

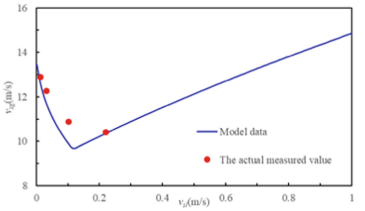

(c)

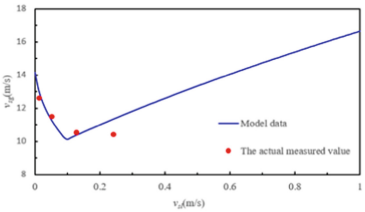

(d)

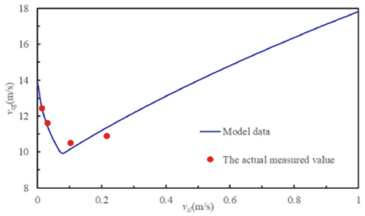

(e)

Fig. 7. Comparison between model calculated value and experimental data: (a) experimental liquid viscosity is 1 mPa·s; (b) experimental liquid viscosity is 18 mPa·s; (c) experimental liquid viscosity is 33 mPa·s; (d) experimental liquid viscosity is 40 mPa·s; (e) experimental liquid viscosity is 51 mPa·s.

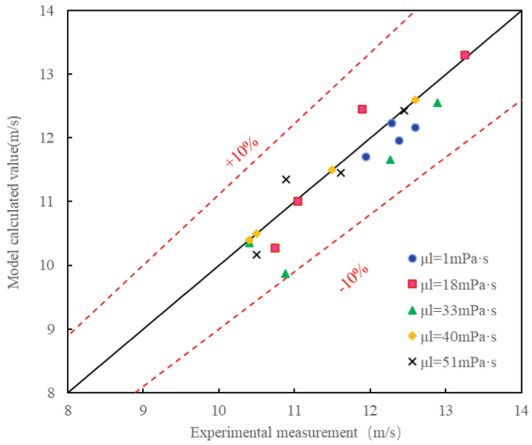

Fig. 8. Error comparison between model calculated value and experimental data

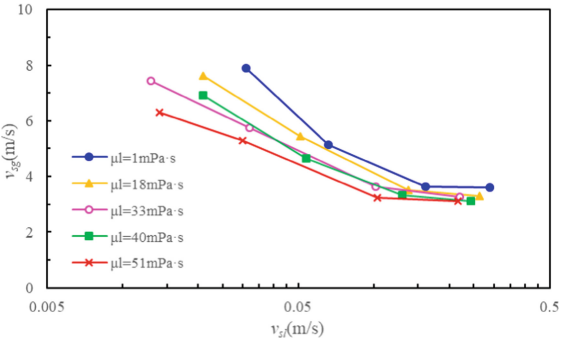

Fig. 9. Relationship between complete drop point of kill fluid and fluid velocity and viscosity

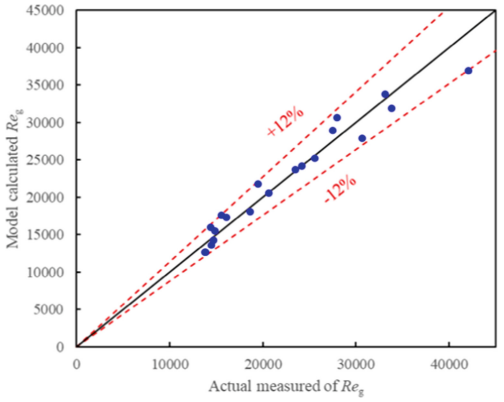

Fig. 10. Error comparison between model calculated value and experimental data

5 Conclusion

The problem of killing fluid falling in unconventional killing is studied. Using the independently designed vertical and visual "killing fluid falling flux experimental device", the killing fluid falling experiments under different apparent gas velocity, apparent liquid velocity and different killing fluid viscosity are carried out.

(1) It is found that the falling of kill fluid is not the relationship between "0" and "1", that is, when the gas velocity is lower than the critical gas velocity, the kill fluid will fall completely, otherwise the kill fluid will rise. The kill fluid injected into the wellbore will rise and fall partially.
(2) According to the working condition of partial falling of kill fluid injected into the wellbore, for the two critical gas velocities of kill fluid falling, the kill fluid falling judgment models are established respectively. Compared with the experimental data, the errors are less than 10% and 12% respectively. The kill fluid drop judgment model established in this paper can accurately predict the partial drop gas velocity and complete drop gas velocity of kill fluid.
(3) Reynolds number, bond number and Froude number are used to fit the experimental data, and the discrimination model of complete falling point of kill fluid is obtained. Compared with the experimental data, the error is less than 10%.For the critical gas velocity of killing fluid part falling, at high liquid holdup, Barnea's flow pattern transformation boundary of slug flow annular mist flow is used to distinguish the falling point of kill fluid. Under low liquid holdup, the model of Li Jinchao is used to distinguish the falling point of kill fluid. Combining the two models, the falling point discrimination model of kill fluid is obtained. Compared with the experimental data, the error is less than 12%.
(4) The kill fluid drop discrimination model established in this paper can determine the critical gas velocity of partial and complete drop of kill fluid, improve the drop proportion of kill fluid, reduce the waste of kill fluid, shorten the kill time, and ensure the safe and efficient deep-water kill operation.

Symbol Description

τ—Shear stress between liquid films at Y from the pipe wall; R—Pipe radius; ρ_L—Liquid density; ρ_L—Gas density; v—Liquid film speed; τ_I—Shear stress at the gas-liquid interface; δ_F—Liquid film thickness; τ_{WL}—Shear stress between liquid film and wall; f_I—Coefficient of frictional resistance at gas-liquid interface; Rsm—The minimum liquid holdup that forms a bridge to block the gas channel; α_L—Liquid holdup rate; Re_g—Gas Reynolds number; Re_L—Liquid Reynolds number.

References

1. Gong, P.: Design of Hydraulic Parameters in Unconventional Well Kill Methods. China University of Petroleum (East China) (2013)
2. Jin, Y.: Numerical simulation of gas-liquid two-phase flow in wellbore. Southwest Petroleum Institute (2005)

3. Dou, J.: Study on gas-liquid two-phase flow characteristics and critical liquid carrying model in gas well bore. Xi'an University of Petroleum (2020)
4. Zhang, S.: Research on dynamic kill parameter design of rescue well. China University of Petroleum (East China) (2019)
5. Wu, C.: Numerical simulation of unconventional well killing technology. China University of Petroleum (Beijing) (2019)
6. Zhao, X.: Research on application technology of dynamic kill drilling. China University of Petroleum (Beijing) (2019)
7. Oudeman, P.: Kill procedures to avoid formation damage in the high rate gas wells of an underground storage project. In: SPE European Formation Damage Conference. OnePetro (1999)
8. Records, L.R.: Mud system and well control. Pet. Eng. **44**, 97–108 (1972)
9. Santos, O.L.A.: A mathematical model of a gas kick when drilling in deep waters. Colorado School of Mines (1982)
10. Van't Westende, J.M.C.: Droplets in annular-dispersed gas-liquid pipe-flows (2008)
11. Skopich, A., Pereyra, E., Sarica, C., et al.: Pipe-diameter effect on liquid loading in vertical gas wells. SPE Prod. Oper. **30**(02), 164–176 (2015)
12. Turner, R.G., Hubbard, M.G., Dukler, A.E.: Analysis and prediction of minimum flow rate for the continuous removal of liquids from gas wells. J. Petrol. Technol. **21**(11), 1475–1482 (1969)
13. Jinchao, L., Daoming, D., Weiwei, S., et al.: The mechanism of gas well fluid accumulation and a new model for predicting critical gas velocity. Acta Petrolei Sinica **41**(10), 1266–1277 (2020)
14. Zhuang, X.: Study on theory and control method of gas well effusion. University of Petroleum (Beijing) (2003)
15. Barnea, D.: Transition from annular flow and from dispersed bubble flow—unified models for the whole range of pipe inclinations. Int. J. Multiph. Flow **12**(5), 733–744 (1986)
16. Barnea, D.: A unified model for predicting flow-pattern transitions for the whole range of pipe inclinations. Int. J. Multiph. Flow **13**(1), 1–12 (1987)

A New Method for the Prevention of Natural Gas Hydrate During Transportation and Production

Ming-bo Wang(✉), Wei Wang, and Rui-lin Wang

School of Petroleum Engineering, China University of Petroleum (East China), Qingdao 266580, China
wangmb@upc.edu.cn

Abstract. The high-pressure and low-temperature environment prevailing in the process of offshore oil and gas development is very prone to the formation of hydrate in the wellbore to block the tubing, which leads to production reduction and shutdown and causes a series of production accidents. Current mainstream hydrate prevention and treatment methods have the disadvantages of high cost, high toxicity and high pollution, and new and more effective hydrate prevention and treatment methods are urgently needed in the deep-water offshore well development. In this paper, the thermal effect of cavitation is introduced into the hydrate prevention and treatment process of deep-water offshore production wells, and the upper section of the completion tubing structure is designed to be applicable to the actual field. With the help of indoor experimental system, we have analyzed the influences of several working parameters such as the injection pressure, injection frequency, initial temperature of the fluid and the pressure inside the cavitator on the development of cavitation thermal effect. Preliminary conclusion drawn from both numerical simulation and experimental observations provides a new and possible way of natural gas hydrate prevention in near future.

Keywords: Deep-water · Natural gas hydrate · Cavitation · Thermal effect · Experimental study

1 Introduction

New energy sources such as solar, wind, hydro, geothermal and hydrogen are in fast development, yet conventional fossil energy still accounts for a large share of the energy structure in all countries. How to maintain the production of conventional fossil energy while maintaining the growth of the proportion of new energy is an issue that countries need to consider. During the development of oil and gas resources, when the crude oil, especially the natural gas, flows through high-pressure, low-temperature, water-bearing environments, methane in the stream will combine with water to form solid, ice-like natural gas hydrates, blocking pipelines and wellbores and causing risks and hazards, which is especially obvious in the process of offshore oil and gas development [1]. With the increasing depletion of onshore oil and gas resources and the difficulty of succeeding reserves, the development of offshore oil and gas resources is receiving

B. Sun et al. (Eds.): DWOG-Hyd 2021, LNCE 246, pp. 282–290, 2022.
https://doi.org/10.1007/978-981-19-0960-3_28

increasing attention. The problem of natural gas hydrate in the process of offshore oil and gas development poses a serious challenge to the efficient development of oil and gas resources, and the adoption of cost-effective and safe hydrate control technology is of great significance to the efficient development of offshore oil and gas.

The existing hydrate prevention and treatment methods mainly include heating, pressure reduction, drying and chemical inhibitor injection, among which the chemical injection method is most commonly used [2]. However, this method requires continuous injection of chemical agents such as methanol into the well or pipeline, which is costly, and methanol as the representative chemical agent usually has certain toxicity, poor environmental friendliness, and high cost of recycling. Therefore, it is imperative to develop efficient, adaptable, non-polluting or low-polluting hydrate control technologies and equipment.

In this paper, a combination of numerical simulations and indoor experiments has been applied to carry out a study of the cavitation thermal effect applied to hydrate control, and propose a new and feasible method for cavitation hydrate control.

2 Drawbacks of Current Hydrate Prevention Technologies

Current methods of natural gas hydrate control are: drying, pressure control, heating and chemical inhibitor injection.

The drying method is to control the water content in natural gas within a reasonable range by certain means, so as to prevent and control the formation of natural gas hydrates [3]. Among them, the air drying method has the characteristics of no pollution and uniform drying effect, and is generally applied to long-distance natural gas pipelines, but air drying cannot be used for unblocking, and is not applicable to offshore gas wells. In addition, moisture-absorbing organic solvents can be injected into the pipeline through the equipment, and the solvent can be combined with water by absorbing water molecules through hydrogen bonding, so as to achieve the purpose of drying, but the method is costly and the construction process is complicated.

The pressure control method reduces the overall system pressure to prevent hydrate formation. This method is easy to operate, simple equipment, low operating cost, and the pipeline pressure needs to be maintained within a certain range [4]. When the hydrate is blocked in the pipeline, the generated hydrate can be decomposed by the pressure reduction method, but the practical application of this method is easily restricted by factors such as reservoir and production pressure, and the hydrate generation is not fundamentally prevented.

Heating method is to heat up the fluid in the pipeline by pipeline heating equipment, so that the hydrate will be decomposed by heat to achieve the purpose of suppressing hydrate generation. This method can inhibit hydrate generation as well as deal with hydrate blockage, but the equipment consumes a lot of energy and is more expensive [5].

The chemical inhibitor injection method is to inhibit the generation of natural gas hydrate or unblock the blocked pipeline by injecting inhibitors directly into the pipeline, equipment and wellbore through physical and chemical actions [6–8]. Although the chemical inhibitor inhibition effect is good, but not easy to recover, and the deeper the

well or the longer the transmission pipeline, the more chemical inhibitor injection is required, and the cost is high.

3 Historical Review of Cavitation Thermal Effects

Cavitation is the process of incipient, development and collapse of vapor or voids inside the liquid or at the liquid-solid interface when the local pressure within the liquid is reduced [9]. During the evolution of cavitation, the voids follow the fluid from the low-pressure region where cavitation occurs to the high-pressure region, the pressure outside the voids gradually increases, the voids undergo depression and collapses sharply in a very short time. During the rapid contraction and collapse of the void or bubble, the non-condensable gas inside the bubble is continuously compressed and the pressure and temperature are continuously increased. When the bubble shrinks to its minimum size, the pressure and temperature of the gas inside the bubble reach their peak, forming a local extreme high-temperature and high-pressure environment around the bubble, accompanied by shockwaves, micro-jets and free radicals. Due to the very short collapse time, the gas inside the bubble is not cooled by the surrounding liquid, and the temperature rises suddenly, forming multiple local high-temperature points inside the liquid, heating the gas inside the bubble and the ambient fluid [10]. During this process, various effects are induced, such as mechanical (perturbation, shear and impact, etc.), thermal, optical and chemical effects.

According to the method of how a bubble is formed, cavitation can be classified as hydrocavitation, ultrasonic cavitation, optical cavitation and particle cavitation [11]. Both ultrasonic cavitation and hydraulic cavitation are popular among industrial applications. Ultrasonic cavitation uses the principle of pressure change within the liquid caused by the propagation of ultrasonic waves in the liquid to produce cavitation, which is costlier and has a low energy utilization rate [12]. Hydraulic cavitation is achieved by changing the hydraulic structure of the flow (such as throttle valves, orifice plates, venturi, high-speed culverts or other geometric structures that can cause changes in liquid pressure, such as high-speed rotation) to achieve liquid cavitation. When the liquid flows through the nozzle, for example, the internal structure of the nozzle, the fluid flow velocity increases sharply, the pressure drops sharply, when the flow field somewhere in the pressure drops to the liquid saturation vapor pressure will trigger cavitation.

Cavitation is a multi-phase, transient, microscopic and stochastic complex process, it occurs not only with the liquid properties themselves, but also with the ambient flow field environment [13]. Studies have shown that local hot spots with extreme high temperature and pressure will form during the bubble collapse along with powerful shockwave and high-speed micro-jets. the energy release during bubble collapse is in direct relation with bubble collapsing intensity [14].

Tomita and Shima obtained a temperature of 8800 K in the center of the collapsed bubble based on the adiabatic theory with viscosity and compressibility of the liquid considered [15, 16]. Suslick et al. measured the temperature of the central region of the bubble during acoustic bubble collapse in different liquids by spectroscopic experiments, in which the central collapse temperature of the bubble was 4000–6000 K for aqueous medium, 4100–4500 K for benzene, and 4920–5240 K for silicone oil [17]. It can be seen

that although the bubble collapse time is very short, the heat transfer effect between the gas inside the bubble and the liquid outside the bubble is very important due to the great temperature gradient between bubble and ambient wall, and the small spatial distance at the moment of collapse [18].

Under the synergistic effect induced by cavitation, the cavitation process will induce chemical bond disassembly, aqueous phase combustion, high-temperature decomposition or free radical reactions of harmful organic matter in waste water [19–22], prevent or retard the scale formation [23], improve the coal permeability [24], enhance the rate of oxidation and deterioration of transformer oil [25, 26].

Kim et al. conducted an experimental study on the cavitation priming of a turbopump inducer under different conditions and obtained the corresponding quantized and dimensionless thermal effect parameters for the cavitation incipiency [27], and the conclusions showed that (1) the critical cavitation number decreases with the increase of the dimensionless thermal effect parameter at a fixed Reynolds number; (2) when the dimensionless thermal effect parameter is less than 0.105, the critical cavitation number is not sensitive to Reynolds number; (3) when the dimensionless thermal effect parameter is larger than 0.105, the critical cavitation number increases with the increase of Reynolds number.

Qiu designed a close-loop experimental device and used numerical simulation to analyze the cavitation distribution inside the device. Moreover, the influence of working parameters on the thermal effect of cavitation was performed and conclusions were analyzed [28].

Wang et al. proposed to apply the thermal effect of cavitation to natural gas hydrate prevention, a schematic process of upper completion tubing string is provided and the thermal effect of cavitation was studied numerically and experimentally [29].

Conclusions drawn from previous research on the thermal effect of cavitation reveal that: (1) research on the thermal effect of cavitation should be further enhanced. (2) The energy utilization efficiency of the hydraulic cavitation is high and needs further study.

4 Application of Cavitation Thermal Effect on the Prevention of Natural Gas Hydrate in Offshore Gas Wells

Take an offshore producing well as an example, the possible hydrate formation area is generally located at a certain depth interval below mudline. To prevent the formation of natural gas hydrate at specific depth, the following hydrate prevention program was proposed: (1) during the installation of downhole completion tubing string, an insulation jacket or wrapped coiled pipe is pre-installed outside the tubing around the possible hydrate formation area; (2) a cavitation heater, a water tank (which can be filled with other fluids, such as insulation oil), an intelligent control box and supporting accessories such as cables are installed around the subsea wellhead; (3) the insulation jacket or flexible coiled pipe is connected with the cavitation heater and water tank to form a closed-loop system. Heat from the cavitation heater is then transferred from the wellhead down into the completion string, eliminating the possibility of natural gas hydrate formation [29].

To understand the evolution of temperature and pressure development during the bubble collapse, numerical simulation on a bubble of a certain diameter near the rigid wall was carried out using Volume of Fluid method, simulation results were compared and validated with the previous studies [30]. The physical model used in the simulation is shown in Fig. 1.

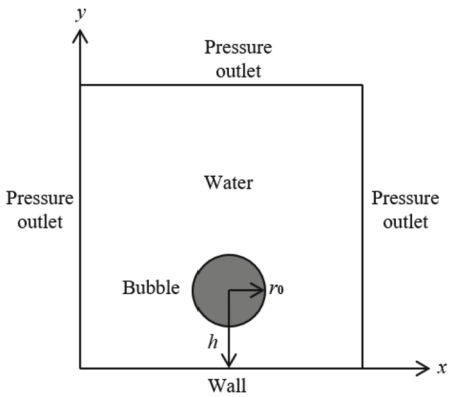

Fig. 1. Physical model of bubble collapse simulation

The simulation results show that: (1) As the bubble-wall distance increases, the restriction from the solid wall gradually decreases, the pressure difference between the upper and lower sections of the bubble gradually decreases, and the bubble tends to compress simultaneously in the radial direction with micro-jets generated and collapses in the late stage. (2) At the early stage of bubble deformation, pressure change inside the bubble is not obvious. At the late stage of collapse, the bubble volume shrinks sharply and the pressure inside the bubble rises sharply until it reaches a peak, and then decreases rapidly. (3) During the bubble expansion, the temperature inside the bubble remains almost constant. The gas inside the bubble is rapidly compressed and the pressure and temperature increase sharply during the contraction phase. (4) The greater the ambient pressure, the greater the pressure difference inside and outside of the bubble, the faster the contraction of the bubble, and the shorter the time period required to reach the peak pressure.

Along with simulation analysis, experimental observations of thermal effects during bubble cavitation were also carried out, and Fig. 2 showed the schematic figure of the experimental setup.

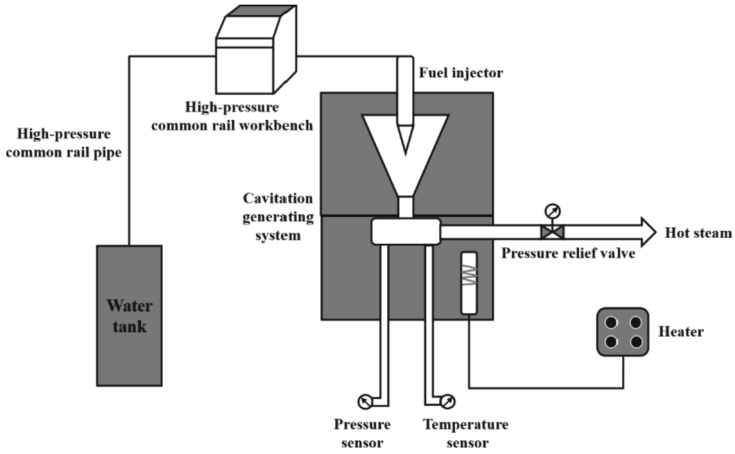

Fig. 2. Schematic figure of the experimental setup

The liquid temperature evolution was measured experimentally for different operating conditions (injection pressure, injection frequency, initial liquid temperature and chamber pressure). The observations of the experimental study show that: (1) The liquid temperature increases gradually as the injection pressure increases (Fig. 3).

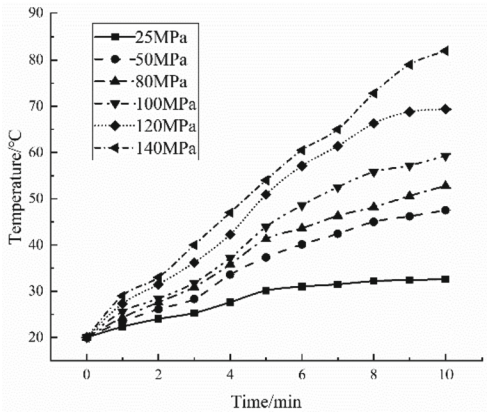

Fig. 3. The influence of injection pressure on fluid heating

(2) As the injection frequency increases, the fluid temperature increases, but the heating effect is not very pronounced (Fig. 4).

(3) The initial temperature of the fluid has a limited effect on the final fluid temperature under the same injection time interval (Fig. 5).

(4) Under current experimental conditions, the effect of chamber pressure on fluid heating is limited (Fig. 6).

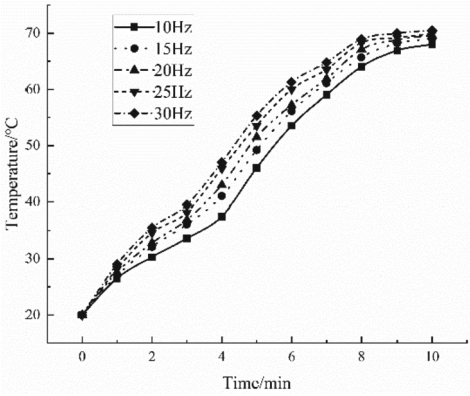

Fig. 4. The influence of injection frequency on fluid heating

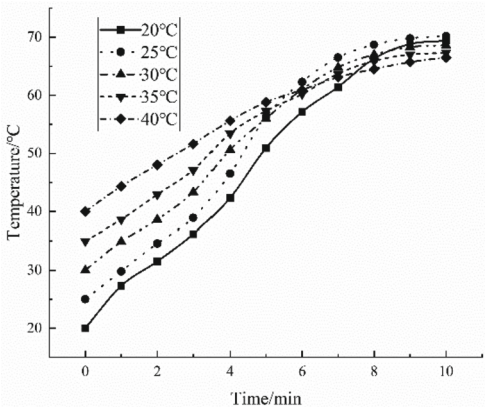

Fig. 5. The influence of initial temperature on fluid heating

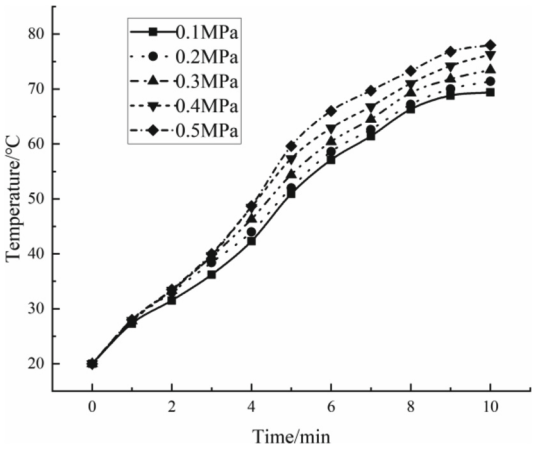

Fig. 6. The influence of chamber pressure on fluid heating

5 Conclusions

(1) Traditional hydrate control method as chemical inhibitor injection, has the disadvantages of high cost, high toxicity and high pollution. It is of great practical significance to develop efficient, adaptable and environment-friendly hydrate control technologies.
(2) To address the natural gas hydrate prevention in offshore production wells, a method of applying the cavitation thermal effect to hydrate prevention is proposed, and a hydrate control program for the upper section of completion tubing string is also provided.
(3) Experimental studies on the thermal effects of cavitation under different operating conditions have been carried out, and the experimental observations is to provide technical support for the natural gas hydrate prevention in offshore wells in near future.

References

1. Sloan, E.D.: A changing hydrate paradigm-from apprehension to avoidance to risk management. Fluid Phase Equilib. **228–229**, 67–74 (2005)
2. Guo, Y.L., Sun, B.J., Zhao, K.K., et al.: A prediction method of natural gas hydrate formation in deepwater gas wells and its application. Petroleum **2**(3), 296–300 (2016)
3. Creek, J.L.: Efficient hydrate plug prevention. Energy Fuels **26**, 4112–4116 (2012)
4. Xu, P., Lang, X., Fan, S., et al.: Molecular dynamics simulation of methane hydrate growth in the presence of the natural product pectin. J. Phys. Chem. C **120**(10), 5392–5397 (2016)
5. Xu, X.H.: Experimental study on the feasibility of natural gas hydrate injection heat extraction. China University of Petroleum (East China), Qingdao (2014)
6. Zhao, X., Qiu, Z.S., Huang, W.A., et al.: Mechanism of action of thermodynamic inhibitors of natural gas hydrates and optimal design. ACTA Petrolei Sinica **36**(6), 760–766 (2015)
7. Sa, J.H., Kwak, G.H., Han, K., et al.: Gas hydrate inhibition by perturbation of liquid water structure. Sci. Rep. **5**(1), 1–9 (2015)
8. Yan, K.F., Li, X.S., Chen, Z.Y., et al.: Molecular dynamics simulation of the crystal nucleation and growth behavior of methane hydrate in the presence of the surface and nanopores of porous sediment. Langmuir **32**(31), 7975–7984 (2016)
9. Pan, S.S., Peng, X.S.: Mechanisms of Cavitation. National Defense Industry Press, Beijing (2013)
10. Cai, J., Huai, X.L., Liu, B., et al.: Applications of Liquid Cavitation Technology. Science Press, Beijing (2019)
11. Zheng, X.: Study of sub-Bjerknes force between two bubbles under the action of acoustic field. Shaanxi Normal University, Xi'an (2016)
12. Kong, W.D.: Research on hydrocavitation-enhanced chlorine dioxide degradation of phenol wastewater. North Central University, Taiyuan (2017)
13. Huang, J.T.: Principles and Applications of Cavitation and Cavitation. Tsinghua University Press, Beijing (1991)
14. Luo, X.W., Ji, B., Peng, X.X.: Theory and Applications of Cavitation. Tsinghua University Press, Beijing (2020)
15. Tomita, Y., Shima, A.: On the behavior of a spherical bubble and the impulse pressure in a viscous compressible liquid. Bull. Jpn. Soc. Mech. Eng. **20**(149), 1453–1460 (1977)

16. Fujikawa, S., Akamatsu, T.: Effects of the non-equilibrium condensation of vapor on the pressure wave produced by the collapse of a bubble in a liquid. J. Fluid Mech. **97**(3), 481–512 (1980)
17. Suslick, K.S., Hammerton, D.A.: Sonochemical hot spot. J. Am. Chem. Soc. **89**(18), 5641–5645 (1986)
18. Kim, D.J., Sung, H.J., Choi, C.H., et al.: Cavitation instabilities during the development testing of a liquid oxygen pump. J. Propul. Power **33**(1), 187–192 (2017)
19. Kikuta, K., Yoshida, Y., Watanabe, M., et al.: Thermodynamic effect on cavitation performance and cavitation instabilities in an inducer. J. Fluids Eng.-Trans. ASME **130**(11), 111302 (2008)
20. Tong, D.S.: Research on cavitation jet treatment technology for oilfield produced water. China University of Petroleum (East China), Qingdao (2009)
21. Fu, J.S., Li, G.S., Shi, H.Z., et al.: A novel tool to improve the rate of penetration-hydraulic-pulsed cavitating-jet generator. SPE Drill. Complet. **27**(3), 355–362 (2012)
22. Melyanyuk, M.V., Akhlyan, I.A.: Technological application of cavitating jet streams in the oil and gas industry. Neftyanoe Khozyaystvo-Oil Industry **11**, 130–133 (2019)
23. Li, H.X.: Experimental study on ultrasonic cavitation anti-scaling and hydraulic cavitation anti-scaling and enhanced heat transfer. Graduate School of Chinese Academy of Sciences (Institute of Engineering Thermophysics), Beijing (2009)
24. Lu, Y.Y., Ding, H., Ge, Z.L., et al.: Experimental study on the influence of thermal effect of cavitation water jet on coal permeability. Rock Soil Mech. **35**(5), 1247–1254 (2014)
25. Ming, X.L.: Oxidative deterioration effect of cavitation heat generation on hydraulic oil. IEEE Access **19**(9), 11–21 (2020)
26. Yu, B.: Hydraulic cavitation performance enhancement and its application research. Jiangsu University, Zhenjiang (2014)
27. Kim, J., Song, S.J.: Measurement of temperature effects on cavitation in a turbopump inducer. J. Fluids Eng. **138**(1), 011304 (2016)
28. Qiu, J.J.: Experimental study of thermal effect of fluid cavitation. China University of Petroleum (East China), Qingdao (2018)
29. Wang, M.B., Qiu, J.J., Chen, W.Q.: Towards the development of cavitation technology for gas hydrate prevention. R. Soc. Open Sci. **8**, 202054 (2021)
30. Ohl, C.D., Arora, M.: Surface cleaning from laser-induced cavitation bubbles. Appl. Phys. Lett. **89**(7), 102–103 (2006)

The Adaptability Analysis of Hydrocyclone Separation for Sand and Natural Gas Hydrate to Back Pressure

Dang-fei Wang, Guo-rong Wang(✉), Lin Zhong, and Xing Fang

School of Mechanical Engineering, Southwest Petroleum University, Xindu Avenue 8, Xindu District, Chengdu 610500, Sichuan, China
200331010023@swpu.edu.cn

Abstract. Solid fluidization is a promising method for the development of marine hydrate resources. In-situ separation is the key to realize the purification of NGH and desanding, which can effectively reduce the energy consumption of slurry transportation and backfill the produced sand to downhole. However, in the fluidization mining process, the downhole pressure is complex and fluctuating. Due to the possible imbalance between underflow pressure and overflow pressure, the back pressure comes into being. The influence of back pressure environment on cyclone separation performance in hydrate exploitation has not been reported. The purpose is to analyze the adaptability of hydrocyclone separation for sand and NGH to back pressure in the range of 30 kPa. In this study, RSM and the Mixture model simulate the back pressure of underflow by setting different pressure-outlet boundary conditions. The results showed that when the back pressure increases from 0 to 30 kPa, the purification efficiency increases to 99.8%, but the desanding efficiency sharply drops to around 53% . Within the back pressure of 20 kPa, the comprehensive efficiency maintains over 70%, and peaks of 88.7% at 10 kPa. In the research scope, the hydrocyclone has good adaptability to back pressure. To a certain extent, the existence of back pressure may help to improve the comprehensive separation efficiency. This paper provides guidance for structural design of hydrocyclone and optimization parameters of mining process in marine hydrate mining.

Keywords: Solid fluidization · In-situ separation · Back pressure · Purification · Desanding

1 Introduction

Natural gas hydrate (NGH) is a kind of ice-like solid formed under the condition of high pressure and low temperature, which is also called combustible ice. Conversion of NGH reserves to methane is $(1.8–2.1) \times 10^{16}$ m^3, equivalent to twice the world's known total reserves of traditional fossil fuels such as coal, oil and natural gas [1]. Such abundant NGH resources have increasingly become a hot spot for energy development in the world. Therefore, many countries have formulated a series of long-term research plans

B. Sun et al. (Eds.): DWOG-Hyd 2021, LNCE 246, pp. 291–301, 2022.
https://doi.org/10.1007/978-981-19-0960-3_29

to carry out corresponding exploration and development research [2]. NGH is widely distributed in permafrost and marine sediment, among which shallow non-diagenetic hydrate (mainly silt clay sediment, 83.25% of particles below 40 μm) accounts for over 90% [3–5]. The shallow non-diagenetic reservoir features are weak cementation, shallow depth, non-diagenesis, and non-dense cover [6, 7]. Based on these characteristics, Zhou et al. [6] proposed a solid fluidization method for the safe and sustainable mining of marine hydrates, and which was successfully attempted in the NGH trial exploitation in South China Sea. The detailed description of this method has been reported by references [4, 6]. Then, this paper is no longer redundant. Based on the solid-state fluidized mining, the approach of sand entering the wellbore for in-situ separation and backfilling to wellhole is adopted, which can reduce the energy consumption of transportation and the risk of reservoir collapse, and realize the controllable mining of marine hydrate. However, in the fluidization mining process, the downhole pressure is complex and fluctuating. The principle of desanding and purification of NGH is shown in Fig. 1. Due to the possible imbalance between underflow outlet pressure (P_u) and overflow outlet pressure (P_o), the back pressure (i.e. underflow pressure minus overflow pressure) comes into being. The existence of back pressure in the separation process will make it difficult for the separation of sand and NGH, reducing the separation performance and seriously leading to the failure of the separator. Fang et al. [8] carried out adaptability analysis of operating parameters of hydrate cyclone separator based on CFD simulation, and provided the basis for using downhole hydrocyclones in the process of NGH solid fluidized mining. Chang

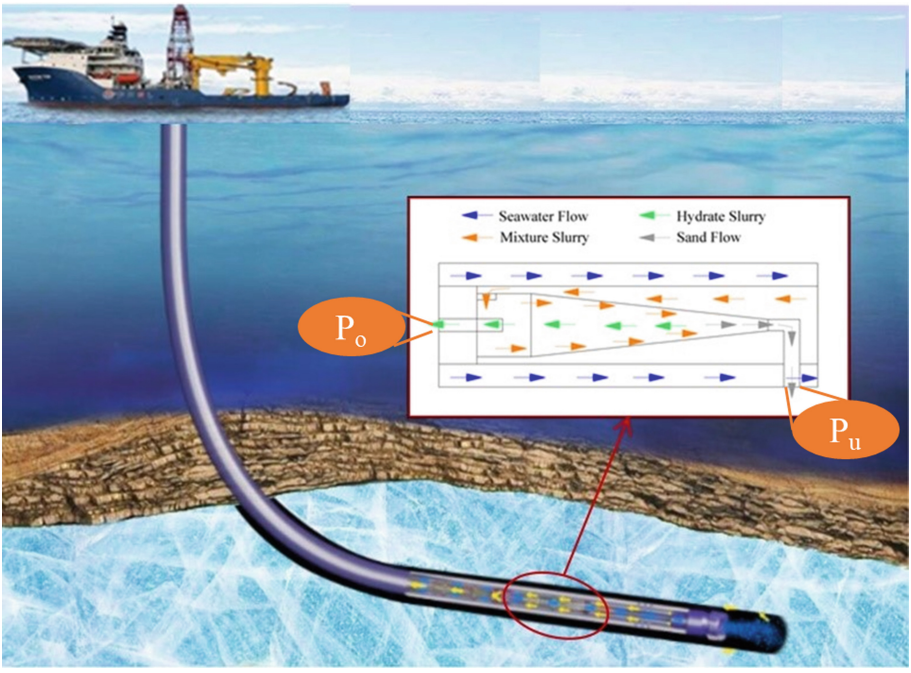

Fig. 1. The principle of desanding and purification of NGH.

et al. [9] designed a hydrocyclone suitable for subsea gas hydrate extraction, and studied the hydrocyclone performance on the effects of operating parameters and geometric parameters. But there is no report on the adaptability of hydrocyclone for desanding and purification of NGH to back pressure. Therefore, the purpose of this study is to analyze the adaptability of hydrocyclone separation for sand and NGH to back pressure.

2 Numerical Methods

2.1 Model Description

The Reynolds stress model (RSM) accounts for the effects of streamline curvature, swirl, rotation, and rapid changes in strain rate, naturally, it can generate accurate predictions for complex flows [10, 11]. In this paper, therefore, the RSM was selected for simulation.

The continuity equation:

$$\frac{\partial p}{\partial t} + \frac{\partial(\rho u_i)}{\partial x_i} = 0 \tag{1}$$

The momentum equation:

$$\frac{\partial p}{\partial t}(\rho u_i) + \frac{\partial\left(\rho u_i u_j\right)}{\partial x_j} = -\frac{\partial p}{\partial x_i} + \frac{\partial}{\partial x_j}\left[\mu\left(\frac{\partial u_i}{\partial x_j} + \frac{\partial u_j}{\partial x_j}\right)\right] + \frac{\partial}{\partial x_j}\left(-\rho\overline{u_i' u_j'}\right) \tag{2}$$

The transport equation:

$$\frac{\partial\left(\rho\overline{u_i' u_j'}\right)}{\partial t} + \frac{\partial\left(\rho u_k \overline{u_i' u_j'}\right)}{\partial x_k} = D_{T,ij} + D_{L,ij} + P_{ij} + G_{ij} + \Phi_{ij} + \varepsilon_{ij} + F_{ij} \tag{3}$$

where $D_{T,ij}$ is the turbulent diffusion, $D_{L,ij}$ is the molecular viscous diffusion, P_{ij} is the shear stress generation, G_{ij} is the buoyancy generation, Φ_{ij} is the pressure strain, ε_{ij} is the viscous dissipation, and F_{ij} is the system rotation generation.

In this paper, the slurry in hydrocyclone is a mixture of hydrate, sand and seawater, so it is necessary to use multiphase flow model for numerical simulation. The Mixture model obtains the relative velocity by solving the momentum equation of the mixture, and then characterizes the discrete phase, which is more suitable for particle load flow, bubble flow, settlement, cyclone separator simulation.

The mass conservation equation:

$$\frac{\partial}{\partial t}(\rho_m) + \nabla \cdot \left(\rho_m \overrightarrow{v_m}\right) = \dot{m} \tag{4}$$

where ρ_m is the density of the mixture, $\dot{m}$ is the mass transfer, and $\overrightarrow{v_m}$ is the average velocity of the mixture, which is defined by

$$\overrightarrow{v_m} = \frac{\sum_{k=1}^{n} \alpha_k \rho_k \overrightarrow{v_k}}{\rho_m} \tag{5}$$

where α_k is the volume fraction of phase k and $\overrightarrow{v_m}$ is the velocity of phase k.
The momentum conservation equation:

$$\begin{aligned}&\frac{\partial}{\partial t}\left(\rho_m\overrightarrow{v_m}\right)+\nabla\cdot\left(\rho_m\overrightarrow{v_m}\overrightarrow{v_m}\right)=-\nabla\cdot p+\nabla\cdot\left[\mu_m\left(\nabla\overrightarrow{v_m}+\nabla\overrightarrow{v_m}^T\right)\right]\\&+\rho m\overrightarrow{g}+\overrightarrow{F}+\nabla\cdot\left(\sum_{k=1}^{n}\alpha_k\rho_k\overrightarrow{v_k}^r\overrightarrow{v_k}^r\right)\end{aligned}\tag{6}$$

where n is the total number of phases, μ_m is the viscosity of the mixture, p is the pressure; ρ_k is the density of phase k, $\overrightarrow{F}$ is the volumetric force, and $\overrightarrow{v_k}^r$ is the relative slip velocity of phase k with respect to the mixture, i.e., $\overrightarrow{v_k}^r=\overrightarrow{v_k}-\overrightarrow{v_m}$.

The volume fraction equation for phase k is

$$\frac{\partial}{\partial t}(\alpha_k\rho_k)+\nabla\cdot\left(\alpha_k\rho_k\overrightarrow{v_m}\right)=-\nabla\cdot\left(\alpha_k\rho_k\overrightarrow{v_k}^r\right)\tag{7}$$

2.2 Simulation Conditions

The SIMPLE algorithm was adopted for describing pressure-volecity coupling. The PRESTO discretisation scheme was used for the pressure equations, while the QUICK discretisation scheme was used for other control equations. The inlet velocity of hydrocyclone separation for sand and NGH can be calculated according to the inlet flow, so the velocity-inlet boundary condition is selected, and the velocities of seawater, sand and hydrate were all 8.33 m/s. The pressure-outlet boundary conditions were set as outlet conditions. The solid wall boundary used standard wall function. Table 1 shows the physical parameters of medias.

Table 1. The physical parameters of medias.

Name		Characteristic
Seawater	Density	1025 kg/m^3
	Viscosity	0.0017 kg/(m/s)
	Volume fraction	75%
	Diameter	–
Sand	Density	2600 kg/m^3
	Viscosity	–
	Volume fraction	15%
	Diameter	30 μm
Seawater	Density	910 kg/m^3
	Viscosity	–
	Volume fraction	10%
	Diameter	30 μm

2.3 Structure Geometry and Grid Independence

The hydrocyclone is composed of cylindrical section, cone section, overflow tube, underflow tube and tangential inlet. The main diameter of hydrocyclone is 80 mm. Other relevant structural parameters are obtained according to relevant empirical formulas [12], and the specific values are shown in Tables 2. The model is divided into tetrahedral unstructured meshes by ANSYS Mesh software. In order to better reflect the actual motion of the fluid in the cyclone, the grid refinement method is used to deal with the key parts. In this paper, the same method is used to mesh the hydrocyclone model, generating 5 levels of 32530, 56285, 99528, 161716 and 416747. As shown in Fig. 3, it reveals the static pressure with different mesh numbers. The results show that when the number of grids reaches 161716, increasing the number of grids will no longer have a significant impact on the numerical simulation results. Therefore, in the subsequent research, the hydrocyclone model is divided into 161716 grids (Fig. 2).

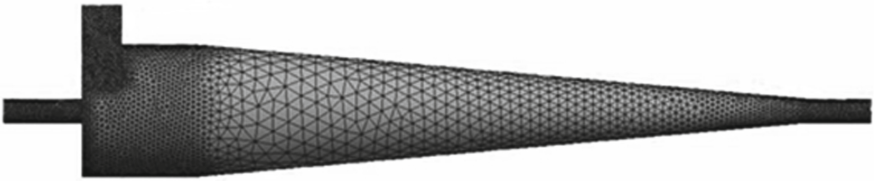

Fig. 2. The hydrocyclone meshed representation.

Table 2. The main structural parameters of hydrocyclone.

Name	Size
Dominant diameter (D)	80 mm
Overflow pipe diameter (d_o)	20 mm
Underflow pipe diameter (d_u)	16 mm
Cylindrical length (H)	100 mm
Overflow pipe length (h_1)	90 mm
Insertion length of overflow pipe (h_2)	40 mm
Underflow pipe length (h_3)	70 mm
Cone angle (θ)	12°
Inlet height (a)	20 mm
Inlet width (b)	10 mm

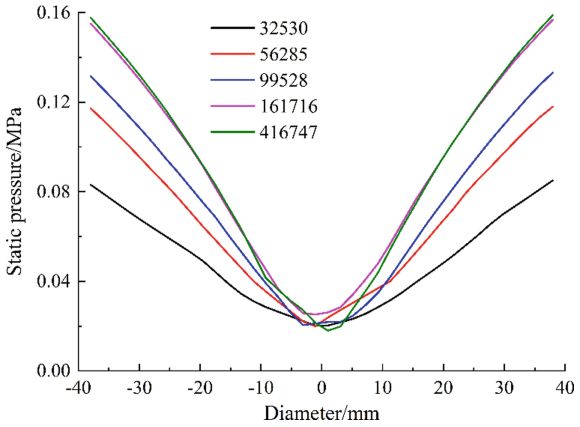

Fig. 3. Grid independence detection.

3 Results and Discussion

3.1 Model Validation

In order to verify the correctness of the numerical model, the results of flow ratio and pressure drop are compared by the simulation and experiment. Figure 4 shows the distribution curves of split ratio and pressure drop under variable flow rates. In this study, the split ratios of both simulation and experiment decrease slightly with the flow rate increasing, and the simulation is generally consistent with the experiment, retaining the average relative error within 2%. With the flow rate increasing, the pressure drop increase significantly, and the simulation of pressure drop is in good agreement with the experiment, and the average relative error is 9%. Obviously, the RSM and Mixture model can be well applied to the hydrocyclone of NGH.

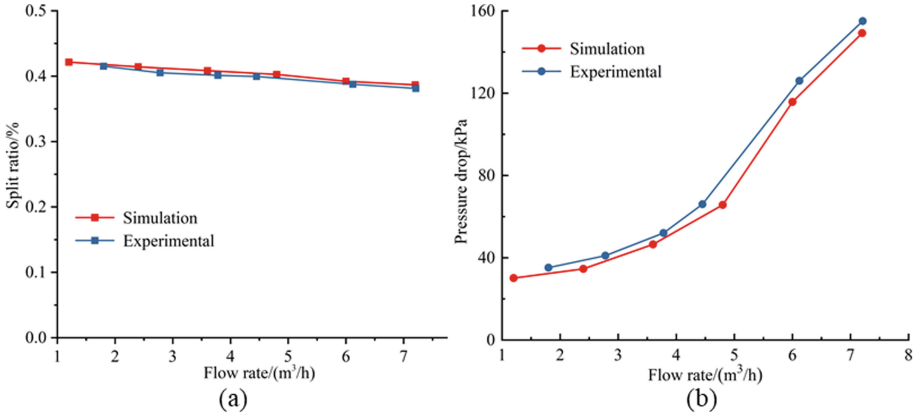

Fig. 4. Comparisons between the simulation and the experiment: (a) the split ratio, (b) the pressure drop.

3.2 Volume Fraction Distribution of Sand

As shown in Fig. 5, it can be seen that with the increase of back pressure, the volume fraction of sand near the underflow pipe gradually increases. The seawater and hydrate in the fluid, due to the smaller density, are more susceptible to the influence of back pressure, then resulting in the accumulation of sand near the wall. In the case of no back pressure, the sand volume fraction near the axis is basically zero, but when the back pressure is 30 kPa, a large amount of sand is accumulated at the same position. This is due to the existence of back pressure, and the area of upward movement expands, resulting in the decrease of split ratio. Obviously, the presence of back pressure is not conducive to sand removal.

3.3 Volume Fraction Distribution of NGH

As shown in Fig. 6, it is the volume fraction distribution of NGH with different back pressures. We can see that the volume fraction of NGH increases rapidly from the wall to the axis along the radial direction, and reaches the maximum near the axis. Besides, the volume fraction of NGH in the lower part of the overflow pipe increases rapidly, while the volume fraction of hydrate in the conical section decreases. This is because the back pressure hinders the underflow flow, resulting in the NGH migrating and accumulating to the axis under the action of centrifugal force in hydrocyclone. It can be seen that the existence of the back pressure of the underflow is conducive to the recovery of NGH.

3.4 Split Ratio

The split ratio represents the relationship of flow distribution between the overflow-outlet and underflow-outlet, which is an important process parameter of the hydrocyclone. In this paper, the split ratio refers to the split ratio of the underflow, and it is given by the following formula [13, 14]:

$$F = \frac{Q_u}{Q_i} \times 100\% \tag{8}$$

where Q_u and Q_i are the underflow-outlet and inlet volume flow rates of the hydrocyclone (m^3/s), respectively.

Figure 7 shows that the distribution curve of split ratio under different back pressures. Clearly, we can see that the split ratio decreases sharply as the back pressure increases. When the back pressure increase from 0 to 30 kPa, the split ratio reduces rapidly from 39% to 11%. This is due to the existence of back pressure, which generates the resistance for sand removal of hydrocyclone, forcing the underflow fluid to change its direction of motion and carrying sand and hydrate out of the overflow outlet. Obviously, it will make a challenge to the separation for sand and NGH.

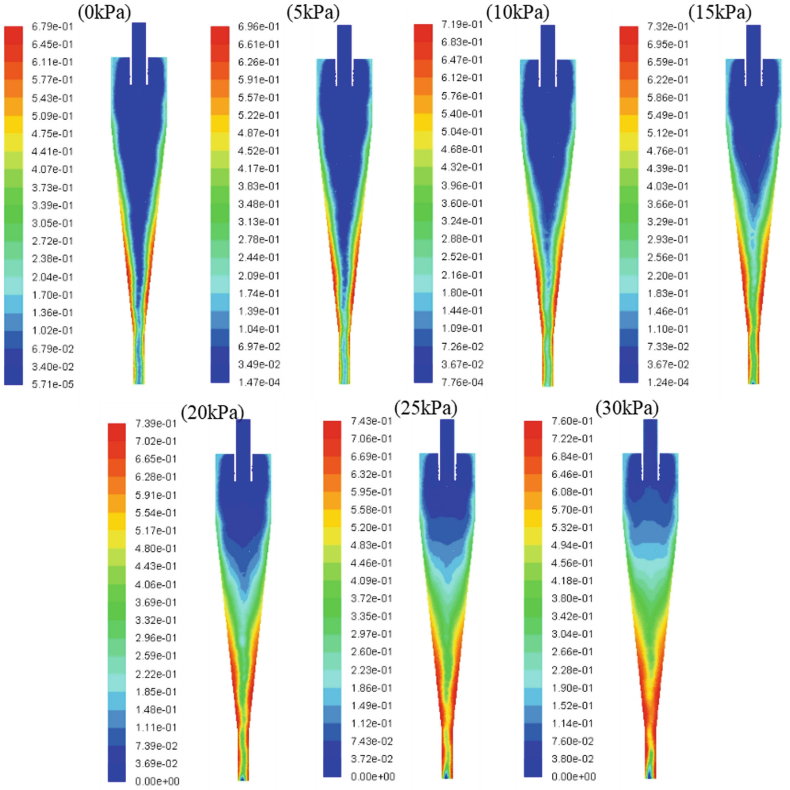

Fig. 5. Volume fraction distribution of sand with different back pressures

3.5 Separation Efficiency

The separation efficiency is an important technical index to evaluate the separation performance of hydrocyclone. The desanding efficiency and purification efficiency are calculated by the following formulas:

$$E_s = \frac{M_{us}}{M_{is}} \times 100\% \tag{9}$$

$$E_h = \frac{M_{oh}}{M_{ih}} \times 100\% \tag{10}$$

where E_s refers to the desanding efficiency (%), M_{is} and M_{us} refer to the inlet and underflow sand mass flow rates (kg/s), respectively; E_s refers to the purification efficiency (%), M_{ih} and M_{oh} refer to the inlet and overflow NGH mass flow rates (kg/s), respectively.

However, the separation efficiency of one phase of gas hydrate or sand cannot be only considered in the evaluation of separation performance, and the technical indexes of the both should be comprehensively considered. This paper uses the deformation formula of Hancock comprehensive efficiency [12]:

$$E = E_s \cdot E_h - (1 - E_s) \cdot (1 - E_h) \tag{11}$$

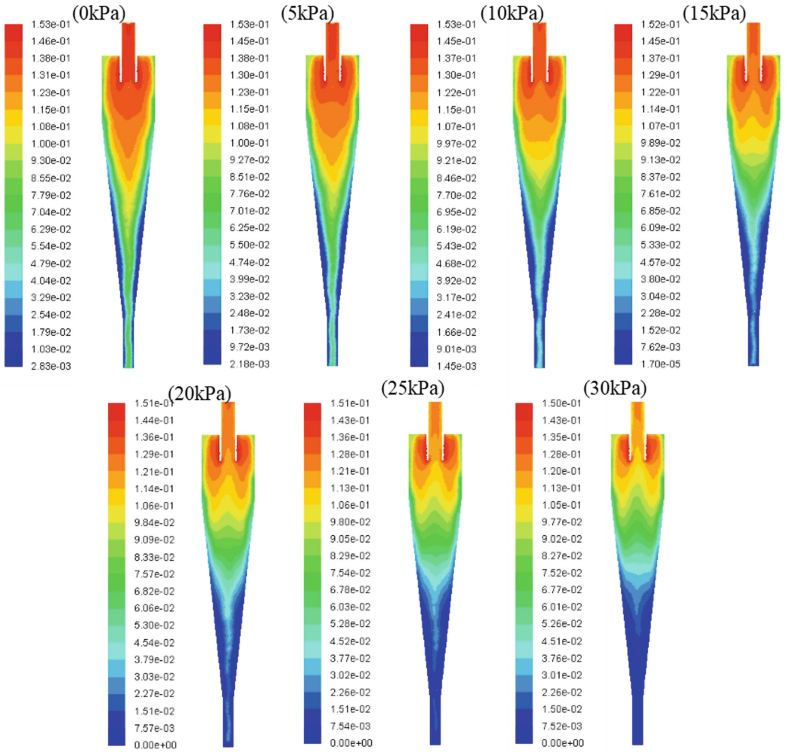

Fig. 6. Volume fraction distribution of NGH with different back pressures

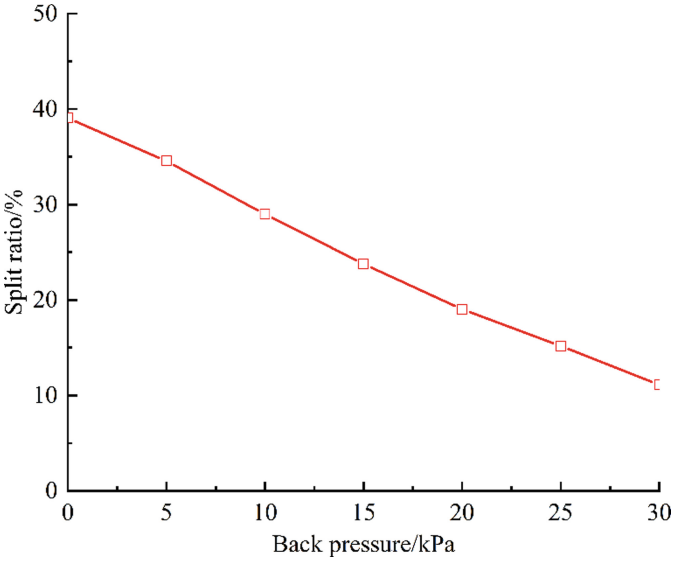

Fig. 7. The distribution curve of split ratio under different back pressures.

As shown in Fig. 8, it is the distribution curves of purification efficiency, desanding efficiency and comprehensive efficiency under different back pressures. It can be seen that the desanding efficiency decreases sharply from 97.7% to 53% with increasing of back pressure. On the contrary, the purification of NGH continues to increase from the initial 86.2% to 99.8%. At the same time, the comprehensive efficiency of hydrocyclone first increases slightly and then decreases sharply with the increase of back pressure, peaking 88.7% at 10 kPa. This is due to with the back pressure increasing, the split ratio of hydrocyclone drops, which leads to most of the fluid carrying unseparated sand and hydrate to discharge directly from the overflow. Obviously, the back pressure will result in the decrease of the comprehensive separation performance. Therefore, it is necessary to strictly control the back pressure in the engineering application, so that the hydrocyclone can maintain a good separation performance.

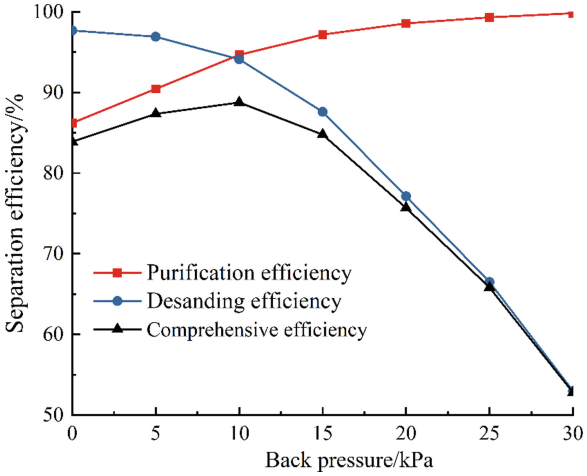

Fig. 8. The distribution curves of purification efficiency, desanding efficiency and comprehensive efficiency under different back pressures.

4 Conclusions

Numerical simulations were performed to investigate the adaptability of hydrocyclone separation for sand and NGH to back pressure. The following conclusions are made:

(1) When the back pressure increases from 0 to 30 kPa, the purification efficiency increases to 99.8%, but the desanding efficiency sharply drops to around 53%. So that, the existence of back pressure is unfavorable for sand removal.
(2) For the separation of hydrate slurry, we cannot only consider the one phase separation efficiency of sand or NGH. Therefore, it is necessary to evaluate the separation performance by comprehensive efficiency. Within the back pressure of 20 kPa, the comprehensive efficiency maintains over 70%, and peaks of 88.7% at 10 kPa.

(3) In the research scope, the hydrocyclone has good adaptability to back pressure. To a certain extent, the existence of back pressure may help to improve the comprehensive separation efficiency.

Acknowledgements. This work was supported by the National Key R&D Program of China (Grant No. 2019YFC0312305).

References

1. Sloan, E.D., Koh, C.A.: Clathrate Hydrates of Natural Gases. CRC Press, Boca Raton (2007)
2. Ye, Y.G., Liu, C.L.: Natural Gas Hydrate: Experimental Techniques and Their Applications. Springer, Heidelberg (2013). https://doi.org/10.1007/978-3-642-31101-7
3. Boswell, R., Collett, T.S.: Current perspectives on gas hydrate resources. Energy Environ. Sci. **4**(4), 1206–1215 (2011)
4. Zhou, S.W., Chen, W., Li, Q.P., et al.: Research on the solid fluidization well testing and production for shallow non-diagenetic natural gas hydrate in deep water area. China Offshore Oil Gas **29**(4), 1–8 (2017)
5. Fu, Q., Wang, G.R., Zhou, S.W., et al.: Development of marine natural gas hydrate mining technology and equipment. Strateg. Study CAE **22**(06), 32–39 (2020)
6. Zhou, S.W., Chen, W., Li, Q.P.: The green solid fluidization development principle of natural gas hydrate stored in shallow layers of deep water. China Offshore Oil Gas **26**(05), 1–7 (2014)
7. Liu, W.G., Liu, R., Zhang, M.M., et al.: Rheological properties of hydrate slurry formed from mudflows in South China Sea. Energy Fuels **35**(13), 10575–10583 (2021)
8. Fang, X., Wang, G.R., Zhong, L., et al.: Adaptability analysis of operating parameters of hydrate hydrocyclone separator based on a CFD simulation. Sep. Sci. Technol. **3**, 1–11 (2021)
9. Chang, Y.L., Ti, W.Q., Wang, H.L., et al.: Hydrocyclone used for in-situ sand removal of natural gas-hydrate in the subsea. Fuel **285**, 119075 (2021)
10. Wang, A., Yan, X.K., Wang, L.J., et al.: Effect of cone angles on single-phase flow of a laboratory cyclonic-static micro-bubble flotation column: PIV measurement and CFD simulations. Sep. Purif. Technol. **149**, 308–314 (2015)
11. Yang, Q., Li, Z.M., Lv, W.J., et al.: On the laboratory and field studies of removing fine particles suspended in wastewater using mini-hydrocyclone. Sep. Purif. Technol. **110**, 93–100 (2013)
12. Pang, X.S.: Hydrocyclone Technology and Application. China Petrochemical Press (2011)
13. Svarovsky, L.: Solid-Liquid Separation. Elsevier, Amsterdam (2000)
14. Yang, Q., Wang, H.L., Liu, Y., et al.: Solid/liquid separation performance of hydrocyclones with different cone combinations. Sep. Purif. Technol. **74**(3), 271–279 (2010)

Numerical Simulation Research on Spiral Transportation of Non-diagenetic Gas Hydrate Fluidized Mining in Sea Area

Feng Chen, Xiaofang Lv(✉), Shuli Wang, and Shu Jing

School of Petroleum Engineering, Changzhou University, Changzhou 213000, Jiangsu, China
lvxiaofang5@cczu.edu.cn

Abstract. In order to improve the safety and efficiency of hydrate slurry transportation in submarine horizontal pipelines in hydrate solid fluidized mining technology, it was proposed to use the tangential velocity of spiral flow to improve the transportation capacity, and a CFD/Fluent numerical model was established. The guide bar in the pipeline starts to rotate all the way, the setting angle of the guide bar was 23°, and the initial concentration of hydrate particles and the inlet Reynolds number were set. The distribution law of velocity field, pressure field and particle concentration in the tube was systematically analyzed when the initial particle concentration was from 10% to 40% and the initial Reynolds number was from 5000 to 20000. The results showed that the cross-sectional velocity of the hydrate slurry in the pipe was 120° rotationally symmetrical about the center of the circle. The greater the initial concentration of hydrate, the smaller the maximum velocity area in the pipe; in the simulated liquid-solid system, the smaller the initial concentration of particles or the larger the Reynolds number, the greater the flow friction of the slurry in the pipeline; An increase in the Reynolds number of a spiral fluid will make it more capable of carrying liquid. The hydrate concentration on each section of the pipe was irregularly distributed, but no hydrate particles were deposited in the whole pipe section. Among the two main factors controlled by this research, the Reynolds number had a greater impact on the friction of the slurry flow in the horizontal pipe that spins along the guide bar. Compared with straight pipes without guide strips, the full rotation of the guide strips can extend the hydrate transportation distance and expand the flow safety boundary.

Keywords: Hydrate · Spiral flow · Guide strip · Numerical simulation

1 Introduction

In 2016, the National "Energy Technology Revolution and Innovation Action Plan (2016–2030)" proposed breakthroughs in key technologies for hydrate exploration and development, and carried out pilot drilling and trial production tests, in 2017, the State Council approved the listing of natural gas hydrate as the 173rd mineral. In this context, in May 2017 and March 2020, China completed two trials of natural gas hydrate production in the South China Sea, setting two new world records for "total gas production and

B. Sun et al. (Eds.): DWOG-Hyd 2021, LNCE 246, pp. 302–319, 2022.
https://doi.org/10.1007/978-981-19-0960-3_30

average daily gas production". However, Large-scale development of natural gas hydrate needed to be explored. Academician Zhou Shouwei creatively proposed a solid-state fluidized hydrate mining method based on the physical characteristics and accumulation characteristics of marine non-diagenetic hydrates in our country [1]. Among them, the transportation law of hydrate into the pipeline after being broken and its safe and efficient lifting technology was one of the current world's leading innovation technology problems [2, 3]. The law of slurry flow in submarine horizontal pipelines was of great significance in solid fluidized mining technology.

Numerical simulation provided data supplement to the development of computational fluid dynamics experiments. Based on the Euler two-fluid model and particle dynamics theory, Wei Xuelei et al. [4] studied the flow pressure drop and the slurry velocity distribution during the flow of heterogeneous particle hydrate slurry at different hydrate particle volume fractions and different flow rates. The results showed that the slurry flow the pressure drop was mainly affected by the flow rate, the greater the speed, the greater the pressure drop. Subsequently, Sun Xian et al. [5] took the hydrate slurry transportation process in the curved pipe system as the research object, and conducted numerical simulations on the two factors (particle diameter, pipe diameter) that affect the maximum volume fraction of hydrate particles in the curved pipe system. The analysis results showed that when the hydrate slurry flow rate was small, the maximum hydrate volume fraction in the elbow system was more affected by the particle size, and when the slurry flow rate was faster, the maximum hydrate volume fraction was more affected by the flow velocity. Yao Shupeng et al. [6] based on the group balance of the hydrate particle aggregation dynamics, conducted an orthogonal test study on the hydrate flow characteristics in the vertical pipeline during the mining process, and the results showed that it has the greatest impact on the hydrate slurry flow friction in the vertical pipeline. The factor was the average flow velocity of the hydrate slurry. Cao et al. [7] established a hydrate slurry multiphase flow model considering particle separation and behavior. Based on the intrinsic dissociation kinetics theory, the hydrate dissociation model was carried out. Improved and studied the particle behavior and dissociation rate flow characteristics under different hydrate volume fractions and flow rates. The results showed that The increase of the average particle size of the hydrate volume fraction will lead to the greater the viscosity and pressure drop of the mud.

Wang Shuli's research group of Changzhou University [8, 9, 10] combined the spiral flow theory with hydrate transportation technology to study the hydrate flow and deposition laws of spiral flow in pipelines. Rao Yongchao et al. [11] adopted the RNG k-ε model numerical simulation research was carried out on the flow characteristics of the spiral flow swirling in the horizontal tube with the impeller, and the accuracy and reliability of the mathematical model were verified through experiments. Wang Ziwen [12] obtained through simulation research that the best placement angle of the guide bar was 23° and the number of guide bars was 3. Later, Rao et al. [13] used RSM and DPM models to analyze the flow of low-concentration CO_2 hydrate slurry. Numerical simulations were carried out and it was found that the heat transfer efficiency was also related to the Reynolds number and particle concentration. Compared with ordinary pipelines, the swirling flow can significantly increase the transport distance of the hydrate slurry.

In this article, we used the Euler-Euler two-fluid model to simulate the liquid-solid two-phase flow process in a spiral flow pipe. The DPM model was used to calculate the interaction between particles and particles and between particles and walls. At the same time, considering the resistance and rotational lift of the fluid relative to the particle phase, the concentration distribution, trajectory, velocity, pressure and velocity of hydrate particles under different working conditions were obtained. Distribution etc. The flow situation of spiral flow and ordinary pipe flow was compared and analyzed. The research results can provide reference for the research of submarine horizontal pipeline transportation in solid fluidized mining technology.

2 Model Building

2.1 Geometric Model

As a spinning device, the guide strip was first adopted by the hydraulic sediment transport research group of Taiyuan Polytechnic [14]. In this study, the design of 360° ring winding installation was adopted. The cross-section structure diagram of the guide bar was shown in Fig. 1, and the guide bar was fixed on the inner wall of the spiral pipe section, so the outer diameter of the ring formed by the guide strip should be consistent with the inner diameter of the pipe. The guide strip was twisted from the ribbon plate, and the tie was installed in the pipe wall, in which one side was fixed on the pipe wall, and the short edge of the tie pointed to the pipe axis everywhere. The placement angle of the guide bar, the number of the guide bar and the height of the guide bar were taken as the three parameters to accurately describe the guide bar, in which the placement angle of the guide bar was the angle between the intersection line and the axis formed by the contact between the guide bar and the pipe wall, and the height of the guide bar was the length of the short side of the tie. When the guide bar was installed in the pipe, it was installed on the inside of the pipe wall according to the number of the guide bar. In this paper, the whole process of rotation was studied, and the installation length of 360° ring winding of guide bar should be consistent with the length of pipe L.

The pipeline was placed horizontally, with a diameter of $D = 0.032$ m and a length of $L = 2$ m. Install guide strips from the entrance. The number of guide strips was 3 and the height was D/6, as shown in Fig. 2. The calculation adopted a rectangular coordinate system, the origin of the coordinates was at the center of the pipe entrance surface, the Z axis was the flow direction, and the Y axis was the direction of negative gravity.

The whole pipe section was divided into unstructured meshes, and the meshes of the wall and the edge of the guide strip were densified by 5 layers, the thickness of the bottom layer was 0.2 mm, under the same working condition, the number of meshes of 2×10^5–2×10^6 was simulated. The average axial flow velocity and tangential flow velocity at the same section position of the pipe were taken for comparison, and the results were shown in Fig. 3. It can be found that the grid number increases to 8×10^5 after that, the grid number continued to increase had little effect on the tangential and axial velocity variations, while the greater the grid number, the longer the computation time. When the accuracy of the calculation was met, an 8×10^5 the number of meshes was calculated, and the final mesh subdivision was shown in Fig. 4.

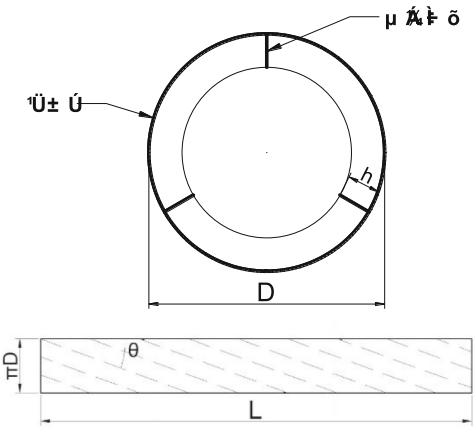

Fig. 1. Schematic diagram of the cross-section structure of the guide strip. D-pipe wall inner diameter; h-guide bar height; θ-guide bar placement angle; πD-pipe circumference; L-pipe total length

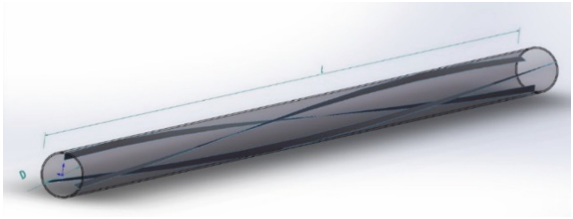

Fig. 2. Geometric model

2.2 Basic Assumption of Model

The model included five basic assumptions, namely: ① incompressible fluid; ② Without considering the formation, decomposition and coalescence of hydrate particles; ③ Without considering the temperature difference; ④ Without considering the adhesion of particles to the pipe wall; ⑤ The initial particle size of hydrate particles was 10 μm.

2.3 Multiphase Flow Model and Turbulence Model

The Euler-Euler two-fluid model was selected for this simulation. The governing equations include momentum equation and continuity equation, as shown in Eqs. (1) and (2) respectively.

$$\frac{\partial(\rho_i \alpha_i)}{\partial t} + \nabla(\rho_i \alpha_i v_i) = 0 \tag{1}$$

$$\frac{\partial}{\partial t}(\rho_i \alpha_i v_i) + \nabla(\rho_i \alpha_i v_i) + \alpha_i \nabla p = \nabla \cdot \tau_i + \rho_i \alpha_i g + M_i \tag{2}$$

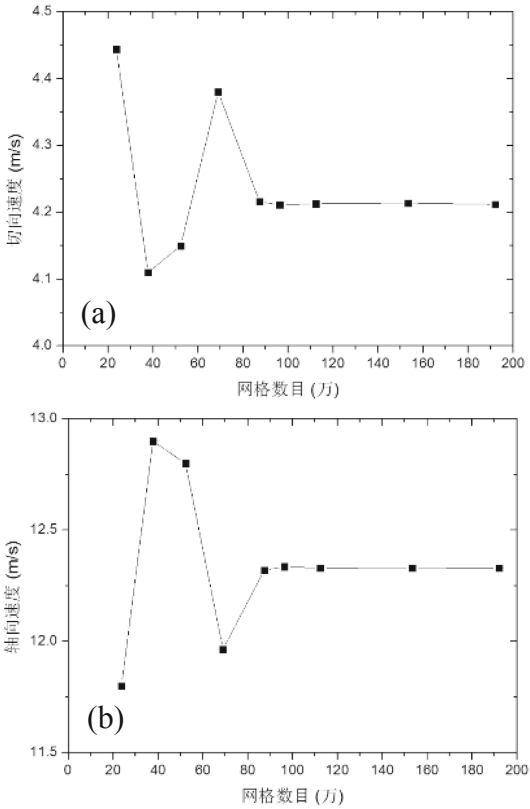

Fig. 3. Grid independence verification. (a) Tangential speed (b) Axial speed

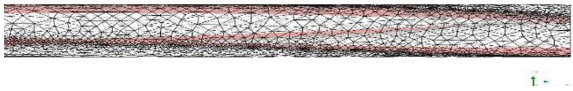

Fig. 4. Mesh division

Where i was water phase or hydrate particle phase, ρ was density, kg/m^3; v was the velocity vector, m/s; P was pressure, Pa; τ_i is the stress tensor, Pa; M_i was the interphase momentum exchange quantity, kg/(m $\cdot$ s)^2. In this paper, the phase transition of hydrate particles was not considered in the simulation study of liquid-solid two phases, so the coupling between liquid and solid should be considered. The interaction between fluid and solid in the flow process will generate momentum exchange. When momentum M_i exchange occurs, the interphase drag force M_{dl} and turbulent diffusion force M_{tl} should be taken into account in momentum exchange, and the interphase force model should be established to close the multiphase flow model, as shown by formula (3).

$$M_i = M_{dl} + M_{tl} = k_{ls}\left(v_r - \frac{\mu_t}{\rho_m \alpha_s \sigma_d}\nabla\alpha_l\right) \tag{3}$$

Where v_r was the phase-to-phase relative velocity; μ_t was turbulent viscosity, $kg/(m \cdot s)$; ρ_m was the density of mixed phase, σ_d was Planck diffusion coefficient; α_s was the volume fraction of hydrate particles; α_l was the volume fraction of water phase. k_{ls} was coefficient of momentum transfer, since the hydrate slurry was formed by the mixing of water and hydrate particles, the swaying force had a large effect on the breaking and polymerization situation in.

The equations of motion of solid particle trajectories in the Z direction as shown by formula (4)

$$\frac{d}{dt}u_p = F_D(u - u_p) + \frac{g_z}{\rho_p}(\rho_p - \rho) + F_Z \tag{4}$$

Where u was the fluid phase velocity, m/s; u_p was the particle velocity, m/s; g_z was the component of the gravitational acceleration in the z direction, m/s^2; ρ was the density of the fluid, kg/m^3; ρ_p the density of the particles, kg/m^3; other acting forces were mainly Staffman lift, additional mass force, Brownian force, etc. Should be considered due to the fact that when flow occurs perpendicular to the direction of particle movement, a poor staffman lift was generated. An additional mass force was considered when the particle density was less than the fluid density. Brownian force should be considered when the particle size was submicron (0.1 m–1 m), which was not considered here because the size was 10 μm.

Where, F_D was defined as:

$$F_D = \frac{18\mu}{\rho_p d_p^2}\frac{C_D \mathrm{Re}}{24} \tag{5}$$

Where d_p was the particle diameter, m.

The drag coefficient CD can be expressed as follows:

$$C_D = a_1 + \frac{a_2 + a_3}{\mathrm{Re}} \tag{6}$$

2.4 Model Solving

Fluent16.0 version was used for the simulation calculation. Velocity-inlet was used as the boundary condition of the inlet end of the pipe, and Reynolds number of 5000–20000 was used as the velocity inlet condition. Outflow end boundary condition was set as Outflow, and wall boundary condition was set as fixed non-slip wall. Gravity direction along the - y direction, the magnitude of gravity acceleration was 9.81 m/s^2. The pressure base implicit solver was used to simulate the three - dimensional transient. The RNG $k - \varepsilon$ turbulence model was adopted and Coupled algorithm was used to calculate the pressure and velocity. The pressure adopted the second-order upwind scheme. The velocity and concentration of seawater and hydrate particles were set at the inlet of the pipe. The simulation was ended when the residual error of each factor converged to 10^{-6}.

The initial conditions were set as follows: the basic physical parameters of seawater phase and hydrate phase were measured at 277K at standard atmospheric pressure. The continuous phase fluid was seawater with a density of 1025 kg/m^3 and dynamic viscosity of 0.0017 Pa·s. The discrete phase was natural gas hydrate particles with particle size of 10 μm and density of 650 kg/m^3.

2.5 Model Validation

According to the related experiment [15], 8 working conditions were selected in this paper, as shown by Table 1. The comparison between the measured pressure drop and the simulated pressure drop can verify the feasibility of this model to a certain extent.

Table 1. Part of the numerical simulation parameter

	Initial particle concentration α_0, %	Converted flow rate v, m/s	Re
1	10	0.2764228	5000
2	40		
3	10	0.5528455	10000
4	40		
5	10	0.8292683	15000
6	40		
7	10	1.1056911	20000
8	40		

Figure 5 was a graph showing the comparison of experimental and numerical values under different conditions. From the comparison results, the flow pressure droped in the hydrate tube at operating condition 1–4 was Lower Reynolds number, although with some margin of error, but the error between the numerical calculation and the experimental data at operating condition 5–8 was smaller, the experimental results were in good agreement with the numerical simulation, which showed that this method can be used to simulate the hydrate slurry flow in helical pipes. As a whole, the whole process of liquid-solid two-phase spiral flow with guide bars can be numerically simulated.

3 Numerical Simulation Results and Analysis

This chapter mainly analyzed the effects of different concentrations and different Reynolds on the velocity distribution, concentration distribution, and pressure distribution in the hydrate slurry pipeline. In this paper, 16 working conditions with hydrate particle concentration of 10%, 20%, 30% and 40% were set under different Reynolds numbers. The data parameters were selected according to the content of the research, as shown in Table 2:

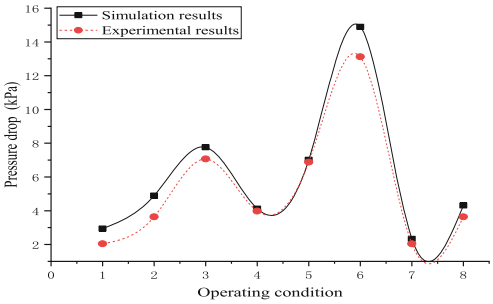

Fig. 5. Variation curve of pressure drop under different working conditions

Table 2. Numerical simulation parameter

	Initial particle concentration α_0, %	Particle size D_k, μm	*Re*	Diversion bar height *h*, m
1	10	10	5000	D/6
2	20			
3	30			
4	40			
5	10	10	10000	D/6
6	20			
7	30			
8	40			
9	10	10	15000	D/6
10	20			
11	30			
12	40			
13	10	10	20000	D/6
14	20			
15	30			
16	40			

3.1 Influence of Hydrate Particle Concentration and Reynolds Number on Velocity Distribution

In order to explore the velocity distribution in the hydrate slurry pipeline, the full cycle position of the cross-section was selected (the guide bar completely rotates 360° from the inlet end, here was the full cycle position) to see that the initial concentration of hydrate particles was 10%–40% of cases. As shown in Fig. 6 was a cloud diagram of the

velocity distribution of hydrate particles at the second full cycle position and the fourth full cycle position with different concentrations under Re = 15000 conditions. From the figure, it can be seen that the cross-sectional flow velocity in the tube rotates 120° with respect to the center of the circle. Symmetrical, with the increase of the flow distance, the velocity in the tube hardly attenuates, and the velocity in the axial center area was the largest. The hydrate particle movement velocity near the pipe wall and the guide bar decreases faster. This was due to the wall roughness causing the velocity decrease near the pipe wall. The velocity of the laminar bottom layer near the wall tends to 0, and the kinetic energy of the slurry impacting the guide bar decreases, so that the velocity near the guide bar tends to 0; while the axis area was not blocked, the axial velocity was fully functional and promotes the hydrate The slurry flows in the tube.

By comparing the maximum velocity area, it can be found that as the initial concentration of hydrate particles increases, the maximum hydrate velocity area at this section was shrinking, and the maximum velocity in the pipeline was decreasing, this was because the hydrate concentration increases, which increases the possibility of hydrate sedimentation and aggregation. Part of the hydrate was dragged by the viscosity of the precipitate, which reduces the flow rate; on the other hand, the hydrate concentration increases, which enhances the collision between hydrate particles. There was a chance that the hydrate particles will lose energy after the collision, and the kinetic energy will decrease.

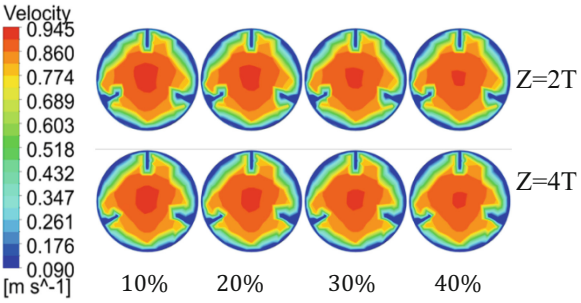

Fig. 6. Cloud diagram of the velocity distribution of hydrate particles at the same section of the pipeline under different concentrations

As shown in Fig. 7, the velocity and vector distribution at different cross-sections of the hydrate slurry pipeline under the condition of Re = 20000 and $\alpha_0 = 30\%$. From the velocity vector line, it can be seen that the vector line near the guide bar in the entire flow was always the densest, the vector line near the guide strip has not attenuated, indicating that the start-up of the guide strip effectively maintains the tangential velocity of the spiral flow without attenuation, and the tangential velocity generated by the spiral flow was to ensure that the hydrate does not quickly deposit and adhere to It was an important factor of the pipe wall, so the rotation of the guide strip can help solve the problem of hydrate deposits blocking the pipe.

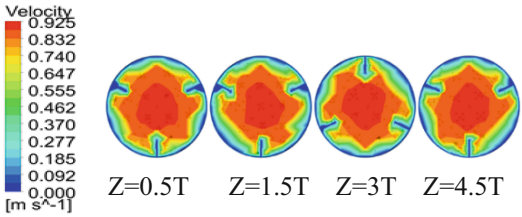

Fig. 7. Velocity and vector distribution at different positions of the pipeline

The initial concentration of hydrate particles was $\alpha_0 = 40\%$, took the velocity on the axis of the pipeline to make a broken line diagram of the centerline velocity change as shown in Fig. 8. It can be seen from the figure that after the hydrate slurry enters the ordinary pipeline, the velocity will change First increase to the maximum value, then slightly attenuate and maintain the speed until the entire pipeline flows. As the Reynolds number increases, the position of the maximum speed in the pipeline gradually moves away from the starting point.

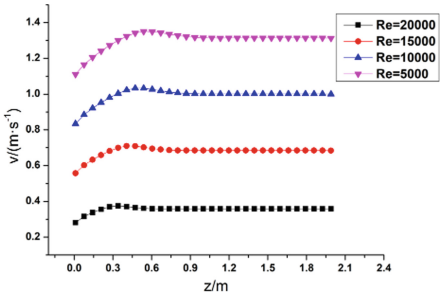

Fig. 8. Variations of center line speed under four working conditions under different Re

As shown in Fig. 9, at the section position of $z = 3T$ under the condition of $\alpha_0 = 30\%$, make a center line in the x direction to observe the influence of Reynolds number on the tangential velocity and the axial velocity. It can be clearly found from the figure that the greater the Reynolds number, the greater the tangential velocity and the greater the axial velocity. The maximum value of the tangential velocity appears at about 0.4D near the tube wall, and the tangential velocity in the axial area tended to zero. The area of maximum axial velocity appears at the axis of the pipe, and the closer to the pipe wall, the lower the axial velocity. This showed that the increase of Reynolds number can effectively improve the conveying effect of hydrate slurry by the rotating pipeline.

3.2 Influence of Hydrate Particle Concentration and Reynolds Number on Concentration Distribution

Hydrate particles flow in the pipeline with seawater, and the distribution of hydrate particles at each section of the pipe was different, starting from the entrance every other

half cycle (the guide bar completely rotates 180° from the entrance end, here was Half-period position) establish a datum level, and obtain the distribution of hydrate particles at different sections of the pipeline under the working condition of Re = 15000 and initial concentration of 40% as shown in Fig. 10. As can be seen from the figure, in the first half-period section, it can be seen that the actual concentration of hydrate particles on both sides of the guide strip at the upper left was slightly higher, and the distribution of hydrate particles in the remaining sections was relatively uniform, and the volume fractions on the same section were slightly different. This was because the hydrate slurry flows into the pipeline, and the swirling effect of the spiral flow at the inlet was not obvious, and the hydrate particles were lighter than seawater. At this time, the shear stress was small and cannot carry all the hydrates. With the extension of the transportation distance, the swirling effect After stabilization, the hydrate particles were more evenly distributed in the pipeline on each section, and there was no sign of hydrate accumulation and deposition.

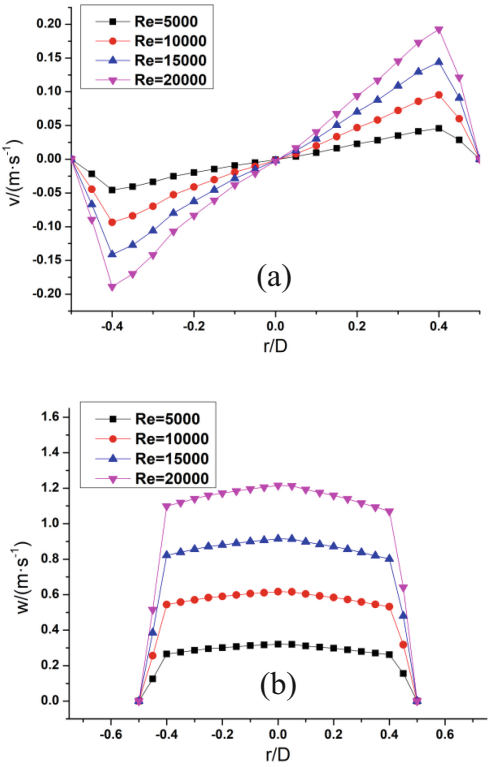

Fig. 9. The influence of different Reynolds numbers on tangential velocity and axial velocity. (a) Tangential speed (b) Axial speed

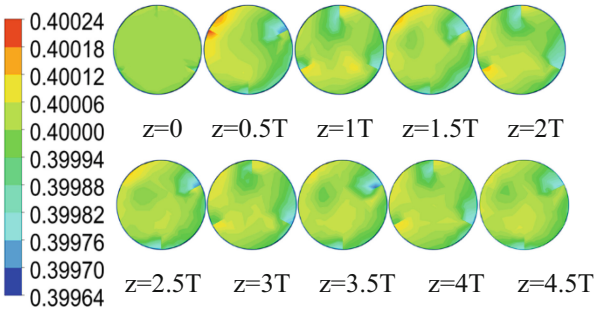

Fig. 10. Re = 15000, α_0 = 40%, hydrate distribution at different cross-sections

Import the simulation results into tecplot to see the specific situation of the two-phase distribution in the pipeline, as shown in Fig. 11. From the figure, it can be found that the seawater on the windward side of the guide strip occupies the main space, and the hydrate particles were almost distributed on the leeward side. The tangential velocity produced by the spiral flow separates the denser seawater from the less dense hydrate particles. After being thrown out, the hydrate particles were partially retained on the leeward side. The actual concentration of hydrate particles on the leeward side of the guide strip was slightly Greater than the concentration on the windward side.

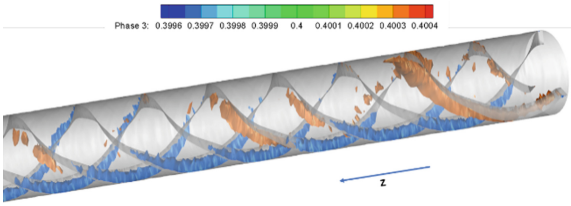

Fig. 11. Two-phase distribution in the hydrate slurry pipeline

As shown in Fig. 12, the initial concentration of hydrate particles was α0 = 40% and the distribution of hydrate particles under four working conditions under different Reynolds numbers. The concentration cloud diagram shows that the actual concentration was within the range of 39.90%–40.05% to see Reynolds more intuitively. The influence of the number on the distribution law of hydrate particle concentration, the comparative analysis can find that with the increase of Reynolds number, the distribution of hydrate particles in the tube gradually tends to be uniform. When the Reynolds number was 15000, there was almost no sign of hydrate particles agglomerating. On the contrary, Conversely, the Reynolds number becomes smaller, that is, the lower the conveying speed, the smaller the tangential velocity produced by the guide strip, the easier it was for hydrate particles to accumulate between the guide plate and the pipe wall, and the speed was still low under Re = 20,000. Enough strong vortex area was generated to attract hydrate particles, and the hydrate particles were distributed near the pipe wall under the combined action of shear stress and buoyancy.

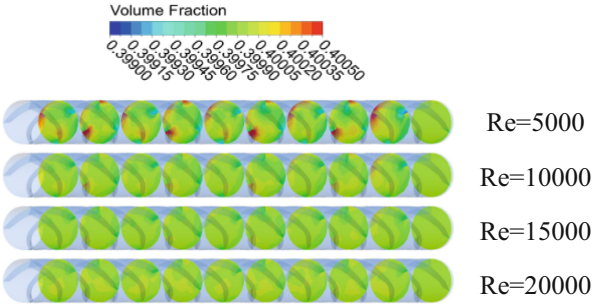

Fig. 12. The actual concentration distribution of hydrate particles under four working conditions under different Reynolds numbers

3.3 Influence of Hydrate Particle Concentration and Reynolds Number on Pressure Distribution

Taking the maximum pressure of the initial section of the pipeline and making the difference between the minimum pressures on the remaining sections to obtain the pressure drop under four working conditions with Re = 15000. Different initial hydrate concentrations was shown in Fig. 13. It can be seen from the figure that as the initial concentration increases, the pressure drop across the pipeline gradually decreases. This was because as the initial concentration of hydrate particles increased, the volume fraction of the seawater phase became lower, and the density becomes smaller after the two phases were mixed. Finally, after the same distance was conveyed, the concentration of hydrate particles was higher, but the pressure consumed was lower.

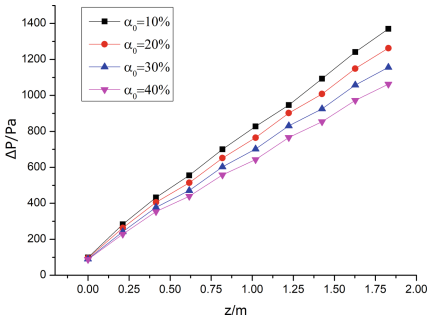

Fig. 13. Pressure drop changes at different concentrations

Take the maximum pressure of the initial section of the pipeline, and make the difference between the minimum pressures on the other sections. As shown in Fig. 14, the effect of Reynolds number on the pressure dropped under the condition of the initial concentration of hydrate particles α0 = 40%, the abscissa. It was the flow distance in the axial direction, and the ordinate was the pressure drop. It can be seen from the figure that as the transportation distance increases, the influence of the Reynolds number on the pressure drop across the pipeline gradually increases.

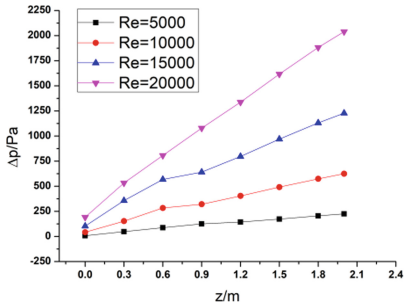

Fig. 14. The influence of Reynolds number on pressure drop

3.4 Comparative Analysis of Spiral Flow and Ordinary Pipeline

In order to compare the influence of the ordinary pipeline and the guide strip on the speed change of the pipeline, take the initial concentration of hydrate particles $\alpha 0 =$ 40% and the axial velocity with the Reynolds number of 10000 and 20000 respectively to make the speed change along the way, as shown in the figure as shown in the figure, it can be seen from the figure that the flow velocity in the ordinary pipeline was always greater than that in the swirling pipeline along the way, which shows that the deflector has a more obvious effect of blocking the hydrate slurry. The collision causes the loss of kinetic energy and the larger the Re, the difference in speed in the two pipelines bigger (Fig. 15).

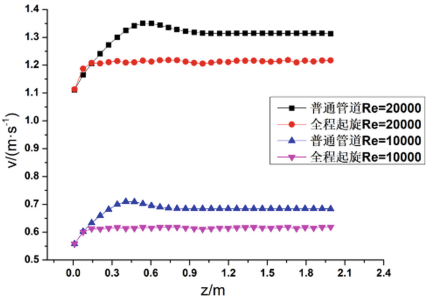

Fig. 15. Changes of axial velocity of different pipelines along the way

In order to compare the influence of ordinary pipelines and guide strips on the distribution of hydrate particles in the pipeline, Re = 15000 and the initial concentration of 10% on the YZ plane to see the distribution of hydrate particles along the way, as shown in Fig. 16. As can be seen from the figure, after the hydrate particles in the ordinary pipeline flow for a certain distance with seawater, due to the influence of buoyancy, they begin to gather and adhere to the upper side of the pipe wall, and the initial concentration of this working condition was not high, only 10% Based on this, it can be inferred that hydrate slurry was easy to accumulate in ordinary pipelines, and there was a great risk of blockage. When the hydrate particles flow in the pipe swirling along the guide strip,

the actual concentration fluctuation was very small, which indicates that the shear stress generated by the spiral flow can effectively prevent the hydrate particles from gathering on the pipe wall and can partially weaken the buoyancy effect. There will be a large number of aggregation of hydrate particles.

The position where the hydrate particles just begin to deposit was the critical position of deposition. Here, it was stipulated that the critical position of deposition was when the actual concentration was higher than 2% of the initial concentration. Table 3 showed the critical position of hydrate particle deposition under different working conditions with an initial concentration of 10% and the maximum actual concentration on this surface. From Table 3, it can be found that as the Reynolds number increases, the critical deposition position of hydrate particles was farther away from the inlet. As mentioned above, the increase in velocity enables seawater to carry hydrate particles for longer distances, which will not lead to rapid deposition. There was no tangential velocity in ordinary pipelines, so under the action of buoyancy, hydrate particles will inevitably accumulate and adhere to the pipe wall after flowing for a certain distance with seawater, resulting in hidden safety hazards of pipe blockage, which shows that pipeline transportation of hydrate slurry should be improved. Ability to increase the flow rate was one of the most direct methods.

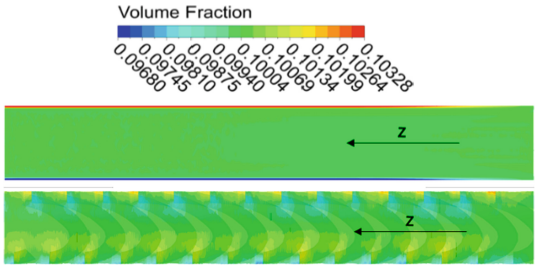

Fig. 16. Contour of the distribution of hydrate particle volume fraction in ordinary pipelines

Table 3. Critical deposition position and deposition concentration of hydrate particles

Re	5000	10000	15000	20000
Critical position, z/m	0.09	0.22	0.36	0.52
Deposition concentration, α	0.10195	0.10203	0.10200	0.10200

In the pipeline where the guide strip spins along the way, there was no cross section where the actual concentration of hydrate particles was greater than 2% of the initial concentration. The critical position was at the pipeline outlet z = 2 m. By comparing the ordinary pipeline and the guide strip spinning along the pipeline under different working conditions It can be found that when the Re was 10000 and 15000, the particle carrying distance of the swirling pipe along the guide strip was about 10 times and 5.6 times that of the ordinary pipe.

In order to better compare the influence of ordinary pipelines and guide strips on the flow friction of the pipelines, the axial pressure under the working conditions of 5000 and 20000 was used to compare the pressure changes along the way, as shown in Fig. 17, from It can be seen from the figure that when the Reynolds number was small, the pressure drop of the ordinary pipeline and the spiral pipeline along the way were not much different. With the increase of the Reynolds number, the barrier effect of the guide bar on the hydrate slurry becomes more and more significant. The pressure difference along the spiraling pipeline with the guide strip was getting larger and larger. When the same hydrate slurry was transported, the pressure consumed by the spinning pipeline along the guide strip was nearly twice that of the ordinary pipeline.

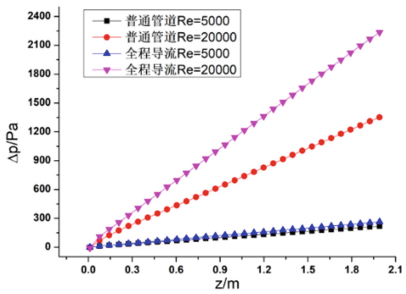

Fig. 17. Changes of axial pressure of different pipelines along the way

In the numerical simulation study of the safe flow of natural gas hydrate mining in the sea, the slurry velocity was not an important factor to measure the transportation efficiency. Therefore, even if the guide strip rotates along the way, the hydrate slurry velocity was slightly lower, but this was not enough to deny the spiral flow to the slurry transportation. Promoting effect; the carrying distance of seawater to hydrate particles and the energy consumption of the whole line were two of the key factors. Under the 15000 Reynolds number condition, the hydrate carrying distance of the swirling pipeline was 5.6 times that of the ordinary pipeline. Correspondingly, the pressure consumption of the whole line It was about 1.2 times that of the ordinary pipeline. It can be seen that the guide strip can effectively improve the transport capacity of hydrate slurry.

4 Conclusion

This paper analyzed the influence of the concentration of hydrate particles and the Reynolds number at the inlet position on the velocity distribution, pressure distribution and concentration distribution in the horizontal pipe that spins along the guide strip, and the main conclusions were as follows:

(1) The cross-sectional flow velocity in the tube was 120° rotationally symmetrical about the center of the circle, and the velocity in the axial center area was the largest. The vector lines near the guide bar were the densest and it didn't attenuated with the increase of the flow distance. Maximum cutting speed output Currently,

the position of the near tube wall was about 0.4D, and the area of maximum axial velocity appears at the axis of the pipe. The increase of the initial concentration of hydrate would result in the decrease of the maximum velocity area in the pipeline.

(2) The increase of the inlet Reynolds number will cause the friction of the mud flow in the pipeline to increase. The increase of the initial concentration of hydrate particles will reduce the flow friction of the slurry in the pipe.

(3) The increase of the imported Reynolds number would increase the ability of the spiral flow to carry liquid. The initial concentration of hydrate had almost no effect on the carrying effect of the spiral flow. The hydrate concentration distribution on each section of the tube was irregular. The areas with low particle concentration were concentrated near the three guide strips, and hydrate particles were not deposited in the entire pipe section.

(4) Among the two main factors controlled in this study, the Reynolds number had a greater impact on the flow friction of the horizontal pipe that spined along the guide bar. Compared with ordinary straight pipes, in a pipeline with a total length of 2 m, the guide bar spins along the way under the $Re = 15000$ working condition, which increased the particle carrying distance by 460%. The full rotation of the guide strip for the hydrate transportation of natural gas hydrate solid-state fluidized mining would play a significant role in expanding the safety boundary and improving the transportation capacity.

References

1. Zhou, S., Chen, W., Li, Q.: Deep-water shallow gas hydrate solid-state fluidized green mining technology. China Offshore Oil Gas **26**(05), 1–7 (2014)
2. Zhou, S., Li, Q., Lv, X., et al.: Thoughts and suggestions on the research direction of natural gas hydrate development. China Offshore Oil Gas **31**(04), 1–8 (2019)
3. Zhang, X., Lu, X., Li, P.: Research review of natural gas hydrate mining methods. Sci. China Phys. Mech. Astron. **49**(03), 38–59 (2019)
4. Wei, X., Liu, B., Pan, Z., et al.: Numerical simulation of hydrate slurry flow characteristics in horizontal pipelines. Chem. Eng. **46**(03), 41–46 (2018)
5. Sun, X., Liu, D., Wang, W., et al.: Analysis of slurry flow in elbow system. Chem. Eng. **47**(06), 58–63 (2019)
6. Yao, S., Li, Y., Wang, W., et al.: Simulation of hydrate slurry flow characteristics in vertical pipes based on population balance model. Oil Gas Field Surf. Eng. **38**(12), 9–15+37 (2019)
7. Cao, X., Yang, K., Wang, H., et al.: Modelling of hydrate dissociation in multiphase flow considering particle behaviors, mass and heat transfer. Fuel **306**, 121655 (2021)
8. Cai, Y., Rao, Y., Wang, S., et al.: Numerical simulation study on the attenuation law of hydrate spiral flow transportation. Ind. Saf. Environ. Prot. **45**(4), 46–51 (2019)
9. Chang, K., Rao, Y., Wang, S.: Numerical simulation of spiral flow of hydrate particles in gas pipeline. Petrol. Mach. **45**(3), 107–113 (2017)
10. Liang, J., Rao, Y., Wang, S., et al.: Experimental study on solid particle transportation based on spiral flow. Oil Gas Field Surf. Eng. **37**(3), 1–5 (2018)
11. Rao, Y., Zheng, Y., Wang, S., et al.: Numerical simulation of spiral flow swirling in a horizontal tube. Fluid Mach. **44**(4), 17–22 (2016)
12. Wang, Z., Rao, Y., Li, L., et al.: The influence of the setting angle of the guide strip on the gas-solid two-phase spiral flow characteristics. Petrol. Mach. **48**(04), 125–134+148 (2020)

13. Rao, Y., Liu, Z., Wang, S., et al.: Numerical simulation of swirl flow characteristics of CO_2 hydrate slurry by short twisted band. Entropy **23**(7), 913 (2021)
14. Sun, X.: Experimental study on hydraulic characteristics and solid particle suspension mechanism of horizontal axis circular tube spiral flow. Xi'an University of Technology, Xi'an (2000)
15. Ji, L., Chu, K., Kuang, S., et al.: Modeling the multiphase flow in hydrocyclones using the coarse-grained volume of fluid—discrete element method and mixture-discrete element method approaches. Ind. Eng. Chem. Res. **57**(29), 9641–9655 (2018)

Experimental Study on Methane Hydrate Particle Cohesive Force Under High Pressure Condition

Pengfei Li, Zhiyuan Wang(✉), Shikun Tong, Jianbo Zhang, Jihao Pei, and Lichen Guan

School of Petroleum Engineering, China University of Petroleum (East China), Qingdao 266580, China
wangzy1209@126.com

Abstract. The environmental characteristics of low temperature and high pressure in deep water are easy to cause hydrate deposition and blockage in wellbore and transportation pipeline. Previous studies mainly focused on the deposition blockage in the macro flow process, but there were few studies on the micromechanics between hydrate particles. In this paper, from a microscopic point of view, a high-pressure micromechanical force device was used to study the cohesive force between hydrate particles in a high-pressure CH4 system, and the cohesive force experiment between hydrate particles was carried out under the conditions of pure water and 10 wt% ethylene glycol. It is found that the cohesive force between hydrate particles decreases first, then increases and then decreases with the increase of subcooling under the condition of 10 wt% ethylene glycol and pure water. At the same subcooling, the cohesive force between hydrate particles under 10 wt% ethylene glycol condition is less than that under pure water condition, 10 wt% ethylene glycol can reduce the cohesive force between hydrate particles and reduce the risk of pipeline blockage to a certain extent.

Keywords: Methane · Hydrate · MMF · Ethylene glycol · Experiment

1 Introduction

Natural gas hydrate (NGH) is a type of ice-like compounds formed by natural gas and water at low temperatures and high pressures. The environmental characteristics of low temperature and high pressure in deep water are easy to cause hydrate deposition and blockage in wellbore and transportation pipeline. Pipeline blockage caused by hydrate is one of the most urgent problems faced by oil and gas transportation in deep water. The macroscopic aggregation and blockage of hydrate can be studied by conventional research methods such as stirring kettle, flow loop, rocking kettle, but it has some limitations in defining the mechanism of hydrate aggregation. Micro-mechanical force device can directly measure the cohesive force between hydrate particles from the micro point of view to make up for the shortcomings of macro-experiment. Micro-mechanical force device is used at an early stage to test the cohesive force between two glass balls [1].

B. Sun et al. (Eds.): DWOG-Hyd 2021, LNCE 246, pp. 320–330, 2022.
https://doi.org/10.1007/978-981-19-0960-3_31

At present, the effects of subcooling, particle size and chemical additives on the cohesive force of hydrate particles can be studied by microcomputer mechanical experiments. Yang and others first measured the adsorption force between tetrahydrofuran hydrate particles at different temperatures by using the MMF test instrument developed by themselves [2–6]. According to the research of Yang and Taylor, the micro force between hydrate particles can be explained by the theory of liquid bridge capillary force, when the volume of liquid bridge increases, greater liquid bridge force will be obtained [2–6]. Lee, Wang, Hu et al. Improved the micromechanical force test device, and investigated the effects of contact time and other factors on the cohesive force of hydrate particles [7–11]. At present, most of the microcomputer mechanics experiments are atmospheric pressure systems under the condition of cyclopentane or tetrahydrofuran, but in actual production, the pressure in the pipe string is high, and the produced fluid is mostly light hydrocarbon gas dominated by CH_4. The results of the existing micro mechanical force experiments are of limited significance for field operation guidance. The experimental equipment used in this study is the self-developed high-pressure hydrate micromechanical force experimental equipment, which can carry out the micro-mechanical force experiment under high-pressure conditions. Through the micro-mechanical force experiment of methane hydrate particles under pure water and ethylene glycol, the micro-mechanical law of methane hydrate particles under high-pressure conditions is revealed, which provides guidance for the risk prevention and control scheme of deep-water hydrate.

2 Experimental Section

2.1 Materials

The materials and reagents used in the experiment are shown in Table 1.

Table 1. Materials used in the experiments

Name	Specification	Manufacturer
Deionized water	18 MΩ · cm	Laboratory self-made
CH_4	99.9%	Qingdao De Yi Gas Co., Ltd.
Ethylene glycol	>99.5%	Shandong Titan Scientific Co., Ltd.

2.2 Apparatus

Figure 1 is a schematic diagram of the high pressure micromechanical force (MMF) system. The cohesive force between hydrate particles can be measured directly by using the device. The pressure limit of the experimental device is 25 MPa and the temperature limit is −50 °C. The operating pressure range of this study is 0 MPa to 12 MPa and the temperature range is −15 °C to 1.7 °C. The temperature of the high-pressure sealed chamber is controlled by a constant temperature water bath (accuracy 0.1 °C), and the cooling jacket contains a 1:1 mixture of ethylene glycol and water. A temperature

sensor is installed in the middle of the high-pressure sealed cabin to measure the cavity temperature, and a pressure sensor is installed at the bottom air inlet pipeline to measure the cavity pressure. Observe and record the experimental results with a microscope. Two cantilevers are installed in the high-pressure sealed cabin: the static cantilever is fixed on the wall of the cavity, and the movable cantilever is controlled by the three-dimensional axis moving table in the cavity.

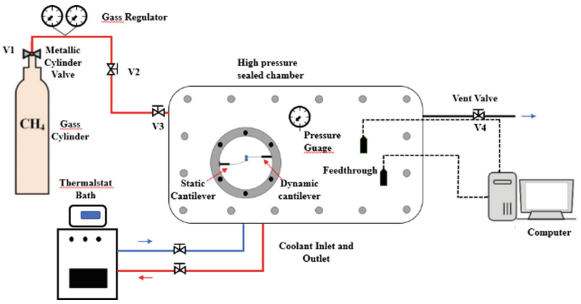

Fig. 1. Experimental setup of high-pressure micromechanical force apparatus

2.3 Experimental Steps

The experiment includes four parts: ice particle preparation, induced hydrate formation, hydrate shell annealing and pull-off test. The experimental steps are as follows:

(1) Firstly, a droplet is placed at the tip of the cantilever, and the droplet is quenched in liquid nitrogen to form ice particles before being put into the high-pressure sealed chamber;
(2) Put the ice particles into the high-pressure sealed chamber, inject methane gas, and gradually pressurize to the experimental pressure. During the pressurization process, the temperature is maintained below 0 °C to prevent the surface collapse of hydrate particles caused by the melting of ice particles;
(3) Take the hydrate particle formation time as the starting time, set the temperature to 1.7 °C and anneal for 2 h to ensure that the hydrate shell is strong enough to withstand at least 40 tests;
(4) Conduct 40 pull-out tests under the experimental temperature and pressure, record the displacement of hydrate particles at the fixed end, and conduct at least 3 groups of experiments under each subcooling condition to ensure the accuracy of the experimental results.

The measurement of cohesive force between hydrate particles is divided into four steps, as shown in Fig. 2;

(1) The hydrate particles on the moving end cantilever are contacted with the hydrate particles on the fixed end cantilever by operating the three-dimensional axis moving table;

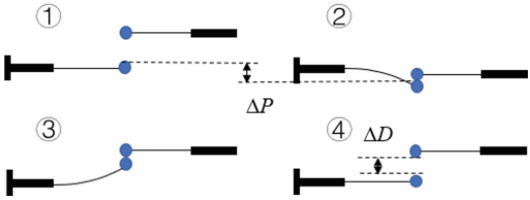

Fig. 2. Procedure of cohesive force measurement

(2) Move the preload displacement ΔP downward, and the contact time of two hydrate particles is 10 s;
(3) Control the moving end to move upward at a uniform speed until the particles are separated;
(4) Measure the maximum displacement ΔD of particles at the fixed end, and the final cohesive force value is the average value of repeated tests.

3 Experimental Results and Discussion

In this study, the microcomputer mechanical force experiment between hydrate particles under different subcooling conditions in high-pressure CH_4 system was carried out. The cohesive force between hydrate particles under pure water and 10 wt% ethylene glycol was tested, and the phenomenon of hydrate formation induced by ice particles was observed.

3.1 Hydrate Formation

The whole process of transforming ice particle surface into hydrate shell is divided into two parts. Firstly, a thin hydrate shell is rapidly formed on the surface of ice particles, and then a thicker hydrate is gradually formed on the outer layer of hydrate shell. This experimental phenomenon can be observed in pure water and 10 wt% ethylene glycol, especially in 10 wt% ethylene glycol.

It can be seen from Fig. 3 that the whole process of ice particle surface conversion to hydrate under the condition of 10 wt% ethylene glycol in the air inlet process, the ambient temperature is - 7 °C, the process takes 4.17 s, and the ice particle diameter is 0.78 mm. The whole process of transforming ice particle surface into hydrate shell is divided into two parts. The first layer of hydrate shell began to grow at 0.00 s, the surface coverage rate of 1.03 s particles reached 50%, and 1.90 s was completely covered; The second hydrate shell of 0.77 s began to grow, the surface coverage of 2 s particles reached 50%, and 4.17s completely covered the surface of particles.

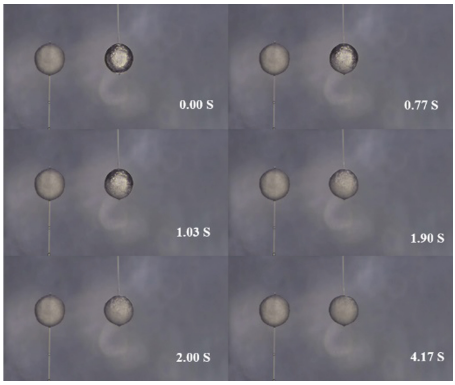

Fig. 3. Hydrate formation induced by ice particles under ethylene glycol condition

3.2 Experiments Under Pure Water Condition

A pure water droplet of similar size is placed at the tips of the two cantilevers respectively, and the ice particles are frozen by liquid nitrogen and put into the high-pressure sealed cabin for subsequent operation. The experimental temperature is 1.7 °C, and the phase equilibrium pressure is calculated by PVTsim software. The experimental conditions of each group are shown in Table 2.

Table 2. Experimental pressure and temperature under water condition

Experimental temperature-1.7 °C		
Phase equilibrium temperature	Phase equilibrium pressure	Subcooling
2.7 °C	3.4 MPa	1 °C
3.7 °C	3.75 MPa	2 °C
5.7 °C	4.56 MPa	4 °C
8.7 °C	6.17 MPa	7 °C
11.7 °C	8.47 MPa	10 °C

Figure 4 is the scatter diagram of the maximum displacement of the fixed end cantilever with the number of tensile tests. It can be seen from Fig. 4 that under the same subcooling conditions, the 3 groups of experimental results are similar, and the displacement value of the fixed end fluctuates within a certain range. Figure 5 is the histogram of particle displacement distribution at the fixed end. It can be seen from Fig. 5 that 120 data points under each subcooling condition basically show normal distribution, and the experimental results have high reliability.

Each group of experiments uses the same arm, the diameter of the hydrate particles is 0.75 ± 0.05 mm, and the maximum stretch distance of the particles is used as the evaluation standard. Table 3 shows the fixed end particle displacement corresponding to different subcooling under pure water condition.

Table 3. Particle displacement in pure water

Subcooling (°C)	Displacement (mm)
1	0.9724
2	0.8679
4	0.7459
7	0.8838
10	0.7563

As shown in Table 3, in the CH_4 system, under the condition of pure water, with the increase of subcooling, the cohesive force between particles first decreases, then increases, and then decreases gradually.

There is a layer of liquid film on the surface of hydrate particles. The cohesive force between particles is mainly affected by two forces: the liquid bridge force provided by liquid bridge and the hydrate bridge force provided by hydrate bridge. Under the condition of low subcooling, the liquid bridge force plays a major role. With the increase of subcooling, the liquid film is gradually transformed into hydrate. With the increase of subcooling, the liquid film gradually transforms into hydrate. The decrease of liquid film thickness leads to the decrease of liquid bridge volume, and finally leads to the gradual decrease of cohesive force, corresponding to the subcooling of experiment 1–4; With the increase of subcooling, the speed of liquid bridge conversion into hydrate gradually accelerates. Under a certain subcooling condition, hydrate bridge force plays a major role, resulting in a sudden increase in cohesive force, corresponding to the experiment of 4–7 subcooling; Under the condition of high subcooling, the increase of subcooling leads to the gradual decrease of liquid film thickness, and the decrease of liquid bridge volume leads to the decrease of hydrate bridge volume and the gradual decrease of cohesive force, which corresponds to the experiment of 7–10 subcooling.

3.3 Experiments Under 10 wt% Ethylene Glycol Condition

A 10 wt% ethylene glycol droplet with similar size is placed at the tips of the two cantilevers respectively, and the ice particles are frozen by liquid nitrogen and put into the high-pressure sealed cabin for subsequent operation. The experimental temperature is 1.7 °C, the phase equilibrium pressure is calculated by PVTsim software. The experimental conditions of each group are shown in Table 4.

Figure 6 is the scatter diagram of the change of the maximum displacement of the cantilever at the fixed end with the number of tensile tests. It can be seen from Fig. 6 that under the same subcooling conditions, the three groups of experimental results are similar, and the displacement value at the fixed end fluctuates within a certain range. Figure 7 is the histogram of particle displacement distribution at the fixed end. It can be seen from Fig. 7 that 120 data points under each subcooling condition basically show normal distribution, and the experimental results have high reliability.

Each group of experiments uses the same arm, the diameter of the hydrate particles is 0.75 ± 0.05 mm, and the maximum stretch distance of the particles is used as the

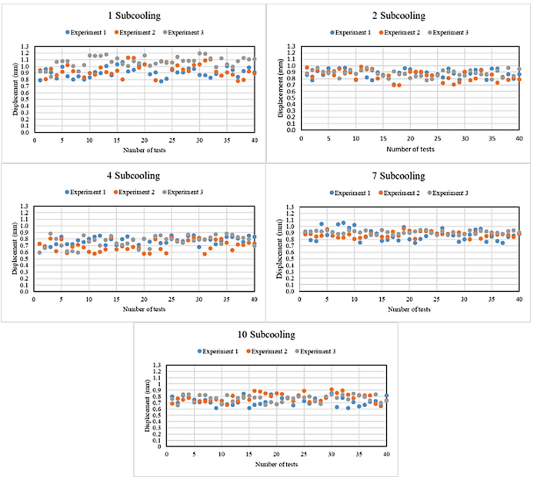

Fig. 4. Variation diagram of displacement with tensile test times

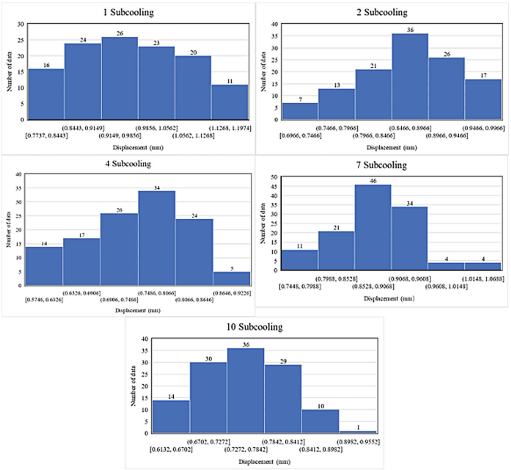

Fig. 5. Displacement distribution histogram

evaluation standard. Table 5 shows the fixed end particle displacement corresponding to different subcooling under ethylene glycol condition.

As shown in Table 5, in the CH4 gas system, under the condition of 10 wt% ethylene glycol, with the increase of subcooling, the cohesive force between particles first decreases, then increases, and then gradually decreases, the change trend is consistent with that in pure water. The reasons for this change trend have been described in detail in Sect. 3.3 and will not be described here.

The experimental results show that the variation trend of hydrate particle cohesive force with subcooling under the condition of 10 wt% ethylene glycol is similar to that under the condition of pure water, which first decreases, then increases and then decreases

Table 4. Experimental pressure temperature under ethylene glycol condition

Experimental temperature-1.7 °C		
Phase equilibrium temperature	Phase equilibrium pressure	Subcooling
2.7 °C	4.3 MPa	1 °C
3.7 °C	4.76 MPa	2 °C
5.7 °C	5.83 MPa	4 °C
8.7 °C	8.05 MPa	7 °C
11.7 °C	11.2 MPa	10 °C

Table 5. Particle displacement at 10wt % ethylene glycol

Subcooling (°C)	Displacement (mm)
1	0.7842
2	0.5917
4	0.4293
7	0.6516
10	0.4316

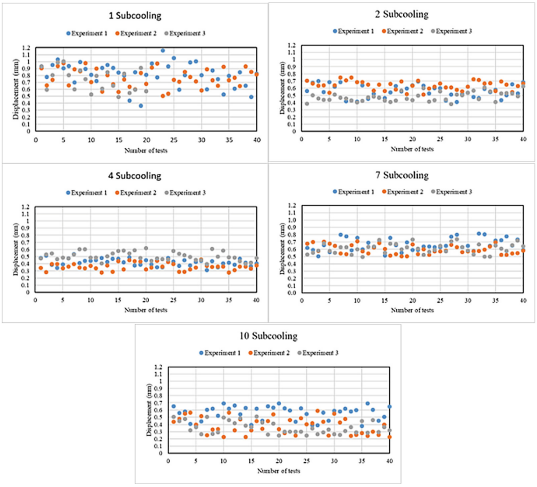

Fig. 6. Variation diagram of displacement with tensile test times

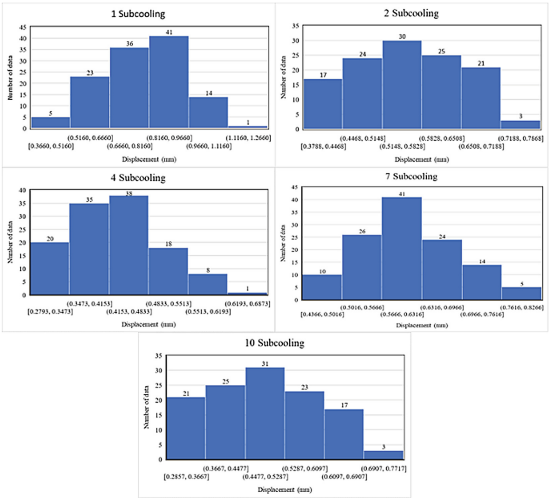

Fig. 7. Displacement distribution histogram

with the increase of subcooling. And under the same subcooling condition, the cohesive force between hydrate particles under 10 wt% ethylene glycol condition is less than that under pure water condition. Figure 8 is the variation curve of displacement with the degree of subcooling.

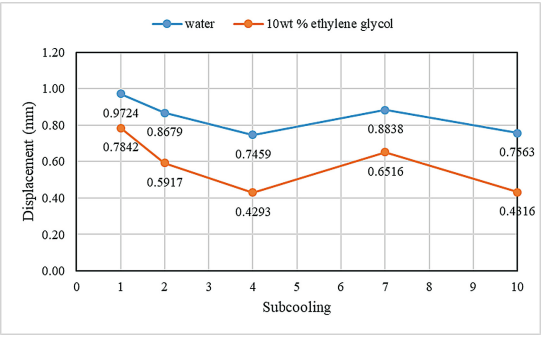

Fig. 8. Variation curve of displacement with the degree of subcooling

4 Conclusion

In this study, the high-pressure micromechanical force device was used to study the cohesive force between hydrate particles in high-pressure CH_4 gas system, carry out the cohesive force experiment between hydrate particles under the conditions of pure water and 10 wt% ethylene glycol, and test the cohesive force between CH_4 hydrate particles under 1–10 subcooling conditions respectively.

Under the experimental conditions in this paper, the variation trend of hydrate particle cohesive force with subcooling under 10 wt% ethylene glycol condition is similar to that under pure water condition, both of which first decrease, then increase and then decrease with the increase of subcooling. This is because the liquid bridge force plays a major role under the condition of low subcooling. With the increase of subcooling, the liquid film consumption leads to the decrease of liquid bridge volume, and finally leads to the gradual decrease of cohesive force. With the increase of subcooling, the conversion rate of liquid bridge into hydrate gradually accelerates. Under a certain subcooling condition, hydrate bridge force plays a major role, resulting in the increase of cohesive force. Under the condition of high subcooling, the increase of subcooling leads to the gradual consumption of liquid film, the decrease of liquid bridge volume leads to the decrease of hydrate bridge volume, and the cohesive force shows a gradual decreasing trend. At the same subcooling, the cohesive force between hydrate particles under 10 wt% ethylene glycol was lower than that under pure water. Therefore, 10 wt% ethylene glycol can reduce the cohesive force between hydrate particles to a certain extent, so as to reduce the risk of hydrate blockage, The micromechanical law of methane hydrate particles under high pressure has guiding significance for the risk prevention scheme design of deep-water hydrate.

Symbol Description

ΔP—Preload displacement
ΔD—Maximum displacement of fixed end cantilever

Acknowledgement. The authors would like to thank their tutors and senior brothers for their guidance.

References

1. Gröger, T., Tüzün, U., Heyes, D.M.: Modelling and measuring of cohesion in wet granular materials. Powder Technol. **133**(1–3), 203–215 (2003)
2. Yang, S., Kleehammer, D., Huo, Z., et al.: Temperature dependence of particle-particle adherence forces in ice and clathrate hydrates. J. Colloid Interface Sci. **277**(2), 335–341 (2004)
3. Taylor, C.J., Dieker, L.E., Miller, K., et al.: Micromechanical adhesion force measurements between tetrahydrofuran hydrate particles. J. Colloid Interface Sci. **306**(2), 255–261 (2007)
4. Dieker, L.E.: Cyclopentane hydrate interparticle adhesion force measurements. Colorado School of Mines, Golden (2009)
5. Dieker, L.E., Aman, Z.M., George, N.C., et al.: Micromechanical adhesion force measurements between hydrate particles in hydrocarbon oils and their modifications. Energy Fuels **23**(12), 5966–5971 (2009)
6. Taylor, C.J., Dieker, C.J., Miller, K.T., et al.: Hydrate particles adhesion measurements: effects of temperature, low dosage inhibitors, and interfacial energy. In: Proceedings of the 6th International Conference on Gas Hydrates (ICGH), Vancouver, British Columbia, Canada (2008)

7. Lee, B.R., Koh, C.A., Sum, A.K.: Development of a high pressure micromechanical force apparatus. Rev. Sci. Instrum. **85**(9), 095120-1-4 (2014)
8. Wang, S., Hu, S., Brown, E.P., et al.: High pressure micromechanical force measurements of the effects of surface corrosion and salinity on CH4/C2H6 hydrate particle-surface interactions. Phys. Chem. Chem. Phys. **19**(20), 13307–13315 (2017)
9. Hu, S., Koh, C.A.: Interfacial properties and mechanisms dominating gas hydrate cohesion and cohesive force in liquid and vapor hydrocarbon phases. Langmuir **33**(32), 11299–11309 (2017)
10. Brown, E.P.: Study of hydrate cohesion, cohesive force and interfacial properties using micromechanical force measurements. Colorado School of Mines, Golden (2016)
11. Liu, C., Li, M., Zhang, G., et al.: Direct measurements of the interactions between clathrate hydrate particles and water droplets. Phys. Chem. Chem. Phys. **17**(30), 20021–20029 (2015)

Fundamentals and Emerging Technologies of Clathrate Hydrate

Visualization of TBAB Hydrate in Confined Small Channels

Qi-rong Zuo, Ming Gao(✉), Lin-xin Zhang, and Liang Yang

School of Energy and Power Engineering, University of Shanghai for Science and Technology, Shanghai 200093, China
gaoming@usst.edu.cn

Abstract. TBAB (tetrabutylammonium bromide) can generate semi-cage hydrate at atmospheric pressure, which has high energy storage density and can be applied to cold storage technology. Small channel has the characteristics of high heat exchange efficiency and can generate hydrate more efficiently. In this paper, 2 mm and 3 mm quartz tubes with inner diameter were used as experimental tubes. The hydrate crystal morphology and agglomeration morphology generated by the flow in the tube were captured by industrial microscope. The effects of undercooling degree and diameter of solution concentration and flow rate on the blockage time and agglomeration process of hydrate morphology were studied. It was found that the density of single crystal hydrate formed by TBAB (10 wt%–20 wt%) at the same undercooling is low, and its front end is needle or sword, which is beneficial to mass and heat transfer and continues to grow. High concentration TBAB solution (30 wt%–40 wt%) formed hydrate crystals closely, and the tip effect was significantly weakened. For low concentration TBAB solution, the increase of flow rate can accelerate the formation of new nuclei and inhibit the growth of large crystals. Adjusting the flow rate can help to obtain slurry solutions with different particle sizes. The growth and aggregation process of TBAB hydrate were reviewed, and the microscopic physical model of TBAB hydrate growth and aggregation process was established. It is found that the initial morphology of TBAB hydrate crystal includes spherical and columnar, and the morphology evolution process of single hydrate crystal is similar. The optimal solution concentration and flow rate range for continuous hydrate formation can be preliminarily determined by experiments, which has reference significance for the development of efficient and continuous hydrate formation process.

Keywords: TBAB hydrate · Morphology · Flow · Small channel

1 Introduction

Natural gas hydrate is one of the most well-known hydrates and is considered as one of the most potential new energy sources in contemporary times. Its guest molecule is mainly methane, but gas hydrate can be generated and exist stably under low temperature and high pressure, so it is difficult to study it directly. Quaternary ammonium salt and water molecules can also form hydrate, such as tetrabutylammonium bromide [1].

B. Sun et al. (Eds.): DWOG-Hyd 2021, LNCE 246, pp. 333–341, 2022.
https://doi.org/10.1007/978-981-19-0960-3_32

At atmospheric pressure, the phase equilibrium temperature range of TBAB solution for hydrate formation is 3–12 °C, and the formation conditions are relatively mild. Although the structure of semi-cage hydrate is not exactly the same as that of natural gas hydrate, it has sufficient similarity and the experimental conditions are not as strict as those of natural gas hydrate, which has certain reference significance for the study of natural gas hydrate. At the same time, TBAB hydrate can also be used as phase change material for refrigeration and cold transfer in the field of air conditioning and refrigeration [2, 3].

Shimada [1] and Koyanagi [4] recorded the static growth morphology of hydrates in TBAB solution and TBAB + CO_2 gas system in the reactor, respectively. The hydrate morphology generally appeared tip, showing wedge-shaped columnar and sword-shaped, respectively. The experiments of Shimada showed that the tip protrusions in the front of the growth direction of columnar crystals gradually tended to be flat with the increase of undercooling. The hydrate morphology characteristics were also mentioned in the flow characteristics experiments of hydrates. The hydrate morphology after stirring in the reactor was mostly needle-shaped or flake-shaped [5].

2 Experimental Section

2.1 Experimental Equipment

In this experiment, a self-designed reaction system was used for TBAB hydrate formation experiment. The experimental system consists of test pipeline circuit, constant temperature system, temperature system and video camera system. The observation of formation experiment is shown in Fig. 1.

Test pipeline circuit is mainly composed of test small channel and peristaltic pump. The hydrate formation experiments were performed in a fully visual flow loop. The flow pipeline was constructed of quartz glass tubes, which was 1 mm, 2 mm and 3 mm, respectively. In order to narrow the scope of observation, test pipes are made into serpentine pipes. Peristaltic pump flow range is 0.000166-570 mL/min, flow resolution is 0.01 μL/min, peristaltic pump and test section through rubber pipe connection. constant temperature system is composed of chiller and organic glass box(180 × 240 × 50 mm^3). The organic glass box is placed above the microscope and filled with ethanol glycol to ensure a stable temperature environment for the hydrate to form in the quartz glass tube. The temperature of the TBAB solution is recorded by a thermocouple and a corresponding data logger.

2.2 Experimental Materials

The main materials used in the experiment included TBAB and pure water. TBAB was provided by China National Pharmaceutical Group Corporation. In addition, pure water was also produced in the laboratory, and the pure water machine (Milli-Q IX7003) was produced by Merck Millipore.

2.3 Experimental Process

Firstly, The experimental tube was cleaned via warm pure water for 3–5 times to ensure that no other impurities were attached to the experimental tube, in order to avoid memory effects in the next set of experiments.

Then the TBAB solution was configured in advance, and 30 mL TBAB solution was poured into the measuring cylinder in each experiment. After the preparation work was finished, running the thermostatic system to ensure temperature drop to test temperature in organic glass box. After the chiller reaches the experimental operating temperature, turn on the peristaltic pump, and start image and temperature data acquisition. Compared with the whole test pipeline range, the field of view of the microscope is much smaller, so the first observation position is artificially selected, which is defaulted in the middle of the organic glass box. After hydrate formation, the observation range will be selected again according to the actual growth of hydrate.

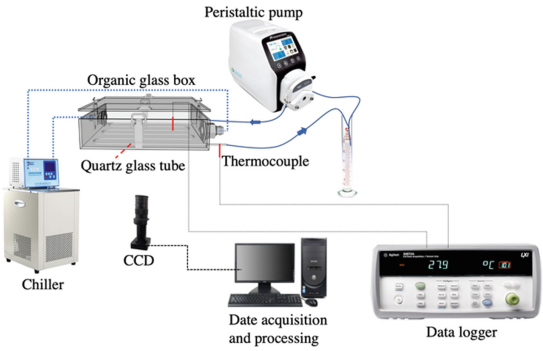

Fig. 1. Observation system for morphology of TBAB hydrate growth

3 Experimental Results and Discussion

3.1 Morphology of TBAB Hydrate

Figure 2 shows the crystal morphology of in-situ growth at low flow rate ($q < 20$ mL/min). Due to the low dynamic pressure of the liquid at low flow rate, the crystal nucleus did not flow with the solution in the tube for a long time after the hydrate crystal was formed in the small pore channel.

10 wt% TBAB solution first formed the crystal nucleus in the straight tube center 90 mm away from the channel outlet, and then formed a new crystal nucleus in the outlet with the flow direction. Finally, the hydrate was blocked in the pipeline. After the flow stopped, the hydrate began to adhere to the wall and grow rapidly in the direction of the solution, which lasted only 11 s and occupied the whole field of vision. As shown in Fig. 2(a_1) and Fig. 2(a_2), 10 wt% hydrate was white crystal, and its shape was similar to pine branch. It basically grow linearly before encountering resistance. When it touched the wall or was squeezed by the surrounding hydrate in the growth process, the hydrate in the blocked direction will change its growth trajectory like the vine, and will not stop

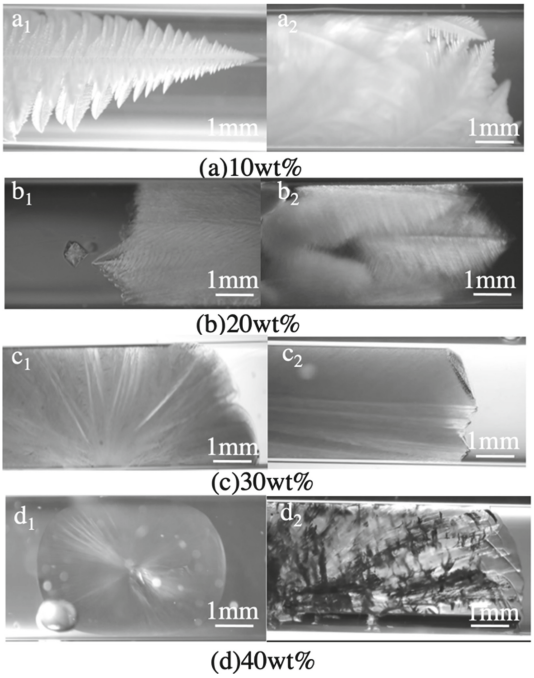

Fig. 2. Typical hydrate growth morphology of TBAB solutions in small pipes at low flow rates ($d = 3$ mm, $\Delta T = 17$ °C, $q < 20$ mL/min)

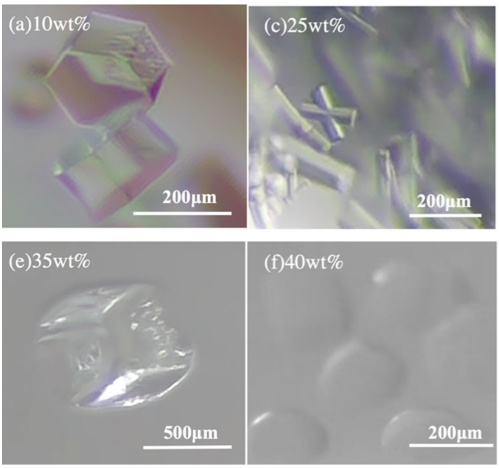

Fig. 3. Typical single crystal morphology of hydrate with different mass fractions in flowing state

growing directly. The transparency of hydrate crystal was very low, and the generated hydrate is more like frost.

It can be observed from Fig. 3 (a) that the hydrate formed at the initial mass fraction of 10 wt% was hexagonal short columnar. The hydrate growth process of 25 wt% TBAB solution is the same as that of Fig. 3(a), also prone to cross-linked polycrystals of two or more single crystals. Darbouret [6] tested the rheological properties of hydrate slurry and found that columnar crystals were very fragile. After the hydrate crystals have been stirred in the reactor and flowed in the pipeline, it is considered that the hydrate morphology is closer to spherical. The single crystal morphology of hydrate formed in TBAB solution with hydrate size of about 10-100 μm and 35 wt% is regular cube, as shown in Fig. 3(c). The hydrate is in a very unstable state at the initial stage of growth, and the crystal nucleus morphology will change greatly after continuous growth. The crystal size of hydrate formed by 40% TBAB solution is small, and the crystal is irregular spherical, as shown in Fig. 3(d). At this time, the morphology of single crystal nucleus did not increase with the increase of size. The morphology change of spherical hydrate crystals generated at this mass fraction is mainly due to the deformation caused by the extrusion of multiple grains.

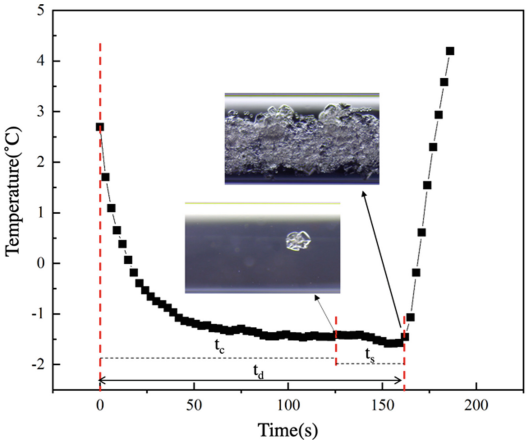

Fig. 4. Schematic diagram of temperature variation during the formation process of typical TBAB hydrate in small tube

The hydrate growth process includes nucleation stage and growth stage. In this experiment, the process from initial equilibrium state to crystal visualization can be regarded as nucleation stage. In this experiment, the quartz tube selected as the test tube, and the thermocouple is placed at the outlet of the tube. Quartz small pipe was selected for the test tube, and thermocouples were placed at the outlet of the pipe. The small pipe has high heat exchange efficiency, which can timely take away the heat generated by hydrate production. The temperature will not rise significantly before the complete blockage, and the change of temperature can only be used to judge whether the pipe was blocked.

As shown in Fig. 4, starting from the solution passing through the temperature measurement point for the first time to the time when the outlet temperature rises when the pipe is blocked, it is the blocking time (t_d). Nucleation time (t_c) referred to the time from the first temperature measurement point of solution to the first appearance of visible hydrate crystal nucleus. The hydrate growth time (t_s) referred to the period when the hydrate crystal continues to grow until it is blocked after the formation of hydrate crystal core, and the time above that can be basically extracted by image and video.

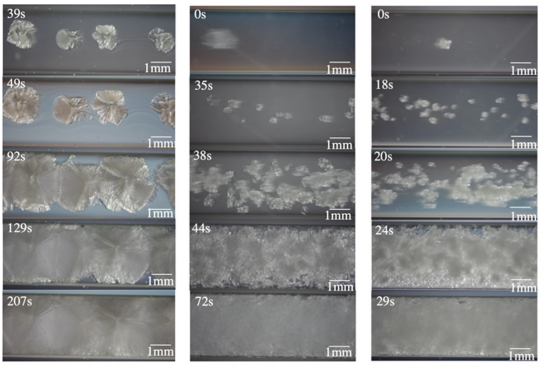

Fig. 5. Hydrate morphology in small pipe at different flow rates (d = 3 mm, w = 25 wt%, ΔT = 16 °C)

Figure 5 shows the growth of hydrate crystals in a small tube under different flow rates of 25 wt% TBAB solution. As shown in Fig. 5, hydrate crystals still grow in the middle of the pipeline. Due to the uneven concentration of solution at the solid-liquid interface caused by hydrate growth, it can be clearly seen from Fig. 5 (t = 49 s) that TBAB solution is still in the flow state at this time. It can be observed that in the process of hydrate growth, the crystals with smaller sizes are separated from the original crystals and continue to flow and grow, which is equivalent to providing new nuclei, while the increase of flow rate indirectly provides more nuclei. From Fig. 5(a) and Fig. 5(c), it can be inferred that if there is no local blockage in the hydrate growth process, more nuclei will be generated when the flow rate increases, resulting in tube blockage. Joshi studied the plugging mechanism of high water-cut natural gas hydrate in large pipelines, and considered that high flow rate can reduce hydrate nucleation time, which is the same as Joshi's [7] experimental results.

The TBAB content in the liquid phase affects the morphological evolution of single crystal particles. As shown in Fig. 6, when the solution concentration is 40 wt%, the spherical crystal ratio can be observed in the experiment, which is larger than that of other concentrations. The proportion of amplification of the hydrate basically grows at the initial stage of growth. When the hydrate crystal has begun to burst, the growth of the hydrate interface will begin to appear ripples, and the cylindrical single crystal that continues to increase the size of the last sphere against the radiation growth can evolve into square, square and hexagonal columns. The columnar hydrate crystals continue

to grow in low concentration TBAB solution, the center of the column axis will be depressed, and the side will continue to grow lamellar or acicular crystals.

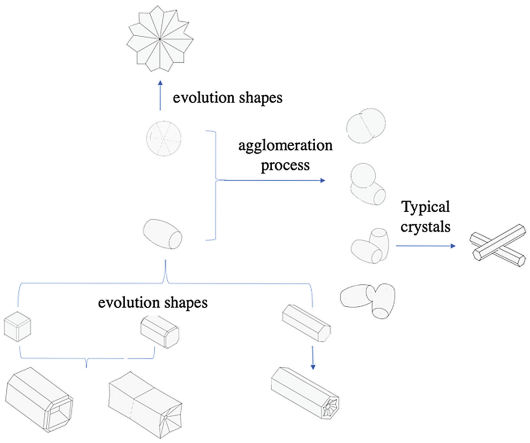

Fig. 6. Microscopic model of TABAB hydrate formation and agglomeration process

Large-size crystals tend to grow into divergent crystals, and the aggregates are more irregular, but the shape of TBAB hydrate particles with smaller sizes is relatively regular. The agglomeration is mainly achieved by forming TBAB hydrate between particles and connecting the two particles. Therefore, the agglomeration between TBAB hydrate particles is related to the TBAB content in the liquid phase. For columnar single crystal particles, the contact between spherical and columnar single crystals also occurs in the side contact position of TBAB between spherical and columnar crystals to form hydrate, which makes the two single crystal particles aggregate and the interface between the contact positions gradually disappear. With the consumption of TBAB in the liquid phase, the particle size further increases, and the proportion of aggregates increases. Many single crystal particles gather together to form large-sized clusters with extremely irregular shapes.

3.2 Influence of Various Factors on Hydrate Flow

Due to the rapid blockage after hydrate nucleation, the nucleation time can be directly determined by the blockage time. From Fig. 7, it can be seen that the increase of concentration and undercooling can effectively increase the nucleation rate of hydrate, and large flow rate can also shorten the nucleation time of hydrate to a certain extent. However, too large concentration and undercooling also make hydrate blockage easier. By comparing multiple sets of experiments, it can be predicted that TBAB hydrate can be continuously generated in the environmental range ($w = 20$ wt%, $\Delta T = 15$–16 °C) and the hydrate with uniform particle size can be obtained by changing the flow rate.

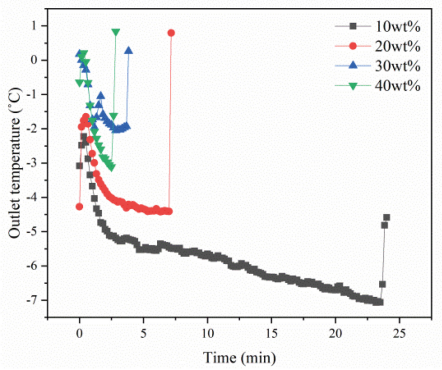

(a) d=3mm, q=30ml/min, ΔT=16℃）

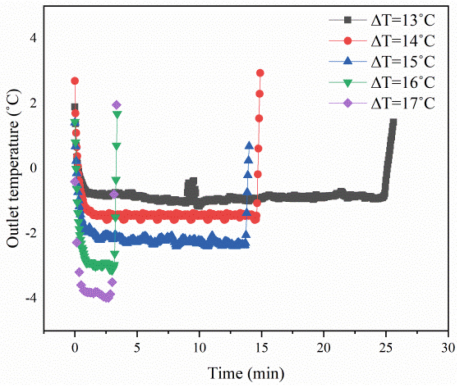

(b) d=2mm, w=30wt%, q=10ml/min

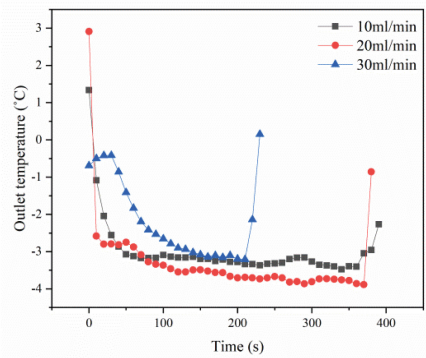

(c) d=3mm,w=25wt%, ΔT=16℃

Fig. 7. Variation of outlet temperature of TBAB solution with different factors

4 Conclusion

(1) With the increase of concentration, the tip effect of hydrate growth weakens, and the front end of hydrate growth changes from dendritic to arc. As the single crystal concentration changes from columnar to cubic and then to spherulite, the nucleation time is effectively reduced, and the nucleation time is shortened from 25 min to 5 min.
(2) The crystal morphology did not change with the flow rate in the experimental range, but the increase of flow rate leads to the increase of hydrate grains. It is found that increasing the flow rate within a certain range can reduce the nucleation time, and the hydrate crystal particle size is more average at high flow rate.
(3) The initial morphology of hydrate single crystal is spherical and cylindrical, and the single crystal evolution mode is the same. However, due to different concentrations or undercooling conditions, the boundary sizes of hydrate crystal morphology change are different.

Acknowledgement. This work was supported by National Natural Science Foundation of China through Grant No. 51976127.

References

1. Shimada, W., Ebinuma, T., Oyama, H., et al.: Free-growth forms and growth kinetics of tetra-n-butyl ammonium bromide semi-clathrate hydrate crystals. J. Cryst. Growth **274**(1–2), 246–250 (2005)
2. Zhang, P., Ye, J.: Experimental investigation of forced flow and heat transfer characteristics of phase change material slurries in mini-tubes. Int. J. Heat Mass Transf. **79**, 1002–1013 (2014)
3. Zhang, P., Ma, Z.W., Bai, Z.Y., et al.: Rheological and energy transport characteristics of a phase change material slurry. Energy **106**, 63–72 (2016)
4. Koyanagi, S., Ohmura, R.: Crystal growth of ionic semiclathrate hydrate formed in CO2 gas+ tetrabutylammonium bromide aqueous solution system. Cryst. Growth Des. **13**(5), 2087–2093 (2013)
5. Kumano, H., Hirata, T., Kudoh, T.: Experimental study on the flow and heat transfer characteristics of a tetra-n-butyl ammonium bromide hydrate slurry (first report: flow characteristics). Int. J. Refrig. **34**(8), 1953–1962 (2011)
6. Darbouret, M., Cournil, M., Herri, J.M.: Rheological study of TBAB hydrate slurries as secondary two-phase refrigerants. Int. J. Refrig. **28**(5), 663–671 (2005)
7. Joshi, S.V., Grasso, G.A., Lafond, P.G., et al.: Experimental flowloop investigations of gas hydrate formation in high water cut systems. Chem. Eng. Sci. **97**(7), 198–209 (2013)

Molecular Dynamics of CH_4 Hydrate Growth in Confined Space of ZIF-8: Micro-insights in Technology of Adsorption-Hydration Hybrid to CH_4 Storage

Jun Duan[1], Yiheng Xu[1], Shujun Chen[1,2,3(✉)], Qianchuan Li[1], and Xingyu Jiang[1]

[1] College of Pipeline and Civil Engineering, China University of Petroleum (East China), Qingdao 266580, China
shujunchenfu@126.com

[2] Qingdao Engineering Research Center of Efficient and Clean Utilization of Fossil Energy, Qingdao 266580, China

[3] Shandong Key Laboratory of Oil and Gas Storage and Transport Safety, Qingdao 266580, China

Abstract. The behavior of CH_4 hydrate growth and CH_4/H_2O migration in confined interconnectivity space between the surface of ZIF-8 is studied by molecular dynamics simulation. To investigate the main growth position and direction of hydrate when CH_4 is dissolved in aqueous solution and the effect of CH_4/H_2O migration to promote hydrate growth on the surface of hydrophobic ZIF-8 with pre-adsorbed water. The system of three-phase and four components containing CH_4, H_2O, hydrate and ZIF-8 is constructed before MD simulation. Microstructure properties are analyzed for regions containing hydrate near the surface of ZIF-8 (region1) and hydrate in the center of interconnectivity space (region2). The self-diffusion coefficients of H_2O, CH_4 are calculated, self-diffusion coefficients of CH_4 and H_2O are 0.47, 0.85 m^2/s and 0.37, 0.54 m^2/s in region1 and 2, respectively. The results demonstrate that the hydrate preferentially grows near the surface of ZIF-8 rather than the region of center. Because of the competitive adsorption for CH_4 between ZIF-8 and hydrate surface, CH_4 distribution is mainly concentrated in cavities and center of confined interconnectivity space, whereas H_2O distribution is focused in the region near surface of ZIF-8 and center water shows the ordered structures by facilitating hydrogen bonds formation. Therefore, two-way migration of CH_4/H_2O further promote cooperativity between physical adsorption and hydrate growth in confined space, the nanopores of ZIF-8 could serve as sites of CH_4 adsorption and preferentially enhance hydrate growth near the region of ZIF-8 and expand by a layer-by-layer mechanism for growth of the hydrate. Furthermore, hydrate growth in confined space is directional. The preferential growth directions of hydrate are boundary and center rather than the surface of ZIF-8. This study provides microscopic insight into CH_4 storage by adsorption-hydration hybrid in ZIF-8, which can be favorable for the investigation of storage and utilization of hydrate in future.

Keywords: Methane adsorption-hydration hybrid · CH_4 hydrate · Metal-organic framework · Molecular dynamics simulation

B. Sun et al. (Eds.): DWOG-Hyd 2021, LNCE 246, pp. 342–349, 2022.
https://doi.org/10.1007/978-981-19-0960-3_33

1 Introduction

The challenge of climate and environmental issues in the past decades has paid more attention of governments towards clean and renewable energy rather than relies on traditional fossil fuels. However, due to the limitation of renewable energy technology, it could not replace fossil fuels as the main source of energy in the world at a short period of time. It necessary to find a new clean and abundant alternative energy source that serves as a bridge to transition and reduce the emissions of CO_2 [1]. Natural gas (NG) is the fastest-growing primary energy source in the world [2] and has always being one of the paramount energy resources before the large-scale application of renewable energy due to high energy density and low carbon dioxide emission [1]. As global acceleration in the consumption of natural gas, new technologies that can attain the efficient storage and transportation of NG are increasingly required.

The technology of adsorption-hydration hybrid has investigated to store CH_4 by physisorption and hydrate formation in confined spaces [3], which combined with the advantages of Adsorbed natural gas (ANG) and natural gas hydrate (NGH). Compared with dry materials, CH_4 storage capacity has a significant jump using pre-humidified porous materials, which is partly due to the formation of CH_4 hydrate in the material [3, 4]. The porous materials could not only as physisorption media, but also provide the sites of hydrate nucleation and growth [4]. Metal-organic frameworks (MOFs) materials have been postulated as the best candidates to storage CH_4 due to their specific advantages [5]. However, there is not a clear understanding of the micro-mechanism of hydrate growth and CH_4/H_2O migration in confined space.

In this work, the microscopic mechanism of hydrate growth and CH_4/H_2O migration in different regions of confined interconnectivity space were investigated by MC and MD simulations, which further explore the effect of hydrate growth after the methane dissolves in water to form a mixture during the process of CH_4 adsorption-hydration hybrid in ZIF-8.

2 Model and Simulation Method

2.1 Molecular Model

The illustration of the representative unit cell and force filed atomic types of ZIF-8 were adopt by our previous work [6]. A surface model of ZIF-8 crystal ($33.98 \times 33.98 \times 169.91 Å^3$) containing intrinsic micropores and confined interconnectivity space was established by removing the outermost imidazolate linkers connected to the Zn atoms on the surfaces of ZIF-8 cubic cells, which is consistent with the description by Proenza et al. [7] and the interaction between surface and water molecules [6]. To obtain the three-phase and four components (CH_4/H_2O/hydrate/ZIF-8) configuration within confined space of CH_4/H_2O mixture solution, as shown in Fig. 1. Firstly, the mixture solution was composed of 3900 H_2O and 488 CH_4 molecules within the region of $33.982 \times 33.982 \times 118.858 Å^3$, the numbers of H_2O and CH_4 molecules in the system are selected such that it corresponds to the stoichiometry of the CH_4 hydrate. Then, three equidistant regions of gas-liquid phase were replaced by three $2 \times 2 \times 2$ supercells of CH_4 hydrate ($23.75 \times 23.75 \times 23.75 Å^3$). In addition, the initial surface configuration of pre-humidified ZIF-8

containing eight unit cells was generated using MC simulation in the NVT ensemble at T = 298 K, 56 water molecules were suggested to adsorb on ZIF-8 surface when the water content is 0.3 by our previous study [6] Finally, the models of H_2O and CH_4 in this system were described by the TIP4P/Ice [8] and OPLS-UA [9], respectively.

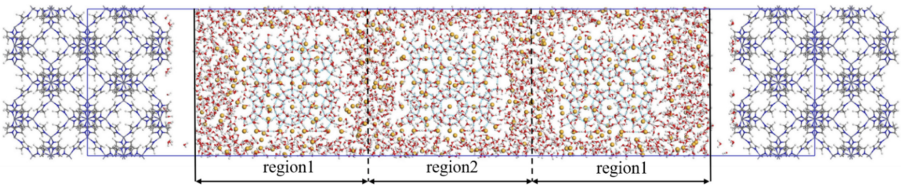

Fig. 1. Initial three-phase and four components configuration of the simulation system. Orange spheres represent CH_4 molecules. Red, white, purple, blue, and silver spheres represent O, H, Zn, N, and C atoms, respectively. Cyan dotted lines represent hydrogen 8 bonds in the hydrate phase.

2.2 Simulation Method

The MD and MC simulations were performed using LAMMPS packages [10] and Materials Studio package [11], respectively. Motion equations were integrated according to leap-frog algorithm with a time step of 2 fs and periodic boundary conditions were applied in all three dimensions, the L-J interactions cut-off distance was set to 1.4 nm, whereas long-range electrostatic interactions were calculated using the PPPM summation technique with a precision of 1×10^{-4}. Temperature was controlled using Nosé-Hoover algorithm with a relaxation time of 0.4 ps and pressure barostat with the relation time of were used 2 ps. The bond and angle of H_2O molecules were fixed by rigid command using SHAKE algorithm [12]. The system was first equilibrated at 275.15 K with a 250 ps NVT run, the atomic positions of the hydrate were frozen. Then, it was performed in the NPT ensemble at 275.15 K and 10 MPa for a few tens of nanoseconds with no position restraint on the hydrate phase. Furthermore, the cages identification algorithm was used to analysis hydrate growth in this work, which is referred by the literature [13].

3 Results and Discussion

3.1 Hydrate Evolution in Different Regions of Confined Space

Figure 2(a)–(d) displays that the evolution of hydrate in different regions of confined space with simulation time from 0.02 ns to 40 ns. It should be noted that the CH_4 hydrate grew clearly in two regions by cages identification, however, there are some discrepancies between region1 and 2. Firstly, it can be seen from the CH_4 hydrate configuration at about 10 ns in region1 that the cages preferentially grew towards the boundary of system (xy-dimension) rather than the center of interconnectivity space (z-dimension). The volume of hydrate in region1 was larger than that of region2, it indicates that the surface of pre-humidified ZIF-8 can provide a nucleation site to promote faster and greater hydrate crystal growth, which is similar with the phenomenon reported by Cha [14].

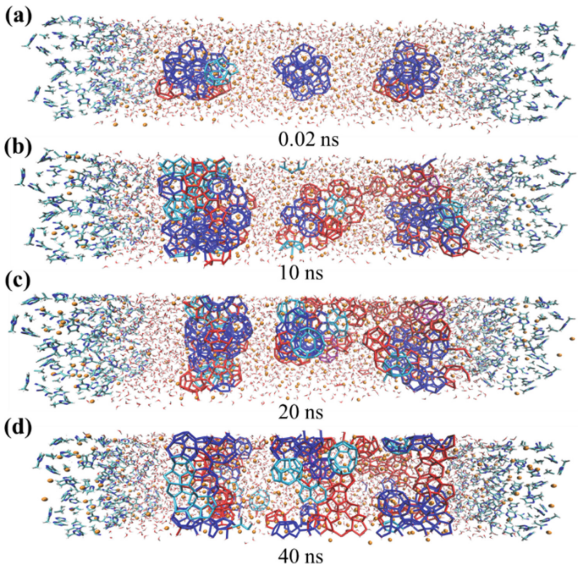

Fig. 2. Snapshots of the ZIF-8 interconnectivity space simulation at different moments. CH_4 and H_2O molecules are represented as orange spheres and light red thin lines, respectively. Hydrate cages are shown as sticks with different colors (red for 5^{12}, yellow for $5^{12}6^2$ green for $5^{12}6^3$ and blue for $5^{12}6^4$)

The preferential adsorption sites of H_2O are located proximal to the C = C bond of the 2-methylimidazolate linker, which causes pre-adsorbed H_2O to occupy the effective adsorption sites of CH_4 [6]. Therefore, more H_2O molecules were interacted to form clusters and this observation is in general associated with the results of H_2O adsorption in MIL-100(Fe) [15], whereas CH_4 molecules in this region were force to diffuse to region1 and pores of ZIF-8. As shown in Fig. 3(a) the 5^{12}, $5^{12}6^2$ and $5^{12}6^3$ cages grow rapidly during the first 10ns followed by reaching equilibrium throughout the simulation process. CH_4 hydrate growth mainly occurred in region1 within the initial 10ns and grew towards the boundary continuously with the time from 10ns to 40ns, which is due to the existence of capillary force in confined space. Furthermore, Fig. 3(b) shows that the H_2O molecules move from region1 to region2 during the hydrate formation. Both hydrate cages in region1 and 2 gradually formed towards near region during the equilibrium and the hydrate in region1 promoted evolution of hydrate in region2. This observation is regarded as a layer-by-layer mechanism also reported by the CO_2 hydrate growth [16].

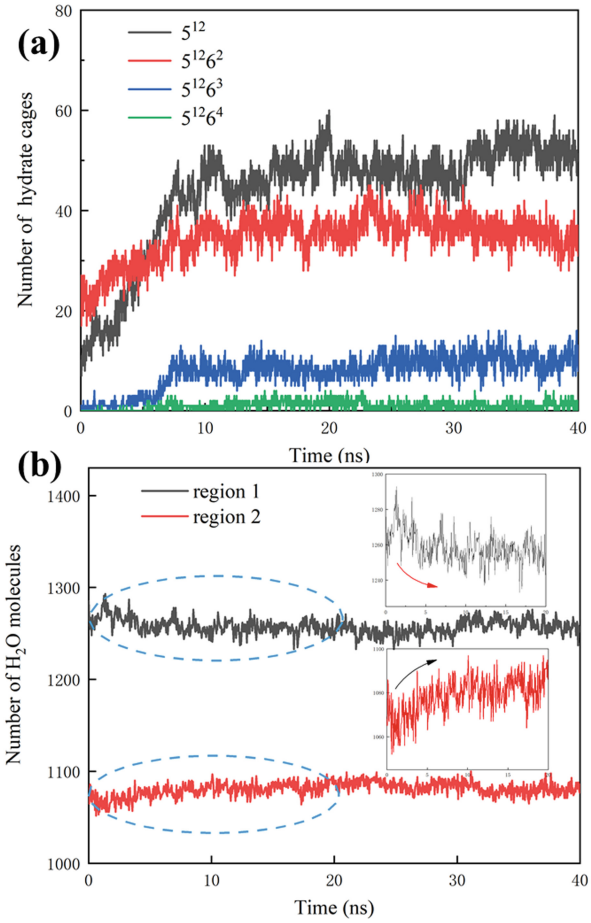

Fig. 3. Time evolution of the number of (e) hydrate cages and (f) H_2O in different regions.

3.2 Effect of CH_4/H_2O Migration on Adsorption-Hydration Hybrid

Figure 4 shows the density distribution for CH_4 and H_2O in system with different time at 275.15 K. It can be seen from Fig. 4(a)−(d) that CH_4 molecules evenly distributed over the interconnectivity space within the initial 10ns, whereas some CH_4 molecules had migrated in ZIF-8 pores, which are shown in Fig. 5 and Fig. 6 (a)–(b). It indicated that the competitive adsorption for CH_4 between ZIF-8 and hydrate surface. Furthermore, the diffusion coefficient of CH_4 and H_2O in region1 are 0.47 and 0.37 m^2/s, respectively. In region2 are 0.85 and 0.54 m^2/s, respectively. It is found that the value of CH_4 and H_2O in region1 both lower than region2, indicating the preferential growth of hydrate is in region1, because the hydrate formation inhibits the diffusion of CH_4 and H_2O molecules. Some H_2O molecules on surface of ZIF-8 were migrated into interconnectivity space

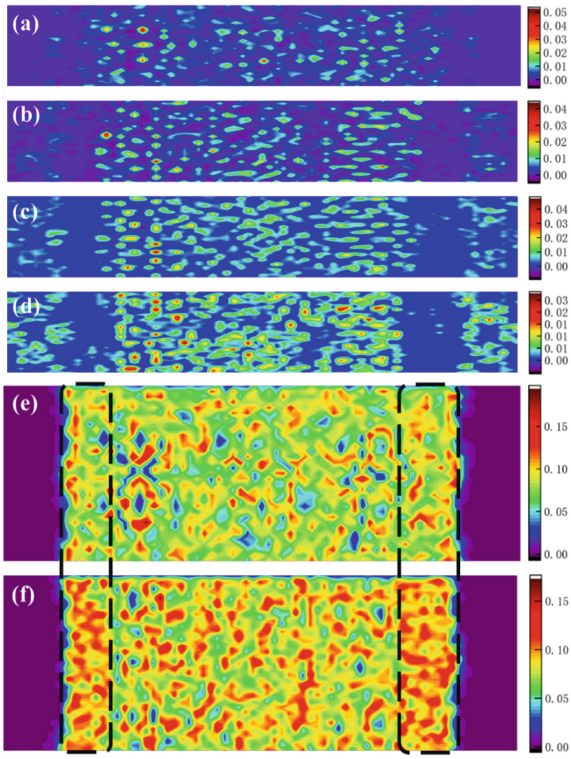

Fig. 4. Density distribution for CH_4 and H_2O in system with different time. CH_4:(a) 0.02 ns, (b) 10 ns, (c) 20 ns and (d) 40 ns. H_2O: (e) 0.02 ns and (f) 40 ns at 275.15 K.

and the CH_4 molecules were migrated into the pores. The result showed that the two-way migration [17] is also observed in MD simulation, indicating that CH_4 molecules penetrate the obstruction of H_2O molecule clusters and enter micro pores induced by strong physical adsorption, while water molecules migrate outwards.

In Fig. 4 (c)–(d), density distribution for CH_4 is displayed the significant difference after about 20 ns, which was mainly focused in both ZIF-8 pores and interconnectivity space. It indicates that the physical adsorption and hydrate growth are occurred at the same time during the process adsorption-hydration hybrid. Compared with Fig. 4 (e) and (f), the liquid water gradually formed the ordered structure and the migration of H_2O molecules tended to be stable. The H_2O molecules focused in the region near the surface of ZIF-8, which differed widely with the density distribution for CH_4.

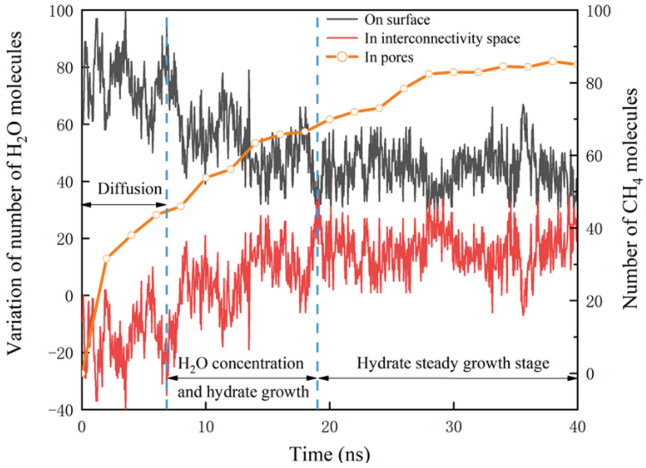

Fig. 5. The evolution of H_2O and CH_4 molecules in different regions of ZIF-8 is shown in different colors: on surface (black), in region1-2-1 (red), and CH_4 in pores (orange).

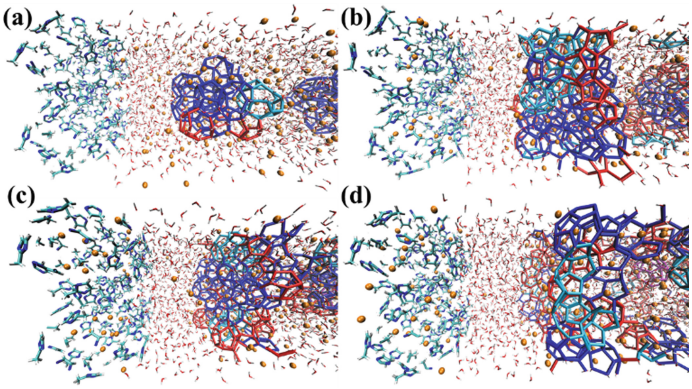

Fig. 6. The migration of H_2O and CH_4 near the surface of ZIF-8 with time of (a) 0.02 ns, (b) 10 ns, (c) 20 ns and (d) 40 ns at 275.15 K.

4 Conclusion

In this study, the behavior of CH_4 hydrate growth and CH_4/H_2O migration in confined interconnectivity space between the surface of ZIF-8 were investigated using MC and MD simulations. The results showed that the hydrate growth in interconnectivity space with pre-humidified ZIF-8 followed by a layer-by-layer mechanism and preferred growing towards boundary. During the process of CH_4 adsorption-hydration hybrid, the value of diffusion coefficient for CH_4 in region1 was lower than region2, indicating the preferential growth of hydrate was in region1. The competitive adsorption for CH_4 was existed between ZIF-8 and hydrate surface, a number of CH_4 molecules were adsorbed in pores by physical adsorption, which promoted the two-way migration

of CH_4/H_2O and further enhanced hydrate growth near the region of ZIF-8. Combined with two mechanisms, CH_4/H_2O migration and hydrate growth in confined interconnectivity space in ZIF-8 were further investigated. Finally, this simulation study is helpful to understand the microscopic mechanism of CH_4 storage in ZIF-8 by the technology of adsorption-hydration hybrid.

Acknowledgements. We acknowledge funding support from the project 52176028 supported by National Natural Science Foundation of China, the project ZR2019MEE005 supported by Shandong Provincial Natural Science Foundation, and the project 18CX02080A supported by the Fundamental Research Funds for the Central Universities.

References

1. Kumar, K.V., Preuss, K., Titirici, M.-M., Rodríguez-Reinoso, F.: Nanoporous materials for the onboard storage of natural gas. Chem. Rev. **117**(3), 1796–1825 (2017)
2. EIA: International energy outlook (2020)
3. Casco, M.E., et al.: Methane hydrate formation in confined nanospace can surpass nature. Nat. Commun. 255 (2019)
4. Casco, M.E., et al.: Paving the way for methane hydrate formation on metal–organic frameworks (MOFs). J. Am. Chem. Soc. **7**(6), 3658–3666 (2016)
5. Peng, Y., et al.: Methane storage in metal–organic frameworks: Current records, surprise findings, and challenges. J. Am. Chem. Soc. **135**(32), 11887–11894 (2013)
6. Wang, Z., Zhang, Y., Chen, S., Fu, Y., Li, X., Pei, J.: Molecular simulation of adsorption and diffusion of CH4 and H2O in flexible metal-organic framework ZIF-8. Fuel **286**, 119342 (2021)
7. Proenza, Y.G., Longo, R.L.: Simulation of the adsorption and release of large drugs by ZIF-8. J. Chem. Inf. Model. **60**(2), 644–652 (2020)
8. Abascal, J.L.F., Sanz, E., García Fernández, R., Vega, C.A.: Potential model for the study of ices and amorphous water: TIP4P/Ice. J. Chem. Phys. **122**(23), 234511 (2005)
9. Martin, M.G., Siepmann, J.I.: Transferable potentials for phase equilibria. 1. United-atom description of nalkanes. J. Phys. Chem. B **102**(14), 2569–2577 (1998)
10. Plimpton, S.: Fast parallel algorithms for short range molecular dynamics. J. Comput. Phys. **117**(1), 1–19 (1995)
11. Akkermans, R.L.C., Spenley, N.A., Robertson, S.H.: Monte carlo methods in materials studio. Mol. Simul. **39**(14–15), 1153–1164 (2013)
12. Ryckaert, J.-P., Ciccotti, G., Berendsen, H.J.C.: Numerical integration of the cartesian equations of motion of a system with constraints: molecular dynamics of n-alkanes. J. Phys. Chem. C **23**(3), 327–341 (1977)
13. Jiménez-Ángeles, F., Firoozabadi, A.: Nucleation of methane hydrates at moderate subcooling by molecular dynamics simulations. J. Phys. Chem. C **118**(21), 11310–11318 (2014)
14. Cha, S.B., Ouar, H., Wildeman, T.R., Sloan, E.D.: A third surface effect on hydrate formation. J. Phys. Chem. **92**, 6492–6494 (1988)
15. Mileo, P.G.M., et al.: Unraveling the water adsorption mechanism in the mesoporous MIL-100(F-e) metal-organic framework. J. Phys. Chem. C **123**, 23014–23025 (2019)
16. Bai, D., Chen, G., Zhang, X., et al.: Microsecond molecular dynamics simulations of the kinetic pathways of gas hydrate formation from solid surfaces. Langmuir **27**(10), 5961–5967 (2011)
17. Zhang, G., Sun, M., Liu, B., Wang, F.: Adsorption-induced two-way nanoconvection enhances nucleation and growth kinetics of methane hydrates in confined porespace. Chem. Eng. J. **396**, 125256–125265 (2020)

Prediction Evaluation on $CH_4/C_2H_6/C_3H_8/CO_2$ Hydrate Phase Equilibria in NaCl/KCl/$CaCl_2$ Aqueous Solutions by Water Activity Measurement

Changhong Yu, Baojiang Sun, Xin Jiang, Mingyue Zhao, Haotian Wang, Cheng Yue, and Litao Chen(✉)

School of Petroleum Engineering, China University of Petroleum (East China), Qingdao 266580, China
chenlt@upc.edu.cn

Abstract. Phase equilibria studies are of great significance for the development of hydrate-based techniques. In our previous work, a prediction method based on water activity measurement (WAM) has been developed for the efficient prediction of hydrate phase equilibria conditions. In this study, aiming at further testifying its universality and effectiveness, the water activity of NaCl/KCl/$CaCl_2$ solutions was measured. The hydrate-water-vapor phase equilibria conditions of $CH_4/C_2H_6/C_3H_8/CO_2$ hydrate in different aqueous salt solutions were predicted by WAM method. The validity of the prediction method was subsequently evaluated by using related literature data. It was shown that the predicted result and literature data are in good agreement. This study further demonstrates the reliability and wide applicability of the WAM method for predicting hydrate phase equilibria conditions.

Keywords: Hydrate · Phase equilibria · Water activity · Chen-Guo model

1 Introduction

Gas hydrate is a cage-like crystalline compound in which guest gas molecules are trapped [1]. In nature, natural gas hydrate (NGH) is widely distributed in permafrost and submarine sediments, which is regarded as the alternative energy in future [2]. The prevailing NGH production methods mainly development include depressurization, thermal stimulation, inhibitor injection and their combinations [1, 2]. The production of NGH has raised wide interests. Hydrate formation also occurs during the production and transportation of offshore oil and gas, leading to safety hazards and significant economic losses as hydrates can block pipelines [1, 3]. The injection of hydrate inhibitors is commonly adopted for hydrate prevention as well as the flow assurance. In general, both hydrate production and hydrate-based flow assurance are conducted based on the system temperature/pressure regulation or the hydrate phase equilibrium control. Therefore, hydrate phase equilibria studies is the fundamental of these hydrate-based technologies.

B. Sun et al. (Eds.): DWOG-Hyd 2021, LNCE 246, pp. 350–361, 2022.
https://doi.org/10.1007/978-981-19-0960-3_34

The accurate and rapid determination of hydrate phase equilibria is of great significance for the flow assurance during the offshore oil and the gas production and NGH production [1–3].

Obviously, hydrate phase equilibria experiment is the most convincing way to determine the phase equilibria conditions of hydrate. In the last several decades, numerous hydrate phase equilibrium data have been reported [1]. However, the experimental determination requires the establishment of high pressure apparatus and the complex hydrate formation/dissociation process, which tend to be time-consuming and costly. In order to simplify the hydrate phase equilibria determination process, some thermodynamic hydrate models are proposed for their prediction. The prevailing models are mainly of two types including van der Waals-Platteeuw (vdW-P) type and Chen-Guo type [1, 3]. Water activity is a key parameter for hydrate phase equilibria models. During the prediction, the effect of salt or alcohol on hydrate phase equilibria is mainly characterized by related water activity calculations. However, the calculation of the water activity tends to be complex, and the system composition must be known, which limits its practical applications. the experimentally determined water activity can provide great convenience. Fortunately, there have been commercial water activity meter put in use. For a sealed system, the water activity can be experimentally determined based on the following relationship.

$$a_{\mathrm{w}} = f_{\mathrm{w}} / f_{w0} \cong P_{\mathrm{w}} / P_{\mathrm{w}0} \tag{1}$$

When the water activity is experimentally determined, the prediction of hydrate equilibria conditions can be achieved using the classical hydrate thermodynamic models incorporated with the measured water activity data. When the water activity is experimentally determined, the prediction of hydrate equilibria conditions can be achieved using the classical hydrate thermodynamic models incorporated with the measured water activity data. In our previous work, a prediction method based on water activity measurement (WAM) has been developed for the efficient prediction of CH_4 hydrate phase equilibria conditions [4]. In this study, the water activity of NaCl/KCl/$CaCl_2$ solutions was measured, then the hydrate-water-vapor phase equilibria conditions of $CH_4/C_2H_6/C_3H_8/CO_2$ hydrate in different aqueous salt solutions were predicted by WAM method. This study further verified the effectiveness of the WAM method.

2 Experimental Section

The materials used in the experiment are shown in Table 1. A GYW-1M water activity meter (Guanya Inc., Shenzhen) was adopted for the water activity measurement. The accuracy of water activity measurement is 0.012, and the temperature range is 273.15–323.15 K. Before the measurement, the water activity meter has been calibrated. For each run, some silica gel was first placed in the sample chamber of the apparatus to remove the initial water moisture. Then the aqueous solution to be measured was injected into the chamber of water activity meter by using a syringe. The solutions of different concentrations were prepared by adding related chemicals to deionized water on the mass basis. The water activity can be automatically output after the measurement is initiated for 15 min. To ensure the reliability of the measurement, each sample was measured

for more than 4 times, and the average value was adopted. Finally, Chen-Guo hydrate model incorporated with the measured water activity was adopted for the prediction of hydrate phase equilibria conditions. The detailed modeling process for the prediction of hydrate phase equilibrium conditions has been well-described in the literature, [5, 6] so there is no further elaboration.

Table 1. Materials used in experiments

Chemicals	Purity	Supplier
NaCl	≥0.995	Sinopharm Chemical Reagent Co., Ltd.
KCl	≥0.995	
$CaCl_2$	≥0.960	
Deionized water	18.2 MΩ.cm	Lab-made

3 Experimental Results and Discussion

Before predicting the hydrate phase equilibria conditions of measured samples, the validation of the Chen-Guo model in this work was confirmed by comparisons between predicted results and literature data of bulk hydrate equilibrium conditions [7–12]. It was shown in Fig. 1 that the predicted results and literature data are in good agreement. Figure 2 presents the measured water activity data of aqueous solutions including NaCl, KCl, $CaCl_2$ and their mixed solutions. The labels in Fig. 1 denotes the combination of the mass fraction of salt in aqueous solution and the salt type. For example, 5Na means that the mass fraction of NaCl is 5 wt%. It was shown that the measured water activity is within the range of 0.853–0.983. The measured water activity was then substituted into Chen-Guo model for related predictions.

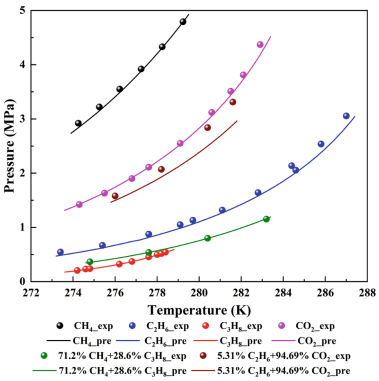

Fig. 1. Validation of Chen-Guo model in this work

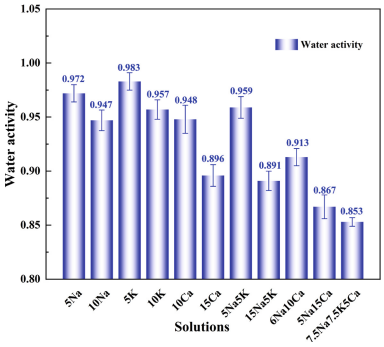

Fig. 2. Experimental determined water activity in different aqueous solutions

3.1 CH_4 Hydrate

In our previous work, the WAM method was proposed for predicting CH_4 hydrate phase equilibria conditions in aqueous solutions. In this study, the validity of the method was further confirmed using binary mixed salt solutions. The comparison between the predicted phase equilibria pressure of CH_4 hydrate by WAM method and the literature data [13] is given in Fig. 3. The error bars are calculated based on the accuracy of 0.012. Table 2 shows the predicted phase equilibrium temperature compared to literature data. With the temperature prediction deviation less than 1.2 K, it can be seen that the predicted results are in good agreement with literature data.

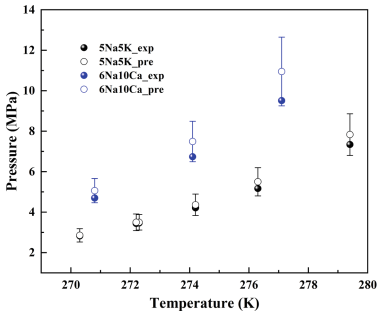

Fig. 3. Comparisons between the experimental and predicted CH_4 hydrate phase equilibria pressure in aqueous solutions

3.2 C_2H_6 Hydrate

Figure 4 presents the comparison between the predicted phase equilibria pressure of C_2H_6 hydrate by WAM method and the literature data [14]. Table 3 shows the predicted phase equilibrium temperature compared to literature data. The predicted results are in good agreement with literature data. The maximum deviation of the predicted phase equilibrium temperature of hydrate in 10 wt% NaCl solution is lower than 1.3 K.

Table 2. Comparisons between the experimental and predicted CH_4 hydrate phase equilibria temperature in aqueous solutions

Solutions	T (K)	P (MPa)	T_pre (K)	ΔT (K)
5Na5K Ref. [13]	272.3	3.464	272.1	0.2
	270.3	2.829	270.1	0.2
	274.2	4.215	273.9	0.3
	276.3	5.169	275.7	0.6
	272.2	3.439	272.0	0.2
	281.2	9.379	280.9	0.3
	279.4	7.34	278.9	0.5
6Na10Ca Ref. [13]	274.1	6.739	273.2	0.9
	277.1	9.514	276.0	1.1
	270.8	4.699	270.1	0.7

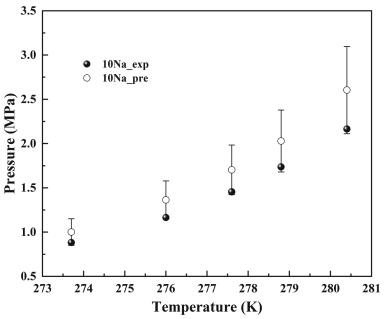

Fig. 4. Comparisons between the experimental and predicted C_2H_6 hydrate phase equilibria pressure in aqueous NaCl solutions

Table 3. Comparisons between the experimental and predicted C_2H_6 hydrate phase equilibria temperature in aqueous solutions

Solutions	T (K)	P (MPa)	T_pre (K)	ΔT (K)
10Na Ref. [14]	273.7	0.883	272.8	0.9
	276.0	1.165	274.8	1.2
	277.6	1.455	276.5	1.1
	278.8	1.737	277.7	1.1
	280.4	2.165	279.2	1.2

3.3 C_3H_8 Hydrate

Figure 5 presents the comparison between the predicted phase equilibria pressure of C_3H_8 hydrate by WAM method and the literature data [14–17]. The predicted phase equilibrium temperatures compared to literature data for aqueous NaCl, KCl, $CaCl_2$ and their mixed solution were shown in Table 4, Table 5 and Table 6, respectively. The predicted results are in good agreement with literature data. The maximum deviation of the predicted phase equilibrium temperature of hydrate is all lower than 1 K.

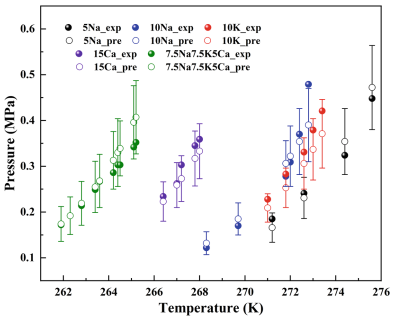

Fig. 5. Comparisons between the experimental and predicted C_3H_8 hydrate phase equilibria pressure in aqueous solutions

Table 4. Comparisons between the experimental and predicted C_3H_8 hydrate phase equilibria temperature in aqueous NaCl solutions

Solutions	T (K)	P (MPa)	T_pre (K)	ΔT (K)
5Na Ref. [15]	271.2	0.185	271.7	0.5
	272.6	0.241	272.8	0.2
	274.4	0.324	274.0	0.4
	275.6	0.448	275.4	0.2
10Na Ref. [16]	268.3	0.122	268.0	0.3
	269.7	0.170	269.3	0.4
	271.8	0.278	271.4	0.4
	272.0	0.309	271.8	0.2
	272.4	0.370	272.6	0.2
	272.8	0.479	273.7	0.9

Table 5. Comparisons between the experimental and predicted C_3H_8 hydrate phase equilibria temperature in aqueous KCl or $CaCl_2$ solutions

Solutions	T (K)	P (MPa)	T_pre (K)	ΔT (K)
10K Ref. [14]	271.0	0.228	271.4	0.4
	271.8	0.283	272.3	0.5
	272.6	0.331	273.0	0.4
	273.0	0.379	273.4	0.4
	273.4	0.421	273.9	0.5
15Ca Ref. [14]	266.4	0.234	266.6	0.2
	267.0	0.262	267.1	0.1
	267.2	0.303	267.6	0.4
	267.8	0.345	268.1	0.3
	268.0	0.359	268.3	0.3

Table 6. Comparisons between the experimental and predicted C_3H_8 hydrate phase equilibria temperature in aqueous NaCl/KCl/$CaCl_2$ mixed solutions

Solutions	T (K)	P (MPa)	T_pre (K)	ΔT (K)
7.5Na7.5K 5Ca Ref. [17]	261.9	0.172	261.9	0
	262.3	0.192	262.3	0
	262.8	0.214	262.7	0.1
	263.4	0.249	263.3	0.1
	263.6	0.267	263.6	0
	264.2	0.286	263.9	0.3
	264.4	0.303	264.1	0.3
	264.5	0.303	264.1	0.4
	265.1	0.342	264.5	0.6
	265.2	0.352	264.6	0.6

3.4 CO_2 Hydrate

The KCl, $CaCl_2$, and some binary salt solutions were prepared for the predictions of CO_2 hydrate phase equilibria conditions. The comparison between the predicted phase equilibria pressure of CO_2 hydrate by WAM method and the literature data [18] is shown in Fig. 6a and 6b. The predicted phase equilibrium temperatures compared to literature data were shown in Table 7 and Table 8, respectively. It was found that the predicted results are in good agreement with literature data. The maximum deviation of the predicted phase equilibrium temperature of hydrate is all lower than 3.6 K.

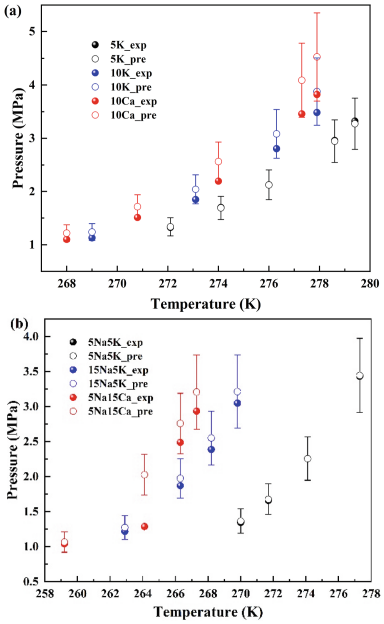

Fig. 6. Comparisons between the experimental and predicted CO_2 hydrate phase equilibria pressure in aqueous solutions of single (a) or binary mixed (b) salts

3.5 Hydrate of Mixed Gas

Phase equilibrium predictions on hydrates of mixed gas can provide guidance on practical hydrate-based flow assurance. In this work, we also analyzed the performance of WAM method on the prediction for hydrate of mixed gas. The comparison between the predicted phase equilibria pressure by WAM method and the literature data [18] is given in Fig. 7. The predicted phase equilibrium temperatures compared to literature data were shown in Table 9. It was found that the predicted results and the literature data [18] are in good agreement. The maximum deviation of the predicted phase equilibrium temperature of hydrate is all lower than 1.3 K.

Table 7. Comparisons between the experimental and predicted CO_2 hydrate phase equilibria temperature in aqueous KCl or $CaCl_2$ solutions

Solutions	T (K)	P (MPa)	T_pre (K)	ΔT (K)
5K Ref. [18]	280.5	3.905	280.7	0.2
	280.4	3.861	280.6	0.2
	279.4	3.324	279.5	0.1
	278.6	2.960	278.7	0.1
	276.0	2.129	276.0	0
	274.1	1.700	274.2	0.1
	272.1	1.325	272.0	0.1
10K Ref. [18]	277.9	3.485	277.2	0.7
	276.3	2.807	275.6	0.7
	273.1	1.848	272.3	0.8
	269.0	1.130	268.2	0.8
10Ca Ref. [18]	270.8	1.511	269.8	1.0
	268.0	1.102	267.2	0.8
	274.0	2.198	272.8	1.2
	277.3	3.460	276.2	1.1
	277.9	3.824	276.9	1.0

Table 8. Comparisons between the experimental and predicted CO_2 hydrate phase equilibria temperature in aqueous binary solutions

Solutions	T (K)	P (MPa)	T_pre (K)	ΔT (K)
5Na5K Ref. [18]	270.0	1.347	269.9	0.1
	271.7	1.660	271.6	0.1
	274.1	2.258	274.1	0
	277.3	3.432	277.2	0.1
15Na5K Ref. [18]	262.9	1.218	262.5	0.4
	266.3	1.872	265.9	0.4
	268.2	2.388	267.7	0.5
	269.8	3.050	269.5	0.3
5Na15Ca Ref. [18]	267.3	2.935	266.7	0.6
	266.3	2.490	265.6	0.7
	264.1	1.288	260.6	3.5
	259.2	1.042	259.0	0.2

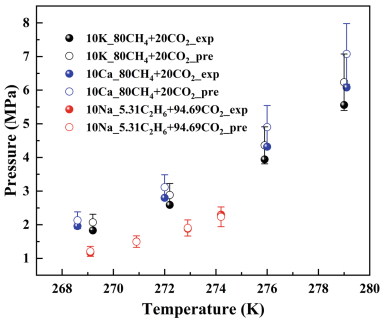

Fig. 7. Comparisons between the experimental and predicted phase equilibria pressure for hydrate of mixed gas in aqueous solutions

Table 9. Comparisons between the experimental and predicted phase equilibria temperature for hydrate of mixed gas in aqueous solutions

Systems	T (K)	P (MPa)	T_pre (K)	ΔT (K)
10K 80%CH_4 20%CO_2 Ref. [18]	275.9	3.94	274.8	1.1
	269.2	1.83	268.3	0.9
	272.2	2.59	271.3	0.9
	279.0	5.56	278.0	1.0
10Ca 80%CH_4 20%CO_2 Ref. [18]	268.6	1.96	268.0	0.6
	276.0	4.32	275.0	1.0
	272.0	2.80	271.1	0.9
	279.1	6.08	277.9	1.2
10Na 5.31C_2H_6 94.69CO_2 Ref. [18]	269.1	1.17	269.0	0.1
	270.9	1.50	271.0	0.1
	272.9	1.88	273.0	0.1
	274.2	2.30	274.3	0.1

4 Conclusion

In this study, the performance of WAM method on phase equilibria prediction of $CH_4/C_2H_6/C_3H_8/CO_2$ hydrate in single or mixed NaCl/KCl/$CaCl_2$ solutions are investigated. The predicted results and literature data were found in good agreement. The predicted deviations of phase equilibrium temperature were all lower than 3.6 K. This study further verified the reliability and universality of the WAM method for predicting hydrate phase equilibria conditions.

Symbol Description

a_w—Water activity
f_w—Vapor water fugacity of system
f_{w0}—Vapor fugacity of pure water
NGH—Natural gas hydrate
P—Pressure
P_w—Vapor water pressure of system
P_{w0}—Vapor pressure of pure water
T—Temperature
T_pre—Predicted temperature
ΔT—Predicted temperature deviation

Acknowledgement. The authors would like to appreciate the financial support from National Natural Science Foundation of China (grant Nos. 51991365, 51876222) and CNPC Major R&D Project (grant No. ZD2019-184-002).

References

1. Sloan, E.D., Koa, C.A.: Clathrate Hydrates of Natural Gases, 3rd edn. CRC Press, Boca Raton (2007)
2. Boswell, R., Collett, T.S.: Current perspectives on gas hydrate resources. Energy Environ. Sci. **4**(4), 1206–1215 (2011)
3. Chen, G.J., Sun, C.Y., Ma, Q.L.: Gas Hydrate Science and Technology. Chemical Industry Press, Beijing (2007)
4. Zhao, M.Y., Sun, B.J., Yu, C.H., et al.: Predicting methane hydrate equilibrium conditions in ethylene glycol and NaCl/KCl/$CaCl_2$ aqueous solutions by water activity measurement. J. Chem. Eng. Data **66**, 4159–4165 (2021)
5. Chen, G.J., Guo, T.M.: Thermodynamic modeling of hydrate formation based on new concepts. Fluid Phase Equilib. **122**(1–2), 43–65 (1996)
6. Chen, G.J., Guo, T.M.: A new approach to gas hydrate modelling. Chem. Eng. J. **71**(2), 145–151 (1998)
7. Nakamura, T., Makino, T., Sugahara, T., et al.: Stability boundaries of gas hydrates helped by methane-structure-H hydrates of methylcyclohexane and cis-1, 2-dimethylcyclohexane. Chem. Eng. Sci. **58**(2), 269–273 (2003)
8. Roberts, O.L., Brownscombe, E.R., Howe, L.S.: Methane and ethane hydrates. Oil Gas J. **39**, 37–43 (1940)
9. Kubota, H., Shimizu, K., Tanaka, Y., et al.: Thermodynamic properties of R13 ($CClF_3$), R23 (CHF_3), R152a ($C_2H_4F_2$), and propane hydrates for desalination of sea water. J. Chem. Eng. Jpn. **17**(4), 423–429 (1984)
10. Adisasmito, S., Frank, R.J., Sloan, E.D.: Hydrates of carbon dioxide and methane mixtures. J. Chem. Eng. Data **36**(1), 68–71 (1991)
11. Deaton, W.M., Frost, E.M.: Gas Hydrates and Their Relation to the Operation of Natural-Gas Pipe Lines. U.S. Bureau of Mines Monograph (1946)

12. Fan, S.S., Guo, T.M.: Hydrate formation of CO_2-rich binary and quaternary gas mixtures in aqueous sodium chloride solutions. J. Chem. Eng. Data **44**(4), 829–832 (1999)
13. Dholabhai, P.D., Englezos, P., Kalogerakis, N., et al.: Equilibrium conditions for methane hydrate formation in aqueous mixed electrolyte solutions. Can. J. Chem. Eng. **69**(3), 800–805 (1991)
14. Tohidi, B., Burgass, R., Danesh, A., et al.: Hydrate inhibition effect of produced water: ethane and propane simple gas hydrates. In: Proceedings SPE Offshore European Conference, SPE-26701, Aberdeen (1993)
15. Patil, S.L.: Measurements of multiphase gas hydrates phase equilibria: effect of inhibitors and heavier hydrocarbon components. University of Alaska, Anchorage (1987)
16. Kobayashi, R., Withrow, H.J., Williams, G.B., et al.: Gas hydrate formation with brine and ethanol solutions. In: Proceedings of the Annual Convention Natural Gasoline Association America (1951)
17. Englezos, P., Ngan, Y.T.: Incipient equilibrium data for propane hydrate formation in aqueous solutions of sodium chloride, potassium chloride and calcium chloride. J. Chem. Eng. Data **38**(2), 250–253 (1993)
18. Dholabhai, P.D., Bishnoi, P.R.: Hydrate equilibrium conditions in aqueous electrolyte solutions: mixtures of methane and carbon dioxide. J. Chem. Eng. Data **39**(1), 191–194 (1994)

Molecular Study on the Mechanism of Methane Hydrate Formation in Formate Solution

Jiafang Xu(✉), Jie Chen, Shuai Du, and Bowen Wang

Institute of Offshore Oil, Gas and Hydrate, China University of Petroleum (East China), Qingdao 266580, China
xjiafang@upc.edu.cn

Abstract. The formation of gas hydrate can block wellbore and drilling equipment during deep sea oil and gas exploitation and transportation, causing high flow pressure and bringing serious threat to the safe production and transportation. Therefore, it is urgent to develop efficient natural gas hydrate inhibitors. In this paper, the formation detail process of methane hydrate in three formate solution was studied by molecular simulation technology, and the micro mechanism of formate in the formation of methane hydrate was revealed. The results show that formate can significantly inhibit the formation of methane hydrate. The order of inhibition ability of three formates is HCOONa > HCOOK > HCOOCs. The detailed analysis shows that the inhibition mechanism of formate on the formation of methane hydrate mainly includes: (1) inhibiting the dissolution of methane gas and weaken the nucleation and growth power of methane hydrate, (2) affecting the water molecular structure of methane hydration, reducing the tetrahedral water substructure in methane hydration, and inhibiting the transformation of water molecular orientation to the direction conducive to the formation of methane hydrate, and (3) delaying the mutual transformation between multi-component rings of water molecules in solution. In addition, (4) The ions can replace the water molecules in the hydrate cage at the methane hydrate growth interface to form an unstable hydrate cage structure and slow down the hydrate growth. This study explores the mechanism of formate inhibiting the formation of methane hydrate from the micro level, which can provide theoretical support for the evaluation and research and development of methane hydrate salt inhibitors.

Keywords: Methane hydrate · Molecular dynamics · Formate solution · Inhibitor

1 Introduction

Natural gas hydrate usually formed in the process of oil and gas drilling, production, storage and transportation, which brings great potential safety hazards to the operation [1–3]. With the development of offshore oil and gas exploration and drilling in the deep sea, where the high-pressure and low-temperature environment is conducive to the formation of gas hydrate, so the problem of gas hydrate blocking pipelines and equipment is becoming more and more common [4–6].

B. Sun et al. (Eds.): DWOG-Hyd 2021, LNCE 246, pp. 362–370, 2022.
https://doi.org/10.1007/978-981-19-0960-3_35

Natural gas hydrate inhibitor is one of the most common methods to control gas hydrate formation. Gas hydrate inhibitors mainly include thermodynamic inhibitors, kinetic inhibitors, and anti polymerization agents [7, 8]. Among them, thermodynamic inhibitors can also be used as chemical injection agents in the development of natural gas hydrate to accelerate the exploitation of natural gas hydrate. Thermodynamic inhibitors mainly include salts (NaCl, KCl, $CaCl_2$, etc.) and alcohols (methanol, ethylene glycol, etc.) [9–11]. Inorganic salts can reduce the vapor pressure at the gas-liquid interface, destroy the cluster structure of water molecules, affect the interaction between water molecules and gas molecules, and thus change the phase equilibrium conditions of natural gas hydrate [12–17]. The inorganic salts have been widely used in natural gas hydrate all over the world, which has been proved that it can effectively inhibit the formation of natural gas hydrate [12, 15, 16]. However, thermodynamic inhibitors have some defects, such as large dosage, high cost, environmental pollution, and difficult recovery. The formation of natural gas hydrate will interact with formate in drilling fluid during the process of deep-sea drilling. The experimental results show that formate can inhibit the formation of hydrate, but the mechanism of formate affecting gas hydrate formation is unclear.

Herein, we constructed a two-phase model of "methane bubble + formate solution", and studied the spontaneous nucleation and growth of methane hydrate at 250 K and 650 bar by molecular simulation. The effects of formate on methane hydrate nucleation and growth were studied by analyzing structural order parameters, system energy, and water molecular structure. Furthermore, the mechanism of formate on methane hydrate formation was explored.

2 Simulation Methods

In this study, the initial configuration of the simulation system after pre-equilibrium is shown in Fig. 1, where the simulation box is $50 \times 50 \times 50$ Å^3. The solution phase contains 3487 water molecules and 3.5wt% formates (HCOONa, HCOOK, and HCOOCs). The gas phase contains 550 methane molecules. The four-site TIP4P/Ice water model proposed by Abascal *et al.* (2005) [18] and the single-site model proposed by Guillot and Guissani (1993) [19] was adopted for water and CH_4, respectively [20]. The L-J potential energy and charge parameters of particles in the model are shown in Table 1 [21, 22]. The interactions between different species were determined by the Lorentz − Berthelot combining rules. The combination of these potential energy models can well predict the phase boundary of methane hydrate related to our simulation conditions and was widely used in previous studies [23–28].

MD simulations were performed with GROMACS package version 5.1.5. The equation of motions was integrated using the Leap-frog algorithm with a time step of 1 fs. For the long-range electrostatic interaction, particle mesh Ewald (PME) was used with a cutoff radius of 1.0 nm. The Lennard-Jones interaction was implemented with a cutoff radius of 1.0 nm. Nosé-Hoover thermostat and Parrinello-Rahman barostat algorithms were used to control temperature and pressure with time constants of 1.0 and 0.1 ps, respectively. Periodic boundary conditions were applied in all three dimensions.

Energy minimization was first performed to relax liquid water at the methane bubble surface and formate solution at the target temperature and pressure (250 K and 65 MPa).

Then, a 1 ns-long simulation under NVT ensemble was followed by a 2 ns simulation under NPT ensemble. The production run lasts 1500 ns and two parallel runs at 250 K and 65 MPa.

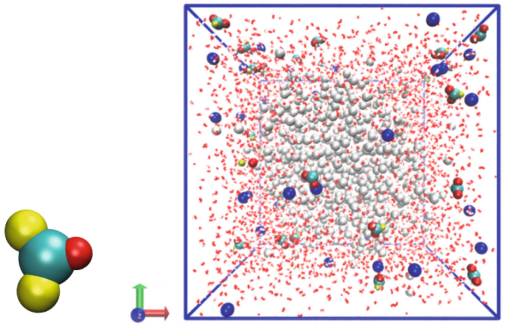

(a) Formate model (b) Initial conformation of simulated system

Fig. 1. The initial configuration of the methane bubble + 3.5 wt% HCOONa (a) solution system (b). Here, the blue and white balls represent the Na^+ and CH_4, respectively. The red, cyan and yellow balls represent oxygen, carbon and hydrogen in HCOO-. The red and white sticks are water.

Table 1. L-J potential energy and charge parameters of particles [21, 22]

Formate molecule	σ/nm	ε/(kJ.mol^{-1})	q/e
Na^+	0.26378	0.5438	1.0
K^+	0.37423	0.4184	1.0
Cs^+	0.43002	0.4184	1.0
H	0.25	0.12552	−0.0616
C	0.355	0.29288	0.3690
O	0.296	0.87864	−0.6537

3 Results and Discussion

3.1 The Methane Hydrate Formation in Different Formate Solutions

Figure 2(a) shows the variations of total energy of all simulated systems with simulation time. The total energy of all systems showed an obvious downward trend, which indicate the formation of gas hydrate. The methane hydrate nucleation time in pure water and HCOOCs solution was significantly earlier than that in HCOOK and HCOONa solution. As shown in Fig. 2(b), We further calculated F_4 for different systems. The results show that the induction phase of all formate systems was longer than that of 0 wt% system. The induction time of methane hydrate nucleation in HCOONa and HCOOK systems is

longer than that in other systems, which indicate HCOONa and HCOOK solutions have a stronger inhibitory effect on the formation of methane hydrate than other systems.

Based on the variations of the number of water molecules in methane hydrate with time and F_4 data, we obtained the induction time and critical size of methane hydrate in different formate systems. As shown in Table 2, the induction time of hydrate in salt containing system is longer than that in the pure water system, and the order of induction time is 0 wt% > HCOOCs > HCOOK > HCOONa, in which the induction time of HCOOK and HCOONa system is 3.4 and 4.4 times that of pure water system, respectively. In the formate containing system, the critical size of crystal nucleus is larger than that of the pure water system. The critical size of HCOONa system is the largest. Therefore, whether in the induction stage or rapid formation stage, the inhibitory effects of the three formates on methane hydrate are as follows: HCOONa > HCOOK > HCOOCs.

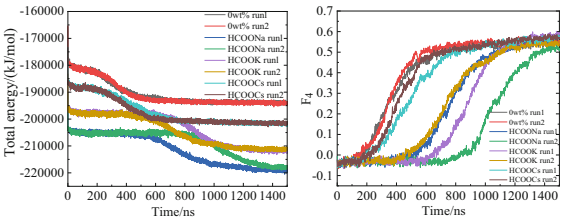

(a) Total energy of the simulated system (b) The F_4 of the simulated system

Fig. 2. The variations of total energy of the simulation system and F_4 with simulation time.

Table 2. Hydrate induction time and critical size of crystal nucleus

System name	Induction time/ns	Critical size/number of water molecules
0 wt%	161	191
HCOONa	715	264
HCOOK	560	220
HCOOCs	237	215

As shown in Fig. 3, to analyze the growth process of methane hydrate in formate containing system, we intercepted the snapshot of methane hydrate formation from three formate systems. It is found that methane hydrate clusters tend to form in places with low ion concentration, which due to high concentration ions are not conducive to the stability of methane hydrate clusters. In the three formate containing systems, the growth of methane hydrate is towards methane bubbles, because the methane concentration gradient around the bubbles is the largest, which is conducive to the growth of methane hydrate. At the later stage of methane hydrate growth, methane hydrate competes with formate ions for water molecules, and the hydrate growth rate is slow, such as 800 to

1500 ns in HCOOCs system. Finally, many aggregation regions of liquid water and formate ions will be formed in the salt containing system. In addition, formate crystallization was also observed in HCOONa system (Fig. 4).

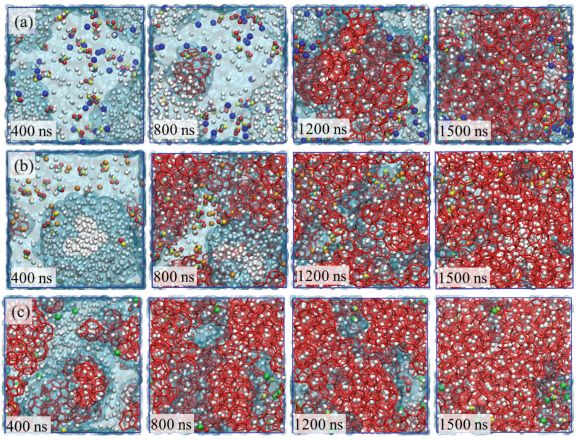

Fig. 3. The snapshots of methane hydrate growth in HCOONa solution (a), HCOOK solution (b) and HCOOCs solution (c). Here, the blue, orange, green and white balls represent the Na^+, K^+, Cs^+, and CH_4, respectively. The red, cyan, and yellow balls represent oxygen, carbon, and hydrogen in $HCOO^-$, respectively. The red and white sticks are water. The ice blue blocks are liquid water.

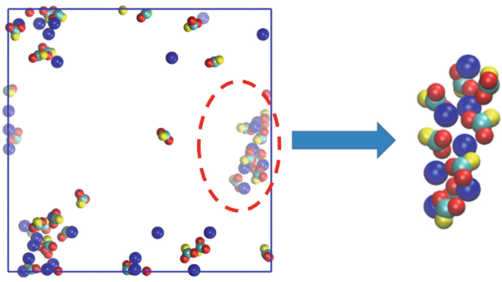

Fig. 4. HCOONa crystals formed during hydrate formation. The color scheme is the same as Fig. 3.

3.2 The Mechanism of Formate Inhibiting Methane Hydrate Formation

To clarify the mechanism of formate inhibiting hydrate formation, we analyzed the changes of the number of dissolved methane and hydrogen bonds in different formate containing systems with simulation time, and counted the proportion of tetrahedral water molecules and the orientation distribution of water molecules in methane hydration layer (Fig. 5).

Figure 5(a) shows the change of dissolved methane amount with time in different systems 100 ns before simulation. It can be shown that the number of dissolved methane

in three formate containing systems is less than that in the pure water system. Therefore, the formate inhibits the dissolution of methane and weakens the nucleation power of hydrate. At 100 ns, the most dissolved methane is HCOOCs system, followed by HCOOK and HCOONa system. As shown in Fig. 5(b), due to ionic hydration, the number of initial hydrogen bonds in salt containing systems decreases, and the order of the number of initial hydrogen bonds in all systems is 0 wt% > HCOOCs > HCOOK > HCOONa. While reducing the hydrogen bond in the system, ions also affect the water molecular network structure in the methane hydration layer. As shown in Fig. 5(c), the proportion of tetrahedral water molecules in the dissolved methane hydration layer of different systems before 100 ns of simulation is calculated. Ions reduce the tetrahedral water molecular structure in the methane hydration layer. Compared with the pure water system, the tetrahedral water molecules in HCOOCs system are reduced by ~1%, less than ~4% and ~5% in HCOOK and HCOONa systems. Then, the effect of ions on the orientation of water molecules in the methane hydration layer is further analyzed (Fig. 5(d)). The results indicate the formats can change the orientation of water molecules in methane hydration layer and inhibit the transformation from water molecular orientation in methane hydration layer to water molecular orientation in hydrate. Among them, the inhibitory effect of HCOOCs is weaker than that of HCOOK and HCOONa.

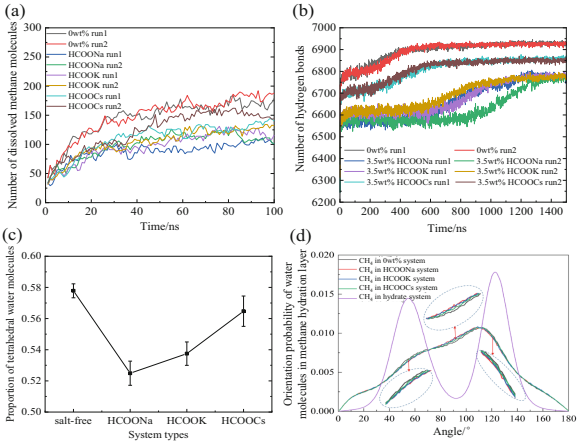

Fig. 5. (a) The number variations of dissolved methane with simulation time. (b) The number variations of hydrogen bonds with simulation time. (c) The ratio of tetrahedral water within the hydration layer of dissolved methane. (d) Orientation distribution of water molecules in methane hydration layers

As shown in Fig. 6, we counted the number variations of 12 common hydrate cages in the generated amorphous methane hydrate. In all systems, the 5^{12}, $5^{12}6^2$, $5^{12}6^3$ and $4^15^{10}6^2$ cages are four kinds of cages with a large number. Among them, 5^{12} cages have the fastest growth rate and the largest number, followed by $5^{12}6^2$ and $5^{12}6^3$ cages, and $4^15^{10}6^2$ cages are the least and close to the number of other 8 cages. It can be concluded that formate slows down the formation rate of hydrate cages and is not conducive to

the growth of hydrate clusters, but does not change the main types of methane hydrate cages.

Based on the crystallization calculation method from Jacobson *et al.* [29], we calculated the change of crystallinity of type I and II hydrates with time. As shown in Fig. 7, after the induction stage, the crystallinity of methane hydrate in most systems increases rapidly. This is due to the methane hydrate cage is mainly 5^{12}, which is easy to form a standard hydrate structure. With the growth of methane hydrate, the number of water molecules in hydrate increases and the crystallinity of methane hydrate decreases. Comparing the hydrate crystallinity curves of each system, it can be seen that the final methane hydrate crystallinity of the two rounds of simulation is quite different in pure water system and HCOOCs system. In HCOONa and HCOOK systems with strong inhibition, the crystallinity difference of methane hydrate simulated in the two rounds is small. This is because in pure water system and HCOOCs system, methane hydrate grows rapidly, which is not conducive to methane hydrate crystallization, and the randomness of hydrate crystallization is large. In HCOONa and HCOOK systems, salt ions destroy the unstable methane hydrate structure, slow down the growth rate of methane hydrate, facilitate the crystallization, and reduce the randomness of methane hydrate crystallization.

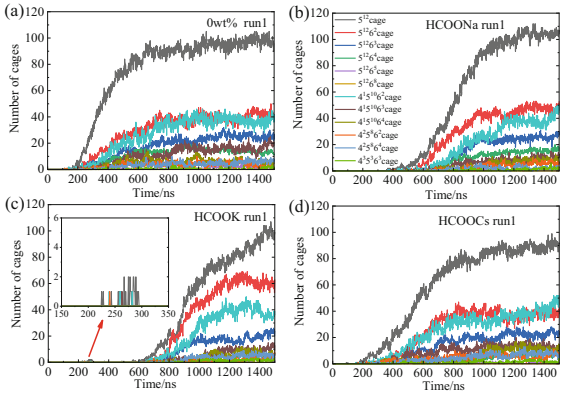

Fig. 6. The number variations of different types of cages in 0wt% system (a), HCOONa system (b), HCOOK system (c), and HCOOCs system (d).

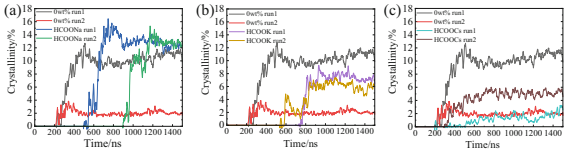

Fig. 7. The crystallinity variations of methane hydrate in HCOONa system (a), HCOOK system (b), and HCOOCs system (c).

4 Conclusion

Through molecular dynamics simulation, the formation process of methane hydrate in different formate solutions with 3.5wt% was simulated, and the formation mechanism of methane hydrate under the effects of formate was explored. The following conclusions were obtained:

(1) The formate used in the simulation has a certain inhibitory effect on the formation of methane hydrate. Compared with pure water system, the methane hydrate induction time in formate solution is longer and the growth rate is slower. The inhibitory effect of the three formates on hydrate formation was 3.5 wt% HCOONa > 3.5 wt% HCOOK > 3.5 wt% HCOOCs.
(2) The inhibition mechanism of formate on methane hydrate formation mainly includes: inhibiting the dissolution of methane bubble, reducing tetrahedral water molecular structure in methane hydration, and inhibiting the transformation of water molecular orientation from methane hydration layer to hydrate. In addition, the formate can delay the mutual transformation between water molecules, and the ions can replace the water molecules at the interface of methane hydrate to form unstable hydrate cages, thus delaying the growth of methane hydrate.

References

1. Prassl, W.F., Peden, J.M., Wong, K.W.: Mitigating gas hydrate related drilling risks: a process-knowledge management approach. Paper Presented at the SPE Asia Pacific Oil and Gas Conference and Exhibition, Perth, Australia, October 2004. (SPE-88529-MS)
2. Parlaktuna, M., Öztürk, M.T.: Wellbore temperature assessment for generic deep water well in black sea and mitigation of hydrate dissociation risk. In: Conference Proceedings, 19th International Petroleum and Natural Gas Congress and Exhibition of Turkey, p. 380-00045. European Association of Geoscientists & Engineers, May 2013
3. Zarinabadi, S., Samimi, A.: Problems of hydrate formation in oil and gas pipes deals. Aust. J. Basic Appl. Sci. **5**(12), 741–745 (2011)
4. Xu, T., Lang, X., Fan, S., Wang, Y., Chen, J.: The effect of electric fields in methane hydrate growth and dissociation: a molecular dynamics simulation. Comput. Theor. Chem. **1149**, 57–68 (2019)
5. Bai, D., Wu, Z., Lin, C., Zhou, D.: The effect of aqueous NaCl solution on methane hydrate nucleation and growth. Fluid Phase Equilib. **487**, 76–82 (2019)
6. Sloan, E.D., Koh, C.A., Sum, A.K.: Natural Gas Hydrates in Flow Assurance. Gulf Professional Publishing, Burlington (2011)
7. Kamal, M.S., Hussein, I.A., Sultan, A.S., et al.: Application of various water soluble polymers in gas hydrate inhibition. Renew. Sustain. Energy Rev. **60**, 206–225 (2016)
8. Balson, T., Craddock, H., Dunlop, J., et al.: The development of advanced kinetic hydrate inhibitors. In: Chemistry in the Oil Industry VII, pp. 264–276 (2002)
9. Mohammadi, A.H., Tohidi, B.: A novel predictive technique for estimating the hydrate inhibition effects of single and mixed thermodynamic inhibitors. Can. J. Chem. Eng. **83**(6), 951–961 (2005)

10. Zare, M., Haghtalab, A., Ahmadi, A.N., et al.: Effect of imidazolium based ionic liquids and ethylene glycol monoethyl ether solutions on the kinetic of methane hydrate formation. J. Mol. Liq. **204**, 236–242 (2015)
11. Dong, F., Zang, X., Li, D., Fan, S., Liang, D.: Experimental investigation on propane hydrate dissociation by high concentration methanol and ethylene glycol solution injection. Energy Fuels **23**(2), 1563–1567 (2009)
12. Yagasaki, T., Matsumoto, M., Andoh, Y., Okazaki, S., Tanaka, H.: Dissociation of methane hydrate in aqueous nacl solutions. J. Phys. Chem. B **118**(40), 11797–11804 (2014)
13. Saw, V.K., Das, B.B., Ahmad, I., Mandal, A., Laik, S.: Influence of electrolytes on methane hydrate formation and dissociation. Energy Sources **36**(15), 1659–1669 (2014)
14. Lv, Q., Li, L., Li, X., Chen, Z.: Clathrate hydrate dissociation conditions and structure of the methane + cyclopentane + trimethylene sulfide hydrate in NaCl aqueous solution. Fluid Phase Equilib. **425**, 305–311 (2016)
15. Mimachi, H., Takeya, S., Gotoh, Y., Yoneyama, A., Murayama, T.: Dissociation behaviors of methane hydrate formed from NaCl solutions. Fluid Phase Equilib. **413**, 22–27 (2016)
16. Wen, Z.H., Fang, C.Y., Dong, L.L., Shi, J.H., Jiang, L., Han, X.T., et al.: Perturbation simulation of invasion of drilling fluid containing thermodynamic hydrate inhibitors into natural gas hydrate formation
17. Yagasaki, T., Matsumoto, M., Tanaka, H.: Effects of thermodynamic inhibitors on the dissociation of methane hydrate: a molecular dynamics study. Phys. Chem. Chem. Phys. **17**(48), 32347–32357 (2015)
18. Abascal, J.L.F., Sanz, E., Fernández, R.G., Vega, C.: A potential model for the study of ices and amorphous water: TIP4P/Ice. J. Chem. Phys. **122**(23), 268–342 (2005)
19. Guillot, B., Guissani, Y.: A computer simulation study of the temperature dependence of the hydrophobic hydration. J. Chem. Phys. **99**(10), 8075–8094 (1993)
20. Luis, D.P., Herrera-Hernández, E.C., Saint-Martin, H.: A theoretical study of the dissociation of the sI methane hydrate induced by an external electric field. J. Chem. Phys. **143**, 204503 (2015)
21. Cygan, R.T., Liang, J.J., Kalinichev, A.G.: Molecular models of hydroxide, oxyhydroxide, and clay phases and the development of a general force field. J. Phys. Chem. B **108**(4), 1255–1266 (2004)
22. Dodda, L.S., Cabeza de Vaca, I., Tirado-Rives, J., et al.: LigParGen web server: an automatic OPLS-AA parameter generator for organic ligands. Nucleic Acids Res. **45**(W1), W331–W336 (2017)
23. Michalis, V.K., Costandy, J., Tsimpanogiannis, I.N., Stubos, A.K., Economou, I.G.: Prediction of the phase equilibria of methane hydrates using the direct phase coexistence methodology. J. Chem. Phys. **142**(4), 044501 (2015)
24. Zhang, Z., Guo, G.-J., Wu, N.Y., Peter, G.K.: Molecular insights into guest and composition dependence of mixed hydrate nucleation. J. Phys. Chem. C **124**(45), 25078–25086 (2020)
25. Zhang, Z., Liu, C.J., Walsh, M.R., Guo, G.-J.: Effects of ensembles on methane hydrate nucleation kinetics. Phys. Chem. Chem. Phys. **18**(23), 15602–15608 (2016)
26. Zhang, Z., Guo, G.-J.: The effects of ice on methane hydrate nucleation: a microcanonical molecular dynamics study. Phys. Chem. Chem. Phys. **19**(29), 19496–19505 (2017)
27. Zhang, Z., Kusalik, P.G., Guo, G.J.: Bridging solution properties to gas hydrate nucleation through guest dynamics. Phys. Chem. Chem. Phys. **20**(38), 24535–24538 (2018)
28. Zhang, Z., Kusalik, P.G., Guo, G.-J., Ning, F., Wu, N.: Insight on the stability of polycrystalline natural gas hydrates by molecular dynamics simulations. Fuel **289**(9), 119946 (2021)
29. Jacobson, L.C., Matsumoto, M., Molinero, V.: Order parameters for the multistep crystallization of clathrate hydrates. J. Chem. Phys. **135**(7), 7457–8233 (2011)

Adsorption and Hydration Coupling on a Novel Material of MIL-101(Cr)/Graphene Oxide Composites with High Capacities Methane

Yaxue Zhang[1], Ming Zhang[1], Shujun Chen[1,2,3(✉)], and Di Wang[1]

[1] College of Pipeline and Civil Engineering, China University of Petroleum (East China), Qingdao 266580, China
chensj@upc.edu.cn

[2] Qingdao Engineering Research Center of Efficient and Clean Utilization of Fossil Energy, Qingdao 266580, China

[3] Shandong Key Laboratory of Oil and Gas Storage and Transport Safety, Qingdao 266580, China

Abstract. To reach the carbon peak by 2030 and carbon neutrality by 2060, a kind of clean energy of natural gas acts as a key energy to achieve the target, and the high capacities of methane is significance for large-scale utilization of natural gas. In this study, a novel MIL-101(Cr)/GO composites were synthesized by hydrothermal synthesis, characterized and studied for storage of CH_4. A lower mass ratio of GO will not damage the structure of MIL-101(Cr). The adsorption experiment of CH_4 was carried on MIL-101(Cr)/GO composites, the adsorption capacity of dry MIL-101(Cr)/2.5GO composites for CH_4 reached 27.39 mmol/g, at 8 MPa and 275.15 K; the adsorption capacity of CH_4 on MIL-101(Cr)/2.5GO composites with H_2O was higher than dry material, reaching 33.98 mmol/g (0.54 g/g) at 8 MPa and 275.15 K, much higher than other MOFs reported and over the standard of DOE (0.5 g/g), the results confirmed that CH_4 hydrate formation on MIL-101(Cr)/GO composites. It is the first indicated that adsorption-hydration coupling of CH_4 on MIL-101(Cr)/GO composites and increase the storage capacity of CH_4, MIL-101(Cr)/GO composites can be developed as an effective storage material to storage CH_4 and provide a way for natural gas storage and transportation applications.

Keywords: Natural gas · Methane hydrate · Graphene oxide · MIL-101(Cr)/GO composites · Adsorption-hydration coupling

1 Introduction

The greenhouse effect has become a challenge all world, which is caused by the carbon dioxide that is produced through the burning of fossil fuels [1]. China promises to reach the carbon peak by 2030 and carbon neutrality by 2060 [2]. Natural gas is a kind of clean and potential energy, large-scale utilization of natural gas is the key technology to achieve the target. Therefore, the high-density storage of methane is significance for large-scale utilization of natural gas.

B. Sun et al. (Eds.): DWOG-Hyd 2021, LNCE 246, pp. 371–376, 2022.
https://doi.org/10.1007/978-981-19-0960-3_36

Natural gas by adsorption method has aroused widespread attention and research of scholars due to its moderate condition, however, the adsorption capacity of CH_4 is still a certain distance from the DOE standard [3]. Scholars [4, 5] found that the presence of water in porous materials increases the storage of CH_4 due to hydrate formation, which combines the advantages of adsorbed natural gas (ANG) and natural gas hydrate (NGH).

MIL-101(Cr) has been widely used in gas storage due to the advantages of high specific surface area, adjustable pore size, large porosity and surface modification [6]. However, MIL-101(Cr) also have disadvantages such as poor chemical stability and low atomic density [7]. Some studies found that introduction of GO to MOFs improved the disadvantages [8]. Therefore, the MIL-101(Cr)/GO composites with H_2O storage CH_4 may provide a new method to natural gas storage and transportation.

In this study, firstly, MIL-101(Cr) and MIL-101(Cr)/GO composites with different GO contents were synthesized successfully by the hydrothermal synthesis method and were characterized via various techniques. Then, the effect of different GO contents on the CH_4 adsorption performance of MIL-101(Cr) were systematically investigated, besides, the adsorption and hydration coupling of CH_4 in MIL-101(Cr)/GO composites with water was discussed in detail.

2 Materials and Experimental Setup

2.1 Materials

All chemicals were of analytical reagent and used without further purification. Chromium nitrate nonahydrate ($Cr(NO_3)_3{\cdot}9H_2O$), terephthalic acid $H_2BDC(C_6H_4(CO_2H)_2$, terephthalic acid ($HCON(CH_3)_2$), ethanol and CH_3COONa were purchased from Titan Science and Technology Co., Ltd. Graphene oxide was purchased from Beijing Innochem Science Technology Co., Ltd. High-purity CH_4 (99.99%), CO_2 (99.99%) were used in experiments, which were provided by Yantai Deyi Gas Co., Ltd. Deionized water was produced in the laboratory.

The MIL-101(Cr)/GO composites were synthesized by hydrothermal synthesis, synthesis steps reference [9, 10]. The MIL-101/GO composites were synthesized with different GO mass ratios (1%, 2.5%, 5%, 10%, and 15%) of $Cr(NO_3)_3{\cdot}9H_2O$, which were recorded as MIL-101(Cr)/1GO, MIL-101(Cr)/2.5GO, MIL-101(Cr)/5GO, MIL-101(Cr)/10GO, MIL-101(Cr)/15GO.

2.2 Experimental Setup

Schematic illustration of the experimental setup was shown in Fig. 1.

The main experimental steps are as follows: First, MIL-101(Cr) and MIL-101(Cr)/GO composites were degassed at 493K for 6 h to remove any adsorbed species. Second, Checking the airtightness of the set up by through gas of He. Then, temperature is cooled to experimental required by water bath and CH_4 flow into adsorption tank. As the same time, the change of pressure was recorded by the data acquisition system every seconds. Finally, system reached equilibrium when the pressure of adsorption tank no change. The number of mole of methane consumption at any given time was calculated using a modified ideal gas equation [11].

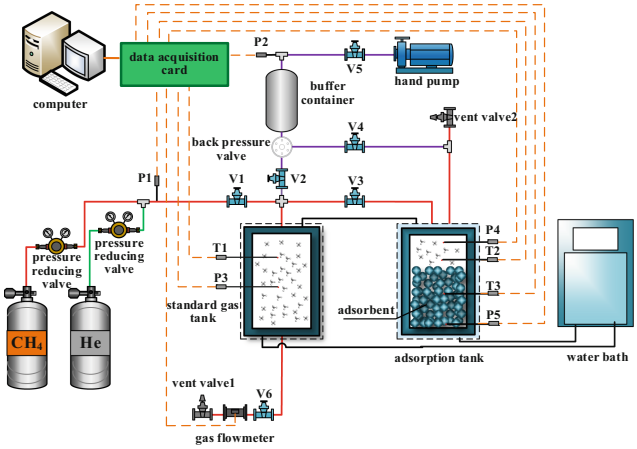

Fig. 1. Schematic of the experimental setup

3 Results and Discussion

3.1 Structural Characterizations

The XRD patterns of the MIL-101(Cr) and MIL-101(Cr)/GO composites are shown in Fig. 2. As shown in Fig. 2 (1GO to10GO), the major diffraction patterns of MIL-101(Cr)/GO composites are consistent with MIL-101(Cr), which indicates that the presence of GO does not prevent the development of bonds between chromic nitrate and terephthalic acid and MIL-101(Cr)/GO composites were synthesized successfully [8]. However, the major diffraction patterns of MIL-101(Cr)/15GO composite is not a good match with MIL-101(Cr), which indicates that high content of GO prevent the structure of MIL-101(Cr) growth. In addition, the major peak of MIL-101(Cr)/5GO, MIL-101(Cr)/7.5GO, MIL-101(Cr)/10GO composites show lower intensity than MIL-101(Cr), which demonstrate the introduce of GO embedded in the pores of MIL-101(Cr), but the remaining main structure is still MIL-101(Cr).

3.2 The Experiment of CH_4 Storage on MIL-101(Cr) and MIL-101(Cr)/GO Composites

The adsorption experiments of CH_4 on MIL-101(Cr) and MIL-101(Cr)/GO composites with different *Rw* at 275 K and pressure from 0 to 8.5 MPa. *Rw* represents that the mass of water to mass of materials. When the water content is $Rw = 1$ on MIL-101(Cr), it is suitable for CH_4 storage [12]. The results are shown in Fig. 3. It can be seen from Fig. 3(a) that the adsorption capacity of MIL-101(Cr)/GO composites to CH_4 is higher than that of MIL-101(Cr) to CH_4. This is due to the addition of GO that increases the atomic density and enhances the dispersion force of MIL-101(Cr), thereby increasing the adsorption capacity of CH_4 [13]. The adsorption capacity of CH_4 on MIL-101(Cr)/2.5GO reached 27.39 mmol/g (0.44 g/g) and close to the standard of DOE.

The adsorption and hydration coupling experiments of CH_4 on MIL-101(Cr) and MIL-101(Cr)/GO composites with $Rw = 1.0$ at 275 K, 0–8.5 MPa. Compared with

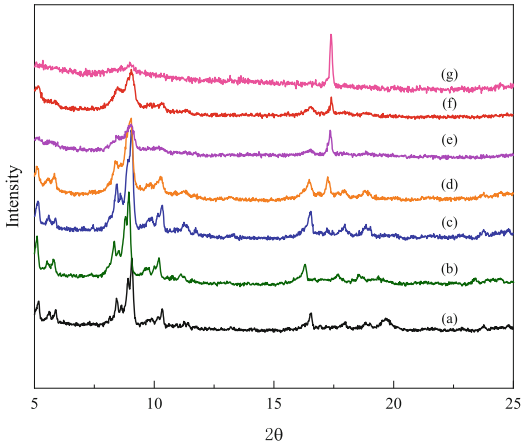

Fig. 2. XRD patterns of materials, (a) MIL-101(Cr); (b) MIL-101(Cr)/1.0GO; (c) MIL-101(Cr)/2.5GO; (d) MIL-101(Cr)/5.0GO; (e) MIL-101(Cr)/7.5GO; (f) MIL-101(Cr)/10GO; (g) MIL-101(Cr)/15GO.

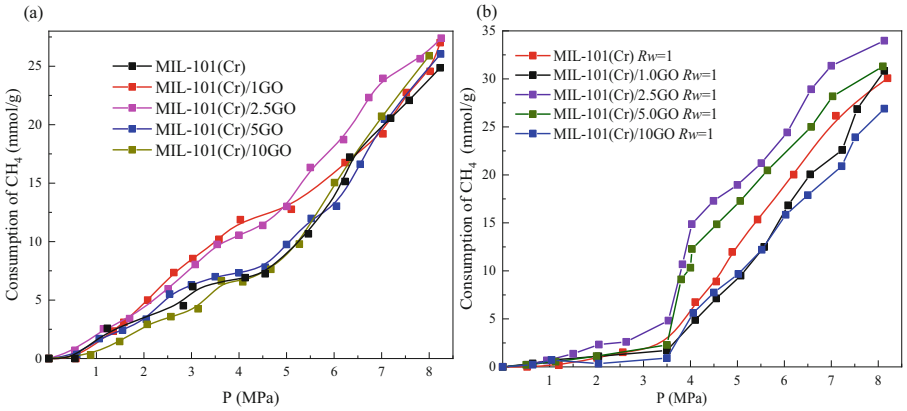

Fig. 3. Consumption of CH_4 at 275 K, (a) adsorption capacity of materials with $Rw = 0$; (b) adsorption capacity of materials with $Rw = 1$.

Fig. 3(a), the Fig. 3(b) shows that the adsorption hydration coupling capacity of CH_4 on MIL-101(Cr) and MIL-101(Cr)/GO composites are higher than materials with $Rw = 0$, which suggested that CH_4 hydrate form under this condition. Especially, the adsorption hydration coupling capacity of CH_4 in MIL-101(Cr)/2.5GO composites reaches 33.98 mmol/g (0.54 g/g), over the standard of DOE (0.5 g/g). In addition, the adsorption capacity of CH_4 on wet materials is lower than dry materials under the pressure of 0–3.5 MPa, this result is obtained that MIL-101(Cr) is a kind of typical hydrophilic material. Water would occupy the adsorption sites of the CH_4 gas, and no CH_4 hydrate is formed. Interestingly, consumption of CH_4 increases sharply over 3.5 MPa, suggesting that CH_4 hydrate begin to form, and the picture in Fig. 4 confirmed that CH_4 hydrate formation

in MIL-101(Cr)/2.5GO composites. CH_4 forms a hydrate membrane on the surface of the materials.

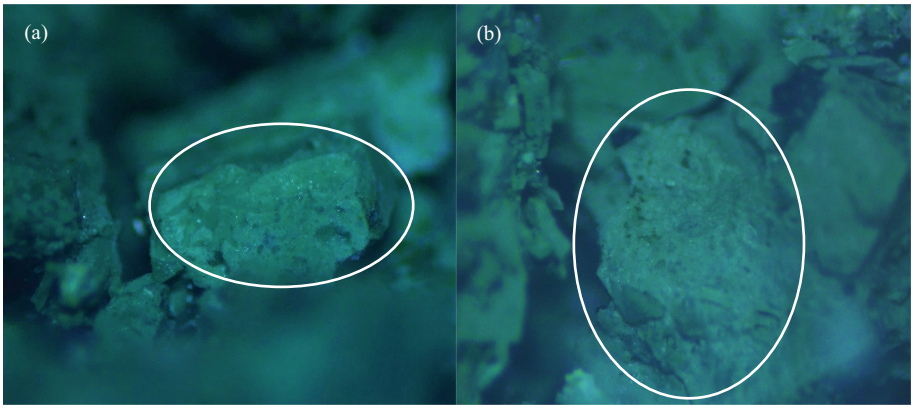

Fig. 4. Pictures of CH_4 hydrate on MIL-101(Cr)/2.5GO composites

4 Conclusion

In this study, a novel MIL-101(Cr)/GO composites were successfully synthesized by the hydrothermal method. The storage capacity toward CH_4 was testified by MIL-101(Cr) and MIL-101(Cr)/GO composites, the results shows that adsorption capacities of CH_4 on the MIL-101(Cr)/GO composites were higher than that on the MIL-101(Cr) owing to GO increases the dispersion force of MIL-101(Cr). Moreover, the consumption of CH_4 on MIL-101(Cr)/GO composites with $Rw = 1$ was higher than that on the MIL-101(Cr) with $Rw = 1$ due to CH_4 hydrate formation, up to 33.98 mmol/g (0.54 g/g). These findings suggest that adsorption and hydration coupling on MIL-101(Cr)/GO composites with high capacities of CH_4 are suitable for natural gas storage.

Acknowledgments. We acknowledge funding support from the project 52176028 supported by National Natural Science Foundation of China, the project ZR2019MEE005 supported by Shandong Provincial Natural Science Foundation, and the project 18CX02080A supported by the Fundamental Research Funds for the Central Universities.

References

1. Ma, S., Zhou, H.C.: Gas storage in porous metal–organic frameworks for clean energy applications. Chem. Commun. **46**(1), 44–53 (2010). https://doi.org/10.1039/b916295j
2. Yang, M., An, Q., Ding, T., Yin, P., Liang, L.: Carbon emission allocation in China based on gradually efficiency improvement and emission reduction planning principle. Ann. Oper. Res. **278**(1–2), 123–139 (2017). https://doi.org/10.1007/s10479-017-2682-1

3. DOE MOVE program at: methane opportunities for vehicular energy, Advanced Research Project Agency-Energy, U.S. Department of Energy, Funding opportunity No. DE-FOA-0000672 (2012)
4. Casco, M.E., et al.: Methane hydrate formation in confined nanospace can surpass nature. Nat. Commun. **6**, 6432–6439 (2015). https://doi.org/10.1038/ncomms7432
5. Zhou, L., Liu, J., Su, W., Sun, Y., Zhou, Y.: Progress in studies of natural gas storage with wet adsorbents. Energy Fuels **24**, 3789–3795 (2010). https://doi.org/10.1021/ef100315t
6. Llewellyn, L.P., et al.: High uptakes of CO_2 and CH_4 in mesoporous metalorganic frameworks MIL-100 and MIL-101. Langmuir **24**(14), 7245–7250 (2008). https://doi.org/10.1021/la800227x
7. Ertl, G.: Handbook of Heterogeneous Catalysis. VCH (2008). https://doi.org/10.1002/9783527610044.hetcat0147
8. Petit, C., Bandosz, T.J.: Exploring the coordination chemistry of MOF–graphite oxide composites and their applications as adsorbents. Dalton Trans. **41**(14), 4027 (2012). https://doi.org/10.1039/c2dt12017h
9. Song, N., et al.: Doping MIL-101(Cr)@GO in polyamide nanocomposite membranes with improved water flux. Desalination **492**, 114601 (2020). https://doi.org/10.1016/j.desal.2020.114601
10. Petit, C., Bandosz, T.J.: MOF-graphite oxide composites: combining the uniqueness of graphene layers and metal-organic frameworks. Adv. Mater. **21**(46), 4753–4757 (2009). https://doi.org/10.1002/adma.20090158
11. Hpv, A., Rk, B., Pl, A.: Hydrogen storage in clathrate hydrates: current state of the art and future directions. Appl. Energy **122**, 112–132 (2014). https://doi.org/10.1016/j.apenergy.2014.01.063
12. Chen, S.J., Wang, Y.F., Fu, Y., Liu, Y.Q., Wang. Z.Y.: Study on methane storage characteristics in MIL-101 (Cr) based on adsorption-hydration. J. Liaoning Univ. Petrol. Chem. Technol. (2020). https://doi.org/10.3969/j.issn.1672-6952.2020.04.013
13. Zhou, X., et al.: Enhanced separation performance of a novel composite material gro@mil-101 for CO_2/CH_4 binary mixture. Chem. Eng. J. **266**, 339–344 (2015). https://doi.org/10.1016/j.cej.2014.12.021

The Formation of CH_4 Hydrate in the Slit Nanopore of the Mesoporous MCM-41 by Molecular Dynamics Simulation

Jianlin Pei[1], Shujun Chen[1,2,3(✉)], Zhiqiang Zhang[1], and Xinyu Jiang[1]

[1] College of Pipeline and Civil Engineering, China University of Petroleum (East China), Qingdao 266580, China
shujunchenfu@126.com

[2] Qingdao Engineering Research Center of Efficient and Clean Utilization of Fossil Energy, Qingdao 266580, China

[3] Shandong Key Laboratory of Oil and Gas Storage and Transport Safety, Qingdao 266580, China

Abstract. Methane storage in water-bearing porous media is a new type of methane storage method with high reserves and mild storage conditions. However, the molecular mechanism of aqueous methane storage in porous media is still unclear. In this paper, molecular dynamics simulation (MD) was used to study the growth process of hydrate on the surface and in the channels of mesoporous molecular sieve MCM-41. Its microstructure, growth process and density distribution were analyzed. The results show that water molecules grow preferentially outside the pore, and hydrate continues to grow along the pore center after saturation. The density of methane molecules fluctuates during hydrate growth. When hydrate growth is complete, the density distribution of methane tends to be average. The results are expected to explain the microscopic mechanism of hydrate formation in porous materials with mesoporous pores.

Keywords: Hydrate · Methane storage · Density distribution

1 Introduction

Natural gas is a cleaner fuel than coal and oil, and its proportion in the energy consumption structure is increasing at present [1]. In the future, with the continuous development of international natural gas trade, natural gas storage and transportation technology is an important link in the continuous expansion of natural gas application scale. In recent years, some scholars have proposed the method of using water-bearing porous media to store methane [2]. The storage density of methane can be greatly increased with the formation of methane hydrate. The main reason is that porous materials can change the space of methane hydrate formation, increase the gas-liquid contact area between methane and water, shorten the induction time of hydrate formation, and thus affect the formation characteristics of methane hydrate [3].

B. Sun et al. (Eds.): DWOG-Hyd 2021, LNCE 246, pp. 377–383, 2022.
https://doi.org/10.1007/978-981-19-0960-3_37

Ordered MCM-41 have been widely used in the research of methane storage in water-bearing porous materials due to their high specific surface area and uniform pore size. LiZhou [4] studied the adsorption characteristics of methane stored by water-bearing ordered mesoporous material. By analyzing the relationship between pressure change and temperature during methane adsorption, it is concluded that the formation of hydrate in material pore is the main reason for the increase of methane storage density. LiZhou [5] measured the methane adsorption isotherm of MCM-41 material in the process of wet methane storage, and found that MCM-41 material can reach the maximum reserves in the system at 4MPa, so it has the potential as a wet methane storage material.

MD simulation, as a molecular scale computing tool, has been applied to study the crystallization mechanism of gas hydrate. He [6] used MD simulation to study the formation process of hydrate in mil-101 mesoporous material, and found that water molecules would have a certain adsorption effect on nearby methane molecules in the process of cage formation. Haoqing Ji [7] simulated the formation of hydrate on the surface of silica skeleton, and found that the water structure on the surface of silica is similar to ice, and the hydroxyl group on the surface of silica can promote the growth of hydrate. In this paper, MD simulation method was used to study the growth process of methane hydrate in MCM-41 material and methane aqueous solution. The change of the number of cages and the evolution of the density distribution of water and methane during hydrate growth are reported. The effect of MCM-41 mesoporous material on hydrate growth is discussed.

2 Model and Simulation Method

Specific atoms were first deleted from the amorphous SiO_2 skeleton to build the initial configuration of MCM-41 material [8]. The final initial configuration consists of a 42 Å $\times$ 42 Å $\times$ 22 Å region of MCM-41 with another region of pure water of the same size. The pure water area consists of water molecules and dissolved methane molecules with a density of 0.97 g/cm^3 [9]. The pore area of the MCM-41 material is also filled with a mixture of methane and water molecules of the same density as the pure water system.The whole system contains 1763 water molecules and 232 methane molecules, and the overall density is 1.25 g/cm^3.

All MD simulations were calculated using Lammps software. H_2O molecules and CH_4 molecules are modeled using the TIP4P/ice H_2O model [10] and the optimized potentials for liquid Debris all-Atom (OPLS-AA) Force Field [11]. The simulation parameters of MCM-41 materials are derived from the research literature [12]. The Lorentz-Berthelot combination rule is used to calculate the Lennard-Jones potential parameters between different atomic types for all atoms. The van der Waals force was calculated with A truncation radius of 8.5 Å, and the long distance electrostatic interactions were calculated using the Ewald summation method. Periodic boundary conditions are set along three directions. The NPT simulation is carried out at 270 K and 10 Mpa. The time step is set to 2fs, and the simulation time was 400 ns.

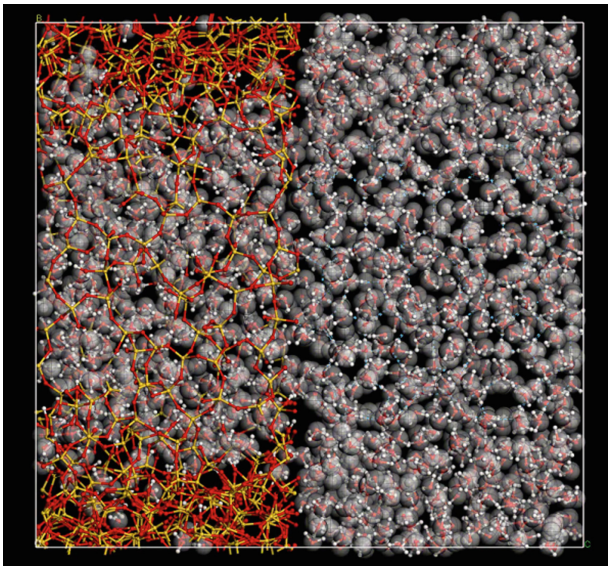

Fig. 1. Molecular configuration at the initial simulation, The red and yellow skeleton material is MCM-41, the water molecule is represented by the red bat model, and the methane molecule is represented by the gray ball.

3 Results and Discussion

3.1 Hydrate Evolution in Different Regions of Confined Space

The MCM-41 material and the methane water layer outside the hole are simulated. Figure 2 shows the change of the number of hydrate cages in the system with time. In 0–400 ns, 5^{12} and $5^{12}6^2$ cages as a whole showed a continuous growth at first, and then reached a balanced trend, and the growth rate gradually decreased. The number of $5^{12}6^2$ cages was significantly higher than 5^{12} cages, and the number of $5^{12}6^2$ cages stopped growing at 125 ns, while the number of $5^{12}6^2$ cages increased to about 250 ns. Figure 3 shows a snapshot of the hydrate cage growth of the simulation system at different simulation times. As can be seen from the figure, the hydrate first grows along the surface of the MCM-41 material in the mixed solution of methane and water on the right. At the time of 100ns, the hydrate cage has occupied most of the space outside the hole, which corresponds to 100–150 ns in Fig. 2. At this time, the hydrate in the MCM-41 hole has not yet been formed, while the hydrate outside the hole has reached its limit along the x-y axis, and the number of 5^{12} cages and $5^{12}6^2$ cages is stable around a value.

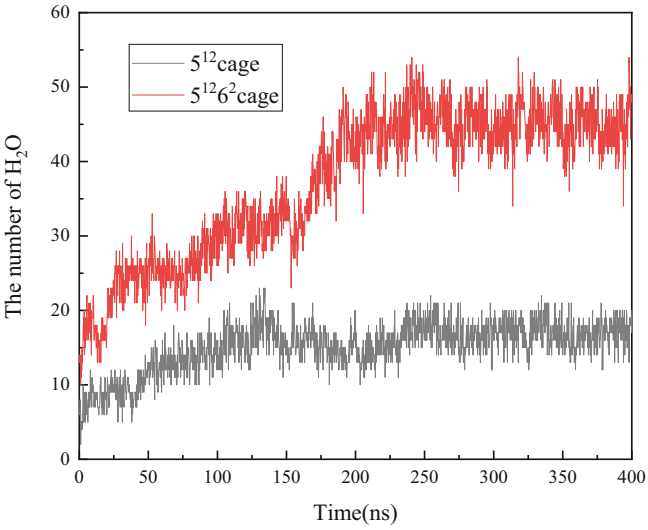

Fig. 2. The variation curve of hydrate cage with simulated time

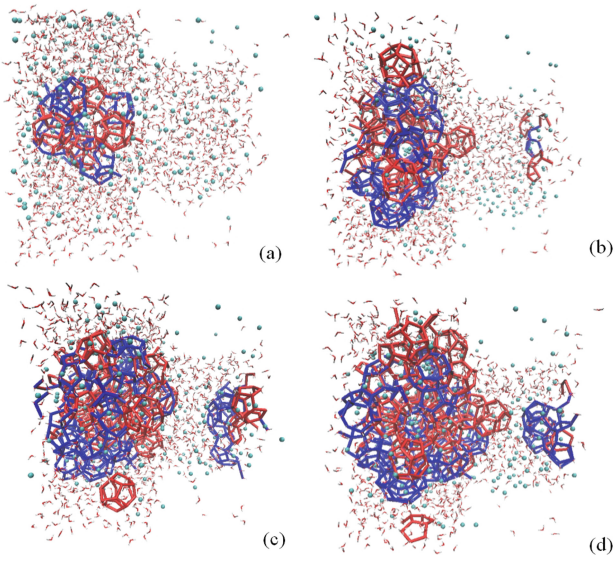

Fig. 3. Snapshots of methane hydrate growth at different simulated times, blue stick indicates $5^{12}6^2$ cage, red stick indicates 5^{12} cage. (a) 0 ns; (b) 100 ns; (c) 300 ns; (d) 400 ns.

When the simulation time is between 150–250 ns, it can be seen from Fig. 2 that 5^{12} cages stop growing, but $5^{12}6^2$ cages begin to grow rapidly during this time. Comparing Fig. 3(c) with Fig. 3(b), it can be found that the hydrate clusters outside the hole begin to grow along the Z-axis. As the hydrate continues to approach along the Z-axis of the MCM-41 material, the hydrate begins to appear in the pores of the MCM-41 material. It

is worth noting that the hydrate cage first appears in the center of the MCM-41 regular cylindrical cavity and is always about 1nm from the inner surface of the MCM-41 hole. KefengYan [9] carried out a similar simulation in the two-dimensional confined SiO^2 skeleton, and found that the hydroxyl groups on the surface of SiO_2 can form a stable half-cage structure with water molecules in the pores and methane molecules adsorbed by the material surface. Like the hydrate cages in the water system, these half-cage structures can exist stably in a certain simulation time. It can be proved that for mesoporous materials, the characteristics of hydrophilic surface can promote the storage of methane in the pore to a certain extent compared with other properties.

Figure 4 shows the change of CH_4 solubility with time in each region during the simulation process. Ring1 is the region along the MCM-41 columnar channel along the hole wall, and ring2 is the central region in the MCM-41 channel except the ring1 region. Free is the methane aqueous solution system on the right side of MCM-41. At 0–100 ns, with the growth of methane hydrate in the methane aqueous solution system, the hydrate growth occupies a large amount of volume, the methane in the aqueous solution system begins to migrate to the MCM-41 pore, and the methane solubility near the MCM-41 surface increases rapidly. At 100–250 ns, the hydrate begins to grow in the pores of MCM-41 materials, and the methane molecules adsorbed on the MCM-41 surface begin to migrate to the center of the pores. Because the potential energy of methane molecules enriched on the solid surface is larger than that of methane molecules in aqueous solution [46] , the methane molecules adsorbed into the MCM-41 pore surface by diffusion begin the equilibrium diffusion in the pore at this stage. Comparing Fig. 2 with Fig. 4, it can be found that the diffusion of methane in the MCM-41 hole corresponds to the process of hydrate growth into the MCM-41 hole.

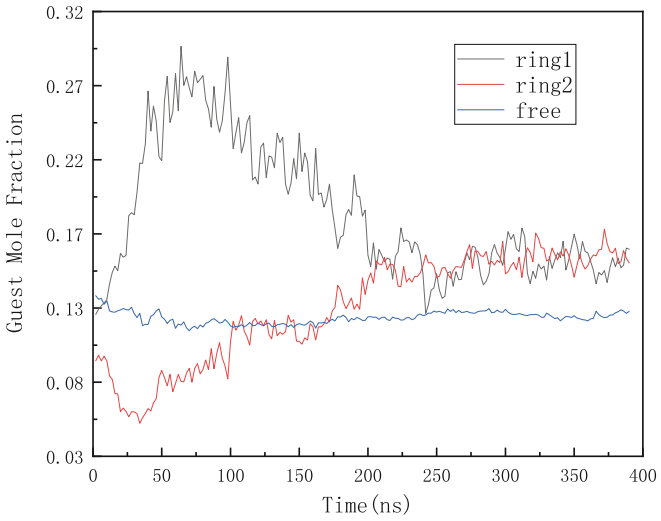

Fig. 4. Variation of CH_4 solubility in each region with time during simulation

3.2 Density Distribution Change of CH_4 and H_2O

Figure 3(a) calculates the evolution of methane quantitative density along the Z-axis.It can be seen that the density distribution of methane molecules in the material hole is slightly lower than that outside the hole. However, it should be made clear that the density of methane molecules in the pore is significantly higher than that outside the pore at the same free volume because the MCM-41 material occupies a certain space, which proves that MCM-41 has a certain adsorption effect on methane molecules. Methane molecules preferentially enter the pore and are adsorbed on the surface of MCM-41. In addition, it can be clearly seen from the figure that the density of methane fluctuates greatly during the rapid growth stage of hydrate (50 ns and 150 ns). Due to the rapid growth of hydrate, the hydrate cage shows stronger adsorption effect on methane compared with the interaction between methane molecules, resulting in regular fluctuations in the density distribution of methane molecules.

Figure 3 (b) calculates the numerical density evolution of water molecules along the Z-axis. Different from methane, there is an obvious density difference between water molecules inside and outside the MCM-41 hole, mainly because the MCM-41 material itself occupies a large amount of free volume, resulting in the relative quantitative density of water molecules is lower than that of the out-of-hole aqueous solution system. After 150 ns, that is, after the hydrate growth of the out-of-hole aqueous solution system is saturated, there is a dense water layer near the surface of the MCM-41 material (Fig. 5).

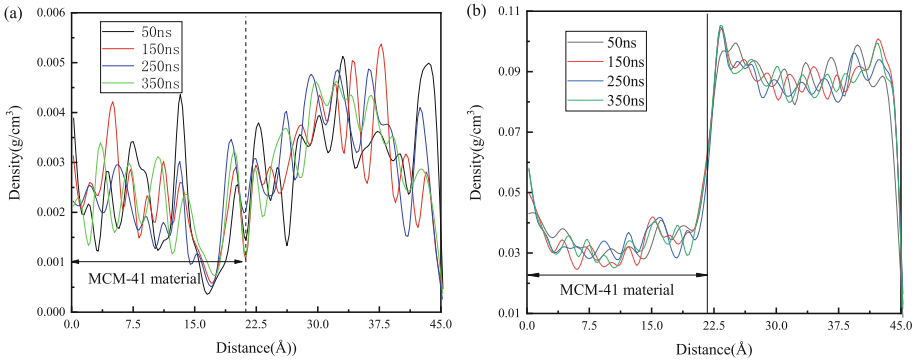

Fig. 5. Evolution of molecular density distribution of methane and water (a) CH_4, (b) H_2O

4 Conclusion

In this paper, the growth process of hydrate in hydrophilic mesoporous material MCM-41 was studied by MD simulation. The results show that hydrate first grows in methane aqueous solution outside the hole. At the same time, this process is accompanied by the migration of methane molecules from outside the hole to the surface of MCM-41 in the hole. After 150 ns, the hydrate began to grow from the center of MCM-41 hole cavity into the hole as the hydrate growth reached saturation state outside the hole. With

the growth of hydrate in the pore, methane molecules migrate to the pore center from the initial adsorption to the inner surface of MCM-41. Finally, the density distribution evolution of water and methane molecules in the simulated system is analyzed. It is found that the growth process of hydrate is accompanied by the drastic fluctuation of methane molecular density. After hydrate growth, the density distribution of methane molecules tends to be average.

Acknowledgements. We acknowledge funding support from the project 52176028 supported by National Natural Science Foundation of China, the project ZR2019MEE005 supported by Shandong Provincial Natural Science Foundation, and the project 18CX02080A supported by the Fundamental Research Funds for the Central Universities.

References

1. Kumar, K.V., Preuss, K., Titirici, M.M., Rodríguez-Reinoso, F.: Nanoporous materials for the onboard storage of natural gas. Chem. Rev. **117**(3), 1796–1825 (2017). https://doi.org/10.1021/acs.chemrev.6b00505
2. Cuadrado-Collados, C., Fauth, F., Such-Basanez, I., Martinez-Escandell, M., Silvestre-Albero, J.: Methane hydrate formation in the confined nanospace of activated carbons in seawater environment. Microporous Mesoporous Mater. **255**, 220–225 (2018). https://doi.org/10.1016/j.micromeso.2017.07.047
3. Borchardt, L., Nickel, W., Casco, M., Senkovska, I., Silvestre-Albero, J.: Illuminating solid gas storage in confined spaces–methane hydrate formation in porous model carbons. Phys. Chem. Chem. Phys. **18**(30), 20607–20614 (2016). https://doi.org/10.1039/c6cp03993f
4. Zhou, L., Liu, X., Sun, Y., Li, J., Zhou, Y.: Methane sorption in ordered mesoporous silica sba-15 in the presence of water. J. Phys. Chem. B **109**(48), 22710–22714 (2005). https://doi.org/10.1021/jp0546002
5. Zhou, L., Liu, J., Su, W., Sun, Y., Zhou, Y.: Progress in studies of natural gas storage with wet adsorbents. Energy Fuels **24**(7), 3789–3795 (2010). https://doi.org/10.1021/ef100315t
6. He, Z., Gupta, K.M., Linga, P., Jiang, J.: Molecular insights into the nucleation and growth of CH4 and CO2 mixed hydrates from microsecond simulations. J. Phys. Chem. C. **120**(44), 25225–25236 (2016). https://doi.org/10.1021/acs.jpcc.6b07780
7. Haoqing, J., et al.: Microsecond molecular dynamics simulation of methane hydrate formation in humic-acid-amended sodium montmorillonite. Energy Fuels **30**(9), 7206–7213 (2016). https://doi.org/10.1021/acs.energyfuels.6b01544
8. Sonwane, C.G., Jones, C.W., Ludovice, P.J.: A model for the structure of mcm-41 incorporating surface roughness. J. Phys. Chem. B **109**(49), 23395–23404 (2005). https://doi.org/10.1021/jp051713c
9. Yan, K., Li, X., Chen, Z., Xu, C., Zhang, Y., Xia, Z.: The formation of ch4 hydrate in the slit nanopore between the smectite basal surfaces by molecular dynamics simulation. Energy Fuels **32**(6), 6467–6467 (2018). https://doi.org/10.1021/acs.energyfuels.8b00195
10. Pascal, T.A., Goddard, W.A.: Interfacial thermodynamics of water and six other liquid solvents. J. Phys. Chem. B **118**(22), 5943–5956 (2014). https://doi.org/10.1021/jp410861h
11. Jorgensen, W.L., Maxwell, D.S.: Development and testing of the OPLS all-atom force field on conformational energetics and properties of organic liquids. J. Am. Chem. Soc. **118**(45), 11225 (1996). https://doi.org/10.1021/ja9621760
12. Williams, J.J., Seaton, N.A., Du Ren, T.: Influence of surface groups on the diffusion of gases in MCM-41: a molecular dynamics study. J. Phys. Chem. C **115**(21), 10651–10660 (2011). https://doi.org/10.1021/jp112073z

Experimental Study on Thermodynamics and Kinetics of Hydrate Formation in TBAB-CO_2-N_2-H_2O System

Haotian Wang[1], Yuxiang Xia[1], Pengcheng Jing[1], Jiakai Ji[1], Ying Wu[1], Changhong Yu[1], and Litao Chen[1,2(✉)]

[1] Petroleum Engineering College, China University of Petroleum (East China), Qingdao 266580, China
chenlt@upc.edu.cn

[2] Key Laboratory of Unconventional Oil and Gas Development, Ministry of Education, China University of Petroleum (East China), Qingdao 266580, China

Abstract. In order to separate CO_2 from power plant flue gas using tetra-butylammonium bromide hydrate, the thermodynamics and kinetics of hydrate formation from CO_2-N_2 gas mixture at lower TBAB concentration and mild temperature-pressure conditions are investigated in this paper. The experiments were carried out using the isovolumetric stepwise warming method with TBAB concentrations of 0.2 mol%, 0.4 mol%, 0.5 mol%, gas-liquid volume ratio of 0.25, and experimental temperatures does not exceed 7 MPa. It was found that there should be an optimal TBAB concentration to make the hydrate formation process relatively mild and the induction time short. When the TBAB concentration is 0.2 mol%, the hydrate formation is low and the induction time is long, so the TBAB concentration below 0.2 mol% is not suitable for the gas separation process. Therefore, we need to consider both thermodynamic and kinetic aspects of hydrate formation to develop a set of the most suitable TBAB concentration, temperature and pressure scheme applied to the gas separation process.

Keywords: Tetra-butylammonium bromide · CO_2-N_2 mixed gas · Induction time

1 Introduction

The widespread use of fossil energy has brought rapid development to industry, but it has also led to the emission of large amounts of greenhouse gases, causing environmental problems such as global warming, and controlling and reducing CO_2 emissions will become a key issue that we need to address now. Therefore, the development of technologies related to the enrichment, separation and recovery of CO_2 has become an urgent task, and it is of great significance for the energy saving and emission reduction of our industry, especially the petrochemical and energy industries [1].

Hydrates are non-stoichiometric caged compounds in which water molecules are held together by hydrogen bonding at low temperature and high pressure and in which

B. Sun et al. (Eds.): DWOG-Hyd 2021, LNCE 246, pp. 384–391, 2022.
https://doi.org/10.1007/978-981-19-0960-3_38

gas molecules are enveloped. Hydrates have a considerable gas storage capacity and the ability to control the operating conditions to allow the desired gas molecules to enter the hydrate. Thus, hydrates show great potential in the field of gas separation. However, hydrate formation conditions are harsh under conditions without any additives, and the realization of high pressure and low temperature accounts for more than half of the energy consumption during gas separation operations. In order to reduce the hydrate formation conditions and energy consumption, many scholars have conducted extensive studies on hydrate promoters. Zhang et al. [2] experimentally investigated, the effect of synergistic interaction of 5.56 mol% tetrahydrofuran and levotryptophan and leucine on hydrate formation from coalbed methane (30% CH_4/70% N_2). Some other authors have also investigated the aspect of surfactants for promoting hydrate. P. Gayet et al. [3] found that some surfactants increase the rate of hydrate formation and the amount of water conversion for hydrate formation without changing the hydrate equilibrium conditions. Zhong et al. [4] studied the effect of surfactants in pure water solution, THF solution and THF/SDS solution on simulated shale gas (CO_2/CH_4) to separate CO_2. It was found that the addition of THF and SDS promoters significantly improved the kinetics of hydrate formation. However, tetrahydrofuran is not only volatile, but also toxic. Therefore, tetrahydrofuran has a major disadvantage as a hydrate promoter applied in industry.

However, some scholars have found that when quaternary ammonium salts are present, the anions of quaternary ammonium salts form hydrogen bonds with water molecules together to form the cage of the hydrate, and the cations of quaternary ammonium salts occupy the large pores of the hydrate and the gas molecules occupy the small pores of the hydrate, which is generally referred to as a semi-clathrate. Quaternary ammonium hydrates are currently used in a large number of applications in the field of hydrate promotion due to their very simple generation conditions. Youssef et al. [5] concluded that tetrabutylammonium bromide hydrates have the advantages of stability, small supercooling and the ability to undergo phase transitions under moderate thermodynamic conditions. Therefore, the application of TBAB hydrate is considered to have a very high potential in the field of gas separation. Hiroyuki Komatsu et al. [6] determined the conditions of hydrate formation in a CO_2-N_2 mixture with a CO_2 molar concentration of 20% in a system in the presence of TBAB. Gupta Pawan et al. [7] determined the hydrate formation in a system with a mass fraction of 5 wt% and 10 wt% of TMAB, TEAB, and TBAB conditions for phase stability experiments of methane hydrate. The gas consumption increased with increasing alkyl carbon chain length of the quaternary ammonium salt and decreased with increasing salt concentration. Lu Tao et al. [8] determined the equilibrium hydrate formation pressure of CO_2-N_2-TBAB and CO_2-N_2-THF systems using isothermal pressure search method. The experiments were conducted in the pressure range of 0.69–14.55 MPa and temperature range of 275.75∼288.15 K. The results showed that both TBAB and THF can be used as additives to effectively reduce the equilibrium formation pressure of gas hydrates. At lower agent concentrations, the equilibrium hydrate formation pressure of CO_2-N_2-TBAB was lower than that of CO_2-N_2-THF system. Sfaxi et al. [9] investigated the phase equilibrium conditions of $CO_2 + N_2$ hydrate in aqueous TBAB solution. Sfaxi concluded that TBAB promoter has

a rather strong thermodynamic promotion effect compared to other conventional thermodynamic promoters. Moreover, the substance is not volatile and has great advantages in the field of gas separation. Yang et al. [10] conducted experiments on the generation of mixed gas ($CH_4 + C_2H6 + C_2H_4 + CO_2 + H_2$) hydrates at TBAB concentrations of 5 wt% and 10 wt%. It was found that there was an inflection point in the phase equilibrium curve of the gas mixture and TBAB system, and TBAB played an inhibitory role when the temperature was greater than this inflection point. Therefore, a medium temperature-pressure range was used for the experiments in this paper. Zhou et al. [11] considered that understanding the crystal properties of semi-cage hydrates is essential for gas separation applications and investigated the phase equilibrium and crystal properties of TBAB-CO_2 hydrates. It was found that the presence of TBAB makes the equilibrium pressure of the hydrate more sensitive to the response of temperature. Pure CO_2 hydrate and TBAB-CO_2 hydrate are a coexisting state when the TBAB concentration is below 20 wt%. Joshi et al. [12] investigated the conditions for the formation of TBAB-CO_2 hydrate at concentrations of 5 wt%, 10 wt% and 15 wt%. It was found that the higher the TBAB concentration, the shorter the time required for hydrate nucleation.

Firstly, most of the current studies only go to the determination of the phase equilibrium conditions of hydrates simply by using integer values of TBAB concentrations, while there are fewer experimental data for the phase equilibrium conditions of TBAB hydrates in the finer concentration range. Secondly, the CO_2 content in the flue gas of power plants is relatively low, generally accounting for about 15% of the total gas, which has a significant impact on the hydrate formation conditions. At present, there are few data on the hydrate formation conditions of CO_2-N_2-TBAB-H_2O system with low CO_2 concentration, so this paper conducts hydrate formation conditions measurement experiments for the main gas composition of power plant flue gas to provide data support for the study of CO_2 capture in flue gas by hydrate method.

2 Experimental Section

2.1 Experimental System

The composition of the experimental system is shown in Fig. 1. The system mainly consists of gas supply system, hydrate reaction system, temperature control system and data acquisition system, which can conduct the experiment of hydrate formation and decomposition in CO_2-N_2-TBAB-H_2O system with the maximum working pressure of 30 MPa and the working temperature range of −60 °C–50 °C. The hydrate reaction system mainly includes the high-pressure automatic stirring reactor, which is made of 316 stainless steel and consists of a stirring device and a reactor. The stirring speed of the stirring device is variable in the range of 0–1000 r/min. The effective volume of the reactor is 1000 mL. The inlet is connected to the gas supply line and the outlet is used for exhausting and evacuating, both of which are installed on the top of the reactor lid. A pressure sensor and a temperature sensor are also installed to record the temperature and pressure inside the reactor in real time. The working range of the pressure sensor is 0–16 MPa with accuracy ±0.01 MPa, and the temperature sensor is Pt1000 platinum resistance with accuracy ±0.05 °C. The reaction kettle is installed in a low-temperature

constant temperature water bath with a temperature range of −10 °C to 100 °C and a temperature control accuracy of ± 0.5/0.05 °C.

2.2 Experimental Materials

CO_2-N_2 mixture with CO_2 molar concentration of 15% (accuracy ± 0.01, Qingdao Xinkeyuan Gas Co., Ltd.), TBAB (purity 99.9%, Aladdin Chemical Reagent Co., Ltd.), and deionized water was obtained by laboratory ultrapure water mechanism.

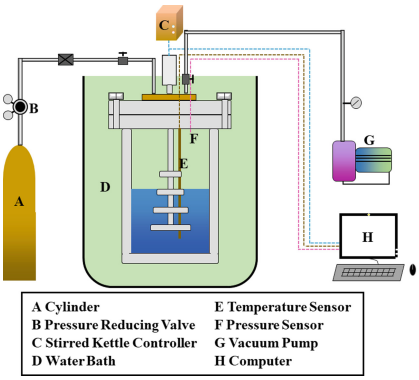

Fig. 1. Flow chart of the experimental setup

2.3 Experimental Steps

(1) Use deionized water to equip the TBAB solution with the required concentration for the experiment.
(2) Wash the reaction kettle 3 times using deionized water and dry it. Fill the equipped TBAB solution into the reaction kettle (V = 1000 mL) and seal the kettle.
(3) Turn on the low temperature thermostat water bath and set the temperature to 22 °C to keep the temperature in the reaction kettle constant.
(4) Connect the vacuum pump to the outlet of the reaction kettle and pump the vacuum.
(5) Inject CO_2-N_2 gas mixture from the inlet of the reaction kettle to a certain pressure, turn on the stirring device of the reaction kettle and set the speed to 1000 r/min to accelerate the dissolution of the gas.
(6) Check the gas tightness. Keeping the state of step (5) for 2 h. if the pressure remains unchanged, the reactor is well gas-tight.
(7) Turn off the stirring device, continue to inject CO_2-N_2 gas mixture to the specified pressure, turn on the stirring device and wait for the pressure to remain constant.
(8) Set the water bath temperature to 2 °C, as the temperature of the water bath decreases, the pressure inside the reaction kettle decreases with the temperature, when the temperature reaches the formation temperature of hydrate, the pressure inside the reaction kettle decreases rapidly, wait for more than 4 h, the pressure no longer decreases indicates that the gas inside the kettle no longer generates hydrate, and the formation experiment is finished.

The steps of the decomposition experiment are as follows:

After the end of hydrate formation, the temperature is gradually increased by 0.5°C each time, and after the temperature-time and pressure-time curves are stabilized, a set of temperature-pressure values are obtained, and the temperature is continued to be increased next time. According to the obtained temperature-pressure value points, the temperature-pressure curves of hydrate formation and decomposition process are drawn, and when the formation and decomposition curves intersect, the hydrate formation conditions of one experimental system are obtained, and the hydrate decomposition experiment is finished.

3 Experimental Results and Discussion

The hydrate formation conditions of the CO_2-N_2-TBAB-H_2O system under mild conditions were measured. The experimental results are shown in Table 1.

Table 1. Thermodynamic and kinetic conditions for hydrate formation in the CO_2-N_2-TBAB-H2O system

TBAB (mol%)	T/K	P/MPa	Induction time /min
0.5	283.45	2.60	46
	284.15	3.60	24
	284.35	4.02	–
	284.75	4.80	69
	285.65	5.91	24
TBAB (mol%)	T/K	P/MPa	Induction time/min
0.4	284.95	6.08	54
	284.55	5.07	57
	284.25	4.70	56
	283.75	4.25	21
	282.95	3.19	31
TBAB (mol%)	T/K	P/MPa	Induction time/min
0.2	281.95	5.61	237

It can be seen from Fig. 2 that the higher the TBAB concentration, the milder the conditions of CO_2-N_2 hydrate formation. However, the phase equilibrium conditions at the two TBAB concentrations do not differ much.

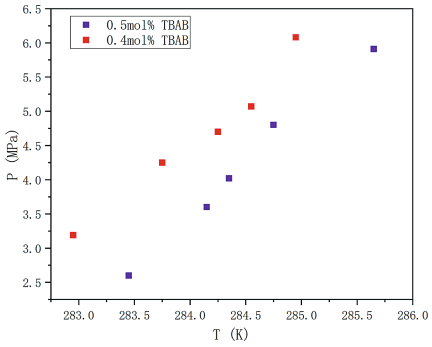

Fig. 2 Phase equilibrium point of CO_2-N_2 hydrate at TBAB concentration of 0.4 mol% and 0.5 mol%

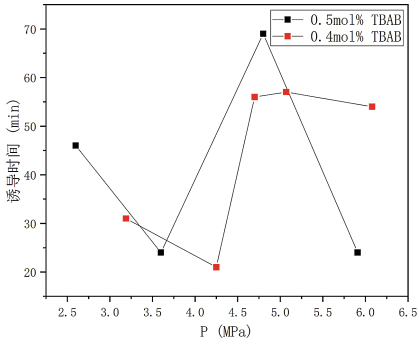

Fig. 3. Induction time of CO_2-N_2 hydrate formation with pressure for TBAB concentration of 0.4 mol% and 0.5 mol%

We define the induction time of hydrate formation in this paper as the difference between the time t2 for starting formation of hydrate and the time t1 corresponding to the phase equilibrium pressure of hydrate. It can be seen from Fig. 3 that the hydrate formation induction time of 0.4 mol% TBAB is generally shorter than that of 0.5 mol% TBAB. Therefore, we infer that it is not the higher TBAB concentration that results in shorter induction time for hydrate formation. We believe that there exists a suitable TBAB concentration that gives the shortest induction time for hydrate formation. Due to the lack of data points in this paper, a large number of experiments will be conducted in the next work to verify the idea.

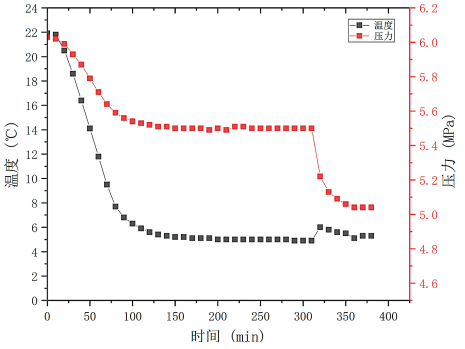

Fig. 4. Curve of CO_2-N_2 hydrate formation conditions with time for TBAB concentration of 0.2 mol%, initial temperature and pressure of 295.05 K and 5.03 MPa

It can be seen from Fig. 4 that the induction time of hydrate formation is 237 min when the TBAB concentration is 0.2 mol%. therefore, the CO_2-N_2 hydrate formation is very slow in the system of 0.2 mL% TBAB concentration at mild temperature and pressure conditions. This concentration can not be applied in gas separation processes based on hydrate methods.

4 Conclusion

In this paper, the thermodynamics and kinetics of hydrate formation from CO_2-N_2 gas mixture at lower TBAB concentration and mild temperature-pressure conditions are experimentally investigated. The experimental results show that although the higher the TBAB concentration, the lower the hydrate formation equilibrium pressure. However, the degree of influence of TBAB concentration on the phase equilibrium pressure is different in different concentration ranges. When the TBAB concentration is lower than 0.2 mol%, the process of CO_2-N_2 hydrate formation becomes very slow. Therefore, we need to consider both thermodynamic and kinetic aspects of hydrate formation to develop a set of most suitable TBAB concentration, temperature and pressure schemes to be applied in the gas separation process.

References

1. Ren, D., Li, Z., Ding, H.: Status and progress of membrane separation technology in water capture in flue gas. IOP Conf. Series: Earth Environ. Sci. **657**(1), 012112 (2021)
2. Qiang, Z., et al.: Coal mine gas separation of methane via clathrate hydrate process aided by tetrahydrofuran and amino acids. Appl. Energy **287**, 116576 (2021)
3. Zhou, X., et al.: Multiscale analysis of the hydrate based carbon capture from gas mixtures containing carbon dioxide. Sci. Rep. **11**(1), 1–9 (2021)
4. Zhong, D.L., et al.: Evaluation of CO2 removal from a CO2 + CH4 gas mixture using gas hydrate formation in liquid water and THF solutions. Appl. Energy **158**, 133–141 (2015)
5. Youssef, Z., Hanu, L., Kappels, T., et al.: Experimental study of single CO2 and mixed CO2+ TBAB hydrate formation and dissociation in oil-in-water emulsion. Int. J. Refrig. **46**, 207–218 (2014)

6. Komatsu, H., et al.: Separation processes for carbon dioxide capture with semi-clathrate hydrate slurry based on phase equilibria of CO2 + N2 + tetra-n-butylammonium bromide+water systems. Chem. Eng. Res. Design **150**, 289–298 (2019)
7. Gupta, P., Sangwai, J.S.: Semiclathrate hydrate of methane and quaternary ammonium salts for natural gas storage and gas separation. In: Offshore Technology Conference Asia (2018)
8. Lu, T., Zhang, Y., Li, S., et al.: Equilibrium generation conditions of hydrate in CO2-N2-TBAB and CO2-N2-THF systems. J. Process Eng. **9**(3), 541–544 (2009)
9. Sfaxi, I.B.A., Durand, I., Lugo, R., Mohammadi, A.H., Richon, D.: Hydrate phase equilibria of CO2 + N2 + aqueous solution of THF, TBAB or TBAF system. Int. J. Greenhouse Gas Control **26**, 185–192 (2014)
10. Yang, L.Y., et al.: Experimental and modeling study on the phase equilibria for hydrates of gas mixtures in TBAB solution. Chem. Eng. Sci. **137**, 656–664 (2015)
11. Zhou, X., et al.: Phase equilibria and the crystallographic properties of TBAB-CO2 semiclathrate hydrates. J. Chem. Eng. Data Acs J. Data **63**(5), 1249–1255 (2018)
12. Joshi, A., Sangwai, J.S.: Experimental investigations on the phase equilibrium of semiclathrate hydrates of carbon dioxide in TBAB with small amount of surfactant. Int. J. Energy Environ. Eng. **4**(1), 1–8 (2013)

Rapid Methane Hydrate Formation in Open-Cell Copper Foam

Jiajie Wang[1,2], Liang Yang[1,2(✉)], Xinxin Shao[1,2], and Hao Zhang[1,2]

[1] School of Energy and Power Engineering, University of Shanghai for Science and Technology, Shanghai 200093, China
lyang@usst.edu.cn

[2] Shanghai Key Laboratory of Multiphase Flow and Heat Transfer in Power Engineering, University of Shanghai for Science and Technology, Shanghai 200093, China

Abstract. Rapid methane hydrate formation with high gas storage capacity is very important for the application of natural gas hydrates technology. Three pieces of open-cell copper foam (CF) with different pore densities (or pores per inch, PPI) herein were immersed in sodium dodecyl sulfate (SDS) solution for enhancing methane storage in solid hydrate. The promotion effects of CF on the methane hydrate formation in the metal-embedded systems were investigated via an unstirred tank reactor. The results demonstrated that the surface of CF skeleton is covered with abundant micro holes and micro grooves, which can provide many metal nuclei for gas-water crystallization. The nest-like metal skeleton acts as crisscross "highway" for the crystallization heat transfer. Methane hydrate was quickly formed in the SDS/CF systems, but CF with the pore densities of 5 and 30 PPI was not favorable for conversion of more water to hydrate. Compared with these two composite systems, the SDS solution with the 15 PPI CF were able to store more methane at a faster formation rate. A theoretical model based highly porous two-phase systems was used to predict the effective thermal conductivity (*ETC*) of the metal foam filled with hydrate. It was found that the *ETC* of the hydrate/CF composite was significantly enhanced by employing CF matrix, and the low pore density CF had a more positive impact on improving the *ETC* of the composite. Further comparative experiments conducted at various pressures indicated that the solutions with 15 PPI CF exhibited higher methane storage capacities and larger hydration rates than the simple SDS solution, especially at the low pressure.

Keywords: Methane hydrate · Formation kinetics · Thermal conductivity · Copper foam

1 Introduction

As an environmentally friendly energy, natural gas can not only be used as urban gas and industrial fuel, but also an important chemical raw material. The premise of large-scale application of natural gas is the development of its efficient storage and transportation technology. Natural gas hydrates are ice-like crystalline compounds composed of water

B. Sun et al. (Eds.): DWOG-Hyd 2021, LNCE 246, pp. 392–399, 2022.
https://doi.org/10.1007/978-981-19-0960-3_39

and gas. The gas molecules (guests, e.g. methane, ethane, and propane) are trapped in water cavities (host) formed by hydrogen-bonded water molecules at low temperature and high pressure [1]. One volume of the solid hydrate can stably capture 160–180 standard volumes of gas that is equivalent to an energy density of a highly compressed gas [2]. The advantages of high stability and competent energy density make hydrate a new material for natural gas storage. However, industrial limitations of hydrate-based gas storage technology lie in the unsatisfactory practical formation rate and storage capacity.

The hydrate formation is essentially a phase change process of gas-liquid to solid, accompanied by a large amount of hydrate heat generated (e.g. 438.54 ± 13.78 kJ·kg^{-1} for methane hydrate) [3]. An efficient hydration process involves sufficient gas-liquid contact (mass transfer), rapid nucleation and growth (reaction) [4], and timely removal of hydrate heat (heat transfer) [5]. Therefore, many studies have focused on enhancing mass and heat transfer during the phase change of hydrate. Mechanical disturbances including stirring [6], rocking [7], spraying [8], and bubbling [9] have been employed to enhance the hydrate formation by increasing the gas-liquid contact. However, these methods were undoubtedly energy-intensive and high-cost in the practical applications.

In view of this, improving the effective thermal conductivity of the bulk water/solution is another new strategy for enhancing hydrate formation. Nanofluids with low concentration of suspended metal nanoparticles have been used for promoting the nucleation and growth of hydrate [10]. Similarly, it was also proved that some thermal conductive nonmetal particles [11, 12] suspended in solutions were favorable for reducing the induction time of nucleation. The presence of nanoparticles not only provided abundant nucleation sites, but also promoted the removal of hydrate heat. They found that the installation of the plate was very effective in transferring hydrate heat, and the induction time of nucleation was significantly reduced. Hu et al. [13] studied the effect of stainless steel mesh on methane hydrate formation. The study presented that the metal surface facilitated the reduction of induction time and increased the conversion of water to hydrate. However, the simple structures of metal tube, plate and mesh lead to small contact area between the solid hydrate and the installations. Moreover, they can only induce the hydrate heat to be transferred along one or two dimensions.

Recently, open-cell metal foam has attracted great attention in the field of heat transfer enhancement due to its continuous skeleton structure, large specific surface area and especially excellent thermal conductivity. Bhattacharya et al. [14] studied the effect of open-cell aluminum foam with high porosity on the thermal conductivity of water. They found that the effective thermal conductivity (*ETC*) of water/aluminum was 6 to 12 times higher than that of water. Therefore, it is reasonable to speculate that the porous metal foam may have an elevated effect on the thermal conductivity of gas hydrates.

Inspired by this, here, we attempted to immerse the open-cell copper foam (CF) with different pore densities in sodium dodecyl sulfate (SDS) solution for methane hydrate formation. The formation kinetics of methane hydrate in these composite systems of SDS/CF were investigated via an unstirred tank reactor under different experimental conditions. In addition, a theoretical model based highly porous two-phase systems proposed by Jagjiwanram and Singh [15] was applied to predict the *ETC* of methane hydrate in the CF with above porosities. In this model, methane hydrate was filled in the CF as a continuous phase.

2 Experimental Section

2.1 Materials

The open-cell copper foam with three kinds of pore densities (or pores per inch, PPI) were provided by the Shanghai Zhongwei New Material Co., Ltd. (China). The pore densities of CF used in this work are 5, 15, and 30 PPI. They all have nest-like metal skeleton, but different pore sizes, as presented in Fig. 1. Methane with a purity of 99.99% was purchased from Shanghai Weichuang Gas Co., Ltd. (China). Sodium dodecyl sulfate (SDS) with a certified purity of 99.5% was supplied by Shanghai Bio Science & Technology Co., Ltd. (China). The ultrapure deionized water with a resistivity of 18.3 mΩ·cm was made in the laboratory.

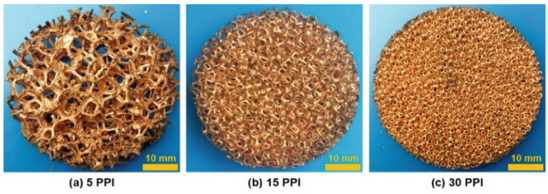

Fig. 1. The samples of open-cell copper foam with different pore densities

2.2 Procedure

In a closed high-pressure space, the formation behavior of gas hydrates can be investigated by monitoring the temperature and pressure changes of the system. The experimental apparatus was the same as that in our previous work [16]. An unstirred stainless steel vessel with effective volume of 300 cm^3 was used as hydration reactor. To conduct methane storage experiments, the vessel was first cleaned with deionized water, and then one piece of CF together with 20.00 g SDS solution (0.05 wt%) were loaded into it. Subsequently the reactor was immersed in a low-temperature thermostatic bath filled with coolant (95 vol% alcohol solution). After that, the air sealed in the reactor and pipe was pumped out via a vacuum pump, and the bath was turned on to cool the circulating alcohol solution. Two type Pt 100 thermal resistance detectors with an uncertainty of 0.01 K, fastened on the vessel cover were used for monitoring the temperature of gas phase and liquid phase. After the designated temperature (274.2 K) was maintained constantly for 5 min, the vessel was pressurized up to the desired pressure (8.0 MPa) with methane. A pressure gauge with an accuracy of 0.1 MPa was used for indicating the intake pressure. The pressure in the vessel was measured using a pressure transducer with the precision of 0.05 MPa. The data of time, temperature, and pressure were collected at steps of 10 s via a data logger that was connected to a computer. The behaviors of methane hydrate formation in the CF with the pore densities of 5, 15, and 30 PPI under above conditions were compared.

3 Experimental Results and Discussion

Enhancing the heat and mass transfer is an effective approach to increasing the formation rate and storage capacity of gas hydrates. Highly porous metal foam has been widely used to enhance the heat transfer in the phase transition process by increasing the effective thermal conductivity. Besides, its reticulate skeleton may contribute many crystal sites for the phase transition of gas-water to solid (e.g. gas hydrates nucleation). Therefore, a faster hydration is expected to occur in the system of SDS solution embedded with CF.

3.1 Effects of CF Pore Density on Methane Hydrate Formation

The CF samples with the pore densities of 5, 15, and 30 PPI employed in this study have different pore sizes and skeleton thicknesses, as shown in Fig. 1. It means that the specific surface areas of these samples are different, and possible crystal nucleation sites and heat transfer pathways provided by the porous metal vary in number. Therefore, the effect of CF pore density on the formation kinetics of methane hydrate is worth studying.

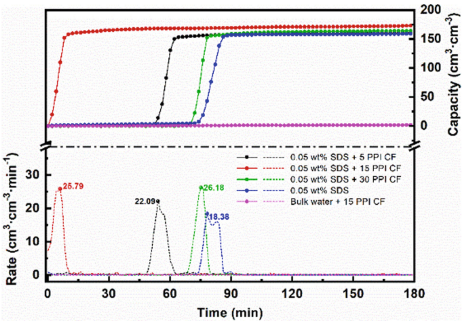

Fig. 2. Methane storage capacities and storage rates of hydrate formed in the bulk water and SDS solution with CF ($P = 8.0$ MPa, $T = 274.2$ K)

The kinetics of methane hydrate formation in the bulk water and SDS solution with CF are descripted in Fig. 2. There was nearly no methane stored in the water/CF system during the whole experimental process, and this may be limited by the insufficient gas-liquid contact for hydrate formation. A note of caution here was that since no hydrate heat was released, the CF matrix was not working for heat removal. In the SDS solution, methane hydrate was formed rapidly whether there is CF or not. Furthermore, it can be seen that gas storage capacities and storage rates of SDS/CF systems were higher than that of SDS solution significantly. Another finding was that the system of SDS solution-saturated CF had shorter induction time than the pure SDS solution. The large gas-solution contact area and sufficient crystallization sites provided by the nest-like metal skeleton might be the main cause of improving the gas storage performance. In addition, the excellent thermal conductivity of CF also could enhance the hydrate heat removal, accelerating the hydrate formation rate. The solution containing CF with various pore densities exhibited different kinetics of methane storage. It seems possible that this result

is due to the various pore sizes leading to differentiated synergistic promotion effect, which includes increasing the nucleation sites and enhancing the thermal conductivity. Especially, the SDS solution embedded with 15 PPI CF had the shortest induction time (2.1 min), largest methane storage capacity (139.0 $cm^3 \cdot cm^{-3}$), and fastest storage rate (25.79 $cm^3 \cdot cm^{-3} \cdot min^{-1}$). The positive effect of 15 PPI CF on the hydrate growth should be due to its more appropriate pore sizes.

The effective thermal conductivity (*ETC*, $\lambda_{e,\,theo.}$) of three pieces open-cell CF filled with methane hydrate were calculated via the highly porous two-phase model proposed by Jagjiwanram and Singh [15]. The experimental *ETC* ($\lambda'_{e,\,expt.}$) of water/aluminum foam (AF) and their theoretical values ($\lambda'_{e,\,theo.}$) were obtained from Bhattacharya et al. [14]. The average deviation between theoretical and experimental values was 5.84%. Moreover, the dotted curve representing calculated values matched well with the scattered points representing measured values in Fig. 3. Therefore, the two-phase model could be adapted to determine the *ETC* of the high porous metal foam-embedded systems in this work. According to the previous study reported by Huang and Fan [17], the effective thermal conductivity (*ETC*, $\lambda_{e,\,theo.}$) of pure hydrate is 0.576 $W \cdot m^{-1} \cdot K^{-1}$. The CF matrix embedded in methane hydrate could improve the thermal conductivity of the composite system for enhancing heat transfer. Figure 3 showed that the *ETC* values of hydrate/CF composite were about 13.0, 15.4, and 18.4 times higher than that of the pure hydrate, respectively. It was also found that the metal foam with lower pore density had a more positive impact on enhancing the *ETC* of the composite, which implied that 5, 15 PPI CF are more beneficial to timely removal of heat during hydration.

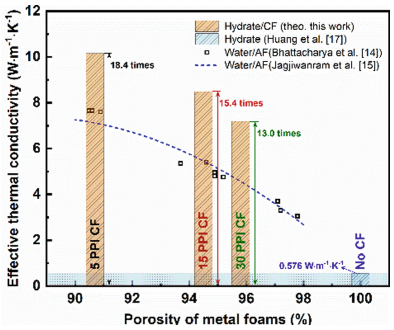

Fig. 3. *ETC* of the hydrate/CF composite

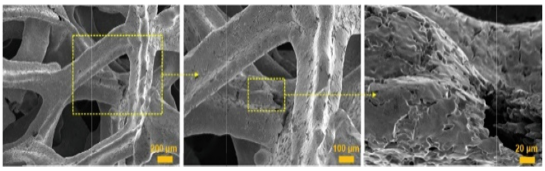

Fig. 4. SEM images of 15 PPI copper foam

As can be seen from the SEM images of copper foam (15 PPI) shown in Fig. 4, the copper matrix is made up of interconnected struts forming a three–dimensional

network of polyhedrons. The rough, irregular metal foam surface of the metal skeleton is expected to serve as the good crystallization zones. Similarly, numerous micro holes and micro grooves are distributing on the reticulate skeleton, which could also provide nucleation sites for hydrate crystallization. In addition, the interconnected struts in CF acts as crisscross "highway" heat transfer, and should be able to accelerate the heat transfer during hydration formation. Therefore, the porous metal foam with synergistic enhancement effect may be a good storage medium, promoting hydrate nucleation and enhancing hydrate heat removal. Therefore, the 15 PPI CF may be a suitable pore density metal foam and could contribute sufficient nucleation sites, while its surface holes would not be blocked by solid hydrate.

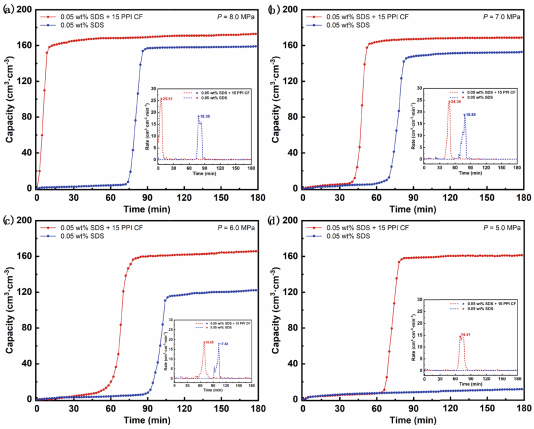

Fig. 5. Storage capacities and storage rates of methane hydrates formation in SDS/CF (15 PPI) systems at various pressures ($T = 274.2$ K)

3.2 Kinetics of Methane Hydrate Formation in CF at Various Pressures

To gain more details on the kinetics of methane hydrate formation in CF, we further compared the hydration behaviors of methane in the SDS/CF (15 PPI) systems at 5.0–8.0 MPa. Gas storage capacities and storage rates in the hydration systems are depicted in Fig. 5. Compared with SDS solution, an obvious promotion effect on the hydrate formation in the SDS/CF system was observed at each applied pressure. The maximum methane storage capacities were increased to 157.89–168.81 $cm^3 \cdot cm^{-3}$, and the corresponding maximum storage rates were significantly elevated to 14.41–23.24 $cm^3 \cdot cm^{-3} \cdot min^{-3}$. There was almost no hydrate formed in the SDS system during the whole test at 5.0 MPa, while the obvious plateau of methane uptake in SDS/CF system was reached within 90 min. It indicated that the addition of CF could improve the gas storage performance of SDS solution to a greater extent at the low pressure. This could be because that the CF matrix with micro holes and micro grooves contributed numerous nucleation sites for hydrate nucleation and growth. Meanwhile, the metal skeleton with high thermal conductivity would provide abundant paths for heat transfer and increase hydrate formation rate.

4 Conclusion

In this study, the open-cell copper foam (CF) with different pore densities were immersed in SDS solution to enhance methane hydrate formation. Gas storage experiments were conducted in a high-pressure static reactor. The experiment results showed that numerous micro holes and micro grooves distributed on the surface of CF skeleton provided many nucleation sites for hydrate crystallization. The three-dimensional copper skeleton could be recognized as crisscross "highway" for the hydrate heat transfer. The fast hydrate phase change occurred in the SDS/CF systems, but the enhancement effect of 5 and 30 PPI CF on hydrate formation was less than that of 15 PPI CF. The SDS solutions with the 15 PPI CF could store more methane within the shorter time than above SDS/CF systems. A theoretical model based highly porous two-phase systems was employed to calculate the *ETC* of the hydrate/CF composite. The *ETC* of hydrate/CF composite were about 13.0, 15.4, and 18.4 times higher than that of the pure hydrate, respectively. It was also found in the further comparative experiments at various pressures that the CF-embedded systems exhibited more excellent methane storage performance than the simple SDS solution, especially at the low pressure.

Acknowledgement. The work was supported by the National Natural Science Foundation of China (grant numbers 52176015, 51606125).

References

1. Sloan, E.D.: Fundamental principles and applications of natural gas hydrates. Nature **426**, 353–359 (2003)
2. Sloan, E.D., Koa, C.A.: Clathrate Hydrates of Natural Gases, 3rd edn. CRC Press, Boca Raton, FL (2007)
3. Gayet, P., Dicharry, C., Marion, G., et al.: Experimental determination of methane hydrate dissociation curve up to 55 MPa by using a small amount of surfactant as hydrate promoter. Chem. Eng. Sci. **60**, 5751–5758 (2005)
4. Lee, J.H., Shin, C.H., Lee, Y.S.: Experimental investigation to improve the storage potentials of gas hydrate under the unstirring condition. Energy Fuel **24**, 1129–1134 (2010)
5. Yang, L., Fan, S.S., Wang, Y.H., et al.: Accelerated formation of methane hydrate in aluminum foam. Ind. Eng. Chem. Res. **50**, 11563–11569 (2011)
6. Hoang, H.M., Oignet, J., Osswald, V., et al.: Impact of pressure on the dynamic behavior of CO_2 hydrate slurry in a stirred tank reactor applied to cold thermal energy storage. Appl. Energy **204**, 641–652 (2017)
7. Zhao, J.F., Wang, B., Sum, A.K.: Dynamics of hydrate formation and deposition under pseudo multiphase flow. AIChE J. **63**, 4136–4146 (2017)
8. Fukumoto, K., Tobe, J., Ohmura, R., et al.: Hydrate formation using water spraying in a hydrophobic gas: a preliminary study. AIChE J. **47**, 1899–1904 (2001)
9. Luo, Y.T., Zhu, J.H., Fan, S.S., et al.: Study on the kinetics of hydrate formation in a bubble column. Chem. Eng. Sci. **62**, 1000–1009 (2007)
10. Mohammadi, A., Manteghian, M., Haghtalab, A., et al.: Kinetic study of carbon dioxide hydrate formation in presence of silver nanoparticles and SDS. Chem. Eng. J. **237**, 387–395 (2014)

11. Deng, Z.X., Wang, Y.H., Yu, C., et al.: Promoting methane hydrate formation with expanded graphite additives: application to solidified natural gas storage. Fuel **299**, 120867 (2021)
12. Najibi, H., Shayegan, M.M., Heidary, H.: Experimental investigation of methane hydrate formation in the presence of copper oxide nanoparticles and SDS. J. Nat. Gas. Sci. Eng. **33**, 315–323 (2015)
13. Hu, P., Wu, G.Z., Zi, M.C., et al.: Effects of modified metal surface on the formation of methane hydrate. Fuel **255**, 115720 (2019)
14. Bhattacharya, A., Calmidi, V.V., Mahajan, R.L.: Thermophysical properties of high porosity metal foams. Int. J. Heat Mass Transfer **45**, 1017–1031 (2002)
15. Jagjiwanram, S.R.: Effective thermal conductivity of highly porous two-phase systems. Appl. Therm. Eng. **24**, 2727–2735 (2004)
16. Yang, L., Liu, Z.Z., Liu, D.P., et al.: Enhanced natural gas hydrates formation in the suspension with metal particles and fibers. J. Mol. Liq. **301**, 112410 (2020)
17. Huang, D.Z., Fan, S.S.: Thermal conductivity of methane hydrate formed from sodium dodecyl sulfate solution. J. Chem. Eng. Data **49**, 1479–1482 (2004)

Effect of Cyclopentane and Graphite on the Kinetics of CO_2/C_3H_8 Formation for Hydrate-Based Desalination

Xialian Xing[1], Jibao Zhang[1], and Tianbiao He[1,2,3(✉)]

[1] Department of Gas Engineering, College of Pipeline and Civil Engineering, China University of Petroleum (East China), Qingdao 266580, China
hetianbiao@upc.edu.cn

[2] Shandong Provincial Key Laboratory of Oil and Gas Storage and Transportation Safety, Qingdao 266580, China

[3] Qingdao Engineering Research Center of Efficient and Clean Utilization of Fossil Energy, Qingdao 266580, China

Abstract. Fresh water plays a vital and irreplaceable role in ecosystems and human societies. Desalination is regarded as a pivotal means to solve the global water crisis for sustainable development. The mainstream of seawater desalination in the world is still traditional technologies based thermal and membrane, which are limited mainly by energy intensive. Hydrate-based desalination (HBD) technology is attractive due to energy-efficient and easy availability of hydrate formers. In order to increase the yield of fresh water, CO_2 was considered to be major hydrate former and C_3H_8 employed as co-guest gas to make the thermodynamic conditions of CO_2 hydrate formation more moderate. Besides, cyclopentane (CP) and graphite were used as promoter in this study. The effects of CP/liquid phase volume ratios from 0.05 to 0.25 and graphite with different sizes (75 μm, 25 μm, 6.5 μm, 1.6 μm) at 275.6 K and 2.5 MPa were discussed to evaluate the kinetics of CO_2/C_3H_8 hydrate. The results showed that CP as additive promoted the formation of CO_2/C_3H_8 hydrate. When CP/liquid phase ratio was increased from 0.05 to 0.15, the rate and final molar mass of gas consumption were both significantly increased. With a CP/liquid ratio of 0.25, the final conversion of water to hydrate was the highest, which could reach 35.63%. Moreover, on the basis of CP/liquid ratio of 0.25, the addition of graphite further promoted the rate of hydrate formation. The graphite particles with smaller sizes provided more sites for hydrate nucleation and growth, however, the low conversion as a result of the limited mass caused by the dense shell with the rapidly growth of hydrate. It was proved that graphite size of 6.5 μm has the most excellent performance in shortening the induction time and increasing the gas consumption rate and the final conversion of water to hydrate. The findings acquired in this study will contribute to select suitable additive in the HBD process for obtaining more fresh water quickly.

Keywords: Gas hydrate · Desalination · Cyclopentane · Graphite · Kinetics

B. Sun et al. (Eds.): DWOG-Hyd 2021, LNCE 246, pp. 400–408, 2022.
https://doi.org/10.1007/978-981-19-0960-3_40

1 Introduction

Fresh water is of vital and irreplaceable importance to ecosystems and human societies. However, the prominent contradiction between supply and demand of fresh water has become a severe challenge around the world due to population growth, agricultural intensification, urbanization and industrial production. From the perspective of sustainable development, seawater with abundant reserves and wide distribution is regarded as an important means to solve the global water resources crisis [1]. Currently, the mainstream of seawater desalination in the world is still traditional technologies including reverse osmosis (RO), multi-stage flash (MSF) and multi-effect distillation (MED), which are limited mainly by high energy consumption and cost [2, 3]. Therefore, there is an urgent need to study a more economical and environmentally friendly desalination method, meanwhile HBD as a promising method with advantages of energy-efficient and cost saving has attracted much attention in recent years [4, 5].

The principle of HBD process is salt removal effect during hydrate formation [6]. Gas hydrate is a clathrate compound formed by connecting water molecules through hydrogen bonds to only envelop guest molecules excluding salt ions under certain temperature and pressure conditions. Although the concept of HBD was proposed as early as 1942, it has not yet been industrially applied which is mainly hindered by the slow rate of hydrate formation, long introduction time and severe production conditions [7]. In order to improve the effect of HBD, extensive studies have been carried out on different types of guest molecules such as methane (CH_4), carbon dioxide (CO_2), propane (C_3H_8) [7–9]. Among them, CO_2 that the main component of greenhouse gas is more suitable as hydrate forming agent owing to its lower pressure for hydrate formation and even higher salt rejection rate compared with CH_4 [10]. In consideration of comprehensive cost and environment, CO_2 hydrate was a research hotspot recently. It has demonstrated that C_3H_8 used as co-guest gas of CO_2 hydrate makes the temperature and pressure conditions of hydrate formation more moderate [11].

To date, most of the studies on CO_2/C_3H_8 hydrate focus on the thermodynamic equilibrium, and a few involve kinetic analysis but are not systematic and comprehensive. The low hydrate formation rate and water conversion to hydrate need to be improved further. CP, a promising former that can form hydrates at atmospheric pressure can also be used as an accelerant to improve the thermodynamic and kinetic effects of hydrates [12]. Moreover, porous media such as graphite is proved to be effective in promoting the formation of hydrates and shortening the induction time [13]. Nevertheless, the certain effects of CP and graphite on the kinetics of CO_2/C_3H_8 hydrate have not been conducted.

In this work, the kinetic properties of hydrate formation employing a gas mixture of 90% CO_2 and 10% C_3H_8 as hydrating agent combined with the effects of CP and graphite were investigated. Under the experimental conditions of 275.6 K and 2.5 MPa, the different volume ratios of cyclopentane to liquid phase from 0.05 to 0.25 were discussed. With the CP ratio that achieved best promotion, the impact of graphite particle size of 75 μm, 25 μm, 6.5 μm, 1.6 μm has been further explored. The results of this study would contribute to the rational selection of accelerators for facilitating hydrate formation and desalination via hydrates.

2 Experimental Section

2.1 Materials

The mixed gas composed of 90% CO_2 and 10% C_3H_8 was supplied by Yantai Deyi Gas Co., Ltd. CP with a purity of 96% and graphite with sizes of 75 μm, 25 μm, 6.5 μm, 1.6 μm and purity over 99.9% were bought from Shanghai Macklin Biochemical Co., Ltd. NaCl with a purity of 99.9% was purchased from Sinopharm Chemical Reagent Co., Ltd. The deionized water was produced by a water deionization system in the laboratory.

2.2 Apparatus

The schematic of the experimental apparatus used for hydrate formation is shown in Fig. 1. The stainless steel crystallizer with a capacity of 180 mL was placed in a refrigerated water bath, and the temperature stability of the water bath mixed with ethylene glycol and water is 0.01 K. The mechanical agitator was controlled by an external controller with a speed range from 0 to 1500 rpm. The temperature of the gas phase and liquid phase in the reactor was monitored by two platinum resistance sensors with an accuracy of 0.01 K, the pressure of the reactor was monitored by a pressure transducer with an accuracy of 0.1 MPa. The temperature and pressure collected by the data acquisition system were recorded in the computer.

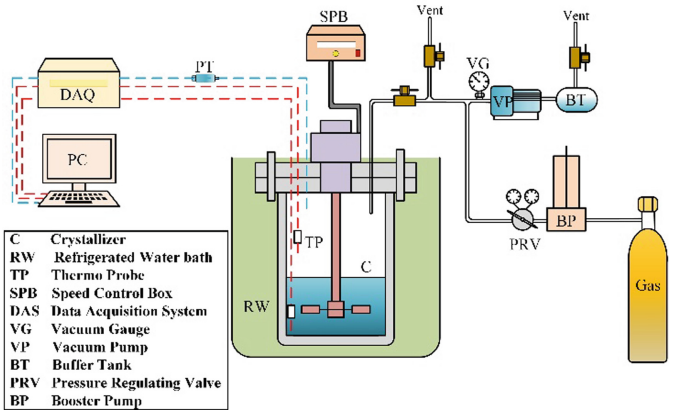

Fig. 1. Schematic of the experimental apparatus used for hydrate formation

2.3 Performance Index

The moles of gas consumed for hydrate formation were calculated using Eq. (1):

$$\Delta \mathrm{n} = V\left[\left(\frac{\mathrm{P}}{\mathrm{z}RT}\right)_0 - \left(\frac{\mathrm{P}}{zRT}\right)_t\right] \tag{1}$$

where V represents the volume of the gas phase in the reactor; P, T represent the pressure and gas phase temperature of the reactor; R is the universal gas constant; and z is the compression factor calculated by the Peng-Robinson equation of state.

The conversion of water to hydrate (CWTH) was calculated using Eq. (2):

$$CWTH\ (\%) = \frac{\Delta n \times hydration\ number}{n_{H_2O}} \times 100 \tag{2}$$

where Δn is the consumed gas moles calculated at the end of hydrate formation; n_{H2O} is the moles of 40ml water in the reactor; and the *hydration number* is the number of water molecules required to form a hydrate per gas molecule, for the 90% CO_2 / 10% C_3H_8 gas used in this study, the hydration number applied is 8.21 [14].

3 Results and Discussion

A total of 16 experimental groups were observed at 275.6 K and 2.5 MPa with 90% CO_2/ 10% C_3H_8 mixed gas as hydrate former to evaluate the influences of CP ratio and graphite size on hydrate formation rate and quantity. Table 1 presented a summary of the experimental conditions and the results explained by induction time, gas consumption, and final conversion of water to hydrate.

Table 1. Summary of experimental conditions and results

Exp. No	CP/ liquid phase volume ratio	Graphite size (μm)	Induction time (min)	Time (h)	Gas consumption (mol/mol of water)	Final conversion of water to hydrate (%)
1	0.00	-	60.56	20.0	0.02856	23.45
2	0.00	-	49.35	21.6	0.02903	23.84
3	0.05	-	30.83	20.7	0.02893	23.75
4	0.05	-	5.67	7.0	0.02794	22.94
5	0.15	-	25.83	19.1	0.03369	27.66
6	0.15	-	27.50	19.8	0.03958	32.50
7	0.25	-	19.17	20.0	0.04124	33.86
8	0.25	-	43.33	39.3	0.04554	37.39
9	0.25	75	28.42	42.4	0.04882	40.08
10	0.25	75	2.25	40.1	0.04737	38.89
11	0.25	25	9.12	54.6	0.04893	40.17
12	0.25	25	13.67	47.7	0.04901	40.24
13	0.25	6.5	3.60	39.0	0.05034	41.33
14	0.25	6.5	1.50	37.8	0.05172	42.46
15	0.25	1.6	45.06	46.23	0.04817	39.54
16	0.25	1.6	27.33	43.12	0.04716	38.71

3.1 Effect of CP/Liquid Phase Volume Ratio on Hydrate Formation

As shown in Fig. 2, the consequences of adding CP in different proportions on hydrate formation have obviously distinction. In general, the formation rate of hydrate was promoted by the addition of CP. Stabilization was reached quickly when CP/liquid phase ratio was 0.05, the final gas absorption was similar to that without CP, both around 0.029 mol/mol of water. When the CP/liquid phase ratio was 0.15, not only the formation

rate was faster but also the final gas absorption was boosted to 0.034 mol/mol of water, which was about 1.21 times of that without CP. The CP ratio was further increased to 0.25, and the formation rate was reduced in contrast to the higher gas consumption. It was speculated that a large amount of CP could be an obstruction to the interaction of carbon dioxide/propane molecules due to the quick CP hydrate formation and water molecules at the beginning.

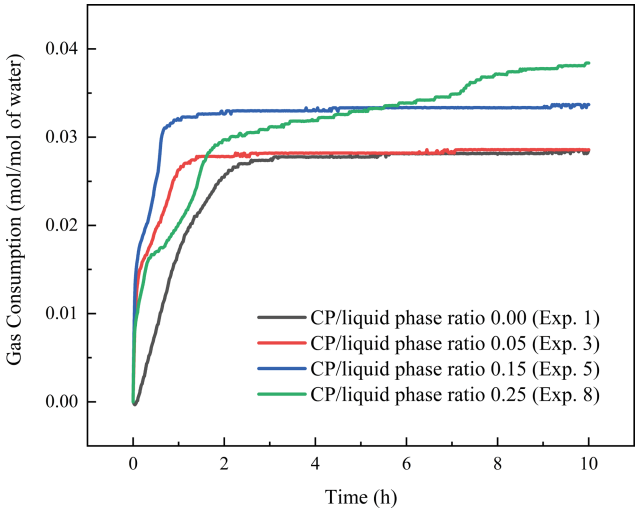

Fig. 2. Effect of CP/liquid phase volume ratio on gas consumption in 3.4wt% NaCl solution.

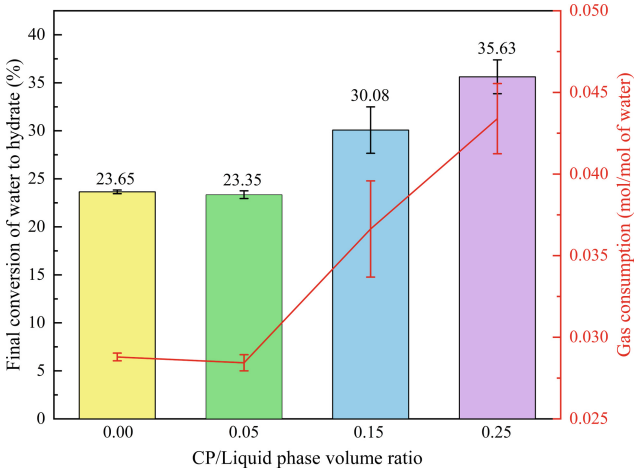

Fig. 3. Effect of CP/liquid phase volume ratio on final conversion of water to hydrate corresponding to final gas consumption in 3.4wt% NaCl solution.

As shown in Fig. 3, the final conversion of water to hydrate was 23.65% and 23.35% at the CP/ liquid phase ratio of 0.00 and 0.05 respectively. The reason for the small difference may be the low content of CP has been completely encased in hydrate as an auxiliary hydrating agent and was not enough to support the formation of more hydrates. When CP/liquid ratio was 0.15 and 0.25, the final conversion of water to hydrate were boosted to 30.08% and 35.63%, respectively. To further promote hydrate formation rate, the CP/ liquid phase ratio of 0.25 was chose for subsequent experiments with graphite addition.

3.2 Effect of Graphite Size on Hydrate Formation with CP

The time-dependent gas consumption was investigated at a CP/liquid phase volume ratio of 0.25 to shed light on the impact of graphite size on the kinetics of hydrate formation. It can be seen from Fig. 4 that all the experiments using graphite with different sizes show increased hydrate formation kinetics which are facilitated by more nucleation sites provided by graphite. Smaller particle size meant more specific surface area that explained why graphite size of 6.5 μm would have a more excellent performance than 75 μm and 25 μm in promoting hydrate kinetics. However, this promotion was not positively correlated with the decrease in particle size. The rapidly formed hydrate was easy to form a relatively dense shell which inevitably limited the mass transfer and subsequent degradation. Therefore, the 1.6 μm graphite as shown in Fig. 4 and Table 1 was only observed to promote weakly far less than 6.5 μm.

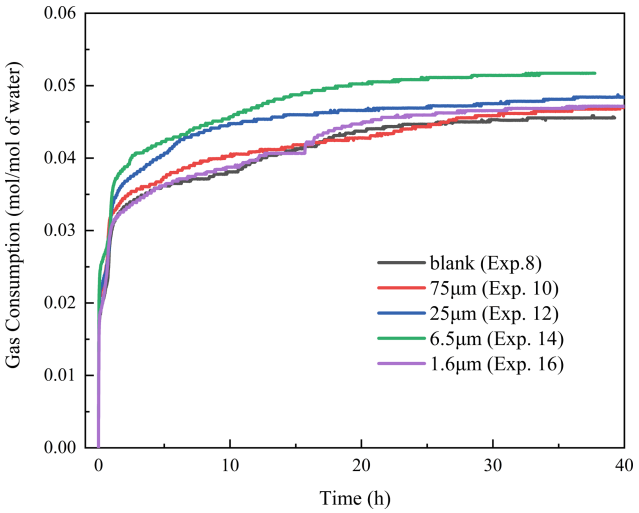

Fig. 4. Effect of graphite size on gas consumption with a CP/liquid phase volume ratio of 0.25.

The effect of graphite size on final conversion of water to hydrate with a CP/liquid phase volume ratio of 0.25 is demonstrated in Fig. 5. When the graphite size was 75 μm, 25 μm, 6.5 μm, and 1.6 μm, the final water conversion of water to hydrate was 39.49%,

40.20%, 41.90%, and 39.13%, respectively. As analyzed by gas consumption, the final water conversion rate of 6.5 μm graphite was the highest, which was 17.6% higher than that without graphite. Moreover, the induction time with 6.5 μm graphite was reduced significantly as shown in Table 1. Therefore, the selection of reasonable graphite size is crucial to achieve the goal of high hydrate conversion and rapid formation for the purpose of desalination.

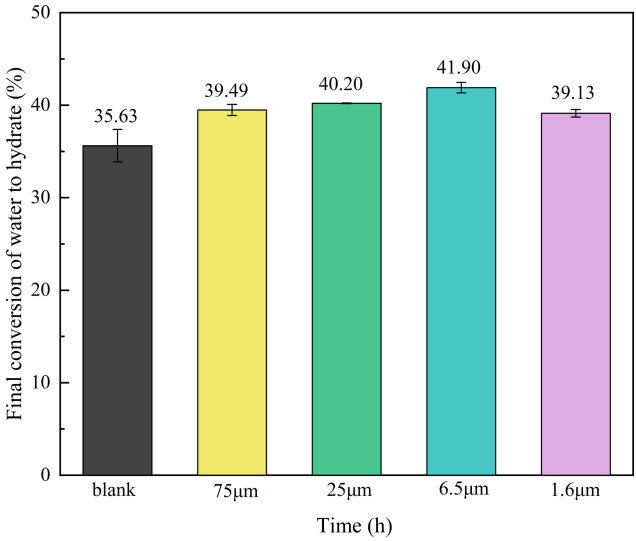

Fig. 5. Effect of graphite size on final conversion of water to hydrate with a CP/liquid phase volume ratio of 0.25.

4 Conclusion

In this study, the effects of different ratios of CP and different graphite sizes on hydrate formation kinetics at 275.6 K and 2.5 MPa were evaluated for the HBD process. It was found that the addition of low content of CP induces higher hydrate formation kinetics but cannot improve the final conversion of water to hydrate than without CP. Increasing CP/liquid volume ratio to 0.25, although the final conversion of water to hydrate is superior which can reach 35.63%, the hydrate formation kinetics is not so fast. On this basis, different graphite sizes were added to further promote the rate of hydrate formation. The graphite particles with smaller sizes provided more sites for hydrate nucleation and growth, however, the low conversion as a result of the limited mass caused by the dense shell with the rapidly growth of hydrate. Hence, 6.5 μm graphite was proved to be the best under the experimental conditions due to its short induction time, fast kinetics and high conversion. The findings acquired in this study will provide a basis for selecting suitable promoter to improve the hydrate formation kinetics in the HBD process.

Acknowledgement. The authors would like to appreciate the funding support of the National Natural Science Foundation of China (No. 51906225).

References

1. Feng, G.: Seawater Desalination—Solutions to Shortage of Freshwater Resource. North China Electric Power (2005)
2. Khawaji, A.D., Kutubkhanah, I.K., Wie, J.M.: Advances in seawater desalination technologies. Desalination **221**(1–3), 47–69 (2008)
3. Lv, Y.N., Wang, S.S., Sun, C.Y., Gong, J., Chen, G.J.: Desalination by forming hydrate from brine in cyclopentane dispersion system. Desalination **413**, 217–222 (2017)
4. He, T., Zhang, J., Mao, N., Linga, P.: Organic rankine cycle integrated with hydrate-based desalination for a sustainable energy–water nexus system. Appl. Energy **291**, 116839 (2021)
5. He, T., Nair, S.K., Babu, P., Linga, P., Karimi, I.A.: A novel conceptual design of hydrate based desalination (hydesal) process by utilizing LNG cold energy. Appl. Energy **222**, 13–24 (2018)
6. He, T., Chong, Z.R., Babu, P., Linga, P.: Techno-economic evaluation of cyclopentane hydrate-based desalination with liquefied natural gas cold energy utilization. Energ. Technol. **463**, 69–80 (2019)
7. Ren, Z., Liu, D., Liu, Z., Pan, Z.: Influence of sodium chloride on the kinetics of methane hydrate formation in the presence of surfactant. J. Nat. Gas Sci. Eng. **83**(1), 103622 (2020)
8. Sahu, P., Krishnaswamy, S., Ponnani, K., Pande, N.K.: A thermodynamic approach to selection of suitable hydrate formers for seawater desalination. Desalination **436**, 144–151 (2018)
9. Nakane, R., Shimosato, Y., Gima, E., Ohmura, R., Senaha, I., Yasuda, K.: Phase equilibrium condition measurements in carbon dioxide hydrate forming system coexisting with seawater. J. Chem. Thermodyn. **152**, 106276 (2021)
10. Zhang, J., Chen, S., Mao, N., He, T.: Progress and prospect of hydrate-based desalination technology. Frontiers in Energy (2021). https://doi.org/10.1007/s11708-021-0740-5
11. Yang, M., Zheng, J., Liu, W., Yu, L., Song, Y.: Effects of C3H8 on hydrate formation and dissociation for integrated CO_2 capture and desalination technology. Energy **93**, 1971–1979 (2015)
12. Zheng, J., Yang, M., Liu, Y., Wang, D., Song, Y.: Effects of cyclopentane on co2 hydrate formation and dissociation as a co-guest molecule for desalination. J. Chem. Thermodyn. **104**, 9–15 (2017)
13. Feng, L., Chen, Z., Dong, H., Shi, C., Wang, B., Lei, Y., et al.: Promotion effect of graphite on cyclopentane hydrate based desalination. Desalination **445**, 197–203 (2018)
14. Nambiar, A., Babu, P., Linga, P.: Improved kinetics and water recovery with propane as co-guest gas on the hydrate-based desalination (hydesal) process. Chemengineering **3**, 31 (2019)

Author Index

B. Sun et al. (Eds.): DWOG-Hyd 2021, LNCE 246, pp. 409–411, 2022.
https://doi.org/10.1007/978-981-19-0960-3